

400 11 700
110 | 55.2273

NASA Conference Publication 2273
ORIGINAL

17th Aerospace Mechanisms Symposium

*Proceedings of a symposium held at
Jet Propulsion Laboratory
Pasadena, California
May 5-6, 1983*

Lockheed



NASA

25

25th Anniversary
1958-1983

NASA Conference Publication 2273

17th Aerospace Mechanisms Symposium

Proceedings of a symposium sponsored by
National Aeronautics and Space Administration,
the California Institute of Technology, and
Lockheed Missiles and Space Company, Inc.,
and held at Jet Propulsion Laboratory
Pasadena, California
May 5-6, 1983

NASA
National Aeronautics
and Space Administration
**Scientific and Technical
Information Branch**

1983

Blank Page

PREFACE

The proceedings of the 17th Aerospace Mechanisms Symposium held at the Jet Propulsion Laboratory on May 5-6, 1983, are in this NASA Conference Publication. The symposium was sponsored by the National Aeronautics and Space Administration, the California Institute of Technology, and Lockheed Missiles and Space Company, Inc.

The purpose of the symposium was to provide a forum for the interchange of information among those active in the field of mechanisms technology. To that end, 24 papers were presented on aeronautics and space flight, with special emphasis on actuators and aerospace applications for ground support equipment, latches, connectors, and other mechanisms for large space structures. The papers were prepared by engineers from a broad aerospace background, including the U.S. aerospace industry, NASA, European, and Asian participants.

The efforts of the review committee, session chairmen, and speakers contributing to the technical excellence and professional character of the conference are especially appreciated.

The use of trade names or names of manufacturers in this publication does not constitute an official endorsement of such products or manufacturers, either expressed or implied, by the National Aeronautics and Space Administration.

Blank Page

TABLE OF CONTENTS

Preface	iii
Organizing and Reviewing Committee	vii
Program	ix
1. TETHERED SATELLITE CONTROL MECHANISM	1
Gilbert M. Kyriazis	
2. CONSIDERATIONS ON THE LUBRICATION OF SPACECRAFT MECHANISMS	19
H. Mervyn Briscoe and Mike J. Todd	
3. SPACE TELESCOPE--SOLAR ARRAY PRIMARY DEPLOYMENT MECHANISM	39
Donald P. Chandler and Adolph Veit	
4. A BROADBASED ACTUATOR CONCEPT FOR SPACEFLIGHT APPLICATION	55
James C. Hammond	
5. THE LINEAR BOOM ACTUATOR DESIGNED FOR THE GALILEO SPACECRAFT	81
Edgar F. Koch	
6. POLARIZER MECHANISM FOR THE SPACE TELESCOPE FAINT OBJECT SPECTROGRAPH	97
Mark D. Thulson	
7. DESIGN OPTIMIZATION OF HIGH-PERFORMANCE ELECTRODYNAMIC ACTUATORS FOR USE IN A CRYOGENICALLY COOLED TELESCOPE	109
J.-N. Aubrun, K. R. Lorell, and K. P. Silveira	
8. CONTROL OF LARGE THERMAL DISTORTIONS IN A CRYOGENIC WIND TUNNEL	121
John C. Gustafson	
9. EVALUATION OF SCANNING EARTH SENSOR MECHANISM ON ENGINEERING TEST SATELLITE IV	143
Masami Ikeuchi, Yasafumi Wakabayashi, Yoshiaki Ohkami, Takashi Kida, Takeo Ishigaki, and Mikio Matsumoto	
10. SECURING MECHANISM FOR THE DEPLOYABLE COLUMN OF THE HOOP/COLUMN ANTENNA	157
Elvin L. Ahl, Jr.	
11. A HIGH STRENGTH, TORSIONALLY RIGID, DEPLOYABLE AND RETRACTABLE MAST FOR SPACE APPLICATIONS	171
Lamont DiBiasi and Richard Kramer	
12. CANNON LAUNCHED ELECTROMECHANICAL CONTROL ACTUATION SYSTEM DEVELOPMENT	181
James G. Johnston	

13.	TWO HUNDRED PASSAGE THREE-WAY VALVE - FRACTION COLLECTOR	199
	Jay L. Keffer	
14.	NUTATION DAMPER SYSTEM	209
	Donald R. Sevilla	
15.	PRACTICAL SMALL-SCALE EXPLOSIVE SEAM WELDING	227
	Laurence J. Bement	
16.	THE MANNED MANEUVERING UNIT FLIGHT CONTROLLER ARM	245
	Ken E. Falkner	
17.	LATCH FITTINGS FOR THE SCIENTIFIC INSTRUMENTS ON THE SPACE TELESCOPE	253
	Jan D. Dozier and Everett Kaelber	
18.	THE DESIGN AND DEVELOPMENT OF A MOUNTING AND JETTISON ASSEMBLY FOR THE SHUTTLE ORBITER ADVANCED GIMBAL SYSTEM	267
	Edward S. Korzeniowski	
19.	ROLLING BEAM UMBILICAL SYSTEM	289
	Bemis C. Tatem, Jr.	
20.	DEPLOYMENT AND RELEASE MECHANISMS ON THE SWEDISH SATELLITE, VIKING	305
	Stefan Eriksson	
21.	DESIGN OF THE GALILEO REMOTE SCIENCE POINTING ACTUATORS	315
	Fredrick W. Osborn	
22.	A COMPACT MAGNETIC BEARING FOR GIMBALLED MOMENTUM WHEEL	333
	K. Yabu-uchi, M. Inoue, S. Akishita, C. Murakami, and O. Okamoto	
23.	HINGE LATCH MECHANISM	343
	John C. Walker	
24.	THE EVOLUTION OF A RELEASE-ENGAGE MECHANISM FOR USE ON THE ORBITER	357
	John Calvert	
25.	PAYOUT RETENTION FITTINGS FOR SPACE SHUTTLE PAYLOAD GROUND HANDLING MECHANISM	375
	Vincent Cassisi	

ORGANIZING AND REVIEWING COMMITTEE

The papers presented at the symposium were selected and reviewed by the Organizing Committee. Responsibility for content and technical accuracy lies with each respective author. The committee included the following members:

General Chairman:	Charles W. Coale, Lockheed Missiles and Space Company, Inc.
Operations/Executive Chairman:	Alfred L. Rinaldo, Lockheed Missiles and Space Company, Inc.
Administrative/Executive Chairman:	David F. Welch, California Institute of Technology
Host Chairman:	Peter T. Lyman, Jet Propulsion Laboratory
Committee Members:	Paul W. Bomke, Jet Propulsion Laboratory
	Aleck C. Bond, NASA Johnson Space Center
	Tom F. Bonner, Jr., NASA Langley Research Center
	H. Mervyn Briscoe, European Space Technology Centre
	Kenneth C. Curry, Jet Propulsion Laboratory
	Charles R. Darwin, NASA Marshall Space Flight Center
	David F. Englebert, NASA Ames Research Center
	Otto H. Fedor, NASA Kennedy Space Center
	Angelo Giovannetti, NASA Ames Research Center
	Harvey H. Horiuchi, Jet Propulsion Laboratory
	Allen J. Louviere, NASA Johnson Space Center
	Frank T. Martin, NASA Goddard Space Flight Center
	James B. Sterett, Jr., NASA Marshall Space Flight Center
	Bowden W. Ward, NASA Goddard Space Flight Center
	Nathan D. Watson, NASA Langley Research Center

Blank Page

PROGRAM

THURSDAY, MAY 5, 1983

8:15 INTRODUCTION

Dr. Peter T. Lyman, Host Chairman
Jet Propulsion Laboratory, Pasadena, California

Dr. Charles W. Coale, General Chairman
Lockheed Missiles and Space Co., Sunnyvale, California

8:30 WELCOME

Dr. Lew Allen, Director
Jet Propulsion Laboratory, Pasadena, California

8:40 SESSION 1

Dr. Hans Hintermann, Session Chairman
Laboratoire Suisse, de Recherches Horlogeres, Neuchatel, Suisse

8:40 - 9:10 TETHERED SATELLITE CONTROL MECHANISM
Gilbert M. Kyriazis
Martin Marietta Denver Aerospace, Denver, Colorado

9:10 - 9:40 CONSIDERATIONS ON THE LUBRICATION OF SPACECRAFT
MECHANISMS
H. Mervyn Briscoe* and Mike J. Todd**
*European Space Technology Centre, European Space Agency,
Noordwijk, The Netherlands
**European Space Tribology Laboratory, UKEA, Risley,
United Kingdom

9:40 - 10:10 SPACE TELESCOPE -- SOLAR ARRAY PRIMARY DEPLOYMENT
MECHANISM
Donald P. Chandler and Adolph Veit
Contraves AG, Zurich, Switzerland

10:10 BREAK

10:30 SESSION 2

Mr. Allen J. Louviere, Session Chairman
NASA Johnson Space Center, Houston, Texas

10:30 - 11:00 A BROADBASED ACTUATOR CONCEPT FOR SPACEFLIGHT APPLICATION
James C. Hammond
Schaeffer Magnetics, Inc., Chatsworth, California

11:00 - 11:30 THE LINEAR BOOM ACTUATOR DESIGNED FOR THE GALILEO
SPACECRAFT
Edgar F. Koch
Jet Propulsion Laboratory, Pasadena, California

11:30 - 12:00 POLARIZER MECHANISM FOR THE SPACE TELESCOPE FAINT OBJECT
SPECTROGRAPH
Mark D. Thulson
Martin Marietta Denver Aerospace, Denver, Colorado

12:00 - 12:30 DESIGN OPTIMIZATION OF HIGH-PERFORMANCE ELECTRODYNAMIC ACTUATORS FOR USE IN A CRYOGENICALLY COOLED TELESCOPE
J.-N. Aubrun, K. R. Lorell, and K. P. Silveira
Lockheed Missiles and Space Co., Palo Alto Research Laboratory, Palo Alto, California

12:30 LUNCH

13:30 SESSION 3
Dr. A. H. Hausrath, Session Chairman
TRW Systems Group, Redondo Beach, California

13:30 - 14:00 CONTROL OF LARGE THERMAL DISTORTIONS IN A CRYOGENIC WIND TUNNEL
John C. Gustafson
NASA Langley Research Center, Hampton, Virginia

14:00 - 14:30 EVALUATION OF SCANNING EARTH SENSOR MECHANISM ON ENGINEERING TEST SATELLITE IV
Masami Ikeuchi*, Yasafumi Wakabayashi*, Yoshiaki Ohkami**, Takashi Kida**, Takeo Ishigaki***, and Mikio Matsumoto***
*National Space Development Agency, Tsukuba Space Center, Ibaragi, Japan
**National Aerospace Laboratory, Tokyo, Japan
***Matsushita Research Institute, Tokyo, Inc., Kawasaki, Japan

14:30 - 15:00 SECURING MECHANISM FOR THE DEPLOYABLE COLUMN OF THE HOOP/COLUMN ANTENNA
Elvin L. Ahl, Jr.
NASA Langley Research Center, Hampton, Virginia

15:00 - 15:30 A HIGH STRENGTH, TORSIONALLY RIGID, DEPLOYABLE AND RETRACTABLE MAST FOR SPACE APPLICATIONS
Lamont DiBiasi and Richard Kramer
Fairchild Space Company, Germantown, Maryland

15:30 BREAK

15:45 SESSION 4
Mr. Donald N. Matteo
Electro Mechanical Engineering, General Electric Co., Valley Forge Space Center, Philadelphia, Pennsylvania

15:45 - 16:15 CANNON LAUNCHED ELECTROMECHANICAL CONTROL ACTUATION SYSTEM DEVELOPMENT
James G. Johnston
Martin Marietta Aerospace, Orlando, Florida

16:15 - 16:45 TWO HUNDRED PASSAGE THREE-WAY VALVE - FRACTION COLLECTOR
Jay L. Keffer
McDonnell Douglas Astronautics Company, St. Louis, Missouri

16:45 - 17:15 NUTATION DAMPER SYSTEM
Donald R. Sevilla
Jet Propulsion Laboratory, Pasadena, California

19:00 SOCIAL HOUR

20:00 AMS BANQUET
Dr. Peter T. Lyman, Master of Ceremonies
Jet Propulsion Laboratory, Pasadena, California

21:00 INTRODUCTION OF GUEST SPEAKER
Dr. Paul Heran
Lockheed Missiles and Space Co., Sunnyvale, California

GUEST SPEAKER
Dr. Lee Tepley, President
Moonlight Productions Motion Pictures, Stock Shot Library, Mountain View, California
"Everything You Wanted to Know About Whales"

22:00 RECOGNITION
Mr. A. L. Rinaldo
Lockheed Missiles and Space Co., Sunnyvale, California

FRIDAY, MAY 6, 1983

8:00 SESSION 5
Mr. Bill M. McAnally, Session Chairman
Rockwell International, Space Division, Downey, California

8:00 - 8:25 PRACTICAL SMALL-SCALE EXPLOSIVE SEAM WELDING
Laurence J. Bement
NASA Langley Research Center, Hampton, Virginia

8:25 - 8:50 THE MANNED MANEUVERING UNIT FLIGHT CONTROLLER ARM
Ken E. Falkner
Martin Marietta Denver Aerospace, Denver, Colorado

8:50 - 9:15 LATCH FITTINGS FOR THE SCIENTIFIC INSTRUMENTS ON THE
SPACE TELESCOPE
Jari D. Dozier* and Everett Kaelber**
*NASA George C. Marshall Space Flight Center, Alabama
**Perkin-Elmer, Danbury, Connecticut

9:15 BREAK

9:35 SESSION 6
Mr. Lloyd W. Briggs, Session Chairman
Hughes Aircraft Co., Los Angeles, California

9:35 - 10:00 THE DESIGN AND DEVELOPMENT OF A MOUNTING AND JETTISON
ASSEMBLY FOR THE SHUTTLE ORBITER ADVANCED GIMBAL SYSTEM
Edward S. Korzeniowski
Sperry Flight Systems, Phoenix, Arizona

10:00 - 10:25 ROLLING BEAM UMBILICAL SYSTEM
Bemis C. Tatem, Jr.
Planning Research Corp., Kennedy Space Center, Florida

10:25 - 10:50 DEPLOYMENT AND RELEASE MECHANISMS ON THE SWEDISH SATELLITE,
VIKING
Stefan Eriksson
Saab-Space AB, Linköping, Sweden

11:00 TOUR
Mr. Larry Dumas and Dr. Paul W. Bomke, Tour Chairmen
Jet Propulsion Laboratory, Pasadena, California

12:30 LUNCH

13:30 SESSION 7
Mr. Bowden W. Ward, Jr., Session Chairman
NASA Goddard Space Flight Center, Greenbelt, Maryland

13:30 - 13:55 DESIGN OF THE GALILEO REMOTE SCIENCE POINTING ACTUATORS
Fredrick W. Osborn
Jet Propulsion Laboratory, Pasadena, California

13:55 - 14:20 A COMPACT MAGNETIC BEARING FOR GIMBALLED MOMENTUM WHEEL
K. Yabu-uchi*, M. Inoue*, S. Akishita*, C. Murakami**,
and O. Okamoto
*Mitsubishi Electric Corp., Amagasaki, Japan
**National Aerospace Laboratory, Tokyo, Japan

14:20 - 14:45 HINGE LATCH MECHANISM
John C. Walker
Ball Aerospace Systems Division, Boulder, Colorado

14:45 - 15:10 THE EVOLUTION OF A RELEASE-ENGAGE MECHANISM FOR USE ON
THE ORBITER
John Calvert
NASA George C. Marshall Space Flight Center, Alabama

15:10 BREAK

15:30 - 16:00 JPL OVERVIEW

16:00 AWARDS
Dr. Richard Pefley
Santa Clara University, Santa Clara, California

CLOSING REMARKS
Dr. Peter T. Lyman
Jet Propulsion Laboratory, Pasadena, California

Dr. Charles W. Coale
Lockheed Missiles and Space Co., Sunnyvale, California

Blank Page

TETHERED SATELLITE CONTROL MECHANISM

Gilbert M. Kyriaz*

ABSTRACT

The tethered satellite system (TSS), under development by the Marshall Space Flight Center (MSFC), is used for deployment and retrieval of instrumented satellites from the Space Shuttle orbiter cargo bay. These satellites can operate at very low orbital altitudes not attainable by conventional satellites. They can also operate above the Space Shuttle (higher orbital altitudes) when called for by specific missions.

The concept of maintaining satellites at low altitude by tether attachment to the Shuttle was first suggested by Professor G. Colombo of the Smithsonian Astrophysical Observatory in 1974.

Martin Marietta Corporation, under contract to MSFC, is developing the Space Shuttle mechanical equipment required to deploy, retrieve, and control a 500-kg satellite of approximately 1.4-m diameter, attached to a tether 100 km (65 to 75 miles) long. Under a U.S.-Italian agreement, Aeritalia was given the responsibility of developing the first satellite.

The system includes the satellite control mechanism mounted on a European spacelab pallet. This pallet is located in the Space Shuttle cargo bay, and includes a tether for attachment to the satellite. Figure 1 is an artist's concept of a deployed satellite and attached tether, with the Space Shuttle in the background.

TSS is a multimission program with broad science- and defense-community interest. One of the early missions selected for the tethered satellite will be operation in a region of the Earth's atmosphere too high for aircraft operations and too low for normal satellites. Presently, this region is accessible using sounding rockets that can return spot information only in areas where launch facilities are available. The tethered satellite will be capable of remaining in this atmosphere during several orbits, returning atmospheric data on a worldwide basis. A possible configuration for this type of satellite is shown in Figure 2.

The first mission selected may be an electrodynamic experiment. This mission will use an electrically conductive satellite with tether that will collect an electrical charge and flow current as it passes through the Earth's magnetic field. Figure 3 shows this type of satellite and its possible complement of instruments.

Many other science experiments are planned for the tethered satellite. It is expected that the tethered satellite will find extensive use for many years and will open the door for development of other applications, such as tethered habitable modules that create artificial gravity.

*Martin Marietta Denver Aerospace, Denver, Colorado

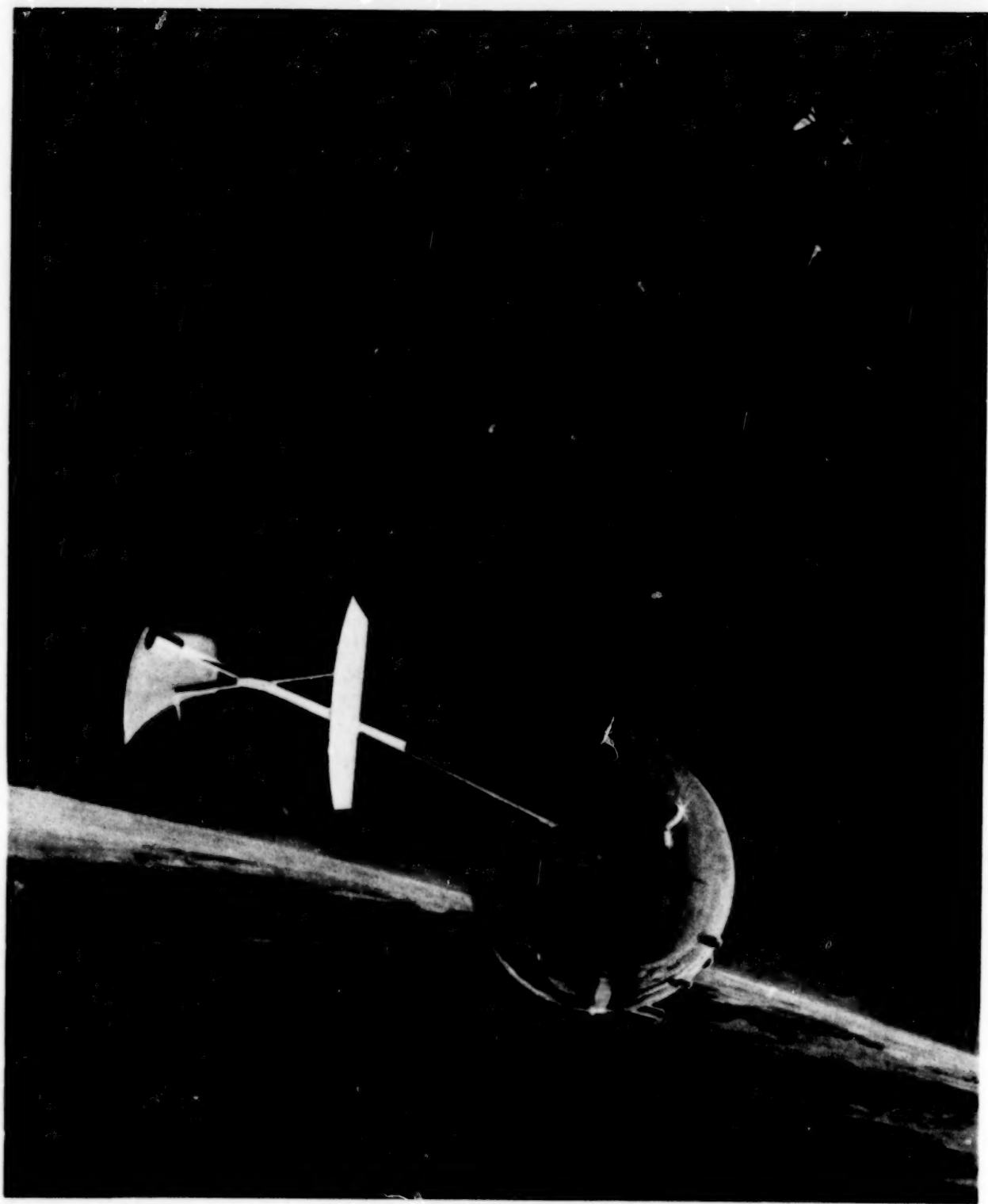


Figure 1 Tethered Satellite

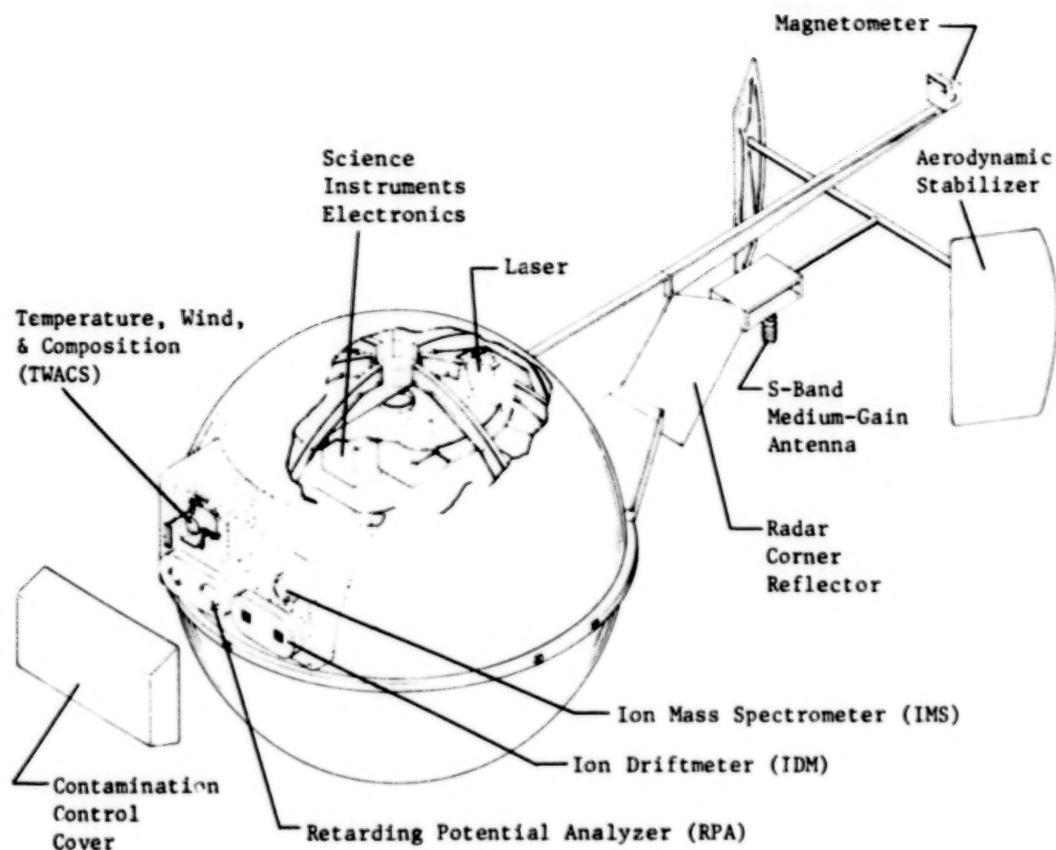


Figure 2 Atmospheric Probe Satellite

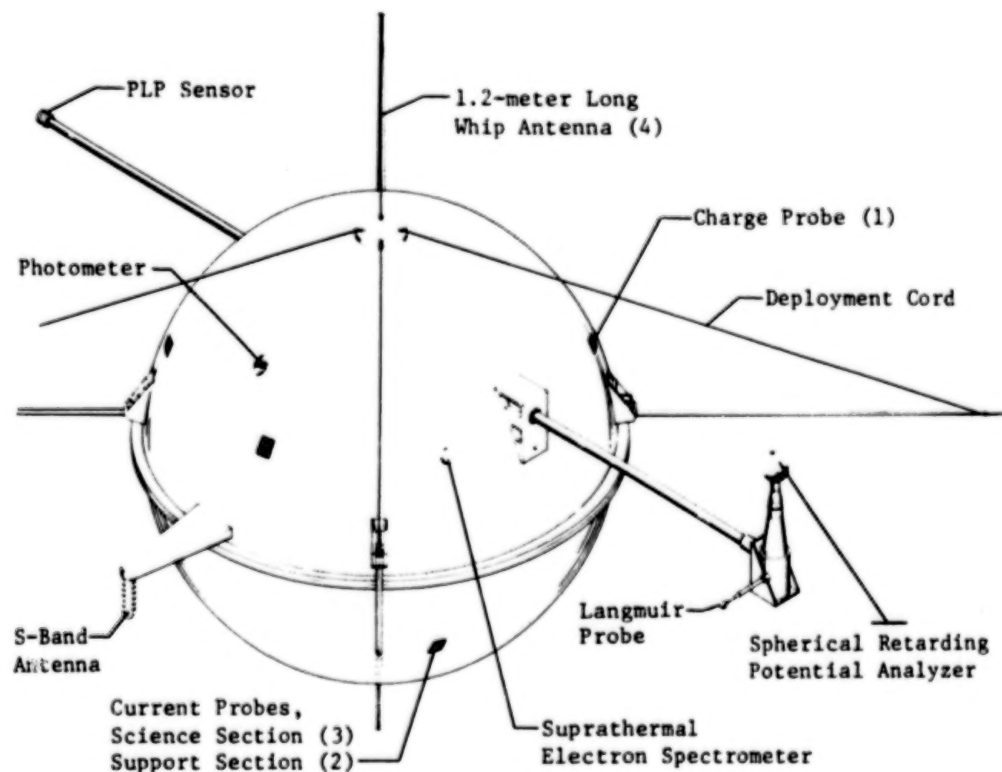


Figure 3 Electrodynamics Satellite

INTRODUCTION

When two masses are linked together (tethered) and separated a distance apart in space, a gravity gradient force between the masses exists, creating tension in the tether. The line of force points to Earth; thus, a gravity gradient stabilization exists. This physical law is the fundamental basis in the operation of a tethered satellite. Whether the satellite is positioned above or below the Space Shuttle, the same rule applies--tether tension is a function of separation distance. When separation is small, tether tension will be nearly zero. Large separations will result in high tether tensions. When the satellite is initially deployed, or is close to the Space Shuttle during retrieval, the gravity gradient force can be as low as a few grams. For practical purposes, this force is too low to affect separation velocity.

As the satellite moves away from the Space Shuttle, the satellite changes orbital altitude. As orbital altitude changes, so does orbital velocity. The result is that the satellite will move ahead of the Space Shuttle when deployed to a lower altitude and then trail behind the Space Shuttle when being retrieved.

Low gravity gradient forces at small separation distances, coupled with the changing orbital velocities of the satellite with respect to the Space Shuttle, require increased control sensitivity during close-in operations. The control sensitivity remains quite high, up to 1-km separation. At this point (1 km), tether tension will be about 2 Newtons (0.43 lb) for a 500-kg satellite. The gravity gradient tension at 125-km separation is about 250 Newtons (56 lb), which will not require such precise control.

Requirements for the tethered satellite control mechanisms, therefore, are dictated by tether and satellite orbital dynamics as they exist at time of deployment, deployment to stationkeeping (at operating orbit), stationkeeping, retrieval, and docking. The wide range of operating parameters dictate challenging design requirements for the mechanical equipment. Tether velocities range from 25 m/h to 10 m/s. At time of deployment and before docking, the tether tension (gravity gradient force) will be about 0.1 Newton (0.04 oz), while early retrieval from stationkeeping can produce tensions as high as 320 Newtons (72 lb). The high retrieval tension forces are a result of the gravity gradient force, acceleration, and aerodynamic drag.

The mission will be flown according to a preprogrammed profile made from a computer-predicted analysis of the tether dynamics. The computer output will specify tether tension, velocity, and position throughout the mission. Data produced by the mechanisms at a given time will be compared to the computer values for control of the system.

It was deemed impractical to depend on natural gravity gradient forces below 1.0 Newton (0.23 lb) for satellite control within the 1-km range. Four 0.5-Newton in-line tether thrusters on the satellite will augment tether tension during close-in operation. Pitch, yaw, and roll thrusters may be included depending on mission requirements.

The tethered satellite control mechanisms described in this paper are designed to be compatible with the characteristics of a tethered mass attached to the Space Shuttle and to accommodate a variety of future satellite missions of various sizes, weights, shapes, and purposes.

A major consideration in the design of these mechanisms is the safety of the Space Shuttle and crew. To prevent Space Shuttle damage, precautions are taken to ensure that the 500-kg satellite is always under control. Operating machinery in this environment requires close attention to safety margins, emergency shutdown, and recovery procedures.

TETHERED SATELLITE CONTROL MECHANISMS

The tethered satellite control mechanisms consist of four major subassemblies. These are shown in Figure 4.

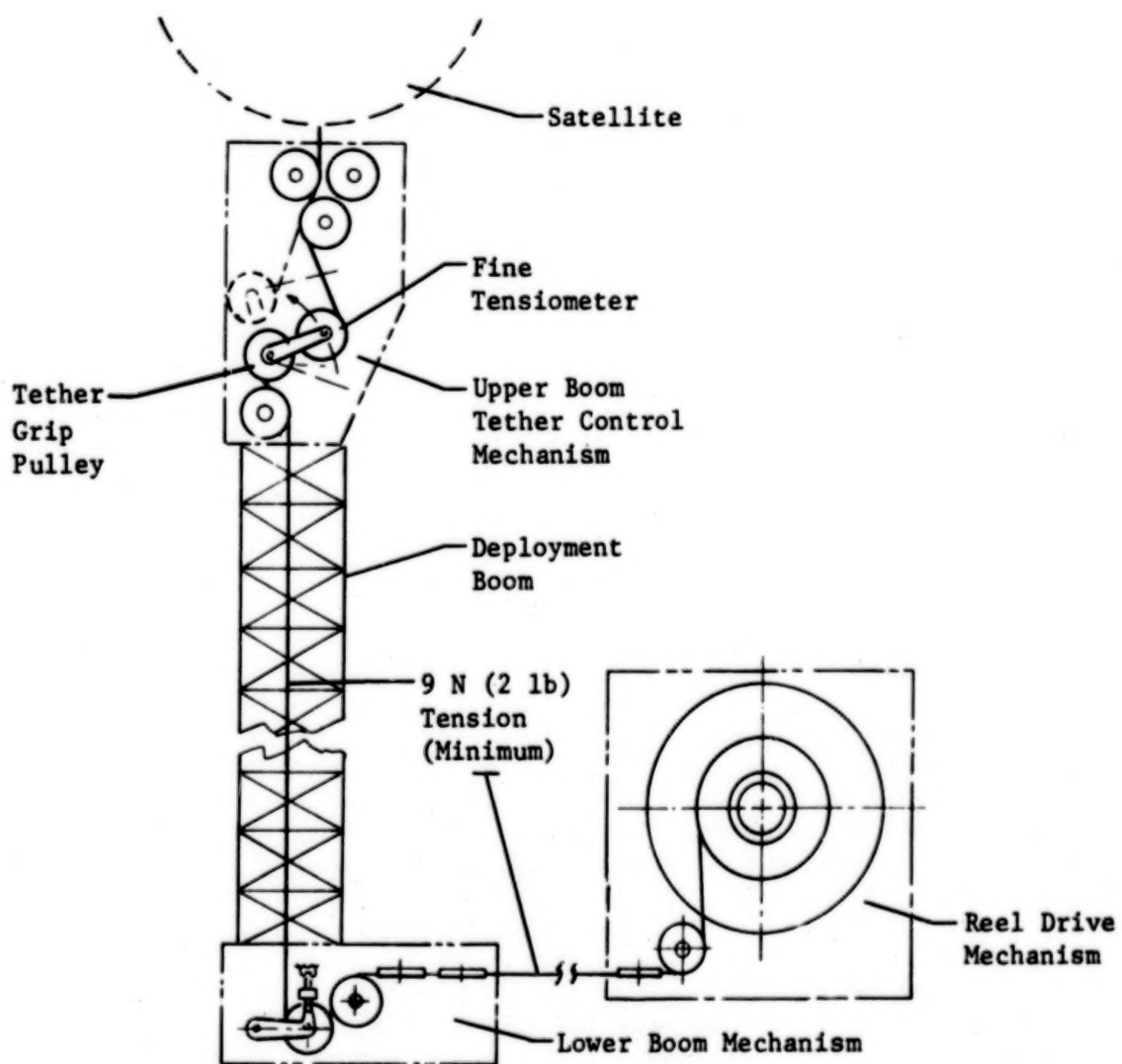


Figure 4 Tethered Satellite Control Mechanisms

Reel Drive Mechanism - This mechanism stores the tether. It is motor-driven and includes a level wind to uniformly feed the tether to the reel.

Lower Boom Mechanism (LBM) - This device serves two primary functions: (1) it measures tether length and velocity as the tether runs through the mechanism, and (2) it reads the tether tension at the reel. It also provides change of direction for the tether from the reel to the upper boom mechanism.

Deployment Boom - The deployment boom positions the upper boom mechanism with satellite out of the cargo bay. The deployment function places the 500-kg satellite 20 m away from the Space Shuttle (producing a small natural gravity gradient force), imparts an initial velocity to the satellite for deployment, and allows for satellite docking at a safe distance from the body of the Space Shuttle.

Upper Boom Mechanism (UBM) - The UBM serves three functions: (1) it provides tether control to the satellite as the satellite swings in and out of plane; (2) it reads tether tension in the low range during the early deployment and final retrieval parts of the mission; and (3) it produces additional tether tension at the reel when tether tension to the satellite is in the low range.

In addition to these four mechanisms required for operations, jettisoning devices provide for emergency ejection of any equipment that may prevent closure of the cargo bay doors.

Figure 5 shows the general arrangement of the total system installed on the European spacelab pallet. Launch and landing configuration is with the boom retracted and the satellite locked in the restraining ring. Satellite flight configuration is with the satellite launch locks released and the boom extended.

Reel Mechanism

The reel drive mechanism consists of the tether storage reel, the tether level-wind device and a 5-hp drive motor. The reel assembly is illustrated in Figure 6.

The size of the reel was determined by tether diameter and length requirements established by a number of candidate missions. Two types of tether, conductive and nonconductive, can be used. Conductive tethers (stainless-steel or copper-core cable) are required for all missions with electrodynamic experiments.

The tether diameter for these missions will range from 1.15 mm to 3.17 mm, including insulation. Nonconductive (Kevlar) tether diameter is 1.70 mm for satellites of the 500-kg size. Figure 7 shows tether reel capacity as a function of tether diameter.

A level wind geared to the reel shaft ensures proper lay of the tether on the reel. Because the tether diameter varies for each mission, the level-wind traverse rate must be variable. The method for changing this rate is shown in Figure 8. The level-wind rate is set by gears and a timing belt between the reel shaft and level-wind ball reverser. Different change-gear sets are needed to obtain the desired level-wind rate.

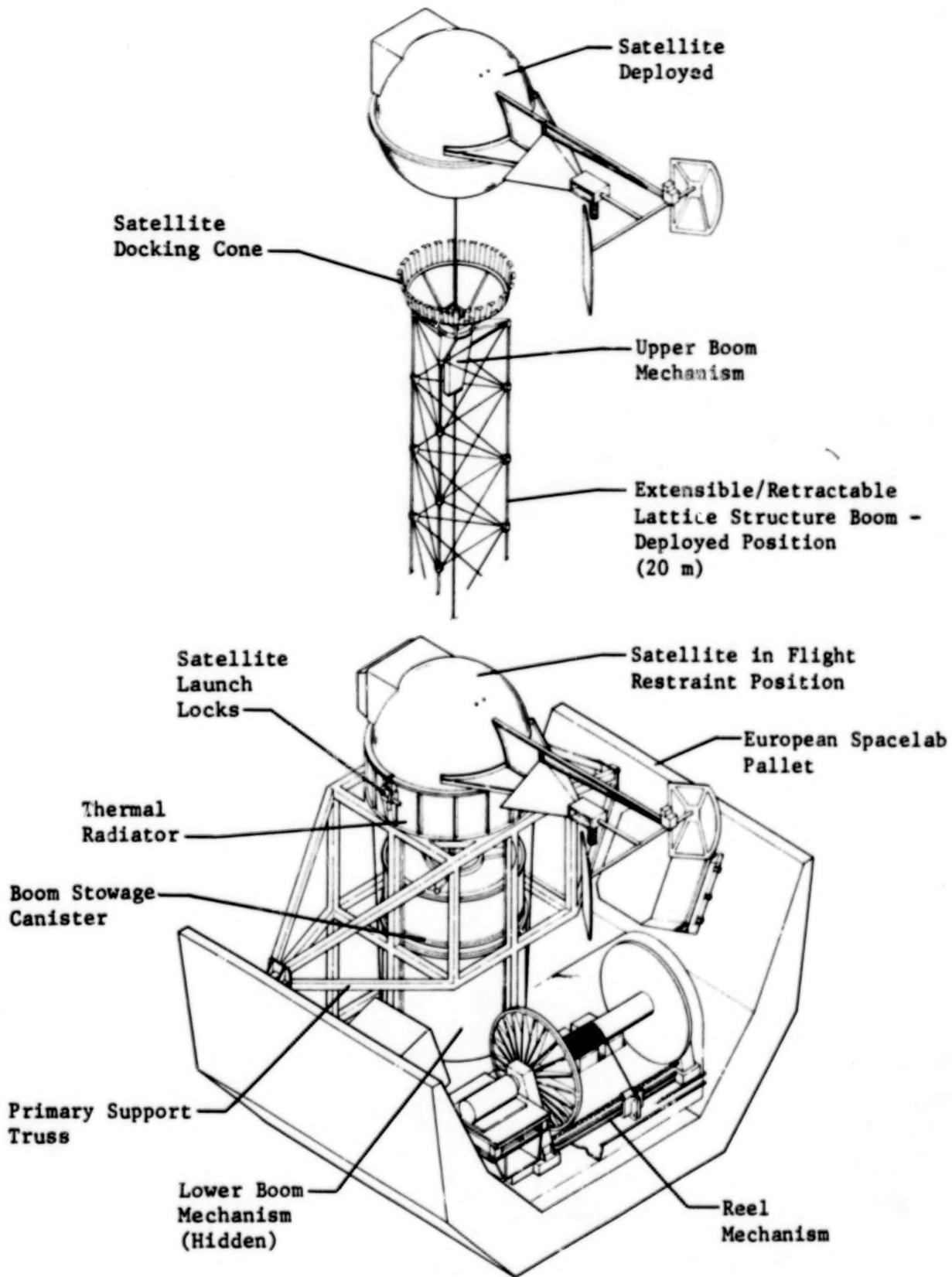


Figure 5 System Installed

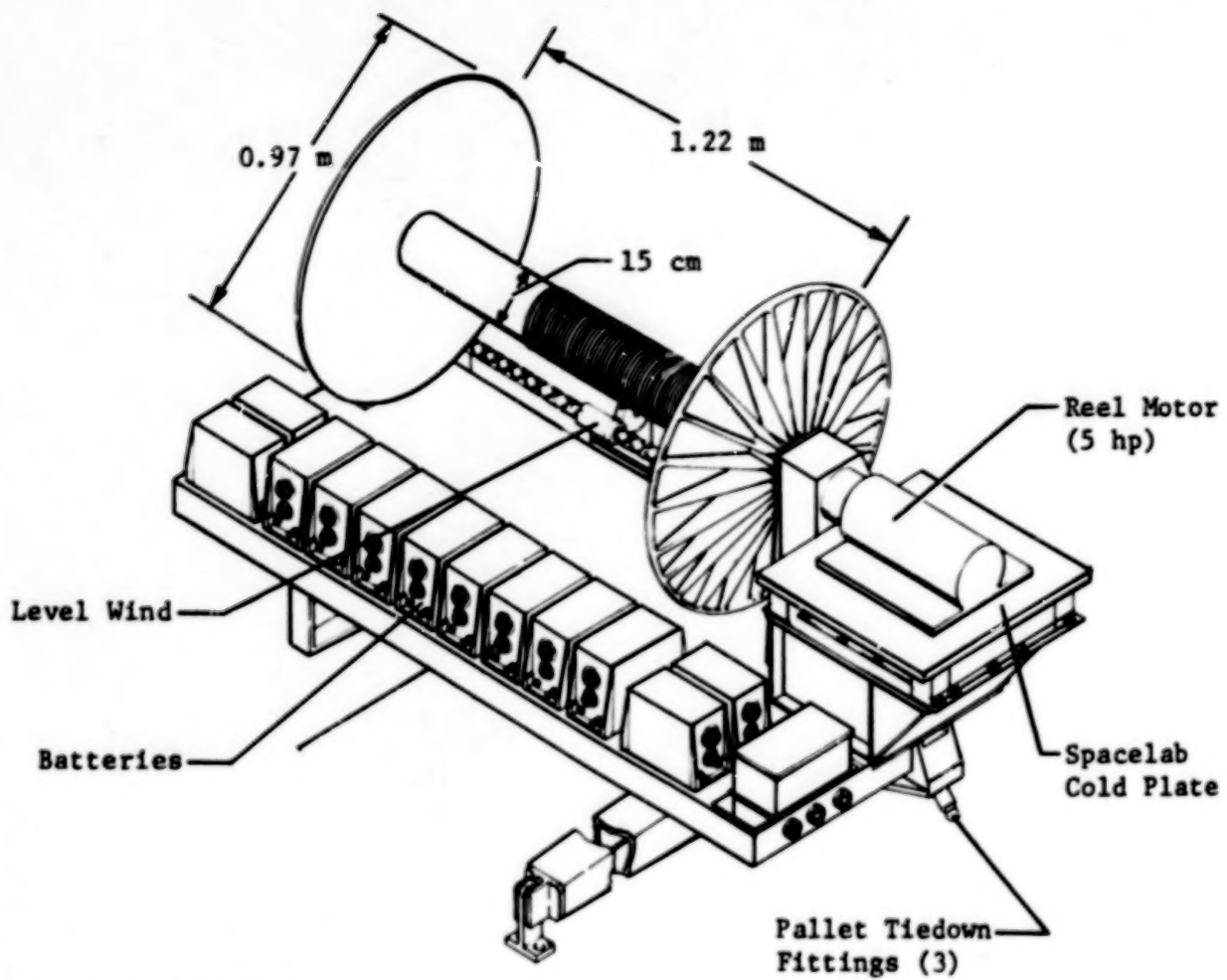


Figure 6 Reel Mechanism

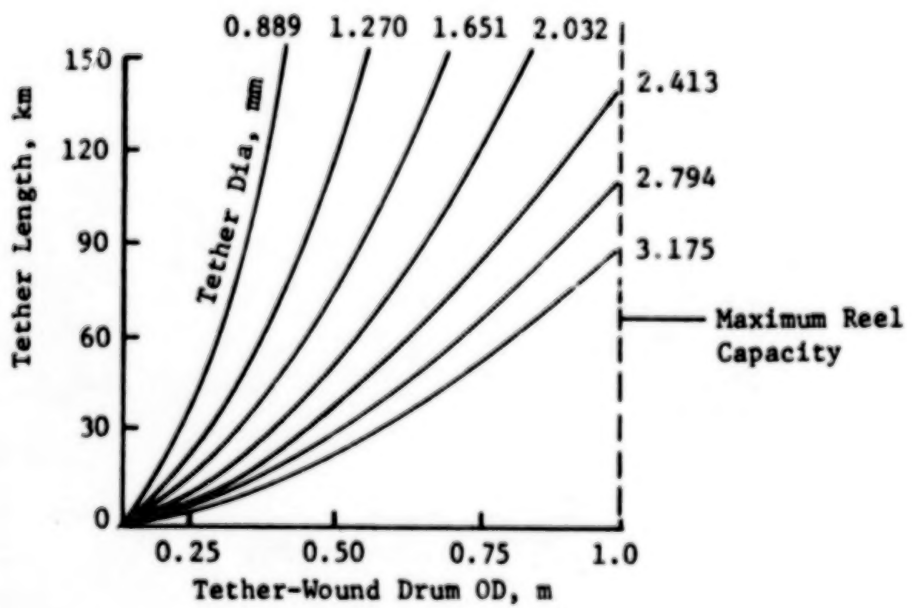


Figure 7 Tether Reel Capacity vs Tether Diameter

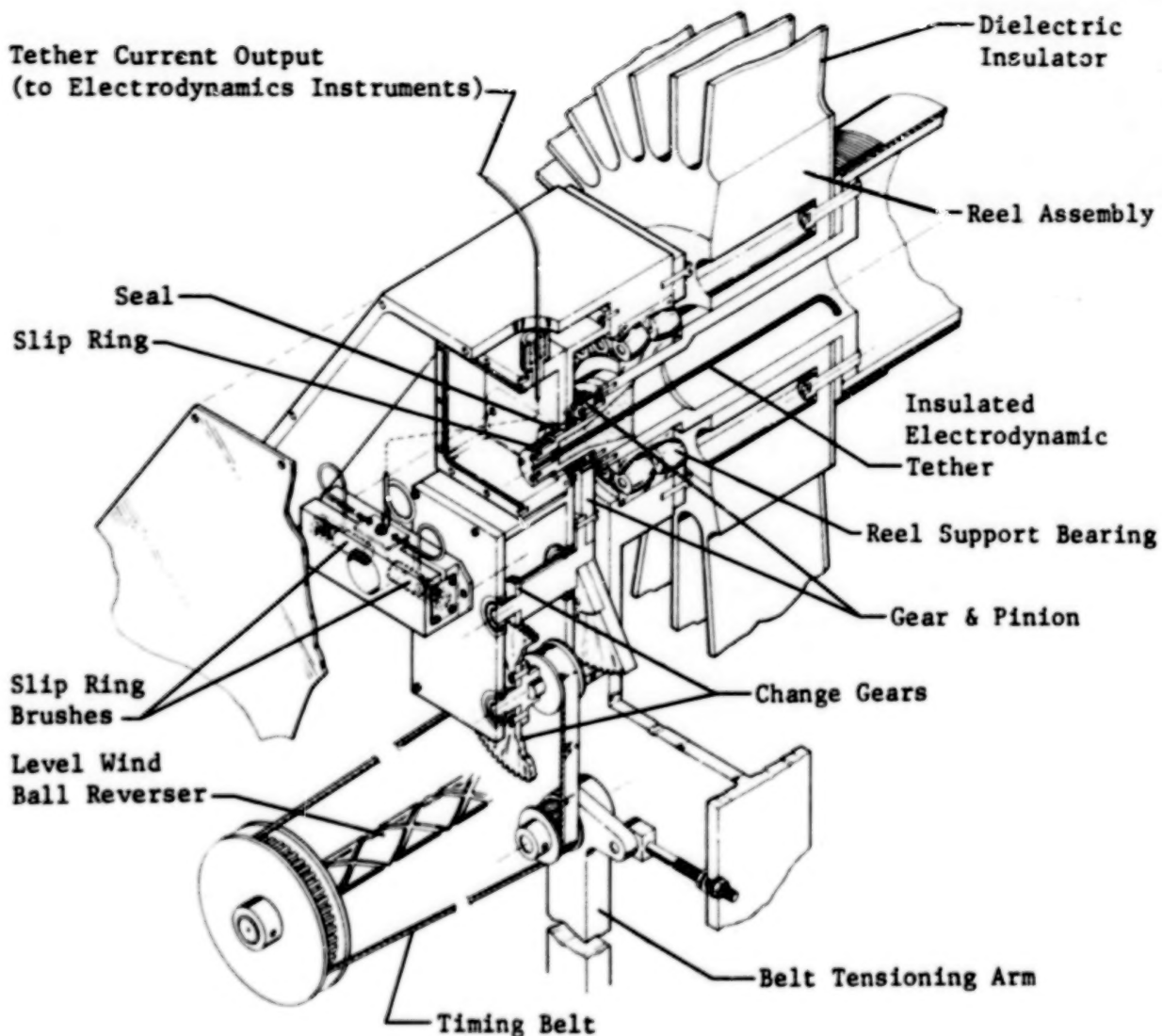


Figure 8 Reel Mechanisms and Tether Current Slip Ring

Figure 8 also shows the method used to carry electrical current out of the conductive tether (electrodynamics experiment) through the rotating reel to the cargo bay supporting equipment. The insulated conductive tether terminates at the slip-ring rotor. Slip-ring brushes complete the circuit to the supporting equipment. If tether insulation becomes damaged, a current leak could occur at any conductive point in the mechanism that is near the tether. To safeguard against arcing, all conductive surfaces near the tether are protected by dielectric material and pulleys are fabricated from nonconductive materials.

The reel is direct-driven by a 5-hp permanent magnet dc motor with tach generator and brake. The motor was selected for its wide operating range. A torque of 25 ft-lb at 2000 rpm is required during the early retrieval period when maximum tether tension may be as great as 320 Newtons (72 lb), with velocities as high as 10 m/s. Early deployment and final retrieval rates are very low (in the 25-m/h range). The motor is capable of operating as low as 3 rev/h. If the spooled tether diameter on the reel is 0.66 m minimum (26 in.), a tether velocity as low as 6 m/h is possible. These slow speeds are accomplished by supplying the motor with pulse-modulated power.

During high-horsepower operation, the motor will generate more heat than can be radiated from the motor housing surface when operating in vacuum. Therefore, the motor must be mounted on an actively cooled cold plate, as shown in Figure 6. During deployment, the motor will not be driving, but will be operating as a generator. The electrical energy generated is dissipated through resistive heaters located above the primary support truss (Fig. 5).

Lower Boom Mechanism

Figure 9 is an exploded view of the lower boom mechanism. The LBM receives the tether from the reel mechanism through a set of flat fairlead rollers. As the reel mechanism level wind traverses the length of the reel, the tether angle changes up to ± 30 deg. The fairlead rollers that also appear on the level wind maintain alignment of the tether into the mechanism.

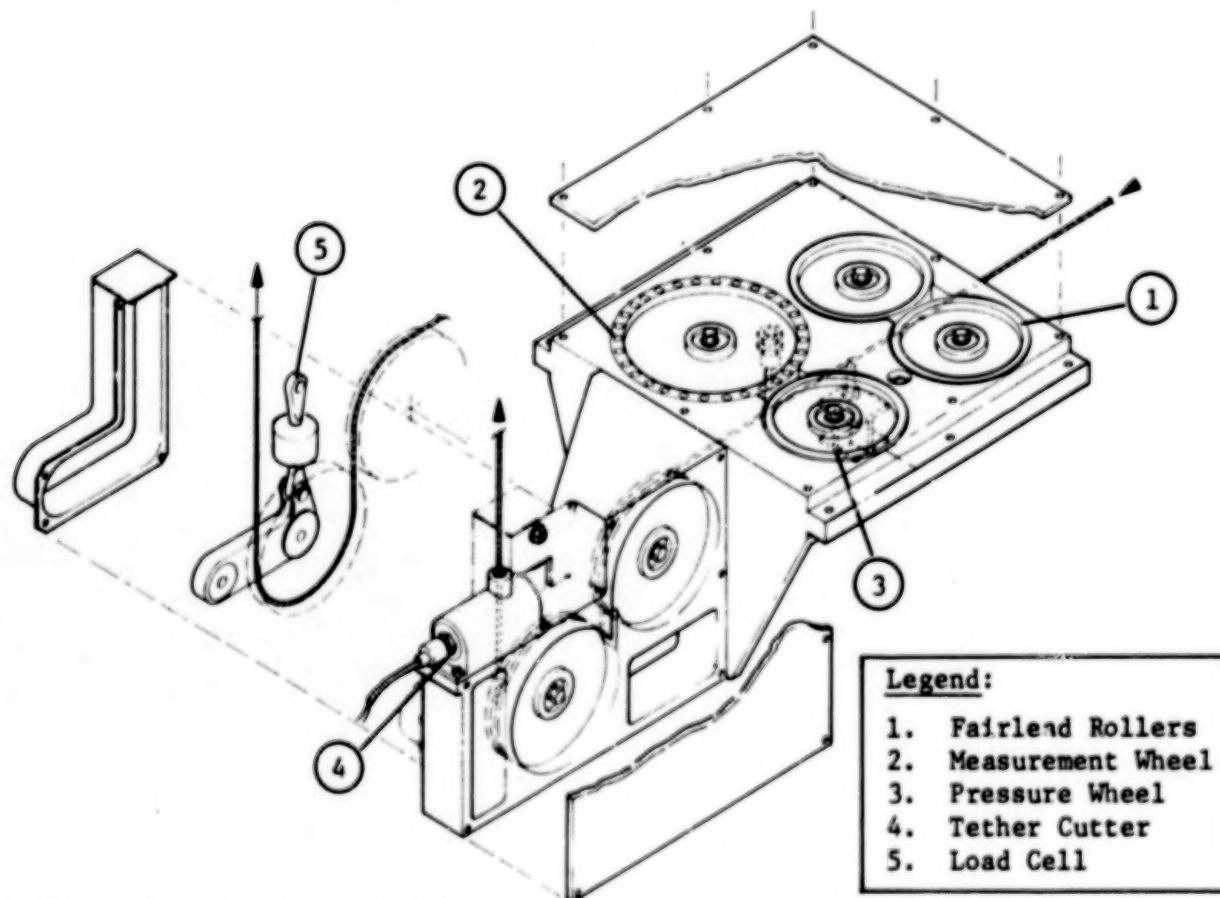


Figure 9 Lower Boom Mechanism

The flat pressure wheel forces the tether onto the flat measuring wheel, ensuring no slip rotation as the tether moves by. The measuring wheel, which is precisely 0.5000 m around, contains 30 permanent magnets at 12-deg spacing. As the wheel turns, the magnets activate the Hall-effect sensor, generating a voltage that is converted into tether velocity. The pulse counter will produce information from 1 per second to 60 pulses per second as the tether velocity varies from 1 m/min to 10 m/s. Each pulse from the Hall-effect device is totaled to supply tether length information.

Tests conducted on a breadboard measurement wheel resulted in measurement accuracies of 99.83% over 800-m lengths. The system should be very accurate for both length and velocity measurements during the first several kilometers of deployment, at which time the orbiter rendezvous radar can be used for updates; however, a computer algorithm will be required to compensate for load and thermal stretch of the tether for length measurements.

From the measuring wheel, the tether passes over a grooved pulley, under the grooved load-cell pulley, through the pyro tether cutter, and into the deployment boom to accomplish a direction change and to produce tension information. The load-cell pulley is attached to a pivoting arm, allowing free movement of the load-cell shaft. The load-cell reading is double the actual tether tension due to stroke reduction, producing a high-resolution output signal. The 890-Newton (200 lb) load cell is identified as the coarse tensiometer, because its job is to ensure adequate tether tension for proper spooling of tether on the reel. A coarse tensiometer is also needed when the tension of the deployed tether exceeds the measuring capability of the fine tensiometer located in the upper boom mechanism.

A pyro-operated tether cutter is located in the LBM in case emergency jettison of the deployment boom is required. Also, the LBM is thoroughly insulated internally and uses nonconductive pulleys for electrical isolation when conductive tethers are in use.

Deployment Boom

Telescoping, furlable tubular- and lattice-structure booms were evaluated in selecting the deployment boom design. The lattice structure boom was chosen because of its inherently greater strength margin and higher damping properties. The boom will be the continuous longeron type stowed in a spiral configuration within a canister. Deployment and retraction is accomplished by feeding the collapsed boom through a motor-driven nut at the canister outlet. This type of boom is available through manufacturers with flight-qualifying experience.

The deployed boom, which extends past the open cargo bay doors, must be capable of emergency jettison if required.

Figure 10 shows the boom canister mounted in tracks on the primary support truss. The canister is restrained by pyro separation nuts at the bottom of the truss, with ball fittings at the midpoint ring frame that react lateral loads. On release of the pyro nuts, the total canister/boom assembly is ejected. Four negator spring motors provide the accelerating ejection force, 267 Newtons (60 lb) over the full 203-cm (80-in.) track travel. The cables release from the bottom of the canister on ejection. Final boom/canister velocity, with satellite seated in the docking cone, is approximately 0.6 m/s, and without satellite is 1.3 m/s.

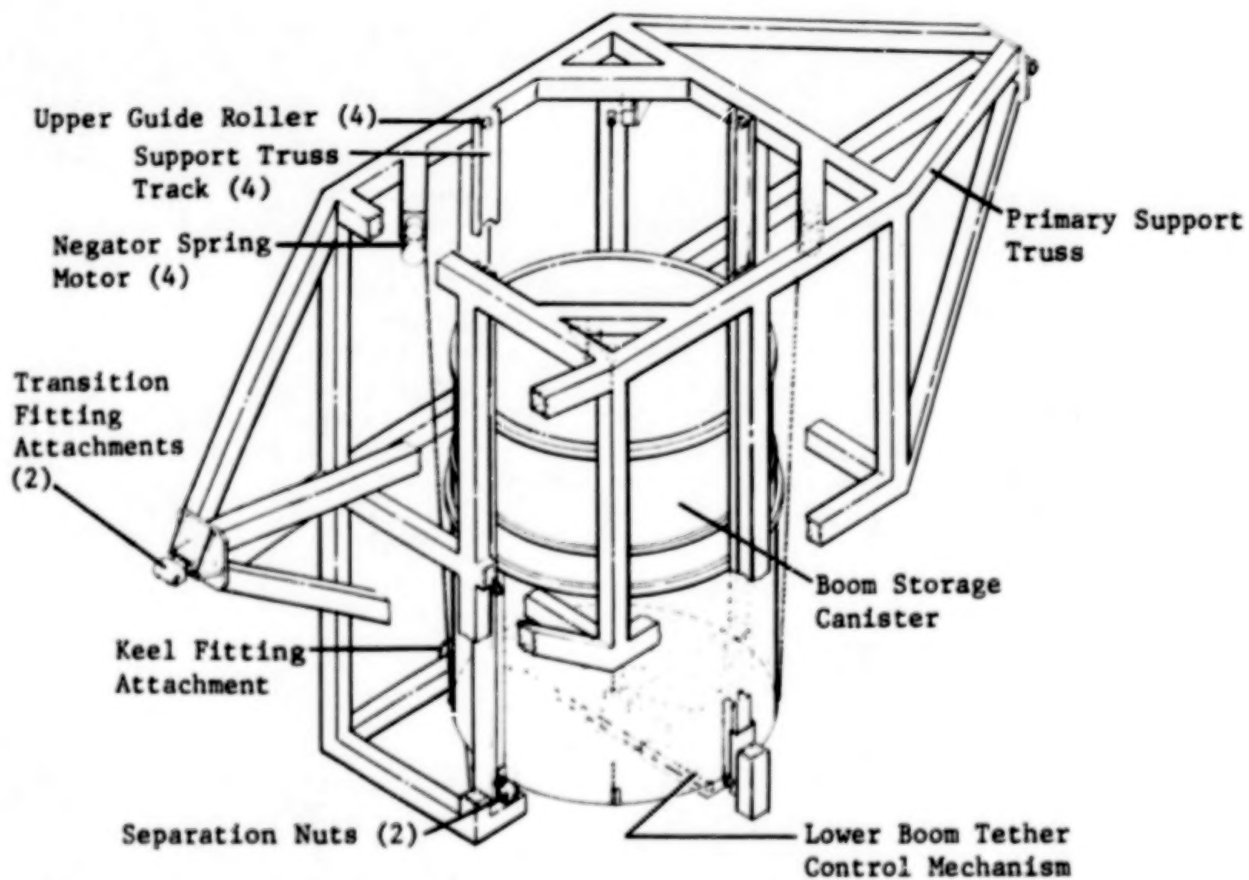


Figure 10 Boom Canister

Two electrical interface connectors are located adjacent to the pyrotechnic separation nut assemblies. These spring-loaded, nonlatched connectors separate passively when the pyrotechnic separation nuts are actuated and the canister is accelerated upward.

Two dual-cartridge tether cutters, one in the lower boom tether-control mechanism and another in the upper boom tether-control mechanism, are actuated before activation of the canister-release separation nuts.

Upper Boom Mechanism

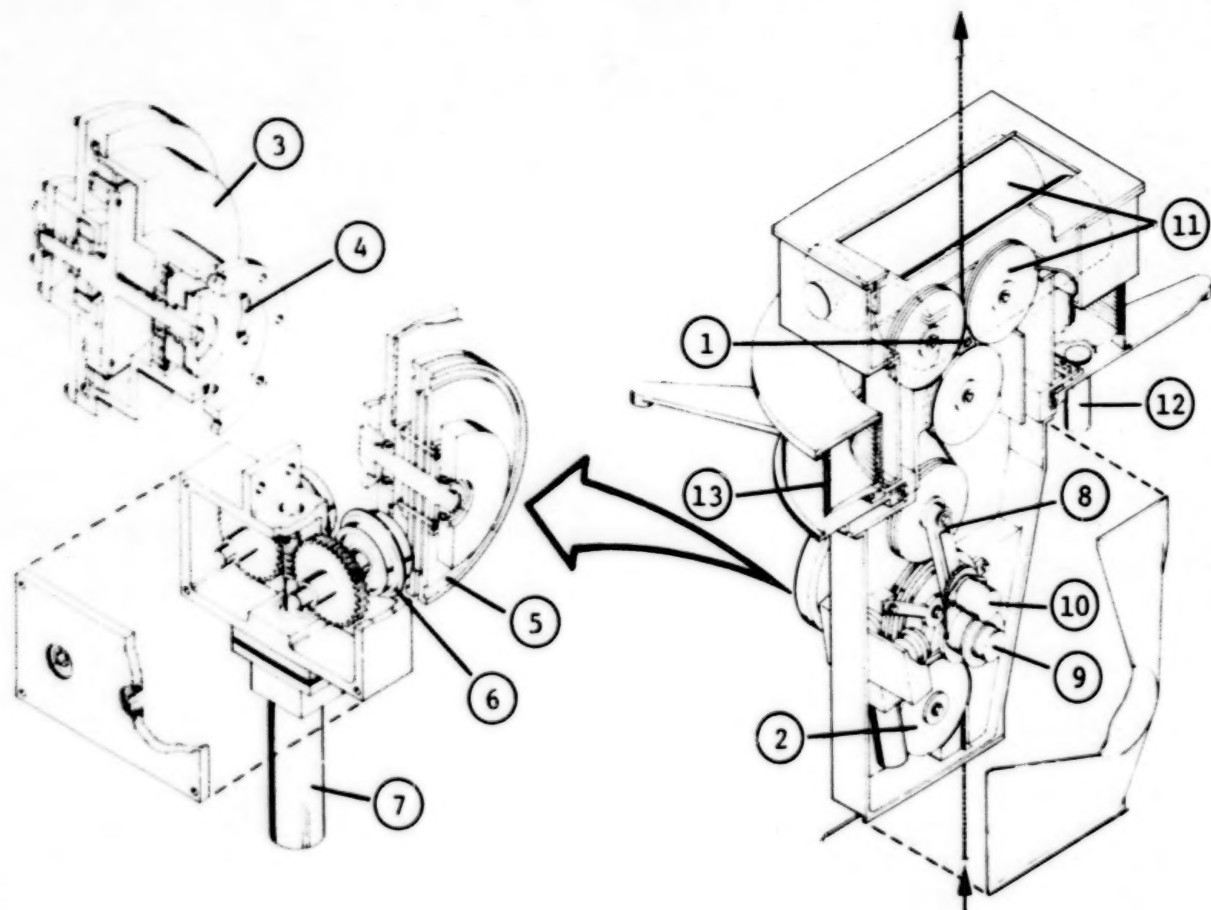
The upper boom mechanism mounts on top of the deployment boom on a large-diameter, double-angular contact ball bearing that allows the mechanism to rotate ± 180 deg with respect to the Space Shuttle cargo bay. A gear motor drives a pinion and gear to cause rotation. The satellite shown in Figure 2 uses an aerodynamic stabilizer for operation in the upper atmosphere. This stabilizer must be aligned with the Space Shuttle cargo bay to allow the cargo bay doors to close, thus requiring satellite rotation before latching in the satellite support ring.

Figure 11 is an open view of the upper boom mechanism. The tether enters the upper boom mechanism from the deployment boom where a second pyro tether cutter is located for emergency jettison. The tether rides over a grooved guide pulley into the tether grip pulley assembly. The purpose of the grip pulley is to provide tether tension between the upper boom mechanism and the reel when gravity gradient tension drops below practical tether-controlling limits. Tests determined this limit to be about 9 Newtons (2 lb). A 9-Newton tension was sufficient to ensure smooth operation through the mechanisms and to give a uniform distribution of the tether on the reel. The grip pulley engages when the fine tensiometer reading drops to 9 Newtons and disengages when the fine tensiometer reading moves above 9 Newtons.

Figure 12 illustrates the grip pulley operation. The pulley is constructed of two grip plates spaced slightly wider than the diameter of the tether. Small-diameter internal shims space the grip plates a predetermined distance from the tether bearing plate to allow for grip-plate deflection. The pinch rollers mounted on eccentric shafts move in, bearing on the grip plates, which cause them to deflect and grip the tether. (Note the deflection line.) This method produces line contact pressure on the tether over an arc of approximately 90 deg and allows the unit load to remain low while generating a high total load. Figure 11 shows the grip pulley with pinch rollers. The pinch rollers are worm gear-driven as a pair by a gear-motor reducer. A potentiometer indicates pinch roller position.

The cable grip pulley that operates only during the low tether tension and low-velocity portion of the mission is coupled directly to a magnetic clutch that engages the drive motor during operation. A dc torque motor is used to drive the grip pulley; it has a dc tachometer generator to measure pulley velocity. It is necessary to match the motor speed with the tether velocity before engaging the tether grip pulley clutch.

From the grip pulley, the tether passes over the fine tensiometer grooved pulley. The tensiometer assembly consists of a torsion spring-loaded arm pivoted about the center of the grip pulley, with a free-turning pulley on the unrestrained end of the arm. The tether passes over this pulley as it exits from the cable grip pulley. The spring-loaded tensiometer arm is free to travel through a 90-deg arc. As the external tether tension increases, the spring-loaded arm pivots from the minimum tension position to the maximum tension position. A potentiometer with a 5-arc-min resolution is used to monitor the angular position of the tensiometer arm. The mechanism can be calibrated after assembly to compensate for spring inaccuracy and to generate precise data output for the rate of tether tension.



Legend:

1. Tether Cutter	6. Pinch Rollers	11. Tether Guide Rollers & Pulleys
2. Guide Pulley	7. Pinch Roller Drive	12. UBM Gear Motor Drive
3. Grip Pulley Drive Motor & Tach Gen	8. Fine Tensiometer	13. Wire-Wrap Housing
4. Grip Pulley Clutch	9. Fine Tensiometer Potentiometer	
5. Grip Pulley	10. Fine Tensiometer Damper	

Figure 11 Upper Boom Mechanism

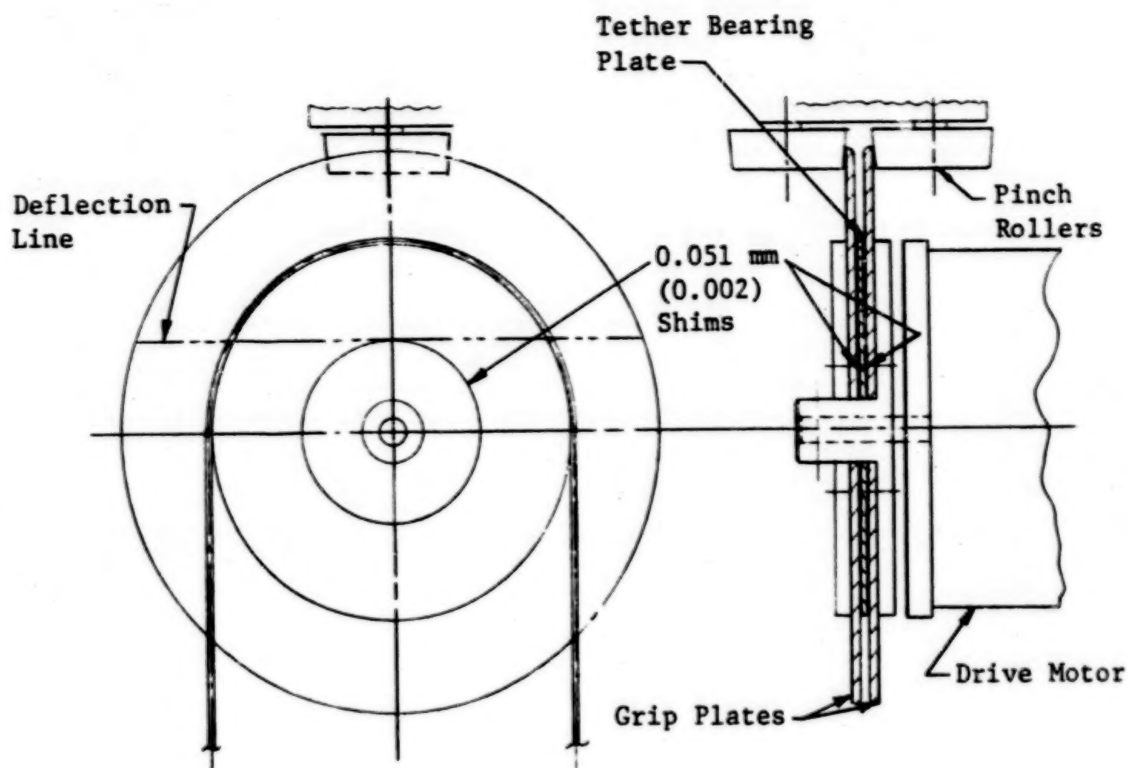


Figure 12 Grip Pulley

Figure 13 illustrates the sensitivity of the fine tensiometer. Large angle changes are generated in the low tension region, providing a 0.0022 Newton resolution. A lower resolution of 0.243 Newton is provided in the higher tension range. The tensiometer peaks at 43.75 Newtons when the arm attains a 90-deg position. The torsion spring is preloaded to 0.25 Newton and is adjusted by rotation of the slotted potentiometer coverplate. A viscous damper that provides 2.8 Newton-cm/rad/s is incorporated on the tensiometer arm.

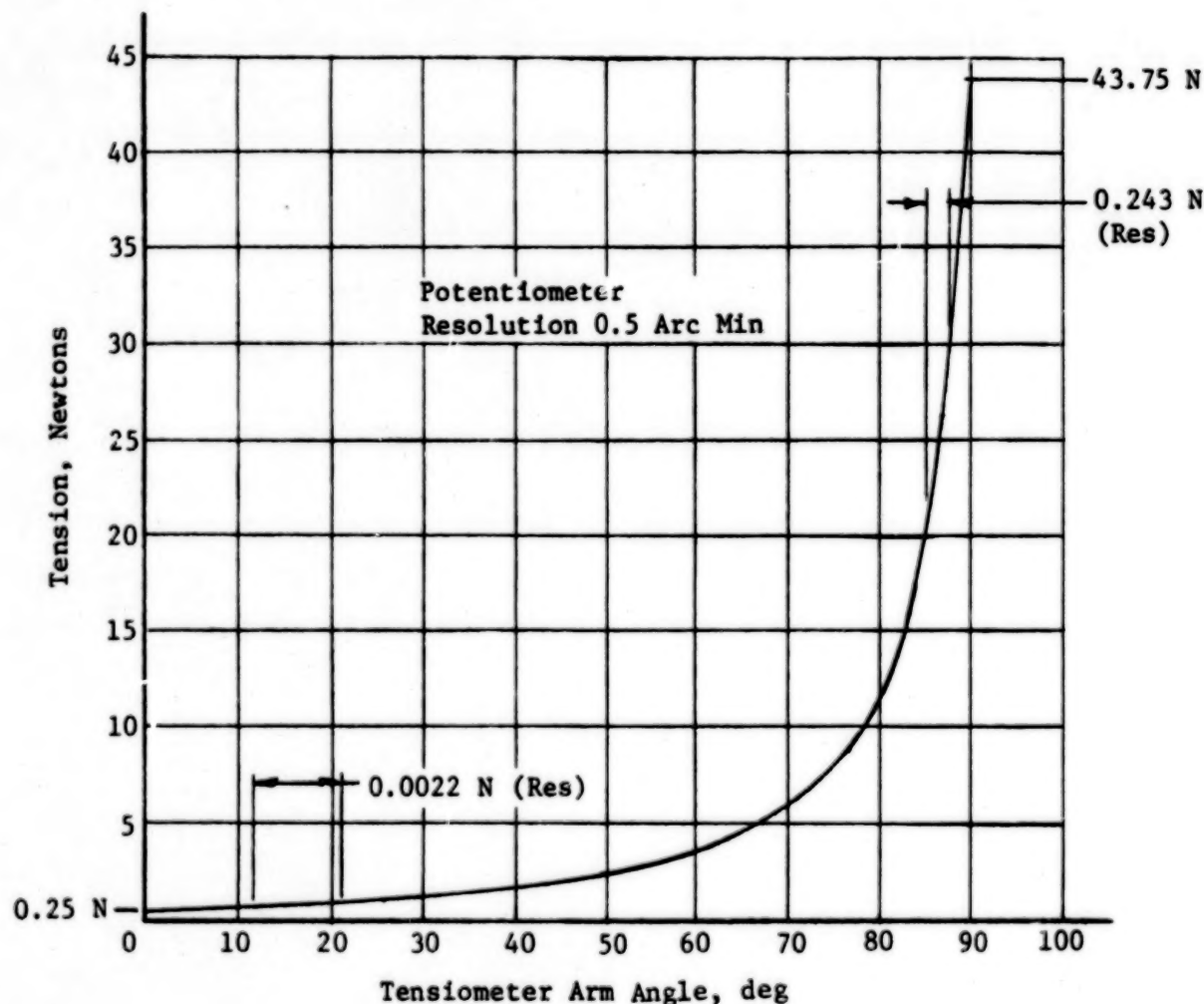


Figure 13 Tensiometer Sensitivity

The tether exits from the tensiometer and passes through the guide pulley assembly that consists of two guide pulleys and two fairlead rollers. The fairlead rollers provide a rolling surface on which the tether may bear as the satellite and tether move out of plane. In-plane tether motion is accommodated by the two guide pulleys as indicated in the drawing. The third guide pulley directs the tether to the tensiometer in a fixed plane and is positioned to set the geometry of the tether direction for proper tensiometer operation.

SATELLITE RESTRAINT ASSEMBLY AND DOCKING CONE

Figure 14 illustrates mechanisms and structures that accommodate the satellite during launch reentry and docking features.

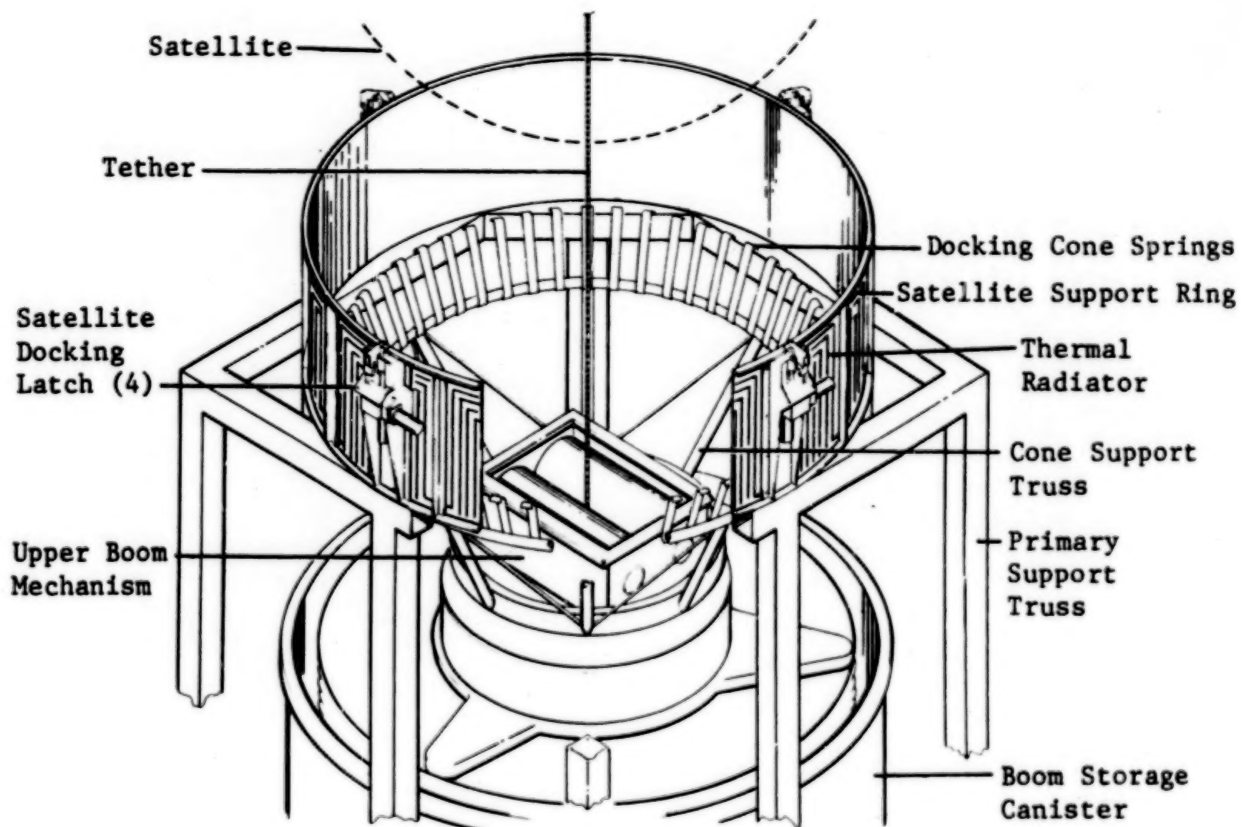


Figure 14 Satellite Restraint Assembly and Docking Cone

The assembly includes a satellite support ring that supports the satellite during launch, orbital flight, and reentry. The assembly, which is mounted on top of the primary support structure, includes an aluminum skin, stringers, ring frame, and longerons. Loads originating at the satellite are reacted into the upper ring frame and through the satellite tiedown latches.

The four satellite latching mechanisms secure the satellite circumferential flange to the restraint assembly support ring frame. The latches and ring frame are designed with enough strength that only two of the four clamps must be activated for safe reentry of the Space Shuttle.

The satellite docking cone and its support structure are mounted to the end of the deployable boom. It serves as a "soft nest" for the satellite when the boom is deployed and tether tension maintained, and during satellite docking. The cone is designed to accept docking velocities up to 0.28 m/s. The soft docking cone consists of 48 individual leaf springs fastened to a tubular, structurally supported ring frame. The docking cone is positioned to avoid tether-line contact up to the maximum tether cone half-angles of 45 deg. Docking angles are not expected to exceed a 20-deg half-cone angle, but tests are required to derive a maximum safe docking angle.

The docking cone design approach does not require precise orientation of the satellite during the docking operation. The satellite can be docked with any yaw (rotational) orientation, and any pitch and roll orientation up to approximately 20 deg. Once docking is accomplished, automatic flight control of the system is ended and boom retraction control is begun. Boom retraction control involves a boom retraction/tether-coordinated retrieval sequence that maintains a 20- to 30-Newton tether tension during boom retraction. At a position of 20 to 30 m above the cargo bay, yaw orientation of the satellite (as determined by the position of the magnetometer boom and aerostabilizer) can be visually determined. The satellite can then be properly orientated in yaw by commanding rotation of the motor-driven cone until the aerostabilizer is oriented approximately along the longitudinal centerline of the Space Shuttle cargo bay. The boom is then retracted until the satellite outer flange contacts the boom canister support ring frame. Continuing retraction of the boom until the docking cone disengages from the satellite, and maintaining tether tension will cause the satellite flange to properly seat on the support ring frame. The four satellite latches are then locked, and the boom is fully retracted.

CONCLUSIONS

Prototype, fully operational models of each tether-related mechanism described in this paper were fabricated and tested in breadboard fashion. Maximum and minimum operating velocities and tensions were simulated using a variety of tether material and sizes. These tests were performed manually (open loop), with no computer control support and with tether lengths up to 1500 m. Phase Two of the TSS project will simulate a complete mission and will incorporate automated control.

The NASA schedule calls for the first of two demonstration flights to occur in early 1987. One of the demonstration missions will be short range (10 to 20 km). The other demonstration flight will be full range (100 km). It is expected that operational tethered satellites will be flown on the average of two times each year thereafter.

CONSIDERATIONS ON THE LUBRICATION OF SPACECRAFT MECHANISMS

by: H. Mervyn Briscoe* and Mike J. Todd**

1. INTRODUCTION

The wide variety of lubrication techniques now available to spacecraft engineers very often makes the choice of an optimum process for a specific application very difficult to select. The ever increasing demand for the reduction of costs in spacecraft engineering has led to the unthinking application of commercial processes with the minimum of either intellectual or practical justification, and sometimes disastrous results.

The purpose of the paper is, therefore, to try to focus space tribology and to propose a number of precepts to guide designers in its application. Of the many techniques available all, without exception, have limitations in performance. Two European processes will be discussed in more detail and their limitations identified. Some performance results on a recently introduced liquid space lubricant will be given.

2. APPLICATIONS AND REQUIREMENTS

Table 1 is a non-exhaustive list of important space mechanisms with brief details of their lubrication needs in which four broad types of application can be identified.

- low speed sliding contact
- high speed sliding contact
- low speed rolling contact
- high speed rolling contact

For each of these there is a number of solutions but the selection of the optimum will depend wholly on the physical details of the mechanism. Which brings us to the first precept of space tribology.

Precept 1 The optimum lubrication system for a space mechanism is an integral part of the mechanism design and not a process to be added when the design is complete.

Even today when space engineering is more than twenty years old the precept is ignored. The authors have personally experienced two instances during the past year where the lubrication system was expected to make a poor design concept work.

*European Space Technology Centre (ESTEC), European Space Agency, Noordwijk, The Netherlands

**European Space Tribology Laboratory (ESTL), UKEA, Risley, United Kingdom

3. LUBRICANT CLASSIFICATION

They may be categorized as:

DRY

- (a) Dichalcogenides (lamellar solids)
- (b) Solid lubricant composites and transfer film lubricants
- (c) Soft metals

LIQUID

- (a) Hydrocarbon oils
- (b) Synthetic oils
- (c) Greases

It is quite impossible in a short paper to review all available techniques and processes so the authors will concentrate on those available in Europe and with which they are most familiar.

4. DRY LUBRICANTS

4.1 Dichalcogenides

These are a group of metal compounds which exhibit a lamellar structure to which current theory attributes their good lubrication properties. In fact only a limited number may be classed as lubricants, amongst which are WS_2 , WSe_2 , MoS_2 , $MoTe_2$, NbS_2 , $NbSe_2$, and $TaSe_2$.

Of these MoS_2 has shown itself to have the best performance in a space environment as a result of years of testing. It has good wear characteristics, low friction and in general performs better in vacuum than in moist air. Its coefficient of friction is load dependent, although some recent work has introduced dispute on this point, and ranges from 0.4 to lower than 0.1. There is a large literature on MoS_2 and ESA is funding a continuous bibliography on its applications to space prepared by A.R. Lansdown. (Ref. 1-5).

MoS_2 may be applied in a number of ways and those of interest to space engineers are reviewed briefly below.

4.1.1 Bonded Films

A bewildering variety of bonded films has been invented, now more than 100, but only a few of them have found general commercial application. The binders may be organic or inorganic, heat cured or simple air drying agents mostly based on cellulose. Some inorganic binders based on ceramics require curing temperatures of 1000°C which limits the materials to which they can be applied.

The thickness of a bonded film may commonly be of the order 10 μm which is enough to degrade the precision of many high grade mechanisms. The debris from the film may also lead to very erratic torque, particularly in rolling bearings. The control of such processes is very operator dependent which makes it difficult to achieve consistently uniform results and tends to preclude their use in critical mechanisms. The authors would not now use a bonded film in an application where high precision was a requirement.

4.1.2 Burnished Films

A moderately adherent thin film of MoS₂ may be achieved by burnishing onto a thoroughly degreased and clean metal surface. Rubbing with chamois leather or a wire brush, or tumbling in a ball mill are established methods of burnishing. It is difficult to achieve consistent results even when the process is most carefully controlled, but the process is readily acceptable for very simple single operation devices such as latches, hinge pins and pyrotechnics. It can be applied to rolling bearings where the life is a few thousand revolutions and loads are moderate. Running-in should be an integral part of the process.

4.1.3 Sputtering

The most recent technique for applying MoS₂ films is by sputtering, first developed by Spalvins and Przybyszewski at NASA Lewis Research Centre. Since then a good deal of work on sputtered MoS₂ in ball bearings has been reported in the USA, chiefly by Spalvins (6) and by Christy and Barnett (7) and also in Europe by Bergman (8). In Europe the process has been developed and refined both at the Laboratoire Suisse de Recherches Horlogères (LSRH) and at the European Space Tribology Laboratory (ESTL) in the U.K.

The very significant advantage to be gained by the process is the achievement of a very thin, about 1µm, film strongly adherent and of controlled composition. However, it has been shown by ESTL that the performance of sputtered films varies widely depending upon the sputtering technique and the stoichiometry of the film. During the past two years films of MoS₂ sputtered by LSRH and ESTL have been compared for performances in 42 mm diameter ball bearings, preloaded to 40N and run at 100 rpm. Results are discussed in para.4.4.

4.2 Solid Lubricant Composites and Transfer Film Lubricants

The number of polymer type materials falling under this heading is now considerable and quite beyond the scope of this paper. In practice only a very few are suitable for use in a space environment and in Europe only PTFE, often filled with MoS₂ and reinforced by glass fibre polyimide and polyacetal (e.g. Delrin) are commonly used for their tribological properties. The disadvantages of polymers in a space environment are:

- high coefficient of expansion
- low load capability
- high wear rate
- limited dimensional stability
- poor thermal conductivity

But these are balanced by the advantages of:

- cheapness and simplicity
- low coefficient of friction
- low outgassing

The lubricating action of these polymers and composites may be by the transfer of a film to the mating material or they may simply provide wear resistant components, but the two actions should not be confused. In consequence they may be used in space either as the base material of one component of a rubbing pair, e.g. gears, or to provide a transfer film to lubricate a rolling or sliding metal pair, e.g. ball bearings.

PTFE + MoS₂ + glass fibre has for many years been used as a cage material in small, lightly loaded, ball bearings. This composite has been studied in detail by Stevens and Todd (Ref.9). Loads must be limited to ensure that the Hertzian contact stress does not exceed 1.2×10^3 MN/m² at 20°C. The MoS₂ appears to have the function of preventing the transfer film of PTFE becoming too thick. Failure is usually by wear-out of the cage, creating large quantities of debris. In oscillatory motion a build up of transfer film at the end of the arc of travel leads to excessive torque peaks. In addition the thickness of the transferred film can be dependent upon speed of operation.

Both polyimide and polyacetal have been used for lightly loaded gears in a space environment running against stainless steel, titanium or aluminium. Work in progress at ESTL, to be reported in the near future, has shown that Vespel, a polyimide, gives the lowest wear rate of all polymers tested. Polyacetal filled with carbon fibre has also been tested and shows lower wear rate than the unfilled polymer but still greater than the polyimide. Maximum loads for all these materials should be limited to 10 N/mm tooth width for gears of module 1.

4.3 Soft Metals

It has long been known that the soft metals such as Ba, Au, Ag, Pb, In and others are capable of providing lubricating films in certain circumstances. In this paper we shall confine ourselves to the use of lead in rolling bearings and gears in space. The work was initiated by the Royal Aircraft Establishment in the UK in the 1960's and a very extensive test programme was carried out by Marconi Space and Defence Systems on 19 mm diameter bearings at 3000 rpm, some of which ran for eleven years. The programme was extended by ESA to bearings of 90 mm diameter running at 100 rpm and six pairs completed more than 60,000 hours without failure. In all these tests the only limitation was the wear debris from the lead bronze cage, and the search for a better cage material is continuing.

The process used by MSDS Ltd. was vacuum deposition, which made film thickness and adhesion difficult to control, so the Agency undertook the development of an ion plating process at ESTL. (Ref.10, 11, 12).

The pre-eminent advantages of an ion plated film over a vacuum deposited one are excellent adhesion and close control of thickness, $0.35 \pm 0.15\mu\text{m}$ at ESTL. At present only the races of the bearing are plated and the film is transferred to the balls during the running-in period in vacuum, which is an integral part of the process. Ion plating of the balls is now possible but, for most applications seems to offer little advantage.

Lead lubricated bearings are flying in the OTS and MARECS Solar Array Drives and will fly in the SADs of ECS, EXOSAT, L-SAT and the French SPOT. The bearings of the de-spin mechanism of GIOTTO, the European Halley's Comet probe, will also be lead lubricated. The selection ad in this case was made to take advantage of its immunity fr. torque changes due to temperature. The torque at -40°C is virtually identical to that at room temperature in a well designed system; a performance which no liquid lubricated bearing can equal. Torque noise, however, will be higher than an equivalent liquid system which was the reason for the final rejection of lead, and all other dry film systems, for the Space Telescope Solar Array Drive, where smoothness of operation is a prime requirement.

Lead lubricated bearings are finding application in scientific instruments and lead lubricated ball screws are flying on Nimbus G. A similar ball screw has performed very well at 4°K and demonstrated the effectiveness of the process at cryogenic temperatures. Ion plated lead is now being applied to gears although it operates better in a rolling than in a sliding contact. Tests have shown it to be a very effective lubricant for gears of nitrided steel on nitrided 440C steel and it has been adopted for the gears of the L-SAT Solar Array Drive. Most importantly the process has been fully established, codified and documented at ESTL to ensure complete repeatability of film parameters and friction and wear characteristics, and it is now offered as a standard process routinely carried out.

The pros and cons for lead lubrication may be listed as:

Pro: - excellent adhesion

- low, consistent and temperature-independent torque
- very long life under vacuum
- applicable to bearings, gears and ball screws
- usable at cryogenic temperatures

Con: - flake wear debris from the lead bronze cage can cause torque noise problems. ESTL is investigating alternative materials for cages.

- operation in air must be limited to fairly low speed and short duration e.g. 10^5 revs. at 100 rpm for a 20mm ID bearing.

4.4 Bearing Torque Characteristics of Solid Lubricant Films in Vacuo.

With the aim of comparing levels of torque and of torque noise from ball bearings under identical conditions, data from ESTL have been assembled to show what is to be expected of the three most common lubricants discussed above.

Table 2 shows the details of the method of lubricant application, the associated cage material, the type, size and preloading of the ball bearings used in this comparison. In all the tests an arbitrary level of torque ten times the initial DC level was chosen to represent torque "failure".

4.4.1 Torque Results

The histories of torque tests over 2 million revolutions (or until torque failure, as defined above) are collected in Table 3. As a comparison the result for an unlubricated, but degreased, bearing is included. Very rapid failure is encountered.

The MoS₂-sputtered bearings tended to start with a moderately high torque (20×10^{-4} Nm) but it soon fell to a $6 - 10^{-4}$ Nm (at 40N preload) where it remained until usually a sudden steep rise and torque failure. Films sputtered at ESTL and at LSRH Switzerland exhibited broadly similar behaviour but bearing lives varied from $0.7 - 3 \times 10^6$ revs for films sputtered at ESTL and from $2 - 3.66 \times 10^6$ revs for films sputtered at LSRH. The torque traces were some of the smoothest that we have observed and we would now recommend sputtered MoS₂ where low torque noise is important and the life requirement is not above 10^5 revolutions, or equivalent rolled distance.

The ion-plated, lead-filmed bearings exhibit reasonably steady DC (average) torque but there is considerable fluctuation in the peak-to peak torque. This latter is defined here as the maximum total swing of torque either side of zero during slow rotation of the bearings in two opposite directions. This bi-directional check of the torque was carried out at regular intervals in these tests. For the lead film there is no effect of a previous run at 100N preload on the torque. None of the lead bearings failed by the above criterion. The PTFE-composite caged bearings were considerably more erratic in their average torque than the lead filmed bearings and the torque was prone to rise quite suddenly over a few thousand revolutions and as quickly to subside. Nevertheless, the peak-to-peak amplitudes of torque were less than those of the ion-plated lead, as Table 3 shows. There was a

discernable effect of previous running at low load (i.e. below critical stress) upon the torque in the 250N run (above critical). The bearings run immediately at 250N showed high DC torque initially but this gradually reduced with time. Such initial high torque was absent if the bearings had been run at sub-critical stress beforehand but there were still periods of high torque during the run. For these bearings 100N preload caused the critical Hertzian stress.

It is appropriate to complete this section with the second precept of space tribology:

Precept 2: In designing a space mechanism avoid making its operation dependent upon close control of the coefficient of friction.

5. LIQUID LUBRICANTS

The use of liquid lubricants in space is not new and it is fair to say that all early American satellites relied upon it. Ball Bros. were the leaders in the field in the USA and the move to dry lubrication has been slow. In Europe we went strongly for dry lubricated systems, largely driven by the success of the lead system, but also because their advantages were clear.

In consequence liquid systems in Europe have received less attention but have not been ignored. A de-spin system which has been running under test in vacuum at ESTL for more than 7 years is liquid lubricated. The Solar Array Drive for Space Telescope, the Instrument Pointing System and the bearings of the Antenna Pointing Mechanism on L-SAT, all have liquid lubricated bearings.

5.1 Hydrocarbon Oils

In Europe BP Ltd (U.K) developed, at the request of RAE, two space oils with very low vapour pressure.

BP 110 is a very fine cut natural hydrocarbon with a claimed vapour pressure of 10^{-10} torr or lower at room temperature.

BP 135 is a synthetic tri-ester with a higher viscosity index than BP 110.

BP. Ltd. further developed two greases upon these oils but of quite different formulation from normal greases. (Ref.13).

The thickener is based on an oleophilic graphite-lead composite capable of forming stable semi-solid structures on dispersion in a suitable base fluid. The proportion of thickener is 17%, which is unusually high, but it also provides a marked improvement in the extreme pressure and boundary lubricating properties.

The use of graphite in a space environment is very unusual since it is well known that graphite in a wholly dry atmosphere acts as an abrasive. In the case of the BP greases the special method of preparing the graphite to render it oleophilic makes it operate in a vacuum environment very satisfactorily.

Both of these oils have been subjected to extensive testing over the past seven years and the BP 110 and its grease BP 2110, have been shown to give longer bearing lives in vacuum than competitive lubricants. In most tests BP 135 has not equalled the life achieved by BP 110 but has given good results for many applications, and is useful where its higher viscosity index may be an advantage.

At ESTL a de-spin mechanism has been running at 60 rp.m. under thermal vacuum conditions for seven years without any change in performance. Lubrication is achieved by a small quantity (about 5% fill) of BP 2110 grease in each bearing combined with Nylasint oil stores charged with BP 110 oil. The thermal conditions in the chamber are maintained at 20°C whilst the shaft of the mechanism is driven between -5°C and + 45°C. The performance of this mechanism has been excellent with no change in any operating parameter except a small rise in motor current attributable to magnet deterioration.

5.2 Synthetic Oils

In general, synthetic fluids usable as space lubricants fall into two broad categories:-

- silicones
- fluorinated polyethers.

In the early years of space many silicones were tried as space lubricants with widely different results. Their advantages are a high viscosity-index, good thermal stability and fair to good lubricating properties, but their volatility in space environment may not be significantly better than some hydrocarbon oils, and their surface creep characteristics are notoriously bad.

Silicones in space have now been displaced by perfluoralkylethers such as the Krytox and Fomblin fluids. However, the lubricating properties of these fluids are not general and only some of them have found application in space. In some applications such as sliprings they can lead to excessive wear rates and the formation of polymers. However used in the right application they can give excellent performance and their extremely low (10^{-11} - 10^{-13} torr) vapour pressures at room temperature makes them most attractive for mechanisms with critical cleanliness requirements.

5.2.1 Fomblin Z25

Probably the most significant addition to space lubricants is a polyfluoralkylether manufactured by Montedison in Milan called Fomblin Z25. The Fomblin Y series of fluids has been well known in the vacuum industry for many years but the introduction of Fomblin Z, which has a different chemical structure, was something of a breakthrough for space lubrication. The fluid has the very high viscosity index of 345 and a vapour pressure that is certainly below 5×10^{-12} torr at room temperature. It is the only oil known to the authors which passes the Agency's material out-gassing test, giving TML/RML % 0.01/0.01 and cvcM% 0.00.

The Bray Oil Co. in the USA have for several years distilled the Italian raw stock to make Bray 815Z, which has been flown on a number of USA satellites mostly in the form of a PTFE thickened grease, Bray 3L38RP, and will fly in Space Telescope in the solar array development mechanism.

During the last two years the fluid has been subjected to numerous tests at ESTL.

Bearings of two different conformities are being run at speeds of 20, 100, 200 and 1400 rpm. Full elasto-hydrodynamic lubrication is achieved at about 250 rpm. In the case of low conformity bearings at 1400 rpm the torque reduces suddenly and torque noise increases after a short time indicating the onset of starvation conditions. A black deposit has been observed in these bearings which has been identified as a polymer. In initial tests the high conformity bearings at 1400 rpm were accidentally contaminated with a hydrocarbon oil which resulted in a good performance but a milky deposit. Repeat tests with rigorously pre-cleaned cages are showing similar deterioration in average torque and torque noise. This work will be fully reported when complete.

The load carrying capacity of the fluid tested on the Falex machine is very good, giving a failure load in excess of 15,500N (3500 lb).

In pin and disc tests to evaluate its boundary lubricating properties it has performed equally with KG 80 and BP 110 for wear rate and coefficient of friction. (Ref.10).

The conclusion to date is that its use is acceptable in low speed applications where boundary lubrication is required and in Europe it is currently being applied to the bearings of IPS, Space Telescope Solar Array Drive and the L-SAT Antenna Pointing Mechanism.

For the present the oil should not be used in sliprings where it may increase the wear rate and can lead to complete failure by the formation of debris.

The grease 3L38RP has been used in small gear boxes but data on permissible tooth loading, shear breakdown or polymer formation is very limited.

Future use of the oil under conditions of EHD lubrication is dependent upon the results of the ongoing test programme at ESTL, the objective of which is to determine the limits of its range of application. Its use in optical instruments is not excluded but has yet to be demonstrated by valid test.

Before any application of this oil to a space mechanism is contemplated it is strongly advised to seek the guidance of ESTL who has carried out most of the relevant work.

6. THE CODIFICATION OF SPACE LUBRICANT SYSTEMS & PROCESSES

The behaviour of any tribological systems is governed by a large number of factors, many of which are difficult to control. Material properties, both macro and micro, surface condition, presence of micro quantities of contaminants, system geometry, speed, load, duty cycle are only some of the variables. In consequence any lubrication process to be acceptable for space must be subject to the following precepts:-

Precept 3: - Any lubrication process used for space application must be fully codified and documented to ensure consistent repeatability of performance.

Precept 4: - The lubricant used must be approved and validated for space to a recognised specification and must be source traceable.

Precept 5: - The test programme to determine the performance of the lubrication system must reproduce all the operational conditions of duty cycle, environment and life that it will experience in the application.

The use of a commercial system for a space application is acceptable only if it fulfils these three precepts. The Agency has issued a guide to the preparation of process procedures. (Ref.14).

7. CONCLUSION

In attempting to cover the whole field of space lubrication in a short paper the authors have set themselves an impossible task. Much relevant and important detail has had to be omitted. But the purpose of the paper is to provide a useful brief overall view which will, it is hoped, give the non-specialist a picture of a highly complex subject, and some guidance in the choice and application of a lubricant in spacecraft mechanisms.

BLANK

PAGE

TABLE 1.

APPLICATION	DUTY	LIFE	ENVIRONMENT	LUB. REQUIREMENTS
Momentum Wheels	Continuous Rotation at 3000-4500 rpm.	7-10 yrs	Closed low pressure He	Liquid: Maintenance of a controlled flow of lubricant into EHL zone to achieve low and consistent torque. Low wear rate.
Solar Array Drive	Continuous rotation at 1-16 revs. per day	7-10 yrs	Space exposed Thermal -40°C to +65°C	Solid or liquid: Boundary lubrication with consistent torque. No contamination, moderate load, corrosion protection.
Antenna Pointing Mechanism	Slow intermittent operation over small angle and occasional fast tracking	7-10 yrs	Space exposed Thermal -40°C to +65°C	Solid or liquid: Boundary lubrication with consistent torque. No contamination. Moderate to high load capacity, corrosion protection
Instrument Pointing Systems	Slow intermittent operation over small angle, very high precision	1-4 weeks 5 yrs storage	Space exposed Thermal -20°C to +60°C	Liquid: Boundary lubrication with low and consistent torque. No contamination. High load capacity, corrosion protection
De-Spin Mechanism	Continuous operation at 15-60 rpm.	7-10 yrs	Space exposed Thermal -40°C to +65°C	Solid or liquid, controlled quantity of oil or grease. Low and consistent torque over temperature range. Low wear rate, corrosion protection.

TABLE 1 (cont.)

APPLICATION	DUTY	LIFE	ENVIRONMENT	LUB. REQUIREMENTS
Solar Array (Hold down points and latches)	Deploy and retract	50 operations	Space exposed Thermal -60°C to -80°C Launch vibration loads	Dry. High load capability, good fretting resistance
Focussing Mechanism	Intermittant operation cycles 10000 to 100000	7-10 yrs	Space exposed Thermal 0°C to 20°C	Dry. Low and consistent friction. Absolute freedom from contamination. Low wear rate. Corrosion protected.
Filter wheels, shutters, beam splitters etc.	Intermittant operation 10.000 - 20.000 cycles	7-10 yrs	Space exposed Thermal 0°C to 20°C	Dry or liquid. Low and Abso- lute freedom from contamin- ation. Corrosion protection.
Slip rings and brushes	1) Low speed continuous	7-10 yrs	Space exposed	Dry. Low and consistent friction. Absolute freedom from contamination. Low and consistent electrical noise.
	2) High speed intermittent	7-10 yrs	Thermal -40°C to +65°C	Dry or liquid, low wear rate, low electrical noise
Gears	1) Intermittent operation 1000 Cycles	7-10 yrs in space	Space exposed Thermal -40°C to +65°C	Dry or liquid. Low and consistent-friction. No contamination
	2) Continuous operation	7-10 yrs	" " "	Dry or liquid. Low wear and low friction. No contamination

TABLE 1. (cont.)

APPLICATION	DUTY	LIFE	ENVIRONMENT	LUB. REQUIREMENTS
Rotating Scanner	Continuous operation operation at 15-60 rpm.	7-10 yrs	Space exposed Thermal -0°C - 20°C	Solid or liquid, controlled quantity of oil or grease. Low and consistent torque. Absolute freedom from contamination.
Booms	1) Deploy only	50 operations	Space exposed -40°C to +65°C	Dry: Consistent friction over temperature range
	2) Deploy and retract.	100 operations after long space stay	Space exposed Launch vibration loads	Dry: Consistent friction over temperature range and life. No contamination.
Solar Array (Hinges)	1) Deploy only	20 operations	Space exposed Thermal -60°C to +80°C	Dry. Consistent friction over temp.range.
	2) Deploy and retract.	50 operations after long space stay	Space exposed Thermal -60°C to +80°C	Dry or liquid. Consistent friction over temp.range for long life required. No contamination.
Antenna Deployment	Deploy only	20-50 operations	Space exposed Thermal -60°C to +80°C	Dry. Consistent friction over temperature range.

TABLE 2

LUBRICANTS AND BEARING DATA

LUBRICANTS

<u>Solid Lubricant</u>	<u>Cage Material</u>	<u>Method of Application</u>
PTFE film	PTFE/glass fibre/MoS ₂ composite (commercially available).	Film formed by transfer from the cage during bearing rotation.
MoS ₂	1% C/1% Cr steel (EN31), machined and ground	RF sputtered film approx. 0.5 micron thickness All bearing components sputter coated.
Pb	11% Pb tin bronze cast alloy (Commercially available)	Raceways ion-plated with lead to thickness between 0.2-0.5 μm Balls not coated

BEARING DATA

Type of bearing	angular contact
Size	20mm ID, 42mm OD
Contact angle	15°
No. of balls	10
Ball diameter	7.14mm
Ball conformity	1.14
Precision	ABEC 7 or 9
Axial preloads used	40N, 100N and 250N

Table 3. Torque Results From Bearing Tests (All Bearings Completed 2×10^6 Revs at 100-600 RPM Unless Stated).

Lubricant	Axial Preload	Range of Average torque ($\text{Nm} \times 10^{-4}$)	Range of Peak-to-peak torque ($\text{Nm} \times 10^{-4}$)	Remarks
NONE (DEGREASED)	40N	12 - 43	105 - 144	Torque failure after 1,340 revs
SPUTTERED MoS ₂	40N	6 - 10 (20 initially)	50 - 100 (up to 220 initially)	Low DC torque noise, but torque failures between 0.7 and 3.6×10^6 revs.
ION-PLATED LEAD	40N	16 - 26	80 - 150	<u>NO TORQUE FAILURES</u>
	100N	40 - 50	150 - 450	
	250N (After 100N)	100 - 180	400 - 1100	DC torque steadier than for PTFE but peak-to-peak torque (noise) greater
	250N (No run-in)	80 - 160	500 - 1300	
PTFE-COMPOSITE CAGE	40N	6 - 50	34 - 160	<u>NO TORQUE FAILURES</u>
	100N (After 40N)	10 - 60	75 - 250	
	250N (After 40/100N)	50 - 500	250 - 1050	-Stress above limit. Periods of high DC torque.
	250N (No run-in)	40 - 500	150 - 700	-Stress above limit. Initially high DC torque.

* Bearing lives with MoS₂ -sputtered film varied from 0.7 to 3×10^6 revs for films sputtered at ESTL to 3.6×10^6 revs for films from LSRH, Switzerland.

REFERENCES

1. Lansdown, A.R., "Molybdenum Disulphide Lubrication", ESRO Contractor Report CR(P)-402, (May 1974).
2. Lansdown, A.R., " Molybdenum Disulphide Lubrication, a Continuation Survey 1973-4," ESA Contractor Report CR(P)-764.
3. Lansdown, A.R., "Molybdenum Disulphide Lubrication, a Continuation Survey 1975-76", ESA Contractor Report CR(P)-1045.
4. Lansdown, A.R., "Molybdenum Disulphide Lubrication, a Continuation Survey 1977-78", ESA/TRIB/4, (February 1981).
5. Lansdown, A.R., "Molybdenum Disulphide Lubrication, a Continuation Survey 1979-80", ESA Contractor Report CR(P)-1518.
6. Spalvins, T. "Bearing Endurance Tests in Vacuum for Sputtered Molybdenum Disulphide Films". NASA TMX 3193 (1975).
7. Christy, R.I and Barnett, G.C. "Sputtered MoS₂ Lubrication System for Spacecraft Gimbal Bearings". ASLE 32nd Annual Meeting, Quebec, 1977.
8. Bergmann, E. et al., "Friction Properties of Sputtered Dichalcogenide Layers". Tribology International December 1981.
9. Stevens, K.T. and Todd, M.J. "Parametric Study of Solid Lubricant Composites as Ball Bearing Cages." Tribology Int. Oct. (1982).
10. Todd, M.J. and Robbins E.J., "Ion Plated Lead as Film Lubricant for Bearings in Vacuum". ESA Trib/l.
11. Thomas, A., Todd, M.J., Garnham, A.L., "Current Status of Lead Lubrication of Ball Bearings". Proceedings 2nd Space Tribology Workshop, ESA SP-158.

REFERENCES

12. Todd, M.J., "Lead Film Lubrication in Vacuum" ASLE Conf. on Solid Lubrication, Denver (1978).
13. Friend, G.C., Groszek, A.J., et al., "Development of New Space Lubricants". First European Space Tribology Symposium 1975. ESA SP 111.
14. "A Guide to the Writing of Process Procedures" ESA PSS 30.

Blank Page

SPACE TELESCOPE - SOLAR ARRAY
PRIMARY DEPLOYMENT MECHANISM

Donald P. Chandler and Adolph Veit
Dept. EKR Contraves AG, Zurich, Switzerland

ABSTRACT

This paper describes the requirements, the design, and the test program which has been carried out in producing the Space Telescope Solar Array (STSA) Primary Deployment Mechanisms (PDM). The PDM will be used to rotate the rolled solar array supporting boom from its launch position alongside the telescope housing, through 90° to its use position. After five years in space the array is to be re-rolled and by use of the PDM swung back to its stowed position alongside the telescope housing for capture and return to earth via the Space Shuttle.

INTRODUCTION

A Primary Deployment Mechanism powered by redundant stepper motors is developed for the primary deploy and stow operations of the Space Telescope Solar Array. The mechanism must lock the array boom in the deployed position and have the capability of releasing the boom at the end of mission for restowing before capture and earth return via the Space Shuttle. Due to a continual growth in the design load of the PDM a condition was reached where the system exhibited instabilities. At this point in the program a redesign was made introducing a planetary gear train between the motors and the primary level arms. This resulted in a very stable system allowing for even more increase in system load if required. Three flight models (two flight and one spare) were produced and successfully tested (see Fig. 1). Acceptance testing, besides ambient operational tests, included vibration and thermal vacuum tests with operational testing being included in the thermal vacuum environment.

SYSTEM REQUIREMENTS

The PDM has been developed to comply with the following basic requirements:

- withstand Shuttle launch and return operations.
- withstand a five year orbital lifetime.

- stiffness in the stowed position to be compatible with an overall first resonance frequency above 25 Hz for the complete array. Stiffness to be at least equivalent to an EI of 3.6×10^4 Nm². This requirement shall still be met after five years in orbit and return to earth.
- deploy and stow rates less than 1 deg./sec. with full deploy or stow in less than 20 minutes.
- an astronaut manual override is to be provided for in-orbit contingency operation.
- each articulation to be positively driven through its angle of rotation.
- capable of five years inactive deployed condition in space followed by correct response to restow commands. The system is to be capable of 50 operations in-orbit after the five years of inactive lifetime.
- the array boom is to be independently locked in the deployed position with release for restow by command, or manually (by astronaut) to permit array retraction.
- ground operation, powered or by hand, shall be possible using a zero-G simulator.
- command capability with either or both motors of the forms:
 - start - continue deploy
 - start - continue stow
 - stop
- redundant μ switches shall signal deployed position.
- redundant temperature measurements will be made at each PDM hinge.
- passive thermal control shall be used.
- thermal control design limits of +65°C and -40°C.
- system reliability for the first two years of operation is 0.9999 and no single point failures which will endanger telescope recovery or affect astronaut safety.

PROGRAM SEQUENCE

The principal tasks for this program were:

- interpret the system requirements and formulate several alternate solutions.
- derive a system concept through trade-off studies.
- identify areas of technological risk.
- develop a "bread-board" model with sufficient fidelity to determine and study potential problem areas.

- produce a high fidelity development model of the mechanism, an accurate dummy load and a zero-G test jig.
- perform parametric tests to determine system limitations:

In parallel with the above an intensive research program was carried out to establish a satisfactory bearing lubrication system.

Additionally, a qualification model was manufactured and successfully passed qualification level testing.

Finally, three flight level models were manufactured and each successfully passed the acceptance test program.

SYSTEM SELECTION

In selecting a suitable drive system several concepts were developed to sufficient depth to allow for a trade-off study to be carried out. The system finally selected for development consisted of redundant stepper motors driving an array support boom by a pair of primary and secondary lever arms. This system displayed redundancy with no single-point failures. Other systems investigated included worm drives, universal gear drives and a harmonic drive system.

During the progress of the development program the driven load increased until a point was reached at which the system exhibited a tendency to become unstable. At this point the specified load had reached twice the original estimated load. A further study was made which resulted in the addition of a set of planetary gears located between the motors and the lever arms. This restored system stability and the system subsequently passed all test requirements.

TECHNICAL DESCRIPTION

The PDM assembly consists of the following principal components:

1. Support Bracket
2. Boom Fork
3. Boom
4. Motors
5. Motor Housing Assembly
6. Motor Housing Support Assembly
7. Planetary Gear Assembly
8. Lever Arm System
9. Deployed Position Holding Clamps
10. Deployed Position Microswitches
11. Thermistor Installation
12. Wire Harness
13. Manual Drive System
14. Cover Plates
15. Thermal Control Provisions.

Motors

The drive motors for the PDM consist of two stepper motors. The motors are independently powered, only one motor being used in a normal operation with the second motor being provided for redundancy. The two motors are mechanically connected together in a housing with the rotors driving the primary lever arms through a planetary gear system. The stepper motor will rotate through approximately 624° in rotating the boom through approximately 90° . This operation requires about 2080 steps giving a step resolution of 0.045° (2.68 min). With a step frequency of 4 Hz the total time for deploy or stow is approximately 8.5 min. The stepper motors are powered with a nominal 360 ma $\pm 10\%$. The PDM has been successfully tested with a minimum current of 310 ma.

Motor Drive Assembly (see FIG. 2)

The stator from each stepper motor is installed into a motor housing unit and positioned with an alignment pin. Alignment between two stators is achieved by means of control screws rotating each stator to obtain a position of maximum torque. The rotors of the two motors are bolted to the shaft of the drive unit. Non-magnetic stainless steel has been used for the shaft and inner housing to minimize thermal induced loads on the bearings. The motor shaft is connected to the sun gear which in turn drives the three planetary gears. The planetary gears are mounted on a disc which replaces the short primary lever arm on one side of the motor housing. The outer or ring gear which meshes with the planetary gears is bolted to the motor housing. The disc on which the planetary gears are mounted is connected by means of a center shaft to the primary lever arm on the opposite side of the motor housing. The astronaut interface is a $7/16$ inch hex fitting designed to interface with the astronaut standard tool. For thermal control purposes thin sheet Aluminum cover plates have been added which cover both the motor assembly and secondary lever arms as well as the motor bracket assembly including the electrical connectors.

Bearing Assemblies

Two sizes of bearing were used in the design of the PDM, 50 mm and 20 mm bore angular contact bearings consisting of:

- Balls - Cemented Tungsten Carbide Steel with TiC coating in place of the standard steel balls
- Races - 52100 Steel (no surface treatment)
- Cages - Lead Bronze in place of the standard Phenolic cages

In selecting a bearing lubrication system several methods were investigated. A comprehensive test program was performed comparing lead, MOS2 and TiC, with the finally selected system being as noted above.

The bearing preloads have been defined as follows:

- Main Trunnion - Total Rigid Preload	100 N
- Secondary Lever Arm/Fork Piece - Total Flexible Spring Ring Preload	118 N
- Secondary Lever Arm/Primary Lever Arm - Lever Arm Flexible Preload	50 N each
- Stepper Motor - Motor Housing Flexible Preload	100 N
- Center Shaft - Total Flexible Spring Ring Preload	124 N
- Astronaut Interface - Rigid Mounted, No Preload	

Flexible spring rings are Nickel plated steel wavy washers. The reason for the rigid and flexible bearing system is best explained as follows:

Since the bearings themselves consist of steel and the assemblies they are built into are made of Aluminium, thermal loads are responsible for the worst case load conditions. In the specified temperature range from -55°C to 80°C the differential expansion of the bearing with respect to the surrounding Aluminium could reach values of up to 0.064 mm. Because on one hand a radial gap of 0.064 mm is not tolerable, and on the other hand, the axial load onto the bearing would be excessive if most of the differential expansion is transformed into stress, two steel interface rings are provided between the bearing races and the Aluminum parts. For the outer bearing race, the steel ring is shrunk into the Aluminum part. Concerning the inner bearing race, the Aluminum axis (required only to transfer axial load) produces a radial gap with respect to the steel bush. Thus the radial thermal expansion of the inner bearing race is independent of the radial expansion of the Aluminum axis. In order to ascertain that all bearing balls maintain contact under all possible loads (especially in a hot case, assuming a reasonable temperature gradient between the outer race and the inner one), the bearing is axially pretensioned.

Deployed Position Holding Clamps

After deployment by the PDM the array is held in the deployed position by spring loaded ball detents mounted on the ends of the primary lever arms. Because the primary and secondary lever arm center lines are aligned together in the deployed position the mechanical advantage of the drive system is maximum in this position. The spring force of the ball detent is easily overcome during the locking and unlocking operation.

Deployed Position Microswitches

Redundant single pole double throw microswitches have been incorporated to provide deployed position information to the motor power control electronics. One switch is mounted on each side of the motor housing and positioned so that when the PDM is fully deployed the primary lever arms actuate the two switches.

Manual Drive

The PDM incorporates provisions for manual operation of the PDM in the event that the power operated system fails. This manual operation has the capability of either deploying or stowing of the array. Operation of the manual drive is performed by a suited astronaut, a hex fitting being designed to interface with the astronaut wrench. The PDM can be rotated in either direction and the rate of PDM rotation can be controlled by the astronaut.

Temperature Measurements

Two thermistors are bonded to the PDM to provide in orbit information on the thermal gradients across the PDM.

Wire Harness Routing and Tie-Down Provisions (see FIG.3)

The solar array power wire bundle from the Solar Array Drive (SAD) enters the PDM through the support bracket. At the point of entry the wire bundle is separated and formed into two equal bundles. These two bundles pass under the main trunnion shaft around the outside of the motor housing and thence down the length of the boom to the Secondary Deployment Mechanism (SDM). The wire bundles are held within two recessed areas on the outside of the motor housing by metal clips. Attachment of the wire harness to the boom is accomplished by means of cable clamps.

Thermal Insulation

Three types of thermal insulation are used for the PDM. The first type consists of standard shop practice material surface finishes such as black anodizing or Alodine 1200 S. A second type of thermal provision used is high reflecting Aluminium type. A third type of thermal provision consists of high performance multilayer insulation blankets.

SYSTEM OPERATION

Launch Configuration (see FIG. 4)

The launch configuration of the PDM is known as the stowed position. In this condition the center line of the PDM boom may be displaced a maximum of 91.5° from the deployed position. The theoretical maximum displacement of the boom, or the point at which the two lever arms form a straight line, is 92.862° . Thus during launch the primary and secondary lever arms are never in a straight line and therefore act to assure no transfer of launch induced loads into the PDM motor unit. In the stowed configuration the PDM and array is restrained by two holding devices mounted on the telescope which interface with each end of the SDM.

Array Release and Deployment (see FIGS. 5 and 6)

After the space telescope is in orbit and ready for deployment the telescope mounted array holddowns are activated to release the solar array. Power is

then applied to either or both of the two PDM stepper motors, rotating the boom at a defined rate until the array reaches the deployed position. At this time the deployed position redundant microswitches signal the control electronics to stop power to the motors. In this deployed position the primary and secondary lever arm center lines are superimposed and the ball detent ensures that this position is maintained.

Array Stowage

At the end of mission the solar array is to be returned to the stowed position. This is accomplished by energizing the stepper motor to rotate in the reverse direction. Final positioning of the stowed array is done by a pull-down device mounted on the telescope and interfacing with the SDM.

SYSTEM MASS

The measured mass of the delivered units is approximately 19.75 kgm.

TEST PROGRAM

During the PDM program three types of tests were carried out: development, qualification and acceptance.

Development tests included:

Bearings

In parallel with the PDM mechanism development program a separate program was initiated to develop a suitable bearing lubrication system. Existing solid lubrication systems proved to be unsatisfactory. Use of oil base lubricants were not seriously considered because of the strict sealing requirements imposed with the use of voltaile materials. A research program was carried out resulting in a bearing system consisting of standard SNFA SEB 20 and EB 50 bearings modified in the following ways:

- the phenolic cages have been replaced with lead bronze cages
- the steel balls have been replaced with cemented carbide balls with a Titanium Carbide (TiC) coating.

Life tests of the bearing systems proved satisfactory and subsequently passed all system tests with no problems.

NOTE: For the lubrication of gears within the PDM the E-metal process has been applied. This is an electrolytic process for Aluminium alloys which produces a hard protective surface on the gear teeth so that in this application no additional lubrication is required.

PDM (see FIG. 7)

During the development of the PDM a significant problem was the steady growth of the specified load. As each new load was imposed a series of operational tests was performed to re-establish system performance margins. The initial specified load was $480 \text{ m}^2 \text{ kg}$ for which the initial design was very adequate. Mid-way through the program this load had increased to $821 \text{ m}^2 \text{ kg}$. The system still functioned but with no margin of safety. A redesign was completed adding a planetary gear train between the motors and the primary lever arms. No discrepancies (instabilities, missing steps etc.) occurred during operation with the following inputs:

- input current 200 to 488 mA
- supply voltage 12 to 28 V
- motor step frequency 2.6 to 10 Hz

QUALIFICATION AND ACCEPTANCE TESTS

Qualification and acceptance level tests were successfully carried out in the sequence shown below:

- bearing system (4 pairs 5000 cycles with maximum allowed torque = 0.08 Nm and maximum measured torque of 0.0095 Nm)
- ambient functional and static load test
- vibration (sine-random-sine in each of the three axes)
- ambient functional
- thermal vacuum and accelerated life test
- ambient functional
- electrical bonding
- mass and center of gravity measurements.

For the thermal vacuum tests the flight configuration boom was replaced with a stub boom (zero-G condition) to accommodate the system to the limited space within the thermal vacuum chamber.

BLANK

PAGE

47

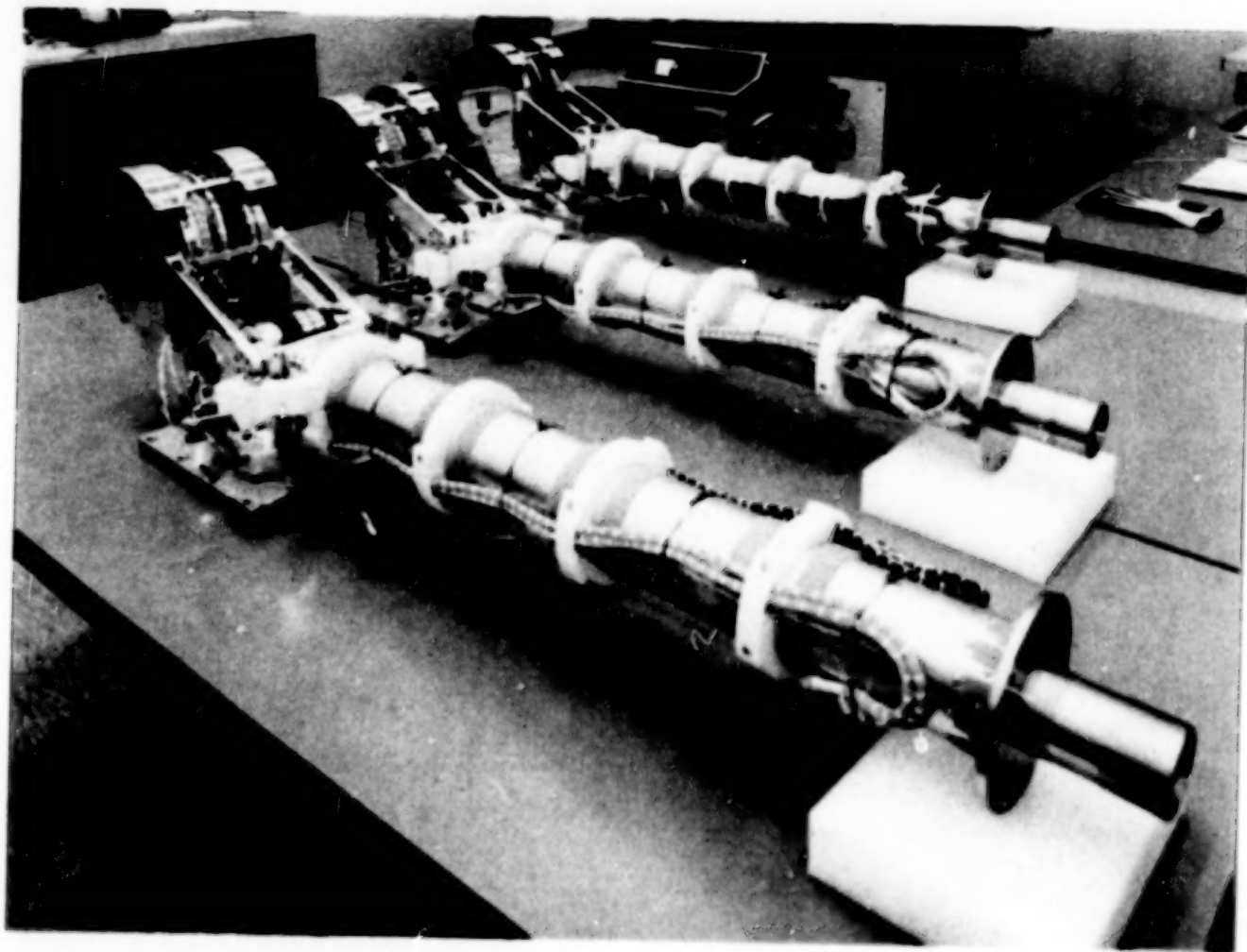


FIG. 1: Two Flight and One Spare Models - Ready for Delivery

47

BEST AVAILABLE COPY

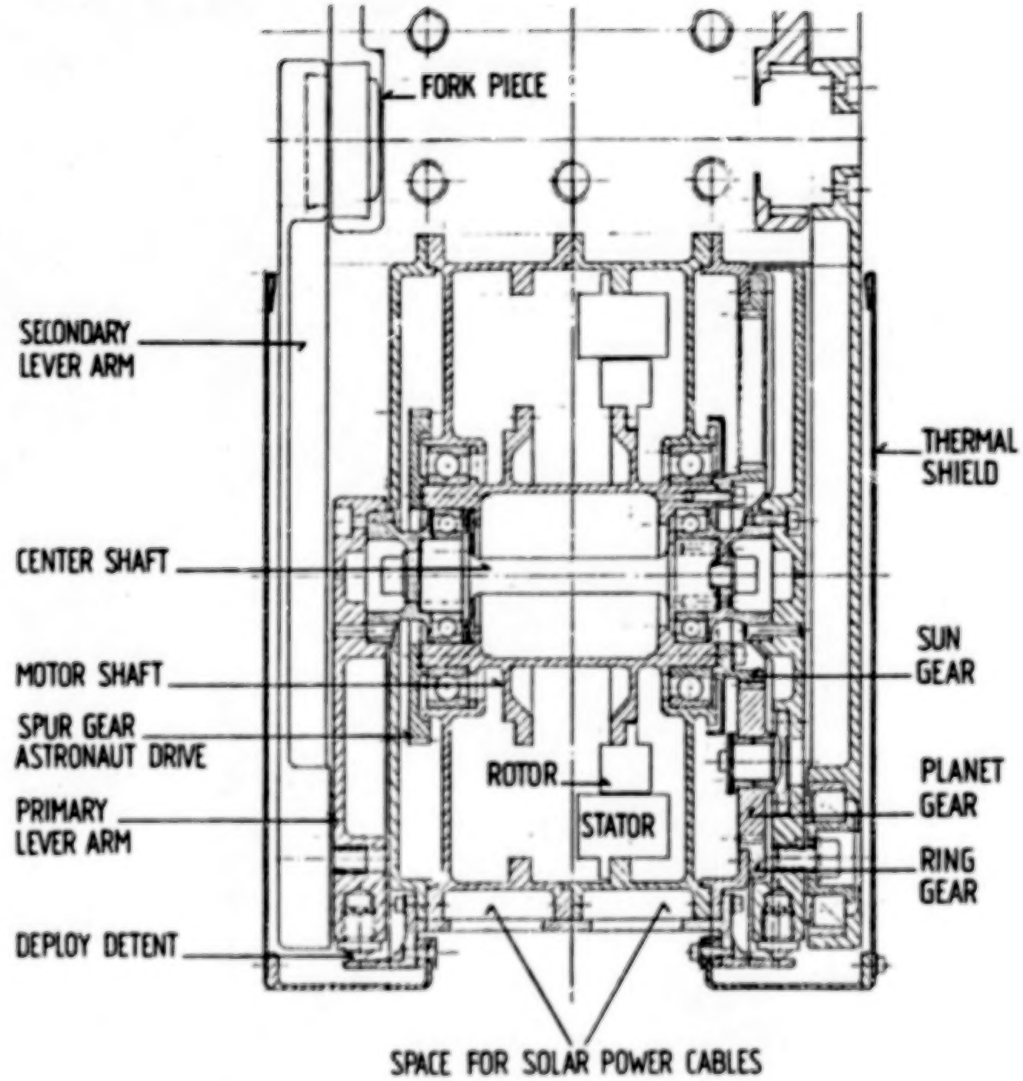


FIG. 2:

MOTOR DRIVE ASSEMBLY (DETAIL)

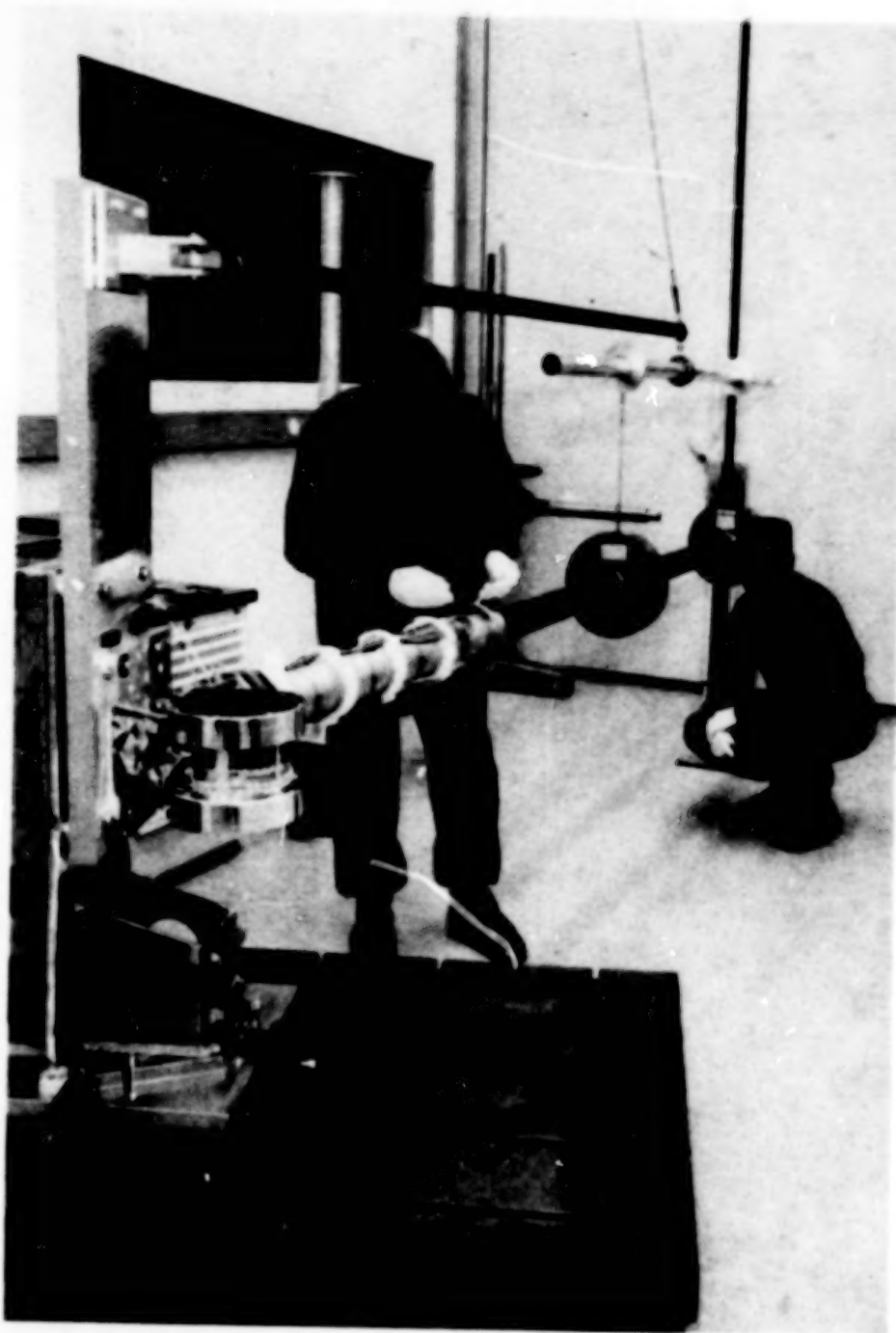


FIG. 3: Installing Dummy Load with PDM Mounted in Zero-G Test Stand

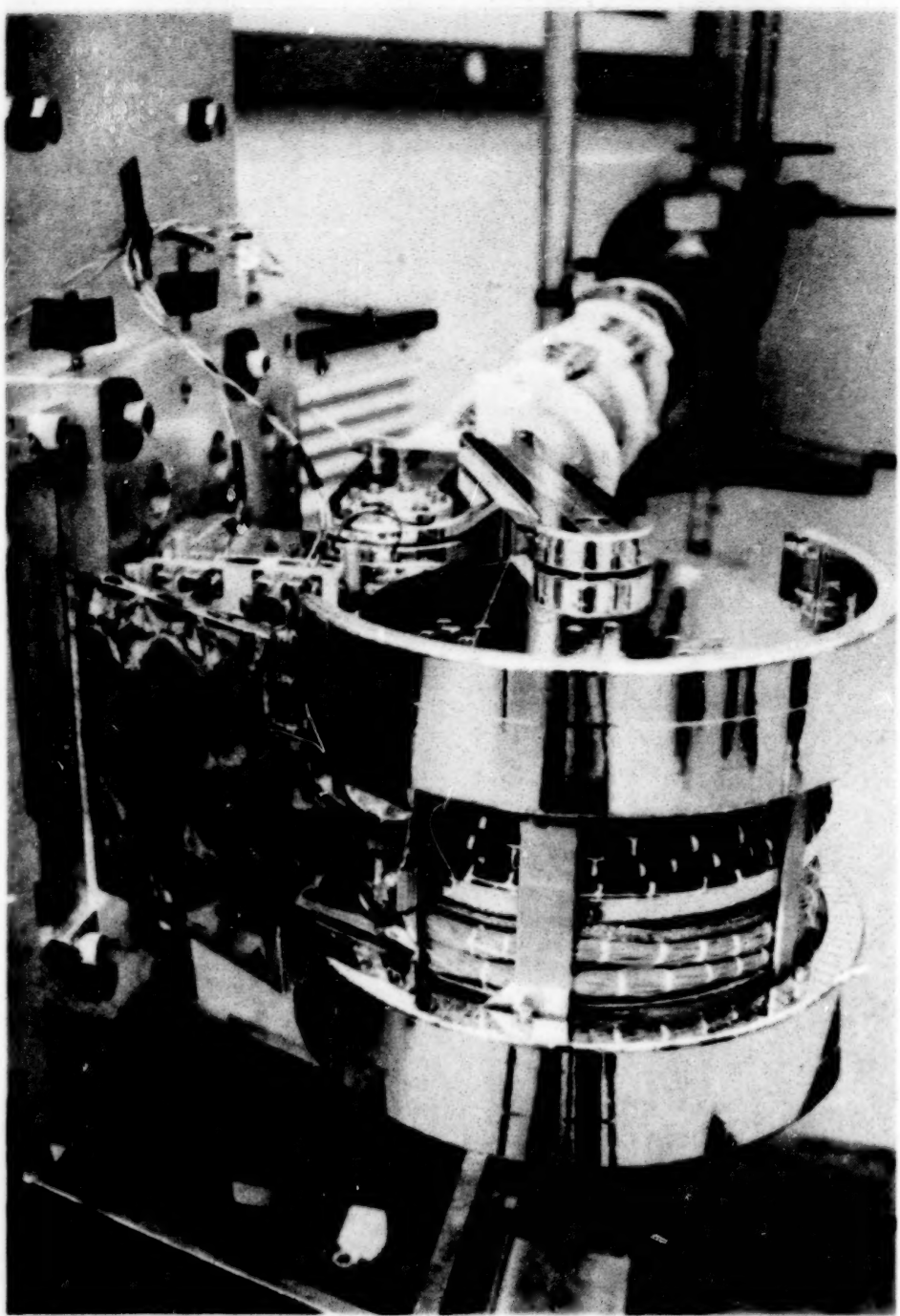


FIG. 4: PDM in Stowed Position in Test Stand
(Launch Configuration)

BLANK

PAGE

51

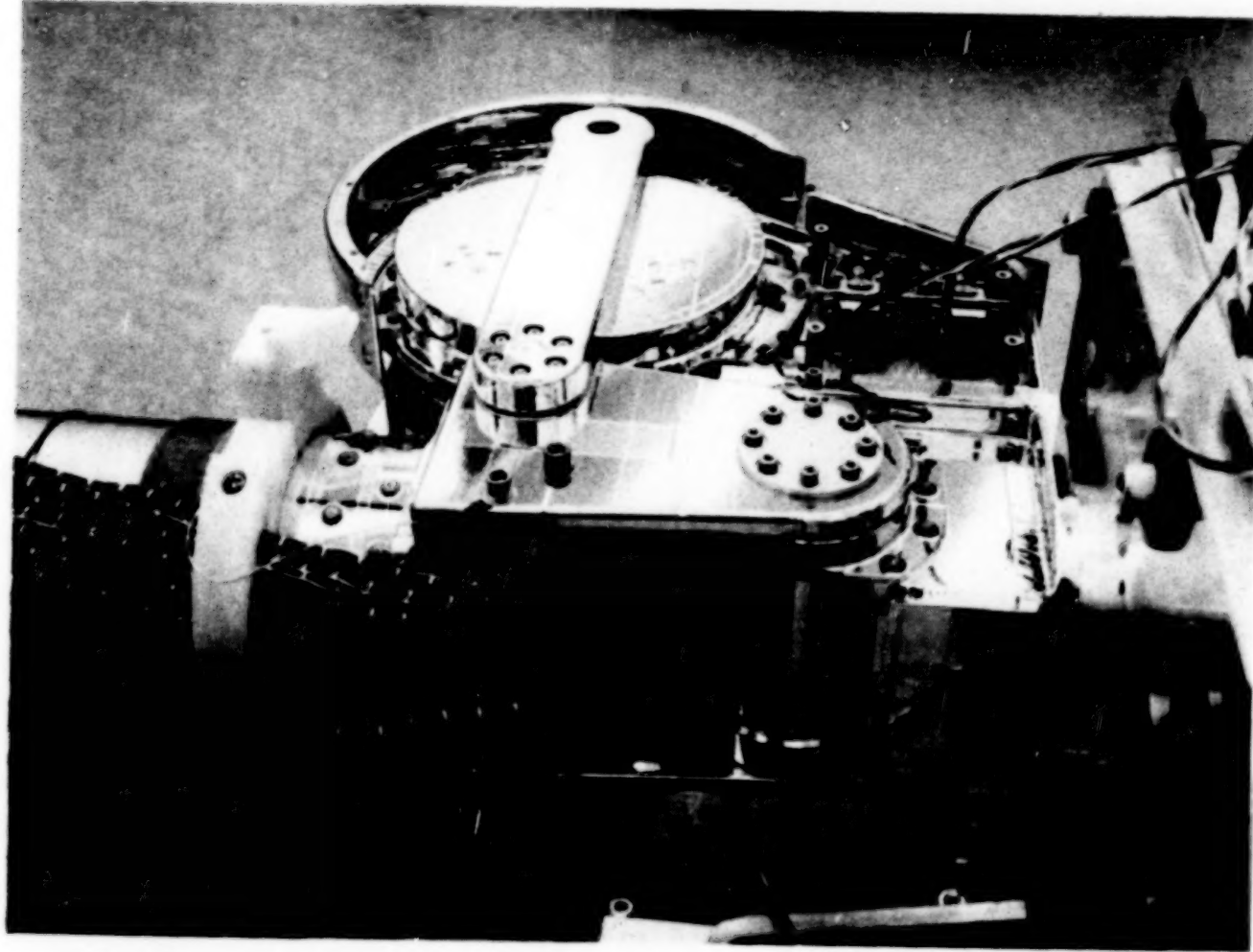


FIG. 5: PDM in Deployed Position

52

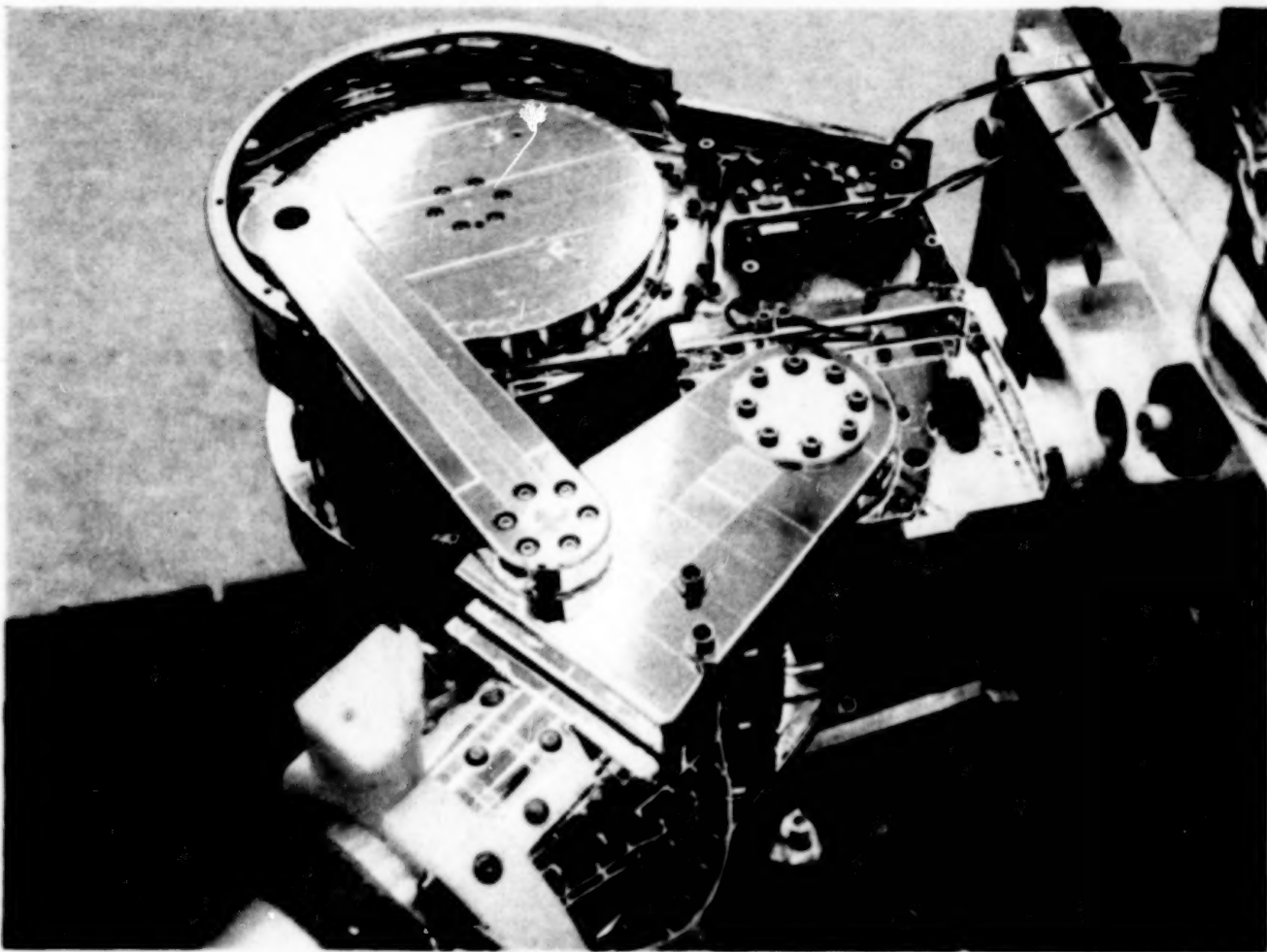


FIG. 6: PDM at Half-Way Position

52

BEST AVAILABLE COPY

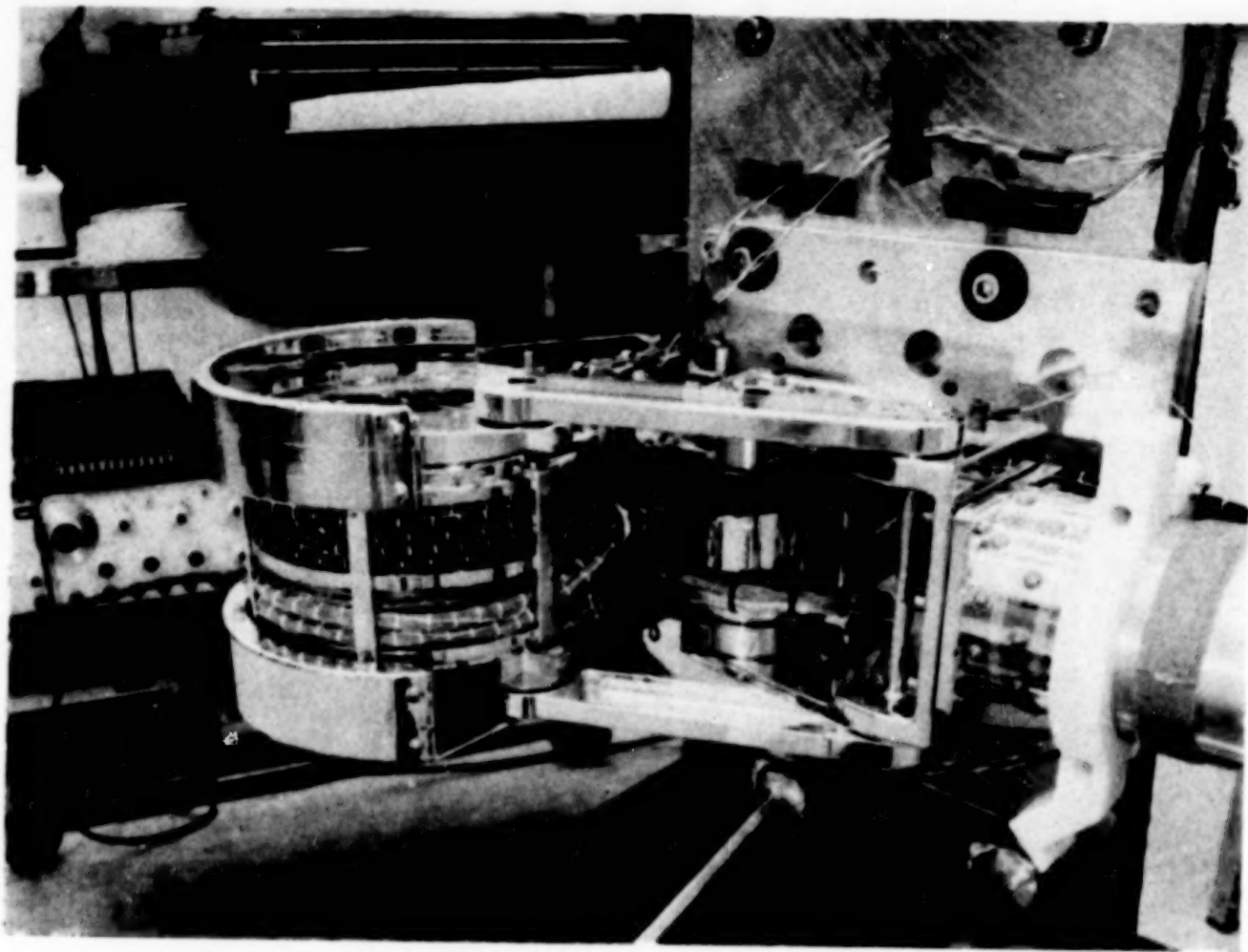


FIG. 7: PDM During Acceptance Test - Note Wire Harness Routing

Blank page

A Broadbased Actuator Concept for Spaceflight Application

James C. Hammond*

ABSTRACT

A recently developed electromechanical actuator has been found to be applicable to a variety of spaceflight requirements. Characterized by high torque and a small output step angle, the device is comprised of a coaxial, symmetrical arrangement in which a cup-type harmonic drive is directly coupled to a pancake configuration drive motor. The motor, with its dual stator driving a common rotor, is one illustration of the concept of Selective Redundancy.

Selective Redundancy promotes the idea that redundancy, to be effective, must not compromise inherent design simplicity nor introduce new failure modes.

The usefulness of the actuator is exemplified by its selection for a broad range of positioning and driving applications including TDRSS Gimbal Drives, Space Telescope deployment and latching mechanisms, and Space Telescope secondary mirror drive, as well as others.

INTRODUCTION

A rotary actuator, broadly applicable to spaceflight service because of its high performance, adaptability, and high reliability, has been developed. The device, which is producible in a range of sizes, derives reliability from its inherent simplicity. Further increases in reliability are achieved by the inclusion of selected redundant features. However, redundancy is used only in those areas where the design is not compromised by the incorporation of those additional features.

Actuators of this type have been employed on a number of spaceflight programs. Details of some of these applications are briefly discussed.

THE ROTARY INCREMENTAL ACTUATOR

The rotary incremental actuator is based on an evolutionary design which was first produced more than ten years ago and has since grown into a family of standard actuators. These are currently being produced in various forms by Schaeffer Magnetics under the designation Rotary Incremental Actuator, Types 1 through 7.

*Schaeffer Magnetics, Inc., Chatsworth, California

Concept

Figure 1 shows a sectional view of that first actuator as produced for the Pioneer 10 planetary probe in 1970. Viewed as state-of-the-art at the time, it illustrates the design thinking of that period.

The device, functioning as a telescope positioner, is required to have a small, accurate step and the ability to hold position with power off. A variable reluctance stepper motor (15 degree step) is used, and initial gear reduction is effected by means of spur gearing, thus minimizing inertia reflected to the motor. On the second shaft is a mechanical detenting device to provide position holding, since the VR motor lacks detent torque. Also fitted to this shaft are a shaft angle encoder and a mechanical damper to assist in controlling step-and-settle time.

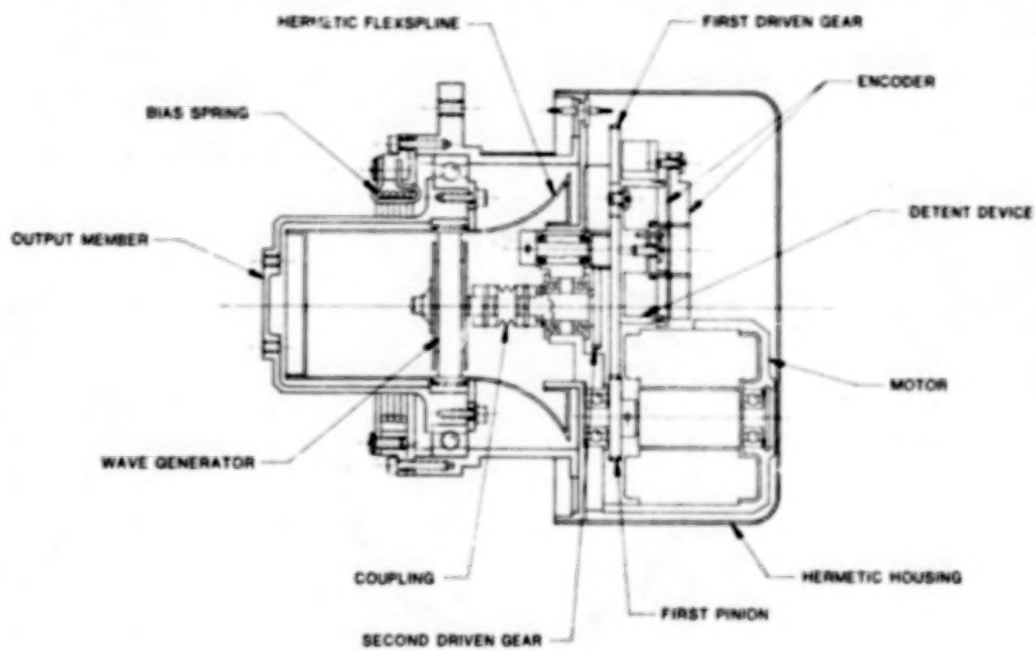
This assembly illustrates an early application of the harmonic drive speed reducer to spaceflight hardware. (Harmonic drive is a proprietary product of the Harmonic Drive Division of USM Corp., Wakefield, Mass.) Its operating principle is shown in Figure 3. Briefly, the device uses a rotating elliptical element (the wave generator) to produce rhythmic deformation of a toothed elastic member (the flexspline) reacting against a toothed reaction member (the circular spline). Differing tooth numbers on the meshing elements produce reduced output motion with corresponding multiplication of torque. Ratios between about 60:1 and 200:1 can be achieved in a single pass with harmonic drive.

After a second pass of spur gearing, power flow in the device of Figure 1 is through a flexible coupling to the harmonic drive wave generator. The Harmonic drive, reflecting the thinking of that period, is hermetically sealed, in turn requiring its flexspline to be grounded against rotation. A large torsion spring provides bias torque to improve positioning accuracy.

After 11 years, these actuators continue to operate on board Pioneer 10 and 11, now near the orbit of Uranus almost two billion miles from earth. That early design embodies some attractive characteristics:

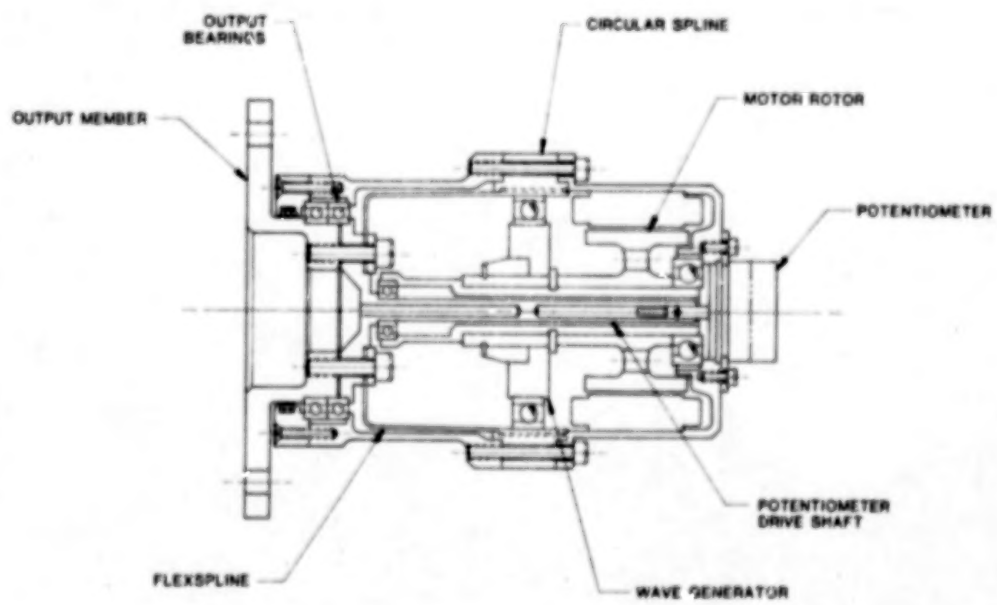
- o Small output step
- o Good positional accuracy
- o High torsional stiffness
- o Unpowered holding torque

But it also displays some not-so-attractive characteristics. First is complexity, with the attendant negative impact of high cost and reduced reliability.



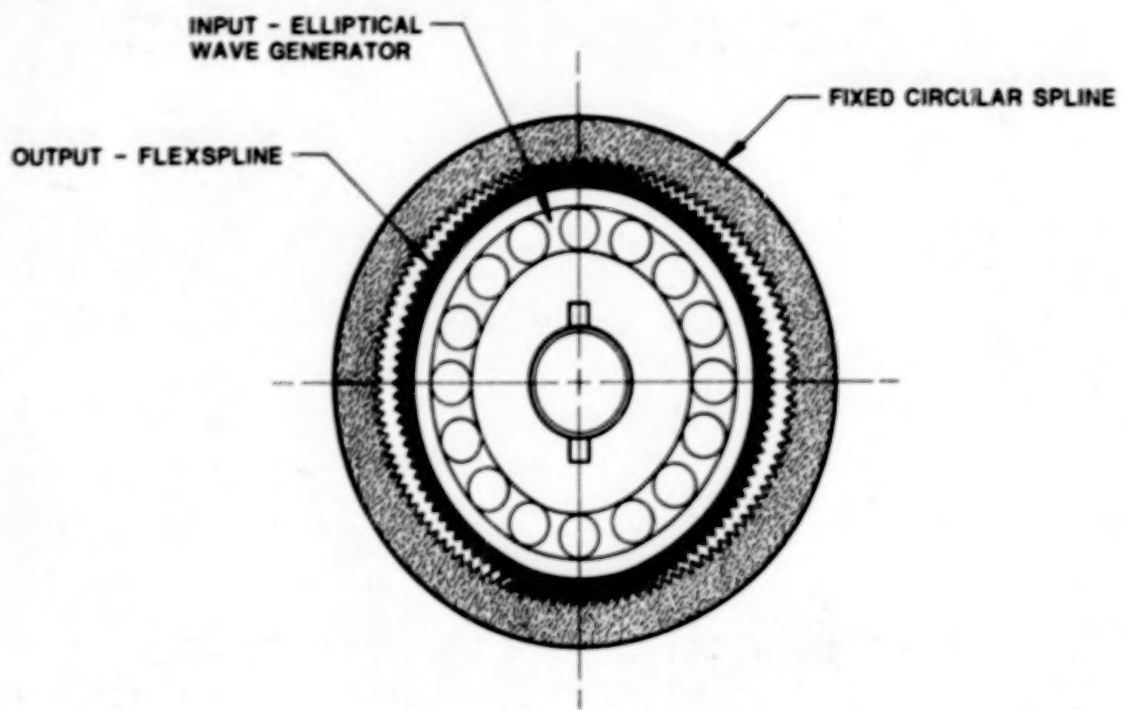
PIONEER II TELESCOPE DRIVE - 1970

FIG. 1



ANTENNA POSITIONER - 1977

FIG. 2



HARMONIC DRIVE PRINCIPLE

Rotation of the elliptical wave generator results in a greatly reduced motion at the toothed output members due to differential action between teeth on flex spline and circular spine.

FIG. 3

A more up-to-date design is depicted in Figure 2. Still based on harmonic drive, its function is the same as the early unit. But a number of changes are evident:

- o Spur gearing eliminated
- o No detent device or auxiliary damper required
- o Output self-supporting and load-capable
- o Non-hermetic

These changes are made possible by the use of a small-angle permanent magnet stepper motor to power the actuator, and by the availability of low-vapor pressure liquid lubricants. Parts count has been reduced sharply, with no loss of performance.

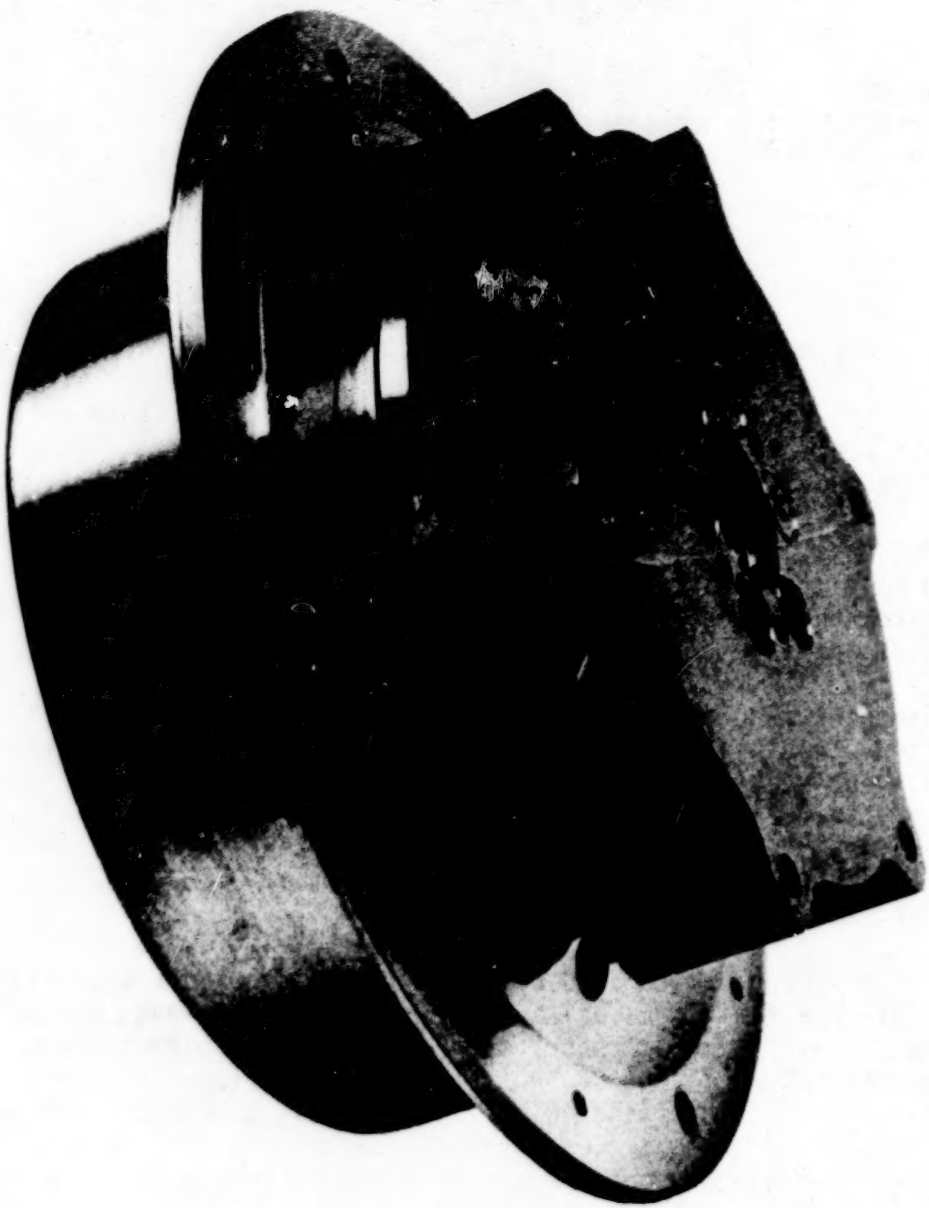
Quickly made obsolete by an even more advanced design, this unit never reached the 'production' stage. It is, however, viewed as the turning point in the design evolution of the product as it is known today. That rotary incremental actuator is seen in Figure 4.

The concept is detailed in the sectional view of Figure 5. It consists of a larger permanent magnet stepping motor, tightly integrated with the harmonic drive, and a larger rotating output flange.

The permanent magnet stepper motor is a unique design. It features a multi-toothed structure with a small step angle and a rotor magnetic structure that is inherently annular in configuration. Because of the small step angle and the use of samarium cobalt magnets, the motor is capable of directly driving considerable inertial loads. This characteristic is exploited by driving the rather large harmonic drive input member directly. Spur gear pre-reduction stages are not necessary.

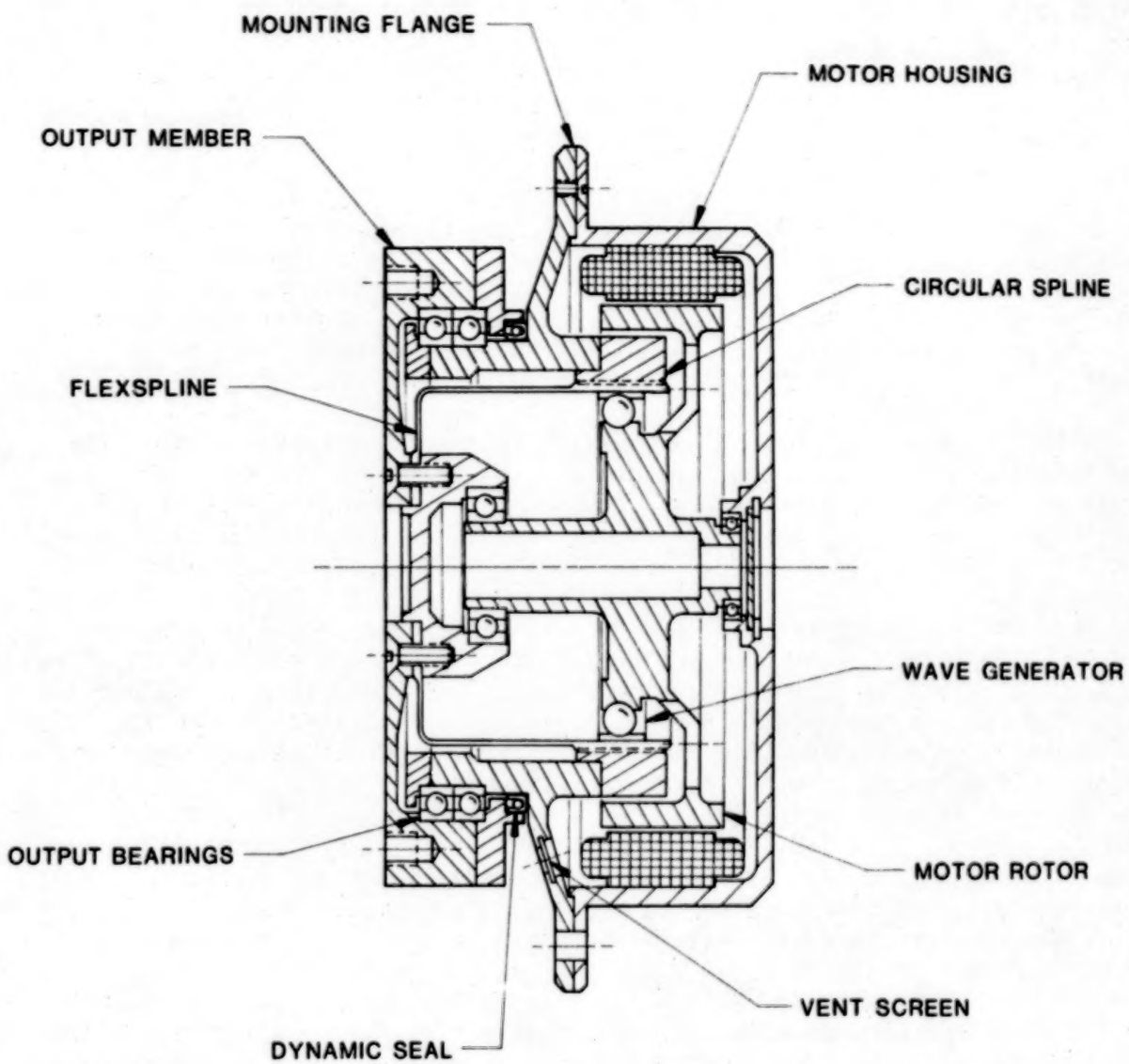
The device employs a standard cup-type harmonic drive rather than a hermetic unit or a flat "pancake" type. The elliptical wave generator is driven directly by the motor rotor, and the flexspline output member is attached to the output flange of the actuator. The circular spline reaction member is attached to the frame of the unit. This is the most common speed reduction mode of harmonic drive -- a large reduction ratio and reversed rotation is achieved. The motor rotor is sized so that it envelops the circular spline at its outer periphery.

The motor drives the harmonic drive wave generator through a flexible coupling. The coupling now is of the Oldham type. It offers adequate radial accommodation, with much higher torsional stiffness than a bellows or similar type of coupling. The coupling allows for slight lateral movements of the rotor and wave generator, which are due to the slight but unavoidable eccentricities created by the wave generator. This feature enables the wave generator to be self-centering within the flexspline and the circular spline.



**TYPE 5
ROTARY INCREMENTAL ACTUATOR - 1983**

FIG. 4



ROTARY INCREMENTAL ACTUATOR

FIG. 5

The output member is large, consistent with the performance capability of the device. The large, duplexed output bearings allow this part to be nested over the cup-type flex spline. The duplex bearing pair offers good rigidity as well as high load capability; so that large cross-axis moments can be resisted. A further benefit of this geometry is the high degree of structural integrity afforded to internal members of the device.

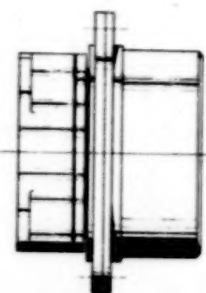
Key features offered by this arrangement can be cited as (a) a very low parts count, (b) relatively open internal structure having few tight clearances, and; (c) because of motor design, a device having no high speed shafts. Additionally, a short load path to ground is afforded for the moments imposed on the output member by overhung loads, and a similarly short thermal path to ground is provided for the flow of dissipated heat from the motor stator.

Although aerospace quality harmonic drive component sets are used, they are standard sizes. Figure 6 illustrates, in relative proportion, the size progression of devices from the Type 1 which uses a harmonic drive of 2.5 cm (1 in.) pitch diameter, to the Type 7 which uses the 2M harmonic drive component set.

The actuator described here is the most basic form of the device. A number of variations have been produced to meet different requirements. One common difference is in the size of the output bearings. Figure 7 shows a basic Type 5 unit, and Figure 8 shows the same unit adapted to withstand very large overhung loads. In this case, the outside diameter is increased at the frame to accommodate a larger pair of duplex bearings. The oversize bearings and seal are located on the output member where the torque level is very high. In Figure 9, a Type 2 unit with output bearings of reduced size is shown. Because this unit is designed for a pure torque output, the overhung load capability of the large duplex bearing pair is not needed. In this way, for a slight increase in the axial length of the unit, considerable weight is saved.

Figure 10 shows another embodiment, this one having an eccentric ball on the output flange, yielding rectilinear output motion. It also has feedback devices on the motor shaft as well as the output shaft.

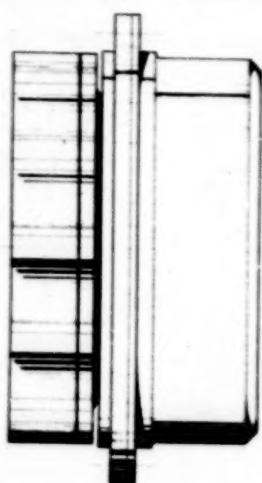
A feature of the arrangement, of particular interest because of its impact on reliability, is the inclusion of redundant elements. The design in Figure 10 has redundant motor stators, redundant potentiometers, and redundant shaft angle encoders. Other components of the actuator assembly are not duplicated. They are of essentially the same size and design as in a similar basic device. Redundant design has a far reaching impact on performance as well as reliability of these units; and because of this, the philosophy of redundancy is given special attention.



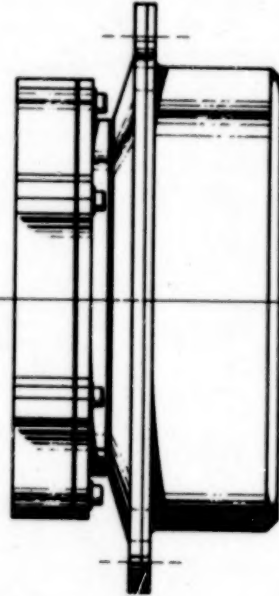
TYPE 1



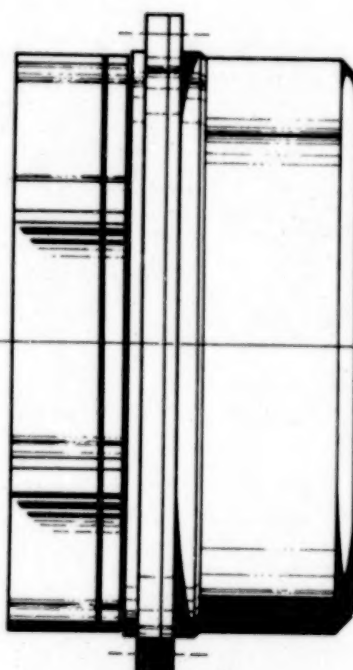
TYPE 2



TYPE 3



TYPE 5



TYPE 6

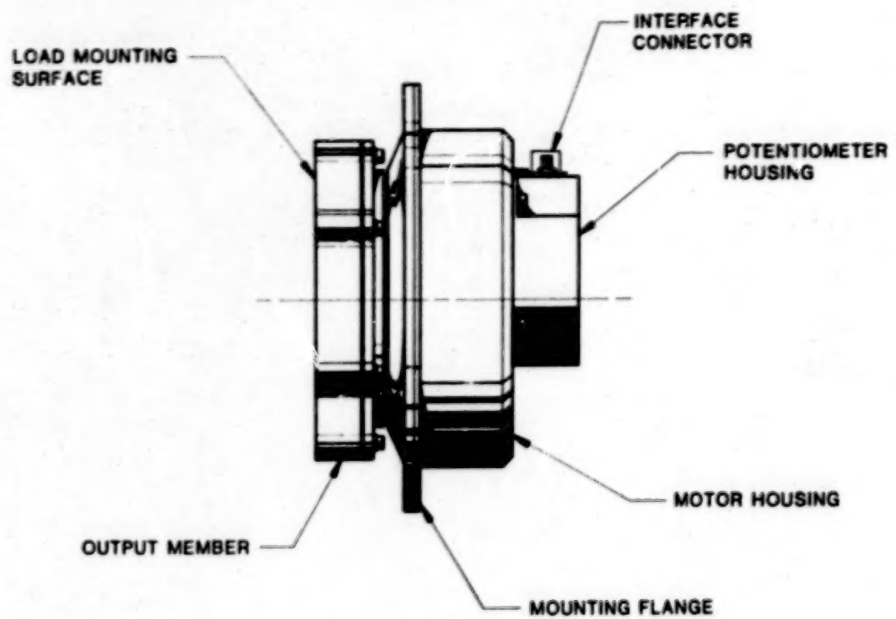


TYPE 7



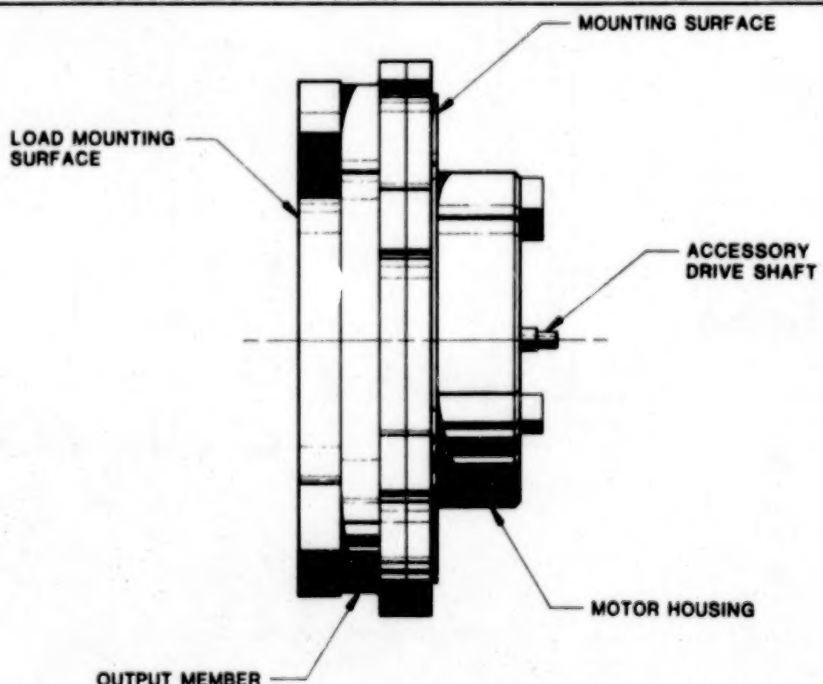
ROTARY INCREMENTAL ACTUATOR FAMILY

FIG. 6



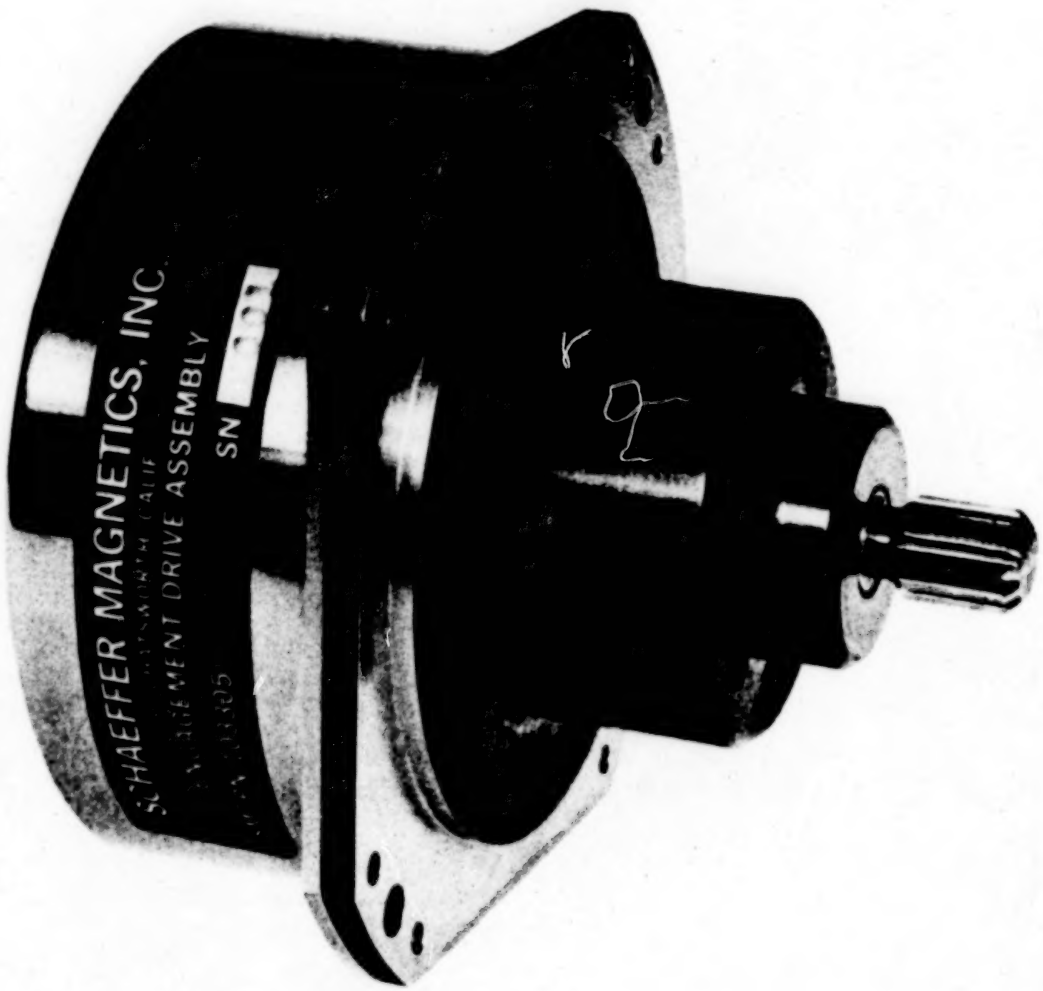
TYPE 5 ACTUATOR

FIG. 7



CONSTRUCTIONAL VARIATION

FIG. 8



TYPE 2 UNIT WITH OUTPUT BEARINGS OF REDUCED SIZE

FIG. 9



**TYPE 5 UNIT WITH ROTOR AND OUTPUT
ANGULAR POSITION FEEDBACK**

FIG. 10

Selective Redundancy

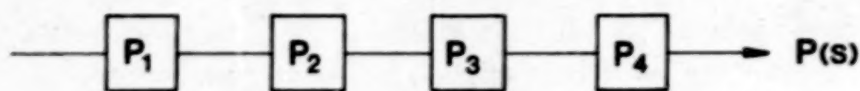
Selective Redundancy is a term aptly applied to the concept of redundancy as used in the design of this rotary incremental actuator family. Although the term may be new, the concept is not. One illustration can be seen in the frequent requirement for 'no system single point failure modes.' But, the attempt to totally avoid such failure modes can easily lead the designer to an arrangement of parts which in the end is distinguished more by its complexity than by its reliability. In devices where the design is aimed at full redundancy, there is almost always the tendency toward an increased parts count.

There are at least two provocative questions that should be asked before the concept of 'reliability via redundancy' is applied: (1) are the relative failure rates and the point of load convergence such that a worthwhile numerical reliability gain is realized? and (2) does the satisfaction of the 'no single point failure mode' requirement lead to the creation of a redundant load path that, in itself, is more prone to fail, thus further compounding the need for a back-up path?

A reliability block diagram of the basic elements of the actuator is shown in Figure 11. P1 represents the reliability of the motor stator, which is the only electrical part present. P2 represents the reliability of the motor rotor, P3 the reliability of the harmonic drive, and P4 the reliability of the output stage of the device. P4 is the output element through which the load is driven.

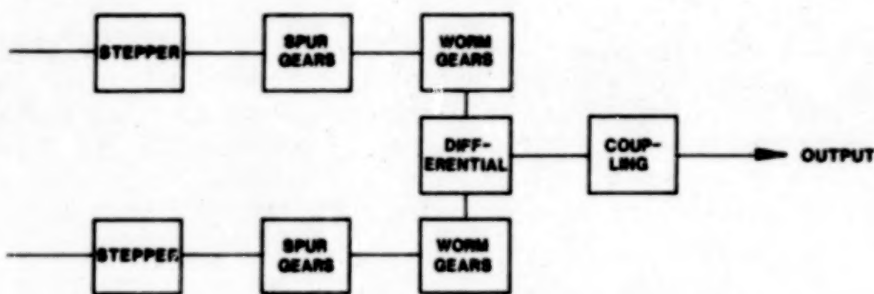
In contrast, a unit designed to be completely redundant is shown diagrammatically in Figure 12. This device was designed by Schaeffer; several have been flown. It uses independent large-angle steppers with spur pregearing and dual worm gear input to a differential, with output taken from the differential spider gear carrier. Actually, this design has many more parts than the newer rotary actuator; but for purposes of comparison it will be assumed that its parts count could be reduced. Here all of the elements P1 through P4 are duplicated in two parallel paths. P5 represents the reliability of the parts required to achieve the switching of mechanical power when a change from one parallel path to the other occurs (the differential spider gears). This branching element is not duplicated, because it appears in the output load path.

Actuators represented by both of these reliability diagrams have been successfully used in orbit, and neither has suffered failure. A further comparison on the basis of performance is as follows:

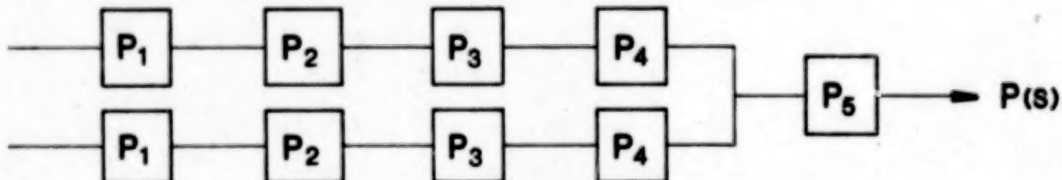


RELIABILITY BLOCK DIAGRAM - BASIC ACTUATOR

FIG. 11



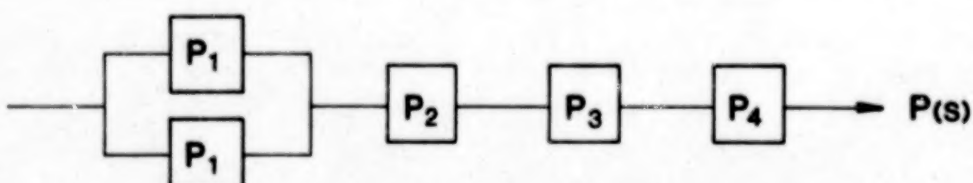
(A) MECHANICAL BLOCK DIAGRAM



(B) RELIABILITY DIAGRAM

REDUNDANT SYSTEM

FIG. 12



RELIABILITY BLOCK DIAGRAM - SELECTIVELY REDUNDANT

FIG. 13

	<u>Redundant Device</u>	<u>Rotary Incremental Actuator</u>
o Output Torque	5.1 nt.m (45 lb-in)	84.8 nt.m (50 lb-in)
o Weight	5 kg. (11 lb.)	1.8 Kg. (4 lb.)
o Output Step	.025 deg.	.0075 deg.
o Assembly Man Hours	T	T/3
o Backlash	30 arc min.	Nil

What this comparison appears to show is that redundant design can have a significant price. Its effect on predicted numerical reliability is powerful, however; and it would be desirable to reap the benefits of redundancy without compromising the inherent simplicity of a device like the rotary incremental actuator.

The reliability diagram of Figure 13 illustrates schematically how this has been done. Major components of the device have about the same failure rate. However, external drive circuitry is associated with the stator, and since electronic components in general have higher failure rates than mechanical components, there is good reason to want redundant motors (redundant motors allow redundant drivers). Although driver electronics are external to the actuator, reliability is ultimately a system concern; and system considerations make two independent electrical systems highly desirable. Therefore, provision of stator redundancy significantly increases system reliability, since additional mechanical elements are not required to effect the transfer of power from one path to the other. Figure 13 shows this concept applied to the actuator. Here only the motor stator is reproduced in a parallel path.

For purposes of illustration, it is assumed that failure rates for components 1, 2, 3 and 4 are identical while the failure rate of component 5 (mechanical switching means) is two times that failure rate. (If component 5 were an active electromechanical device such as a clutch, its failure rate might be higher than that of other components by as much as 7X). When system reliabilities are computed (all for the same mission time) the three approaches illustrated above can be compared. Figure 14 shows calculated reliabilities based on the reliability models (1). Here it can be seen that the fully redundant approach produces an increase in system reliability over that of the basic unit. But, Selective Redundancy is seen to produce a result nearly as good. This is largely an effect of the simplicity of the system. The hazard posed by the additional element P5 is large compared to the gains that can be made by paralleling elements, because there are relatively few elements to begin with.

$$\lambda = 20 \times 10^{-9} \text{ f per hr. (typical)}$$

$$t = 156 \text{ hr. oper. time (typical)}$$

$$\text{Then } \lambda t = 3.12 \times 10^{-6}$$

1. Basic System:

$$\begin{aligned} P(s) &= e^{-\lambda t} \cdot e^{-\lambda t} \cdot e^{-\lambda t} \cdot e^{-\lambda t} \\ &= e^{-4 \lambda t} \\ &= .9999875 \end{aligned}$$

2. Full Redundancy:

$$\begin{aligned} P(s) &= (e^{-4 \lambda t} + 4 \lambda t e^{-4 \lambda t}) e^{-2 \lambda t} \\ &= (1 + 4 \lambda t) e^{-6 \lambda t} \\ &= .9999938 \end{aligned}$$

3. Selective Redundancy

$$\begin{aligned} P(s) &= (e^{-\lambda t} + \lambda t e^{-\lambda t}) e^{-3 \lambda t} \\ &= (1 + \lambda t) e^{-4 \lambda t} \\ &= .9999906 \end{aligned}$$

CALCULATED NUMERICAL RELIABILITIES

FIG. 14

It should also be noted that those design compromises required to package redundant mechanical components within a given space and weight limit will in many cases result in the degradation of individual part reliabilities (P2, P3, P4). Like the addition of new failure modes, this is not demonstrably significant in terms of numerical prediction. The trend is in the wrong direction, however, and is a further argument in support of Selective Redundancy.

This analysis is intended to show numerically that the concept of Selective Redundancy is an effective way to achieve system reliability when applied to devices of the size and scope of these rotary incremental actuators. Selective Redundancy does not entail poorly defined risks and combinatorial failure modes, and is an especially effective approach when other requirements are considered together with reliability.

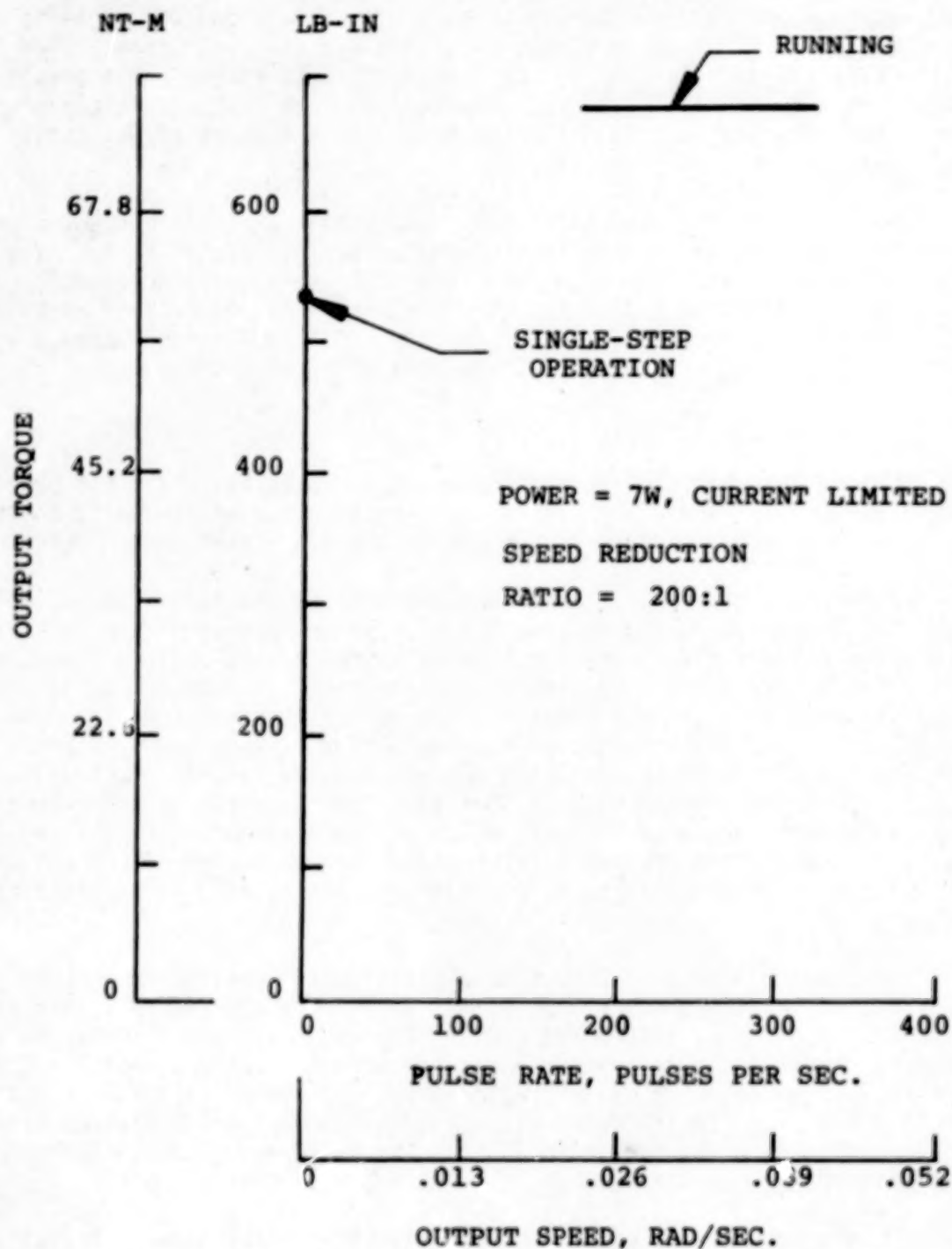
Performance and Testing

Applications of the Rotary Incremental Actuator fall into two broad categories: positioning and driving. Construction of the units and the provision of accessories and other design details varies accordingly.

Performance of a Type 5 unit in a driving application is shown in Figure 15. The torque-speed characteristic curve shown here is of typical shape. Since the devices have a characteristically small step angle at the motor rotor and a moderately high speed reduction ratio (100 to 200 to 1) the speeds achieved are not extremely high. Torque output is high, however. The curve shows torque available for start-stop operation. Higher angular rates can be achieved in slew mode operation in which the pulse rate is started low and ramped up to the operating rate. Not shown by the curve is the unpowered or passive detent torque of the unit which all such permanent magnet devices have. Unpowered and powered driving torque can be traded off to optimize the unit for specific applications, depending on the relative importance of holding torque.

Performance of a Type 5 unit in a positioning application is shown in Figure 16. In this test, groups of 400 steps were applied to a unit having an output step angle of .00013 rad (.0075 degrees), to produce .0524 rad, (3 degree) nominal displacements. Actual measured output positions of the unit are shown together with calculated errors. The typical error is on the order of 73×10^{-3} rad (15 arc seconds). Errors shown primarily reflect harmonic drive positioning accuracy, since motor positioning accuracy is greatly demagnified and the harmonic drive is essentially free of backlash.

Stepper motors as a class are sensitive to the inertia of the driven load. The permanent magnet stepper used in the Type 5 actuator, however, is somewhat less inertia-sensitive, due primarily to the large air gap radius and small step increment. Torque-to-inertia ratio at the motor rotor is greater than with a conventional large angle stepper, and peak kinetic energy of the rotor during stepping is less. Figure 17 shows a large inertia thermal vacuum load test facility. The shaft extending vertically from the vacuum chamber



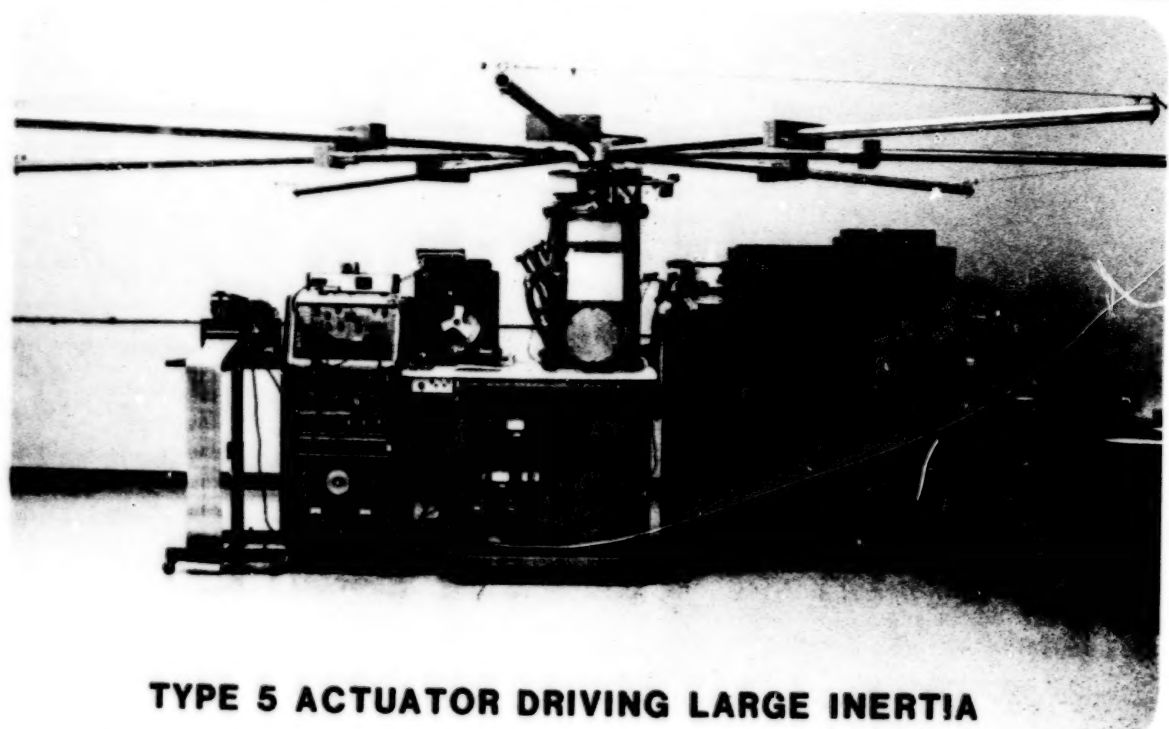
TYPE 5 ACTUATOR PERFORMANCE

FIG. 15

TOTAL STEPS	THEORETICAL POSITION DEGREES	TABLE POSITION DEG, MIN, SEC	POS. ERROR MIN, SEC
0	0	0	0
400	3.00	2 59 34	-26"
800	6.00	5 59 40	-20"
1200	9.00	9 0 16	+16"
1600	12.00	11 59 46	-14"
2000	15.00	14 59 50	-10"
2400	18.00	18 0 12	+12"
2800	21.00	20 59 30	-30"
3200	24.00	24 0 0	0
3600	27.00	27 0 14	+14"
4000	30.00	29 59 42	-18"
4400	33.00	33 0 0	0
4800	36.00	36 0 8	+8"
5200	39.00	38 59 50	-10"
5600	42.00	42 0 0	0
6000	45.00	45 0 10	+10"
6400	48.00	47 59 54	-6"
6800	51.00	51 0 0	0
7200	54.00	54 0 18	+18"
7600	57.00	56 59 46	-14"
8000	60.00	60 0 12	+12"
8400	63.00	63 0 12	+12"
8800	66.00	65 59 44	-16"
9200	69.00	69 0 4	+4"
9600	72.00	72 0 18	+18"

TYPE 5 ACTUATOR POSITIONING ACCURACY

FIG. 16



TYPE 5 ACTUATOR DRIVING LARGE INERTIA

FIG. 17



TYPE 1 ACTUATOR

FIG. 18

can be fitted with a number of inertial masses on the radial arms, to achieve inertias well in excess of 1356 kg.m^2 (1000 slug ft^2). The illustration shows an inertia of 474 kg.m^2 (350 slug ft^2) being driven by a Type 5 actuator under test mounted inside the chamber. The unit will reproducibly start and stop the inertia, at $0.039 \text{ rad per sec.}$ ($300 \text{ pulses per sec.}$), and with a ramped pulse rate can drive the inertia at angular rates up to 0.17 rad per sec ($1300 \text{ pulses per second}$).

APPLICATIONS OF THE ROTARY INCREMENTAL ACTUATOR

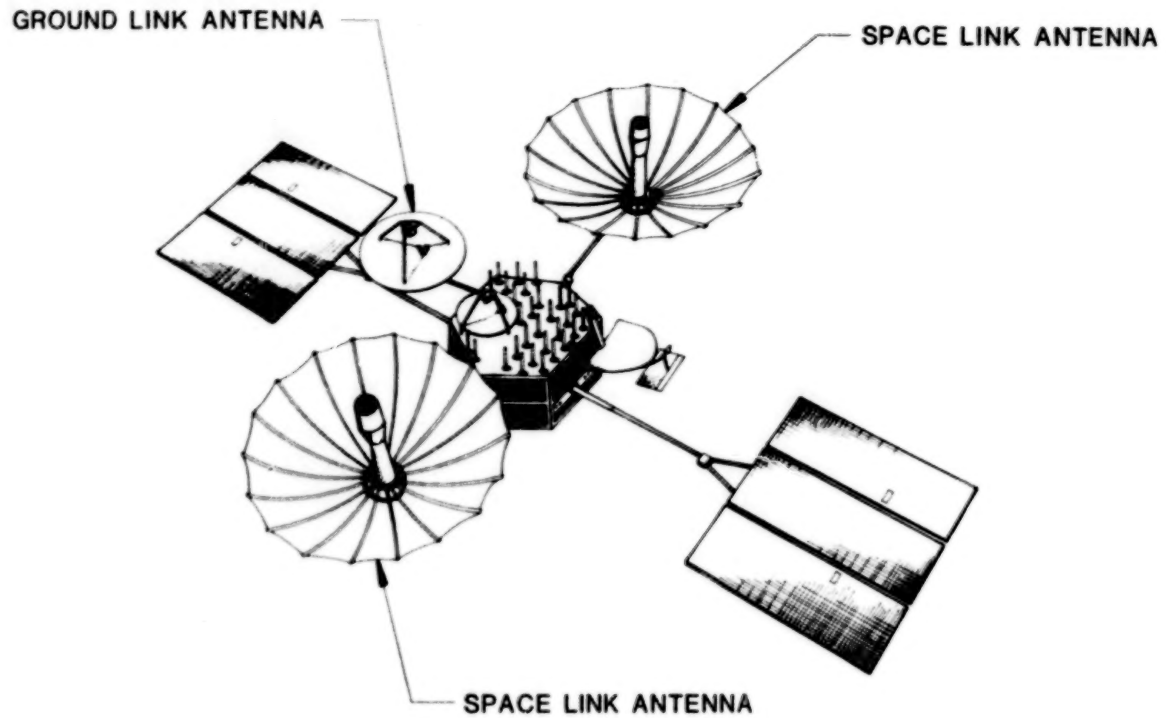
The actuators are used in a broad range of applications. Types 1, 2, and 5 have been built and delivered in numerous forms, and Types 3 and 6 have been proposed or are in development.

The low end of the size spectrum is represented by the Type 1 actuator shown in Figure 18. This unit is used for positioning a scan mirror on Dynamics Explorer. It weighs just over 0.45 kg. (1 lb.), including an integral potentiometer and position-sensing switch assembly. Step angle is 0.0022 rad. (.125 degrees), with worst-case positioning accuracy of about $3 \times 10^{-4} \text{ rad.}$ (1 minute of arc). Its unpowered detent torque is used to hold the output stable during power-off periods. This is a good example of Selective Redundancy. A single motor is incorporated, and a single potentiometer element is used. Position sensing switches, however, are deemed to have significantly higher failure potential, and are therefore duplicated.

A larger unit, used for both positioning and driving, is represented by the TDRSS Gimbal Drive Assembly. Figure 19 shows a view of the TDRSS spacecraft. These 1.8 kg. (4 lb.) Type 5 units are used in two-axis arrays to position the large umbrella-shaped high gain antennas and the ground link antenna. This application requires the actuators to drive an inertia load of 57 kg.m^2 (42 slug ft^2) at a speed of $0.005 \text{ rad. per sec.}$ ($35 \text{ pulses per sec.}$). Required positioning accuracy is $7 \times 10^{-4} \text{ rad}$ ($2 \text{ min } 24 \text{ sec.}$). The unpowered holding torque of 11.3 nt.m. (100 inch-lbs) minimum is relied upon to maintain pointing of the antennas during actuator unpowered periods. These units are electrically redundant, and performance figures are based on operation of one motor. Position feedback is provided by integral redundant potentiometers.

A variation of the Type 5 actuator with oversized output bearings was depicted earlier (Figure 8). The application of this unit is on the ERBE program (TRW, under NASA contract NAS 1-15900). The entire ERBE instrument on the spacecraft is both supported and pointed in azimuth by the output member of this 4 kg. (9 lb.) actuator. The driven inertia represented by the instrument is 27 kg.m^2 (20 slug ft^2) and the mass of the instrument package is 11.3 kg. (25 lbs). No unloading latches are used at launch, so that the actuator output stage carries all inertial loads.

These actuators are used extensively on the Space Telescope mainframe for high gain antenna deployment, for operation of the main aperture door, and for latching of the high gain antennas, the main aperture door, and the solar



APPLICATION OF TYPE 5 ON TDRSS SPACECRAFT

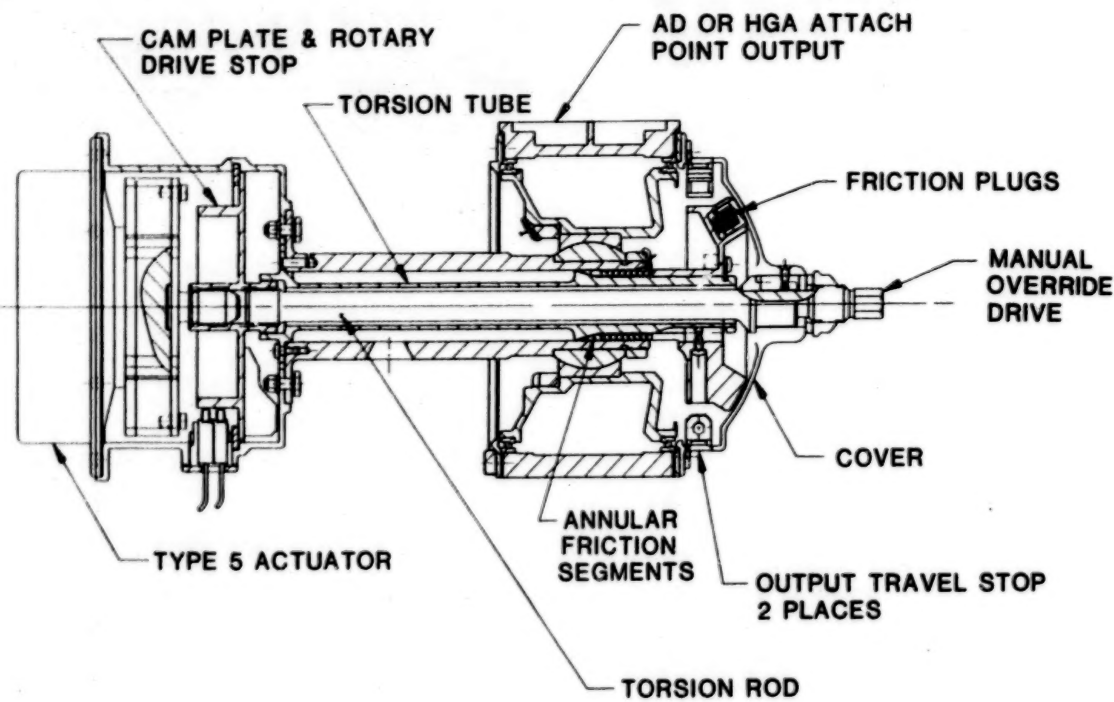
FIG. 19

array panels. The hinge and latch assemblies used for these tasks were developed by Lockheed Missiles and Space Company under NASA Contract NAS 8-32697 (2). Type 5 actuators to power these units are supplied to a common specification which is written to cover the worst case of this set of utility applications. Motors are redundant, and the devices are required, with the operation of one motor only, to meet the following specifications: torque 56.5 nt.m. (500 in-lbs) minimum, operating speed 0.039 rad. per sec, (300 pulses per second) maximum, driven inertia 474.5 kg.m^2 (350 slug ft^2), unpowered detent torque 11.3 nt.m. (100 in-lbs.) minimum/62.2 nt.m. (550 in-lbs.) maximum. (Maximum backdrive torque is limited in order to insure EVA manual re-stow capability). Figure 20 shows the actuator assembled in a typical hinge drive assembly, and Figure 21 shows a latch assembly.

Another Type 5 application on Space Telescope is found in the Optical Telescope Assembly (OTA), where an array of six Type 5 actuators are used to support and to position the secondary mirror. These units, referred to earlier, have an eccentric ball on the output flange in order to convert the output rotary motion into linear motion. Because of the very small angular output increment of the device and the small eccentricity of the ball relative to the center of rotation, an extremely fine rectilinear output step is achieved -- about $0.5 \times 10^{-6} \text{ m}$ (19 microinches) per step. Motors in this device are redundant, and the accessory devices (both potentiometers and optical position encoders) are also redundant. Potentiometers are special units located in the rear cover and are driven by a quill shaft which extends axially through the device. Optical encoders provide feedback of motor rotor position. Although the system control loop is closed through external devices, the combination of optical encoders and potentiometers provides unique position information for each of the six secondary mirror drives.

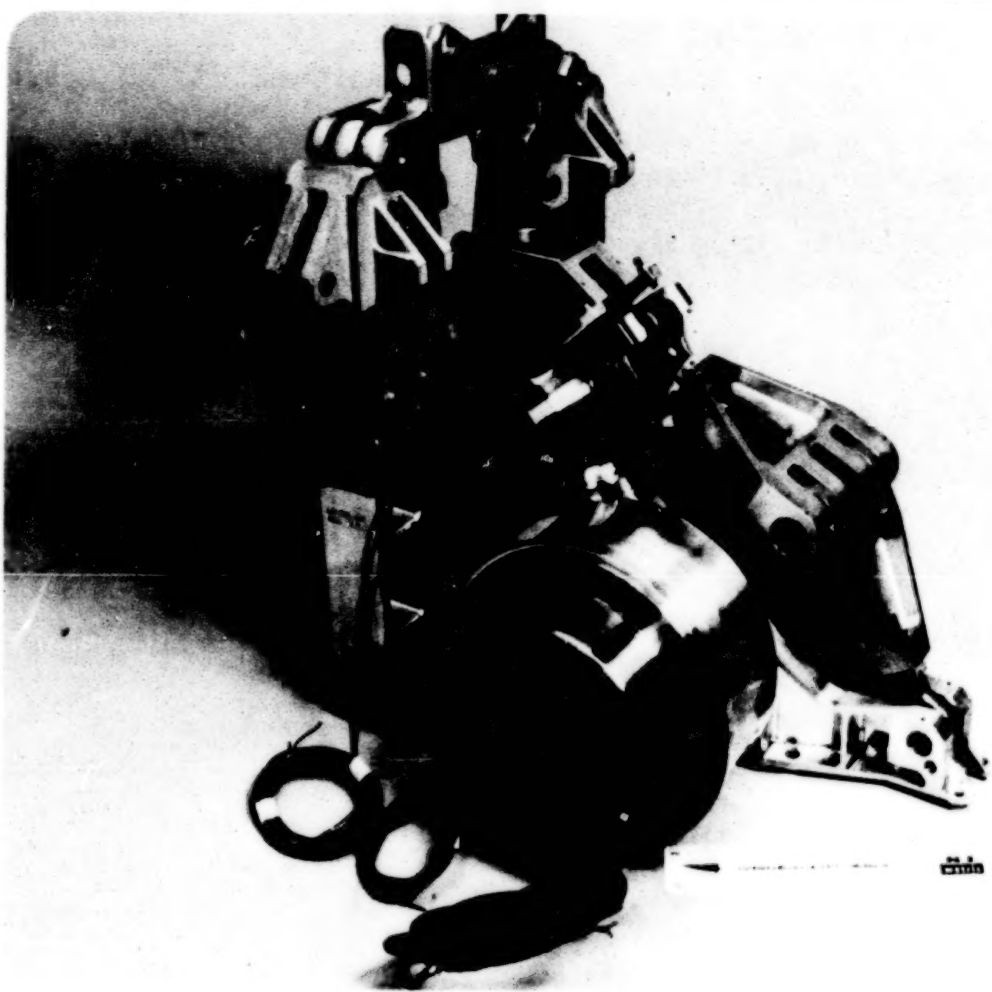
Including some other devices of a different generic type, the total count of Schaeffer Magnetics actuators on board Space Telescope reaches 58.

It appears that future applications of rotary incremental actuators will cover much the same spectrum as those of the recent past, with special interest in driving larger inertias and positioning loads in finer increments. Harmonic drives are available in sizes larger than the 2M size, and there is no inherent upper limit on the size in which the small-angle stepper motor can be built. Fine incremental positioning capability is implicit in the design, without pre-gearing or other auxiliary mechanisms, and without the need for added electronic complexities to effect micro-stepping. It is believed that these characteristics make this rotary actuator type as attractive a candidate for the increasingly demanding spaceflight requirements of tomorrow as it is for the applications of today.



SPACE TELESCOPE HINGE DRIVE ASSEMBLY

FIG. 20



SPACE TELESCOPE LATCH ASSEMBLY

FIG. 21

ACKNOWLEDGMENTS

The author wishes to thank Mr. H. T. Greenfield, Lockheed Missiles & Space Company; Dr. John Craven, University of Iowa Physics Department; Mr. R. I. Gilje, TRW Space and Technology Group; and Mr. Louis A. Watts, Santa Barbara Research Center; as well as others in customer organizations who have provided application details. Thanks also go to Mr. Ernest Schaeffer for providing historical information as well as encouragement and assistance in the production of this paper.

REFERENCES

1. MIL-HDBK-217D, Reliability Prediction of Electronic Equipment.
2. Schmidt, Hubert, Latch Mechanism for Space Telescope, Proceedings of 15th Aerospace Mechanisms Symposium, pp. 331-339.

THE LINEAR BOOM ACTUATOR DESIGNED FOR THE GALILEO SPACECRAFT

Edgar F. Koch*

SUMMARY

The Galileo spacecraft (S/C) is designed to be a Jupiter orbiter launched by the Shuttle/Centaur system in 1986. The spacecraft differs from past JPL spacecraft in that it is not three-axis stabilized but is a dual-spin design. A despun section contains some of the science instruments and camera system, while the spun section contains antenna, propulsion, and power generation systems. Power is supplied by two Radioactive Thermoelectric Generators (RTG's), each of which is mounted at the end of a long boom. A third boom mounts a magnetometer. (See Figure 1.) Nutation of the spinning spacecraft is controlled by an articulated attachment of the magnetometer boom to the spacecraft. Booms that mount the RTG's are hinged at the spacecraft and restrained from rotating to a 90° position with the spin axis

*Jet Propulsion Laboratory, California Institute of Technology,
Pasadena, California

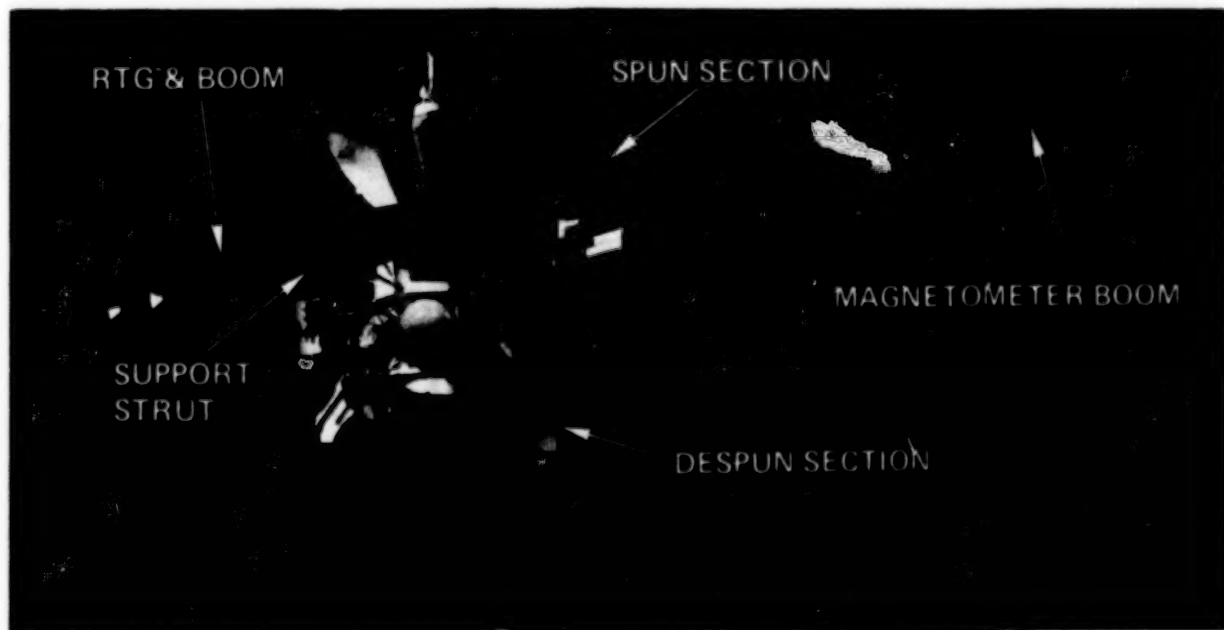


Figure 1. Galileo Spacecraft Configuration

(Z) by a support strut. The support strut is made up of a folding section (for launch configuration reasons), some straight sections, and the Linear Boom Actuator (LBA). (See Figure 2.) Varying the length of the LBA varies the length of the support strut, thereby controlling the distance of the RTG mass from the spin axis. Changing the position of an RTG mass relative to the spin axis controls the wobble of the spacecraft. One LBA is used on each RTG boom support strut to provide both required degrees of freedom needed for wobble control.

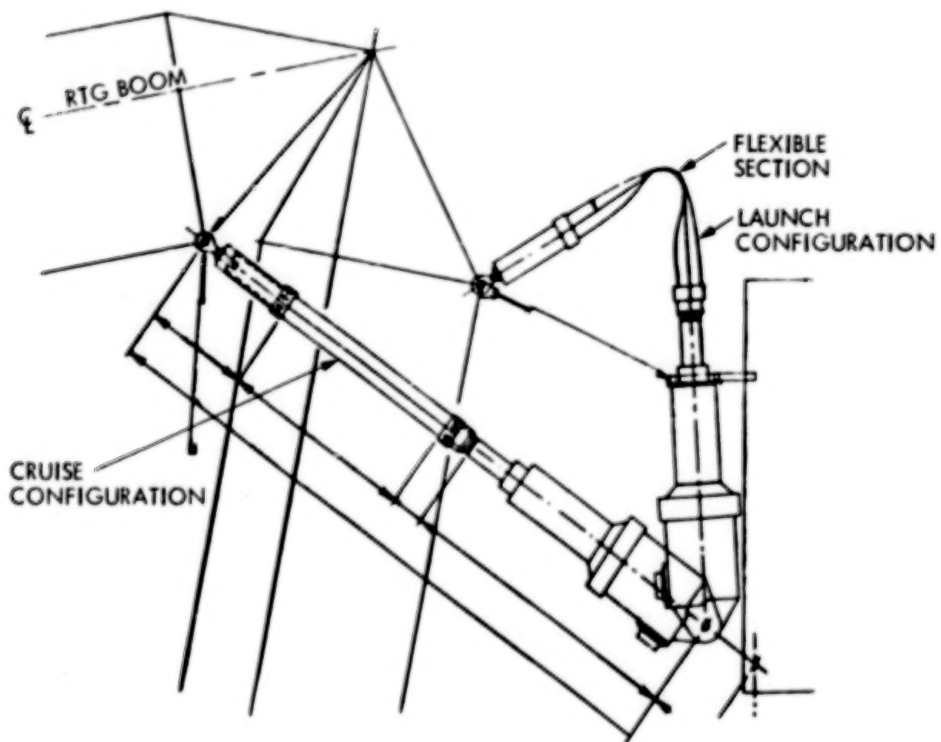


Figure 2. Support Strut Deployment View

LBA REQUIREMENTS

Because this actuator is to be used on a flight spacecraft, as opposed to a ground-based application, there is a comprehensive set of requirements. First, of course, the actuator must be capable of positioning and holding the load. Initially the load was predicted to be 4448 N (1000 lb) but with subsequent spacecraft configuration changes the load has been greatly reduced to a constant tensile pull of 1477 N (332 lb) due to centrifugal force. Lesser compressive loads of 1317 N (296 centrifugal lb) may be experienced during launch and deployment.

Experience on the Voyager spacecraft emphasized the need for redundancy. Accordingly, this actuator must have the maximum redundancy possible.

Life requirements were defined by the 10.16 to 15.24 cm (4 to 6 in.) total linear travel expected during the five-year flight duration.

Linear range required of the actuator was set at plus and minus 5.08 cm (± 2.0 in.) to accomodate configuration changes, although this linear range is not expected to be used in flight. Since the actuator will be used in a digital system, and because fine position control was needed, stepper motors similar to those used on a Voyager actuator were indicated. Maximum allowable power was set at 5 watts at 30 VDC. Overall length, weight, and backlash were to be held to a minimum with no specifications applied. Overall length was important due to the mounting configuration in concert with the folding struts for each boom. Interchangeability between actuators was required; however, interchangeability was carried further in that all parts and/or matched subassemblies are interchangeable.

Redundant readout of boom angles to 0.1 degrees was also required.

Systems engineers indicated that a gear train ratio of approximately 5000 to 1 in combination with a screw lead of 0.318 cm (0.125 in.) would be compatible with a minimum step size required of $0.10 \mu\text{m}$ (step size 1.537×10^{-7} in.).

Magnetic fields about the actuator were to be held to 5 nT at a 1.0 m distance, because of the magnetometer on board.

Because any parts that might come loose during launch vibration could become lodged in the shuttle bay door hinges, shuttle safety required that all actuator parts have redundant attachments and that the materials be analyzed for launch stress and crack sensitivity. Structural safety factor of the actuator was to be set at four.

The Galileo spacecraft, assuming it makes five orbits in the vicinity of Jupiter, will receive an estimated 10^6 rads of radiation from high energy protons and electrons. All parts and lubrication must be either capable of withstanding this radiation directly or shielded to reduce the radiation level to a level within its capability. Electronic components change their electrical characteristics under radiation, while lubricants harden.

The qualification and flight temperature ranges were established early in the development as:

-40 to +75°C for qualification, and

-20 to +55°C for flight.

Vibration levels were likewise established early in the development period as 8 G's rms qualification level and 5.8 G's rms flight.

The above list of requirements is a brief summary of the major requirements and has omitted much of the detail. With these major requirements in mind, the following design concept was followed to a successful conclusion.

DESIGN CONCEPT

After several preliminary starts the design approach shown on Figure 3 was developed. The low torque redundant gear train design is similar to the Scan Platform Actuator for the Voyager spacecraft in that the motors are similar, steel spur gears are used, and porous sleeve bearings impregnated with lubricant are used with a few exceptions. Ball bearings are used in the motors and potentiometers. Output from one gear train drives the ring gear of a planetary stage while output from the other gear train drives the sun gear. An important feature of this design must be pointed out here: the magnetic detent of the motors when de-energized in concert with the gear train advantage holds the associated gear train from coasting or being back-driven. This feature eliminates the need for either a brake or a clutch. Also with the ball screw locked up, one gear train cannot back-drive the other. Other strong points for this actuator design are the many ways in which it can be operated:

1. Each motor can be operated single- or two-phase.
2. Motors can be used singly or in pairs. Care must be observed to operate motors in opposite directions if used in pairs; otherwise, there will be no output movement.

The Galileo spacecraft is designed to operate the actuator single-phase, one motor/actuator at a time.

Some actuator design constants follow:

$$\text{Ball screw } T = PL/2\pi e$$

TOTAL GEAR RATIO: 5164.7895

$$\text{DUAL POWER TRAIN: } \frac{88}{10} \left| \frac{96}{20} \right| \frac{96}{20} \left| \frac{66}{18} \right| = 743.4240$$

COMMON PLANETARY REDUCTION:

$$\frac{44}{19} \left(1 + \frac{88}{44} \right) = 6.9473 \text{ SUN DRIVEN}$$

$$\frac{88}{19} \left(1 + \frac{44}{88} \right) = 6.9473 \text{ RING DRIVEN}$$

POTENIOMETER GEAR TRAIN:

$$\frac{76}{24} \left| \frac{78}{24} \right| \frac{78}{24} = 33.4479$$

$$\frac{32 \times 360}{33.4479} = 344.42 \text{ POT ROTATION}$$

PINTLE EXTENDS WHEN:

1. MOTOR B1 ROTATES CCW AND B2 DE-ENERGIZED
2. MOTOR B2 ROTATES CW AND B1 DE-ENERGIZED

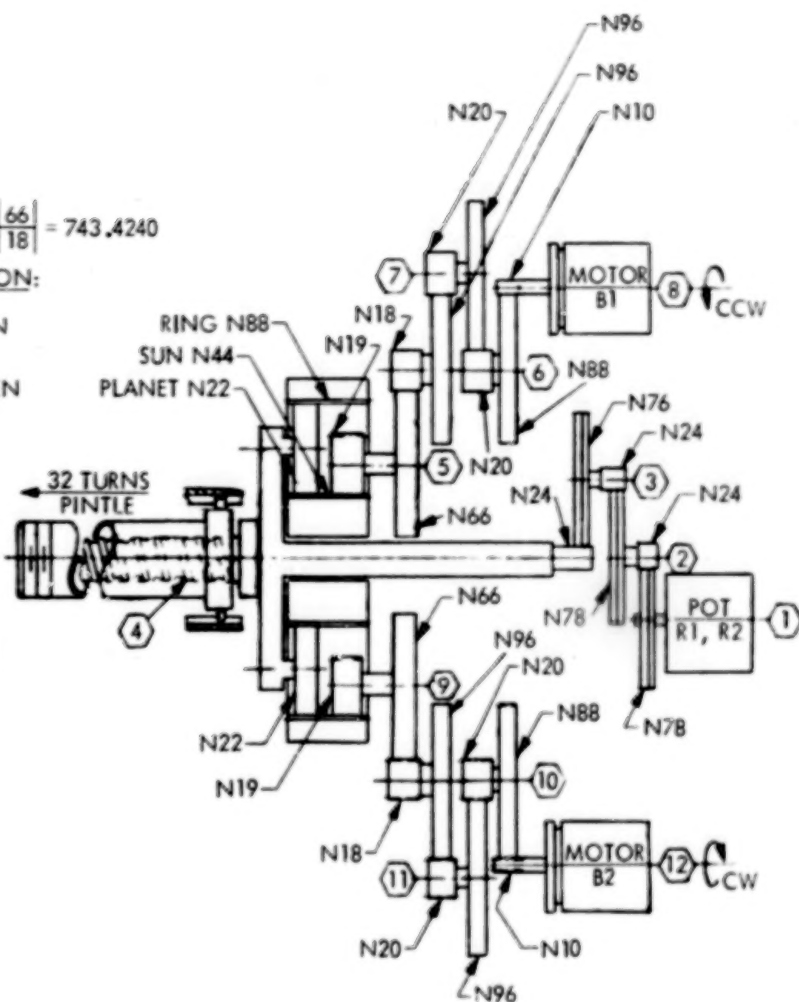


Figure 3. Mechanical Schematic

where

T = torque to drive

P = load

e = efficiency (approximately 0.9)

L = pitch/ 360° = 0.3175 cm (0.125 in.)

Motor max torque at 100 PPS = 0.00127 Nm (0.18 in. ounce)

Motor min detent torque = 0.00113 Nm (0.16 in. ounce)

Gear train efficiency approx 0.8

The 3 planet gears drive the ball screw. Bearings for the planetary stage are all journal type bearings.

The ball screw converts the rotary movement to linear movement at the rate of 0.318 cm (0.125 in.) per one rotation. The ball screw has a total capability of 10.16 cm (4 in.) or 32 turns.

Feedback potentiometers are driven from an extension of the ball screw shaft through a 33.45/1 anti-backlash geared gear train. Total rotation of the potentiometer is 344.4° for the 32 turns of the ball screw. Available electrical rotation of the potentiometer is 347° .

As can be seen from the above discussion and the schematic, the central key element of the actuator is the complex, one-piece ball screw assembly, which includes the planetary spider and the potentiometer drive. (See Figure 4.)

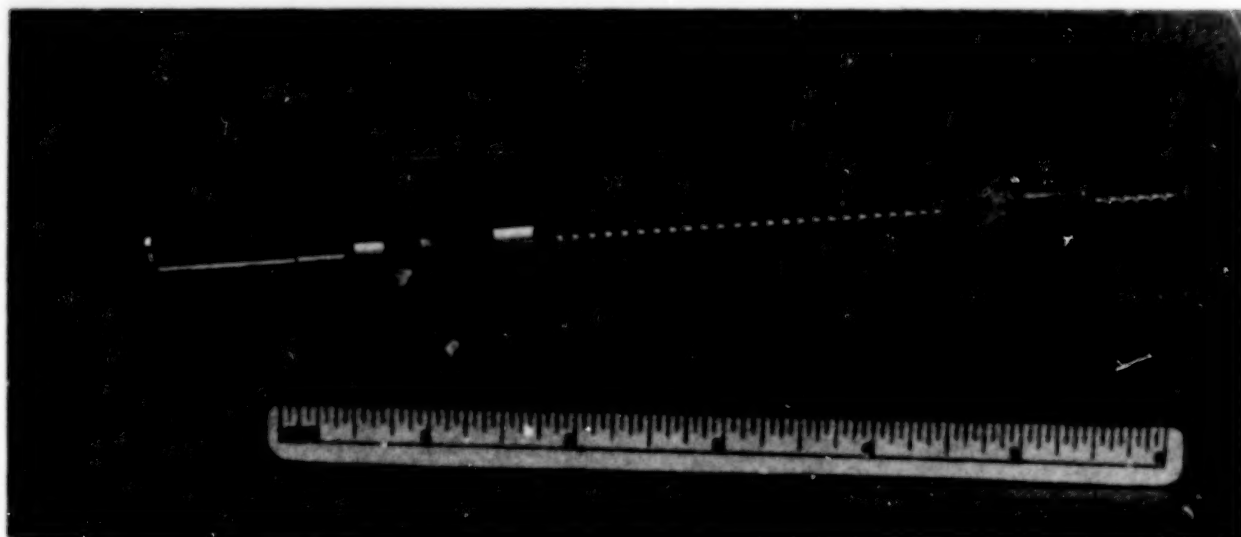


Figure 4. Ball Screw Assembly

The method of driving the ring and sun gears of the planetary gear stage is unique. Both gears (ring and sun) are at least double the width required by the planetary stage in order that the last gear of the power trains could drive the ring and/or sun gears by the same gear track. This also serves to improve the L/D ratio for the plain bearings, and makes fabrication easier. This arrangement also resulted in both gear trains, in combination with the planetary stage, being exactly the same ratio (5164.7895/1).

Travel limits have been incorporated as a part of the ball screw drive by machining stops on both ends of the ball screw nut that engage with similar stops at either end of the ball screw. In so doing, the stops only have to stop the power gear trains and stall the driving motor. The force is much less than stopping the linear motion of the ball screw and is not susceptible to jamming.

The above arrangement of parts results in a very compact design of acceptable length. Keeping the overall length down required the elimination of universal joints and telescoping the ball screw and output tube. However, as was stated before, this arrangement required a great deal of design complexity in one element.

The housing for the actuator maintains a positive pressure of 3.4475 N/cm^2 (5 psig) of GN_2 and incorporates mounting provisions for attachment to the spacecraft. This enclosure, with positive GN_2 pressure, protects the potentiometer from hard vacuum, inhibits lubrication migration and evaporation, and eliminates the entry of Florida salt air.

Materials selection for various elements was based on many factors. The steel gears use 15-5PH CRES, which is a fine-grained, heat-treatable stainless steel, readily available, that has been used with success on Voyager in the same application. The first gear and pinion from the motor, because it rotates as an idler on a steel shaft, is hardened beryllium copper. This makes a dissimilar metal bearing combination which does not readily cold weld or gall. Planet gear shafts and sun gear are made from manganese-silicone bronze per SAE CA674 for reasons similar to the above; good bearing material rotating in association with hardened stainless steel.

The gear train case is made from pure beryllium for two reasons. The primary reason is the matching of thermal expansion characteristics of the steel ($11.39 \times 10^{-6} \text{ cm/cm}/{}^\circ\text{C}$, $6.33 \times 10^{-6} \text{ in./in.}/{}^\circ\text{F}$) and the beryllium ($10.80 \times 10^{-6} \text{ cm/cm}/{}^\circ\text{C}$, $6.00 \times 10^{-6} \text{ in./in.}/{}^\circ\text{F}$). The secondary reason is the weight advantage (1.854 g/cm^3 or 0.067 lb/in.^3).

Journal bearings for the individual gear shafts other than those mentioned above are made from self-lubricating sintered bearings. These bearings are made from a combination of bronze and iron powders and charged with lubricant. The ring gear rotates in a beryllium pocket and is both dry and wet lubricated. The ball screw nut, of course, rides on stainless steel balls. The tube that extends from the actuator was chosen to be titanium (MIL-T-9047) because of its low heat conductivity, light weight, and high strength.

Lubrication at first was to be silicone oil and grease (F-50 and G-300); however, after analysis of a Voyager actuator anomaly, it was decided to change to a teflon derivative system of oil and grease (perfluorinated polyether 815Z oil and 3L-38-1 grease, which has better staying power and better lubricity). The oil is used to impregnate all the porous bearings and the grease is used on the ball screw, ring gear, planet gear shafts, and all gear meshes. "O" rings are also lubricated with the grease. In addition to the oil and grease system, the ring gear O.D., tube O.D. and the first gear idler shaft (shaft #6 and 10 on Figure 3) are ion plated with molybdenum disulfide to a thickness of 1500 to 2500 Å (angstroms). Idler shaft and planet gear shafts were also provided with a minor flat the length of the bearing surface (approximately 20% of the projected area) for lubricant flow or debris relief. Steel and bronze parts were all specified to have an eight micro-inch (0.203 µm) finish in the bearing and/or relative motion areas. (See Figures 5, 6, and 7.) The Voyager anomaly referred to above was the sticking of the instrument platform on the Voyager spacecraft as it was passing Saturn in 1981. This anomaly has been analyzed as a depletion of lubricant between an idler shaft and gear with subsequent galling and sizing of gear to shaft.

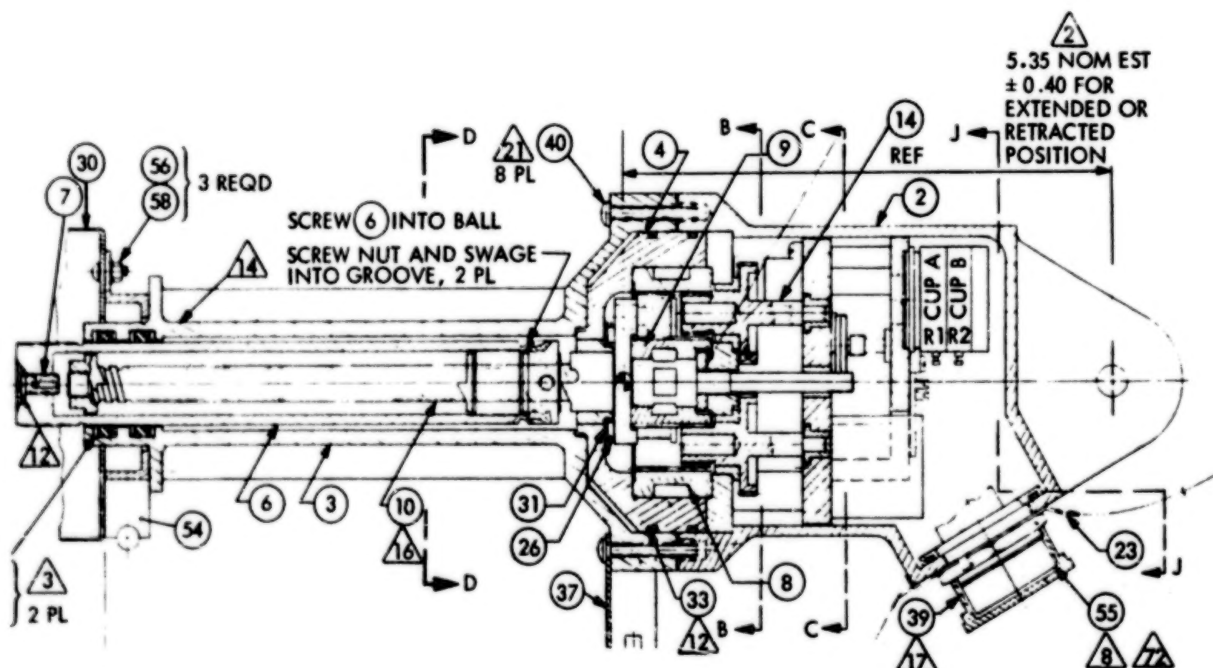


Figure 5. Actuator Cross Section View

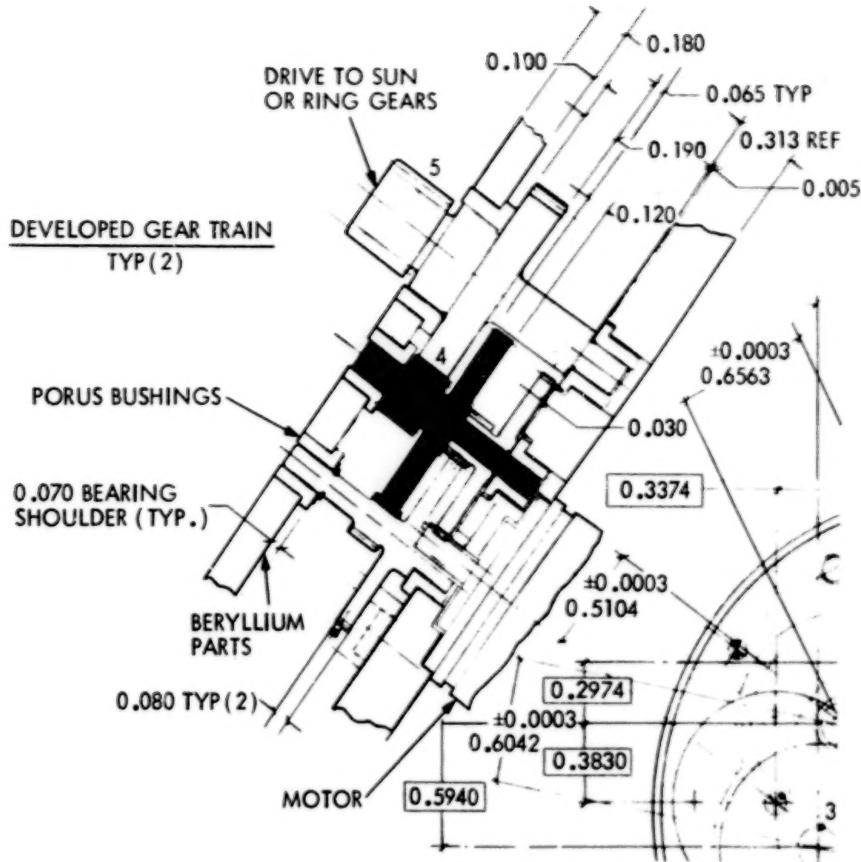
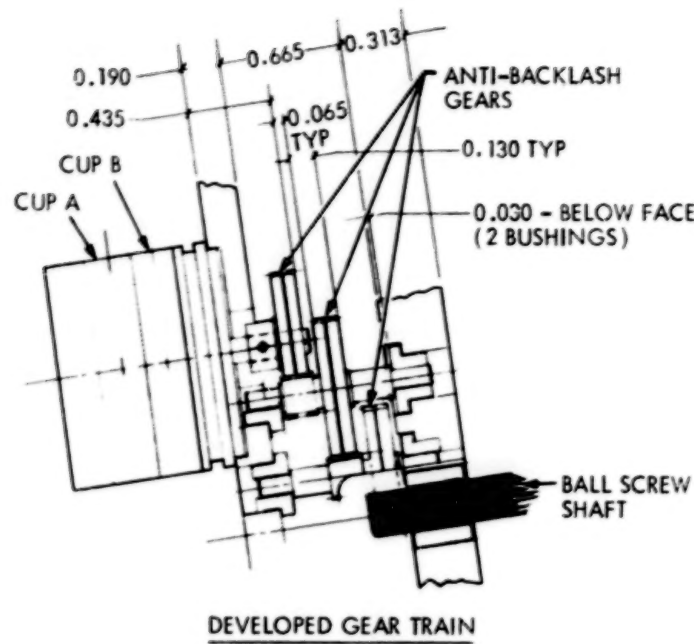


Figure 6. Power Gear Train

Figure 8 shows the method of pressurizing the actuator with GN_2 . A special sealed fixture was designed to thread onto the end of the actuator tube with provisions for an "O" ring-sealed screwdriver shaft and pressurizing port. The screwdriver is used to back off the vent screw to allow pressure to enter the actuator housing, after which the vent screw is closed. The vent screw is also sealed by an "O" ring.

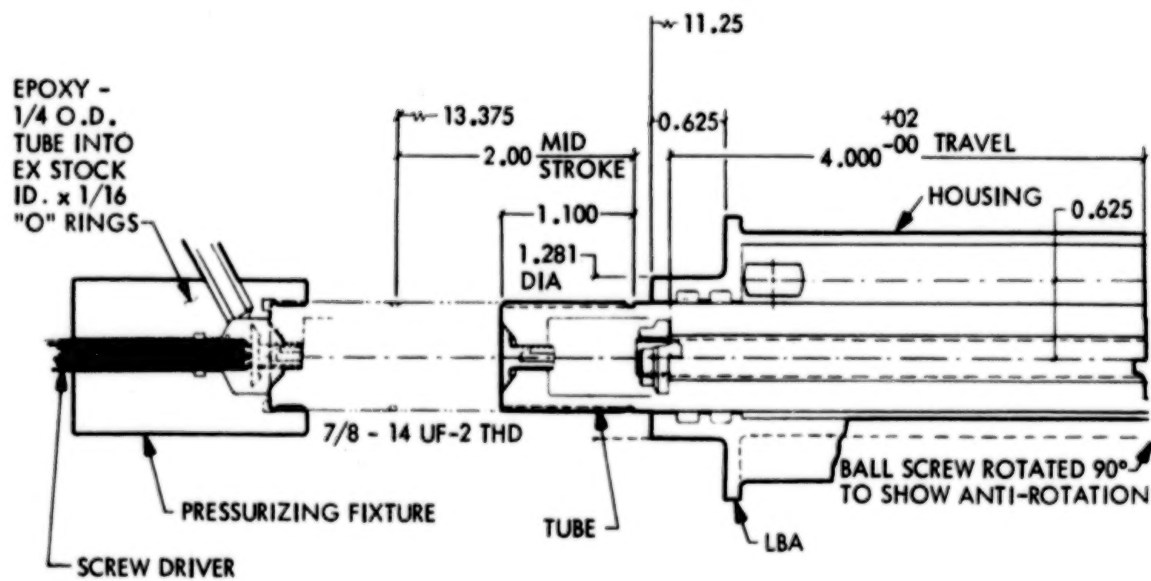
FABRICATION

Fabrication of actuator parts and assembly was more or less straightforward with a few notable exceptions. Instead of fabricating an engineering model first for evaluation and then building the flight models, all parts for both engineering and flight models were fabricated at the same time. The engineering model was then assembled and tested, after which the flight models were assembled. Beryllium parts fabrication was a problem due to the



POTENTIOMETER ROTATES 347°
FOR 32 TURNS OF THE
BALL SCREW SHAFT

Figure 7. Pressurizing Method



SECTION E-E

Figure 8. Potentiometer Gear Train

toxic nature of the beryllium dust. Beryllium parts had to be machined to within a few thousands of an inch of final dimensions and then chemically etched to remove a crazed surface from the cutting operations. This improved the strength characteristics of the metal. Sintered bushings machined on the O.D. to press fit tolerances, cleaned, and lubricant impregnated were then pressed in place. Matching parts of the gear frame assembly were then mounted together, and shaft and gear center lines bored through the bearings to ± 0.0001 in. tolerances on both the bearing diameters and the center-to-center distances. (See Figure 9.)

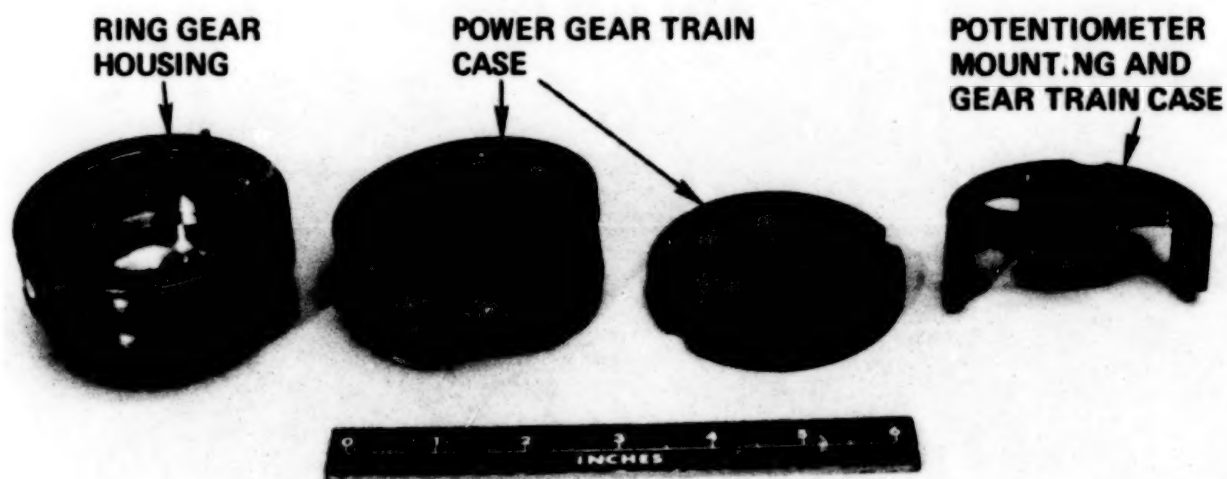


Figure 9. Beryllium Gear Case Parts

All machining of steel gears, beryllium parts, aluminum housing, etc. was accomplished at JPL or local machine shops. The only difference between the engineering model and the flight models is that the gear frame in the engineering model was made from aluminum instead of beryllium. The aluminum gear frame was used as a first article and set-up piece for the fabricators. This difference in material restricted only usage of the engineering model in temperature control and thermal test runs.

TEMPERATURE CONTROL

Originally the design of the actuator called for resistive heaters of the same wattage consumption as the motors, with the idea that when the motors are on the heaters would be off. This would keep power consumption level during operations; however,

power was at a premium and additional weight was tolerable. Therefore the resistive heaters were removed and two Radioactive Heater Units (RHU's) were installed in the two small aluminum enclosures on the outside of the actuator housings. These units will each provide one watt in the form of heat. The RHU's in conjunction with a blanket installed around the LBA will keep the temperature of the actuator between -15 and +50°C. (See Figure 10.) Operation of the LBA motors will add about 3.5 watts to the package and raise the temperature approximately 5°C/hour of operation.

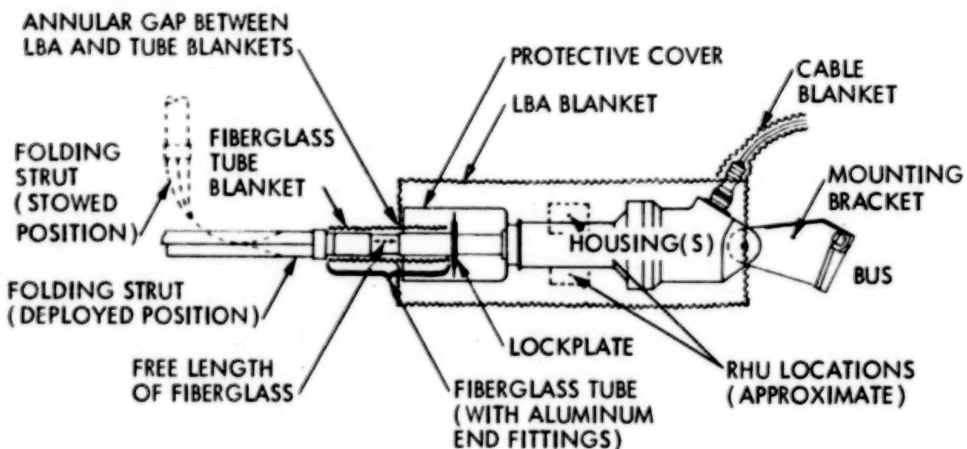


Figure 10. Actuator Insulation Schematic

TESTING AND RESULTS

Testing the LBA to 4448 N (1000 lb) would be a problem if that much force or weight had to be loaded on and off of an actuator test holder or platform; therefore a fixture was designed whereby the actuator could pull against itself thereby springing the fixture. (See Figure 11.) Motor A was stepped at a slow rate (5 PPS) in a retracting direction until the load cell read 1000 lb on the readout instrumentation, then relaxed back to zero; this was done three times, counting the required pulses each time. The average number of pulses were then programmed to 100 PPS to ensure that the torque associated with the higher pulse rate was sufficient to lift the load. There is approximately a 15 - 20% reduction in torque by increasing the pulse rate from 90 to 100 PPS; this provides a torque pad. Spacecraft usage will be at 90 PPS. This test lifted the load with no difficulty even at low voltage. Next the 1000-lb load was increased to 1200 lb (5338 N) at the 100 PPS rate, proving that the actuator could position a 1000-lb load.

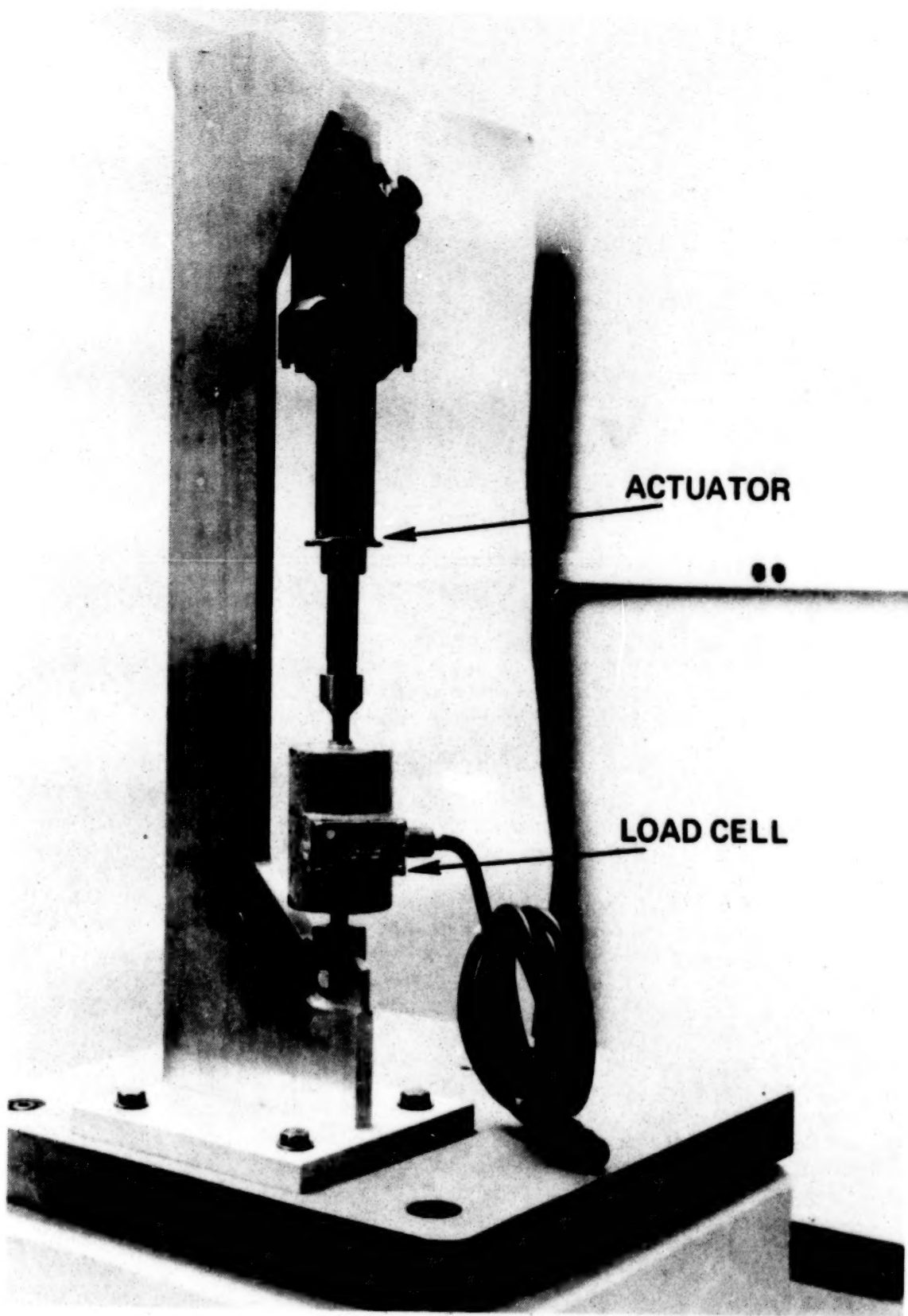


Figure 11. Stress Test Stand

The next step was to reduce the load from 5338 N (1200 lb) to 4448 N (1000 lb) by extending the actuator and checking for overdriving or coasting when the actuator was de-energized at the 4448 N (1000 lb) load point with no difficulty. The load showed no tendency to back-drive the gear train and motor. The above test was then repeated using the motor B, proving that there is no difference in operation between motor A or motor B and their associated gear trains.

Checking travel from stop to stop required 10.269 cm (4.043 in.) of travel, or a total of 668,209 motor steps, each of which was 1.5368487×10^{-5} cm (6.0505854×10^{-6} in.). This test, as well as a calibration test for eventual usage during flight, was conducted with 444.8 N (100 lb) using the calibration fixture pictured on Figure 12.

Power dissipated is in the range of 3 to 5 watts depending on temperature, voltage and initial resistance.

Overall length is 43 cm (16.93 in.); the weight is 2.35 kg (5.18 lb); diameter at the largest point is 10.03 cm (3.95 in.).

The magnetic field at 1 meter was high due to the use of magnetic steels in both ball screw and ring gear. This tested out at close to 10 nT where a maximum of 5 nT was specified; however, a waiver has been approved allowing up to 15 nT.

Qualification environmental testing of actuator serial #002 consisted of 144 hours at 75°C and 24 hours at -40°C in atmospheric launch conditions. After the above environmental exposures, complete functional testing was repeated.

Life testing consisted of a series of cycles of varying length with the actuator mounted in the Calibration Fixture as in Figure 12 and loaded with 22.675 kg (50 lb). Total travel during this test was 609.6 cm (240 in.). The method of monitoring the actuator during the test is shown in Figure 13. Voltage was varied between about 12 and 22 VDC in steps of one volt, recording the time it took to move the actuator tube weights 0.127 cm (0.050 in.). As the voltage was increased, the motor missed fewer steps, and the points formed a sloping line until the voltage was high enough that the motor no longer missed steps, in which case the line became horizontal. Plotting these points gave two straight lines with sharp intersection. Should the gear train wear or lubricant disappear and torque increase, the time would increase and displace the intersection. Throughout the life test the observed intersection did not increase by as much as 0.25 VDC.

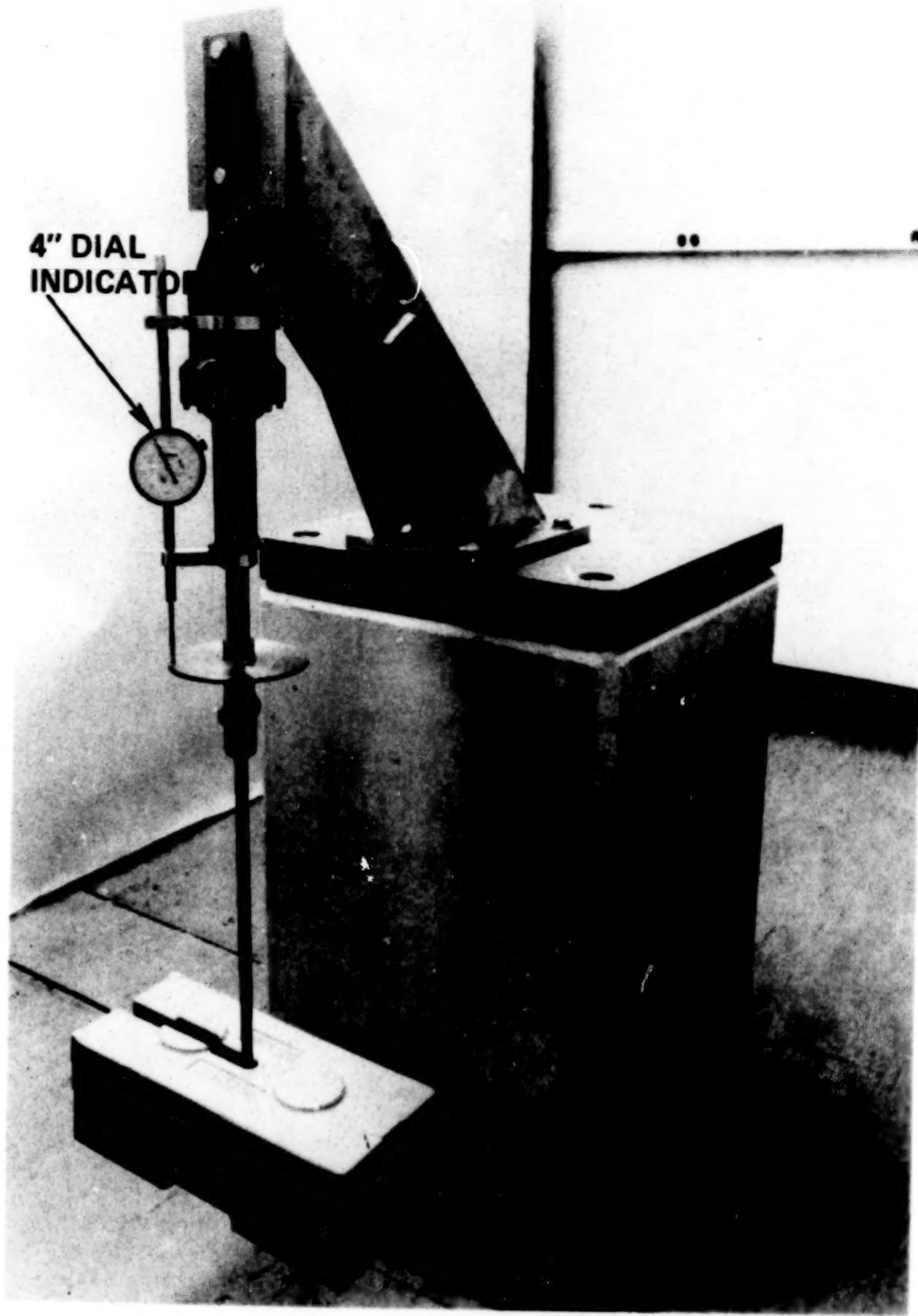


Figure 12. Calibration Test Stand

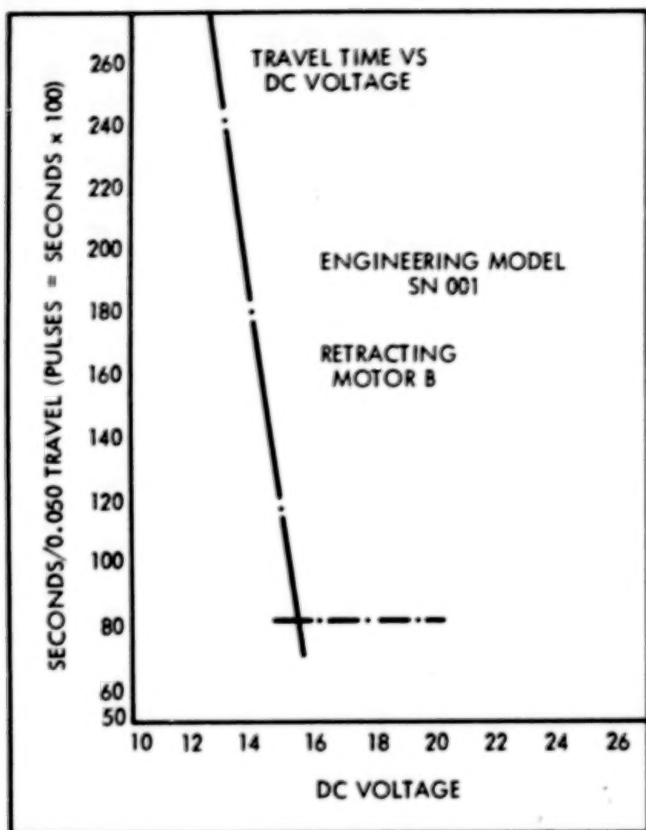


Figure 13. Motor B Actuator Serial #001
Engineering Actuator

STATUS

Weight, power, and length restrictions have been met with a redundant gear train containing no brake or clutch. Four models have been built and tested: One engineering model; one qualification/spare model; and two flight models. Although the flight load (tensile) is not expected to be greater than approximately 1557 N (350 lb), the engineering model was tested to 5338 N (1200 lb) and the flight models to 2224 N (500 lb). All models are awaiting system test and spacecraft assembly.

ACKNOWLEDGEMENTS

The research described in this paper was performed by the Jet Propulsion Laboratory, California Institute of Technology, Pasadena, California, under a contract with the National Aeronautics and Space Administration. The author wishes to thank R. Wendlandt for his diligent effort during the assembly and test of the actuators.

POLARIZER MECHANISM FOR THE
SPACE TELESCOPE FAINT OBJECT SPECTROGRAPH

Mark D. Thulson*

ABSTRACT

This paper describes the polarizer mechanism for the Space Telescope Faint Object Spectrograph. This device will allow spectropolarimetric measurements of faint astronomical objects. The mechanism employs a unique arrangement to meet functional requirements in a compact package and with only one actuator. Detailed tolerance analysis and a variety of tests indicate that the polarizer is capable of accurate and reliable performance.

INTRODUCTION

The polarizer mechanism for the Faint Object Spectrograph (FOS) will allow the Space Telescope to obtain spectropolarimetric data on faint astronomical objects. Measurements made using this device will be quite useful to astronomers studying a wide variety of phenomena, especially with the extension into the far ultraviolet made possible by the Space Telescope.

The FOS, shown in Figure 1, has two distinct light paths and digicon photon counting detectors. One detector is red sensitive (1800-8000 Å) and the other is blue sensitive (1150-5000 Å).

Spectropolarimetric data is obtained by introducing a Wollaston prism and waveplate into either of the light paths. The Wollaston prism forms two dispersed images in opposite senses of polarization at the detector. The waveplate is rotated with respect to the stationary prism to analyze for linear and circular polarization. For better coverage of the spectrum, two waveplates with different retardations are used, each with its own Wollaston prism.

MECHANISM DESCRIPTION

The polarizer mechanism must be able to do the following:

- place either of the Wollaston/waveplate pairs in either of the light paths;
- rotate each waveplate with respect to its Wollaston prism; and
- leave both light paths simultaneously clear when the polarizer is not in use.

The mechanism uses an arrangement which accomplishes these requirements with a single actuator and in a compact package. The two Wollaston prisms are fixed to a drum which also contains two holes to

* Martin Marietta Denver Aerospace, Denver, Colorado

clear the optical paths (see Figure 2). The waveplates are mounted in rotating cylinders inside the drum and ahead of the prisms. Each of these cylinders has a 16 tooth gear cut into its outside diameter. Both of these gears mesh with a stationary 17 tooth gear located on the drum's axis of rotation.

Rotating the drum about its centerline allows either Wollaston/waveplate pair to be inserted into either optical path, or both paths to be cleared simultaneously. Turning the drum 360° rotates the Wollaston prism 360° , and the waveplate $17/16$ times as much, or 382.5° . The net effect of one rotation of the drum, then, is to rotate the waveplate 22.5° . Sixteen revolutions of the drum returns the optical elements to their original positions.

The drum is driven through a two stage, 105:1 gear train by a 900 permanent magnet stepper motor as shown in Figure 3. The motor is driven at 50 pulses per second (750 RPM). This means that one 22.5° increment of the waveplate takes 8.4 seconds.

Two eight-bit pin contact encoders provide position feedback. The encoders are geared in such a way (see Figure 4) that a motor step advances encoder A 3.05 counts and encoder B 3.09 counts. In 16 revolutions of the drum, encoder A rotates 80 times and encoder B 81 times, bringing both back to their starting point. As a result, each of the 6,720 steps of the motor required to complete 16 revolutions of the drum is associated with a unique combination of bits from the encoders. The fact that motor steps are separated by slightly more than three counts guarantees that the outputs are unambiguous.

Positional accuracy of the optical elements is determined by the accuracy of the motor's position plus any error in the gear train. The design includes several features to minimize this error. First, spring loaded antibacklash gears are used wherever possible. The 210 tooth gear is a conventional antibacklash gear with two extension springs. The 18 tooth pinion in the second stage is a special antibacklash gear which is preloaded by a small torsion spring mounted inside the gear.

Space does not permit the 16 tooth waveplate gears to be antibacklash. The fixed 17 tooth gear cannot be, because it is engaged by both waveplate gears. The angular position of the waveplate, however, is not as critical as that of the Wollaston prism. Control of center distance and runout to minimize backlash limits this error to an acceptable range.

Second, all gear ratios are integral. As a result, when the mechanism returns to a previous position, all the same gear teeth are in contact and any errors resulting from gear tolerances, bearing runout, and so on are repeatable. This also means that extremely high precision gears are not required - AGMA Q10 gears are sufficiently accurate.

Third, ABEC 7P bearings are used throughout and comparable tolerances are maintained on all housings and shafts. This minimizes

clearances between bearings and housings or shafts and the resulting angular errors.

Finally, the bearings are preloaded axially to eliminate clearance within the bearings themselves. This is done with belleville washers for the rotating drum bearings, a wave spring washer for the intermediate shaft, and compression springs for the waveplate bearings. The use of springs accomodates thermal changes without large changes in preload.

In the event of a failure, activation of a hot wire pinpuller allows two torsion springs to rotate the mechanism completely out of the optical paths to the position shown in Figure 5, allowing continued use of the remainder of the FOS. The holes engaged by the pin are match drilled at assembly to guarantee proper alignment. As a further precaution against binding of the pin, the bolts which attach the pinpuller to the mechanism are left .025 to .076 mm (.001 to .003 inch) loose to allow the pin to freely align itself with the hole.

The entire assembly is attached by six #6-32 screws to a fitting which is, in turn, bonded to two graphite epoxy tubes that are part of the FOS optical bench. Laminated shims at these six points allow any adjustment required for initial alignment. Figure 6 shows the polarizer after installation into the FOS.

MATERIALS AND LUBRICATION

All gears are 416 stainless steel, heat treated to a hardness of Rockwell C32. After final machining, the gears are case hardened to a depth of 5 to 10 μm (.0002 to .0004 inch) by a nitriding process, resulting in a surface hardness of Rockwell RC 60 to 70. The hardened surface will minimize gear wear during the life of the mechanism. Any wear would result in positional errors as well as the generation of particle contamination.

By using the nitriding process, the gears can be cut, then hardened, thus eliminating the need for final grinding of the teeth. Dimensional changes are well within the tolerances for AGMA Q10 gears. The fact that the hardened case is so shallow allows the gears to be drilled and reamed where required for pinning at assembly.

The bearings are 440C stainless steel. All other major parts are aluminum to save weight. All non-functional surfaces are coated with flat black polyurethane paint to minimize optical reflection.

The bearings and gears are lubricated with Braycote 3L-38RP grease. The shaft about which the mechanism rotates when the pinpuller is activated is lubricated by MoS_2 with an impinged binder.

REPEATABILITY ANALYSIS

Some of the more critical requirements for the polarizer have to do with the repeatability of the angular position of the optical elements.

Two kinds of angular error are possible - 1) rotation about the optical axis, or θ_z ; and 2) rotation about an axis perpendicular to the optical axis, or θ_x and θ_y (tilt). Either of these can result in both motion of the image at the detector and errors in polarization measurements.

To insure that these requirements would be met, a detailed tolerance analysis was performed prior to fabrication of the mechanism. For a particular requirement, all of the potential error sources were identified and their effect on angular position calculated. Root sum square addition of these contributors resulted in a predicted maximum error.

The largest single source of error in θ_z for either the Wollaston prisms or waveplates is the stepper motor. Its actual position is specified to be within $\pm 5\%$ of a step, or $\pm 4.5^\circ$, of its nominal position. The resulting error in θ_z for the Wollaston prisms, then, is $\pm 4.5^\circ / 105 = \pm 2.57$ arc min.

Most of the remainder of the error in θ_z arises from bearing to housing and bearing to shaft clearance. This clearance can induce error in two ways. First, motion of a gear along a line passing through the centers of the mating gears changes the center distance. This results in rotation of the gear which is related to the pressure angle. Motion in a direction perpendicular to a line through the centers also results in rotation of the gear. The resultant of these two components cannot exceed an amount determined by the maximum total clearance in the supporting bearings.

The analysis divides the total possible motion of each gear between these two components in such a way as to maximize the rotational error in question. Bearing runout is also included in the same way to account for the possibility that the outer race rotates with respect to the housing or the inner race with respect to the shaft.

The error in θ_z for the waveplates is somewhat larger than that for the Wollaston prisms. This is because of the extra pair of bearings involved and the backlash in the waveplate gear meshes.

Repeatability error for θ_x and θ_y (tilt) of the Wollaston prisms are calculated from the clearances and runout of the bearings which support the rotating drum. Tilt of the waveplates also includes the effect of the waveplate bearings and manufacturing tolerances for perpendicularity between the waveplate mounting shoulder and bearing lands.

Table 1 summarizes the required, predicted, and measured values for θ_x , θ_y and θ_z for the Wollaston prisms and waveplates. Predicted and measured values compare favorably, and both are well within the requirements.

PROBLEMS AND SOLUTIONS

Minimal problems were encountered during assembly, but one became obvious. Interference between two of the motor mounting screws and the mounting bracket prevented full rotation of the mechanism when the pinpuller was operated (see Figure 4). Two small modifications solved this problem. First, stress analysis showed that three screws were more than adequate to mount the motor, so one was removed. Second, a small area was machined from the mounting bracket to clear the other interfering screws.

TESTING

Functional tests were performed to verify that the polarizer performed as expected. These tests included repeatedly operating the motor a specified number of steps, then reading the two encoders. The encoders consistently produced reliable and repeatable data.

Further testing verified that the polarizer could be operated closed loop, as it will be in the FOS. Here the mechanism is commanded to a position and the encoders are read to determine when it has arrived. This also worked reliably.

Optical tests were performed to measure image motion and polarization measurement errors. These tests indicate that errors are well within required values and that the polarizer is capable of excellent performance.¹

The mechanism was also tested under random vibration with no problems.

CONCLUSION

At this writing (December 1982) the polarizer has been installed (along with the other mechanisms, optics, and detectors) into the FOS. The entire FOS is presently undergoing thermal vacuum testing.

ACKNOWLEDGEMENT

This work was performed under NASA Goddard contract NAS5-24463 and purchase contract E07121-3143 from the Regents of the University of California (Faint Object Spectrograph for the Space Telescope).

¹ Allen, R.G., and Angel, J.R.P., "Performance of the Spectropolarimeter for the Space Telescope Faint Object Spectrograph", Proceedings of the S.P.I.E., Instrumentation and Astronomy IV, 1982.

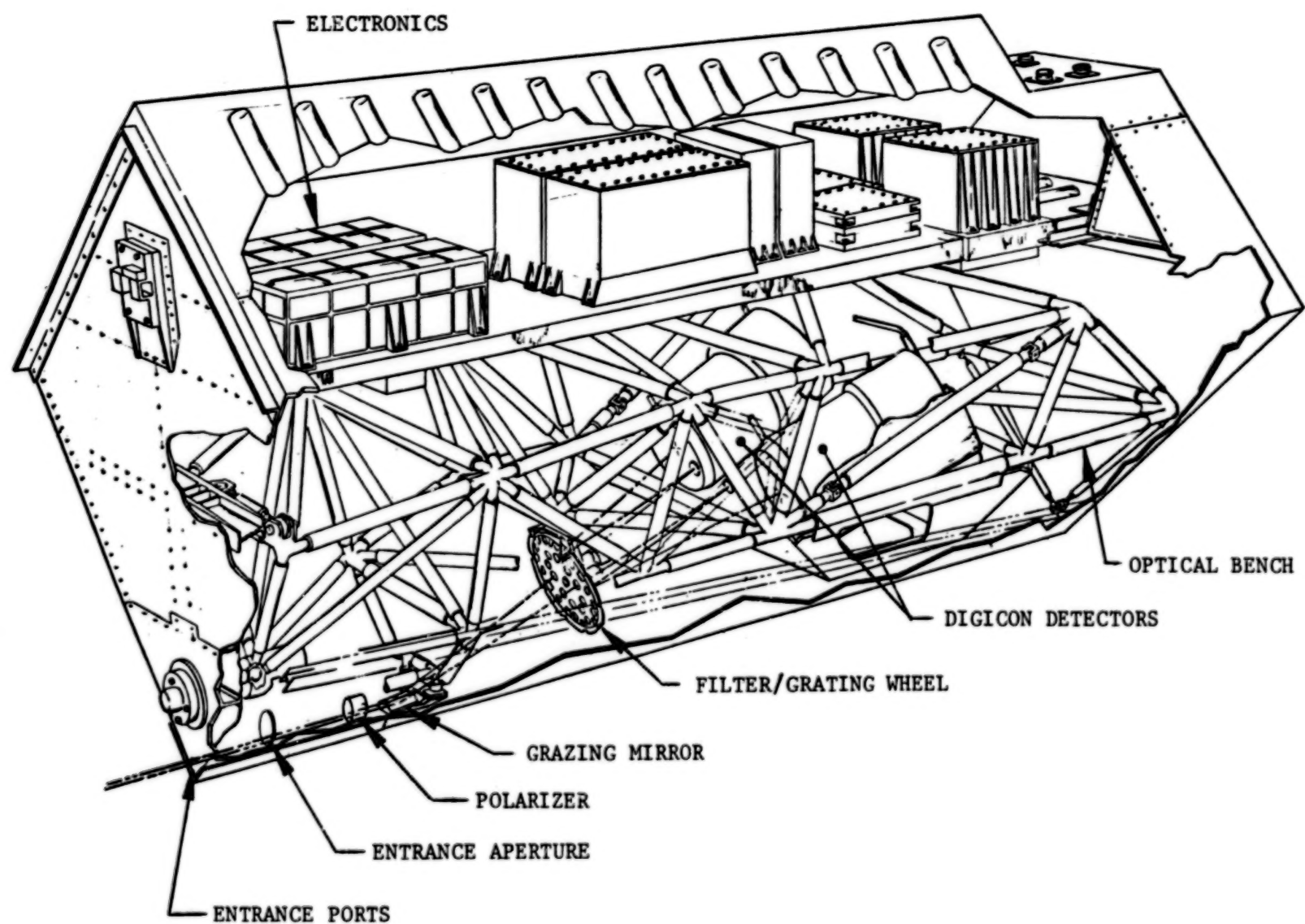


Figure 1. - Faint Object Spectrograph

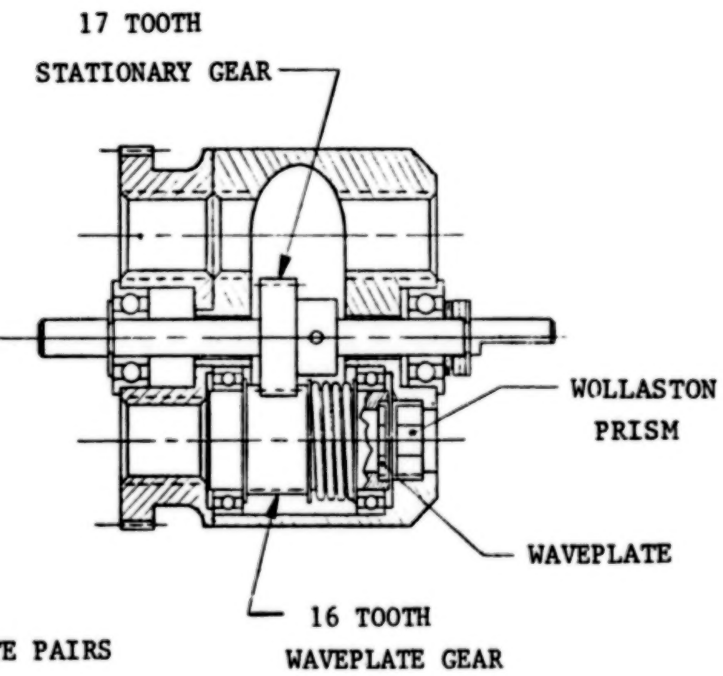
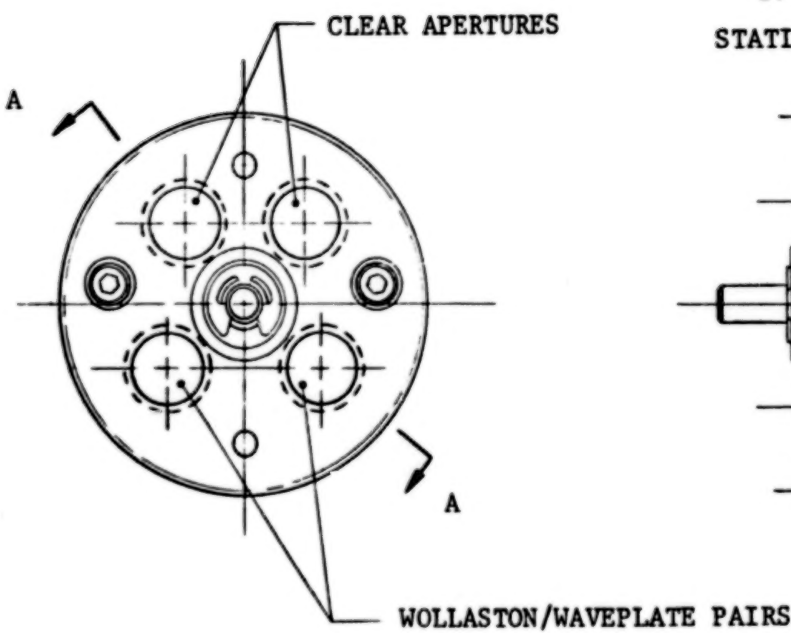


Figure 2. - Rotating Drum

104

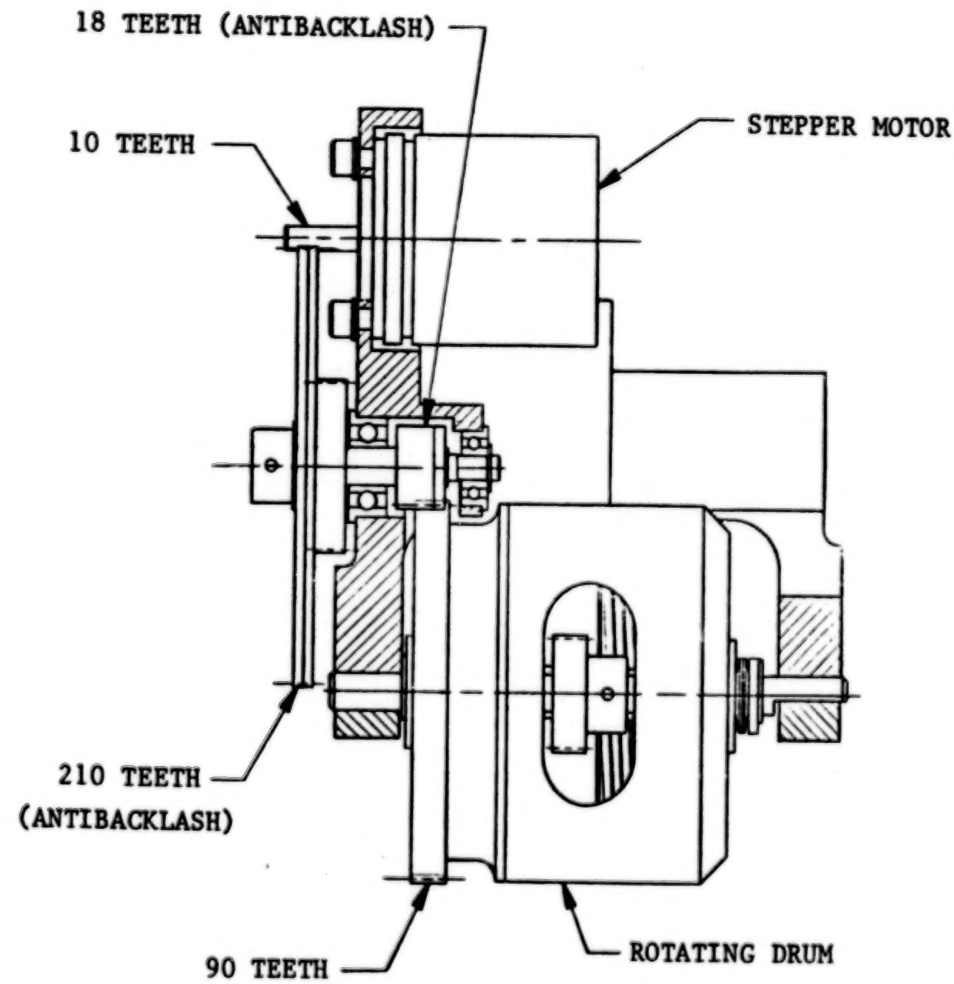


Figure 3. - Gear Train

104

BEST AVAILABLE COPY

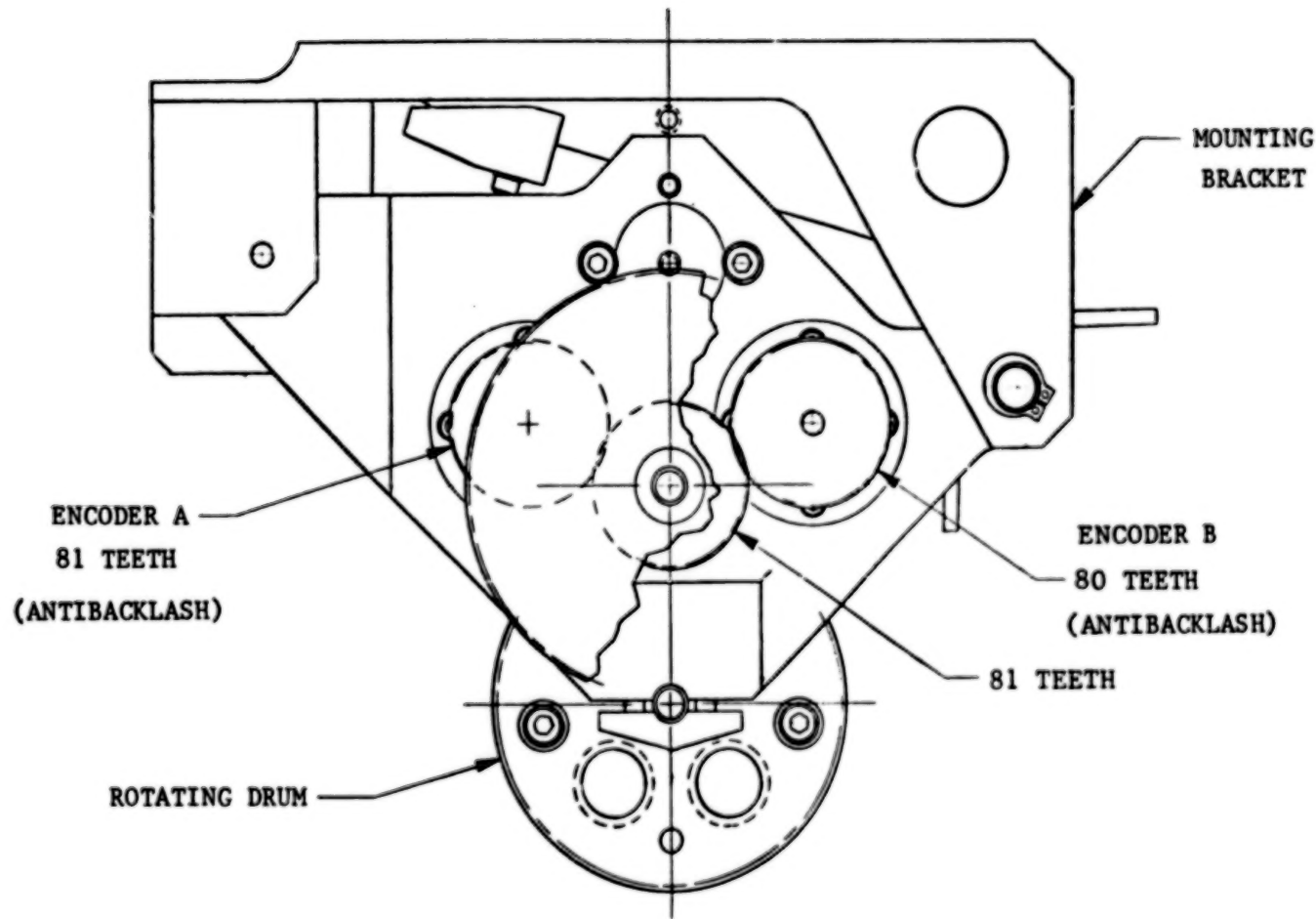


Figure 4. - Encoder Gears

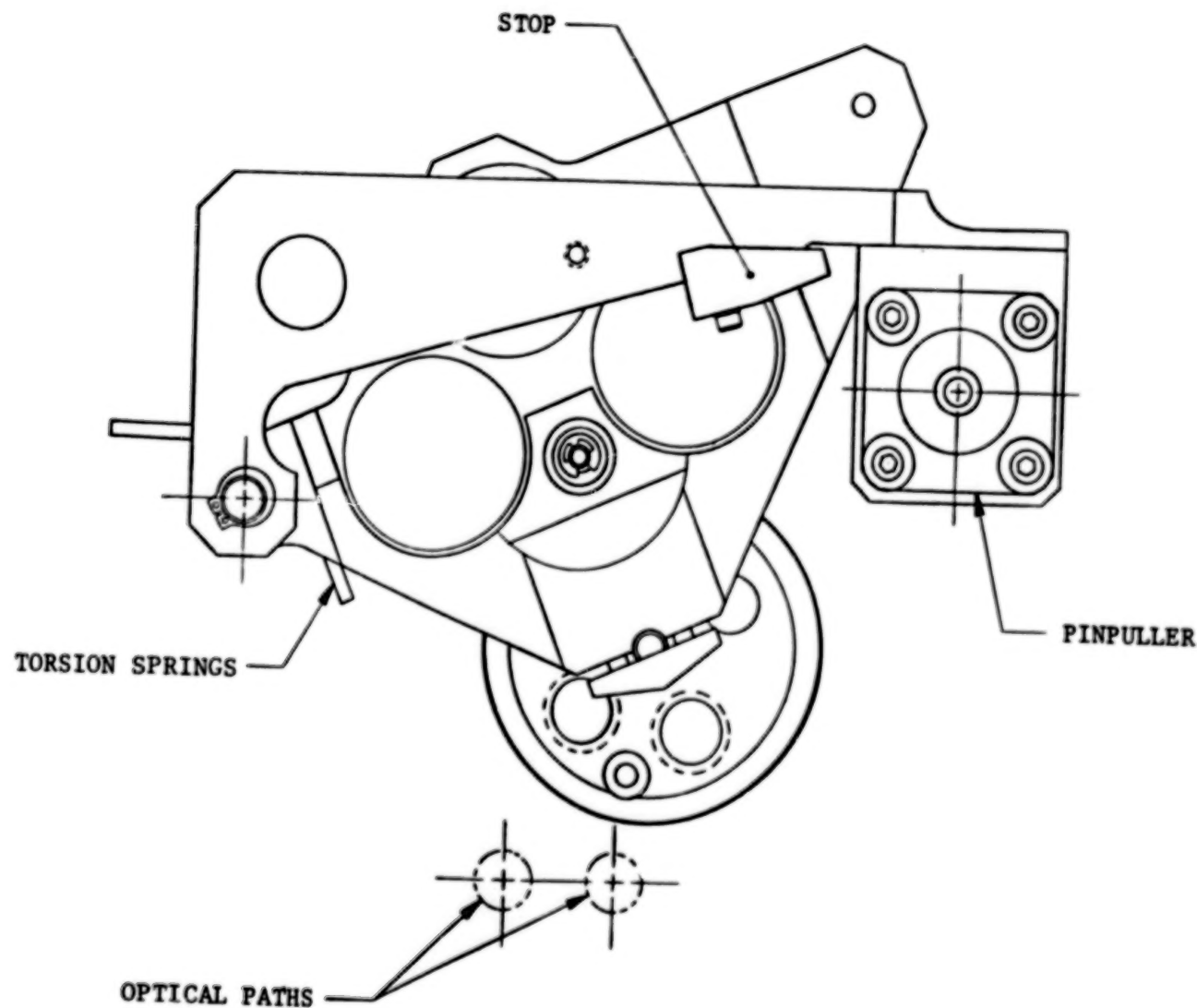


Figure 5. - Fail-safe Mode

107

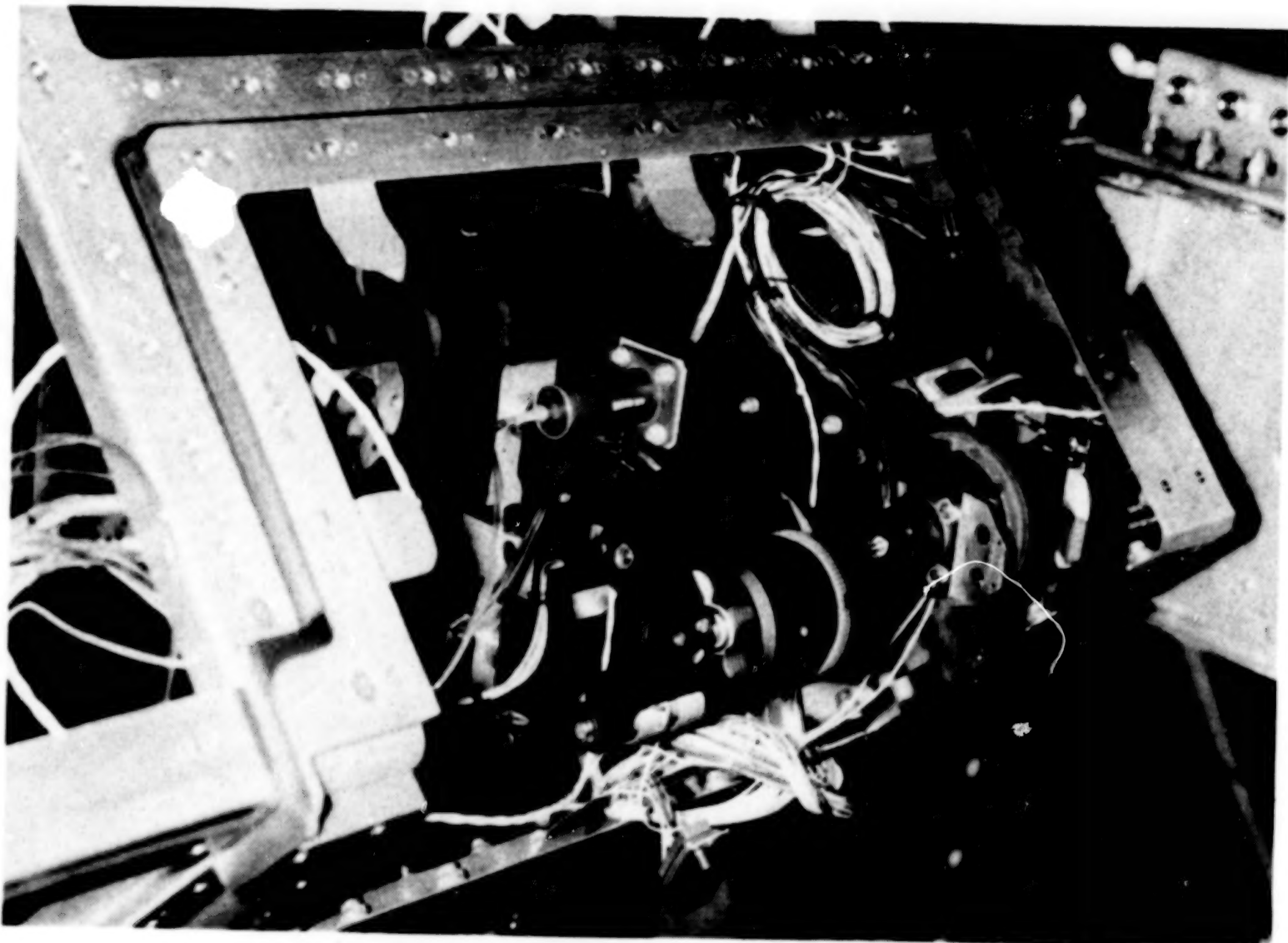


Figure 6. - Polarizer Installed in FOS

107

BEST AVAILABLE COPY

Table 1. Repeatability Tolerances

		Wollaston Prism	Waveplate
θ_x, θ_y (arc min)	Required	± 8	± 8
	Predicted	± 1.1	± 3.2
	Measured	± 1.7	± 3.0
θ_z (arc min)	Required	± 6	± 21
	Predicted	± 3.0	± 12.6
	Measured	± 2.8	± 10.0

DESIGN OPTIMIZATION OF HIGH-PERFORMANCE ELECTRODYNAMIC ACTUATORS FOR USE IN A CRYOGENICALLY COOLED TELESCOPE

J.-N. Aubrun, K. R. Lorell, and K. P. Silveira*

INTRODUCTION

Substantial improvements in infrared sensor technology, the ability to design optics suitable for use at cryogenic temperatures, and the advent of Space Shuttle operations have spurred the development of the Shuttle Infrared Telescope Facility (SIRTF) [Ref. 1]. SIRTF, operating at cryogenic temperatures, will be flown as a shuttle-attached payload for missions up to 14 days. One of the unique advantages of a cooled infrared telescope observing above the earth's atmosphere is its ability to detect and measure extremely faint objects. This ability is further enhanced by using a technique called space chopping. Space chopping requires the telescope secondary mirror to execute a rapid back-and-forth motion in a pattern closely approximating a square wave. This motion, performed at frequencies between 10 and 40 Hz with amplitudes ranging from 5 to 45 arcminutes, permits a continuous comparison of an object-field containing background radiation only with a nearby field containing background radiation plus source radiation. By collecting data from both object fields and subtracting the resultant outputs, the signal-to-noise ratio of very weak sources is substantially improved.

The requirements placed on the secondary mirror actuation system by space chopping are especially difficult to meet. Ideally, of course, the mirror should execute a perfect square wave, exhibit no overshoot or jitter, and be able to operate over a wide range of frequencies and amplitudes. The actuators must be compact enough to fit behind the secondary mirror while developing sufficient force to rapidly accelerate and decelerate the mirror. In addition, the power to operate the actuators must be minimized because any heat dissipated inside the telescope must be removed by the cooling system, which has a limited capacity.

In the sections that follow, an analysis and optimization of a mirror-actuator system for large-excursion/high-frequency chopping is developed. The results of this analysis, combined with laboratory measurements of a prototype actuator operating at cryogenic temperatures, allow performance predictions to be made for a real system utilizing this technology.

PERFORMANCE CRITERIA AND POTENTIAL ADVANTAGES OF ELECTRODYNAMIC ACTUATORS

The performance criteria for the SIRTF secondary mirror are as follows:

- 20 Hz, 90 percent duty cycle chop
- ± 24 arcmin amplitude
- 1000 g-cm² mirror inertia
- Reactionless design
- Energy dissipation of <200 mW
- Actuator dimensions not to exceed secondary mirror envelope

These pose extremely challenging problems for the control system designer. The usual requirements of aerospace systems for small size, light weight, and low power are augmented by the need to generate forces on the order of 50 to 100 N in a time frame of only 200 to 600 μ s.

Electrodynamic actuators are differentiated from the electromagnetic variety (Ref. 2) by their lack of a fixed magnetic field (see Figs. 1 and 2). By using two coils to generate the interactive magnetic fields, electrodynamic actuators are

*Lockheed Missiles & Space Company, Co., Palo Alto Research Laboratory, Palo Alto California.

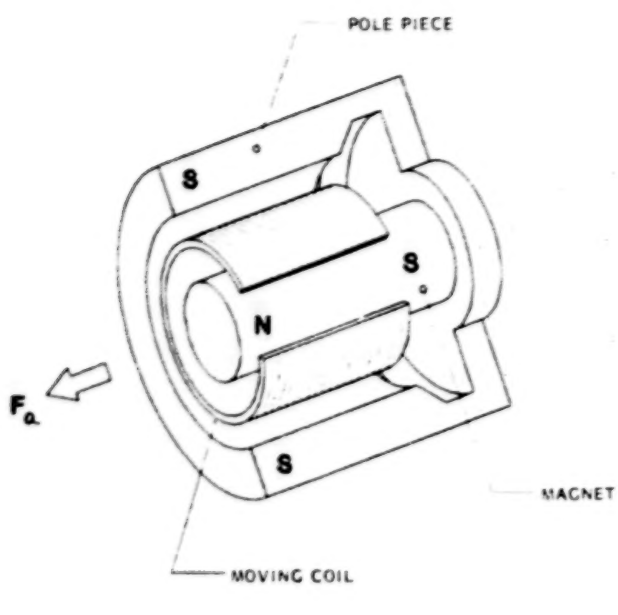


Fig. 1 Electromagnetic Actuator
Cutaway View

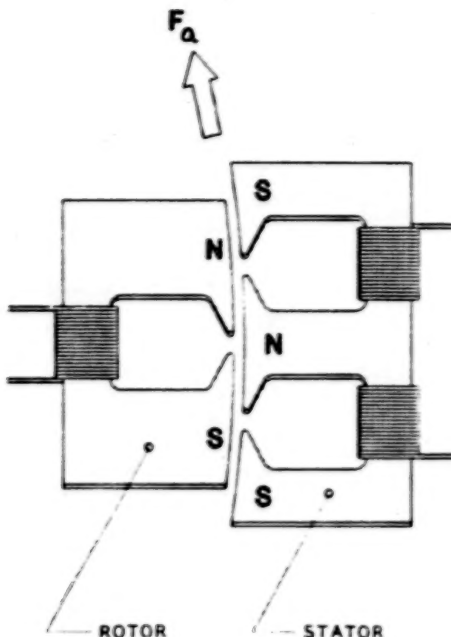


Fig. 2 Electrodynamic Actuator Detail

capable of delivering substantially more force than an electromagnetic device of comparable size. This is possible because higher flux concentrations can be obtained using electromagnets, very small gaps, and special core geometry and material to focus field effects.

Two characteristics of electrodynamic actuators, the comparatively large inertia of the moving portion and the additional power resulting from the use of two coils (rather than the single coil in an electro-magnetic machine) are potential disadvantages for the SIRTF application. Given the performance criteria, the questions to be answered are:

- Could any actuator, with physically realizable dimensions, produce the force required?
- What is the optimum actuator-linkage geometry, given the size and inertia-cancelling constraints on the mirror-actuator system?
- What is the predicted energy dissipation of the proposed design under SIRTF operation conditions?

DEVELOPMENT OF AN ANALYTICAL MODEL FOR ACTUATOR OPTIMIZATION

The relationship between the physical parameters used to describe the geometry of a generic mirror-actuator system are shown in Fig. 3. A real system would, of course, have two actuators to provide symmetric inertia cancellation. The analysis is somewhat simplified, however, by assuming the use of a single actuator.

The control system parameters α and β , which affect the design of the actuator, are illustrated in Figs. 4 and 5. The ratio of the total transition time t_T to the time during which the actuator is used to apply a force t_A (for either acceleration or deceleration) is defined as α . The duty cycle, or percentage of a total chop cycle during which the mirror is actually available to the optical system, is defined as β . Together α and β represent important tradeoff parameters in both the design of the mirror-actuator system and the overall philosophy of the telescope system. Figure 5 demonstrates the impact on the actuator requirements of an 11 percent decrease in data-taking capability during a 20-Hz chop (β changed from 0.9 to

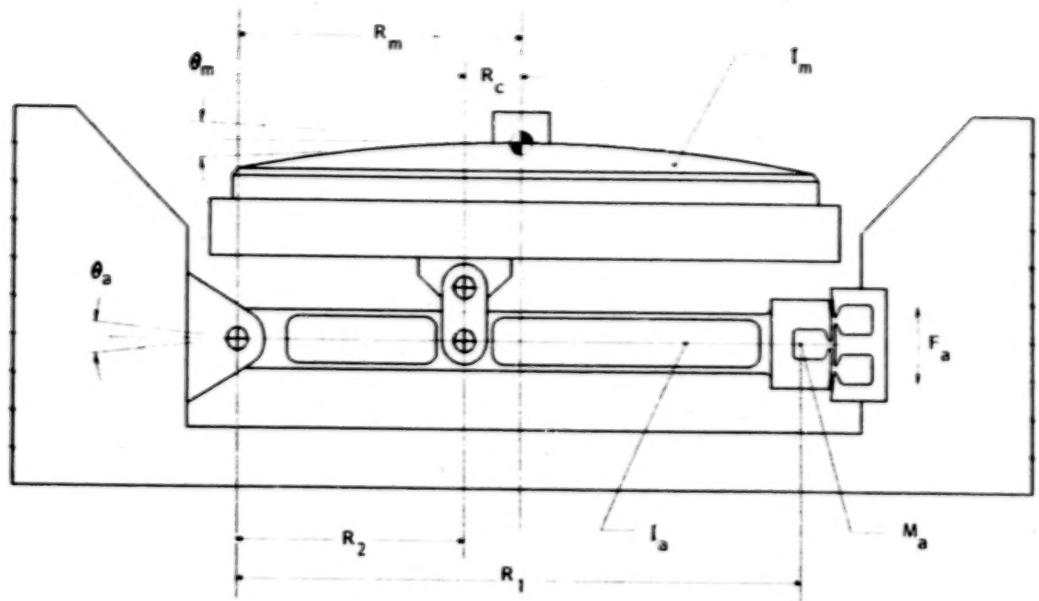


Fig. 3 Secondary Mirror Actuator

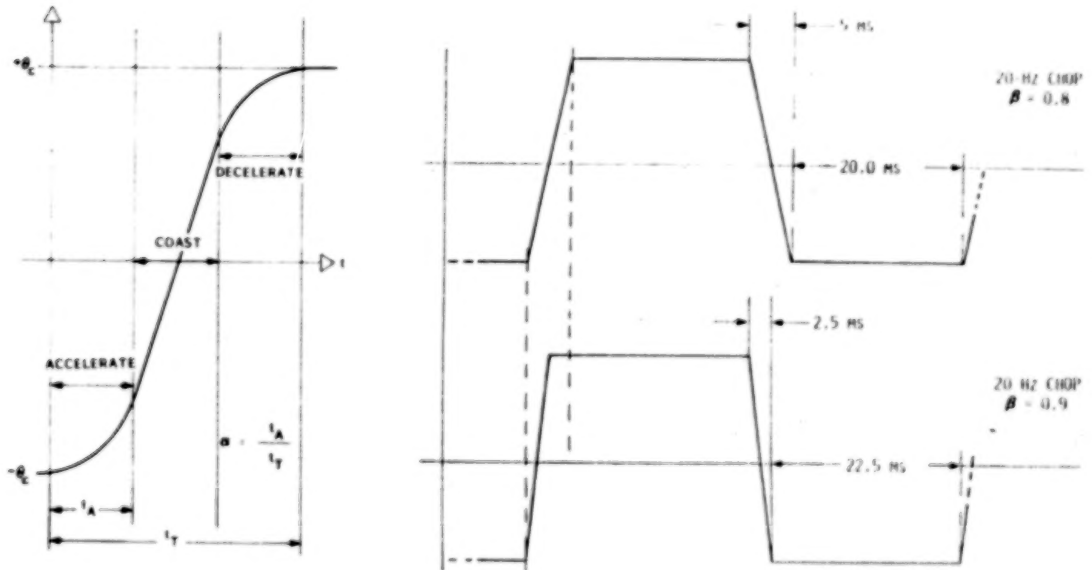


Fig. 4 Transition Period Detail

Fig. 5 Effect of Duty Cycle Variation

0.8). The force required to accelerate the mirror decreases by a factor of almost 10, thus placing substantially lower demands on actuator performance and power consumption.

Relations (1) through (8) were derived by analyzing the requirements for mirror acceleration/deceleration, inertia cancellation, and linkage geometry of the mirror and actuator system. Defining θ_c , v , and γ respectively as the mirror chopping amplitude, the chopping frequency, and the actuator gear ratio R_c/R_2 , the following relations are found:

$$\text{balancing condition: } \gamma = I_m / (I_a + m_a R_1^2) \quad (1)$$

$$\text{force required: } f_r = (I_m + I_a + m_a R_1^2) C_e / R_1 \quad (2)$$

where

$$C_\theta \triangleq 4v^2\theta_c/\alpha (1-\alpha) (1-\beta)^2 \quad (3)$$

force available: $f_a = (K_a/\delta_a) m_a \quad (4)$

The quantity (K_a/δ_a) is the ratio of the force developed per unit active area of the pole pieces to the mass per unit area of the pole pieces. The estimate of available actuator force modeled in Eq. (4) is a highly simplified approximation and is heavily dependent on core material and geometry.

The simultaneous solution of (2) and (4) requires that:

$$K_a/\delta_a > R_1 C_\theta \quad (5)$$

The actuator mass is then given by

$$m_a = \frac{(I_m + I_a) C_\theta}{R_1(K_a/\delta_a - R_1 C_\theta)} \quad (6)$$

Resistive losses in the actuator may be calculated from the basic relationship for energy dissipation in a resistor

$$E_R = \int_0^t R i^2 dt$$

This leads to the expression for the average power dissipated by a pulse-actuated system

$$P_E = \frac{8}{3} v R i_{\max}^2 t_A \quad (7)$$

Assuming that the resistance R is a function of the size of the pole piece (a larger pole piece will result in a longer winding and hence a higher resistance), then Eq. (7) may be written as

$$P_E = \frac{4}{3} R' m_{a \max}^2 \alpha (1-\beta) \quad (8)$$

where R' is the resistance per unit mass of the pole piece.

The mechanical energy imparted to the mirror/actuator system can also be calculated as well as the resultant power. However, the value of the mechanical power (and hence the potential dissipation of energy) is several orders of magnitude less than the typical values obtained for electrical energy losses and so will not be considered here.

PARAMETRIC OPTIMIZATION OF ACTUATOR REQUIREMENTS

From Eq. (6) it can be seen that a minimum value for m_a (and thus for f_r) will be achieved when

$$R_1 = (K_a/\delta_a)/2C_\theta \quad (9)$$

The actuator mass will be in this case

$$m_a = 4(I_m + I_a) C_\theta^2 / (K_a/\delta_a)^2 \quad (10)$$

and thus the optimal gear ratio:

$$\gamma = \frac{I_m}{I_m + 2I_a} \quad (11)$$

Finally, the force required from the actuator is:

$$F_a = 4(I_m + I_a) C_\theta^2 / (K_a/\delta_a) \quad (12)$$

Equation (12) can be obtained either by substituting the value of m_a in (10) into the force available model in (4) or by substitution in (2) with R_1 from (9). This is possible because we have assumed the force required F_a equal to the force available f_a .

Figures 6 and 7 display the results of calculations to determine actuator performance requirements as a function of the parameters β and K_a/δ_a . In all of these calculations, $\alpha = 0.33$. This value minimizes the electrical power in (8) when m_a is provided by (10).

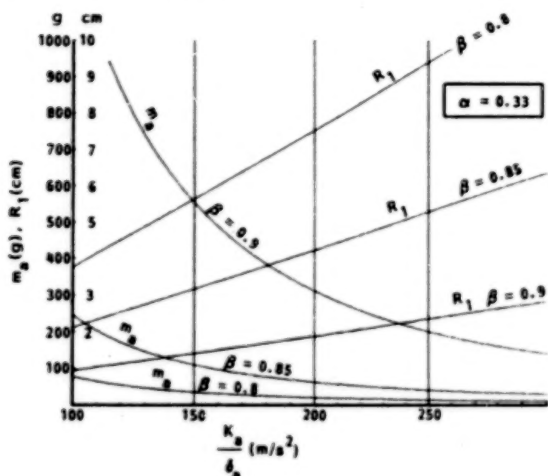


Fig. 6 Optimal Mass (m_a) and Lever Arm (R_1) Versus K_a/δ_a

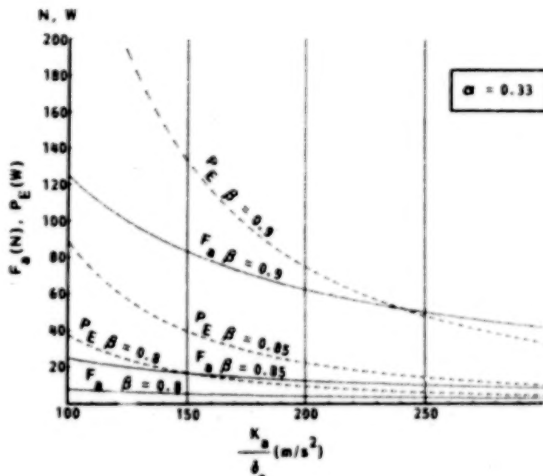


Fig. 7 Force Required (F_a) and Power Dissipated (P_E) Versus K_a/δ_a

Three values of K_a/δ_a , 150, 200, and 250 m/s^2 have been highlighted in Figs. 6 and 7. These values represent the range of K_a/δ_a to be expected from well designed electrodynamic actuators and thus illustrate the region from which design selections can be made for the dependent variables.

In Fig. 6 the changes in actuator pole-piece mass m_a and actuator arm length R_1 are plotted versus K_a/δ_a for three values of duty cycle β . It is clear from both sets of curves that to achieve a $\beta = 0.9$ will require an actuator in the 250- m/s^2 class. A compromise design in which $\beta = 0.85$ (slight degradation in chopping performance at 20 Hz) with $K_a/\delta_a = 200 \text{ m/s}^2$ indicates a required mass of 75 g at a radius of 4.2 cm.

In Fig. 7, the changes in required force F_a and dissipated electrical power P_E are shown as functions of K_a/δ_a . The assumptions of $\theta_C = 24$ arcmin, $v = 20$ Hz, and $R' = 60 \Omega/\text{kg}$ were made for these calculations. The difficulty of meeting the $\beta = 0.9$ requirement is very apparent. Even for a state-of-the-art design, a force of 55 N dissipating 54 W would be required. For a more easily designed actuator with a $K_a/\delta_a = 150 \text{ m/s}^2$, the required force and dissipated power are 85 N and 131 W respectively. These values are too large by a factor of 3. The improvement obtained by

setting $\beta = 0.85$ is dramatic, assuming a 200-m/s^2 design. The power dissipated drops to 25 W while $m_a = 70 \text{ g}$ and $F_a = 17 \text{ N}$.

ACTUATOR EXPERIMENT VALIDATION

Preliminary laboratory experiments were conducted [Ref. 3] to validate the concepts and design of the SIRTF secondary mirror and its actuator(s). Tests were conducted on the actuator to verify force levels and power consumption at ordinary and cryogenic temperatures. The electrodynamic actuator chosen for the test had not been specially optimized; thus the actual performance is below the SIRTF requirements. However, the results are readily scalable to an actual SIRTF design and sufficient to demonstrate feasibility. Moreover, the techniques developed for these tests, particularly at cryogenic temperatures, constitute a solid basis for designing future tests of the fully actuated secondary mirror.

MEASUREMENT PRINCIPLES

Force Measurements

Force measurements are made using a technique similar to that of the ballistic pendulum. This particular method has two advantages: first, the actuator is operating in a mode similar to the actual mode and, second, it is simple to implement and accurate results can be obtained. A short current pulse (200 to 1200 μs) is sent to the actuator coils, communicating a certain amount of kinetic energy to the system, which gradually loads up the spring system constituted by the pivot and the gravity field. The maximum amplitude deflection θ_{\max} is thus a measure of the force applied to the actuator. To quantify these principles, the dynamic model shown in Fig. 8 is used. The actuator is mounted vertically, with its CG below the flex pivot, and the equations of motion are given by:

$$I\ddot{\theta} + (k + Mga)\theta = Fr \quad (13)$$

where I is the actuator inertia about the pivot, k is the pivot spring constant, M is the total mass of the moving part, a is the position of the center of mass, g is the acceleration due to gravity, F is the electrodynamic force generated between the pole pieces at a distance r from the pivot, and θ is the deflection angle.

For a pulse of short duration Δt , it can be shown that the average force F is:

$$F = (\theta_{\max}/r\Delta t) \sqrt{I(k + Mga)} \quad (14)$$

The quantities I and $k + Mga$ are first derived from the measured natural frequencies of oscillation of the actuator in the following cases: (1) nominal position, and (2) nominal position with added mass m at distance d from the pivot.

Actuator Force Coefficient

The force produced by the electrodynamic actuator is directly proportional to the product of the currents in the rotor (i_1) and stator (i_2) coils:

$$F = k_F i_1 i_2 \quad (15)$$

where the coefficient k_F is expressed in Newtons per square Ampere. Because of the coil inductance, saturation of the power amplifiers driving the coils, and other nonlinearities, the pulse shapes are usually not square, especially for short durations. The measurements give an average value of F_{av} , and the force coefficient is determined by the formula:

$$k_F = (F\Delta t) / \int_0^{\Delta t} i_1 i_2 dt \quad (16)$$

In these studies, the maximum achievable F is more important for the design than the actual value of k_F , but linear and saturation ranges must be assessed for scalability and extrapolation to different designs.

Power Measurement Principle

The electrical power dissipated in the actuator is of primary concern for the SIRTF design, and accurate measurement is essential. The method chosen here is purely electrical. A general circuit model for one of the actuator coils is shown in Fig. 9. The main constituents of this circuit are the inductance L , the resistance R , and an induction voltage e , which includes the interactions of the coil with the other part of the actuator and other kinds of losses.

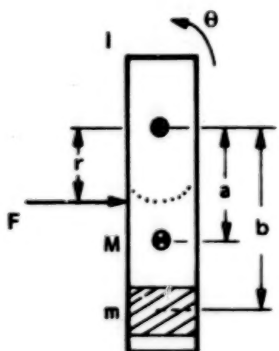


Fig. 8 Dynamic Model

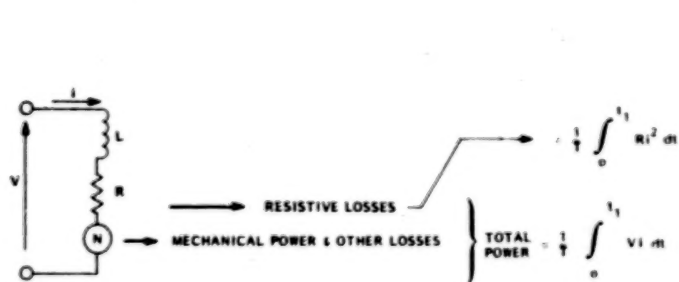


Fig. 9 Power Measurement

Measuring the input voltage V and current i in the coils leads to an evaluation of the total energy fed to the system during the interval Δt ,

$$E_T = \sum_k \int_0^{\Delta t} V_k i_k dt \quad k = 1, 2 \quad (17)$$

The resistive losses are obtained by

$$E_R = \sum_k \int_0^{\Delta t} R_k i_k^2 dt, \quad (18)$$

$$E_m = F\bar{A}t = k_F \int_0^{\Delta t} i_1 i_2 dt \quad (19)$$

The energy balance requires that

$$E_T = E_m + E_R + E_\theta \quad (20)$$

where E_θ represents nonresistive losses. It is thus seen that measurements of V , i , and R can be used to determine the energy losses in the actuator and thus the heat generated.

As shown previously, since the pulse shapes are not square it is necessary to perform an actual integration over some period of time during which there is electrical activity present in the system. (This time may in fact significantly exceed the original pulse width of the input to the power amplifiers.) Thus, each value determined for E_T , E_R , etc., represents the energy per pulse, and the average power is then calculated by multiplying these values by the number of pulses per second.

DATA ACQUISITION AND PROCESSING

The actuator dynamic characterization and the force and power measurements were performed using a sophisticated digital data acquisition and processing system involving an STI/DEC 11-23 microprocessor, A/D and DAC interfaces, a separate digital frequency generator, a pulse generator and power amplifiers, and a data analysis software package (VAMP). This system is used in two different modes (Fig. 10):

- (1) A slow mode in which the actuator is pulsed every 5 or 10 s and the data are taken at a 200-Hz sampling rate.
- (2) A fast mode in which the actuator is pulsed at a 200.1-Hz rate by an independent frequency generator triggering the pulse generator. The 11-23 is still taking data at 200 Hz and, because of the slight difference in frequencies, the equivalent (or virtual) sampling time is about 2.5 μ s.

CRYOGENIC MEASUREMENTS SETUP

These measurements are made using a helium dewar as shown in Fig. 11. A small window allows a laser beam to be reflected from a mirror attached to the actuator. The reflected beam is detected by a linear photosensor whose output is thus proportional to the actuator rotation angle θ . The current into and voltage across the coils are picked up outside of the dewar, near the connector. Thermistors are glued to various parts of the actuator and internal fixtures to determine the local temperatures. Power data are acquired in a short burst to minimize heat dissipation, which would otherwise be significant for 200-Hz operations. Because of the short time available at low temperature due to the limited capacity and insulation of the dewar, all the various measurements are stored in memory to be processed and studied later.

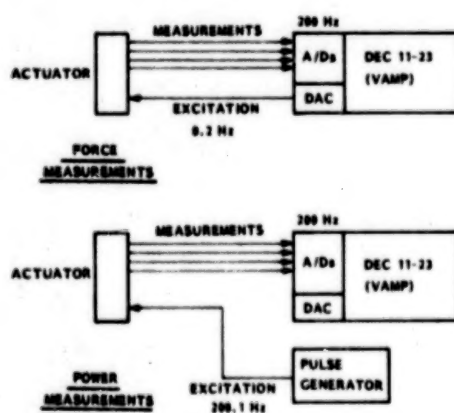


Fig. 10 Data Acquisition and Processing System

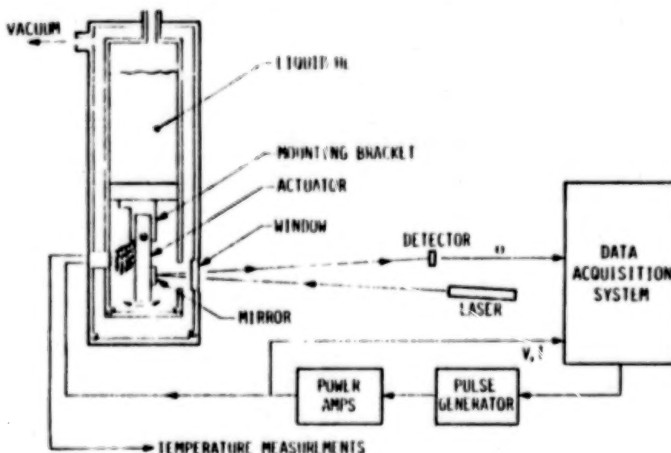


Fig. 11 Cryogenic Measurements Variation

EXPERIMENTAL RESULTS

Data were taken at ordinary temperature and at temperatures around 16 K. In both cases the actuator was installed inside the dewar, except for preliminary measurements of mass/inertia properties.

Mass/Inertia Properties

The actuator under test was found to have the following characteristics:

$$k = 0.69 \text{ N-m/rad} \quad Mga = 2.95 \times 10^{-2} \text{ N-m/rad} \quad I = 1.60 \times 10^{-4} \text{ kg-m}^2$$

The value of r (application point of the electrodynamic force) is 0.0212 m.

Force Measurements

These measurements were taken for commanded pulse lengths of 400, 600, and 1200 μs at room temperature and at 500 and 600 μs at cryogenic temperatures. A typical data set for the cryogenic runs is shown in Fig. 12. Values for the actuator force coefficient were found to be in the range of 0.3 to 0.6 N/A^2 . Fig. 13 plots the relationship between the calculated values and those measured experimentally. The assumption of $K_a/\delta_a = 100 \text{ m/s}^2$ for this actuator appears to be substantially correct based on the fidelity of the computed values in Fig. 13.

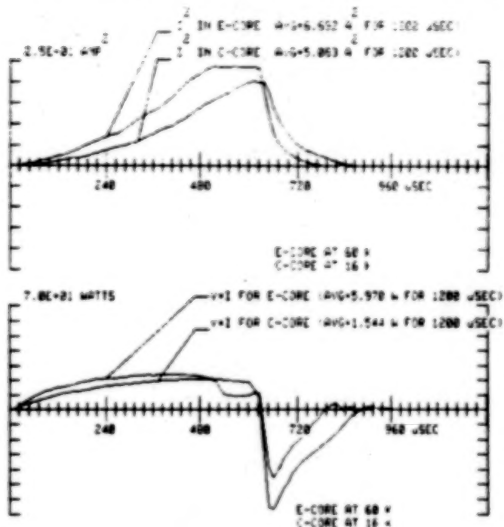


Fig. 12 Total Input Power (VI) and Resistive Losses (i^2) at Cryogenic Temperatures

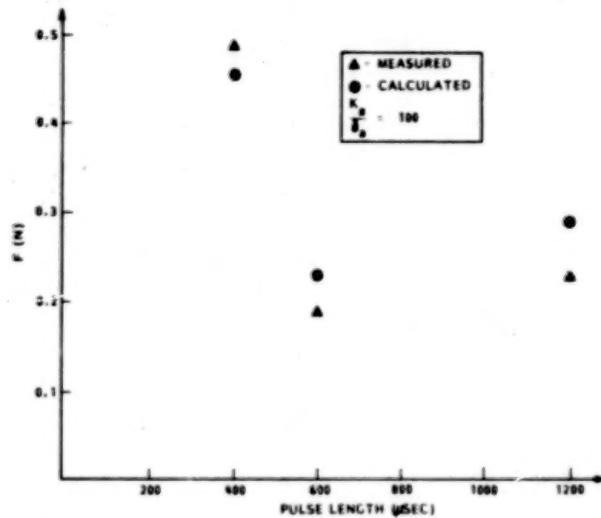


Fig. 13 Actuator Force for Various Pulse Lengths

Power Measurements

Data were taken with the actuator cooled to below LN_2 temperature (E-core at 60 K and C-core at 16 K). The results of these tests are summarized in Table 1:

Table 1 POWER DISSIPATION

Pulse Length (μs)	Average Total Power (W) Per 1200 μs		Average i^2 (A^2) Per 1200 μs	
	C-Core	E-Core	C-Core	E-Core
500	2.785	4.653	3.541	1.886
600	1.544	5.970	5.083	6.692

Measurements of the C-core and E-core winding resistance indicated a drop of approximately a factor of 10 from room temperature values. However a factor of 100

to 150 was expected at 16 K (Ref. 4). To verify the assumption of greatly increased conductivity, a separate test was conducted in which the complete E- and C-cores of a disassembled PPM actuator were cooled directly in an LHe bath until they stabilized at 4.2 K. These data, summarized in Table 2, support the claim that substantially lowered resistivity will occur at SIRTF secondary mirror operating temperatures, even without the use of high-purity, annealed copper wire.

Data from Tables 1 and 2 and Fig. 12 may now be combined to show force generated and the associated energy dissipation (Table 3).

Table 2 RESISTIVITY

Temperature (K)	E-Core Resistance (ohms)	C-Core Resistance (ohms)	Average Reduction
Room Ambient	1.935	1.660	----
77	0.220	0.203	8.5
4.2	0.017	0.013	120.0

Table 3 GENERATED FORCE AND ENERGY LOSS

Commanded Pulse Length (μ s)	Force Generated (N)	Total i^2R Energy Loss (E+C Cores) per Pulse (J)
500	2.91	1.55×10^{-4}
600	3.32	2.16×10^{-4}

Predicted Performance for SIRTF Actuators

Since both the force F generated by this type of actuator and the resistive losses are a function of i^2 , the average power dissipation P_{ave} is thus proportional to F . This scaling relation was used with data from Table 3 to obtain the results in Table 4. Note that even at a 90 percent duty cycle, total power dissipation is less than 150 mW.

Table 4 POWER DISSIPATION

Duty Cycle (500 μ s Pulse)	Force Level Required (20 Hz at 45 arcmin amplitude) (N)	Average Power Dissipated by Resistive Losses $K_a/\delta_a = 200 \text{ ms}^2$ (W)
$\beta = 0.85$ (85 percent) $\alpha = 0.33$	17	0.036
$\beta = 0.90$ (90 percent) $\alpha = 0.33$	65	0.132

REFERENCES

1. F. C. Wittleborn, and L. S. Young, "A Cooled Infrared Telescope for the Space Shuttle - the Shuttle Infrared Telescope Facility (SIRTF)," AIAA Paper 76-174, 21st Annual Meeting of the American Astronautical Society, Denver, 1975.
2. K. R. Lorell, R. R. Clappier, W. F. Barrows, and G. K. Lee, "A Microprocessor-Based Position Control System for a Telescope Secondary Mirror," Proceedings of the Joint IFAC/ESA Symposium on Automatic Control in Space, Noordwykerhout, The Netherlands, 1982.
3. Final Report LMSC-D877125, "Study of SIRTF Long-Life Feasibility," 1982.
4. K. D. Timmerhaus, et al., "Advances in Cryogen Engineering," p. 157, Plenum Press, Inc., New York, 1960.

Blank Page

CONTROL OF LARGE THERMAL DISTORTIONS IN A CRYOGENIC WIND TUNNEL

John C. Gustafson*

ABSTRACT

The National Transonic Facility (NTF) is a recently completed research wind tunnel capable of operation at temperatures down to 89K (160° R) and pressures up to 9×10^5 Pa (9 atmospheres) to achieve Reynolds numbers approaching 120,000,000. Wide temperature excursions combined with the precise alignment requirements of the tunnel aerodynamic surfaces imposed unique constraints on the mechanisms supporting the internal structures of the tunnel. The material selections suitable for this application were also limited. A general design philosophy of utilizing a single fixed point for each linear degree of freedom and guiding the expansion as required was adopted. These support systems allow thermal expansion to take place in a manner that minimizes the development of thermally induced stresses while maintaining structural alignment and resisting high aerodynamic loads.

Typical of the support mechanisms are the preload brackets used in the fan shroud system and the Watts linkage used to support the upstream nacelle. The design of these mechanisms along with the basic design requirements and the constraints imposed by the tunnel system are discussed in detail.

INTRODUCTION

The National Transonic Facility (NTF) is a recently completed cryogenic and high pressure wind tunnel at the NASA Langley Research Center capable of operating at temperatures in the range of 89K (160° R) and at pressures to 9×10^5 Pa (9 atmospheres). This facility is capable of producing Reynolds numbers in the range of 120,000,000 by using cryogenic nitrogen as the test fluid and will provide a marked increase in capability to accurately simulate the full scale aerodynamics of current and future aircraft with small scale models. The tunnel is a recirculating type with a number of internal structures to control and condition the flow through the test section. The internal structures experience wide temperature swings since they are exposed to the cryogenic nitrogen. The tunnel pressure shell is internally insulated and is only exposed to the outside ambient temperature. The design of the mechanisms to support these internal structures from the tunnel pressure shell and still accommodate the thermal and pressure induced relative displacements between the shell and the internals was one of the critical problems to be solved in the facility design.

*NASA Langley Research Center, Hampton, Virginia

This paper discusses the problems associated with the structural design, resulting from thermal expansion, for the entire facility and the general design approach used to deal with it. As typical examples, the design of the supports for two of the major internal structures, the fan shroud system and the upstream nacelle, are examined in detail. The material selection criteria and the constraints imposed by operational considerations are included in the discussion. The final solutions and the major problems experienced in implementing these designs are reviewed in detail.

BACKGROUND

The primary requirement for dynamic simulation of an aircraft at transonic speeds, by a model in a wind tunnel, is the matching of the Reynolds and Mach numbers. While obtaining the required Mach number has readily been achievable in existing facilities, generating full scale Reynolds numbers on scale models has been a considerably more difficult task.

As a result, over the past three decades existing wind tunnels have been unable to accurately simulate the characteristics of the progressively higher performance aircraft that were being developed, Figure 1.

As early as 1920 it was recognized that the Reynolds number in a wind tunnel could be controlled by varying the temperature of the working fluid.⁽¹⁾ Density, viscosity and the speed of sound are all temperature dependent and tend to increase the Reynolds number as the temperature decreases, the effect being most pronounced below 180K (324°R) as shown in Figure 2.

Currently the NASA Langley Research Center is in the process of activating the National Transonic Facility which is designed to achieve full scale Reynolds numbers in the transonic regime and provide a more accurate flight simulation in the wind tunnel testing of the next generation of aircraft. (See Figure 3) The tunnel is a recirculating type operating over a temperature range of 89K (160°R) to 339K (610°R).⁽²⁾ Cryogenic nitrogen is used as a working fluid for the low temperature regime while dry air is used for the ambient case. The general design goals are given in Table 1 with the overall size and configuration shown in Figure 4. To minimize the energy consumption associated with cooling the tunnel system to the cryogenic state and to permit more rapid changes in the working gas temperature, the tunnel insulation system is on the internal surface of the pressure shell, Figure 5. This causes the tunnel pressure shell to remain at near ambient temperature while the temperature of the internal structures, which are supported by the pressure shell, are near the flow stream temperature.

Accommodating Thermal Expansions

The design of large structures such as NTF must, in general, incorporate some provision for thermal expansion between supports. For

instance it is necessary to accommodate the seasonal and daily temperature induced dimensional changes or stresses. While it appears that large dimensions are the root of the problem, combining the equations defining the modulus of elasticity and the expansion of a material under temperature show otherwise. As an example, the tensile stress generated by changing the temperature of a bar fixed at both ends can be defined by

$$\sigma = E \alpha \Delta T$$

where σ = tensile stress

E = modulus of elasticity

α = linear coefficient of thermal expansion

ΔT = change in temperature from the stress-free state

It follows that for parts of any size, manufactured from mild steel or annealed aluminum alloys, a temperature shift of 50K (90°R) will generate stresses on the order of $6.89 \times 10^7 \text{ N/m}^2$ (10,000 psi) or about half of the design allowable stresses. Logically then, it is most efficient to allow the thermal expansion to take place, more or less, unrestrained.

The approach used in the NTF design is the classic one of providing a single fixed point of attachment along a given axis and letting the structure deform as freely as possible away from the anchor point. Typical of this approach is the single point anchoring of the pressure shell at the transfer case, Figure 4, and the use of pivoting supports of the type shown in Figure 6 at other ground anchors.

The internal structures are supported from the inner pressure shell wall. Attachment points between the various internals and the supporting shell are located where a functional requirement dictates a fixed relationship between the two structures. Thermal growth away from these attachment points is guided to maintain critical alignments between the internal components and pressure shell structure. This insures that aerodynamic flow quality is maintained regardless of the operating temperature.

MATERIALS

Material selection on the NTF project was severely limited. The basic criteria utilized for material screening was a Charpy notch toughness value in excess of 34 Joules (25 foot pounds). The material also had to meet the requirement imposed by the ASME Pressure Vessel Code.

Table 2 is a list of the primary structural materials chosen for use in the NTF. The use of two types of 5000 series aluminum alloys was dictated by an upper service temperature limit of 339K (61°R) for the 5083 alloy. The use of 5083 was desirable because of its superior strength properties in the annealed condition. However, temperatures from the fan to the cooling coils will rise to 366K (659°R) during ambient temperature tunnel runs necessitating the use of 5454 for aluminum

structures in this section of the tunnel. While 5454 has a lower allowable design stress, it is not susceptible to stress corrosion cracking at temperatures above 339K (610⁰R).

Despite the internal insulation the shell is required to withstand exposure to the cryogenic environment, including possibly a direct contact with liquid nitrogen. Additional considerations of fabrication ease and the requirement for a 50 year fatigue life resulted in the choice of 304 stainless steel for the shell material.

Aluminum was selected over steel for the primary internal structures to reduce weight, increase thermal conductivity and minimize thermal capacity. In order to maintain the thermal stresses within allowable limits, the system cool down time had to be controlled. Even with the optimum material selections, this time could not be reduced to less than approximately 8 hours.

INTERNAL STRUCTURE TO SHELL ATTACHMENTS

As noted earlier, for operational cost considerations, the tunnel pressure steel shell is insulated from the flow stream and the internal structures stabilize at the flow stream temperature. In operation this results in a temperature differential between the shell and internals of apparently 205K (370⁰R) and can result in large relative motions between initially adjacent points on the two structures.

In general, all connections between the internal structural elements and the shell provide fixity in only one local linear direction. Moments on the gross structures are restrained by couples generated by opposing supports on either side of the structure. Local rotations at the supports will occur due to uneven temperature distributions as the system transitions from ambient to its initial operating setpoint. These rotations are simply allowed to occur since they will essentially disappear as thermal equilibrium is reached prior to system start up.

This approach does not directly address the problem of stresses internal to the structure caused by non-uniform temperature profiles during thermal transitions. These are controlled operationally by a five hour structural conditioning cooldown to approximately 117K (210⁰R). Operational temperature variations of the flowstream are then restricted to a change in temperature of 48K (89⁰R). Since these operational swings cannot be predicted, the design calculations assume that an instantaneous change in the gas temperature equal to the full operational temperature swing can occur at anytime within the limits.⁽³⁾ (See Figure 7)

This design approach of letting the structure deform freely reduces both the complexity of the thermal stress analysis and the magnitude of the tunnel stresses. The transient cases of cooldown and the 48K (86⁰R) operational temperature swing became the dominant concern in this area.

Determination of the final stress levels was done by superimposing the mechanically generated stress distribution over the thermal transient stress distributions.

FAN CONTAINMENT SHROUD ASSEMBLY

The fan containment shroud shown in Figure 8 is one of three sections of a sixty foot shroud assembly located in the fan region of the tunnel. This particular section forms the outer surface of the flow annulus, provides the outboard attachments for the fan inlet and exit flow control vanes and, as the name implies, provides protection for the tunnel pressure vessel in the event of separation of a fan blade from the drive disc. Table 3 summarizes the pertinent dimensions, loads, and design requirements of this structure.

The shroud is supported from the tunnel wall which is reinforced for the high loads in this region by external rings. To deal with the combined thrust and torsional operating loads on the shrouds and concurrently allow thermal expansion of the shroud assembly, independent radial and axial support systems are utilized. Each system provides local support along one linear axis and allows relative freedom of motion in the other two orthogonal axes.

Thrust Support

In operation the absolute pressure inside the shroud assembly increases from the upstream to downstream end. To prevent recirculation between the shroud and the shell wall this flow path was sealed off. It is this seal requirement which generates the majority of the force on the shroud and results in a net force tending to drive the shroud upstream. A single bulkhead seal is used on the upstream end and this provides the single fixed axial support point for the shroud, Figure 9.

To insure the alignment during non-operating conditions a set of four preloaded brackets are placed around the circumference of the shell. Each bracket provides an initial force of 89 kN (20,000 lbs) against the seal, and the shallow angle of the line of action precludes any appreciable change in loads due to a radial displacement of the shroud relative to the shell.

Radial Support

In the cold condition the clearance between the rotating blades and the shroud is designed to be less than 1.8 mm (.070 in). This requirement dictated a support design that:

1. Provides for radial adjustment of the structure position at installation in extremely small increments.

2. Is sufficiently rigid to maintain alignment under operational loads.
3. Allows radial thermal expansion but maintains the alignment of the shroud centerline to the blade rotational axis as the expansion takes place.

The rotational and dead loads from the shroud assembly are transferred by three sets of radial keys on the shroud into matching preload brackets bolted to pads fabricated on the pressure shell. Each set is composed of four assemblies, Figure 10, located symmetrically around the circumference of the shroud. The two brackets on the horizontal react only vertical forces and the two on the vertical react only horizontal forces.

The keys on the shroud are 11.43 cm (4.5 in) thick aluminum plates fitted between adjacent reinforcing rings on the outside of the shroud assembly. The plates are fitted into 2.54cm (1 in) deep slots machined into the ring webs and maintained in position by through bolts.

The brackets, Figure 11, are a welded structure fabricated from 9 percent nickel steel. The loads are transmitted into the shell primarily through a 15.2 cm (6 in) diameter shear pin. The configuration is unsymmetrical with the heavier side positioned to resist the dead loads of the shroud assemblies. Vertical and horizontal alignment of the shroud is provided by opposing A286 stainless steel screws threaded into the bracket arms. The screws react into the key through self aligning pucks. The motion of the pucks over the key surface is restrained only by sliding friction and allows the radial and axial deformation of the shroud to occur relatively unimpeded. To minimize the sliding friction and provide a semblance of lubrication the pucks have a reinforced fluorocarbon pad bonded to the sliding surface.

The bracket itself is exposed to the gas temperature of the tunnel. To minimize local cold spots on the shell, the bracket is separated from the shell pad by machined fiberglass reinforced polyester spacers. The spacers are selectively machined to correct for the relatively coarse tolerances on the "as welded" shell pad and are used as an accurate reference surface for the bracket load bearing assemblies. The shear pin is also thermally isolated from the shell by being totally encased in a load bearing fiberglass envelope.

The design, while straightforward in appearance, proved to be more difficult to implement than expected. The alignment of the shroud to the centerline of the rotating fan, as noted earlier, is critical because of the limited clearance to the blade tips. Once aligned, the support system must maintain this alignment over all of the thermal excursions and operating loads. These criteria were met by preloading the bracket arms to a level in excess of in-service loads. This insures that the entire bracket is fully involved and the effective stiffness of each bracket is maintained at a required value in excess of 1.4×10^8 N/m (8×10^5 lb/in).

Initial closed form analysis indicated that the bracket stiffness would be on the order of 3.5×10^9 N/m (20×10^6 lb/in). The results were highly questionable since the geometry of the bracket does not meet the length to depth ratios assumed in the standard beam equation. A finite element analysis was also made which predicted a much lower stiffness primarily due to flexing of the bottom plate. The difficulty here was correctly modeling to account for the contribution of the mounting bolts, the shear pin, fiberglass spacers and the shell mounting pad to the overall stiffness.

Preload relief during cooldown resulting from the differential expansion between the aluminum key and the steel bracket was also a concern. This imposed a minimum deflection of .25 mm (.01 in) between the two bracket legs before any preload was applied. Depending on the bracket stiffness, the total preload could increase to the point that, under certain loading conditions, stresses in the weld root could approach design allowables.

This prompted a change in weld filler alloy from AWS specification ENiCrFe-3 (normally used for 9 percent nickel on NTF) to specification ENiCrMo-3 which has an ultimate strength in excess of the base material. A rigorous program of NDT weld inspection and post weld machining of the fillets to remove potential stress risers was also imposed.

Finally a test program was initiated on the tunnel site to determine the actual load, deflection, and root area strain relationship in the bracket, Figure 12. The results showed an effective spring constant of 1.2×10^9 N/m (7×10^6 lb/in), which was adequate but considerably lower than expected. A large part of the deflection occurred in the base as predicted in the finite element analysis.

The combined preload (thermal and operational load) was set at 3.3×10^3 N (73,000 lb) and the strain measured at the weld root for this preload. Strain gages were then mounted at the same relative location on the remainder of the brackets and the strain measurement duplicated to set the preload as the final installation step.

UPSTREAM NACELLE

The upstream nacelle, Figure 13, forms the inner aerodynamic surface of the flow annulus. It houses the main radial bearing for the fan shaft, the bearing lubrication supply lines, the inlet guide vane actuator and its hydraulic system. To avoid cryogenic temperatures on the lubrication and hydraulic systems, the internal volume is insulated and maintained at 292 K (525° R) or above.

The upstream nacelle is an L shaped tubular shell structure beginning as a conical shape just downstream of the nitrogen injection assembly, Figure 14, and terminating at the aerodynamic fairings on the fan blades.

The general dimensions and loads are given in Table 4. Here also, the nacelle loads are resisted by independent support systems each providing a single fixed point for the three linear axes.

Thrust Loads

The thrust loads are the main aerodynamic forces and are reacted in two places. Thrust in the X direction, Figure 4, is towards the fan in the fan leg and is reacted at the transfer case structure by pivoting brackets which allow radial motion. Thrust in the Y direction is removed at the corner by an "Invar" thrust link reacted by the tunnel pressure shell, Figure 13.

Radial Loads

Radial support is provided in three locations. At the transfer case a set of brackets similar in concept to that discussed for the shroud are used. Additional vertical supports were needed near the corner and near the nose to eliminate the overturning moment at the transfer case. The supports must cross the flow stream in this area that requires a design having a low flow blockage and an aerodynamic shape to minimize flow disturbance. In addition the supports must provide sufficient rigidity to raise the nacelle first mode frequency above 15 hz and allow independent thermal expansion of the shell and nacelle.

The first two requirements are most efficiently met by tension members between the shell and the nacelle but rigid attachment would not meet the requirement for free thermal expansion. The solution was to use a Watts linkage for a support as shown schematically in Figure 15. At the corner the mechanism is built into the turning vanes. In the upstream section of the nacelle the legs have leading and trailing edge fairings attached to reduce turbulence. Only vertical support is provided since the nacelle structure in this area is sufficiently rigid to react against any horizontal bending moments.

The Watts linkage is attached to the nacelle by a pivot through a support beam at the nacelle centerline. This allows the nacelle to freely expand and contract radially. Seals are incorporated around the vertical members where necessary to prevent intrusion of the cold flow stream into the heated environment inside the nacelle. With the pivot at the center, the tunnel shell is allowed to expand/contract independent of the nacelle with no effect on the alignment of the nacelle to the centerline. Maintenance of alignment is predicated on a uniform radial change of the tunnel shell. This condition is reasonably well met by having this section of the tunnel enclosed in a high bay equipment area. Horizontal motions of the nacelle relative to the tunnel wall are accommodated by the use of a spherical self aligning bearing at each end of the vertical leg attachments, Figure 16.

Material selection is based solely on strength and stiffness since the radial freedom of the system will obviously accommodate changes in leg length. The entire Watts linkage structure is 304 stainless steel except for the pivot pins which are A286 stainless steel. The aerodynamic fairings are 6061 aluminum attached to the legs with slip fittings to accommodate the thermal expansion.

During installation a slight preload is built in to take up fabrication looseness in the various pivot points.

Concluding Remarks

Support systems utilizing preloaded brackets and Watts linkage mechanisms have been applied to a large highly loaded structure operating over a wide temperature range. These systems have been configured to allow relatively unimpeded thermal expansions and still meet close alignment requirements over the operational temperature and load range.

References

1. Kilgore, Robert A.: Evolution of the Cryogenic Wind Tunnel and Experience With Langley 0.3 Meter Transonic Cryogenic Tunnel. Paper #1, Cryogenic Technology Conference, NASA Langley Research Center, November 1979.
2. Howell, Robert R.: Overview of Engineering Design and Operating Capabilities of the National Transonic Facility. Paper #2, Cryogenic Technology Conference, NASA Langley Research Center, November 1979.
3. Ramsey, James W. Jr.: Design for Thermal Stress. 6th Paper, Cryogenic Technology Conference, NASA Langley Research Center, November 1979.

Table 1. General Design Goals

Maximum Reynolds Number	120,000,000 at Mach 1
Mach Number Range	.1 to 1.2
Operating Pressure Range	5.72×10^4 to 8.27×10^5 Pa (8.3 to 130 psia)
Operating Temperature Range	78°K to 339°K (140°R to 610°R)
Input Power	9.7×10^7 Watts (130,000 Hp)
Operating Medium	Nitrogen
Test Section Size	2.5 m x 2.5 m (8.2 ft. x 8.2 ft)

Table 2. Primary Structural Materials

<u>Ferrous</u>	<u>Non-Ferrous</u>
304 Stainless Steel	5083-0 Aluminum
A286 Stainless Steel*	5454-0 Aluminum
9% Nickel Steel	2024-T4 Aluminum*
Invar 36	6061-T6 Aluminum*

*Primarily used as fastening materials

Table 3. Fan Containment Shroud Dimensions and Loads

	<u>SI Units</u>	<u>English Units</u>
Length	4.44 m	14.56 ft
Inside Diameter	6.0 m	19.70 ft
Wall Thickness	5.09 cm	2.0 in
Material	5454 aluminum	
Weight	196000 N	44,000 lb
Diameter Change Over Temp	2.64 cm	1.04 in
Minimum Fan Blade Clearance	1.8 mm	.07 in
Maximum Thrust Load	1.1×10^6 N	246,420 lb
Maximum Torque about axis	4.26×10^6 Nm	3.13×10^6 ft lb
Maximum Differential Pressure	1.52×10^5 Pa	22 psia

Table 4. Upstream Nacelle Dimensions and Loads

Overall Length Along Centerline	13.7 m	45 ft
Maximum Diameter	4.63 m	15.2 ft
Dead Load On System	2.5×10^5 N	55,240 lb
Thrust Load Z Direction	1.08×10^6 N	242,650 lb
Thrust Load X Direction	1.56×10^6 N	350,600 lb
Thermal Motion Z Axis	3.47 cm	1.37 in
Thermal Motion X Axis	3.88 cm	1.53 in
Moments X Axis	2.79×10^3 Nm	2.05×10^3 ft lb
Y Axis	5.22×10^5 Nm	3.84×10^5 ft lb
Z Axis	5.36×10^4 Nm	3.94×10^4 ft lb
Material	5083-0 Aluminum	

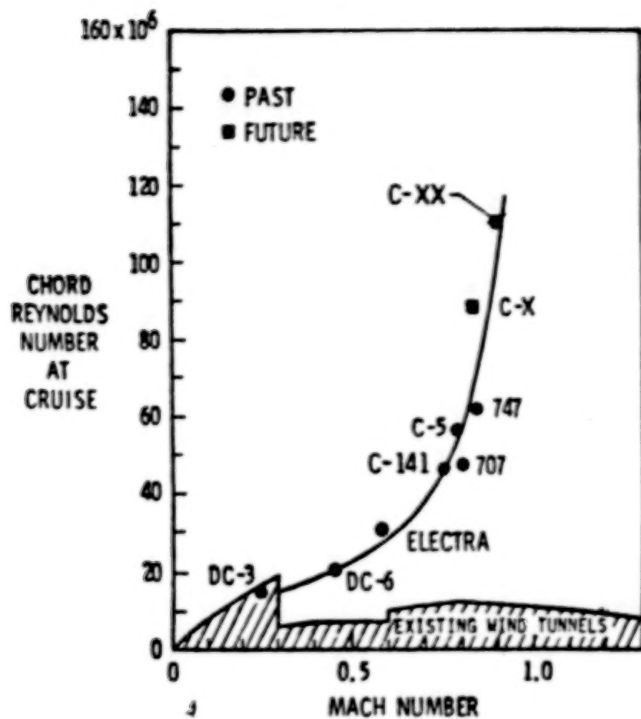


Figure 1.- Flight Reynolds numbers for existing and projected aircraft compared with the capability of existing wind tunnels.

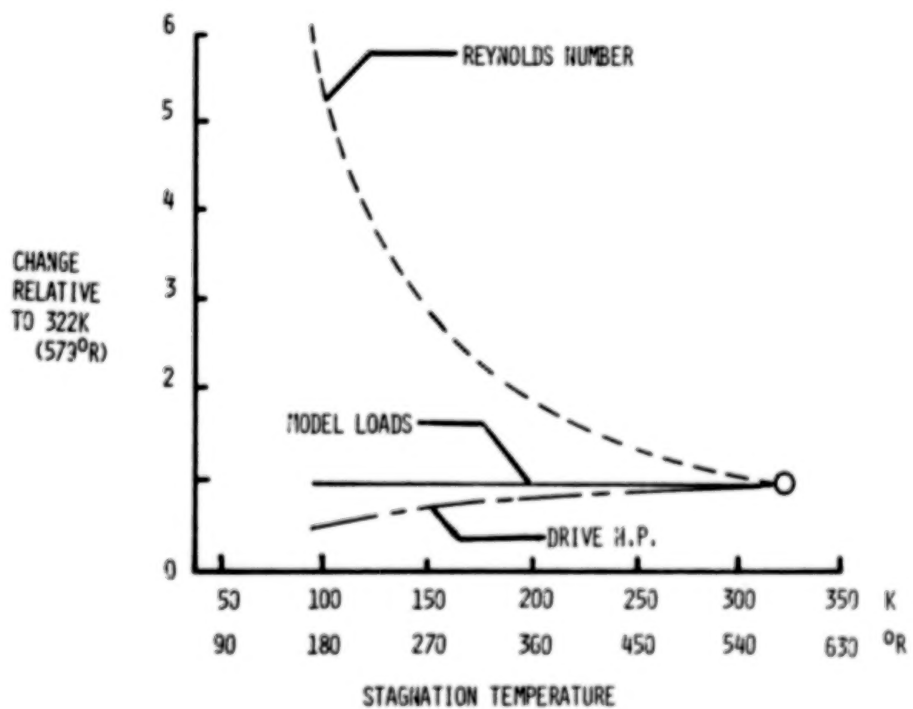


Figure 2.- Cryogenic tunnel concept

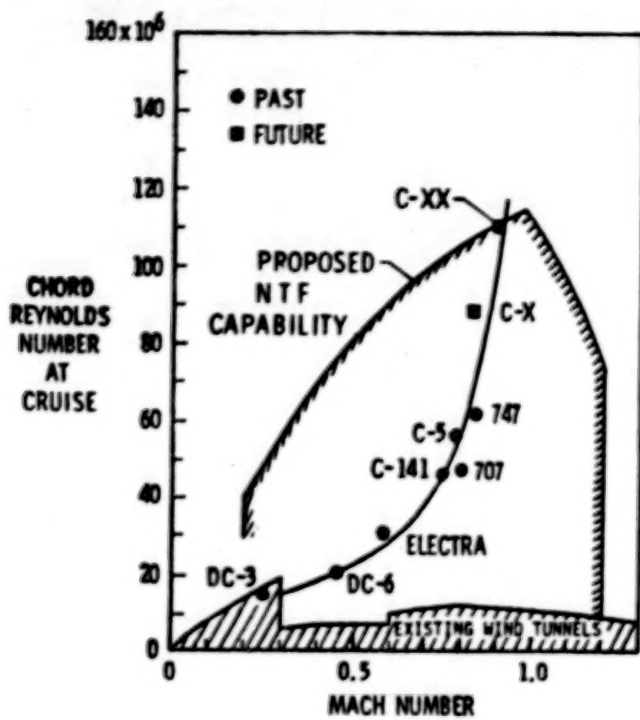


Figure 3.- Flight Reynolds numbers for existing and projected aircraft compared with the capability of the National Transonic Facility.

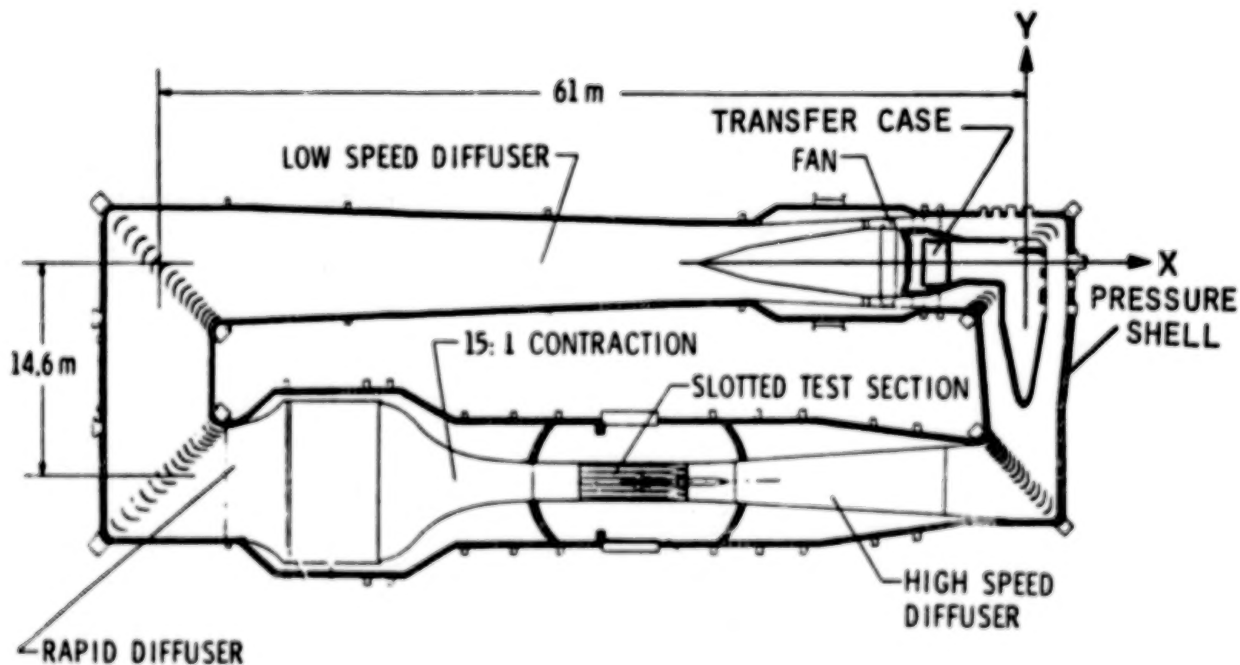


Figure 4.- Plan view of tunnel circuit showing pertinent dimensions and components - National Transonic Facility.

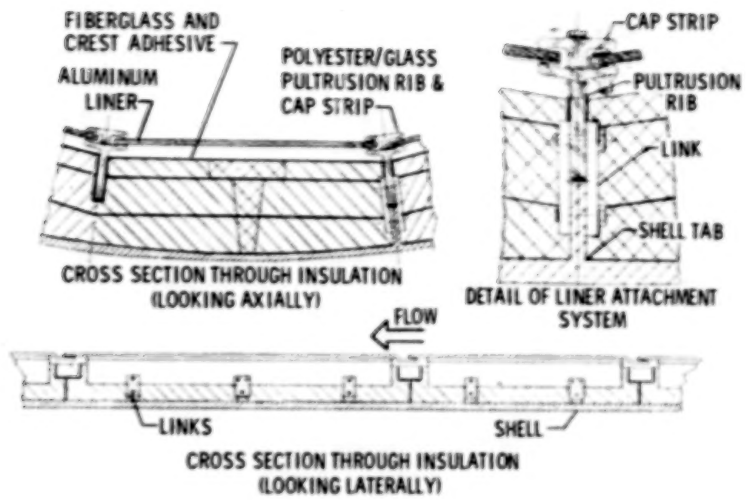


Figure 5.- Typical sections of the internal insulation system.

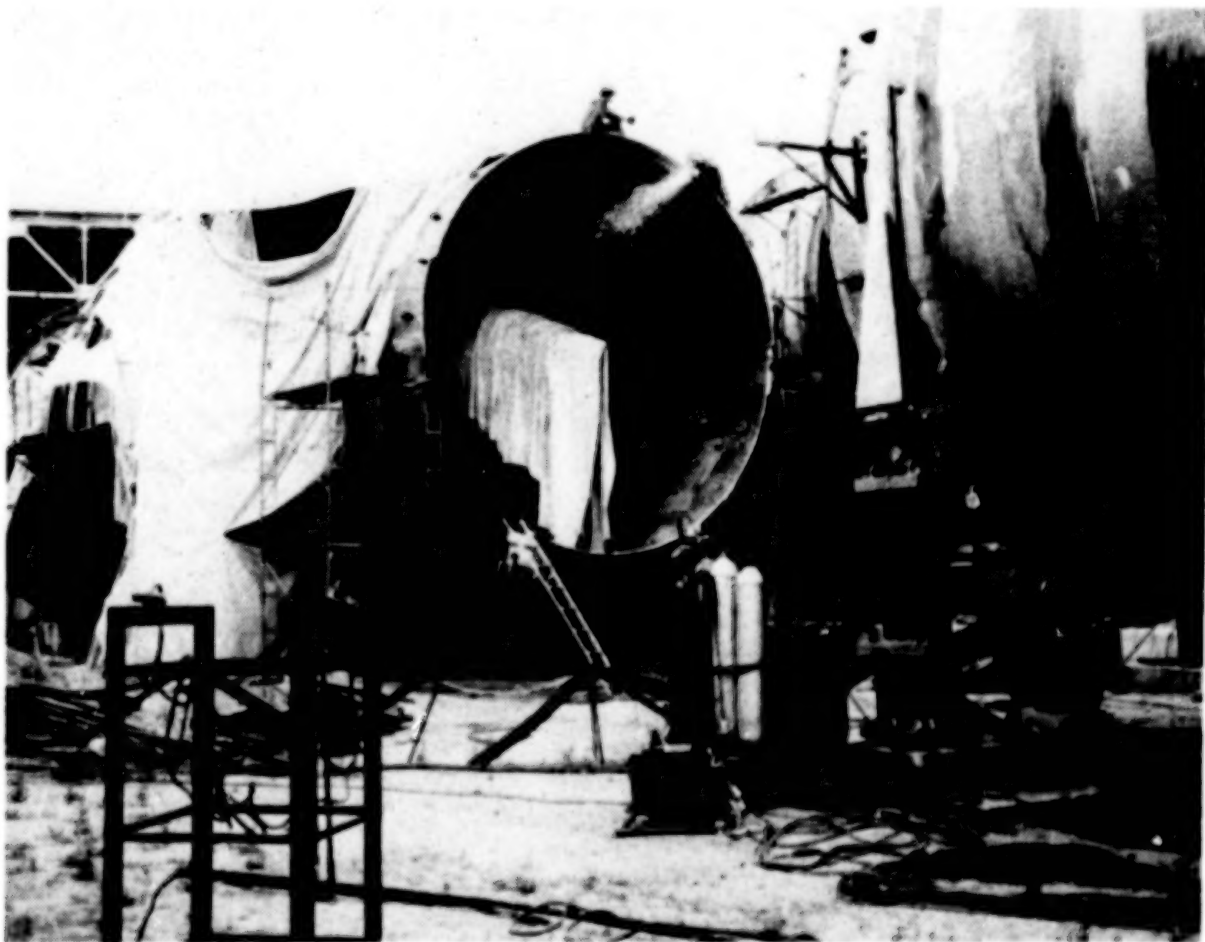


Figure 6.- Tunnel shell support legs.

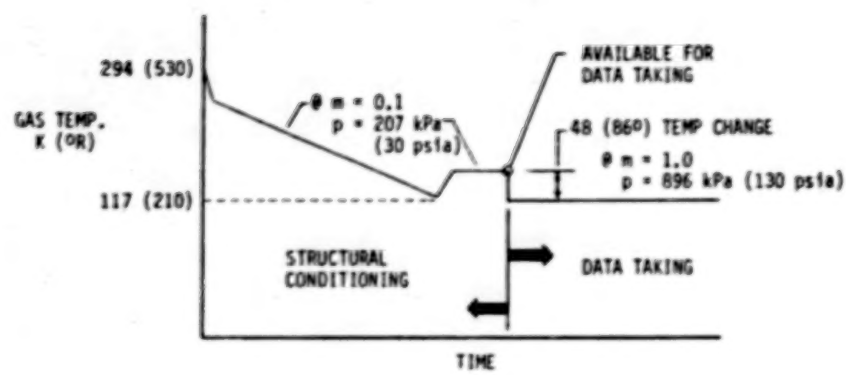


Figure 7.- Thermal forcing function cooldown and operating temperature change.

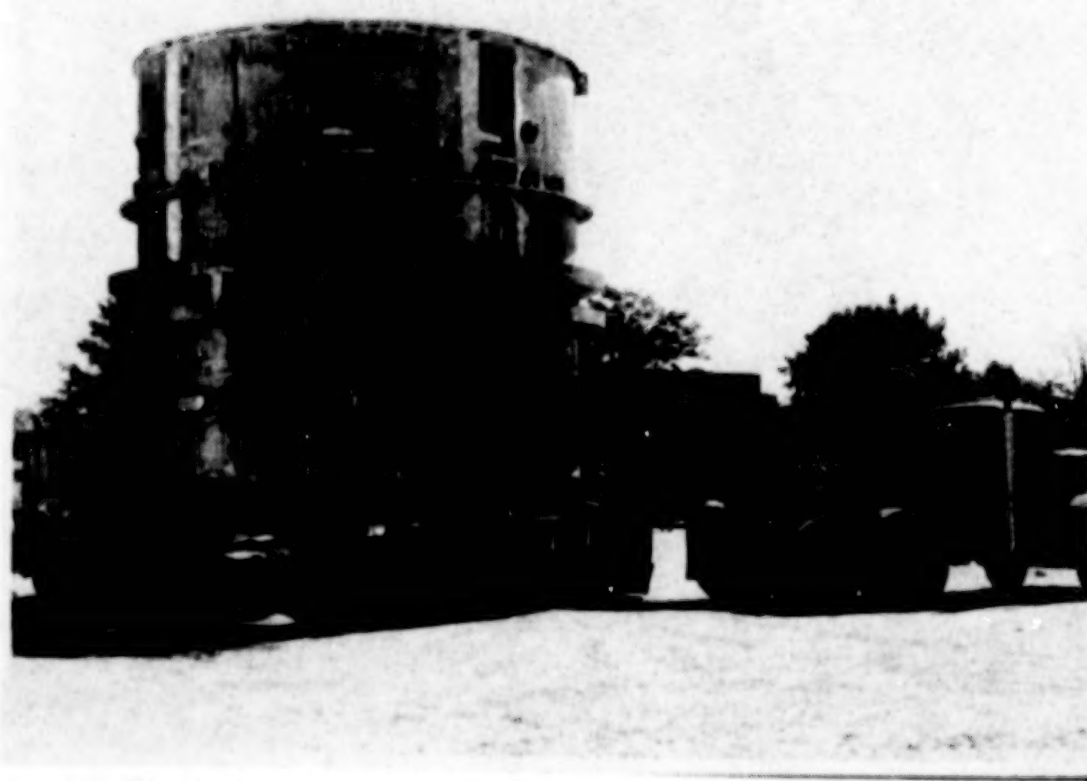


Figure 8.- Fan Containment Shroud

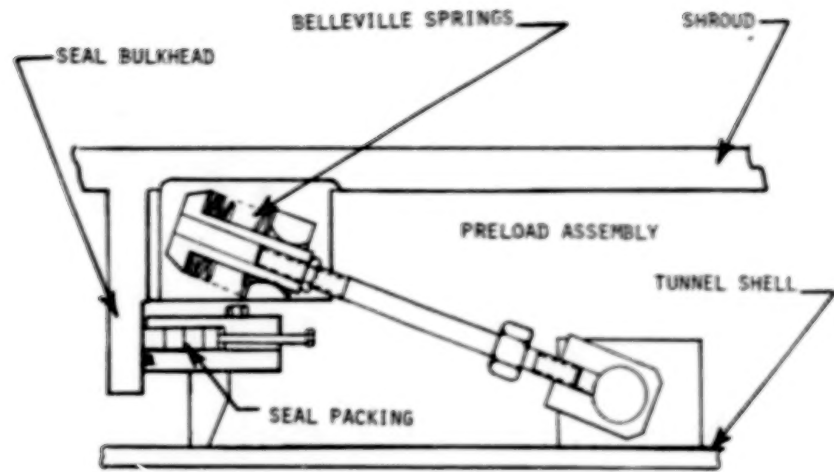


Figure 9.- Seal assembly and thrust brackets for the fan contamination shroud.

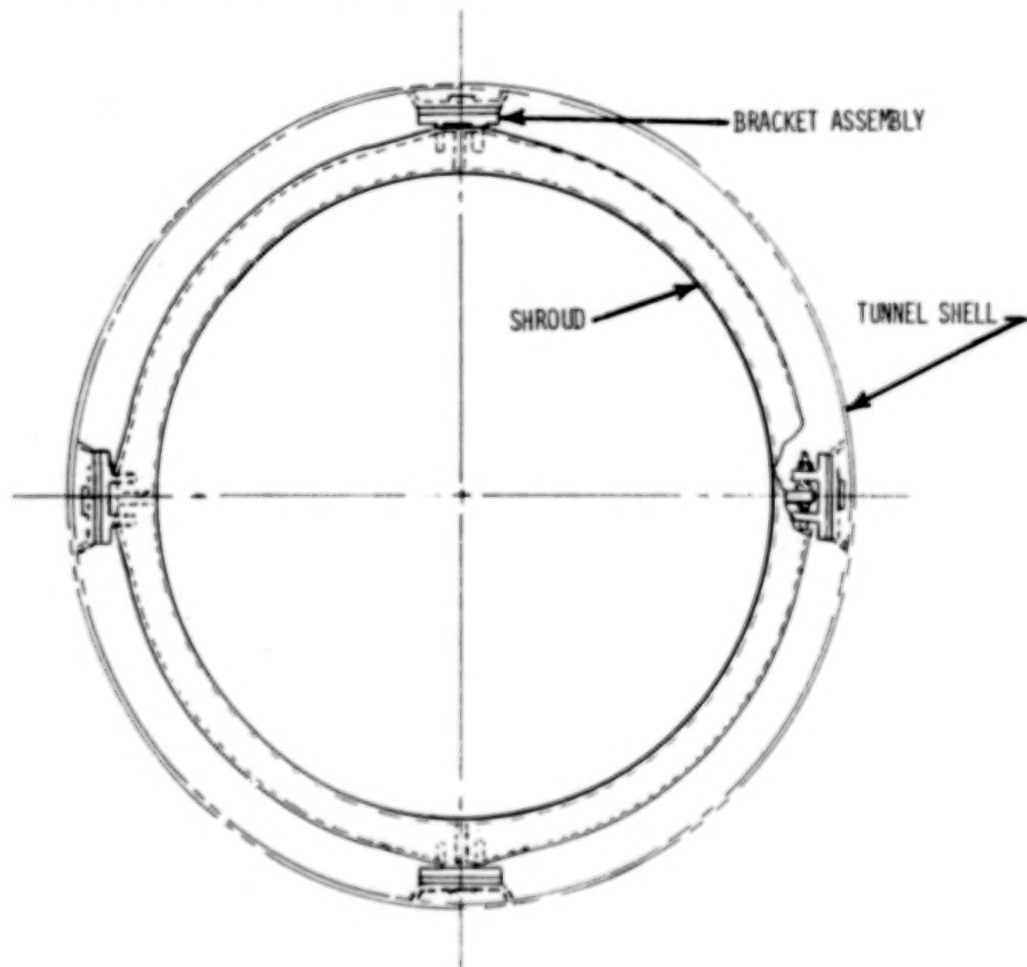


Figure 10.- A fan shroud radial support set.

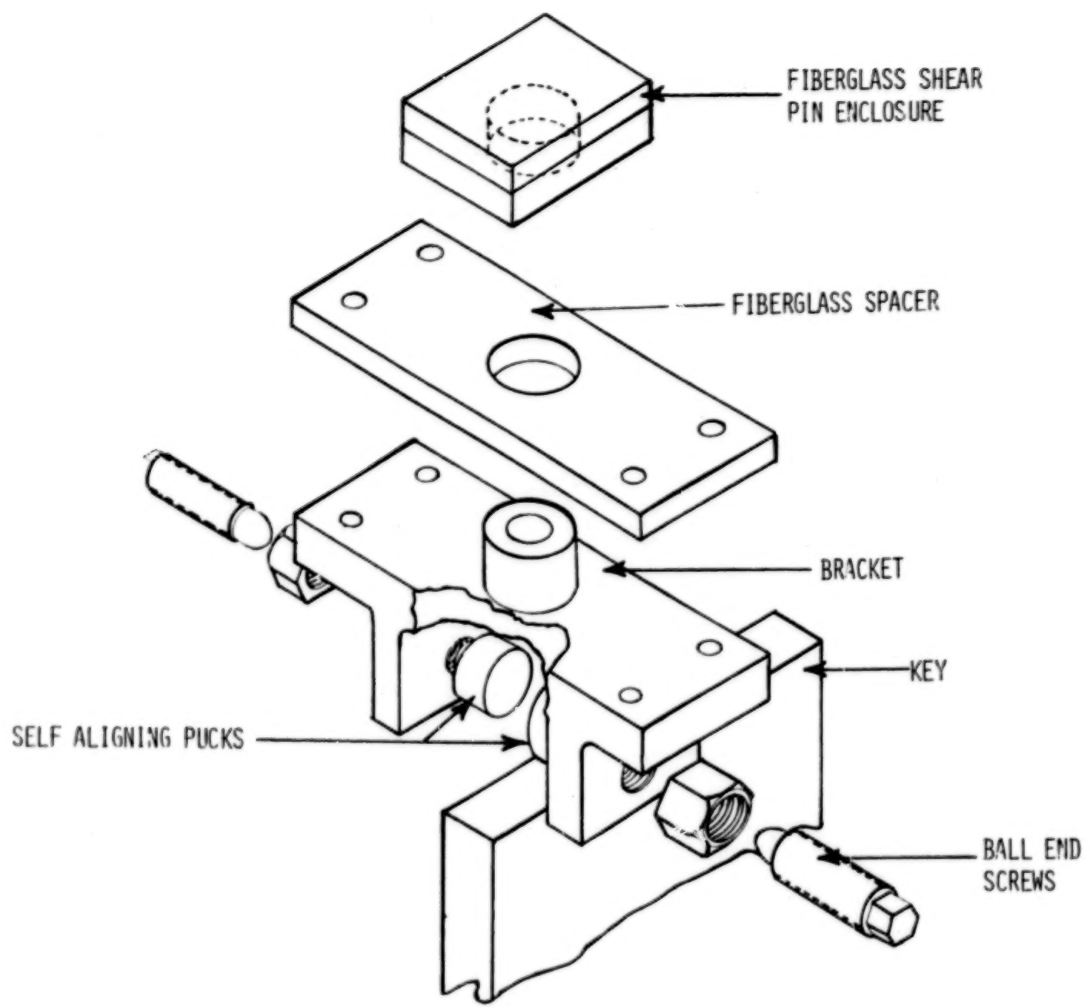


Figure 11.- A fan shroud bracket assembly.

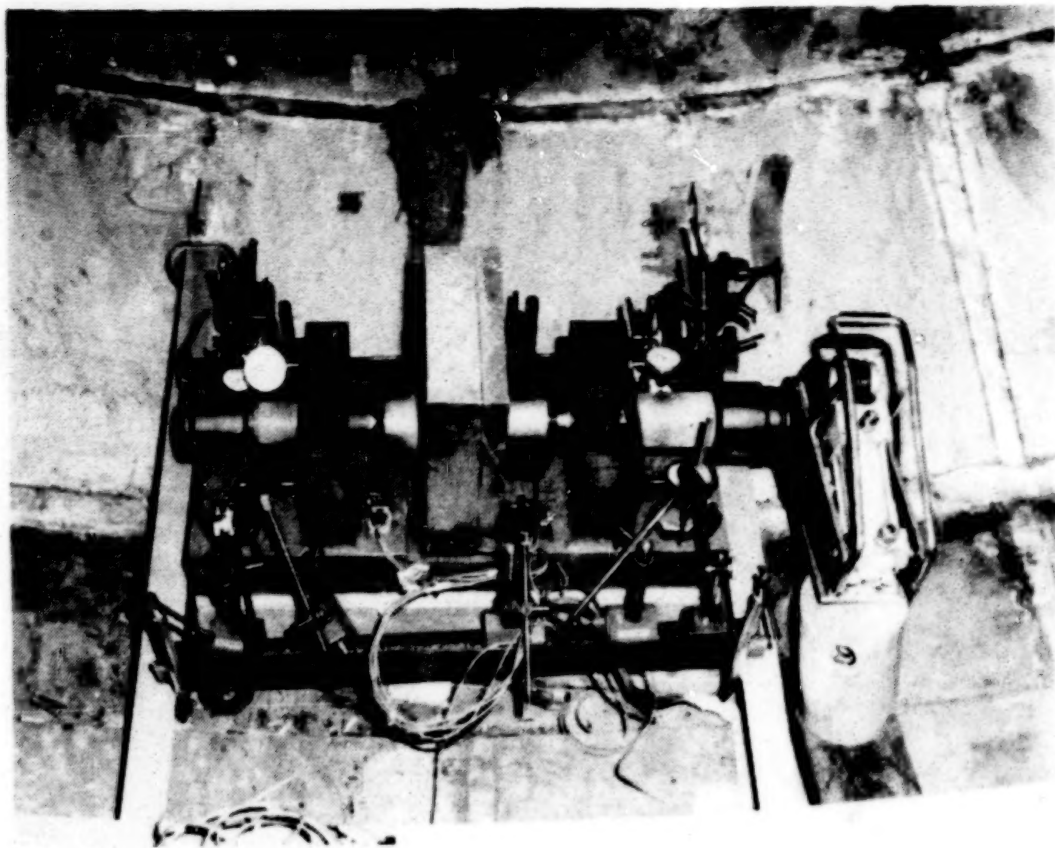


Figure 12.- Fan shroud bracket preload test setup.

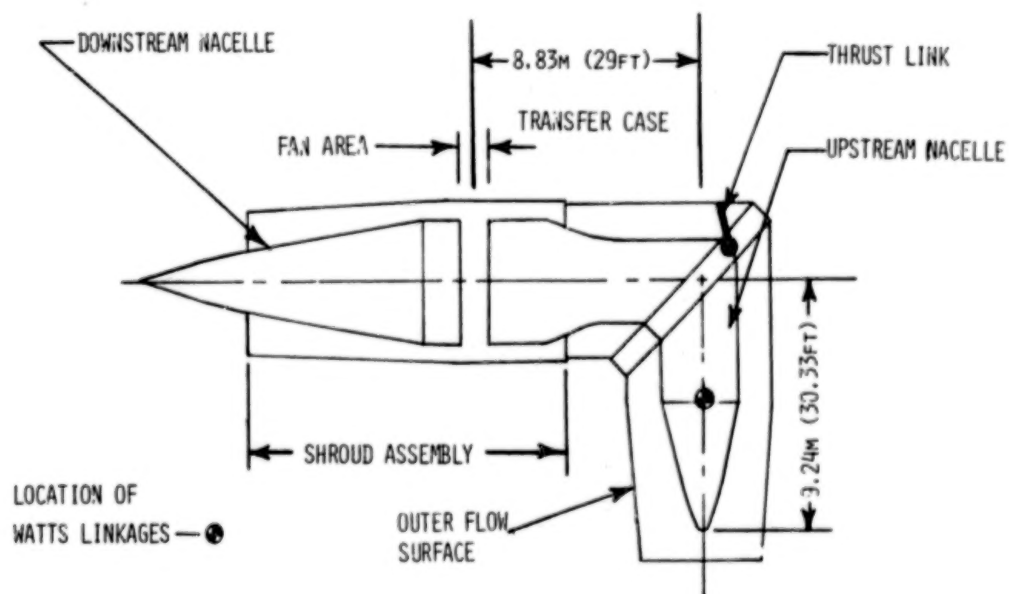


Figure 13.- Upstream Nacelle Configuration.

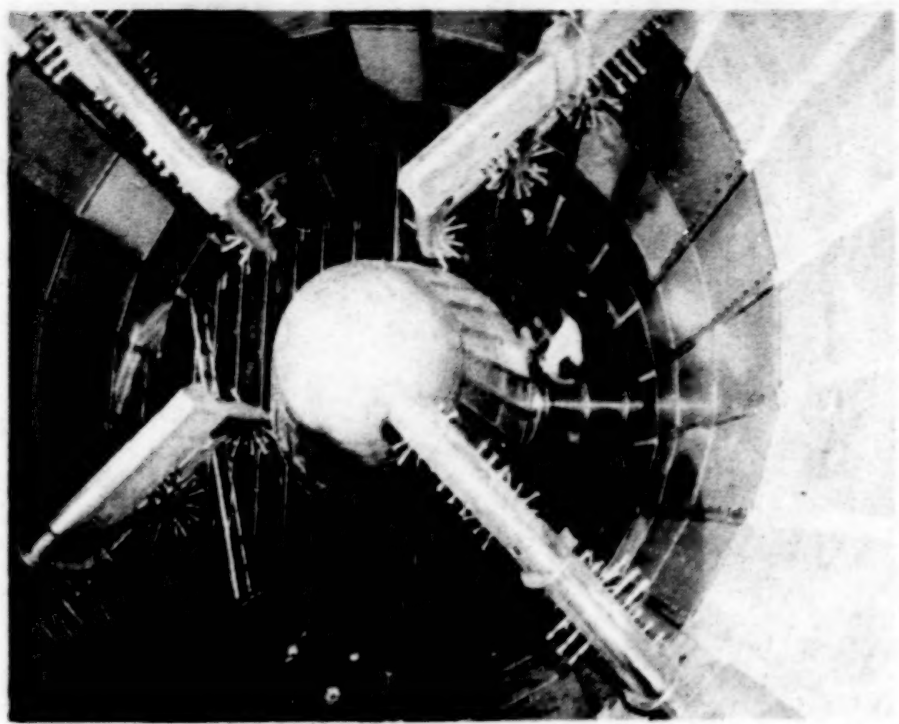


Figure 14.- The upstream nacelle viewed from the N₂ injector assemblies.

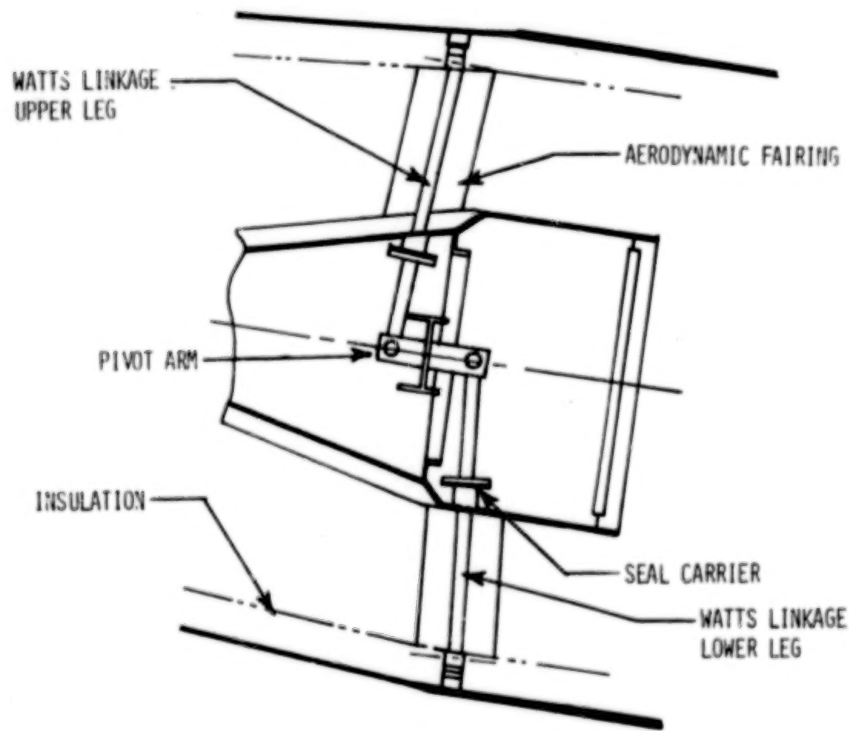


Figure 15.- Watts linkage schematic.

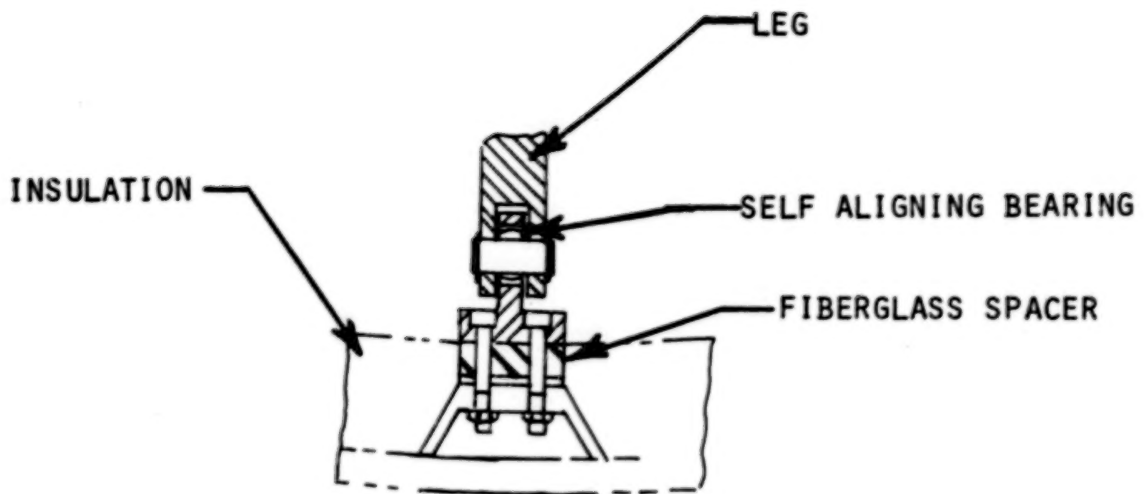


Figure 16.- The Watts linkage leg attachment
to the tunnel shell.

Blank Page

EVALUATION OF SCANNING EARTH SENSOR MECHANISM ON ENGINEERING TEST SATELLITE IV

Masami Ikeuchi*, Yasufumi Wakabayashi*, Yoshiaki Ohkami**
Takashi Kida**, Takeo Ishigaki***, and Mikio Matsumoto***

ABSTRACT

This paper describes the results of the analysis and the evaluation of flight data obtained from the horizon sensor test project conducted jointly by National Aerospace Laboratory and National Space Development Agency of Japan and manufactured by Matsushita Research Institute, Tokyo, Inc.

The rotary mechanism of the scanning earth sensor composed of direct drive motor and bearings using solid lubricant is operated satisfactorily.

The transmitted flight data from Japanese Engineering Test Satellite IV have been evaluated in comparison with the design value and the rotary mechanism is forecasted to be used for a practical satellite.

INTRODUCTION

A scanning earth sensor (called HOST as abbreviation of HOrizon Sensor with Turning head) was originally designed as a roll/pitch attitude sensor of three-axis stabilized spacecraft. The HOST is one of the experimental equipments mounted on the Engineering Test Satellite IV (ETS-IV or 'Kiku 3') which was launched on February 11, 1981 from Tanegashima Space Center of National Space Development Agency of Japan into a transfer orbit with initial apogee and perigee heights of 36000 km and 223 km respectively and with inclination angle of 28.5 degrees.

In comparison with other earth sensors such as the radiation balance type and edge-track type, this conical scanning earth sensor is considered to be one of the main practical earth sensors for low and middle altitude because of its wide acquisition range and little influence to attitude change of spacecraft, but it is difficult to design its rotating mechanism, control its quality, and assure its reliability in general.

The ETS-IV spacecraft is spin-stabilized with nominal spin rate of 60 rpm and the nominal spin axis direction is perpendicular to the earth equatorial plane. The HOST has been tested not only as a horizon crossing indicator for spinning spacecraft, but also as a scanning earth sensor with the scanning axis parallel to the spinning axis.

* National Space Development Agency, Tsukuba Space Center, Ibaragi, Japan
** National Aerospace Laboratory, Tokyo, Japan
*** Matsushita Research Institute, Tokyo, Inc., Kawasaki, Japan

The experimental items of the HOST are as follows.

1. Performance change of rotating mechanism at space environment
2. Characteristic change of infrared optoelectronics in a space environment
3. Data acquisition at infrared input energy
4. Function and performance of attitude angle measurement by the HOST

The HOST has been operated during the primary mission term and the extended mission terms.

This paper describes the rotating mechanism of this HOST and the data analysis and evaluation of the flight experiments in the operating duration.

DESCRIPTION OF THE HOST

The HOST consists of three major components which are two rotary heads (HD1, HD2; Figure 1) and one electronic package. Each rotary head is mounted to both sides of the ETS-IV perpendicular to its spin axis direction. HD1 is on the spacecraft spin axis but HD2 is offset from its spin axis by 0.9 meters. For this reason, HD2 is affected by a centrifugal force of approximately 3.5 G towards the radial direction.

Each rotary head consists of an antireflection coated Ge lens, a pyroelectric infrared detector with an optical bandpass filter, a signal pre-amplifier and a motor for a rotating metal mirror. This rotary mechanism is composed of bearings using solid lubricant (Rulon C) and three phase direct drive motor (DD motor) using phase locked loop (PLL) control. The rotor magnet material of the DD motor is an anisotropic strontium ferrite.

The horizon crossing period of the instantaneous field of view (IFOV) is determined by detecting infrared radiation from the 14 to 16 μm CO_2 band using a narrow IFOV (about 1.4 degrees) conical scan with a cone angle of 120 degrees and rotating rate of 60 rpm. Pitch and roll angles are measured by using two conical scanning rotary heads.

The motors of either head can be turned on and off separately. When the motor is on, the total scanning speed is approximately (60+60) rpm at nominal spin rate and when it is off, it reduces to about 60 rpm, which is spacecraft spin rate.

The dimension and the weight of each rotary head are 160 mm x 230 mm, 3.2 kg respectively.

ROTARY MECHANISM

Figure 3 shows the structure of the HOST rotary head. The scanning mirror and the hollow shaft are driven by a three phase DD motor with a quartz stabilized PLL control which is to be at a constant rotation speed.

Bearing mechanism

A bearing mechanism has a preload structure to inner ring as shown in Figure 2 and has two angular ball bearings using a solid lubricant (Rulon C) retainer. This mechanism's merits are that it is small, easy to assemble and provides a wide distance of work points between two bearings. In order to minimize the precession caused by the HOST head rotation, clearance fit around two bearings was to be as small as possible.

Lubrication

An angular contact ball bearing is adopted and polymer composites having self lubrication are used with a retainer (Table 1). Lubrication is performed when a lubricant is transferred to a ball surface from a retainer by rotating bearings and is then transferred to a raceway of inner and outer rings from the ball surface. The most powerful reason why oil is not used is because the infrared optical system would be contaminated by the oil evaporation and adhesion. The reason why solid lubricant is used is because it is less volatile and less influenced by the large temperature changes and radioactivity of a space environment; this is important because of the HOST's rotating parts which are exposed. MoS₂ is a good lubricant in vacuum, but the ground test data in the air indicates it is not good because of weakness to moisture. Rulon C is a composite type lubricant of fiber reinforced PTFE (teflon) containing lead oxide (Pb₃O₄) and has been used in the Apollo Project of NASA.

This solid lubricant is characterized as follows.

1. Less contamination to the infrared optical system by means of low vapor pressure
2. Radiation resistivity
3. Fitness for use on the ground in the air
4. Comparative high load resistivity

GROUND TEST

An Engineering Model (EM), Protoflight Model (PM) and Flight Model (FM) of the HOST have been developed in turn, and the test levels of PM and FM are Qualified Test level (QT) and Acceptance Test level (AT) respectively (Table 2). Both HD1 and HD2 of the HOST-FM have been operated 20 hours in air and 110 hours in vacuum in the test at the factory, the acceptance test for each head and the inspection at the launching site.

It is confirmed that the measured data were of no difference between in the air and in vacuum of 10^{-5} Pa.

At higher temperature, the average motor torque will be larger, but the torque fluctuation will still be the same level. At larger acceleration, both the average motor torque and the torque fluctuation have larger values (Table 3). Stability of the operation is comparatively good for a short term (several tens of hours), but variations of the average motor torque and the phase jitter are 2.5×10^{-6} N·m, ± 0.076 deg.p-p ($\pm 1.2 \times 10^{-6}$ N·m when converted to torque), respectively, for a long term (several months).

OPERATING TEST ON THE SPACECRAFT

The operating test periods of the rotary mechanism on the ETS-IV are as follows.

1. Mission term (February 1981 ~ May 1981)
 - Continuous operating test (several tens of hours)
 - Function test
2. Extended mission term (May 1981 ~ February 1982)
 - Continuous operating test (several hundreds of hours)
 - Eclipse test
3. Extended mission term (second) (February 1982 ~ August 1982)
 - Continuous operating test (several thousands of hours)
 - Test in maneuvers of the spacecraft

The accumulated operating hours amount to about 4,500 hours for HD1, and about 4,000 hours for HD2 till August 1982. The orbital total hours including nonoperating time amount to about 18 months. The test is continuing.

DATA ACQUISITION

The data acquisition from the ETS-IV spacecraft is transmitted to the ground station by the PCM telemetry. The data of the motor coil current and jitter output are acquired once about 2 seconds and once about 32 seconds respectively. The variation within a short time can not be therefore observed.

Average motor torque

The HD1 has been operated through about 4,500 hours in the temperature range from -34°C to 20°C and its average motor torque is stable at the value of

$4 \sim 8 \times 10^{-6}$ N·m (including iron loss). The HD2 has been operated through about 4,000 hours in the temperature range from -32°C to 25°C and its average motor torque varied from 1.10×10^{-5} to 2.65×10^{-5} N·m but these performance values were well within the limit value of 5×10^{-5} N·m (Figure 4). As HD2 is under stationary acceleration of about 3.5 G, its average motor torque is considered to be increased especially at high temperature in addition to the acceleration.

Motor torque fluctuation

The motor torque fluctuations for HD1 in the period of 20 ~ 30 min. were observed a few times at the beginning of this test schedule, but these phenomena were small and stabilized during the extended mission term. The fluctuations of the motor coil current are coincident with the data from the jitter (AC component) (Figure 5). There were no periodic motor torque fluctuations for HD2. A slight increase of its motor torque fluctuation was found at the middle of this test schedule, but this fluctuation was stable from that time on. The variations of these data are shown in Figure 5.

ANALYSIS AND EVALUATION OF BEARINGS

Table 4 shows the evaluation results of the average motor torque and the motor torque fluctuation including the ground test data. The iron loss is excepted from the average motor torque. The data of the motor torque fluctuation are obtained from the motor coil current output (AC component).

The average motor torque for HD1 varied once or twice from the ground test data, and the periodic variations were observed in the motor torque fluctuation for HD1 which was not found in the ground test data. The average motor torque and the motor torque fluctuation for HD2 are the proper values based on the ground test data.

Concerning the bearings using solid lubricant, temperature and acceleration factors make these characteristics change mainly in the ground test and loading test on the spacecraft. Adhesion that is doubtful especially in high vacuum ($10^{-6} \sim 10^{-11}$ Pa), is not a dominant factor to the solid lubrication in case of slow revolution and light load such as the HOST, but mechanical scratch on the raceway is considered to be a dominant factor mainly due to friction.

As for the motor torque fluctuation, ripple variations occurred, then subsided. This was not abnormal and was observed during the function test of the same type of bearings in the HOST. For the cases which used solid lubrication, the motor torque could be attributed to the fine differences in the adhesive state of the lubricant, mechanical contact state, mechanical accuracy, and surface roughness. Therefore, it is necessary to understand the lubrication properties and to choose the lubrication wisely.

Regarding the motor revolution accuracy, the phase jitter has a slightly large value of about 0.8 deg.p-p (max.) in contrast with the nominal value of 0.2 deg.p-p.

Encoding necessary for obtaining the chord width is the time measurement because the ETS-IV is a spinning spacecraft. This requirement is not essential if an optical encoder is adopted for practical use.

There were two unexpected events that occurred to the motors of HD1 and HD2. First, both HD1 and HD2 were stopped rotating three times by means of operating the current limitter for hours in the continuous operating test. Second, the motors were not driver in the long period eclipse test when HD1 and HD2 were exposed to low temperature below the designed value. In both cases, the motors of HD1 and HD2 were recovered and normally operating after these events. These events were unaccountable by means of no data acquisition when the events were occurred.

Long period eclipse test

A long period eclipse test has been performed during the extended mission term to investigate the characteristics of the rotary mechanism at the large temperature change. This test has been also performed to investigate the temperature change rate dependence of the rotary mechanism by continuously rotating the motor for the eclipse of 90 min. period over maximum eclipse time on the geostationary orbit (about 72 min.). It is shown that HD1 is hardly affected by the temperature change rate of 21°C/hr. and HD2 has large values of the average motor torque of $1.3 \sim 2.2 \times 10^{-5}$ N·m and the motor torque fluctuation of 1.3×10^{-5} N·m by the temperature change rate of 13°C/hr., but a PLL cycle slip does not occur for HD2.

Test in maneuvers of the spacecraft

Maneuvers of the spacecraft have been carried out for the purpose of the interference test by the Sun to the infrared optoelectronics. The motor for HD1 was operating in these maneuvers and the characteristics were observed in case of vibrations. The motor characteristics did not change and had a good operation before/in/after the maneuvers.

EVALUATION OF OTHER LUBRICATION

The long life study of the HOST (HOST-LL) was performed in addition to the lubrication results of the HOST. Several sorts of retainers were attached to the same type bearings of the HOST (a part of bearings have a raceway of inner and outer ring and balls sputtered with MoS₂) and a life test was performed with a revolution of 2,000 rpm and preload of 5 kg in high vacuum ($10^{-6} \sim 10^{-7}$ Pa) and atmospheric pressure. The results show that the bearings using Rulon E have a small average friction torque and are good for the life test over 1,000 hours. Rulon E is composed of PTFE and MoS₂. The bearings assembled along with a Rulon E retainer and a raceway of inner and outer ring and balls sputtered by MoS₂ (0.5 ~ 1.0 μm) are

stable at small friction torque ($4 \sim 5 \times 10^{-6}$ N·m) and small friction loss of retainer. So these bearings exceed the target total revolution of 1.6×10^8 , which is equivalent to the life of the HOST-LL over 5 years.

It is concluded that about one-third of the HOST's average friction torque will occur, given the structure of the HOST-LL and a preload of 2 kg (Table 1).

The friction torque contains dispersive fluctuation and ripple fluctuation and so on. These fluctuation sources are mainly considered to be retainers from the test described above (Figure 6). It is necessary to investigate the following items more clearly.

1. Shape and size of retainers
2. Processing of retainers
3. Uneven materials of retainers
4. Roughness and shape of raceway and balls

It is also necessary to investigate bearings sufficiently for the limit value and design life.

CONCLUSION

Some problems are left unsolved for now, but the rotary mechanism system of the HOST has reached the expected goal through the mission term and the extended mission term. It is shown that the rotary mechanism system using solid lubricant is adequate for space applications.

REFERENCES

1. T. Kida et al. Proc. of the 13th International Symposium on Space Technology and Science (1982)
2. Y. Wakabayashi et al. AIAA Guidance and Control Conference, San Diego (1982)

Table 1. Bearings specifications and structure of the HOST and the HOST-LL

	Items	HOST	HOST-LL
Structure	Method of preload	Preload to inner ring	Preload to outer ring
	Preload	1.5 kg	2 kg
	Clearance fit (between axis and inner ring)	25 μm	5 μm
	Clearance fit (between housing and outer ring)	10 μm	5 μm
Bearings	Grouping	Angular contact ball bearings using solid state lubricant retainer	
	Design	7204C base	
	Ball materials	SUS 440C	SUS 440C
	Retainer materials	Rulon C	Rulon E + MoS ₂
	Inner radius	35 mm	35 mm
	Contact angle	15°	15°
	The number of balls	15	12

Table 2. Test level of the HOST rotary head

	Vibration test		Thermal test in vacuum	Acceleration
	Sine wave	Random		
EM	5.3 G _{o-p} max.	13.1 G _{rms} 60 s.	-20 ~ +50 °C	0 ~ 10 G
PM (QT)	5.3 G _{o-p} max.	19.6 G _{rms} 90 s.	-30 ~ +50 °C	0 ~ 5 G
FM (AT)	—	13.1 G _{rms} 60 s.	-20 ~ +40 °C	0 ~ 5 G

Table 3. Ground test results for the HOST-FM

Test	Condition	Average motor torque ^{a)}		Torque fluctuation ^{b)}	
		HD1 ^{c)}	HD2 ^{d)}	HD1 ^{c)}	HD2 ^{d)}
Temperature	-21 °C	1.75	5.25	2.4	7.8
	+19 °C	2.5	6.0	1.8	3.0
	+36 °C	3.0	12.5	1.2	2.4
Acceleration ^{e)}	1 G		2.5~3.0 ^{c)}		1.2 ^{c)}
	3.5 G		18~23.5 ^{f)}		9.6~15.6 ^{f)}

unit ; $\times 10^{-6}$ N·ma) The data with the exception of iron loss (2×10^{-6} N·m)

b) The data from the HOST jitter output

c) Thrust direction (1 G / earth gravity)

d) Radial direction (1 G / earth gravity)

e) Room temperature in the air

f) Radial direction

Table 4. Evaluation data for the HOST bearings

	Average motor torque ^{a)}		Torque fluctuation	
	HD1	HD2 ^{b)}	HD1	HD2 ^{b)}
Ground test	1.8~3.0	18.0~23.5	1.0~3.0	10.0~14.0
Mission term	2.0~3.0	9.0~15.0	2.0~12.0	2.0~6.0
Long period test	3.0~3.5	13.0~18.0	2.0~7.0	6.0~9.0
Eclipse test	3.0	13.0~22.0	5.0	13.0
Long term	3.0~6.0	14.0~25.0		

unit ; $\times 10^{-6}$ N·ma) The data with the exception of iron loss (2×10^{-6} N·m)

b) Measured value at the stationary acceleration (3.5 G)

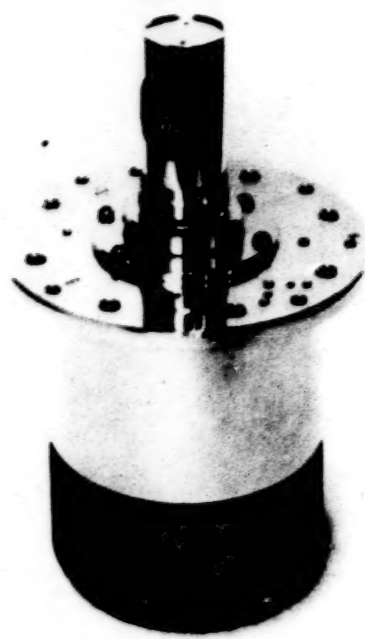


Figure 1. Rotary head of the HOST

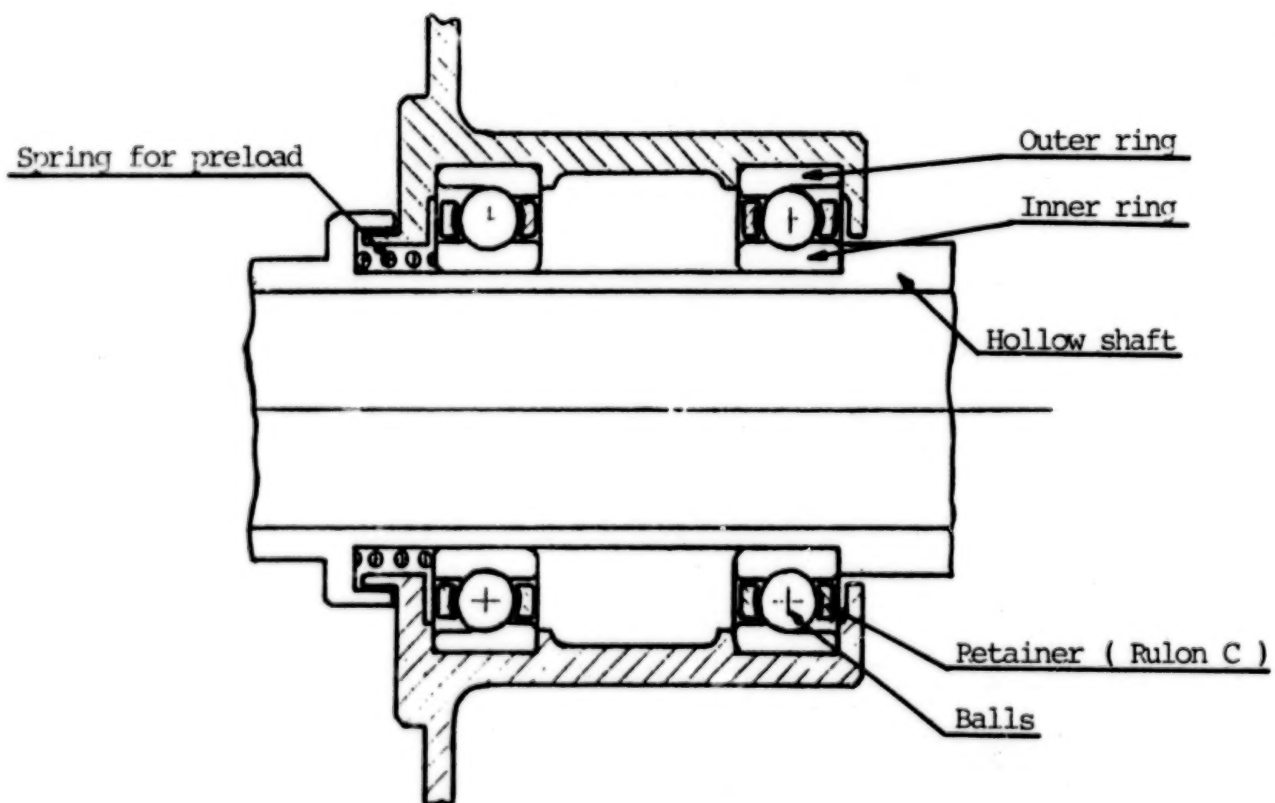


Figure 2. Method of preload

BLANK

PAGE

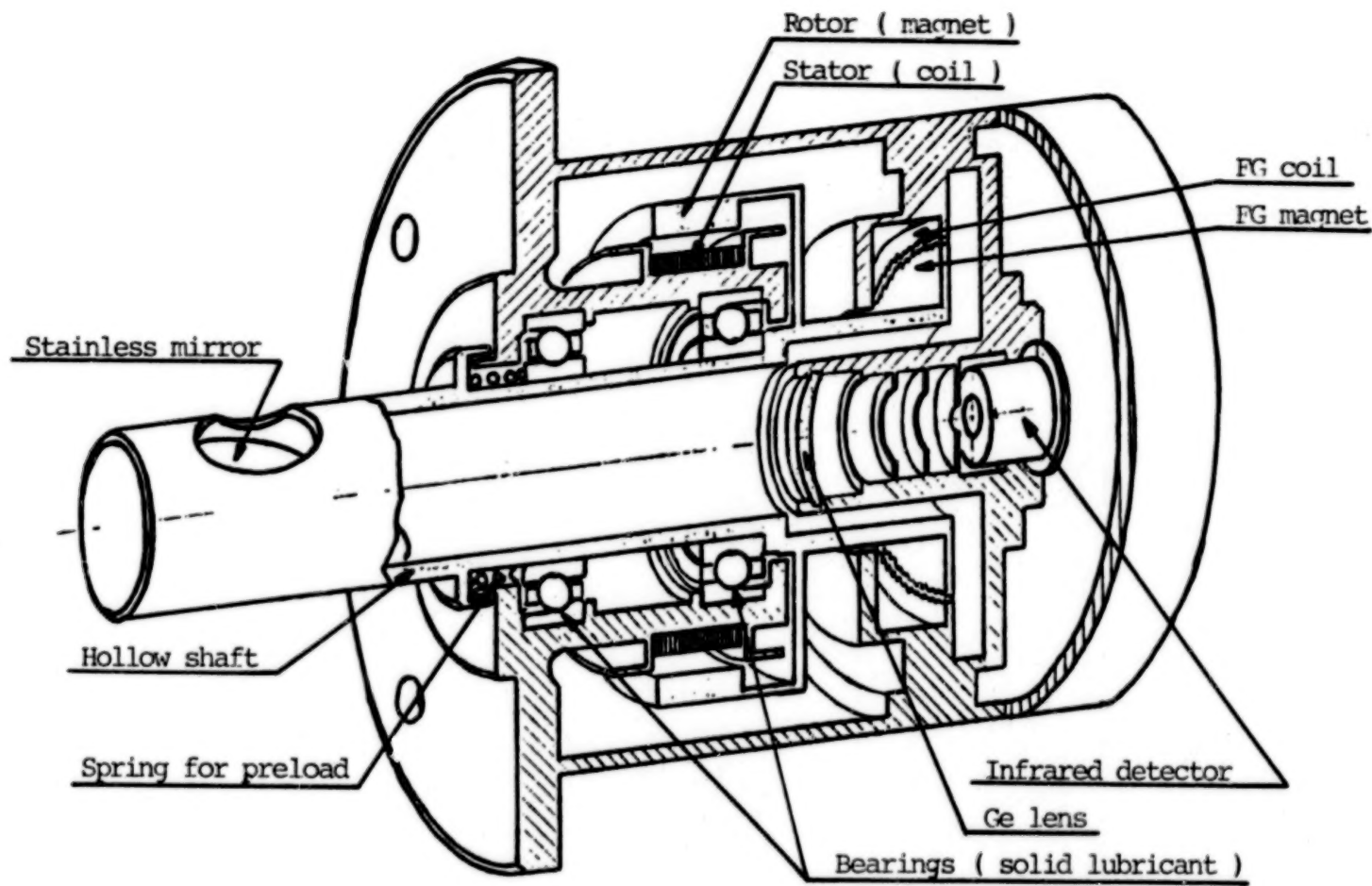


Figure 3. Structure of the HOST rotary head

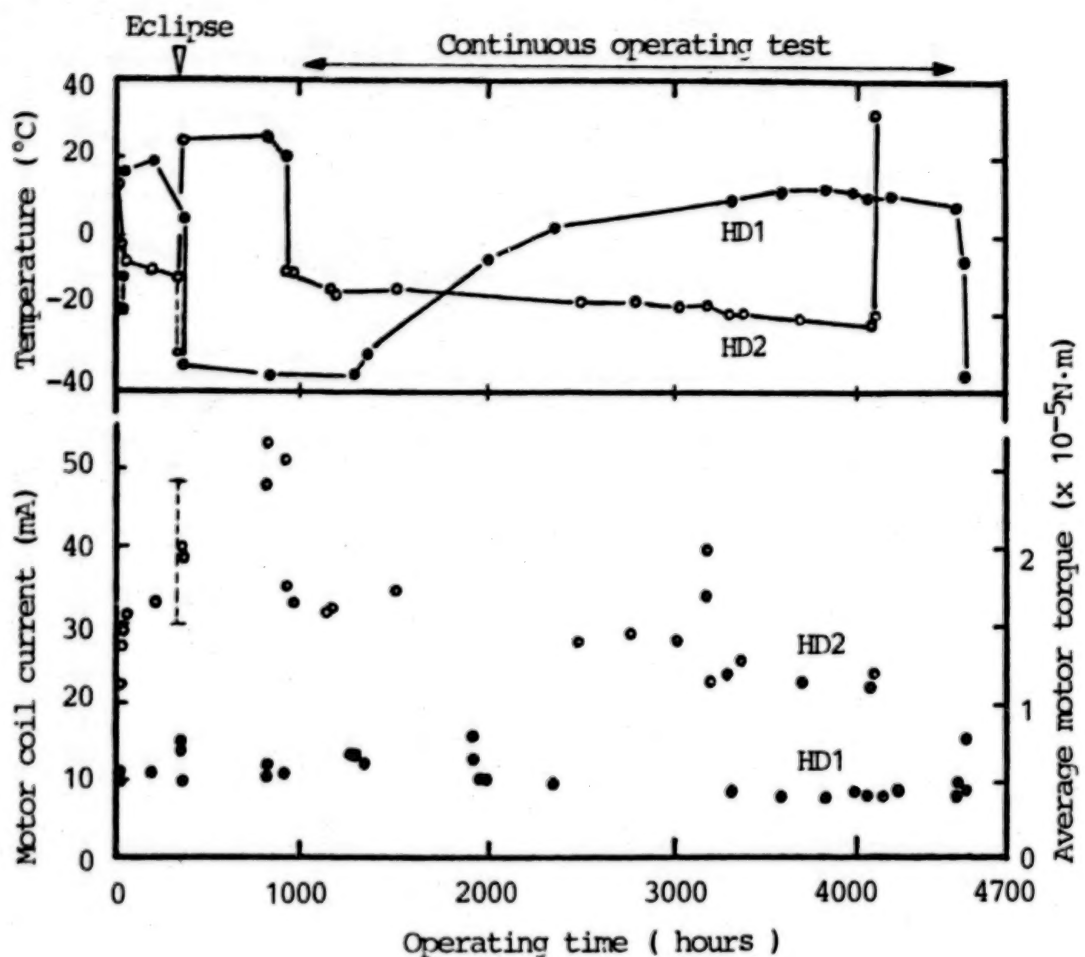


Figure 4. Changes of the average motor torque

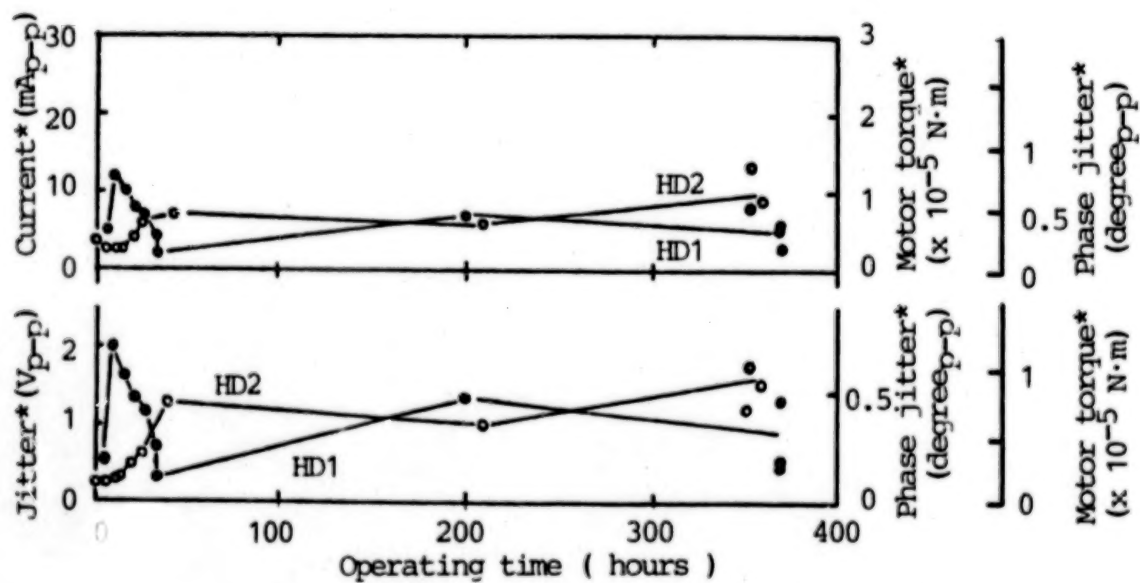


Figure 5. Changes of the motor torque fluctuation
 (* mark shows the data of fluctuation)

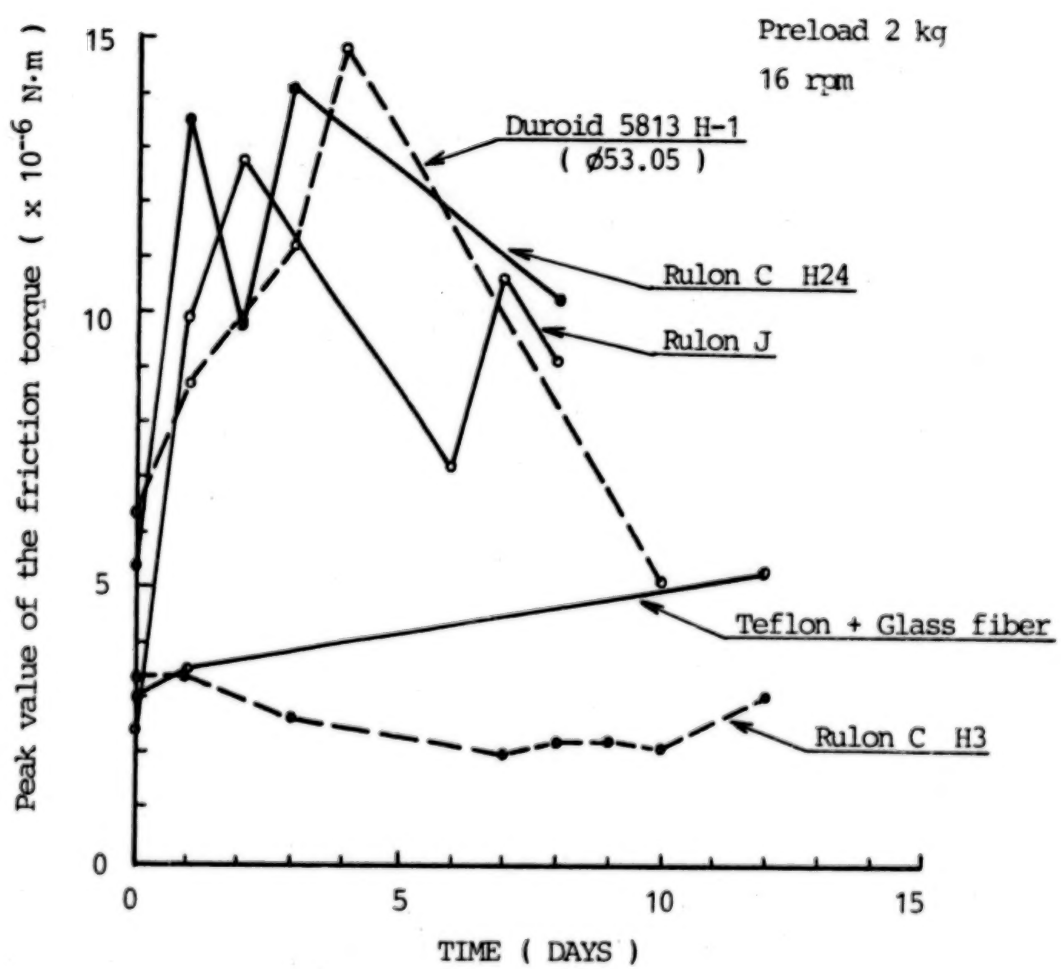


Figure 6. Bearing test of all sorts of retainers
(Equivalent parts of the HOST bearings)

Blank Page

SECURING MECHANISM FOR THE DEPLOYABLE COLUMN OF THE HOOP/COLUMN ANTENNA

Elvin L. Ahl, Jr.*

ABSTRACT

The Column Longeron Latch (CLL) was designed and developed as the securing mechanism for the deployable, telescoping column of the Hoop/Column antenna. The column is an open lattice structure with three longerons as the principal load-bearing members. It is divided into telescoping sections that are deployed after the antenna is placed in earth orbit. The CLL provides a means to automatically lock the longeron sections into position during deployment as well as a means of unlocking the sections when the antenna is to be restowed. The CLL is a four-bar linkage mechanism using the over-center principle for locking. It utilizes the relative movement of the longeron sections to activate the mechanism during antenna deployment and restowing. The CLL design is one of the first mechanisms developed to meet the restowing requirements of future spacecraft which will utilize the STS retrieval capability.

INTRODUCTION

The National Aeronautics and Space Administration currently has a program for development of Large Space Structure Technology (LSST). Some future spacecraft such as the Hoop/Column antenna and the Space Station will be so large that they will have to be either assembled in orbit or deployed once they are clear of the STS cargo bay. One of the Langley Research Center (LaRC) programs is the development of concepts for deployable large space structures.

The Hoop/Column antenna concept, as shown in Figure 1, has been selected as a focus for development of all system disciplines and is being designed as a candidate Shuttle cargo. The antenna, possibly as large as 122 meters (400 ft) in diameter, with the electronic feed system suspended on an 85 meter (279 ft) column, will be stored in the STS cargo bay. It will be deployed while in orbit and then restowed for STS entry/landing.

The main column for antenna deployment is composed of 23 internally-nested telescoping sections. Each section has three longerons spaced 120° apart with a CLL located at the end of the longerons. There are a total of 63 identical CLL's in the column. A servo motor located in the center bay applies a tensile force to cables that are threaded through each set of longerons, as seen in Figure 2, to effect deployment. The same servo-motor may be used for retrieval by pulling on a single cable that is threaded through the center of the column and is attached to the top column section.

*NASA Langley Research Center, Hampton, Virginia

REQUIREMENTS

It is required that the antenna column sections be sequentially locked during extension and unlocked during the restow operation. Each of the longerons when deployed must carry a compressive load of up to 1114 N (250 lb). The CLL was designed to fit within the 19.05 mm (0.75 in) diameter longeron. The design load for the CLL components was taken to be 2304 N (515 lb). This load was developed from the longeron compressive force of 1114 N (250 lb) plus 334 N (75 lb) latch margin in the locked position to allow for some tolerance buildup and to provide column rigidity. The 1447 N (325 lb) force on the latched mechanism and the CLL latching geometry generates a maximum force of 2004 N (450 lb) at the instant the mechanism passes the center point. An additional factor of 1.15 was superimposed to allow for a factor of safety resulting in the design load capability for the CLL of 2305 N (515 lb). Stainless steel (17-4 PH) was selected for the CLL test components to accommodate the design loads in the small sized package.

OPERATION

Deployment of column sections initiates the rotation of the actuator arm that is extended into the housing at the base of each longeron. As longeron B and C move relative to longeron A, the CLL restraining and actuator arms rotate as shown in Figure 3. The actuator arm then rotates into an over-center position, locking the linkage into position. After latching over-center further rotation is stopped when surface A of the restraining arm mates with surface B of the actuator arm in Figure 3. In the action of locking, the stops of longerons A and B merge into position engaging two guide pins, which force alignment and provide shear restraint.

The belleville spring washers and piston housed at the top of each longeron, see longeron A in Figure 3, are an integral part of the latching system. As the restraining arm swings toward the locked position, it drives the piston against the washers causing them to compress. In general, over-center mechanisms rely on the four-bar linkage to deflect when moving to an over-center position. The classic approach was unacceptable for the CLL because the small size caused excessive stress in the pins and linkage. In the CLL design, the belleville spring washers absorb most of the deflections and serve to limit the maximum force necessary to latch. The resulting preload of spring and actuator arms is set to provide a rigid column for the expected external loads.

The single cable attached to the top column section retrieves the column. The bottom of each longeron strikes the extended actuator arm, as seen in Figure 4, unlatching the CLL. This process is continued until all sections are restowed to their original positions.

ANALYSIS

Three analytical models were used in the analysis of the CLL. A kinematic model was used to develop the length and pivot locations of the four bar linkage. The links and pins were sized by closed form mathematical expressions developed from force and moment diagrams. Finally, a finite element model of the restraining arm was generated to allow a more accurate calculation of the stresses in this element, since this was identified as the most critically loaded link from the previous closed form solutions.

The kinematic model of CLL is shown in Figure 5. During deployment, link BC actuates the four-bar linkage consisting of BD, DE, EF, and FB. During restow, link AB actuates the four-bar linkage. Links DB, DE, and GH are loaded in compression while links EF and FG react bending loads. Links FH and FB are loaded in tension to react the bending and compression loads. The linkage is centered when angle I, between links BD and ED, equals 180° . Further counterclockwise rotation of DB into an over-center, locked position decreases angle I to 165° , point G travels in a positive y-axis direction .25 mm (.010 in) as angle I changes from 180° to 165.2° . The belleville spring washers prevent a sharp increase in the stresses in the restraining arm during the over-center travel of the CLL. The perpendicular distance to point D from a line joining point E to point B equals .86 mm (.034 in). This distance represents the margin of safety for the CLL against accidental restow. Point G exerts a maximum compression force of 2004 N (450 lbs) on the belleville spring washers when angle I equals 180° .

All components of the CLL were analyzed by closed form solutions. Forces, moments, free body diagrams and load, shear, and moment diagrams were generated. As a result of the analysis the pins were required to be 3.17 mm (.125 in) in diameter. The maximum force at point C and A respectively, as shown in Figure 5, to latch and unlatch the CLL was calculated to be 150 N (33 lb).

The restraining arm was further analyzed by a finite element model as a check on the closed form stress solution because it is the most highly stressed link and has a complex shape. The maximum bending stress of 454×10^6 Pa (66,000 psi), shown in Figure 6, occurs when angle I, from Figure 5, equals 180° . This stress is within 15 percent of the stress predicted by the closed form solution. The steady state stress, when the CLL is latched, is 289×10^6 Pa (42,000 psi). Corresponding deflections at point A from Figure 5 are 127×10^{-3} mm (.005 in) when angle I equals 180° and 76.2×10^{-3} mm (.003 in) when latched.

TESTING

Four tests were conducted in developing the CLL. A compression test of the top housing, piston, and belleville spring washer assembly was necessary to develop required preload capability shown in Figure 7. A compression test was conducted on the total latch assembly to simulate the

deployed column loading condition, shown in Figure 8. Two tests were conducted to confirm the column longeron loads necessary to latch and unlatch the CLL shown in Figure 9 and 10.

The compression test of the top housing, piston, and belleville spring washer assembly was conducted to determine the number and combination of washers required to obtain a piston preload of 1447 N (325 lb) with the CLL latched while limiting the maximum piston load to 2004 N (450 lb). The combination of 11 belleville spring washers shown in Figure 7 gave the required load conditions with a piston stroke of 0.58 mm (.023 in).

The compression test of the latch assembly gave the preload and the strain in the restraining arm. As a load was applied, the distance between the stop distance A was measured. At a load of 1438 N (323 lbs), a gap was obtained, and the test was stopped. The gap signified that the preload of the latch had been obtained. The steady state strain in the restraining arm was measured at 1.25×10^{-3} corresponding to 258×10^6 Pa (37,500 psi). This differed from the finite element model results by only 11 percent.

The latching load was determined by test, shown in Figure 10, to be 850 N (190 lb). This is six times the value predicted by calculations. The large variance is attributed to a high friction load between the loading longeron and the test housing assembly, and the friction between links and pins. However the peak strain in the restraining arm was 1.76×10^{-3} , which represents a stress of 363×10^6 Pa (52,800 psi). This stress is 20 percent lower than the peak stress predicted by the finite element analysis. The unlatching load was determined by test, shown in Figure 9, to be 530 N (119 lb), which is over three times the calculated value. This difference is attributed to friction between pins and links.

CONCLUSIONS

The test data verified the analysis with the exception of the latching and unlatching loads. These differences are attributed to excessive friction in the test setup. A modification to the latch assembly test housing is being made for retesting of the deployment loads. A modification may be made to the actuator arm to reduce the latching and unlatching loads. Based on the design, analysis and tests, the CLL design shows good potential for a solution to the latch and unlatch problem of a deployable space system where a restow capability is required.

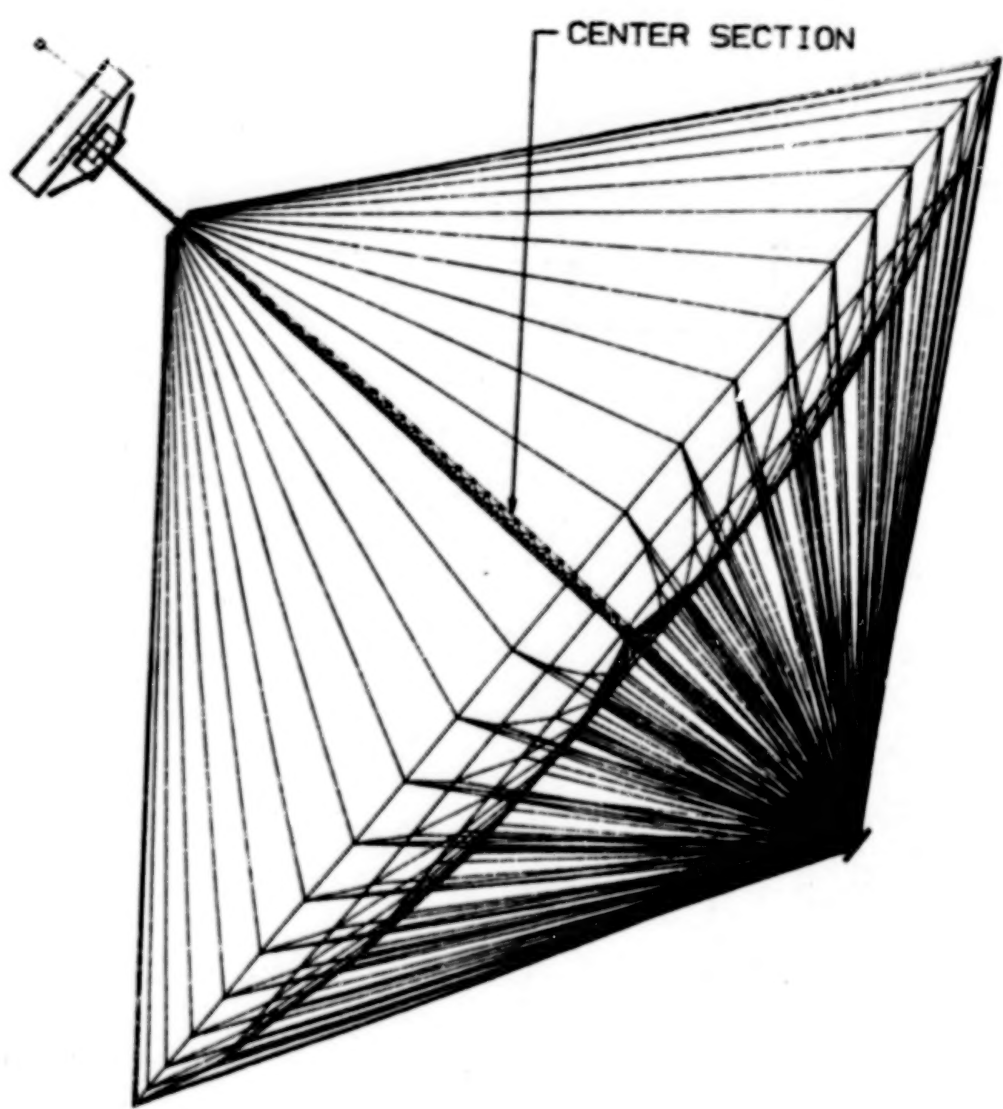


FIGURE 1.- HOOP/COLUMN ANTENNA

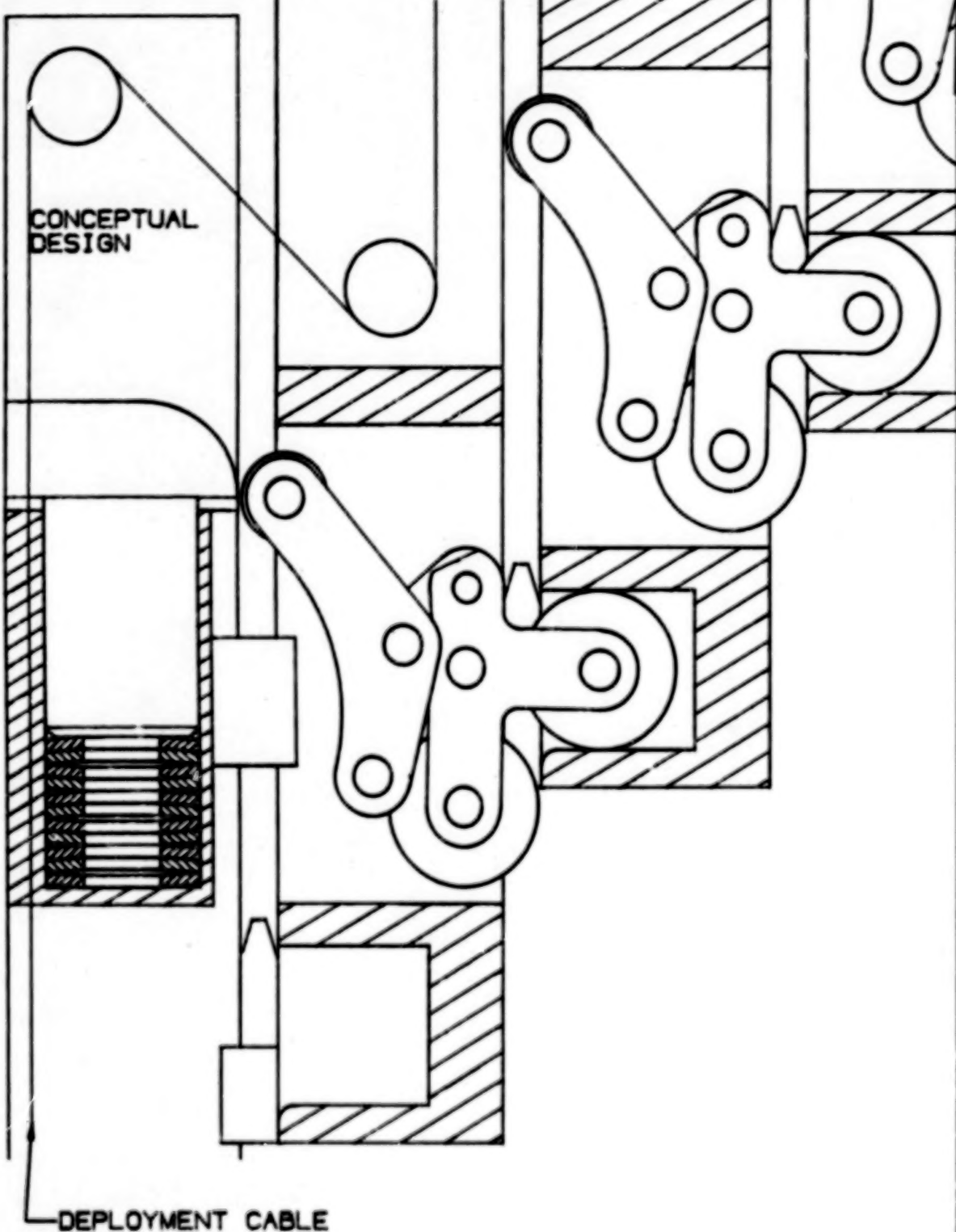


FIGURE 2. - LONGERON DEPLOYMENT

BLANK

PAGE

REQUIREMENTS

The basic requirement of the arm mechanisms design was that its three main mechanisms be prohibited from operating out of sequence.

The arm must be capable of being placed in three positions: "LAUNCH" the arm is fully folded back against the MMU body to permit the MMU to pass through the Orbiter airlock, and to withstand the space shuttle launch vibration environment; "WORK" is when the arm is positioned 82 deg below horizontal to allow the astronaut access to work at a worksite. "FLIGHT" the arm is positioned 30 deg below horizontal, positioning the hand controllers for comfortable operation.

When the crewmember operates the "LAUNCH" locks (See Fig 4) to release the arm from the "LAUNCH" position, the arms, when released, must automatically move into the "WORK" position, then be free to rotate to the "FLIGHT" position without operating additional latches.

In addition, to enable operation of the MMU by crewmembers in the size range from 5 percentile female to 95 percentile male, the arm length must be capable of being adjusted up to 5 in. in half inch increments. This requirement also necessitated that forces required to operate any mechanism be within the capability of the 5 percentile female.

It was also required that the arm be capable of operating in a temperature range of plus 150°F to minus 150°F. To cover the possibility of "LAUNCH" lock malfunction, it was required that a contingency arm release system be incorporated into the design.

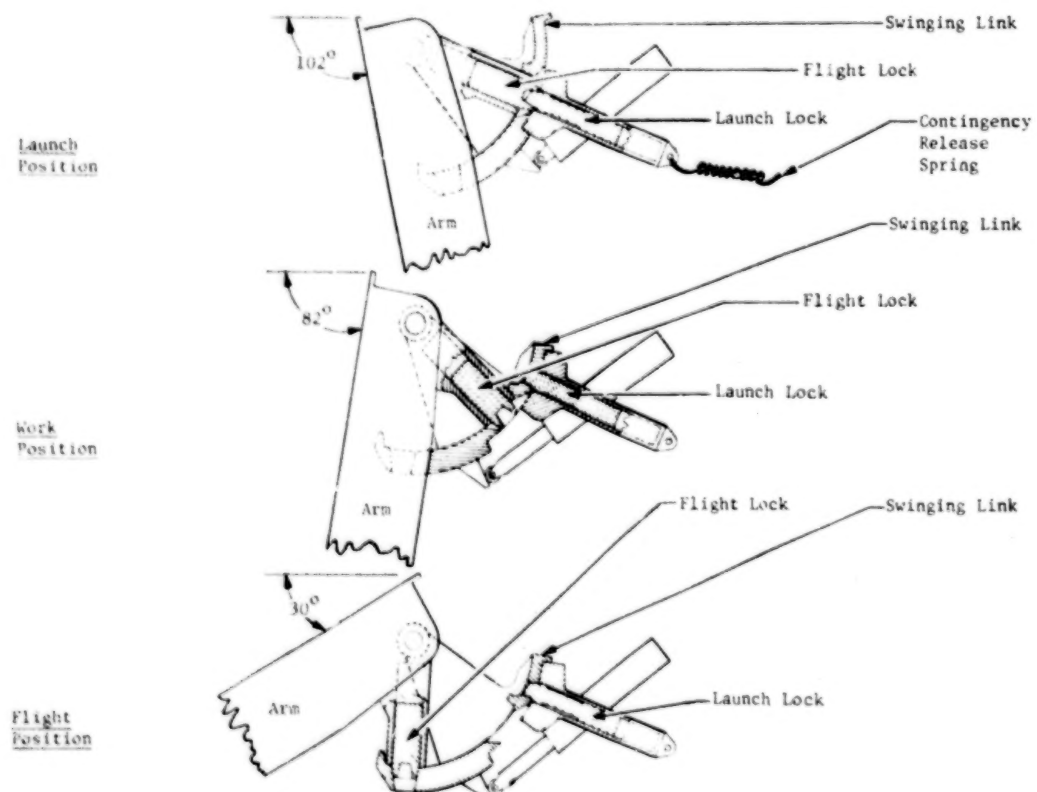


Figure 4. Swinging Link Operations

DESIGN

When the arm design was initiated a potential flight requirement for the MMU to support orbiter tile inspection and repair activities was nine months away. Flight hardware materials and hardware were in short supply at this time, causing delivery lead times that were difficult to meet. An attitude of designing with on-the-shelf hardware had to be adopted, sometimes causing such occurrences as machining simple bolts in small quantities.

The temperature requirements precluded the use of wet lubricants so that surface treatment dry lubricants had to be employed. To ensure there was no danger of cold weld within the moving parts of the mechanisms (assuming the dry lubricant had failed), the materials of any parts contacting while moving were very dissimilar, e.g., a CRES plunger in an aluminum housing.

An early design review demanded that all uses of snap-rings and other spring retaining devices be deleted from the design. This necessitated designing special hinge pin retention devices in very small sizes, having double locking features.

The external envelope of the arm had been determined by crew evaluation with early mockups. This cross section envelope consisted of a 3.75 in. wide by 2.00 in. rectangle. Priority had to be given in this space to two 0.7 in. dia wiring harnesses. Telescoping the arm to meet the arm length adjustment requirement further depleted the envelope, making the remaining space for latch mechanisms very constricted.

The requirement to preclude out of sequence operation of the mechanisms made for a formidable challenge. The worst of these was the requirement that when the flight latch is operated to let the arm down out of "FLIGHT" position, further operation of this latch could not permit the arm to travel beyond the "WORK" position. If the arm should travel past the "WORK" position with a suited astronaut locked into the MMU, his restricted reach might not permit him to reach the arm and return it to the "FLIGHT" position. To fulfill this design requirement, the part known as the "swinging link," which controls arm movement between the three required positions of the arm, was created (see Fig. 4).

The arm length adjustment requirement necessitated the use of some form of sliding action that was compact, easily moved, and prohibited excessive lateral or vertical movements between the arm sections. Cam follower roller bearings were selected. Unfortunately, the material from which commercial bearings are manufactured does not allow their use in temperatures as low as the arm requirements. Therefore, a roller design using approved materials was developed, employing dry lubricants without needles or balls.

When the arm length is adjusted, the length of the electrical harnesses has to adjust accordingly. The first design for the management of these harnesses assumed that it would be necessary for a tension load to be maintained on them to ensure they would retract into the MMU side tower when the arm length was reduced. When flight hardware was available for evaluation it was found that the harnesses were sufficiently stiff to enable them to

be pushed without buckling, making the tension mechanism unnecessary. The present design provides a 180 deg loop in the harness which rolls back and forth inside the MMU side tower when the arm length is adjusted.

If the crewmember in preparation to don the MMU, finds he cannot release the arm from the launch position he has an alternative known as the arm release contingency plan. The launch lock housing is held into the hinge fitting by four special bolts with hexagonal heads which are flush with the MMU sidetower external skins. A dedicated MMU contingency tool is provided in the form of a ratchet drive socket. Using this tool the crewmember is able to remove the four bolts, which releases the launch lock assembly. This action is assisted by a tension spring attached to the launch lock which pulls the launch lock clear, freeing the arm for rotation to the flight position. To maintain the arm in the flight position holes in the side of the arm and the hinge fitting permit the insertion of a pip pin, thus enabling the MMU to still be flown.

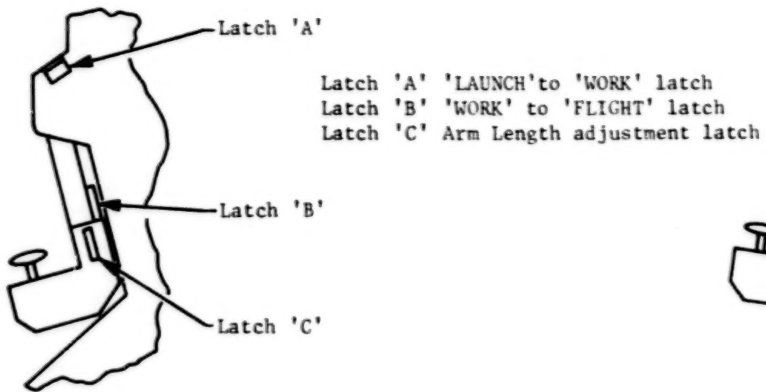
The final arm design is a complicated mechanism designed to meet complicated requirements. Early in the design it was recognized that no matter how the parts were dimensioned, necessary tolerances would not permit guaranteed assembly. It was for this reason that peelable shims were introduced into the design and other modes of adjustment were employed where possible. Even so, assembly proved to be a lengthy, precise exercise using a build plan document which was very detailed in its step by step sequence. This assembly sequence was interrupted on several occasions by parts not going together as intended due to tolerance stackup. Due to the complexity it was not always possible to make a change in the most desirable manner without causing problems further on in the assembly.

ANOMALIES

During crew training it was found that the arm could be locked into an unwanted fourth position. This problem was caused by the automatic push out device which kicks the arm from "LAUNCH" position to "WORK" position coupled with the crewmember tendency not to release the launch latch before the arm pendulum action tried to put the arm in a vertical position. This caused the launch latch to engage the launch position and the "flight" latch to engage the flight position, locking the arm in a position midway between "WORK" and "FLIGHT" positions. (See Figure 5.)

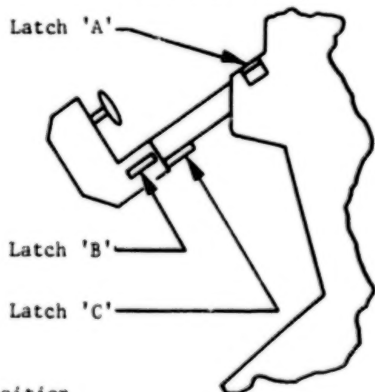
Changes were made to minimize the chances of engaging this position and, if engaged, make it easy to get out of.

The arm was cyclically tested to more than 1.5 lifetimes (3000 cycles). Posttest inspections found that the PTFE impregnated hard anodized material which had been used to provide lubricated surfaces on aluminum had shown very little signs of wear; however, this was not the case with the spray-on types of dry film lube working in line contact on stainless steel.



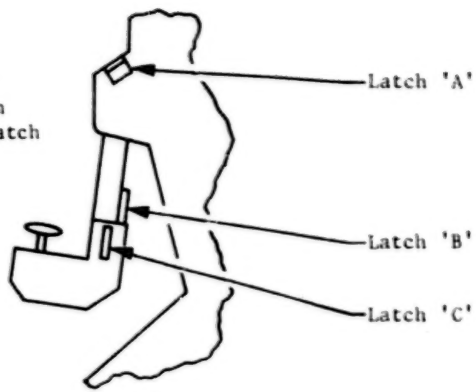
Launch Position

When the arm is in the 'LAUNCH' position, latches 'B' and 'C' are not operable. With the astronaut facing the MMU, actuation of latch 'A' releases the arm which automatically moves it into the 'WORK' position.



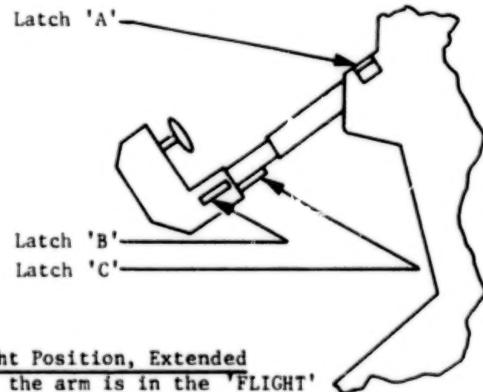
Flight Position

When the arm is in the 'FLIGHT' position latch 'A' is not operable. Latch 'C' is now free to allow arm to be extended to the desired length using aperture in top of arm to read indicator.



Work Position

When the arm is in 'WORK' position latch 'C' is not operable. With the astronaut locked into the MMU the arm is pulled up into 'FLIGHT' without the need to operate any latches; the arm will automatically lock into 'FLIGHT' position.



Flight Position, Extended

When the arm is in the 'FLIGHT' extended position latches 'A' and 'B' are not operable. Note: It is only in the 'FLIGHT' position that the arm length can be adjusted.

Return to Flight Position

Operating latch 'C' allows arm to be retracted. Only when it is fully retracted does latch 'B' become operative. Latch 'A' is still not operable.

Return to Work Position

Operating latch 'B' allows the arm to be pushed down into 'WORK' position. Note:-If when in the work station, latch 'B' is operated, the arm cannot be pushed down toward the 'LAUNCH' position. Latch 'C' is again not operable. (To return to flight position again the arm when lifted automatically locks into 'FLIGHT' position).

Return to Launch Position

With the astronaut facing the MMU, operation of latch 'A' permits the arm to be pushed into 'LAUNCH' position, where it automatically locks. Again latches 'B' and 'C' are not operable.

Figure 5. Arm Operation

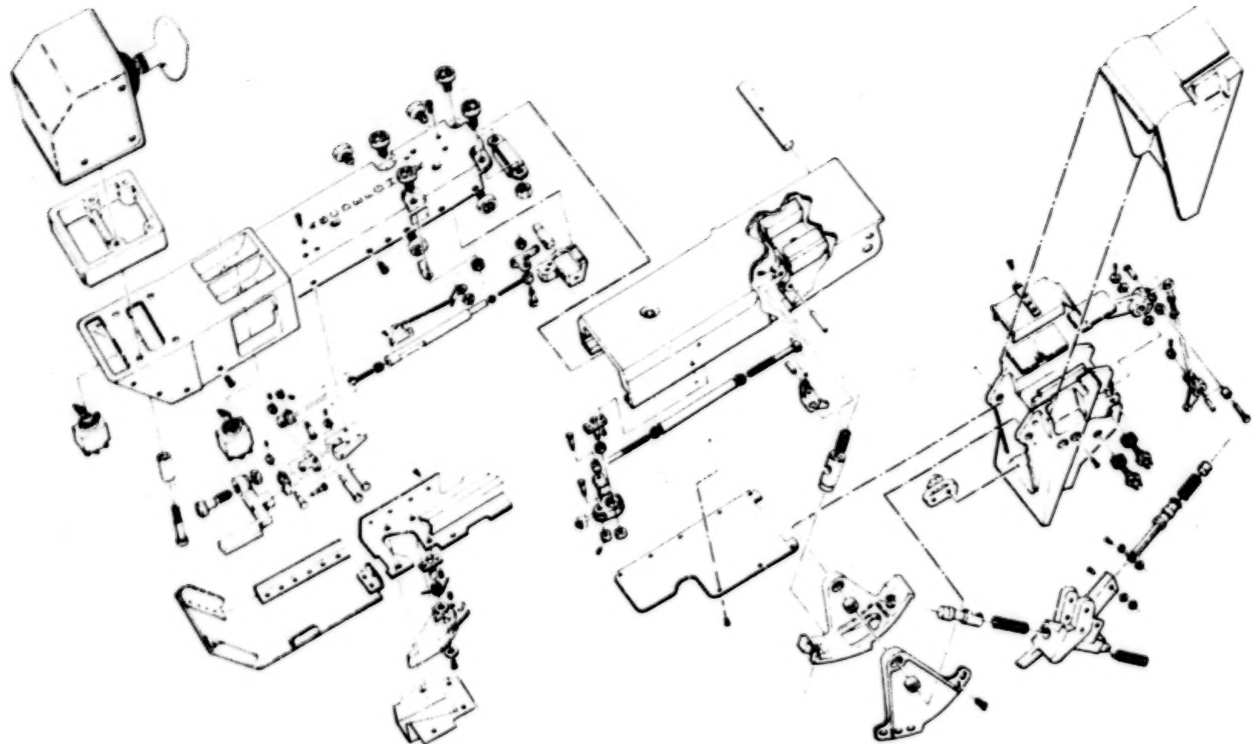


Figure 6. MMU Arm Exploded View

CONCLUSION

The final design consisted of approximately 150 machined parts, not including hardware and springs. (See Fig. 6.)

The arm has now successfully completed all functional, thermal, and vibration testing; and some of the flight hardware has been delivered to the customer.

LATCH FITTINGS FOR THE
SCIENTIFIC INSTRUMENTS ON THE SPACE TELESCOPE

Jan D. Dozier* and Everett Kaelber**

ABSTRACT

Latch fittings which kinematically mount the replaceable scientific instruments onto the Space Telescope must maintain precise alignment and thermal stability for on-orbit observations. Design features which are needed to meet stringent criteria include the use of ceramic isolators for thermal and electrical insulation, materials with different coefficients of thermal expansion for athermalization, precision manufacturing procedures, and extremely tight tolerances. A specific latch fitting to be discussed is a ball-and-socket design. In addition, testing, crew aids, and problems will be covered.

INTRODUCTION

Latch fittings for the scientific instruments (SI) and fine guidance sensors (FGS) on the Space Telescope are mechanisms which structurally support the instruments during launch and orbital operations. Designed to allow on-orbit replacement of an SI or FGS, the latch fittings must maintain precise registration of the instruments, provide alignment and stability during scientific observations, and minimize thermal conductance.

The latch fittings mount each SI or FGS onto the graphite-epoxy focal plane structure (FPS) of the ST in a statically determinate manner. Each of the four axial SI's is mounted with three latch fittings (Figure 1), the radial SI is mounted with three latch fittings (Figure 2), and each of the three Fine Guidance Sensors (FGS) is mounted with four latch fittings (Figure 3). Every latch fitting consists of one half mounted to the FPS and one half mounted to the SI (or FGS). Accounting for mirror image designs, there are a total of 20 different latch configurations.

The stringent alignment and functional requirements of the SI latch fittings make their design, manufacture, assembly, and qualification a challenging and unique engineering task. This paper will discuss design requirements of the latch fittings, the general design features needed to meet these requirements, a specific latch fitting of a complex design, verification and qualification testing, and problems.

*National Aeronautics and Space Administration, George C. Marshall Space Flight Center, Alabama

**Perkin-Elmer, Danbury, Connecticut

DESIGN REQUIREMENTS

The design driver for the SI latch fittings is the stringent alignment requirement. The instrument position during initial alignment must be known within 10 μm . If the instrument is replaced, the alignment must be repeated within 15 μm . Furthermore, during scientific observation, the twenty-four hour stability requirement for the latch fittings is that the SI alignment must be maintained to within .0013 arc second. Alignment and stability are verified by analysis.

In order to minimize heat loss between the SI and the FPS, the mount point conductance for each latch half must be less than 0.050 Watt/ $^{\circ}\text{C}$. Conductance is verified by analysis. Distortion due to thermal deformation of an instrument or the FPS may also induce a moment across a latch fitting interface. Therefore, the maximum residual moment, or breakaway torque of a latch fitting, is restricted. The maximum breakaway torque for each latch fitting is determined by test.

Structurally, the latch fittings are designed to support the instruments and to withstand the shuttle launch and landing loads. For the stress analysis, a factor of safety of 1.4 is used on ultimate strength and 1.1 is used on yield strength. Strength is verified with a static load test on each mated latch fitting. Dynamic tests of all-up SI simulators and latch fittings are used to verify mechanical integrity. These tests will be discussed later.

Other design requirements include crew systems compatibility and constraints on physical dimensions and weight.

DESIGN FEATURES

Each latch fitting is designed to take loads in one, two, or three directions so that the instrument is supported with a statically determinate system. Therefore, a set of latch fittings kinematically mounts each SI or FGS with six degrees of freedom.

The thermal paths between the FPS and SI must be isolated to meet the alignment requirement and the .050 Watt/ $^{\circ}\text{C}$ conductance requirement. Therefore, a common design feature of the latch fittings is the use of glass-mica to insulate the attachment bolts and shear pins. Machined inserts are used to insulate the attachment bolts and injection molds are used to surround each shear pin. Because of the brittle nature of the glass-mica ceramic, it is capable of compression loading only. Therefore, shear load paths must be separated from the tension/compression load paths and the design of the latch fittings becomes complex. Thermal load paths for a typical fitting are shown in Figure 4. Additional thermal requirements are met using materials with low, yet compatible, coefficients of thermal expansion.

Two of the latch fittings, point A of the radial SI and FGS, and point A of the axial SI, are designed to take loads in three directions. Although of different detail configurations, each of these latch fittings is basically a ball-and-socket design. Rotation of the ball is restricted by the space limitation, and it is self-aligning. The 440C stainless steel ball is machined to a sphericity within 1 μm (40 $\mu\text{-in.}$) Each of these latch fitting designs is actuated with a rod which can be torqued and untorqued by an astronaut during an on-orbit mission. The axial SI point A latch has titanium jaws which close on the ball when a 60 Nm (44 ft-lb) torque is applied. During manufacturing, these jaws are clamped, then thermally aged and stabilized for one week before final machining to a sphericity within 1 μm . The clearance between the ball and jaws is 2 μm on the diameter and the maximum moment transmitted is less than 31 Nm (23 ft-lb) when preloaded. Point A of the radial SI and FGS is a ball captured with a threaded rod and seated with a 60 Nm (44 ft-lb) torque. This latch fitting will later be discussed in detail.

Point B of the axial SI is designed to transmit loads in two directions and applies a 3560 N (800 pound) preload along the longitudinal axis of the axial SI. This latch fitting has a large spring at the aft end of the instrument which applies the preload through a linkage mechanism. A threaded actuation rod applies a 10 Nm (90 in-lb) torque and enables an astronaut to engage the fitting. The maximum residual moment allowed across point B is 54 Nm (40 ft-lb).

Switches for crew aid indicator lights are located on each radial SI and FGS point A latch, axial SI point A latch, and on the axial SI guiderail. These lights tell the astronaut when the ball is seated in its socket, when to begin torquing, or when the preload has been applied.

The remaining latch fittings take load in one or two directions only and do not transmit moments. Basically, the design is a self-aligning cylinder which registers against a flexure within a mating receptacle. A spherical stem is sprayed with aluminum oxide coating and cylindrical shells of 440C stainless steel are clamped around the ball with a retaining ring. The clearance between the shells and the ball allows a 2° rotation, thus giving the ball its self-aligning capability. This cylinder is inserted into a rectangular titanium receptacle and registers against a 15-5 Ph steel flexure. Thus, the load path is along the line of contact between the ball and the flexure. All of these types of latch fittings are passive, in that they become engaged when the active fittings are torqued and latched.

SPECIFIC DESIGN

A complex latch fitting design is that of point A of the radial SI and FGS. As described earlier, this ball-and-socket design takes load in three orthogonal directions. The fitting is lightweight, yet strong enough to meet the strength criteria. It also enables on-orbit instrument removal and installation by an astronaut, and realigns the new instrument to extremely

close tolerances. Thermal conductance and electrical resistance requirements are also included in the design.

The 24-hour stability requirement combined with the space limitation of the FPS hub forces complexity into the fitting design. Governed by the 24-hour stability requirements, the allowable thermal expansion between the radial SI and the FPS is .5 μm (19 $\mu\text{-in.}$). Thus, an athermalized design is required and, as shown in Figure 5, consists of nested parts of titanium, Invar, and aluminum. The thermal growth of the titanium base and the Invar stem is counteracted by the growth of the aluminum cover. Aluminum or Invar shims are used for adjustments at the final assembly. Athermalization of the FPS half of the fitting is analytically determined, but can be verified with an interferometer.

The Ti-6Al-4V titanium ball depicted in Figures 5 and 6 is able to swivel 2° and the clearance between the ball and its titanium housing is 1-1.5 μm (40-60 $\mu\text{-in.}$) on the diameter. By referring to Figure 7, it can be seen that vertical load taken by the ball is transmitted to the Invar stem and aluminum cover through a center bolt, then to the titanium base through the stiff axis of three steel flexures. Each flexure has only one attachment bolt per end, necessitating a tapered interference fit to react the moment. One end of the flexure is attached to the titanium base and the other end attaches to the aluminum cover. Therefore, these flexures are designed to deflect outward under distortion resulting from the different coefficients of thermal expansion between aluminum and titanium. Radial load taken by the ball is transferred to the titanium base with shear slugs. As shown in Figures 5 and 6, these shear slugs consist of a glass-mica insert bonded to a self-aligning set of spherical washers. Any remaining "kick" load is taken up by the weak axes of the three flexures.

A threaded rod inserted into the ball engages the fitting when a 60 Nm (44 ft-lb) torque is applied. Springs between the ball and the SI half of the fitting apply 1245 N (280 lbs) of preload to ensure that the ball remains registered to the upper half of its housing.

TESTING

Factors of safety used by Marshall Space Flight Center for untested flight hardware are 2.0 for ultimate strength and 1.25 for yield strength. However, structural verification by test is required if the 1.4 and 1.1 factors of safety are used for ultimate strength and yield strength, respectively. The test criteria were chosen for the SI latch fittings in order to conserve weight and to reduce complexity in design. Each mated latch fitting configuration is statically tested to loads equivalent to shuttle launch or landing. Before the test, baseline dimensions are measured and strain gages are applied at locations determined by the brittle lacquer technique. A functional test is performed after exposure to 1.0 times the limit load. After applying 1.1 times the limit load, measurements are taken to determine the degree of permanent yielding. After the latch fitting is tested to 1.4 times the limit load, it is disassembled and inspected for cracks.

A dynamic test is conducted on each axial SI, radial SI, and FGS configuration, with their respective latch fittings mounted. The most severe load case is simulated by a series of transient shock spectra and random vibration tests for each axis. From these tests, alignment and stiffness data are obtained, as well as information on the mechanical integrity of the latch fittings.

Crew aids accessibility and functional requirements of the latch fittings are tested in Marshall Space Flight Center's Neutral Buoyancy Simulator. Full scale mock-ups of the ST are placed in a large water tank, where weightlessness is simulated by the buoyant effect of the water. The astronauts then remove and install instruments in a simulated zero g environment. Further information on these tests is given in NASA Technical Memorandum 82485 ("Space Telescope Neutral Buoyancy Simulations - The First Two Years," Fred G. Sanders, June 1982).

PROBLEMS

Glass-Mica (Injection molded)

Injection molded glass-mica surrounds a knurled steel pin and is molded into a titanium base. The glass-mica is injected at 276 MPa (40,000 psi) and 760°C (1400°F), requiring extensive tooling. Initial samples exhibited "knit" lines in the direction of the flow, at the point of injection, and at the juncture where the material flowed around the pin. These knit lines appeared as cracks and contained some machining oil, causing contamination. The knit lines were virtually eliminated by a change in the stress relief cycle. This cycle consisted of increasing and decreasing the temperature at 38°C (100°F)/hour. Machining oil was eliminated from the process and the bases were baked out to reduce contamination.

Also, the glass-mica was loose at the titanium base interface after the bases were stress-relieved. This looseness could have contributed to misalignment of the instrument. Looseness which exceeded the alignment error budget tolerance was brought within tolerance by vacuum impregnating the glass-mica interfaces with the epoxy.

Glass-Mica (Bar stock)

Bolt isolators and shear slugs are machined from bar stock glass-mica. During assembly and during the strength tests, this glass-mica was found to be very brittle, especially under point loads. Tighter control of coplanarity and parallelism to the drawings of the bolt isolator bearing surfaces has reduced the occurrence of fracture during assembly. However, a redesign of the shear slugs was necessary. The original design has a set screw tightening a flat washer against the end of a glass-mica cylinder, whereas, the redesigned shear slug has a set screw which bears on a set of spherical washers that are bonded to the glass-mica cylinder. This self-aligning feature prevents the set screw from point loading the glass-mica.

Aluminum Oxide

Aluminum oxide is used to coat some of the spherical surfaces in order to reduce friction. The use of liquid lubrication is severely restricted because of potential contamination. Interior balls in the self-aligning cylinders (axial SI point C, radial SI points B and C, FCS points B, C, and D) and the self-aligning captured balls (axial SI point B, axial SI point A, and radial SI and FGS point A) were plasma sprayed with aluminum oxide.

During the dynamic tests, pieces of the aluminum oxide on the surface of the axial SI point A 440C stainless steel ball chipped off. These broken pieces were abrasive and severely galled the mating titanium jaws. A redesign was therefore necessary and, at this writing, is underway. The proposed design coats the titanium jaws with a tungsten carbide/cobalt material. The aluminum oxide coating has been deleted from the point A ball designs, which now use an uncoated steel ball.

Galling

The self-aligning steel cylinders which register against a 15-5 Ph flexure also bear against a titanium base. During the vibration environment of the dynamic tests, the steel cylinders severely galled the titanium surface and also galled the 15-5 Ph steel surface. This galling is unacceptable if the alignment error budget is to be met. Therefore, the titanium and 15-5 Ph bearing surfaces are now coated with a tungsten carbide/cobalt material. These coated latch fittings will be subjected to more dynamic testing before the proposed design is accepted.

Residual moment

The residual moment, or breakaway torque, at the axial SI points A and B latch fittings was originally limited to 22 Nm (16 ft-lbs). When tested, the fittings transmitted much higher torques. Therefore, lubricant was added to the ball surface to further reduce friction. In addition, the preload at point B was reduced from 4893 N (1100 lbs) to 3560 N (800 lbs). After an evaluation by each scientific instrument contractor, an increase in residual moment at each fitting was approved. The axial SI point A latch fitting residual moment is now a maximum of 31 Nm (23 ft-lb) and the axial SI point B latch fitting has a maximum residual moment of 54 Nm (40 ft-lb).

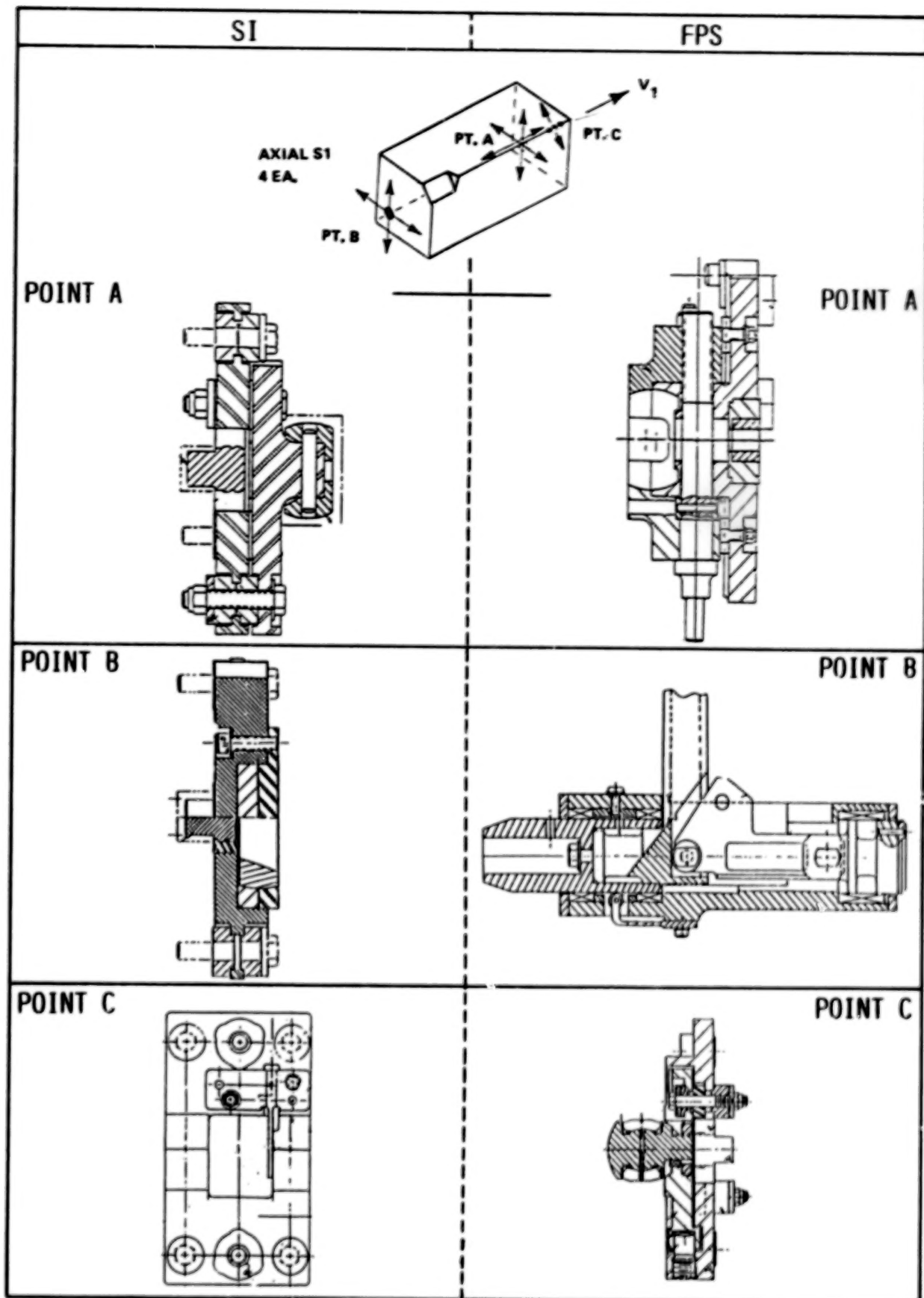


Figure 1. Axial Scientific Instrument Latch Fittings

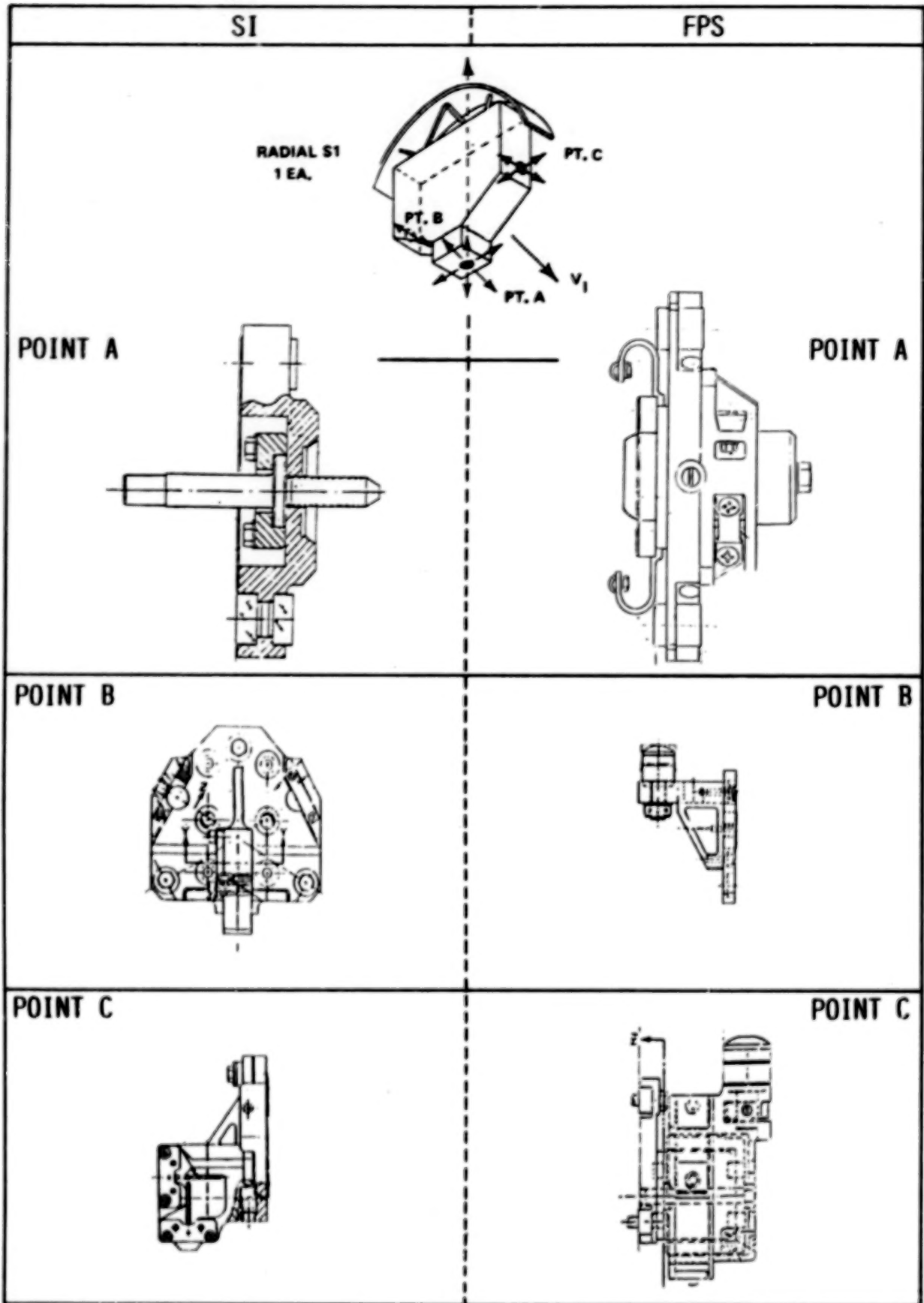


Figure 2. Radial Scientific Instrument Latch Fittings

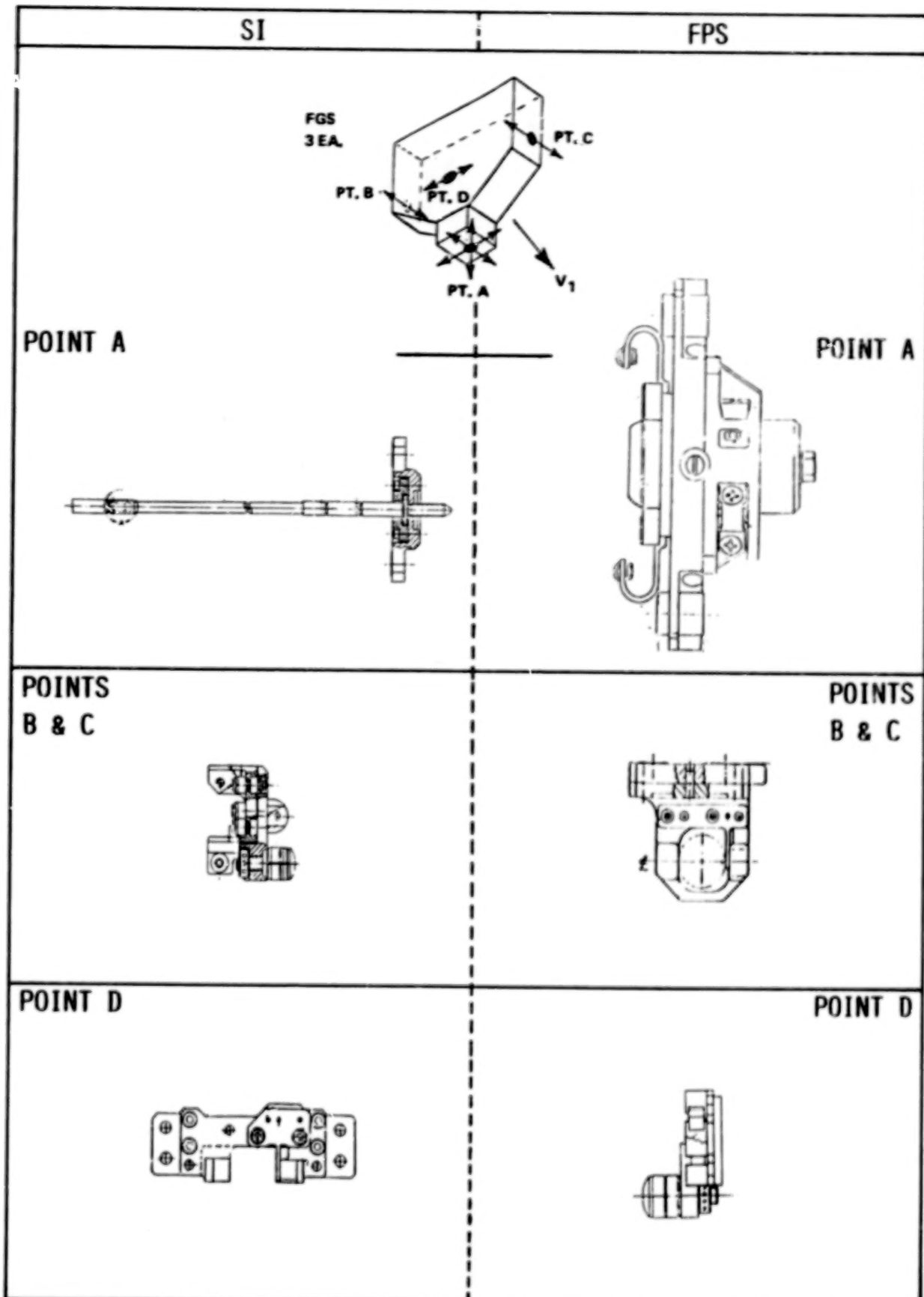


Figure 3. Fine Guidance Sensor Latch Fittings

262

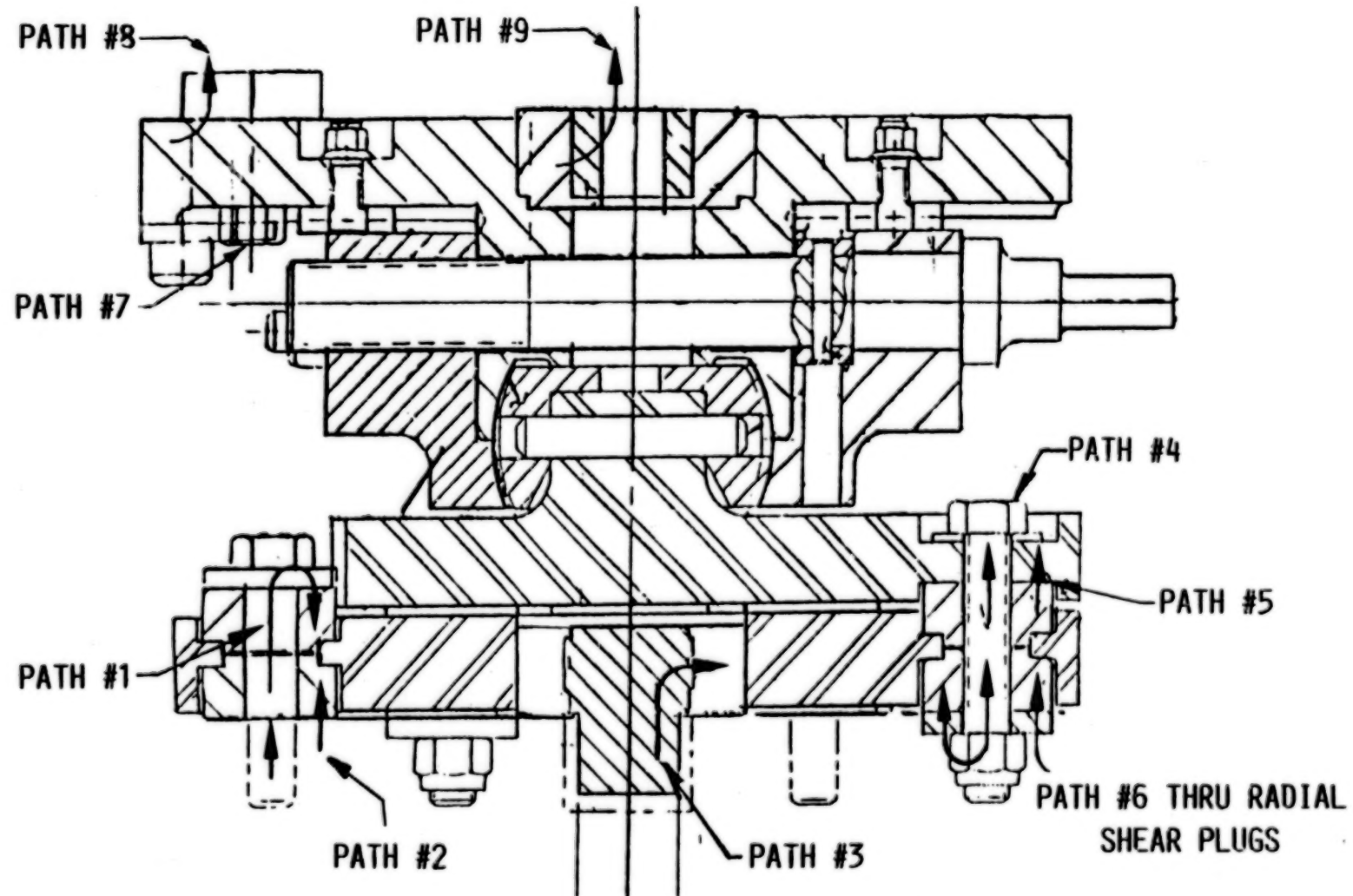


Figure 4. Thermal Paths, Axial SI Point A

262

BEST AVAILABLE COPY

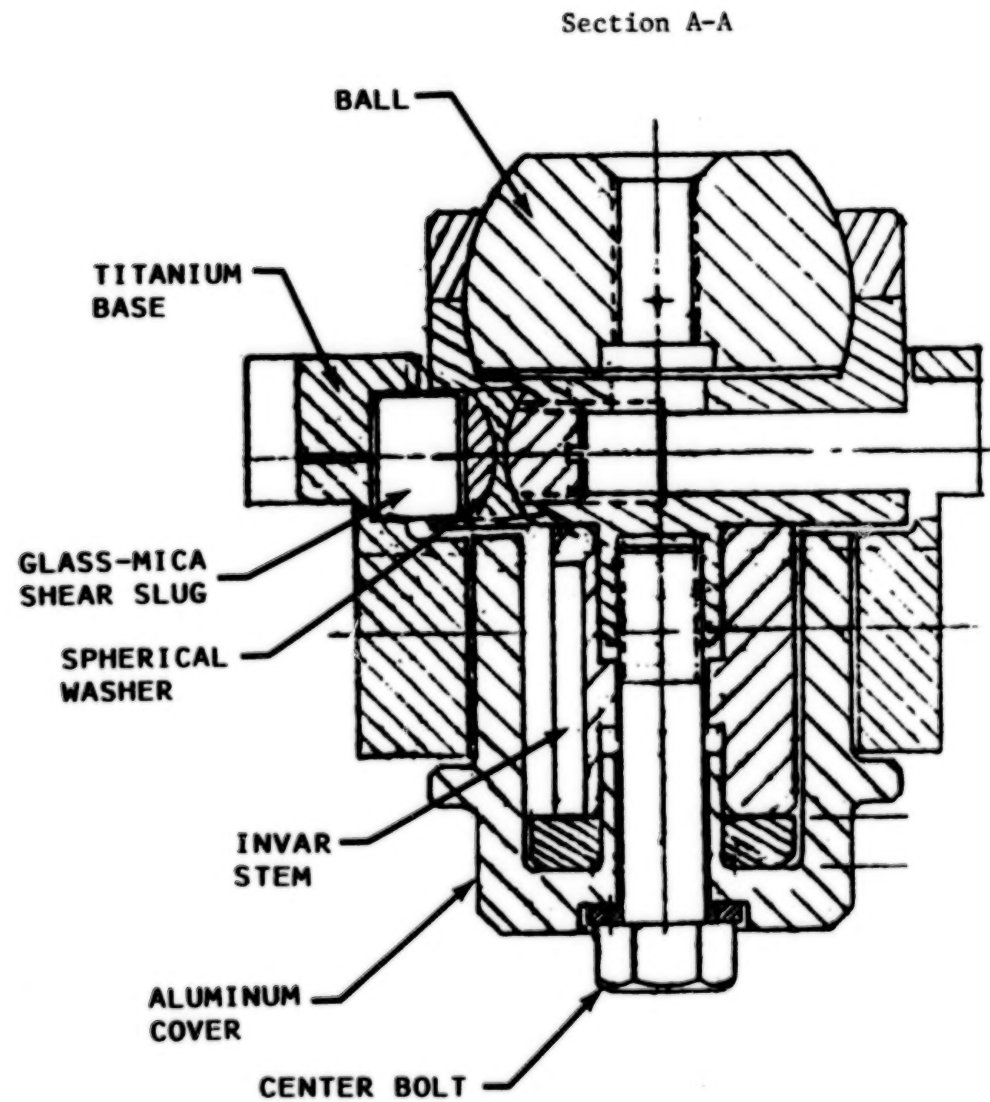


Figure 5. Radial SI and FGS Point A, FPS Half

264

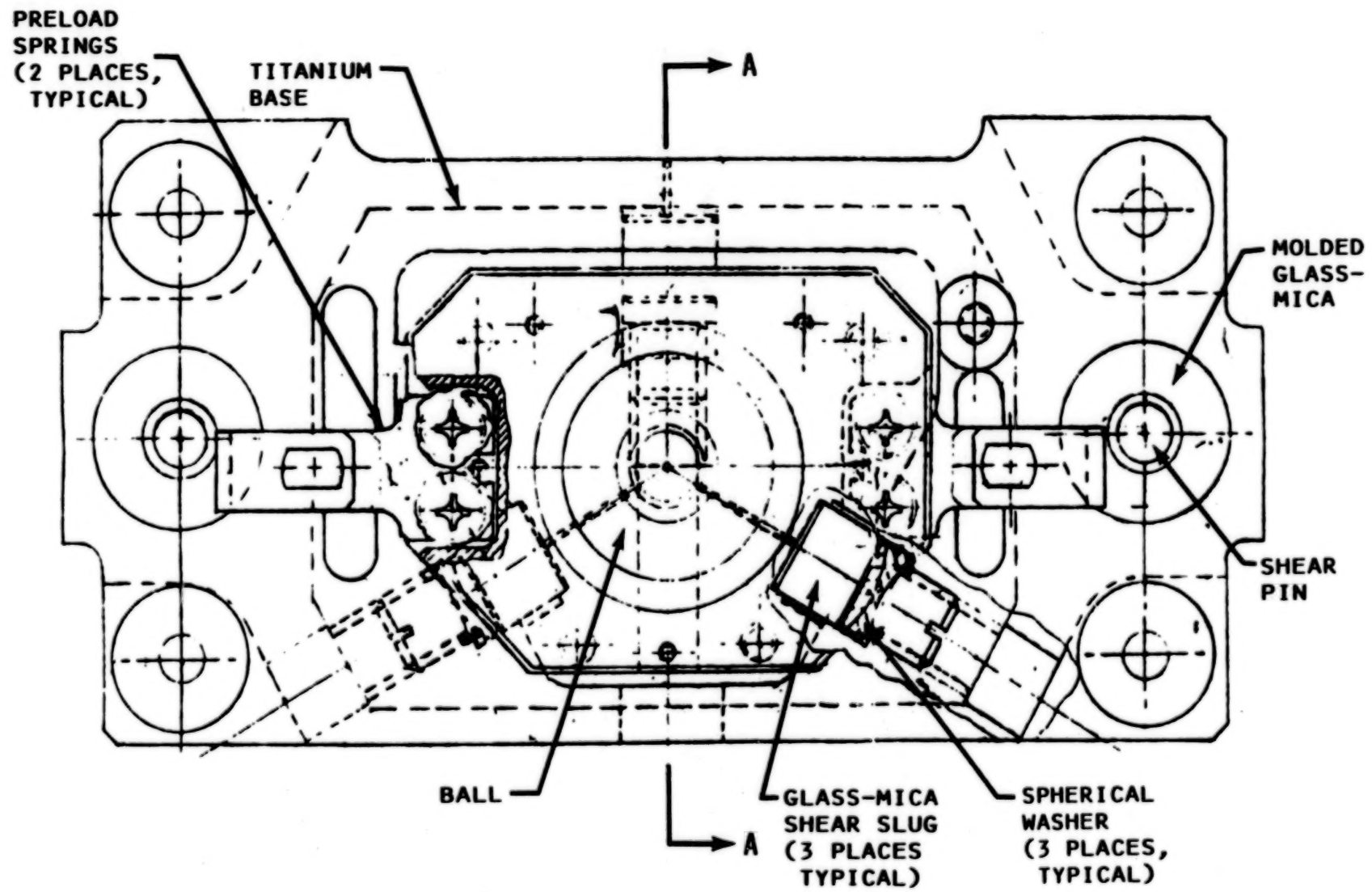


Figure 6. Top View, Radial SI and FGS Point A, FPS Half

264

BEST AVAILABLE COPY

265

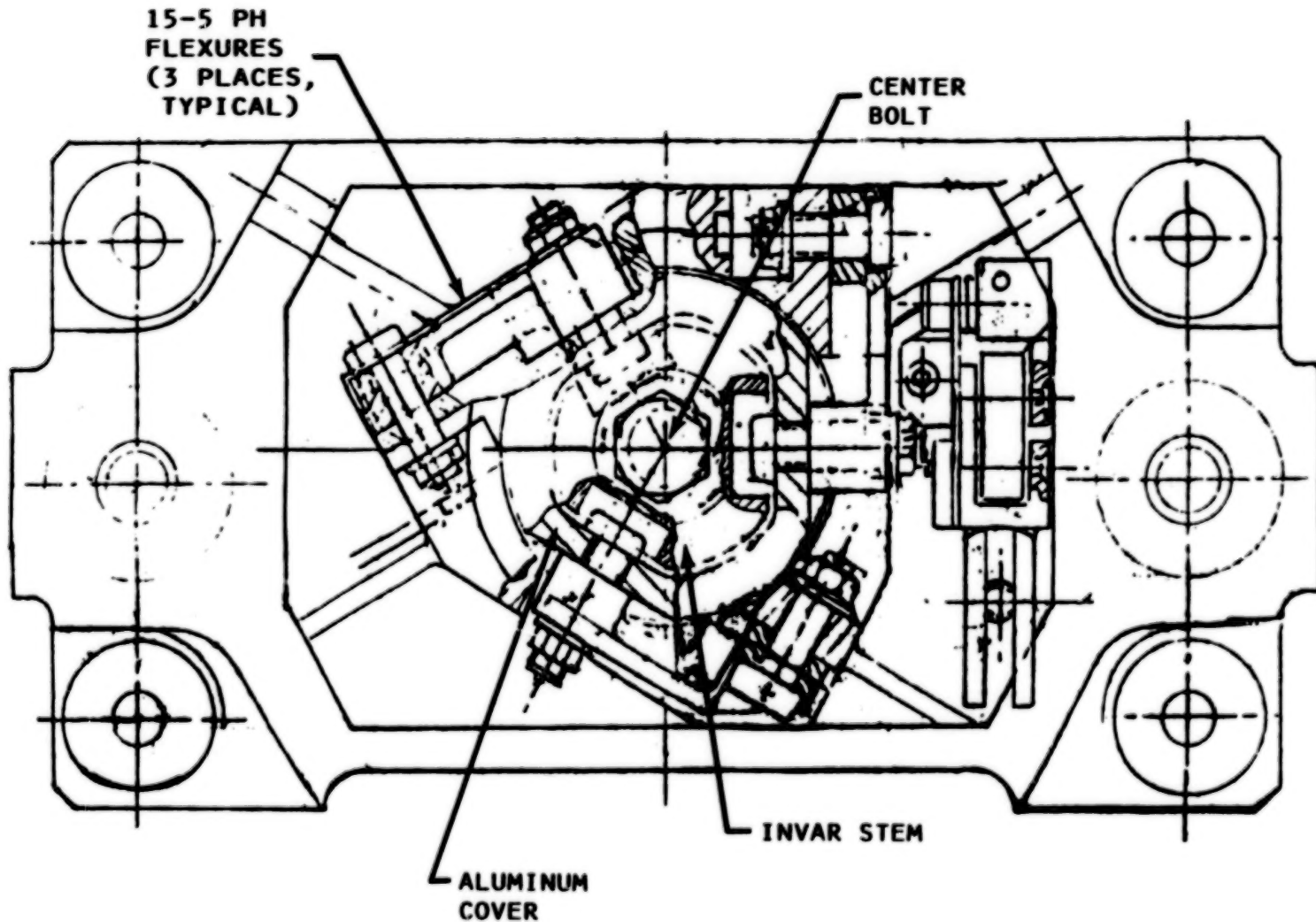


Figure 7. Bottom View, Radial SI and FGS Point A, FPS Half

Blank Page

ABSTRACT

THE DESIGN AND DEVELOPMENT OF A MOUNTING AND JETTISON ASSEMBLY FOR THE SHUTTLE ORBITER ADVANCED GIMBAL SYSTEM

BY

**Edward S. Korzeniowski
SPERRY FLIGHT SYSTEMS
Phoenix, Arizona**

This paper describes the requirements, design, development, and qualification of the mounting and jettison assembly (MJA) which serves as the base structure for the advanced gimbal system (AGS) developed for NASA, Marshall Space Flight Center, for use during shuttle missions.

An engineering model of the MJA has been built and subjected to the following testing: stiffness and modal characterization, sine and random vibration, and a jettison function and energy release. A qualitative summary of the results and the problems encountered during testing, together with the design solutions, is presented.

ADVANCED GIMBAL SYSTEM – OVERALL DESCRIPTION

The AGS is a three-axis pointing system that will be used to point experimental payloads (e.g., a telescope) ranging in mass from 500 to 7200 kg that could span one shuttle pallet or the entire cargo bay. Fig. 1 is a drawing of the AGS flight design. The AGS is shown in Fig 2 in a payload pointing mode, mounted on a shuttle spacelab pallet, and in the launch/landing configuration in Fig. 3.

The mechanical system is composed of a payload mounting structure (PMS), three gimbals, and a MJA. The PMS is a 12.7 cm (5-inch) thick, 2-meter (78.7-inch) diameter honeycomb structure that provides the payload mechanical interface as well as thermal isolation of the payload. Three-axis pointing capability to within $\pm 1/2$ arcsec is provided by the three gimbals (brushless dc torque motors): an elevation and lateral gimbal (each 34 N-m (25 ft-lb)) and a roll gimbal (13.6 N-m (10 ft-lb)). This paper focuses on the MJA that forms the base structure for the AGS. Its main functions are to provide launch/landing load decoupling and jettison capabilities.

MJA REQUIREMENTS

The fundamental MJA requirements are to provide: 1) stiffness for pointing performance, 2) redundant jettison system, and 3) launch/landing load decoupling (separation mechanism). The MJA has been designed to meet these requirements under the following constraints:

- Weight: <75 kg (165 lb)
- Size: 43 cm (17-inch) dia; 41 cm (16-inch) long
- Stiffness: Meet system pointing performance requirements
- Jettison Energy Release to Payload: Minimize
- Operating Life: Fifty missions of 9 days duration each
- Vibration: Shuttle launch environment
- Thermal: Shuttle thermal environment
- Load Decoupling: Protect the AGS gimbals during launch and landing
- Alignment: Maintain initial alignment to within ± 15 arcmin

BLANK

PAGE

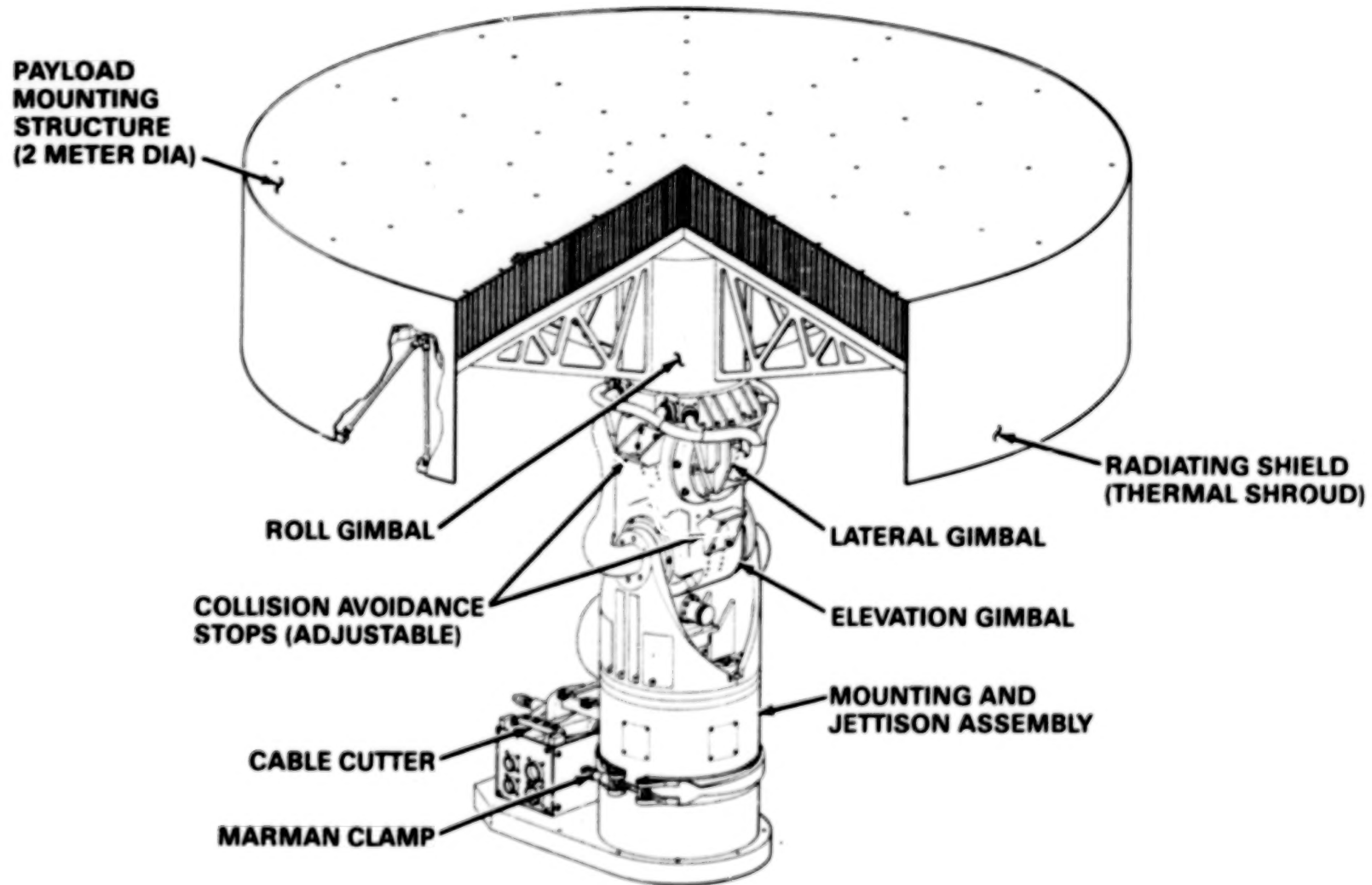


Fig. 1 Advanced Gimbal System Flight Design

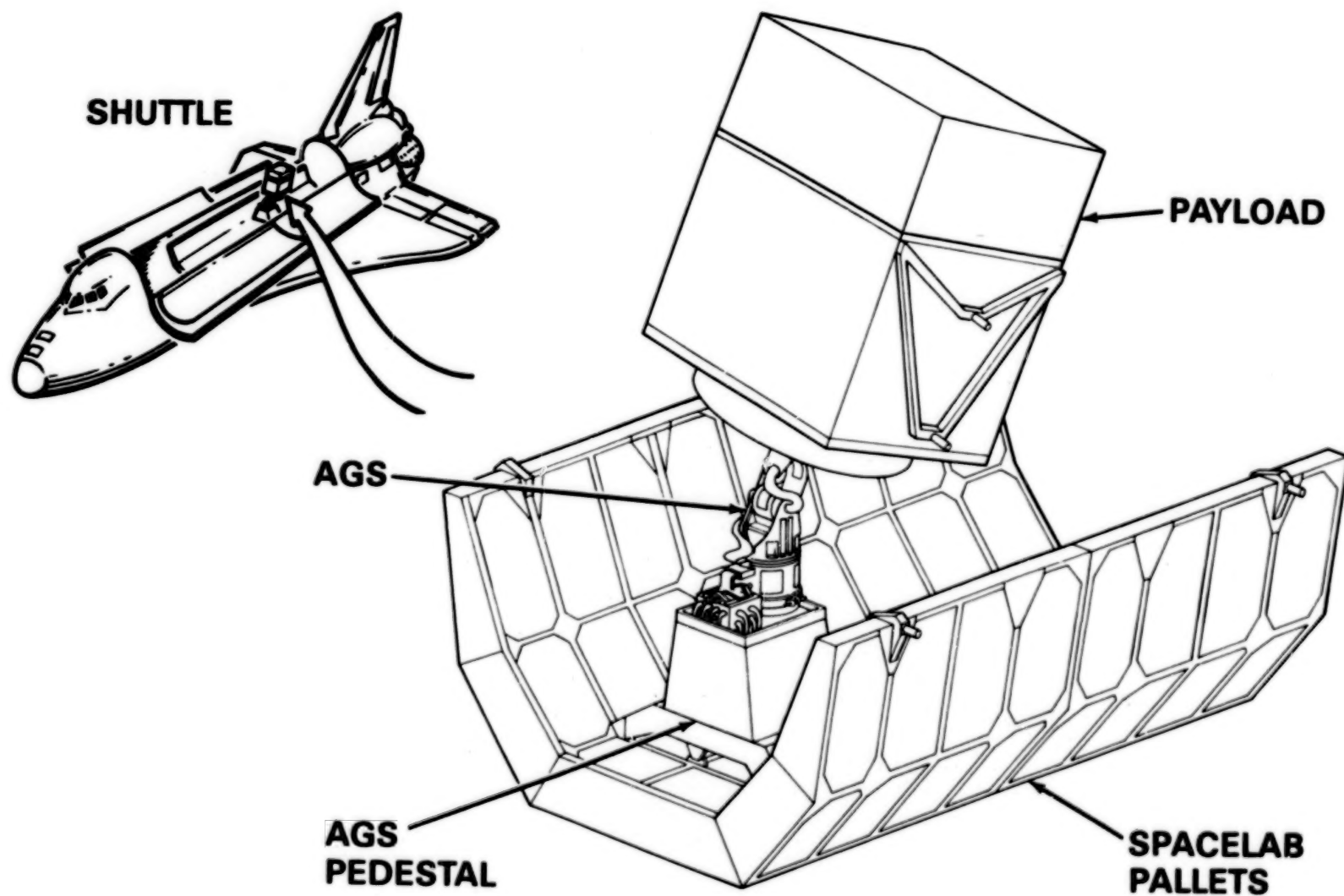


Fig. 2 AGS – Payload Pointing

271

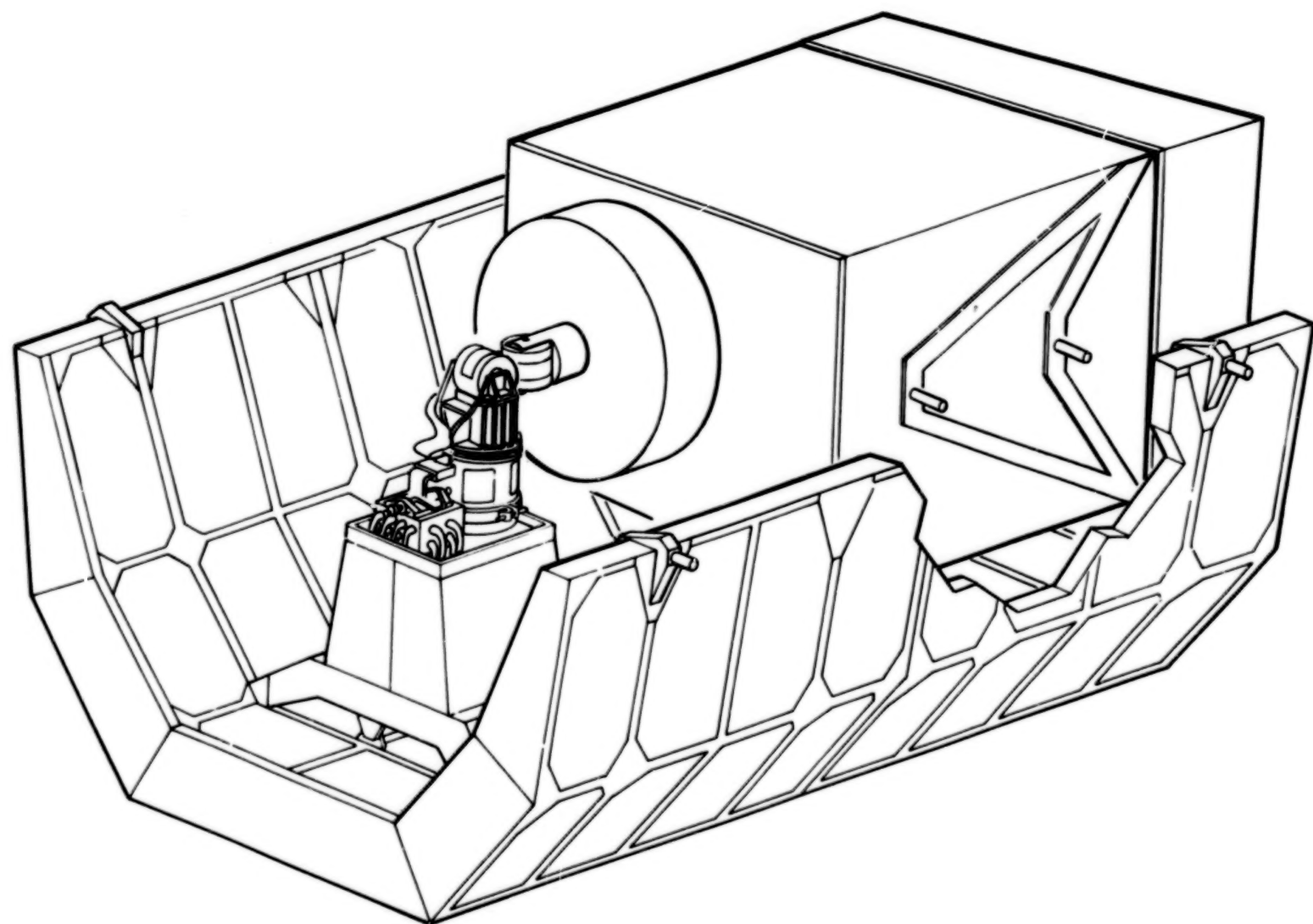


Fig. 3 Payload Caged for Launch or Landing

271

BEST AVAILABLE COPY

ENGINEERING MODEL MJA OVERALL DESCRIPTION

The MJA contains both the separation mechanism and jettison system. The engineering model AGS is shown in Fig. 4; Fig. 5 is a cutaway view of the engineering model MJA. The actual launch and landing separation (3 cm nominal) is provided by the separation mechanism which has the following components: linear actuator, pull down rods, catch plate, and spring seat assemblies, which are primarily located in the upper half of the MJA. Separation occurs between the MJA and gimbal flanges. Launch/landing gimbal constraint is provided by the cantilever beam. The jettison system is pyrotechnically activated and is located in the lower half of the MJA. Its main function is to completely sever all physical ties to the shuttle. Jettison system components (Fig. 6) are jettison clamp, bolt extractor, separation nut, cable cutter, and the jettison interface (curvic coupling).

ENGINEERING MODEL JETTISON SYSTEM DESCRIPTION

The AGS is a two failure tolerant system. As such, the jettison system is a last resort safety backup to be used in the event that the payload cannot be restowed for re-entry. During a jettison sequence, the first action would be to cut the AGS electrical harness. Once microswitch confirmation has been received that the harness has been cut, the jettison interface preload would be released. The shuttle would then back away from the payload. A minimum energy transfer requirement is critical since the AGS can be in any pointing orientation when failure occurs. Any payload c.g. offset will result in payload tumbling when jettisoned, the degree of which is dependent on the amount of energy transferred.

The most desirable jettison operation would completely cut all physical ties and transfer zero energy to the jettisoned payload so that jettison is controlled and the shuttle can simply back away. This condition is very hard to meet in actual practice since there is always some recoverable strain energy associated with the sudden release of the preload at the jettison interface. Every effort has been made to minimize the energy transferred to the jettisoned payload.

Electrically activated pyrotechnic devices are used in the jettison system to attain reliable rapid release. Dual NSI-1 initiated pyrotechnic devices manufactured by Space Ordnance Systems are used in the engineering model jettison system. Three clamp/nut separator devices along with bolt extractors provide the required preload across the curvic coupling (jettison interface) and two cable cutters are used to sever the AGS electrical harness. (See Figs. 5 and 6.)

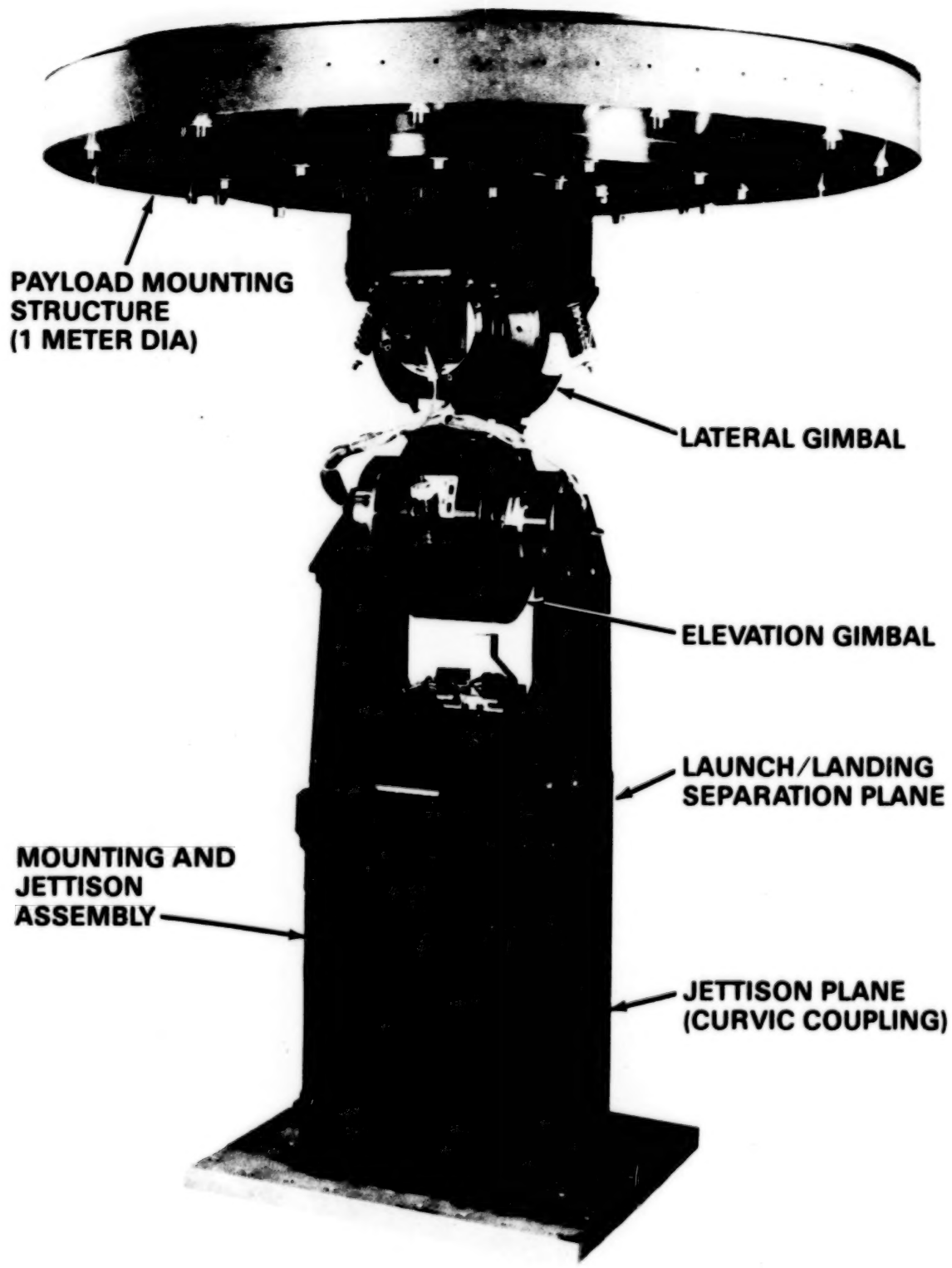


Fig. 4 Advanced Gimbal System – Engineering Model (No Roll Gimbal)

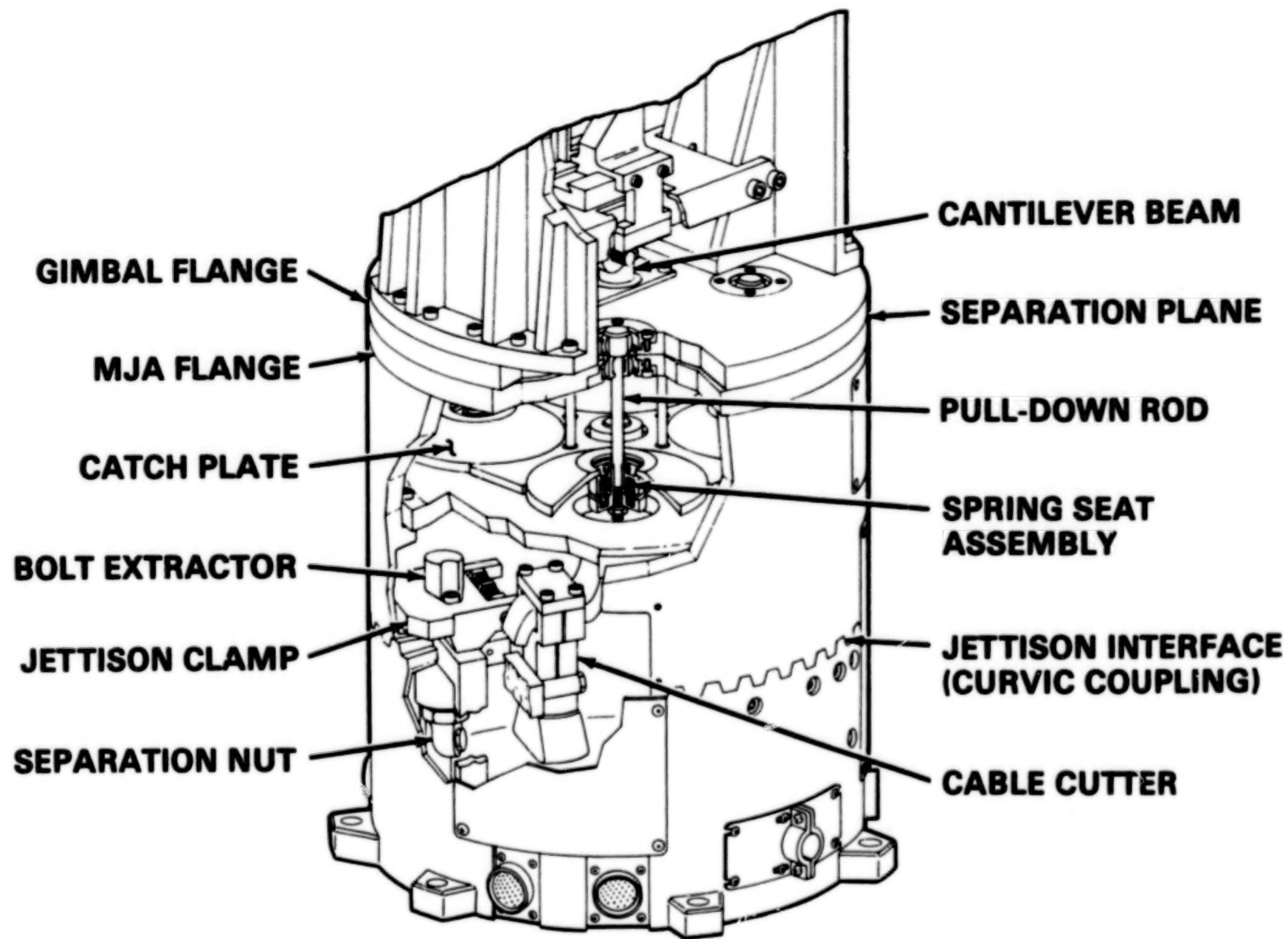


Fig. 5 Engineering Model MJA Cutaway

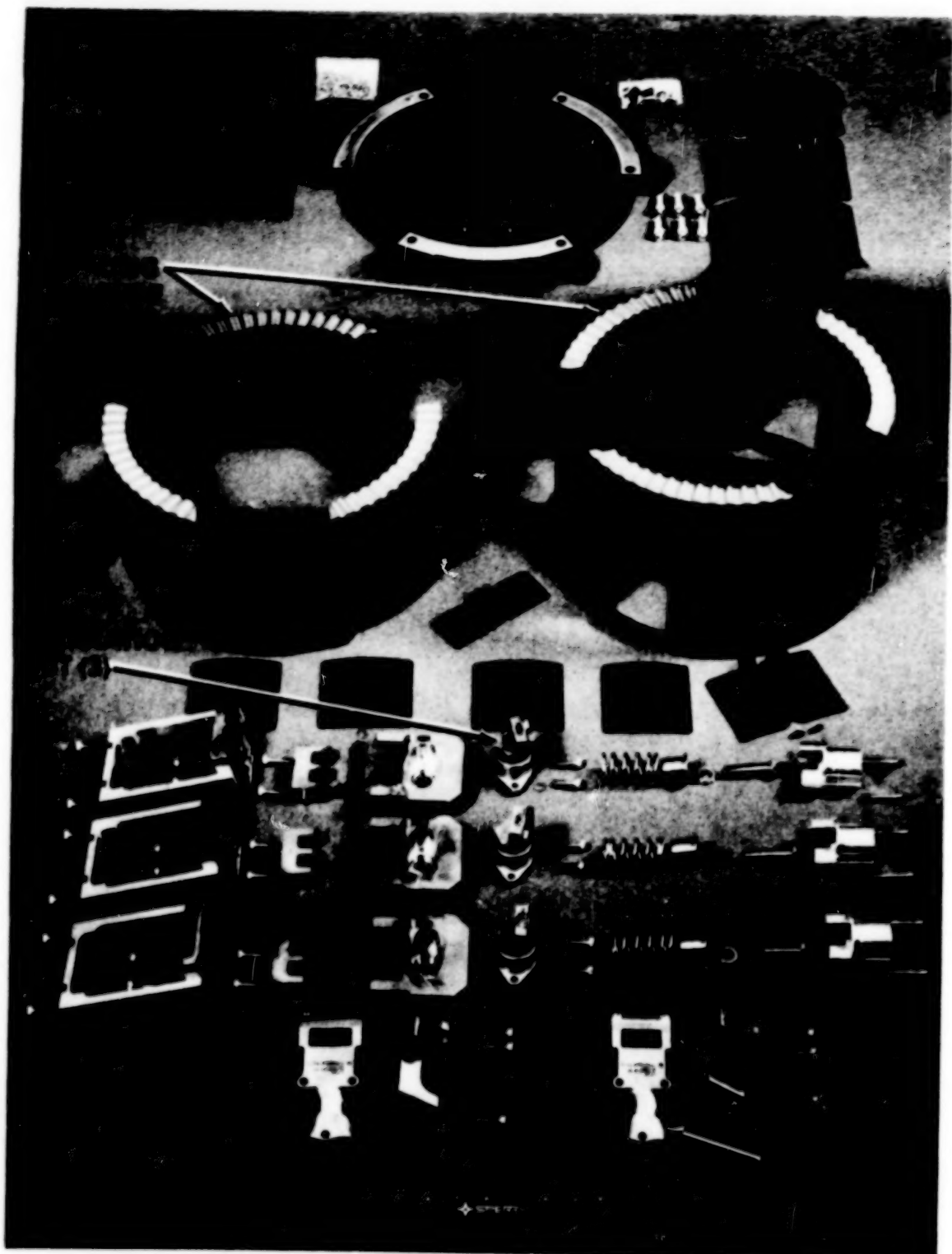


Fig. 6 Engineering Model Jettison System Components

Torsional stiffness at the jettison interface was a design driver. A curvic coupling, which is widely used between turbine rotors to transmit high torques, was selected as the jettison interface. The stiffness requirements are met using this interface as proven by extensive testing.

JETTISON SYSTEM DEVELOPMENT PROBLEMS AND SOLUTIONS

Two problems arose during the jettison development program prior to the full up jettison test. The first involved the separation nut bolt ejection mechanism. For the clamp/separation nut mechanism to open properly, the preload bolts (9.5 mm (3/8 inch) dia) had to be ejected from the clamp to allow the clamps to rotate open. The original design relied on a built in bolt ejector pin and a bolt catcher to get the bolt out of the way. Repeated testing showed that the ejector pin was not ejecting the bolt fast enough for it to clear the clamp and the clamp partially rotated open with the bolt jammed. A spring loaded bolt extraction device was designed to replace the bolt catcher and the full up jettison test of the revised design was successful.

The second problem involved electrical harness growth. The electrical harness diameter grew during the engineering model development program to a point where both cable cutters were completely filled with no growth potential. This problem was corrected by using a single large cable cutter in the flight design.

ENGINEERING MODEL JETTISON TEST

A jettison test was performed on the engineering model MJA in April 1980. The jettisoned portion of the MJA was horizontally suspended at four points using 4 meter (13-foot) lengths of 3 mm (1/8-inch) dia bead chain, and the stationary portion was fixtured to ground. (See Fig. 7 for test setup.) The jettisoned portion was then meticulously aligned so that the bead chain would not load the interface (i.e., cause the jettisoned portion to fall away or be pulled away during the test). Hycam 5000 frame per second movie cameras and photographic targets along with stadia wires were used to record the jettison velocity for the first 1.25 cm of travel. Engineering model jettison velocity was .26 m/sec for a jettison mass of 9.4 kg which is a 0.31 N-m (0.23 ft-lb) energy release.

PROTOFLIGHT JETTISON SYSTEM DESIGN CHANGES

A change in customer requirements to include mechanical as well as electrical jettison redundancy resulted in a design change for flight. The three clamp/nut separators were replaced with a Marman clamp and two pyrotechnic clamp separators positioned 180 degrees apart. (See Fig. 8.) The design is such that the activation of either clamp separator is sufficient to physically disconnect the jettison interface. A single large cable cutter was incorporated into the design to handle the flight harness and allow for future growth.

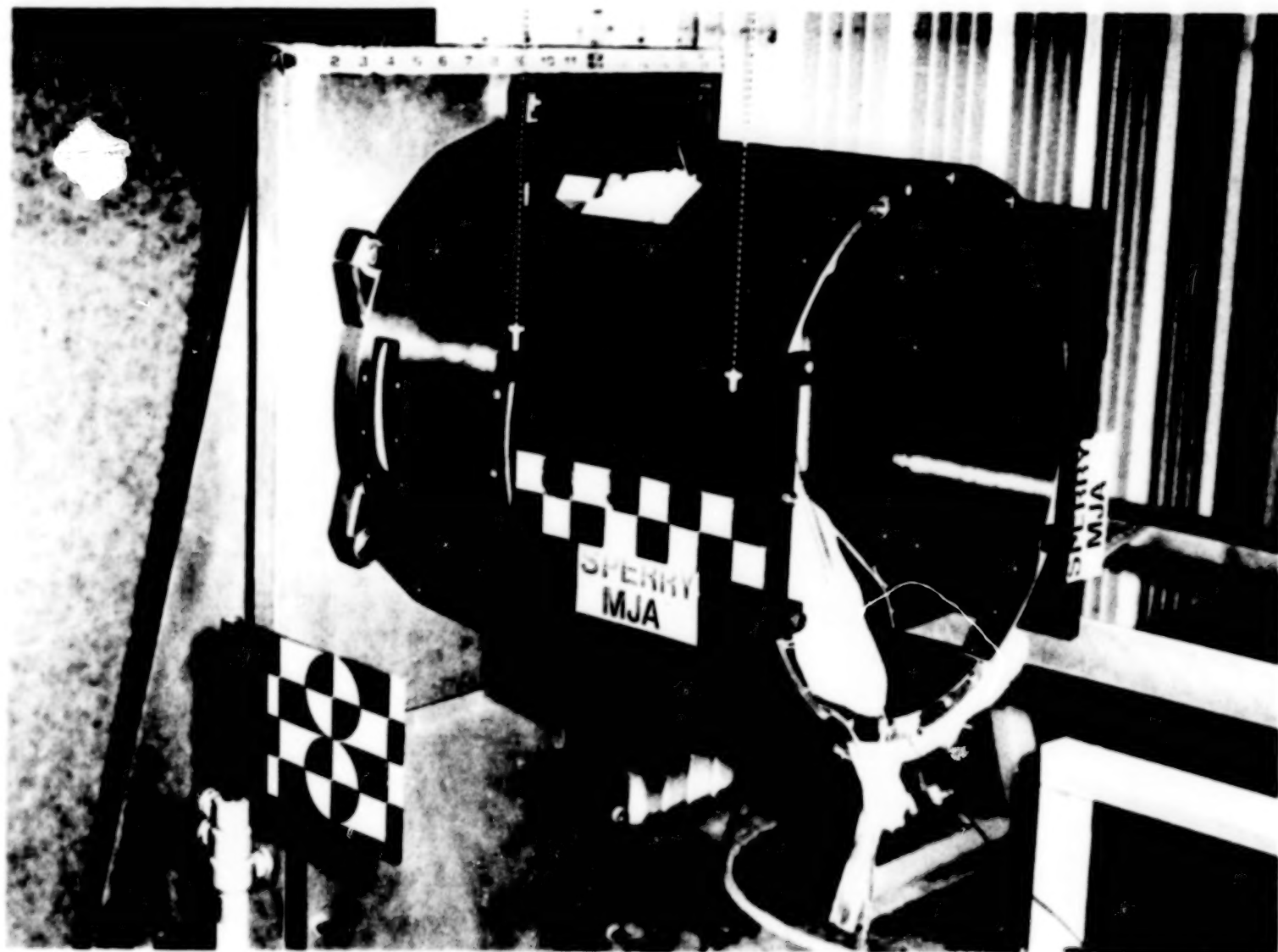


Fig. 7 Engineering Model – Jettison Test Setup

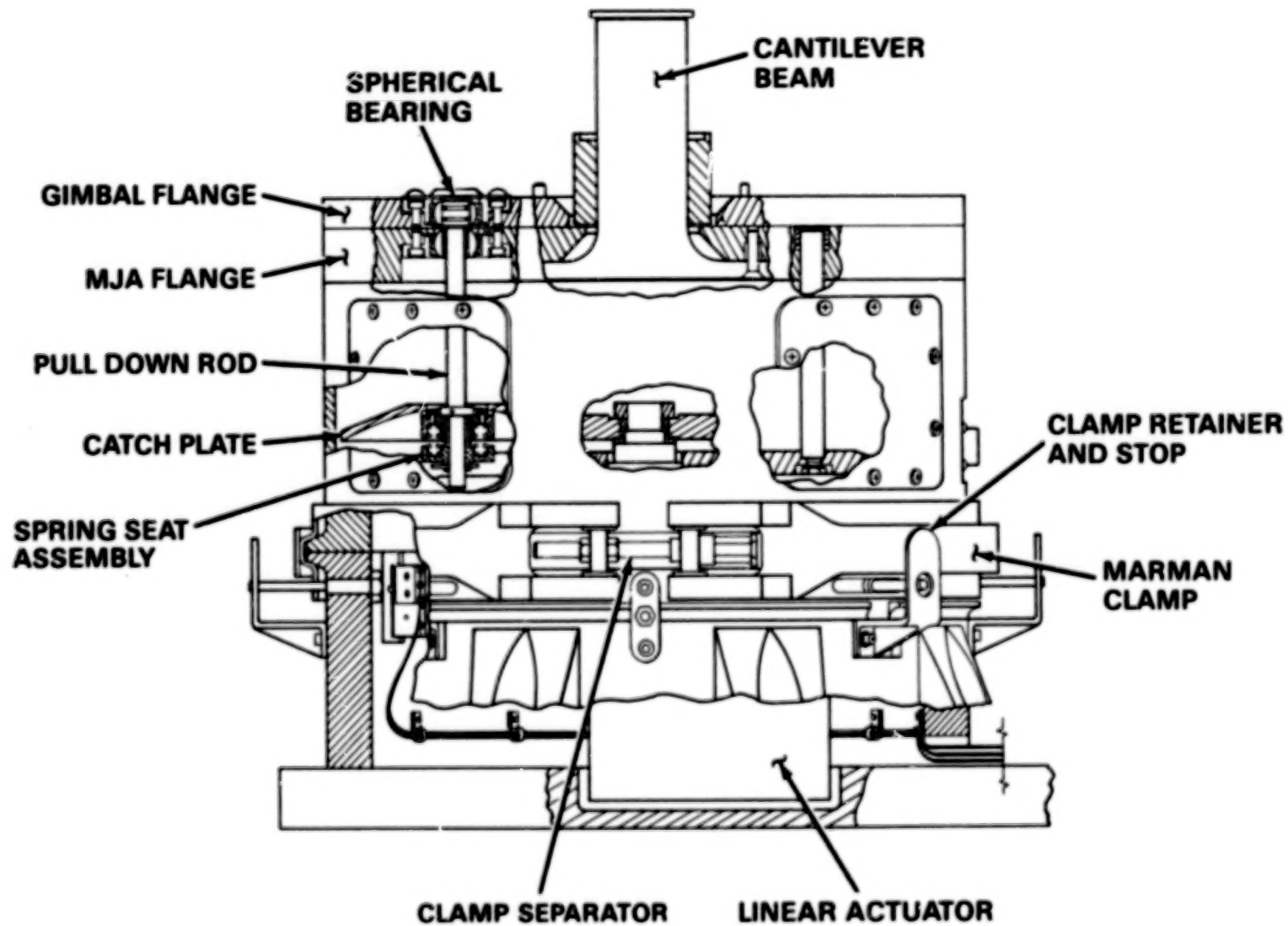


Fig. 8 MJA Flight Design

BLANK

PAGE

The engineering model MJA was modified to simulate the flight configuration, and the jettison test was repeated with a jettison energy release of 0.01 N-m which is considerably lower than the engineering model design. The reduction is due to the slower way in which the Marman clamp releases the interface. The Marman clamp retainer bands (Fig. 8) move radially away from the MJA tube and slide along the MJA tube flanges thereby absorbing some of the released energy.

SEPARATION MECHANISM DESCRIPTION

The AGS payload is secured to the Spacelab pallet with a system of clamps and struts which attach to pallet hard points. The MJA is also attached to pallet hard points through its own separate support structure. (See Fig. 3.) As such, the resultant AGS/payload/pallet assembly constitutes a statically indeterminate structure with the AGS gimbal bearings in the primary load path. The AGS separation mechanism provides a means of decoupling the AGS gimbals during launch and landing to relieve these static loads and to control dynamic loads that are applied to the AGS caused by gravitational, quasi-static acceleration, vibration, and thermal effects. Decoupling is accomplished by the separation mechanism in conjunction with the cantilever beam mechanism which partially constrains the AGS gimbals. The cantilever beam is sized to ensure that the allowable gimbal bearing loads are not exceeded and that minimum launch/landing structural frequency (35 Hz) is maintained across the separation mechanism. During launch and landing, the separation mechanism linear actuator is extended and the gimbal and MJA flanges are separated a nominal 3 cm.

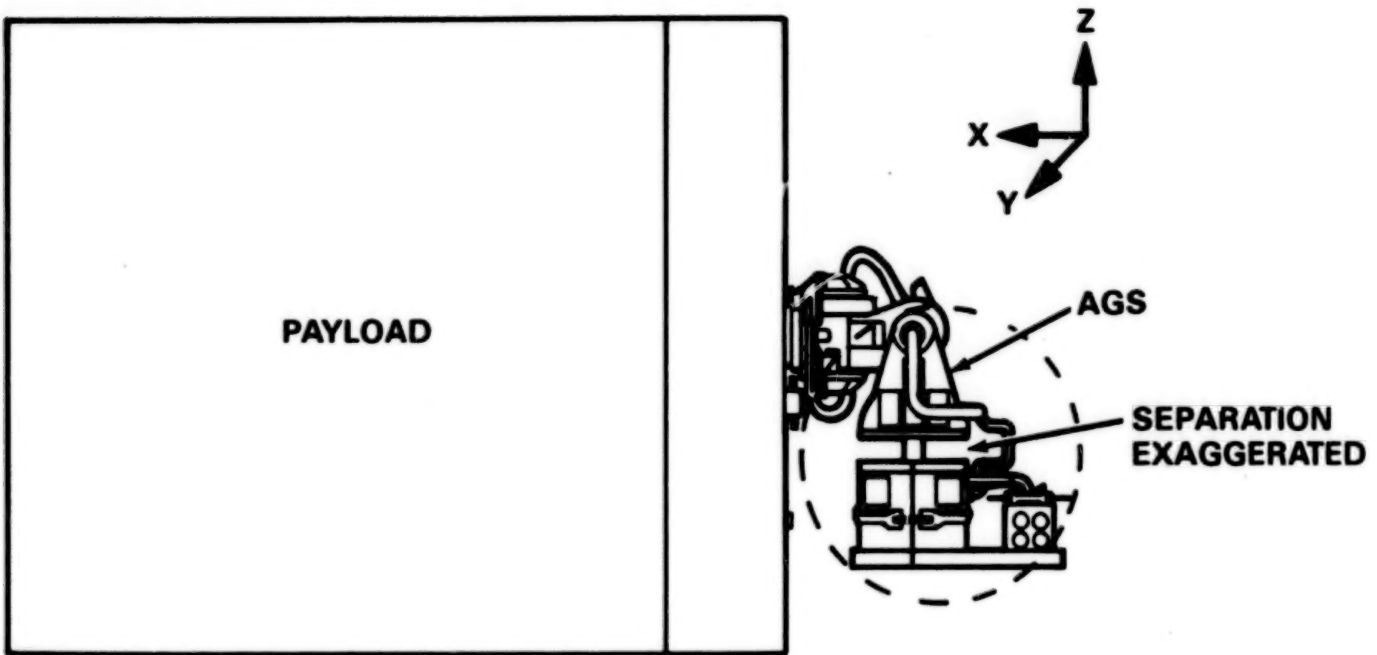
Fig. 9 shows the overall separation mechanism operation. If the base of the MJA is considered to be fixed, translations of the payload are accommodated by the cantilever beam mechanism as follows:

Z-Axis: Translation of the gimbal flange relative to the cantilever

X-Axis: Rotation of the spherical bearing relative to the gimbal flange

Y-Axis: Rotation of the spherical bearing about the cantilever beam

Rotations of the payload about the X, Y or Z axes are accommodated by combinations of the above motions plus rotations about the AGS gimbals. (Note: The gimbals are free to rotate during launch and landing.)



Y-Axis Payload Translation Accommodation by Rotation of the Spherical Bearing About the Cantilever and Tipping of the Gimbal Flange

Fig. 9 AGS Separation Mechanism Operation

BLANK

PAGE

The AGS separation mechanism is made up of a linear actuator, pull down rods, spherical bearings, catch plate, spring seat assemblies, two flanges, and a gimbal launch/landing constraint device (cantilever). (See Figs. 8 and 11.) Functions of these components are as follows:

- Linear Actuator - The linear actuator's main function is to provide the joining force (set at 600 lb) to maintain a preload across the two plates (MJA and gimbal flanges) to provide structural rigidity for pointing. The linear actuator is a 28 volt dc redundant ball screw actuator made by Sperry Electro Components in North Carolina and has a stroke of approximately 6.4 cm (2.5 inches).
- Pull Down Rods - The pull down rods are fixed to the gimbal flange in spherical bearings and pass through similar spherical bearings in the MJA flange. The spring seat assemblies are fixed to their lower ends.
- Catch Plate - The catch plate is fixed to the end of the linear actuator shaft and transmits the actuator joining force to the pull down rods by pushing on the spring seat assemblies.
- Spring Seat Assemblies - The spring seat assemblies are fixed to the lower end of the pull down rods and are made up of two nested springs in a spring cup assembly. Adjustment capability is provided to set preload. The catch plate impacts the integral rulon on the spring seat assembly surface that compresses the springs to provide the precalibrated preload. This spring preload arrangement allows for variation due to thermal growth and assembly tolerance stack up and also allows for a reduction in the actuator microswitch stop setting tolerances.
- Flanges (MJA and gimbal) - The launch/landing separation occurs between these two plates. The gimbal flange provides the top anchor point for the pull down rods, and the MJA flange provides spherical bearing guides and an alignment mechanism to realign the two flanges during the joining sequence.
- Cantilever - A 1.9 cm (3/4 inch) diameter cantilever serves to restrain the gimbals during launch/landing. It is fixed to the MJA flange and rides in a spherical bearing fixed in the gimbal flange that serves to prevent relative planar translation between the two flanges. The spherical bearing is also constrained by pins and roller bearings so that rotation about the X-axis is constrained and rotation about the Y-axis is permitted.

OPERATION

Separation for Launch/Landing

The engineering model AGS in the launch/landing configuration is shown in Fig. 10. The linear actuator is extended and positions the catch plate in the full extend position (6.4 cm (2.5 inch) of travel). This allows the two flanges to be separated by the payload clamp system so that the MJA side of the separation mechanism can be displaced relative to the gimbal side within a 6 cm sphere about the 3 cm nominal position. This relative motion is accommodated by rotations about the AGS gimbals and a tipping about the Y-axis of the gimbal flange relative to the MJA flange. The cantilever constrains $\pm X$ and $\pm Y$ translation plus rotation about the X-axis while allowing $\pm Z$ translation and rotation about the Y- and Z-axes.

Joining

For joining, the actuator is retracted and pulls on the catch plate. The catch plate makes contact with the spring seat assemblies which realign the two flanges about Z. A precision alignment and torque restraint is provided by an alignment core that guides the alignment about Z (alignment in $\pm X$ and $\pm Y$ is provided by the cantilever) within the last portion of actuator travel. The spring seat assembly nested springs are compressed thereby applying the preload between the flanges.

SEPARATION MECHANISM DEVELOPMENT PROBLEMS AND SOLUTIONS

The biggest change in the design occurred with the addition of an optional roll gimbal (the initial contract called for a two gimbal AGS, elevation and lateral). The roll gimbal added another degree of freedom (rotation about the X-axis) that had to be constrained. As a solution, the cantilever spherical bearing was pinned along the Y-axis and the pins were supported with roller bearings. This allowed the cantilever bearing cartridge design to be variable so that a pinned cartridge assembly could be used in the three gimbal system and an unpinned cartridge assembly could be used in the two gimbal system.

Flatness between the MJA and gimbal flanges reduced stiffness across the interface. The initial design utilized a full contact surface which warped when other components were installed and the preload applied. As a solution, both plates were relieved in their centers which left an outer contact ring approximately 1.5 cm wide. Preload across this interface was also increased from 300 to 600 pounds.

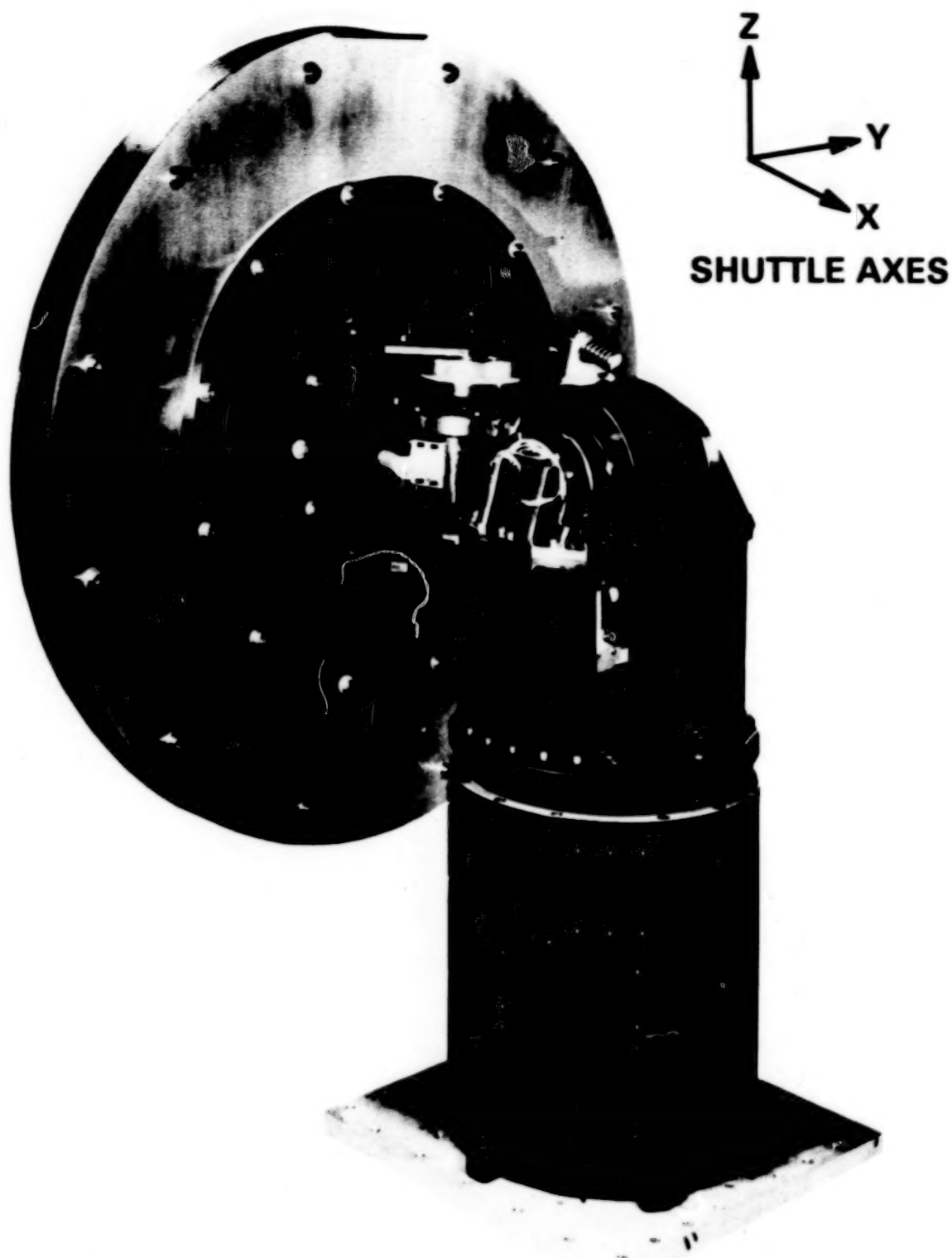


Fig. 10 Engineering Model AGS – Launch/Landing Configuration

284

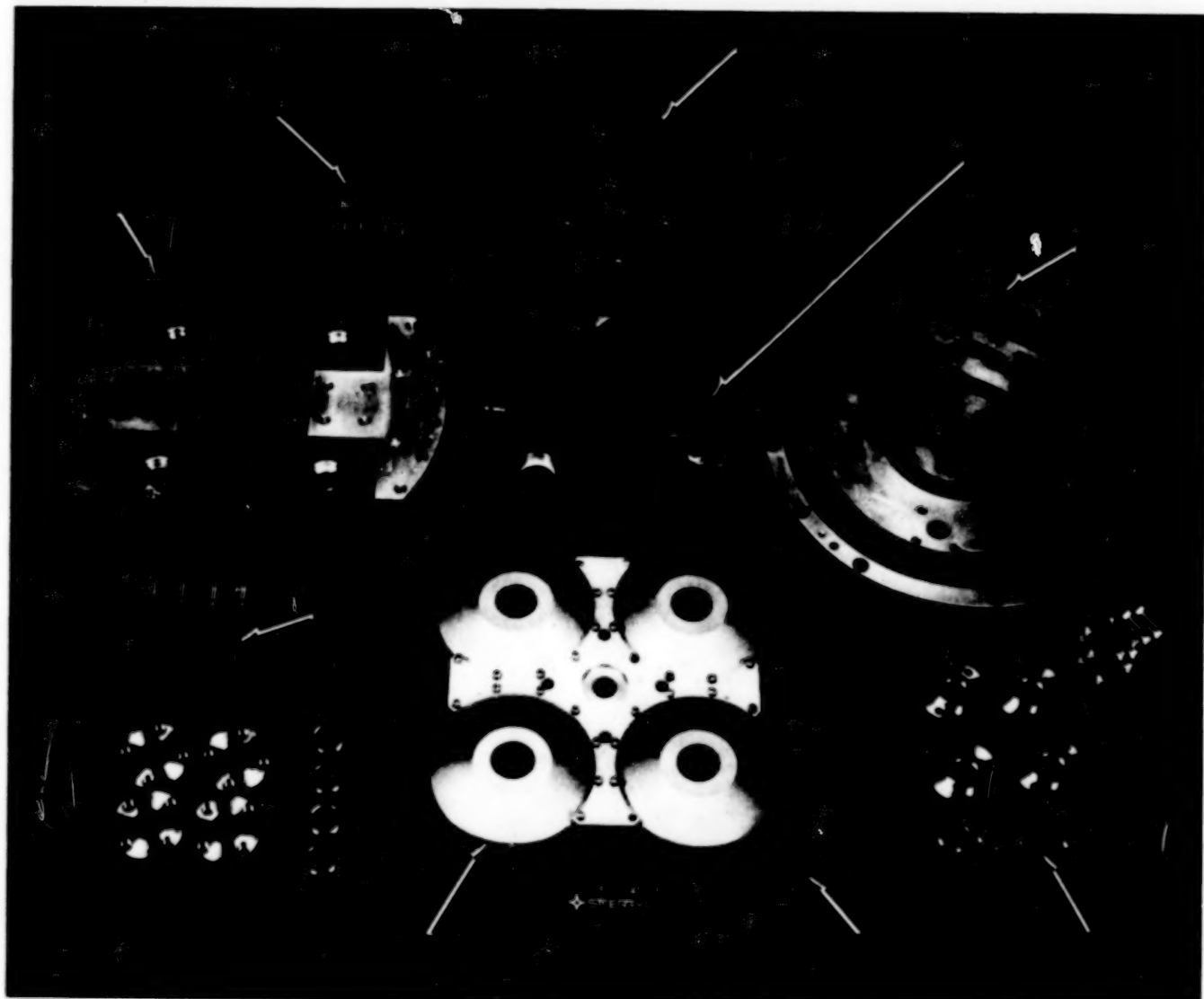


Fig. 11 Separation Mechanism Components

284

BEST AVAILABLE COPY

BLANK

PAGE

PROTOFLIGHT SEPARATION MECHANISM DESIGN CHANGES

The AGS contract was modified for the protoflight design to eliminate the two gimbal version of the AGS. The gimbal bearings were also increased in size to increase stiffness. With this change, the pinned spherical bearing concept was further refined and the cantilever beam was increased in size to 5 cm (2-inch) diameter to increase launch and landing stiffness. The spherical bearing was replaced with a trunnion assembly that was supported in bushings along the Y-axis with a tight running fit for the cantilever in the center.

MJA ENGINEERING MODEL TESTING

The MJA and its components have been subjected to the following testing:

- Subassembly Level:

- Actuator Characterization
- Jettison (See Fig. 7.)

- Assembly Level:

- Separation Mechanism Characterization
- Mode Shape
- Sine and Random Vibration (See Fig. 12.)

The primary problem was encountered during the system flexibility testing. In most analyses, an interface is assumed to be rigid. This is only true if the interface is perfectly flat and there is no misalignment or the interface is preloaded high enough to make up for any inconsistencies. During flexibility testing, many interfaces were discovered where precision machining at the subassembly level significantly increased the overall system stiffness. This knowledge was applied to the protoflight design.

CONCLUSION

The MJA is an innovative design that meets the design requirements for stiffness, alignment, load decoupling, and jettison. During system flexibility and modal testing, it was discovered that mechanical interface characteristics were crucial to ensuring that system stiffness requirements were met. Jettison testing proved the feasibility of designing a system for minimum energy transfer to the jettisoned payload. The vibration testing demonstrated overall mechanical integrity and verified that the separation mechanism/cantilever beam load decoupling does protect the gimbal bearings.

286

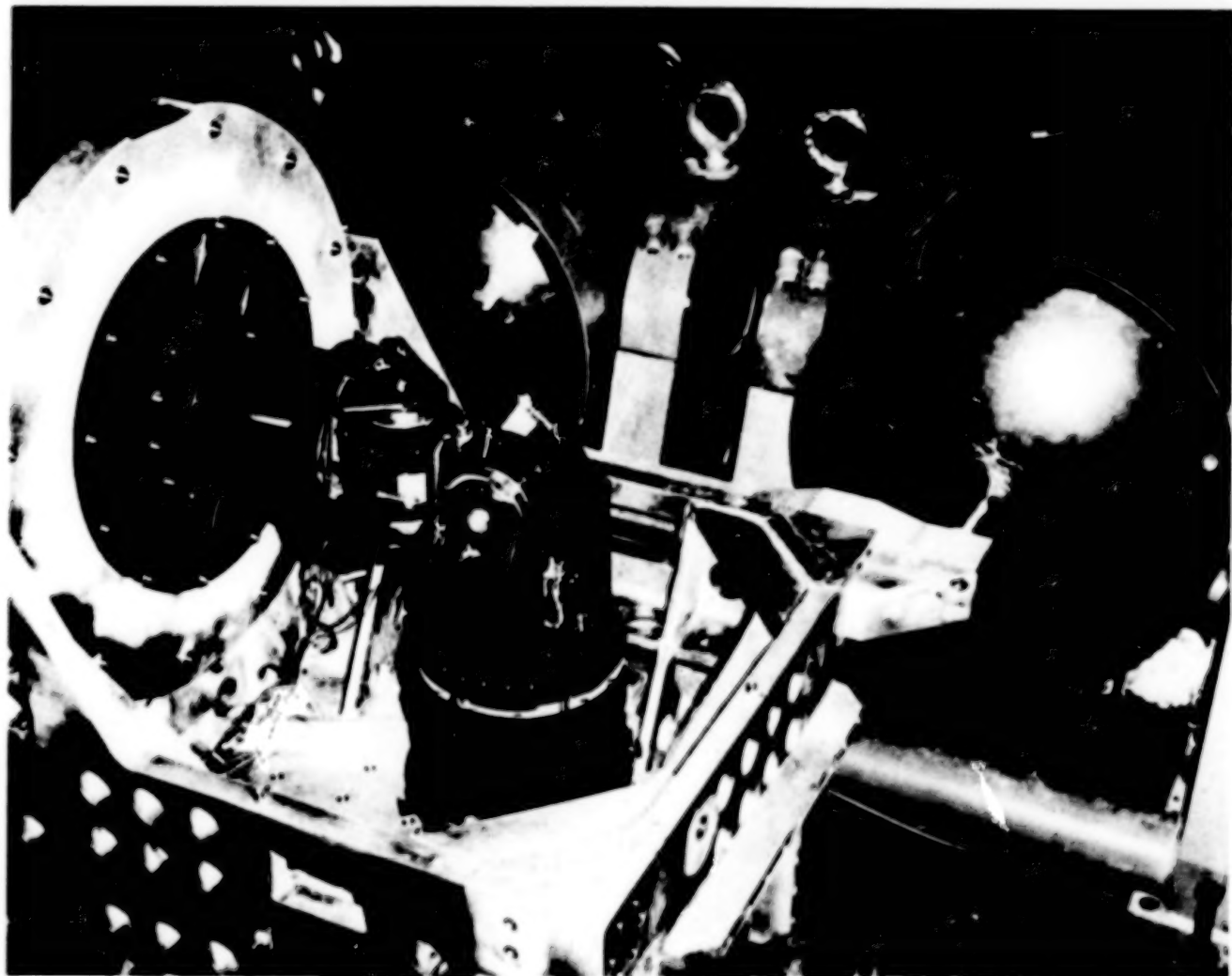


Fig. 12 Y-Axis Vibration Test Setup at Marshall Space Flight Center

ACKNOWLEDGEMENTS

The design and development work presented in this paper was performed under contract with Marshall Space Flight Center, Huntsville, Alabama. The author wishes to thank NASA, Marshall Space Flight Center, and Sperry Flight Systems for their permission to publish this paper and to acknowledge the many engineers, technicians, and designers at Sperry that contributed to this project.

Blank Page

ROLLING BEAM UMBILICAL SYSTEM

By Bemis C. Tatem, Jr.*

ABSTRACT

The decision to make the Centaur vehicle a Space Transportation System (STS) payload meant that new ground support equipment provisions at Launch Pads Pads 39A and 39B were required. These new equipment provisions were needed to service the Centaur vehicle while it was installed in the Orbiter's payload bay prior to launch. This paper describes the design of a new rolling beam umbilical system (RBUS) being added to the pad fixed service structure (FSS) in order to provide the primary functions of liquid hydrogen (LH_2) fill, drain, and vent. The carrier plate itself is a Government-furnished equipment item and of necessity became a T-0 disconnect. This permits quick offloading in the event of an abort prior to lift-off. In addition to the rolling beam structure, mechanisms, and fluid lines, it was necessary to design and build a carrier plate simulator to support early development testing of the mast at the Launch Equipment Test Facility at Kennedy Space Center.

The RBUS is designed to be compatible with the rotating service structure (RSS) to the extent that the umbilical may be deployed with the RSS mated with the vehicle. It is also designed to clear the RSS as the RSS rotates back out of the way. Accessibility to the Orbiter aft compartment via the 50-1 door had to be maintained.

The RBUS consists of an umbilical assembly that supports the carrier plate on the end of a truss beam extending from a carriage assembly that translates on double rails by means of crane track wheels. A porch structure was added to the FSS to mount the incline portion of the assembly that contains the rails. A suitable storage location on the FSS dictated a 6-degree incline up to the Centaur interface located on the port side of the Orbiter in essentially the same location as the previous T-4 interface on the port side. The rolling beam travels a distance of 11 m (36 ft) to the stowed position in the FSS. Power for acceleration of the rolling beam assembly is provided by a dropweight assembly. A linear disk brake decelerates the rolling beam to its parked or stowed position. Upon initial motion of the carriage, the rolling beam separates itself from the ground supply lines as well as from the vehicle. This was dictated by the long retract distance. This paper presents important design approaches considered but not used, in addition to describing the rolling beam, which is in the process of being implemented.

This RBUS was designed by Planning Research Corporation, Systems Services Company under contract to NASA's Kennedy Space Center in Florida.

*Bemis C. Tatem, Jr., Planning Research Corporation, Kennedy Space Center, Florida

INTRODUCTION

In early 1981, an extensive trade study was conducted to determine the best approach to take to provide for the STS/Centaur LH₂ servicing requirements. Numerous concepts were prepared, and the ones considered most promising are:

- a. Tail service mast (TSM) with Centaur service added
- b. RBUS
- c. TSM mounted reusable payload umbilical mast
- d. TSM mounted expendable payload umbilical mast

TSM With Centaur Service Added. Necessary additional lines would be added to the existing TSM's carrier plates as depicted in figure 1. Lines would be routed down the service masts as shown in figure 2. An overriding disadvantage of this approach was its adverse effect on Orbiter flight weight for the LH₂ service functions.

RBUS. An elevation view of this approach is shown in figure 3 and is described in more detail in this paper. The overriding advantage of this approach is that it is located on the FSS with no impact on the Vehicle Assembly Building (VAB) or the mobile launcher platform.

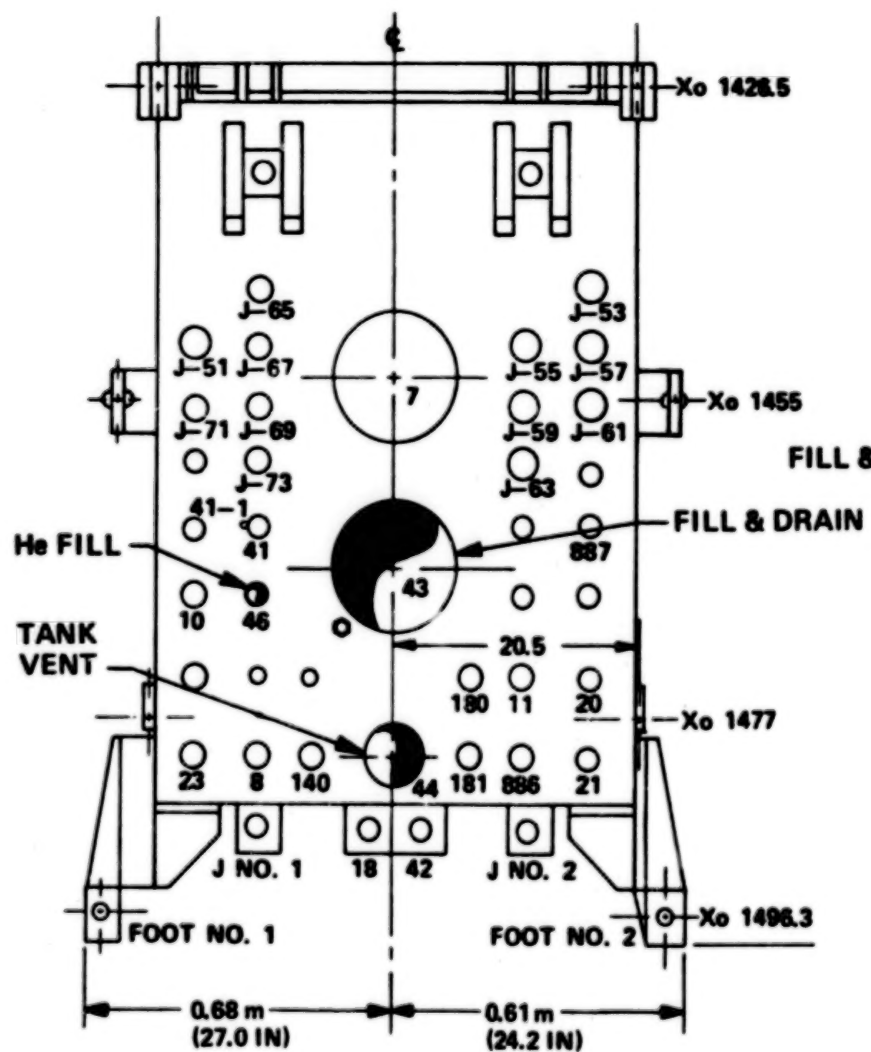
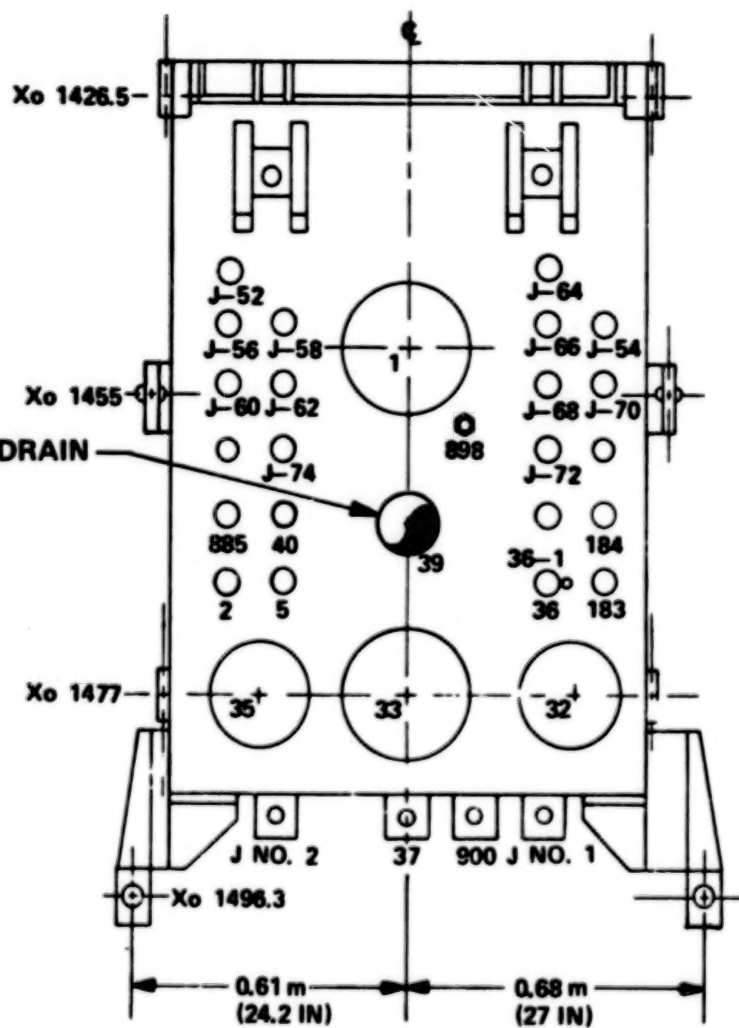
TSM Mounted Reusable Payload Umbilical Mast. An elevation view of this approach is shown in figure 4. This system is similar to a short rolling beam except it retracts into a hardened housing mounted on top of the TSM. The carriage moves on a small track. Dropweight initiation would be by a trigger actuated by the TSM dropweight. The TSM would require structural additions to support the added weight and blast load due to added sail area of the payload umbilical mast. The installation has major impact on VAB platforms as well as the RSS.

TSM Mounted Expendable Payload Umbilical Mast. The carrier plate support is similar to the rolling beam, but a rotating mast with counterweight is used to retract the carrier plate past the vehicle lift-off drift curve. Lanyards penetrate the top of the TSM and use the TSM dropweights for the normal retraction. This approach is depicted in figure 5. This approach was ruled out because of closeness to the Orbiter wing and impact on the VAB.

The conclusion of these studies was that the RBUS approach was selected to perform the task of providing LH₂ service for the STS/Centaur at Launch Pads 39A and 39B. The design of the prototype RBUS was just completed at the time of submission of this paper. This prototype is to be tested at the Launch Equipment Test Facility this summer.

ROLLING BEAM DESCRIPTION

Major assemblies of the selected RBUS include:

LH₂ CARRIER PLATE**LO₂ CARRIER PLATE**Figure 1. LH₂ and LO₂ Carrier Plates - TS1

292

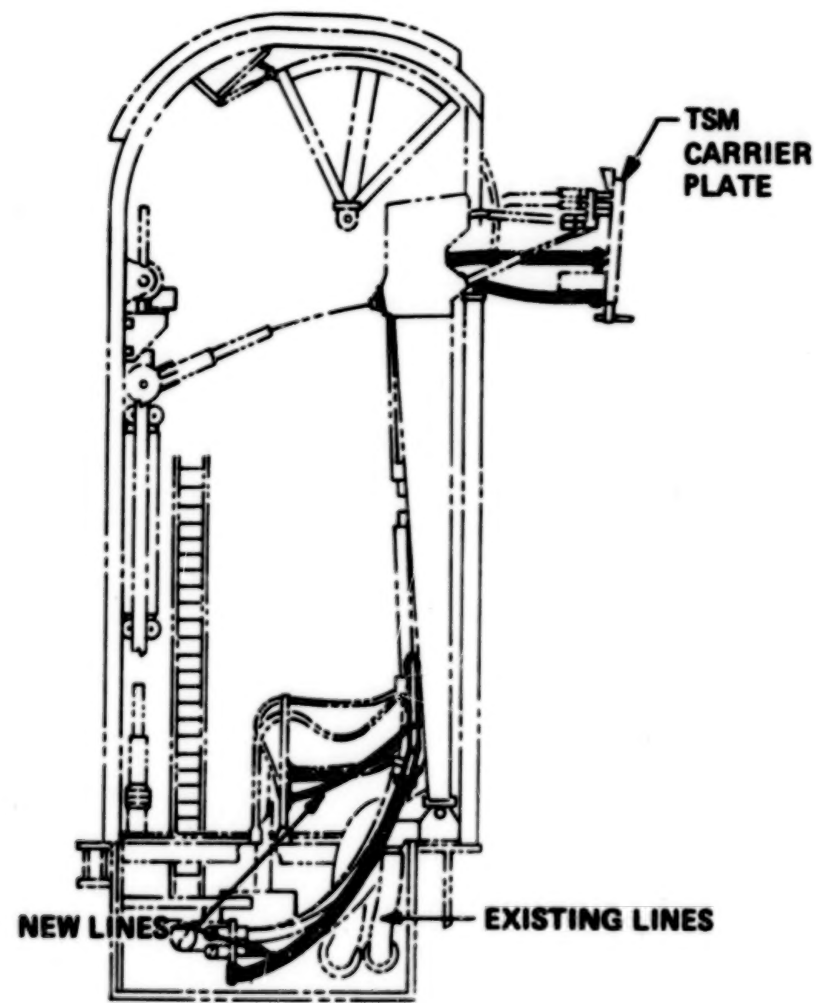


Figure 2. TSM With Centaur Service Added - LH₂

292

BEST AVAILABLE COPY

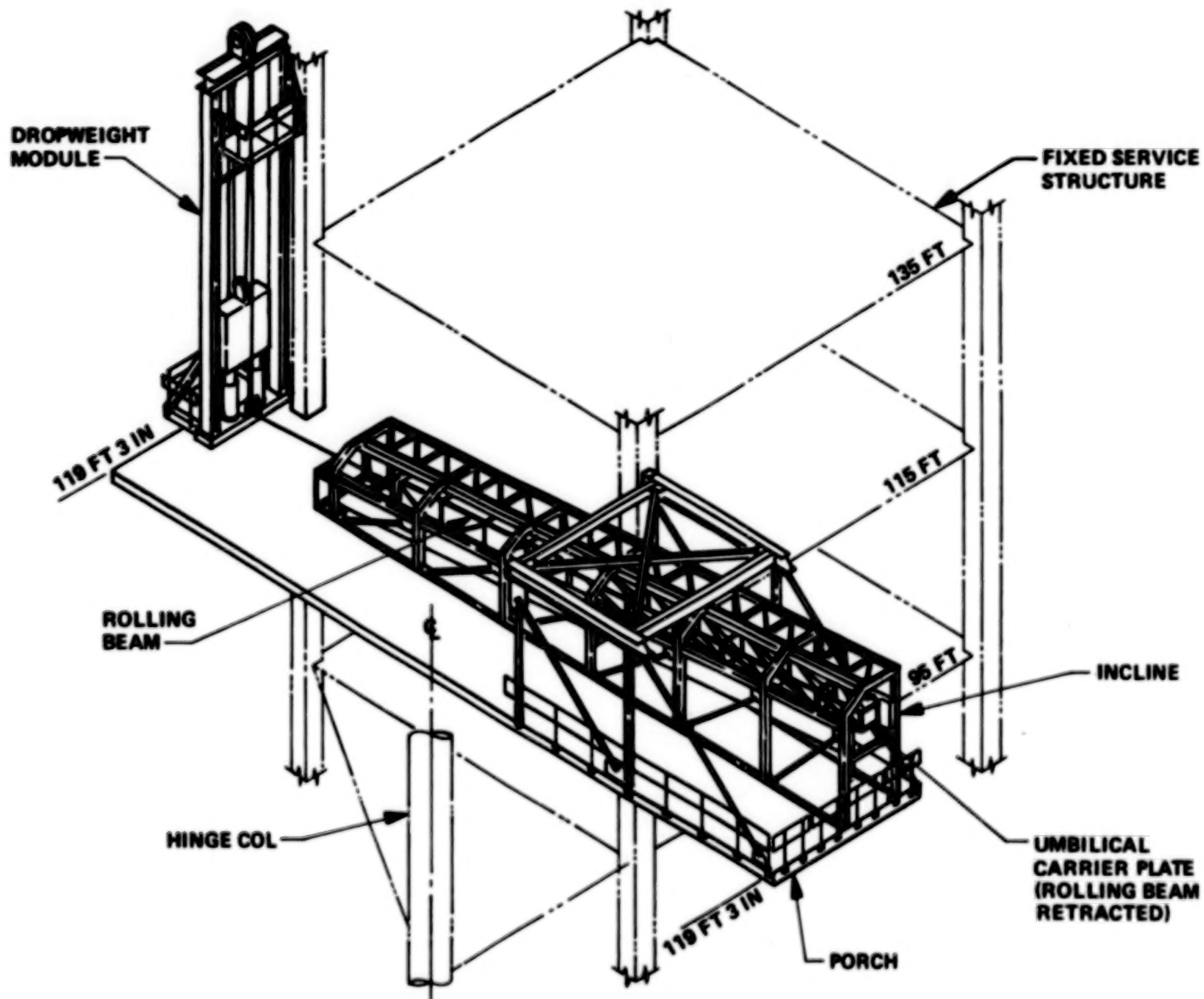


Figure 3. Centaur/STS Rolling Beam Umbilical System-Launch Pad 39A Installation

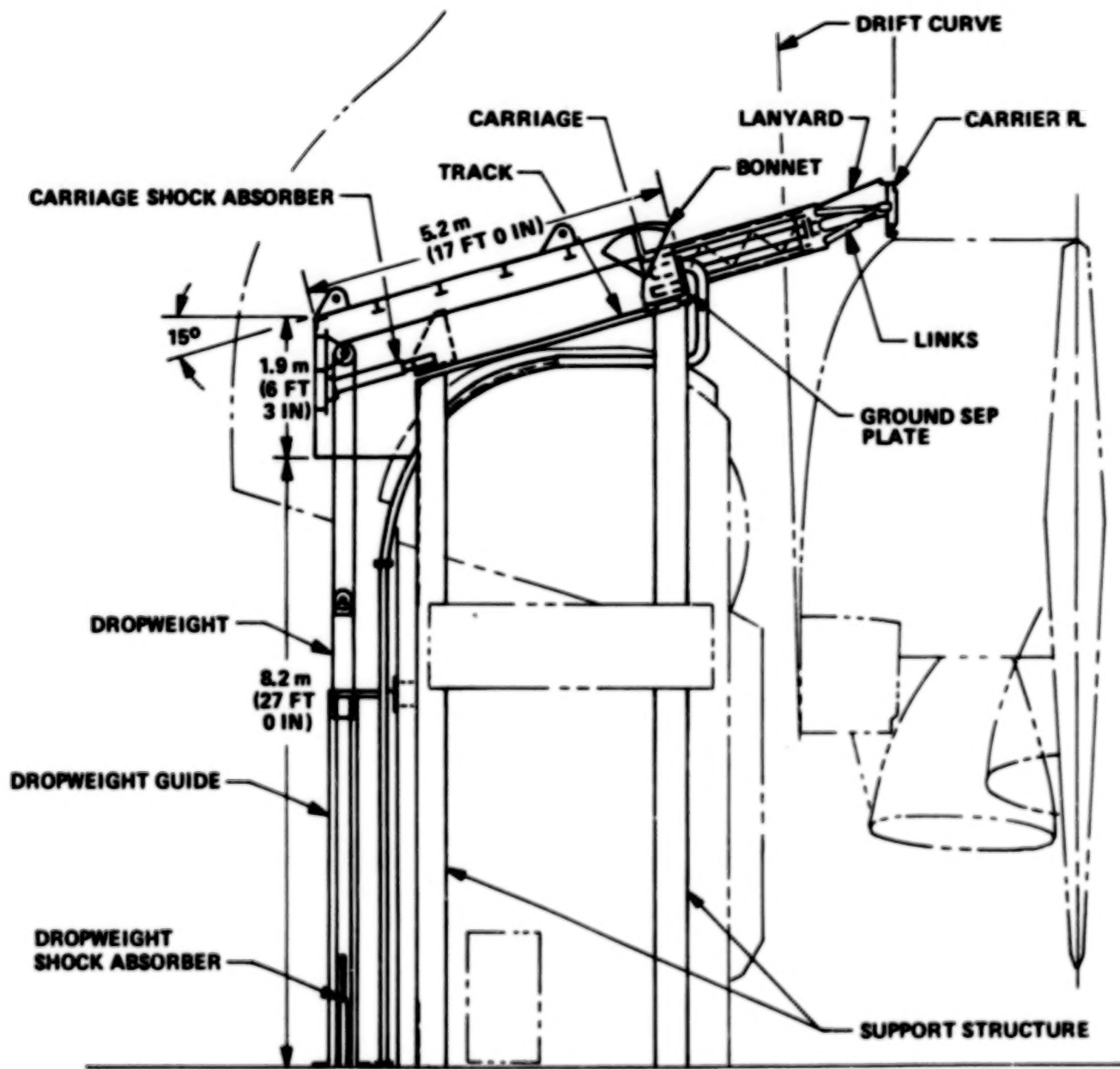


Figure 4. Payload Umbilical Mast - Reusable-Elevation View

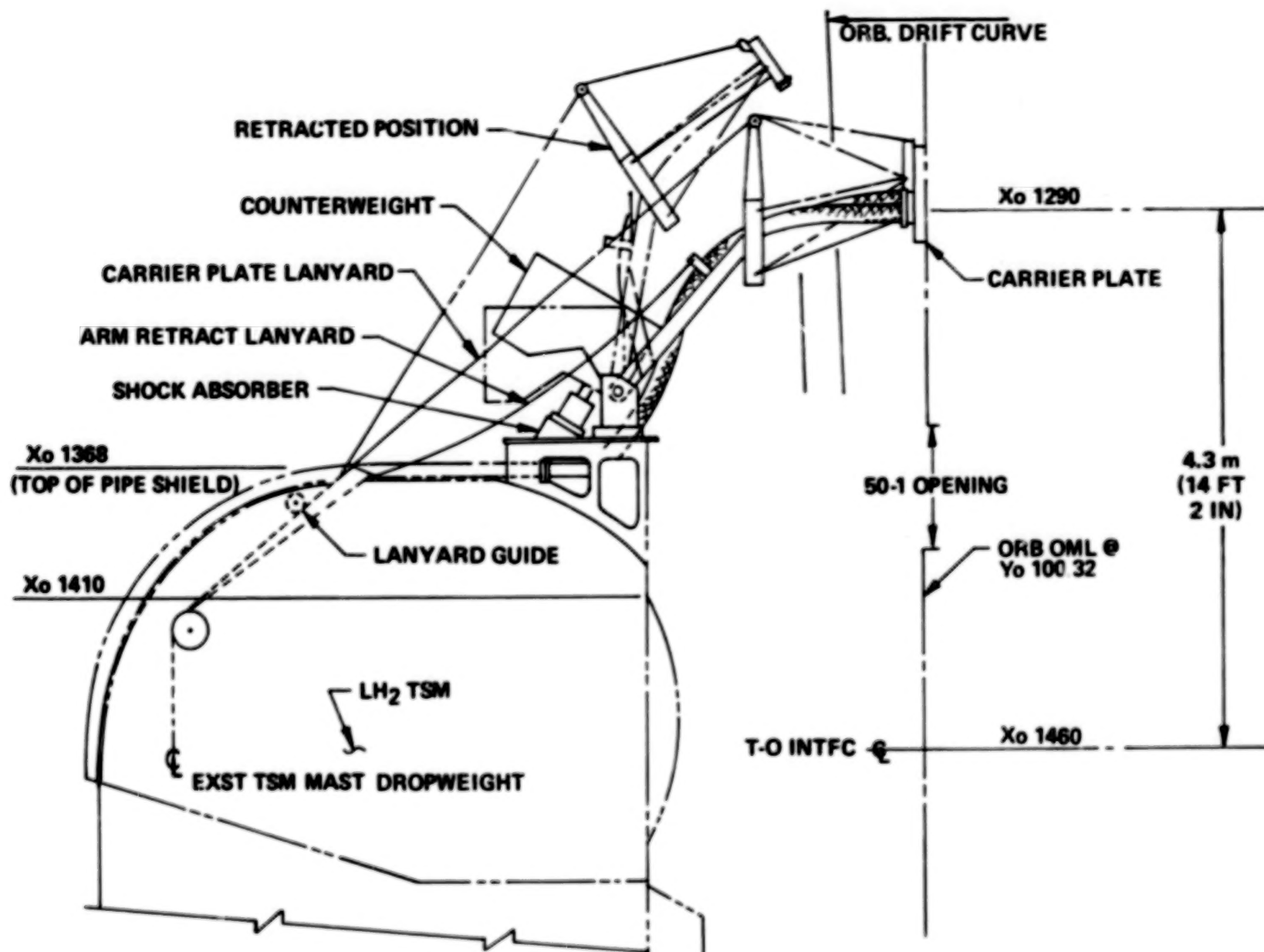


Figure 5. Payload Umbilical Mast - Expendable-Elevation View

- a. STS/Centaur rolling beam assembly (figure 6)
- b. Umbilical carrier plate assembly (figure 7)
- c. Dropweight tower assembly (figure 8)

Installation of this equipment at the Launch Equipment Test Facility for test evaluation and development prior to delivery to Launch Complex 39A is shown in figure 9. A description of the cryogenic supply system is beyond the scope of this paper.

Umbilical Assembly. The umbilical assembly consists of the ground carrier plate (supplied by Rockwell International) supporting links, the LH₂ fill and drain vacuum-jacketed (VJ) flex line, and the LH₂ vent VJ flex line. The links will be equipped with ball joints to permit side-to-side motion as well as up and down. These links support the carrier plate after disconnect. The umbilical assembly includes the hockey stick disconnect lanyards and the static lanyards to prevent rotation of the ground carrier plate towards the Orbiter after disconnect.

Rolling Beam Assembly. The rolling beam assembly consists of a tapered truss beam. One end of the beam supports the umbilical assembly. The other end of the beam is bolted to the carriage assembly. The carriage assembly contains wheels that capture the carriage to the rails. The carriage assembly contains a ground separation plate to support the carriage mounted cryogenic line quick disconnects, the carrier plate purge disconnect, and the various hazardous gas sensing line disconnects. The LH₂ fill and drain lines make a 180-degree turn from the beam to line up in the carriage with the ground separation plate.

Linear Brake. A linear brake acts on a friction plate mounted to the carriage to stop the rolling beam assembly. The brake system includes guide rollers in front of the brake. The brake consists of two spring-actuated caliper-disk-type units that are pneumatically retracted.

Incline Assembly. The incline assembly sets the rolling beam on a 6-degree angle necessary to interface with the Orbiter and provide stowage capability upon retract within the FSS. In addition to the linear brake described above, the incline contains final overrun stop energy absorbers designed for 11,340 kg (25,000 lb) over a distance of 0.472 m (18.6 in). The incline assembly supports the static half of the ground separation plate for the LH₂ fill and drain lines and the gaseous hydrogen vent line. A pneumatically powered winch provides the capability to lift the rolling beam up the incline. Upper guide rail and rollers limit carriage sway. Stairs and access platforms are provided on the incline, giving access to the rolling beam including umbilical and ground separation plates. Cooling water nozzles and piping will be mounted to the incline to protect the umbilical carrier plate.

BLANK

PAGE

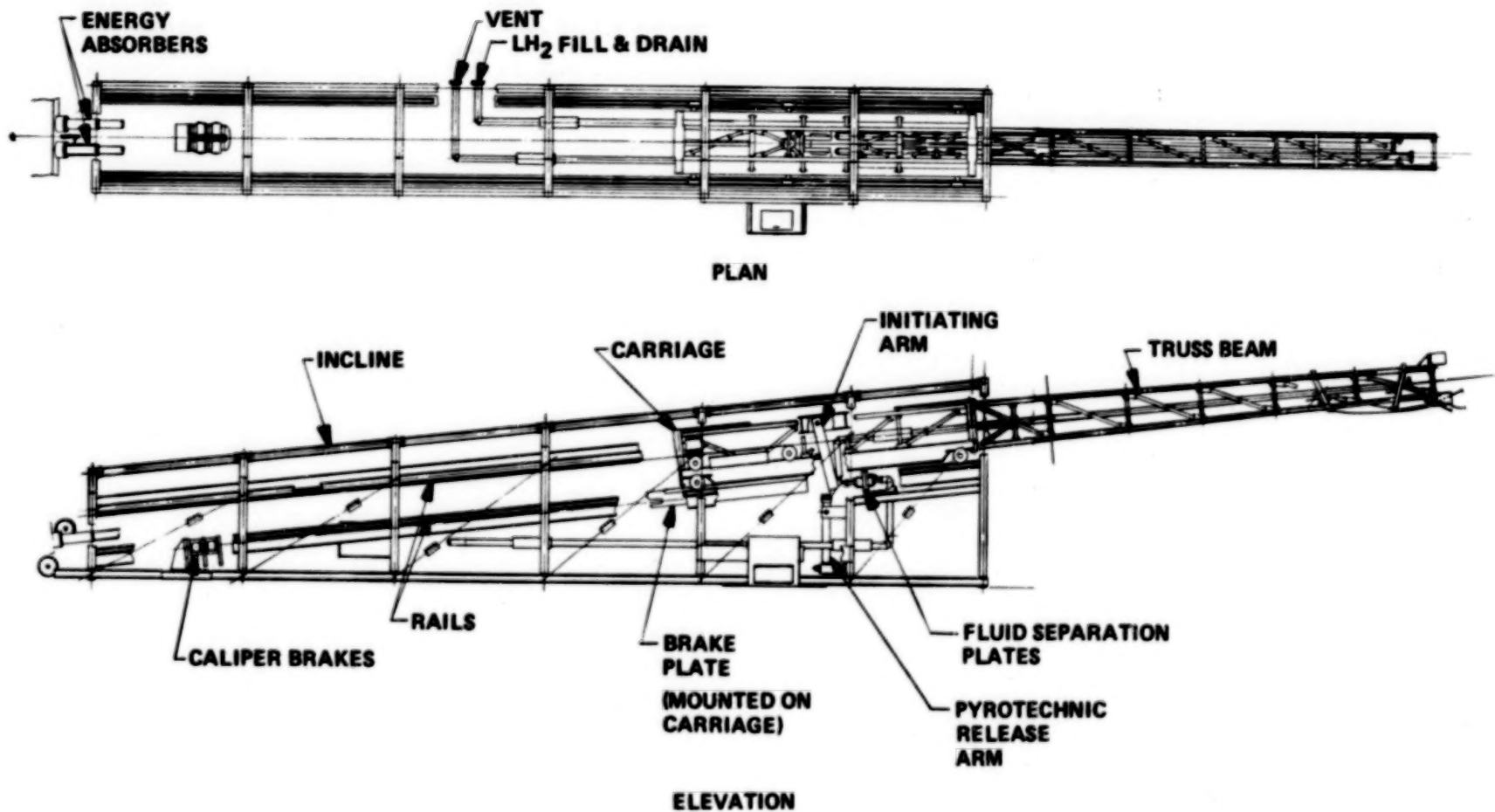


Figure 6. STS/Centaur Rolling Beam Assembly

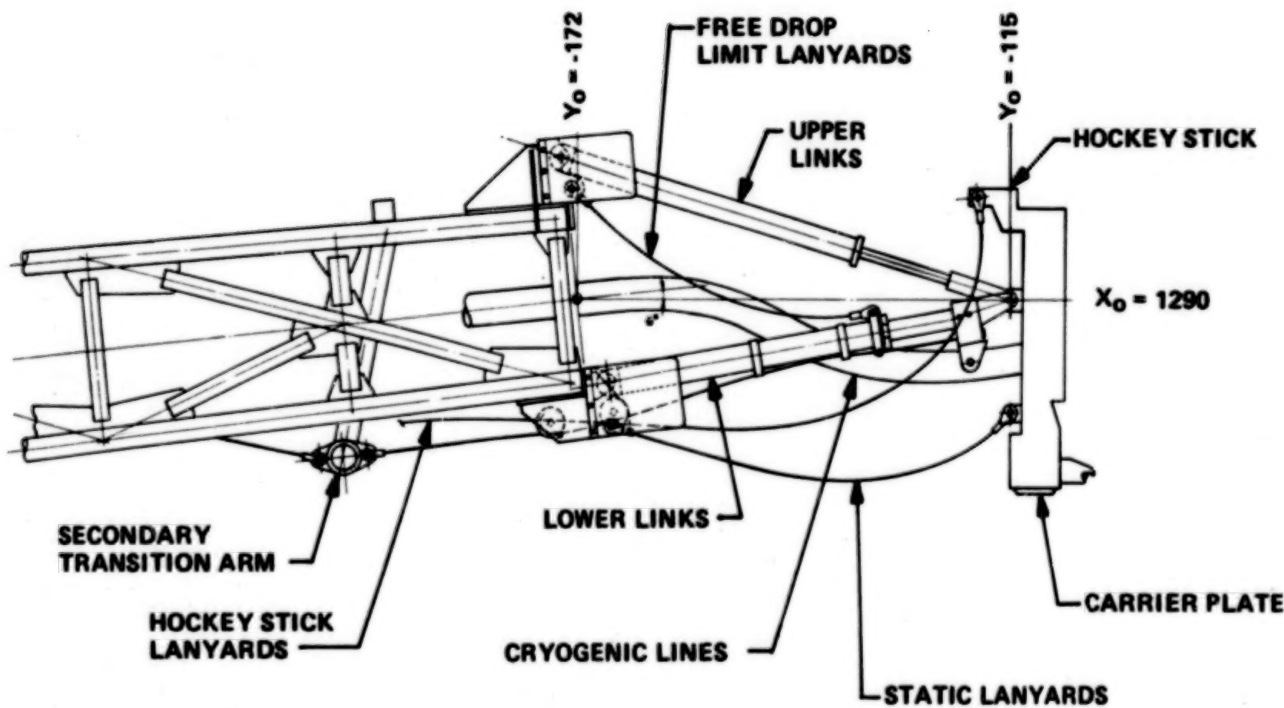


Figure 7. STS/Centaur Umbilical Carrier Plate Assembly

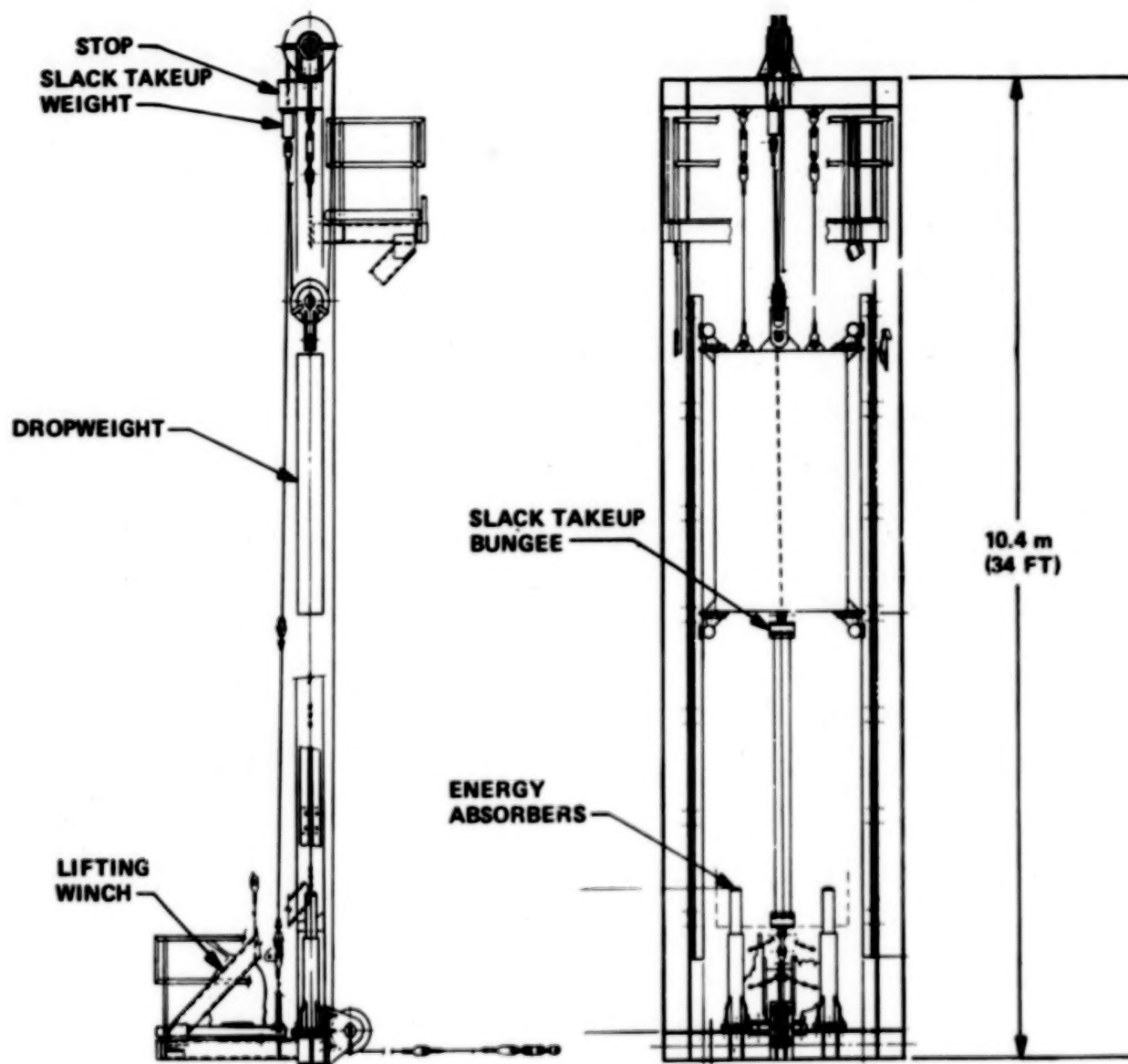


Figure 8. STS/Centaur Rolling Beam Dropweight Tower Assembly

300

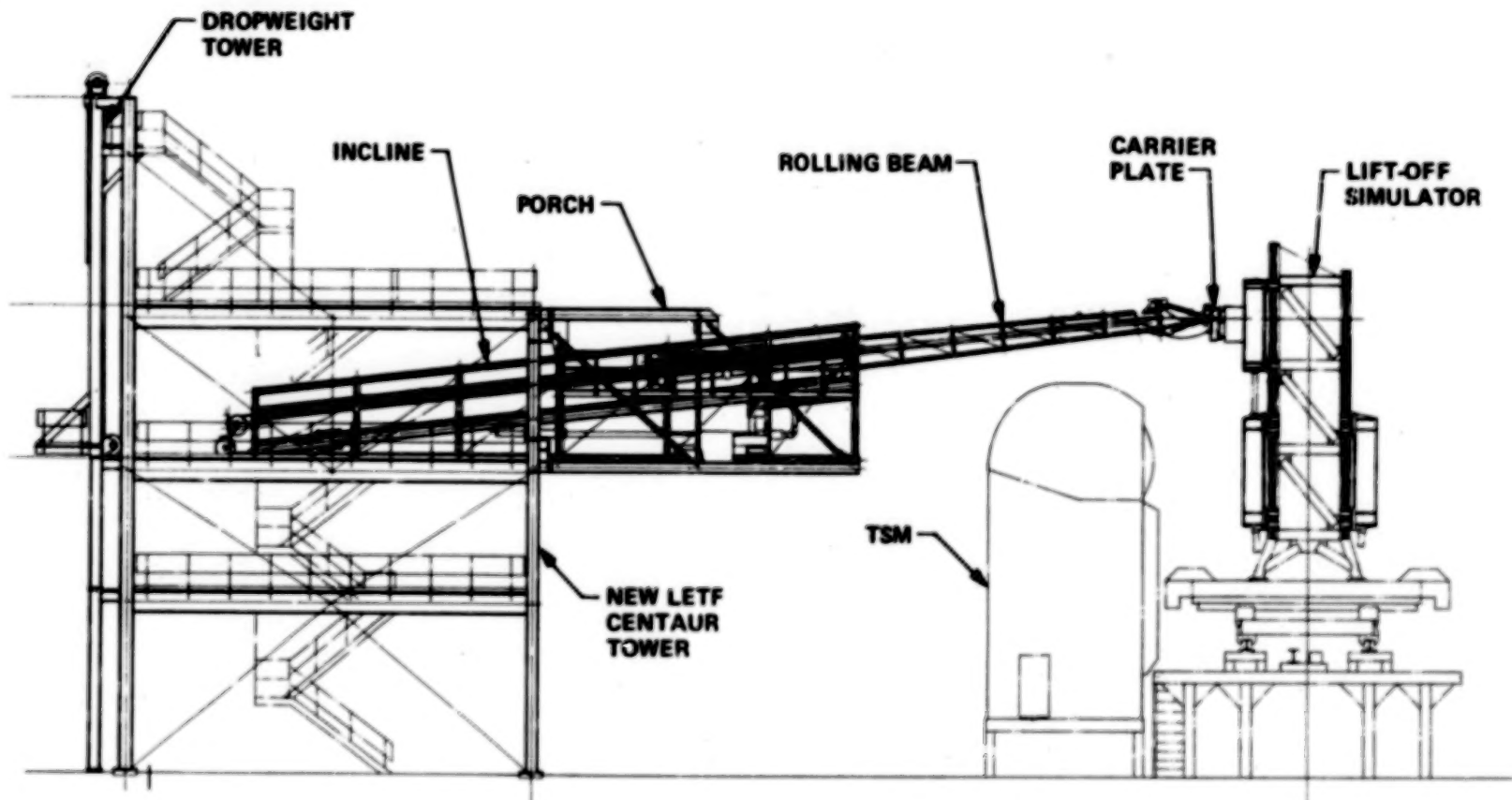


Figure 9. Launch Equipment Test Facility-STS/Centaur Rolling Beam Umbilical System Installation

BLANK

PAGE

Dropweight Tower. The dropweight tower contains the dropweight, drop-weight lifting winch, energy absorbers, kinetic and static sheaves and cables, and cable slack takeup weight, bungee, and pulley. Cable length is adjusted at the attachment to the cable slack takeup weights and pulleys. The main dropweight cable is routed through sheaves to the carriage attach point on the initiating arm, which will be described later. To permit lifting the drop-weight, the carriage end of the main cable is secured either to the carriage or to the incline structure attach point (for weight lifting only).

Porch Assembly. The porch assembly provides the necessary extension of the FSS to support the rolling beam assembly in position to service the Centaur payload in the Orbiter payload bay.

Disconnect Mechanisms. The disconnect mechanisms schematic is shown in figure 10. A latch mechanism holds the rolling beam in Orbiter mated position on the incline prior to launch with the dropweight applying static tension to the dropweight cable. The dropweight cable is attached to the initiating arm mounted in the carriage. This initiating arm first motion activates the hockey stick release lanyards and then transmits the accelerating force of the dropweight to the carriage. A redundant release mechanism triggers this action. Primary release is by a pyrotechnic bolt with dual charges. Either of these discharging will separate the pyrotechnic bolt and release the initiating arm. If the pyrotechnic bolt does not separate, an overcenter mechanism will be released by a lanyard that is activated by carrier plate lower lever extension, which takes place as the Space Shuttle vehicle lifts. The initial prototype rolling beam will incorporate a pyrotechnic bolt simulator that is released by a gaseous nitrogen pressure supply.

Initiating Arm. The initiating arm and its associated pyrotechnic release arm are the heart of the release mechanism, as they coordinate and control the functions of dropweight tension, pyrotechnic release, hockey stick activation, and mechanical secondary release. The trigger that mates with the pyrotechnic release arm is a bellcrank attached to the overcenter linkage. The lanyard action to break this linkage over center will release the trigger and permit rolling beam action to start in the event the redundant pyrotechnic bolt fails to discharge.

DESIGN CRITERIA

Pertinent design criteria for the RBUS are given in table 1. After serving the function of loading LH₂ onto the Centaur payload, the rolling beam must remain mated with the Orbiter until lift-off to provide for quick off-loading in the event of a launch abort requirement. The signal to start the retraction sequence of the rolling beam is initiated at solid rocket booster ignition. Within less than 3 s from the receipt of this signal, the rolling beam is to be retracted the necessary 11 m (36 ft) of incline distance and is stored within the incline structure where it is sprayed with cooling water to protect it for the next required launch.

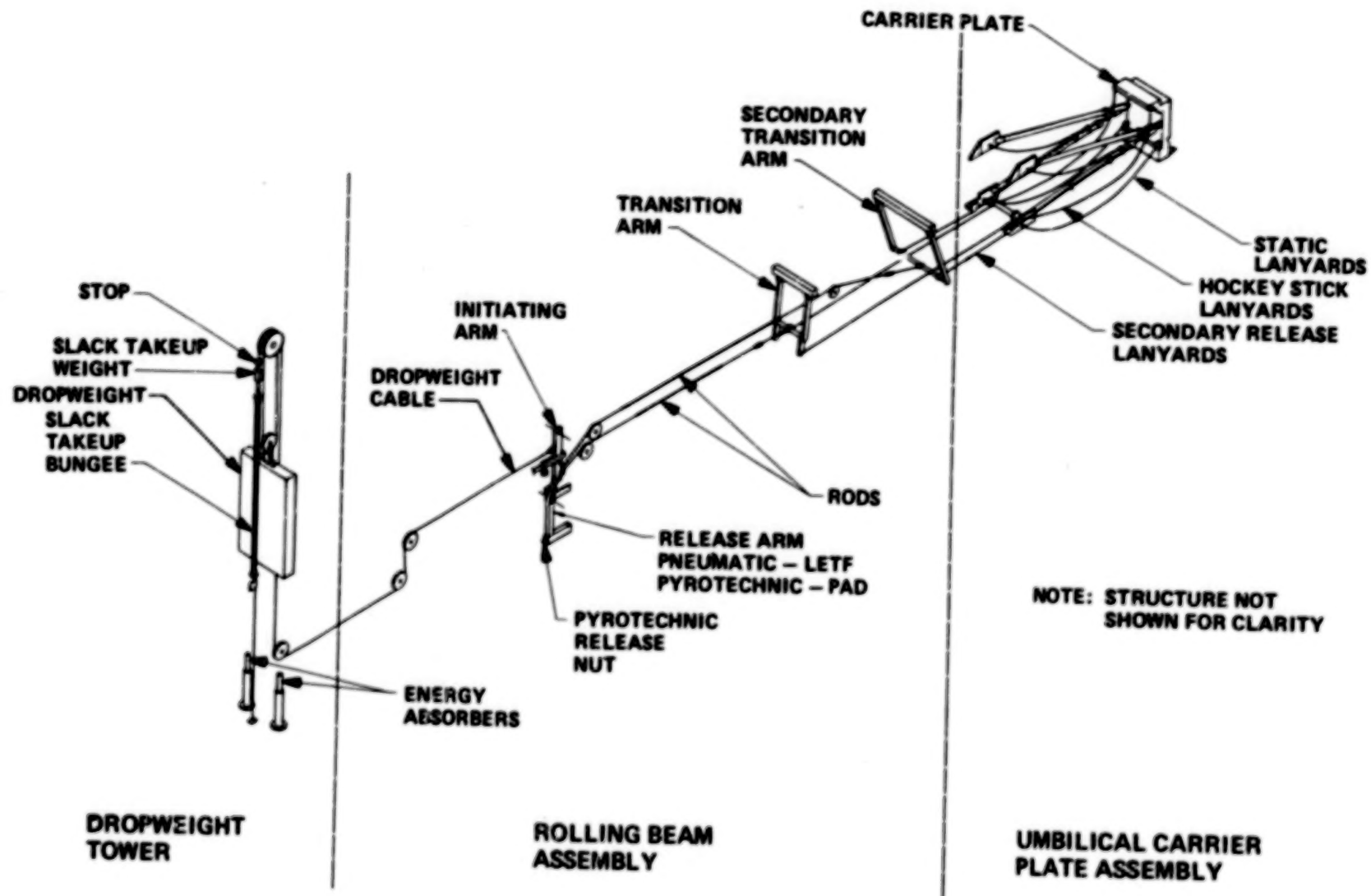


Figure 10. STS/Centaur Rolling Beam Umbilical System-Disconnect Mechanisms Schematic

BLANK

PAGE

Table 1. RBUS Design Criteria

Subject	Criteria
Beam retract distance	11.7 m (38.3 ft)
Acceleration distance	6.1 m (20.0 ft)
Coast distance	3.0 m (10.0 ft)
Deceleration distance	2.5 m (8.3 ft)
Overrun distance	0.46 m (1.5 ft)
Rolling beam weight	4,990 kg (11,000 lb)
Rolling beam material	ASTM A36
Factor of safety - dynamic members	2.0 minimum on yield
Factor of safety - static members	AISC criteria
Beam retract time	<3.0 s
Acceleration G's	<1.0
Deceleration G's (disk brakes only)	<2.5 (normal) <5.0 (abnormal)
Dropweight:	
Rolling beam/dropweight travel ratio	2 to 1
Dropweight travel	3 m (10 ft)
Dropweight energy absorption	2X(14,062 kg)X 0.41 m
Rolling beam module	90% status weight
Rolling beam including umbilical	4,990 kg (11,000 lb)
Incline	15,876 kg (35,000 lb)
Porch	8,618 kg (19,000 lb)
Total weight to be transported	29,484 kg (65,000 lb)
Brake type	Linear disk
Brake force	11,340 kg (<25,000 lb)
Normal coefficient of friction	0.30
Estimated coefficient of friction variation	0.25 to 0.30
Final stop overrun	Energy absorber
Final stop overrun force	2X(5,670 kg)
Incline angle	6.00 degrees
Umbilical type	TSM approach
Cooling provision (water)	1,782 l/min (500 gal/min)
Umbilical release - primary	Lanyard release
Umbilical release - secondary	Collet operation normal Hockey stick activates collet Lanyard release Collet failed
Umbilical release - tertiary	Hockey stick breaks collet shear pin Lanyard release Hockey stick frozen Tension breaks collet shear pin
Rolling beam release - primary	Pyrotechnic bolt
Rolling beam release - secondary	Lanyard release of mechanical trigger

Blank Page

DEPLOYMENT AND RELEASE MECHANISMS
ON THE SWEDISH SATELLITE, VIKING

Stefan Eriksson, Saab-Space AB, Linköping, Sweden

1. ABSTRACT

Two mechanism types are presented, a rigid boom system and a "hold and release" mechanism for spherical sensors. Both mechanisms have been designed, developed and tested by Saab-Space AB, Linköping, Sweden for the VIKING project under a contract from the Swedish Space Corporation.

2. INTRODUCTION (Ref. Fig. 1)

VIKING is a Swedish scientific satellite to be launched together with the SPOT remote sensing satellite by the Ariane Launcher, presently scheduled for late 1984. Its aim is to study a number of physical parameters in the auroral zones of the magnetosphere. The payload consists of five main experiments. Participating scientist groups come from Sweden, Denmark, Norway, Canada, United States of America, West Germany, England and France. Two of the experiments require the spacecraft magnetic influence to be minimized at their sensors. These two sensors are a three axes magnetometer and a loop antenna, located at the tips of the two radial stiff booms.

Two other experiments use six spherical probes ($\varnothing = 10\text{ cm}$), including inner/outer tips, for electric field measurements. These probes are mounted on four wire booms which can each be deployed to a length of 40 m in the satellite's spin plane, and on two tubular-element booms which can be deployed 4 m each, parallel to the spin axis. Until deployment is called for, these probes are to be stowed by Hold and Release Mechanisms (HRM).

Below the requirements of the radial stiff booms and the HRMs are summarized. Their design, performances and test programs are described in detail.

3. STIFF RADIAL BOOMS

3.1 Summary of requirements

The design requirements can be summarized as follows:

Launch Mode (stowed)

Sine vibration, all three axes	5 - 100 Hz	8.0 g _{max}
Random vibration, all three axes	20 - 2000 Hz	0.3 g ² /Hz max

Deployment Mode

Spin rate	8.5 to 14.5 rpm
Release	pyrotechnic device
Deployment shock (on boom tip)	max 50 g
Temperature	-30° to +80°C

Deployed Mode

Boom lateral deflection	within a cone angle of 0.1°
Boom torsional deflection	$\pm 0.2^\circ$ torsional angle

3.2 Detailed description (Ref. Fig. 2 and Fig. 3)

Boom Design

The rigid boom system consists of two identical booms symmetrically mounted. The deployable boom element is an aluminium tube O.D. 53 mm, thickness 1.5 mm and a length of 1385 mm. The limited space available in the launcher adapter and the fact that the boom has to be stowed alongside the payload deck, have set the boom length. Aluminium is also used for the tip sensor mounting flange and the hinge part, both welded to the tube. The other hinge part is designed as a separate unit, fastened to a tubular levelling beam which is mounted on the payload deck. A titanium shaft in two flanged bushings forms the hinge. The bushings have a reinforced P.T.F.E. liner material as lubricant. The hinge also includes the locking mechanism: two beryllium copper leaf springs latching independently on two conical titanium locking pins. These pins are designed with a slope, giving a smooth latching. Between the two spring blades a titanium bolt acts as a stop, taking the collision load at locking. The boom is stowed alongside the payload deck on two supports having a delrin sole. The support nearest to the hinge is elevated with reference to the outer support. The boom is furthermore stowed by means of a "hold down" wire tightening the boom on to the outer support. The boom is thus preloaded to protect the bushings in the hinge from heavy vibration. The preloading also aids in lifting the boom off the supports.

Deployment

Deployment of the booms is initiated by ordinance cutting of the hold down wires. The cuttings are effectuated by electro explosive guillotines through which the hold down wires pass. Nominal spin rate for boom deployment is 11.5 rpm but the boom system has been tested in the required spin rate range from 8.5 rpm to 14.5 rpm. The centrifugal force

generated by the satellite spin provides the booms with deployment energy. At nominal spin rate, deployment takes 2.0-2.2 seconds. When the boom has locked into the deployed position the titanium stop bolt takes the load and the boom is deflected. At the return bending the two leaf springs transfer the load via the two locking pins. Since no damping device is used and the deployment only uses a discrete amount of energy the boom will oscillate until the whole energy is dissipated. The oscillation has a frequency of ~7 Hz. During this oscillation the two leaf springs work their way down further on to the locking pins as the locking pin angle acting against the leaf spring is set below the friction angle for the mating surfaces.

Wiring

The power and signal cables are routed inside the boom and tied down to the tube with brass wires at 15 cm spacings. Through the hinge a flat cable is fed with a free loop length of 14 cm in order to lower the wiring torque. The two boom cables contain:

magnetometer	5 coaxial cables RG 178 1 twisted pair 0.25 mm ²
loop antenna boom	1 coaxial cable RG 178 5 single cables 0.25 mm ²

Mathematical Model

A mathematical model for boom deployment was developed. It was used for design purposes to estimate the deployment loads. The model is simplified to two identical booms deployed symmetrically. Counter torques from friction, cabling and latching were considered. The available energy for boom deployment is the energy dissipated when the spinning satellite changes its moment of inertia during boom deployment. This energy is

$$T_{\text{diss}} = I_p \times \left(1 - \frac{I_p}{I_a}\right) \times \frac{\omega_p^2}{2} \quad (1)$$

where T_{diss} is dissipated energy

I_p moment of inertia prior to boom deployment

I_a moment of inertia after boom deployment

ω_p satellite spin prior to boom deployment

3.3 Boom Tests

Four types of tests were carried out to evaluate the boom system performance. Firstly, deployment tests have been conducted on a spinning table. Secondly, the hinge has been tested separately in a vacuum chamber. A third test has been conducted to determine the boom wiring performance with regard to torque loss changes due to storage and extreme temperatures. Finally, vibration tests have been performed.

Deployment tests

Deployment tests were performed with the booms mounted on a spinning table, with a mounting plate having the same moment of inertia as the satellite itself, and with the spin table drive decoupled just before deployment. Thus the boom deployment was adequately simulated and the interaction of the bodies at locking was not disturbed. To minimize spin rate decrease caused by friction, the spin table bearings were axially off-loaded by means of two support wires from the ceiling. The two booms were also supported at CG location to unload their weight in the g-field. All data acquisition equipment was placed on the rotating table to avoid slip ring arrangements. The main parameters recorded were: the bending moment at the boom root, the tip mounted experiment acceleration, the deployment angle, the latch spring movement and the spin rate. The tests were performed at three spin rates: 11.5 rpm which is the nominal spin rate, 8.5 rpm and 14.5 rpm. After each functional test an alignment check was performed.

Separate hinge test

During the development phase a detached hinge was tested in a vacuum chamber. Deployment was effectuated by means of a pendulum stroke outside the chamber. The counter torque from friction and latching was measured in the axis from the pendulum to the hinge inside the chamber. As the hinge was cooled and heated, the effects of different temperatures and temperature gradients over the bushings were studied.

Wiring test

A test rig for the study of the wiring through the hinge was manufactured. It consisted of an electric motor for simulated deployment with means of measuring deployment angle and counter torque with hinge equivalent wiring. The counter torque changes due to storage of the boom in stowed position and due to the extreme wiring temperatures anticipated were also studied.

Vibration test

For mounting the booms on the vibrator, a fixture shaped as a segment of the payload deck was used. This fixture was also used for mounting on the spin table. Thus the boom could be moved back to the spin table in stowed position for a functional test.

3.4 Test Results

During the functional tests the boom bending moment at the boom root was recorded. The results are presented in fig 4. The maximum recorded bending moment at 14.5 rpm deployment spin rate was 378 Nm. The designed ultimate load was set at 1100 Nm, which resulted in a safety factor of 2.9. The bending moment, 378 Nm, corresponds to an experimental acceleration of 24 g. At nominal spin rate deployment the acceleration was 18 g. A typical interaction of the booms after locking is shown in fig 5.

An alignment check was also performed after each test and the deflections were as follows:

Boom lateral deflection	within a cone angle of 0.05°
Boom torsional deflection	max 0.05°

From the hinge vacuum test and the wiring rig test an energy budget is deduced as follows. The values presented are the maximum obtained. (Ref fig 6)

Action	Energy consumed (J)		
	Pre-locking phase	Locking phase	Temp./Temp.gradient (°C)
- Bearing/shaft friction	0.60	0.05	-30/10
- Harness work	0.05		-30
- Latch work		0.40	N/A
- Latch-locking pins friction		0.40	N/A
Total Energy Consumed		1.5 J	

The figures represent one boom; thus a total energy of 3.0 J is needed for the boom system. The equation (1) given in 3.2 yields the lowest spin rate limit for a feasible latching, which is 5.9 rpm. The safety factor on energy to the predicted lowest deployment spin rate, 8.5 rpm, is 2.1.

During vibration tests the experiment unit experienced an overall RMS level of 6 g. The magnetometer boom configuration resonance frequency at 35 Hz showed a peak value of 46 g at the magnetometer location.

3.5 Problems encountered

Since the vibration level at the magnetometer boom resonance frequency during the preliminary tests was quite high, a 1.5 mm rubber isolator was inserted at the mounting flange. This measure reduced the peak value by a factor of 1.7.

After the preliminary tests a larger safety factor on energy loss was requested. Measures were taken to minimize the energy dissipation during deployment and latching. Decreased width of the leaf springs and adjustment of the locking pins slope resulted in a smoother latching.

A change in the payload deck was found necessary after the deployment tests, because the boom vibrated after release and bounced against a HRM. For protection of the HRM a L-profile with a plastic material on the edge was introduced. The boom now bounces against the profile and the vibration is damped.

4. HOLD AND RELEASE MECHANISM

4.1 Summary of requirements

Stowed Condition

Sine vibration, all three axes	5 - 100 Hz	10.0 g max
Random vibration, all three axes	20 - 2000 Hz	18.1 g ₂ RMS
Resonance frequency	100 Hz min	0.3 g ² /Hz max
No sensor movement		

Release Mode

Temperature	-30° to +80°C
Swing of sensor at release	within a cone angle of 10°
Switch indication at completed armpair deployment	

4.2 Detailed description (Ref. Fig. 7)

The Hold and Release Mechanism (HRM) is used to hold the sensor in stowed position until the wire boom and axial boom deployment is initiated. Ten seconds before boom deployment starts, sensor release is effectuated. The HRM consists of a mounting bracket and two moveable armpairs. The mounting bracket is designed as a flat beam reaching out over the edge of the payload deck. The axes of the two armpairs rotate in bearings similar to those used in the stiff boom hinges. Armpair deployment is effectuated by means of preloaded torsion springs. A wire is used for tightening the armpairs around the sensor rods. The wire is fastened in the armpairs and passing through an electro explosive guillotine in its housing. The holding force is set when the guillotine housing is pulled towards the bracket.

A strain gauge, which is used to measure the holding force, is glued to a beam on one of the armpairs. Each arm is set with 50 N against the sensor tip. The pads (made of delrin) holding the rods have cylindrical grooves for position of the sensor rods. On the sensor outer rod a cylindric pin ($\varnothing = 1$ mm) is used to prevent the sensor from radial and rotational movements. The pin is placed in a track in one of the outer pads. Two micro switches are mounted on top of the bracket for indication of full armpair deployment. The HRM for the two axial tubular element booms is not described in detail but is similar to the unit presented above.

4.3 HRM tests

Release test

The release test was conducted in a vacuum chamber (1×10^{-6} torr) with a heating/cooling arrangement. Three release tests, with a 10°C temperature gradient over the bearings at -30°C, +25°C and +80°C, were performed on each unit. The effect of temperature was studied by comparing the deployment time for each release test. During the test the HRM was vertically mounted such that the sensor dummy used could be studied with regards to side forces. The parameters recorded in these tests were: release initiation (strain gauge voltage drop), armpair deployment angles (potentiometers), switch indication at fully deployed armpairs and the sensor dummy movement. The sensor dummy movement was recorded by the use of a small pick up coil mounted on the rod tip of the dummy. A larger

sending coil induced a voltage variation proportional to the swing of the dummy.

Vibration test

The HRM was tested to the levels specified. During these tests a sensor mass dummy was attached. After vibration test, a release test was performed.

4.4 Test Results

No significant changes due to bearing temperatures of -30°C to $+80^{\circ}\text{C}$, or 10°C temperature gradients over bearings, were found during the release tests. The deployment times for all tests stayed within the interval 50-60 ms. At release, the sensor swing stayed within a cone angle of 5° for four units. Larger swings were recorded for the last unit due to an unintentional torsional preloading of the wire boom cable, caused by the test set up.

4.5 Problems encountered

During the preliminary test two major problems were dealt with. One, the resonance frequency of the mounting bracket was 60 Hz for the first HRM design. By adding a box shaped stiffener the resonance frequency was increased to 130 Hz. Two, a number of different designs of the pads holding the sensor from rotational and radial movements were tested in vibration. The design chosen is such that the wear in the delrin pads during vibration is low. This will minimize the sensor swing after release.

5. CONCLUSION

The two mechanisms described above have successfully passed their qualification and flight acceptance tests and meet the requirements. They are presently being integrated with the VIKING satellite.

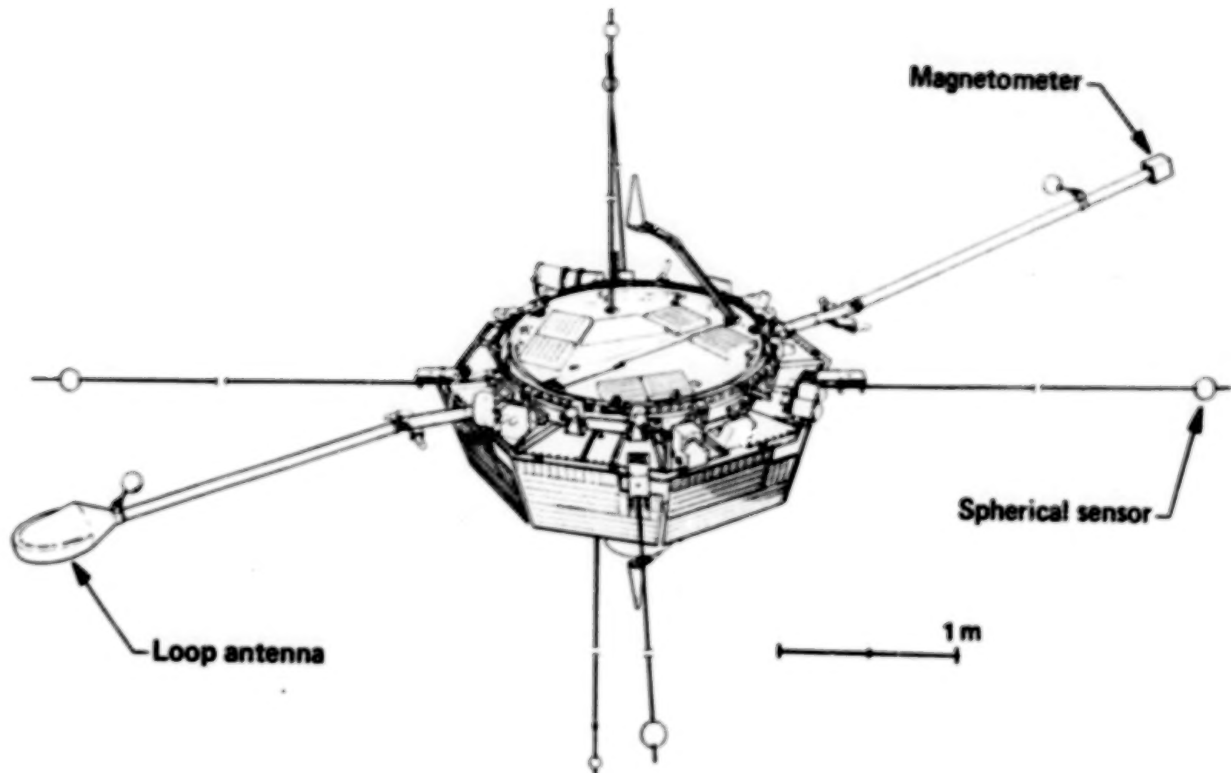


Fig. 1 Viking flight configuration

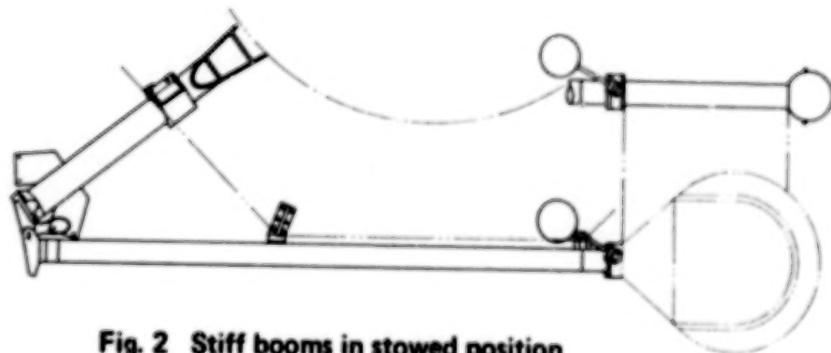


Fig. 2 Stiff booms in stowed position

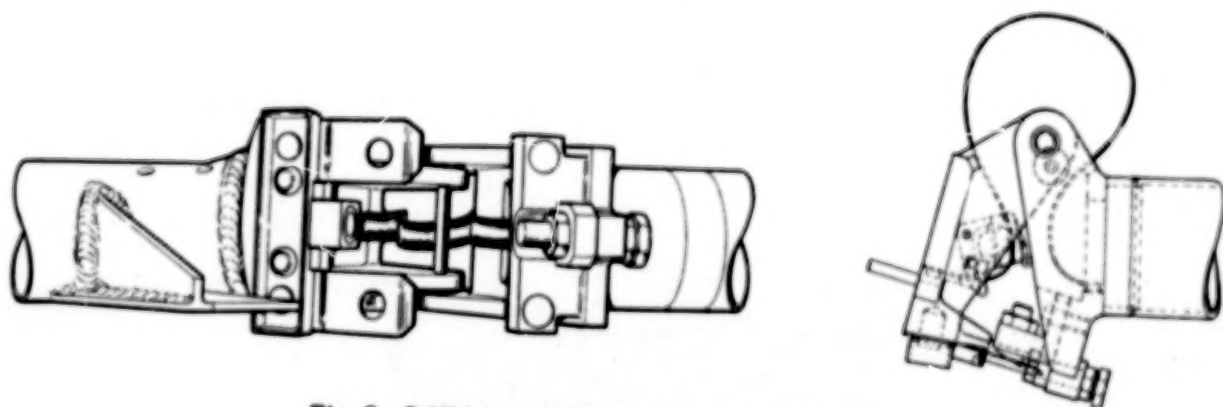


Fig. 3 Stiff boom hinge and latching mechanism

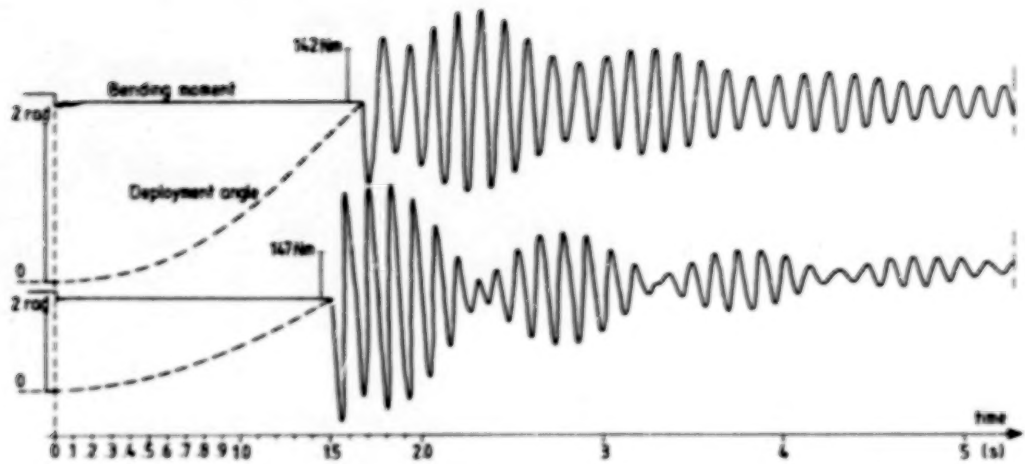


Fig. 5 Boom interaction after locking

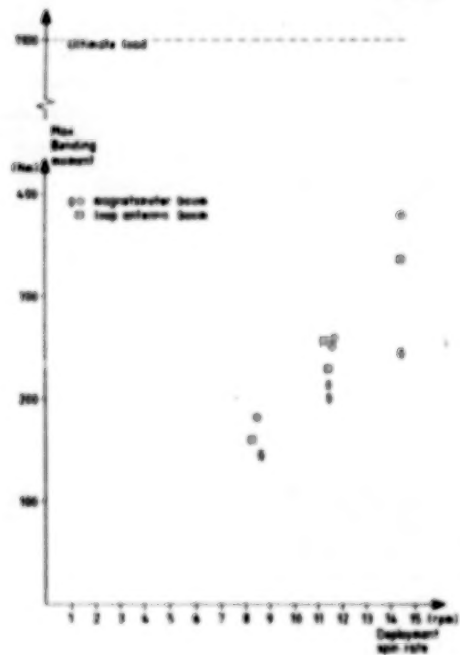


Fig. 4 Max boom bending moment at locking

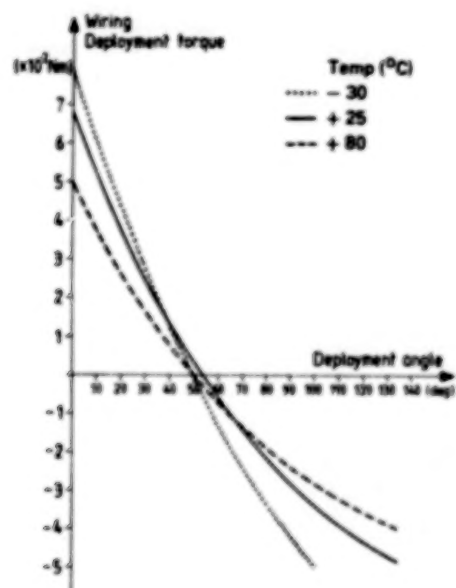


Fig. 6 Boom wiring torque (Temp. 25°C)

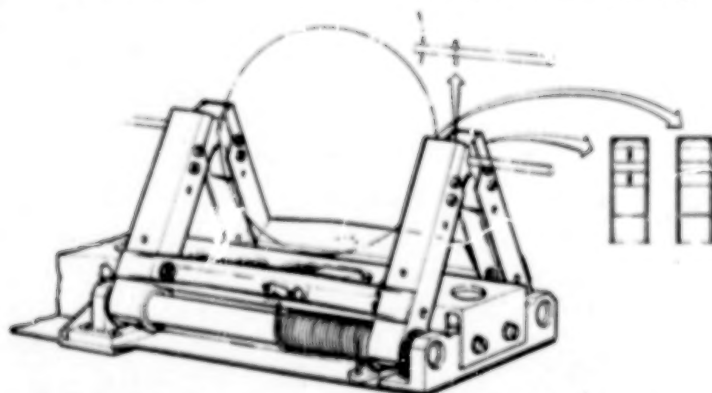


Fig. 7 The HRM with the pads holding the sensor in place

DESIGN OF THE GALILEO REMOTE SCIENCE POINTING ACTUATORS

Fredrick W. Osborn*

ABSTRACT

This paper describes the two actuators developed for pointing the remote science instruments from the spinning Galileo spacecraft. Details of the key elements are presented together with their design features and developmental difficulties. Four techniques used for power and signal transfer across the actuators' rotating joints are also discussed.

INTRODUCTION

The Galileo mission to investigate the planet Jupiter and its satellites will use the dual-spin spacecraft shown in Figure 1. A major portion of this spacecraft, the rotor, will spin continuously at 3.15 revolutions per minute to provide gyroscopically stabilized antenna pointing together with a rotating base for the sky-sweeping fields and particles experiments. Instruments which must be pointed for remote sensing, including the imaging system, will be carried on a non-spinning, or stator, portion of the Galileo Orbiter spacecraft. A Spin Bearing Assembly (SBA) will mechanically and electrically couple these spun and despun Orbiter sections to permit instrument pointing around the spacecraft "clock" axis. The Scan Actuator Subassembly (SAS) will couple the remote science scan platform to the despun stator to provide instrument pointing in the "cone" axis.

Since achievement of the mission remote science objectives is very dependent on the reliable operation of these two mechanisms, they contain redundant elements. Total redundancy was not possible, however, so their development required extensive analysis and testing to insure successful mission completion. Both of the actuators, and their associated electronics, were developed by the Space Systems Unit of Sperry Flight Systems, Phoenix, AZ, under a contract with the Jet Propulsion Laboratory.

Although the two actuators are very dissimilar in configuration, their key design elements, described below, are very much alike.

* Guidance and Control Section, Jet Propulsion Laboratory, California Institute of Technology, Pasadena, CA.

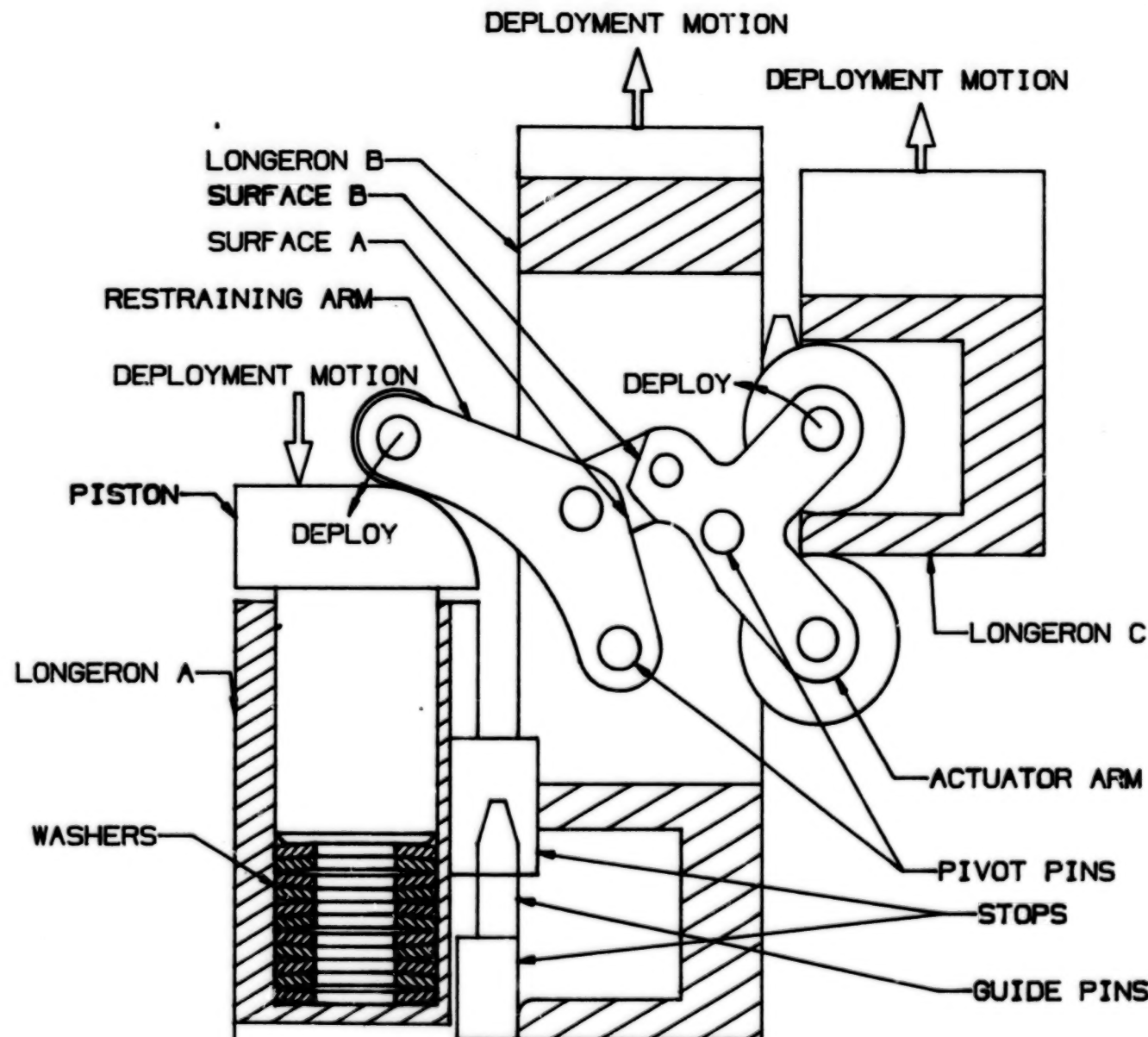


FIGURE 3. - LATCHING MODE

164

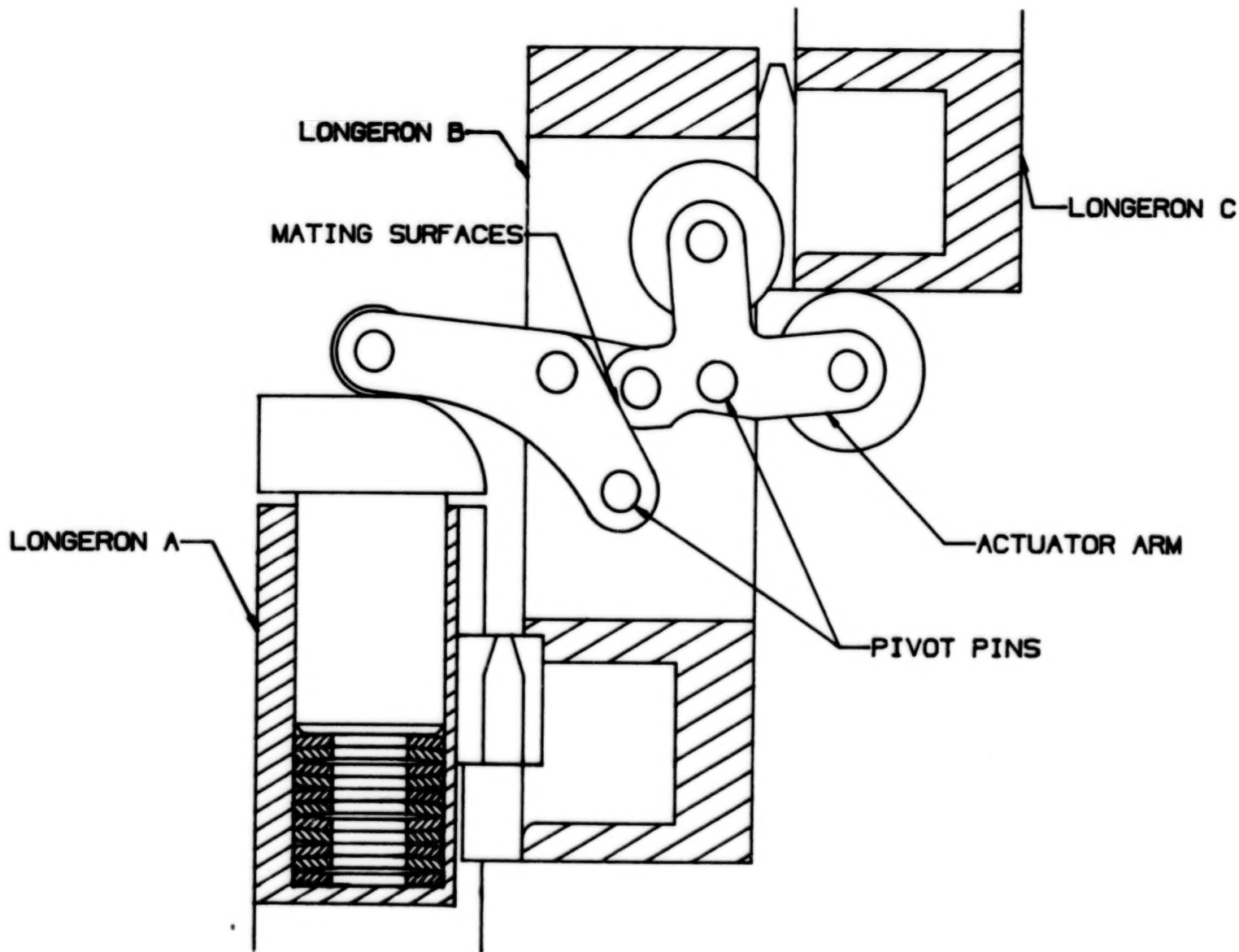


FIGURE 4. - DEPLOYED LATCH

BLANK

PAGE

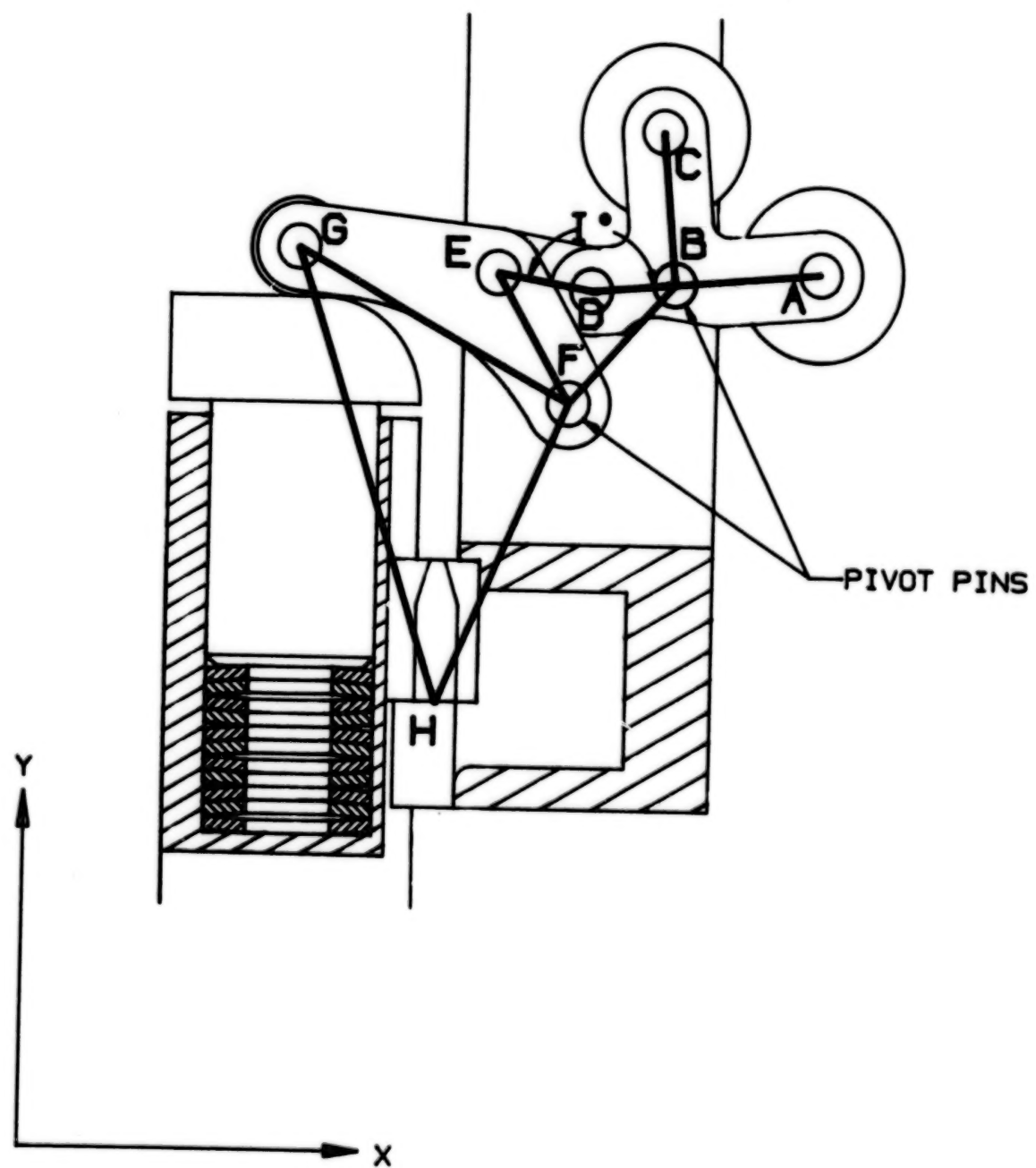


FIGURE 5.- KINEMATIC MODEL

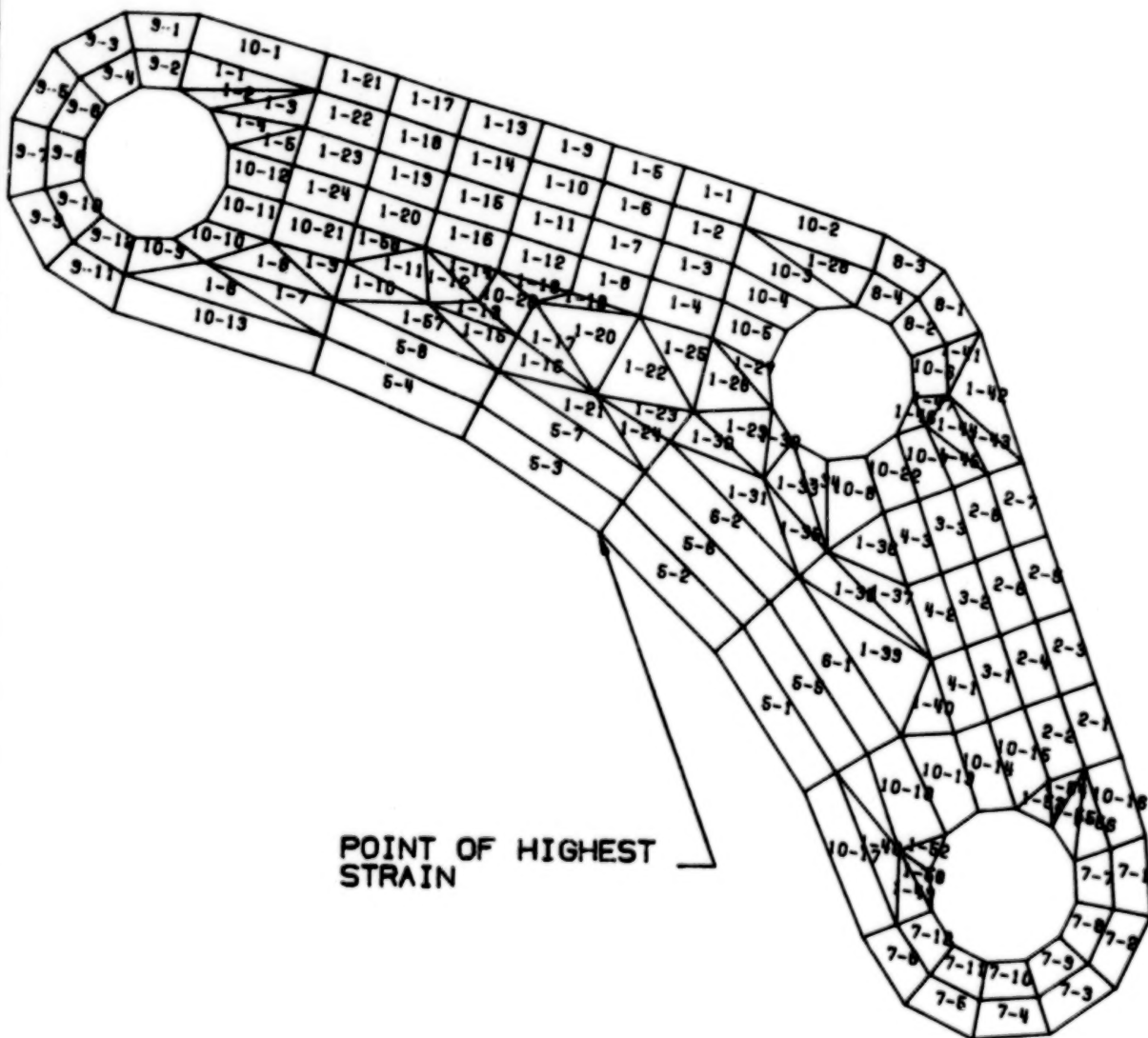


FIGURE 6.- FINITE ELEMENT MODEL

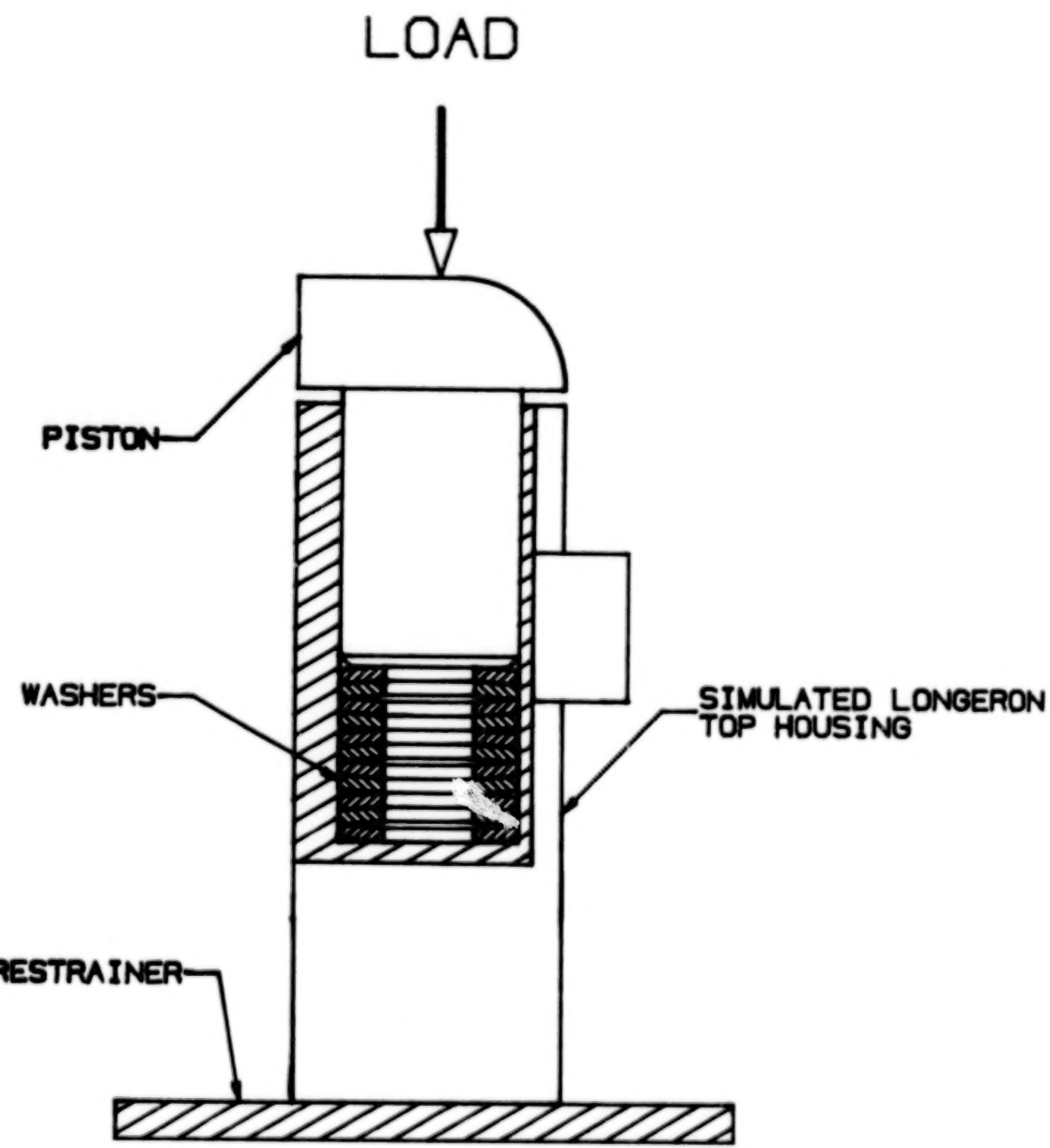


FIGURE 7.- COMPRESSION TEST

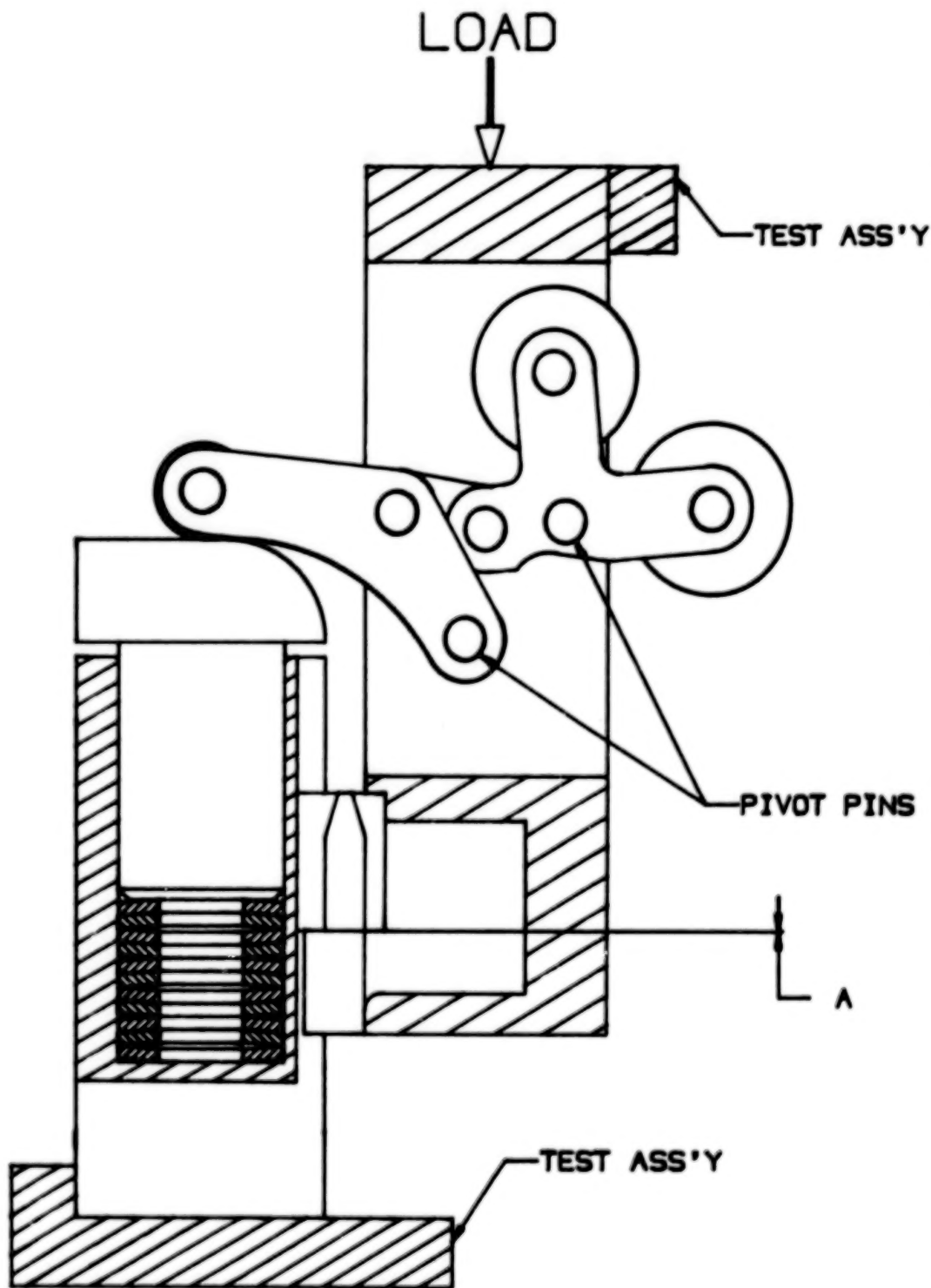


FIGURE 8.- COMPRESSION TEST
ASS'Y LOADED CLL

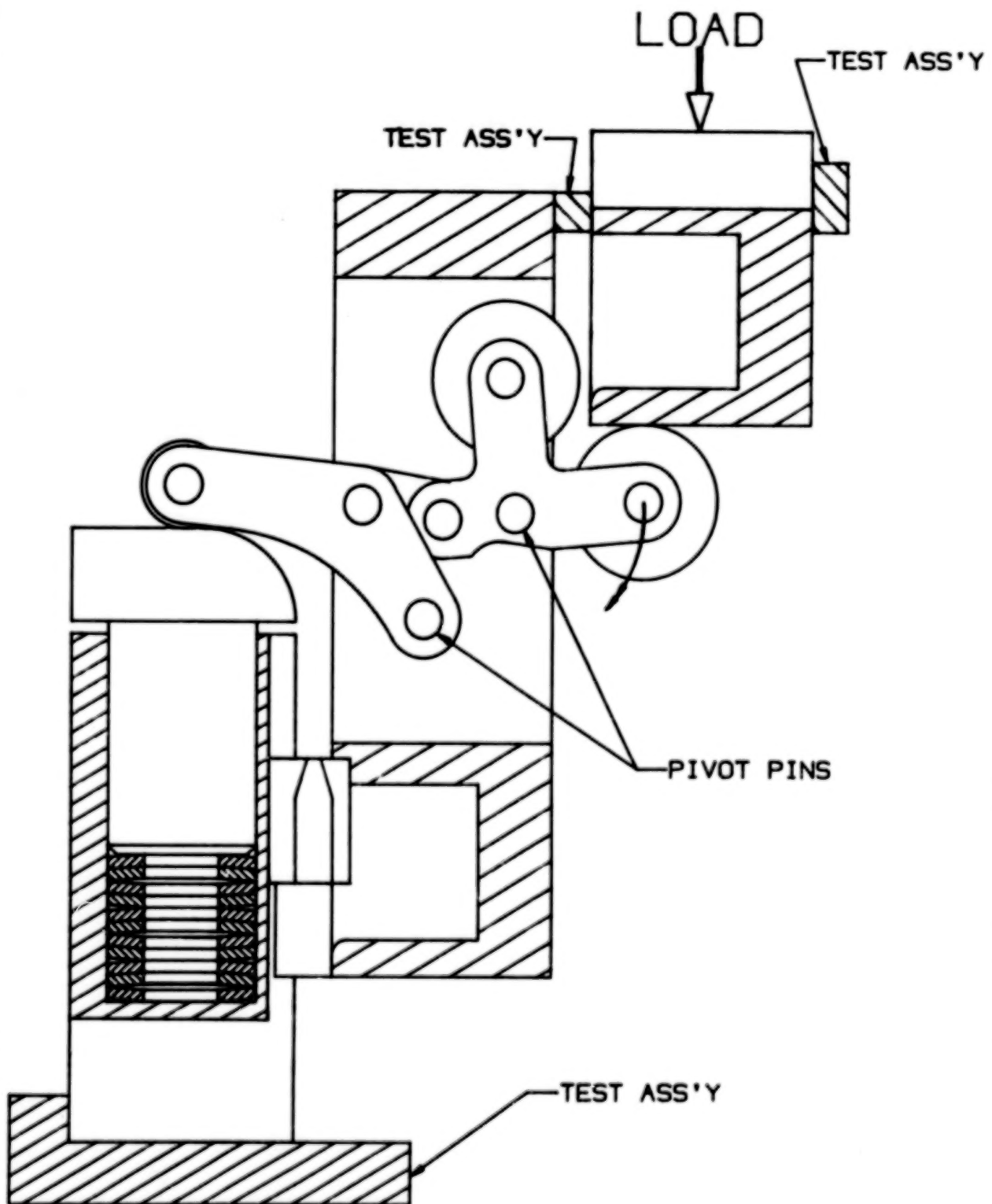


FIGURE 9.- UNLATCHING TEST

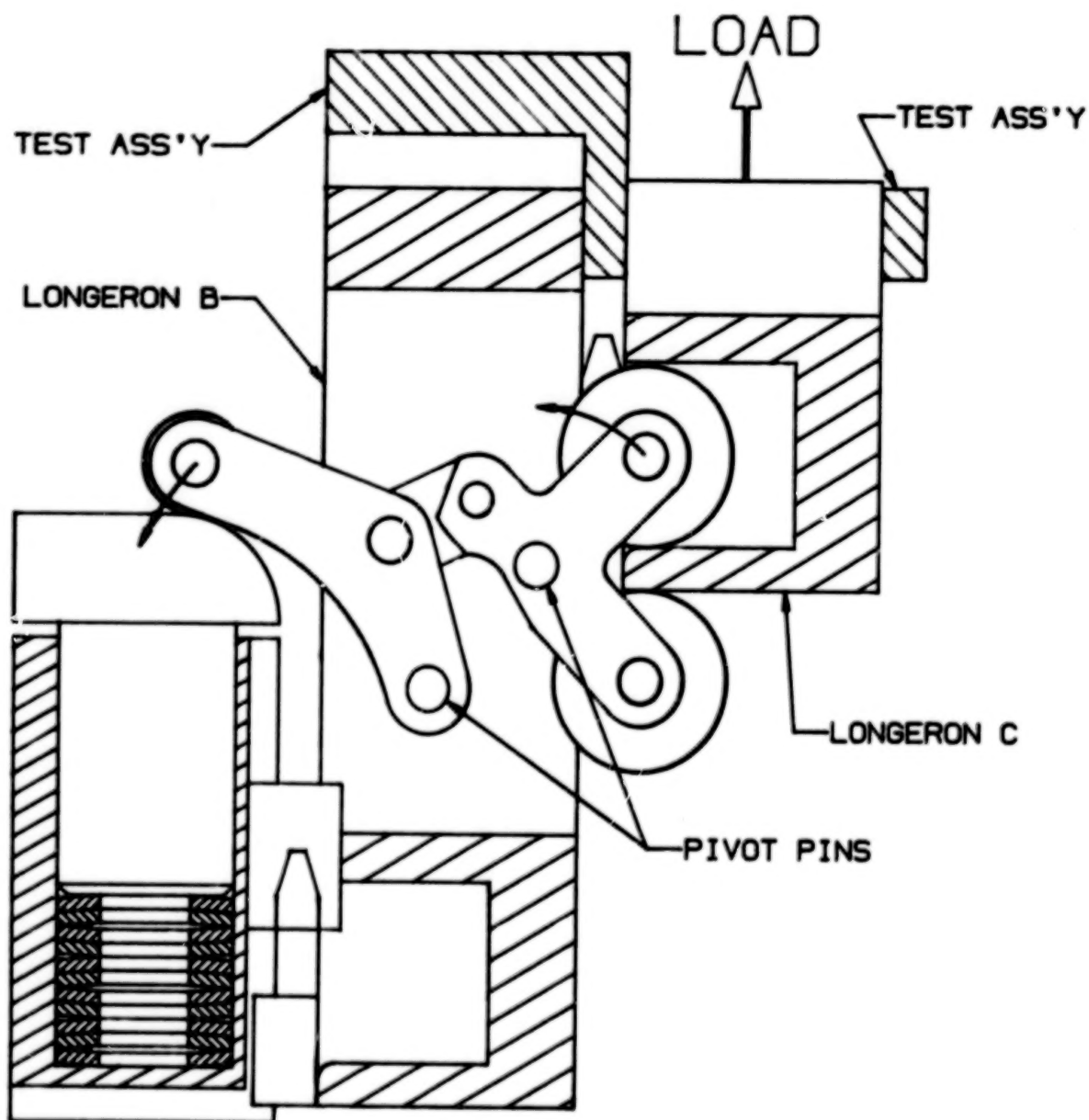


FIGURE 10.- LATCHING TEST

A HIGH STRENGTH, TORSIONALLY RIGID,
DEPLOYABLE AND RETRACTABLE MAST FOR SPACE APPLICATIONS
Lamont DiBiasi and Richard Kramer*

ABSTRACT

The era of retrieving and/or servicing satellites in orbit has mandated that extendable elements, such as those used to deploy solar arrays, thermal radiators, communications antennas, instruments and numerous other appendages have inherent in their design a highly reliable retraction capability. Throughout the past year a structural mast has been developed which during and after full deployment produces a supporting structure with the characteristics of a high bending moment capability, high stiffness and, particularly important for instrument deployment, a high degree of position repeatability and torsional rigidity. These features have been accomplished while providing an easily retractable mast with a high life cycle capability. Since these properties are consistent throughout the full range of deployed lengths, partial deployments or retractions can be utilized for check-out, balance, fine tuning or whatever other reason may be deemed necessary for operation modes or spacecraft stability.

INTRODUCTION

The mast, shown in Figures 1 & 2 to be discussed, is of a triangular cross-section and is formed by the interlocking of three identical strips of material along their common edges. The interlocking of the edges is achieved by a meshing of a series of socket-type inserts permanently attached to rolled tabs alternately spaced along the length of each strip of material. In the stowed configuration, the material is unlocked and is therefore very flexible. This allows great packaging freedom since the three separate storage spools of material can be located remote and in any orientation with respect to the locking station within the mechanism. The packages for a given mast can therefore range from a long cylindrical configuration to a flat rectangular one. Because the strips of material are locked together inside the deployment mechanism, a fully formed mast exits the mechanism and takes all external loading regardless of deployed length. This paper will cover the design requirements, design philosophy, fabrication methods and test methods and results for a specific model mast.

*Fairchild Space Company, Germantown, Maryland 20874-0811



Figure 1

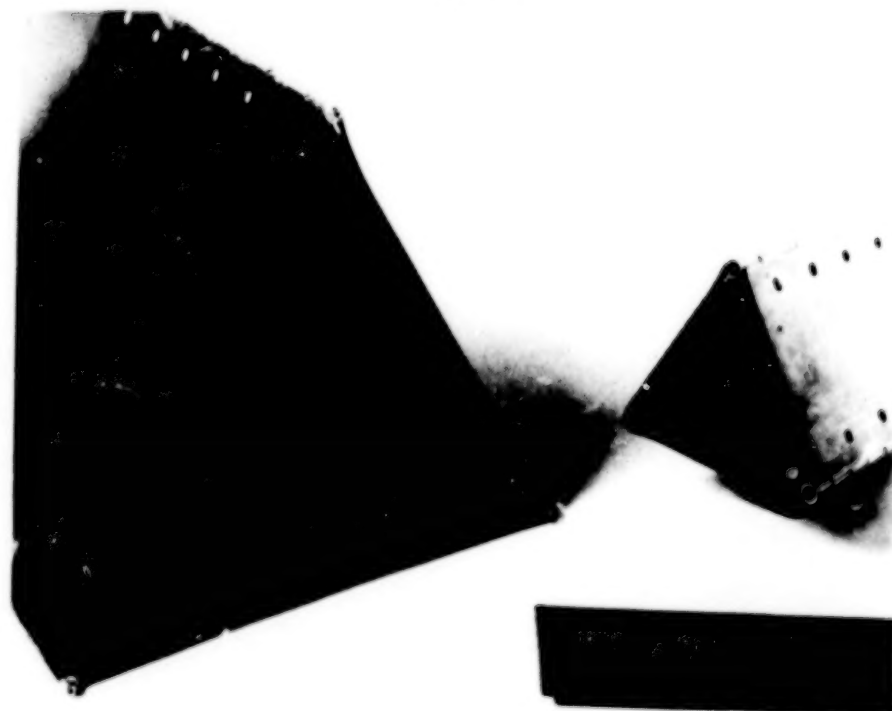


Figure 2

REQUIREMENTS

The design philosophy behind the development of the mast was to select a number of desirable features, establish many as hard criteria and maintain the others as goals which would be studied and traded-off as the program progressed through the design, build and test stages.

Those features considered as hard criteria were:

- Highly reliable
- Extendable and retractable
- Long life cycle capability
- High strength and torsionally rigid
- Provide strength and stiffness throughout the entire deployment/retraction operation
- Provide accurate and repeatable tip position alignment at any extended length
- Thermally controllable
- Packaging flexibility with a minimum boom ploy length

Those features considered preferable but as a goal were:

- Elimination of sharp edges
- Ease of manufacture for cost purposes
- Adaptable to use with various materials, i.e., non-magnetic, low outgassing, etc.
- Adaptability for positive boom drive (not friction drive)
- Lightweight boom
- Adapt to a wide temp range
- Unlimited extended length selection
- Eliminate expensive heat treat operations
- Easily expand boom size without increasing deployment mechanism complexity

DESIGN APPROACH

After reviewing numerous concepts, it was determined that to satisfy most of the criteria the mast should fit the following description:

- Equilateral triangle mast configuration
- Elements stored in an unlocked configuration
- Locking method along edges and internal to the formed mast
- Close tolerance locking pin
- Identical configuration for each element of the mast

The first choice of material for development and proof of concept was beryllium-copper. This was chosen for a number of reasons including familiarity with material from previous programs, non-magnetic for instrument appli-

cations, relatively inexpensive for development work and availability.

The next step was to develop a method for interlocking the individual strips of material. The locking devices had to have the capability of being flexible enough to wrap around the storage spool when in the stowed configuration and yet be stiff and strong enough to take bending and torsional loads when the mast was deployed. The selected design was to utilize a series of tapered cone type of fittings attached within rolled tabs located along the length of each strip of material. These nested fittings along the full length of the deployed mast become the load carrying path of the mast. The rolled tabs were located so that they would be internal to the formed mast, thus creating a smooth external surface which would pose no major deterrent to potential EVA activity in the vicinity of a deployed structure.

A conscientious effort was made throughout the interlocking edge development to keep each element identical to the others. This was done mainly to maintain the commonality of parts and therefore keep the manufacturing costs as inexpensive as possible. As a result of this effort, we were able to meet that objective.

Because results on previous programs with coatings and other methods for controlling thermal distortions have proven our understanding of the problems and our ability to cope with them, it was decided to forego any demonstration of these technologies on this program at this time.

ELEMENT FABRICATION

The following manufacturing method has been formulated for producing 60 inch lengths of elements which are sufficient for proof of concept and properties testing purposes. This method is fairly simple, relatively inexpensive, and very similar to a projected production type operation. To date, test samples have been fabricated in both 2 inch and 4 inch sizes (measured length of each leg of triangle). The following materials are utilized for the various components of the mast:

- Element sides - 7 mil. beryllium copper
- Fittings - 3/16 inch diameter stainless steel
- Bond - Tin lead alloy solder

The mast wall segments have been fabricated from flat, ribbon type, Be Cu material. They have an identical alternating edge tab design that is punched with controlled high tolerance spacing and alignment. After pre-shaping the tabs into a full round tube form, the entire wall segment length is heat treated to a final full strength condition. Interlocking fittings, fabricated from stainless steel, are then inserted into each of the rolled tabs. These patented fittings form the primary interlock between the mast wall segments. They are held into position within the rolled tab by flanges located at each end and, in addition, each of the tabs is secured along the open seam with a resistance solder joint. At this point, the three wall seg-

ments are ready for interlocking into a triangular mast.

The measured weight of a 4 inch wide triangular mast is .54 lb/ft. No attempt was made to make the initial mast configuration weight efficient. However, it was realized that significant lightening could be effected, without significantly reducing mechanical properties, through a pattern of circular, triangular or other cutouts between the triangular apexes.

MECHANICAL TESTS

Mechanical test performed on the mast specimens consist of applications of torsional and lateral loadings. A fixed-free condition was simulated by embedding one end of the mast in Cerrobend as shown in Figure 3.

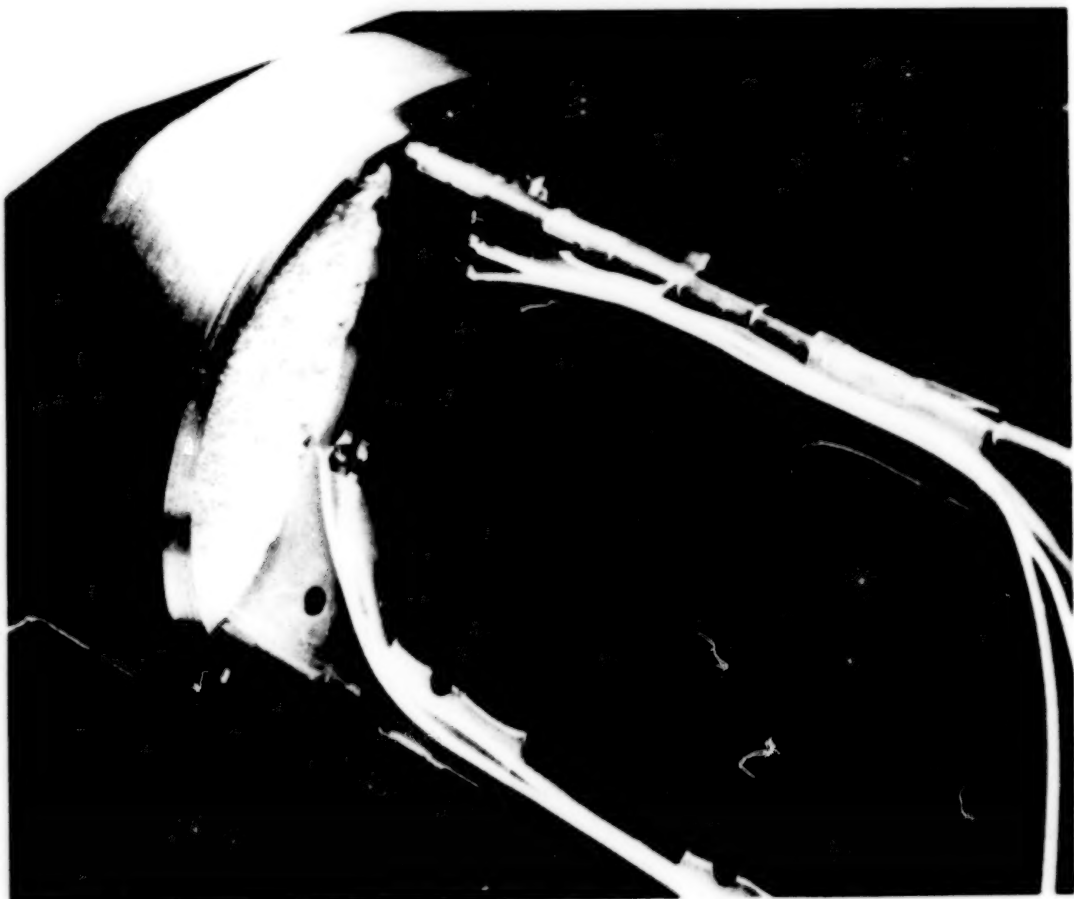


Figure 3

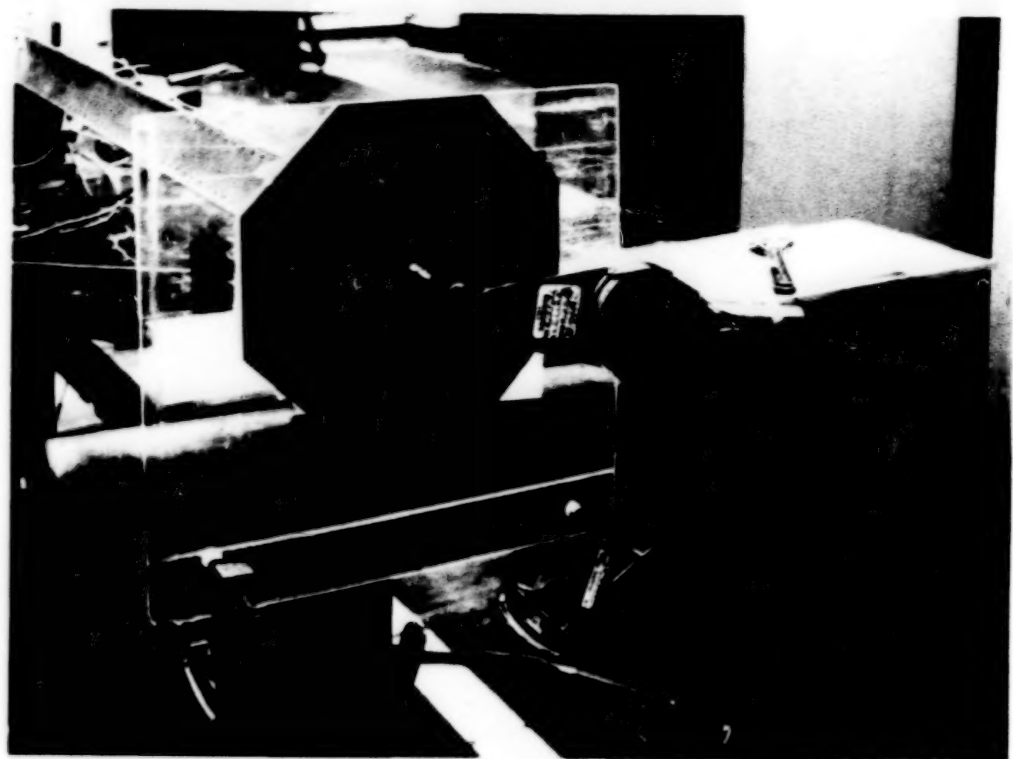


Figure 4

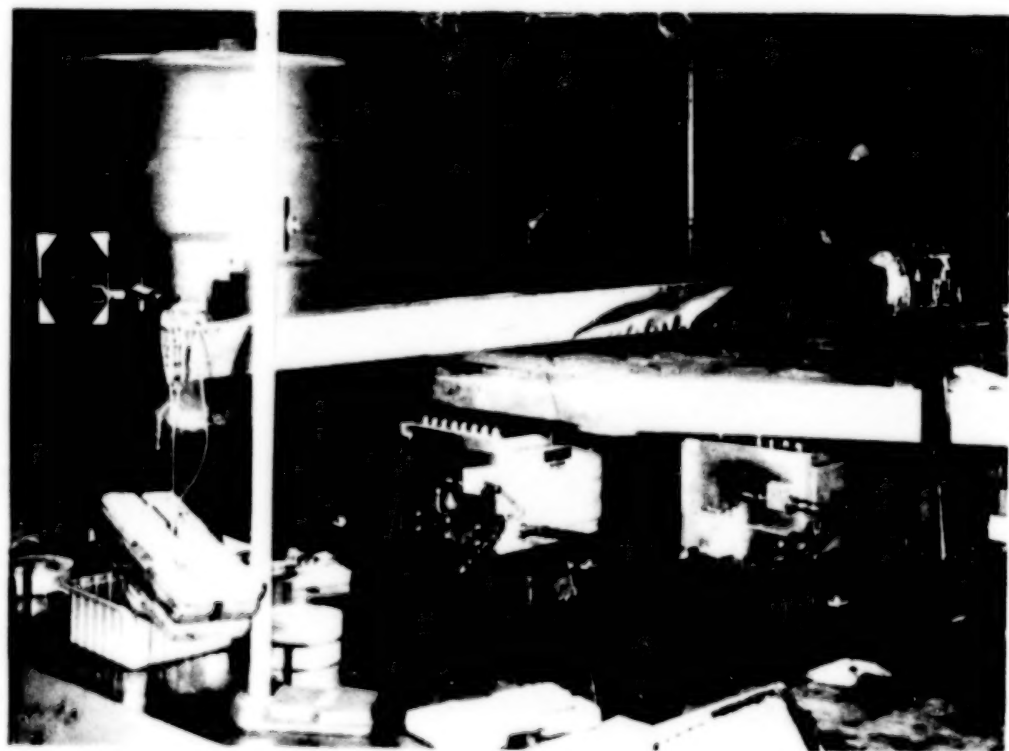


Figure 5

TORQUE TEST

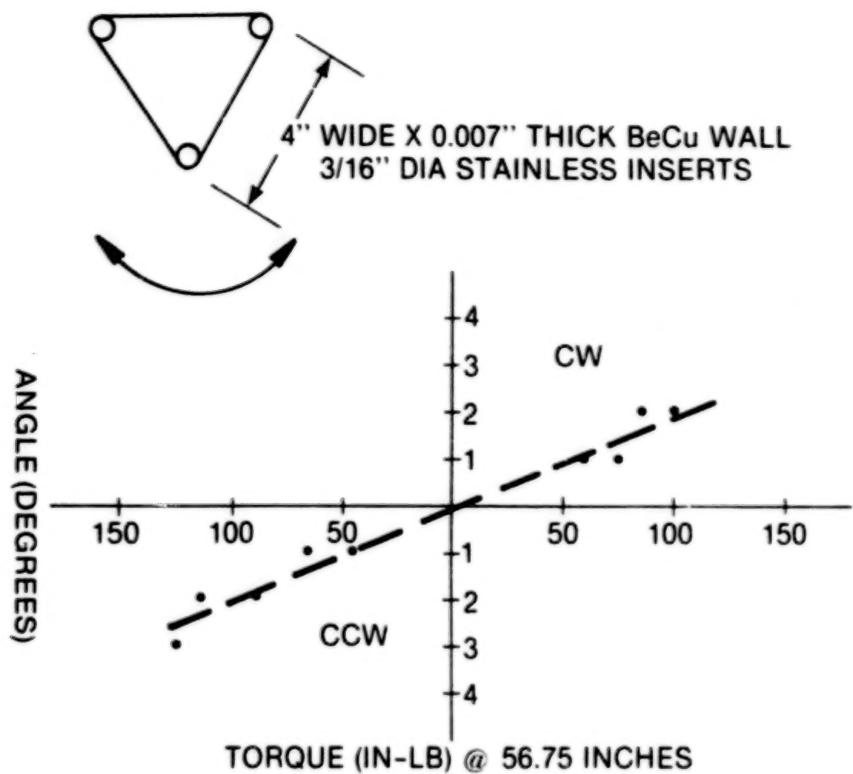


Figure 6

BEND TEST

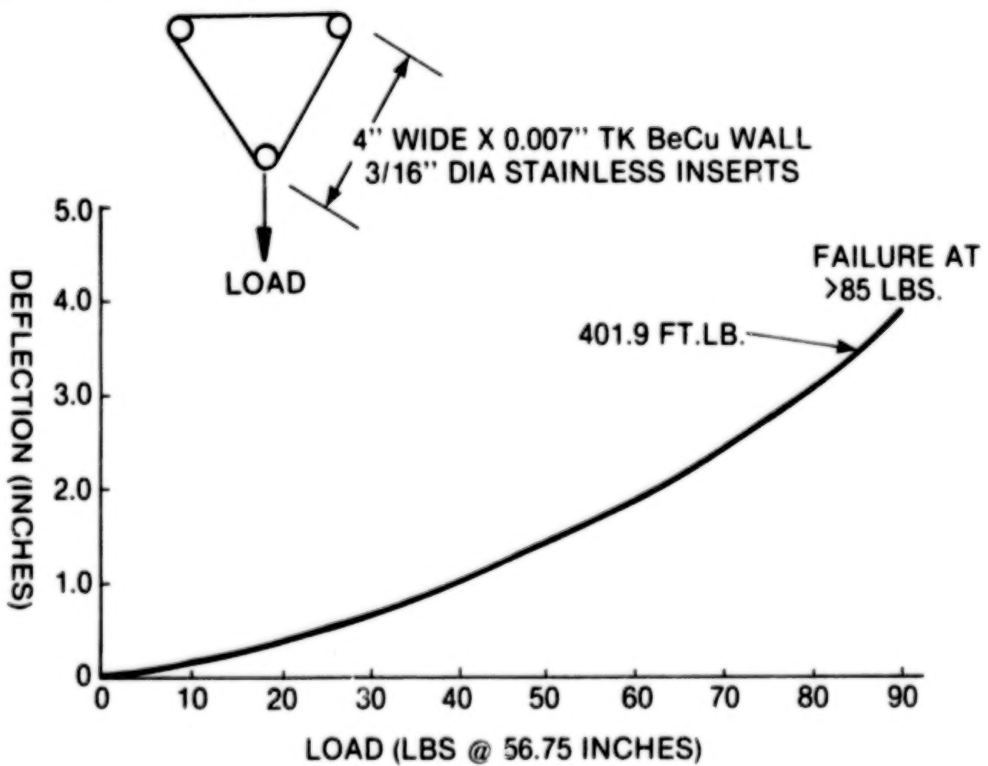


Figure 7

Testing of the mast under torsional and lateral loading conditions was conducted as shown in Figures 4 and 5 respectively. The test results clearly show that the 4 inch wide by 56 inch long mast specimen is capable of torsional forces greater than 100 in. lbs. and lateral forces of greater than 400 ft. lbs. Figures 6 and 7 present recorded load-deflection data.

CYCLE ALIGNMENT TEST

A preliminary deployment alignment/cycle test has been performed with a 2 inch wide triangular mast sample. The mast sample was cycled from a motorized deployment unit. This unit, although designed for demonstration purposes and fabricated from plexiglass, produced sufficient control of the sample mast for optical measurements of the tip position at several extended lengths. The mast was extended vertically under no load conditions and measurements taken between extend/retract cycles numbering 65 through 75.

Measurements of .005 inch maximum variance in both x and y axis were recorded at the full extended tip position of 36 inches. This equates to a repeatable static alignment of .008 degree. The test set up is shown in Figure 8.

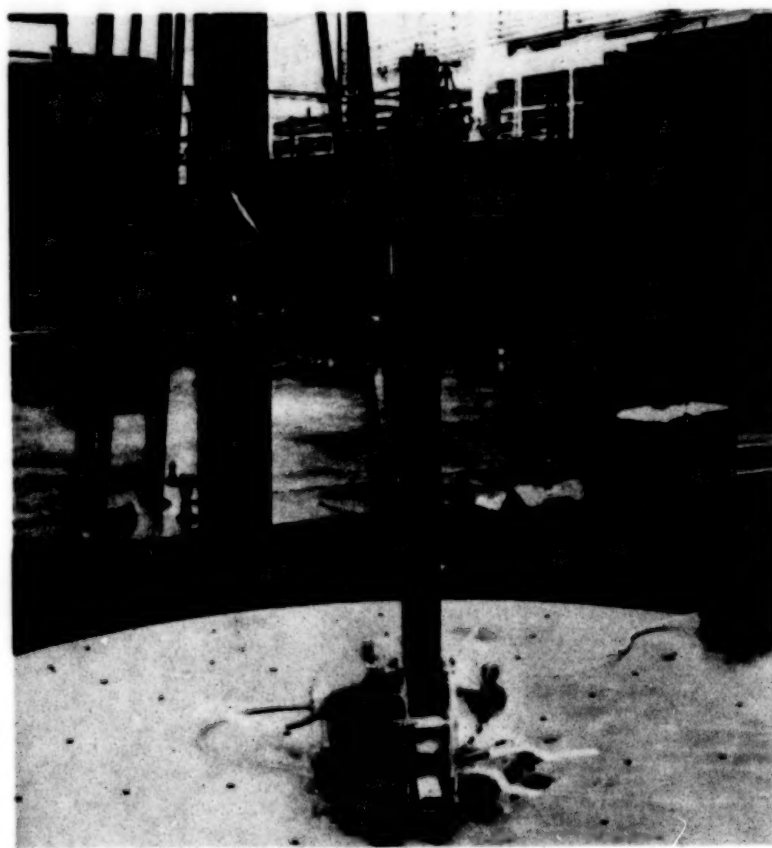


Figure 8

DESIGN EVOLUTION

Finally, after all the concepts have been evaluated and thought out, the real proof is in the fabrication and testing of the hardware. Tolerances that are too tight result in a mast that is difficult to lock and would probably cause jamming of a mechanism. If the tolerances are too loose, the torsional rigidity and bending movement capability is compromised. Some of the problems encountered during the development are hereby presented.

These problems were identified during destructive testing or as a result of test failure mode analysis. The interlocking fittings originally had a stackable straight tubular form and were secured into the curled tabs along the edges of the Be Cu wall by a series of spot welds. These fittings were, at that time, fabricated from brass alloy because of the desirability to utilize as little magnetic materials as possible and because brass is easy to machine and easy to spot weld. Test results of these mast samples showed that the spot welds had failed under test loads. As a result, a structural adhesive, 3M2216A/B, was then selected to replace the spot welds. Test results of these mast samples showed that the failure occurred as a result of compression yielding of the brass fittings and yielding of the fitting bonding agent. The fittings were then redesigned. Flanges were added at each end to provide primary sheer support and positioning within the tab. Also, the fitting material was changed from brass to stainless steel and a solder alloy was selected to secure the curled tabs. To date, testing has demonstrated that this is a successful design combination.

CONCLUSIONS

The mast development has met all the major criteria established at program initiation. The results presented verify that a high bending moment, high stiffness, torsional rigidity and a high degree of positioning/repeatability can be incorporated into a deployable/retractable unit.

Blank Page

CANNON LAUNCHED ELECTROMECHANICAL CONTROL
ACTUATION SYSTEM DEVELOPMENT

JAMES G. JOHNSTON*

ABSTRACT

The evolution of an electromechanical control actuation system (EM-CAS) from trade study results through breadboard test and high-g launch demonstration tests is summarized in this report. Primary emphasis is on design, development, integration and test of the gear reduction system.

INTRODUCTION

Future small missiles will likely use infrared (IR) or radar frequency seekers and are expected to operate over increased ranges. Size, weight, and bandwidth limitations of pneumatic control actuation systems will almost certainly compromise the design of the missile system and necessitate a close examination of possible CAS alternatives.

Trade studies conducted at Martin Marietta Aerospace during 1981 for a Direct Fire Projectile Study resulted in identifying the electromechanical control actuation system (EM-CAS), shown in Figure 1, as the most likely candidate for improved performance at lower weight and cost compared to pneumatic and hydraulic systems. Proper selection of gearing and gear ratios to match load requirements to the dc motor characteristics was important in optimizing the system.

During the last half of 1981, Martin Marietta undertook a program to design and fabricate a breadboard electromechanical actuator which successfully proved performance feasibility.

The 1982 CAS development program was the direct result of CAS Trade Studies, breadboard development, and computerized performance simulation completed in 1981. The long range objective is to develop a baseline design for a family of small missile electromechanical control actuation systems. Specific objectives for 1982 were:

1. To establish and optimize the component parts and assembly configuration of a prototype EM-CAS.
2. To demonstrate the performance capability of the prototype CAS in laboratory tests.
3. To demonstrate the suitability of the prototype CAS for small missile applications by exposure to a high-g launch environment.

During 1982, a prototype EM-CAS for a 155 mm cannon launched projectile was designed, fabricated, tested, and canister launched at temperatures from -45°F to +145°F at 9000 to 10,000g's acceleration with excellent results. Selection of gear reducer types and ratios was of primary importance in ensuring hardness to withstand high acceleration and ensuring a high efficiency gear train to minimize energy consumption from the missile battery system. Reducer trade studies comparing spur gear, ball screws, worm gears, spiroid gears and gear combinations were made with a compromise of acceleration hardness, energy consumption, and complexity to optimize production cost. Design of the dc servomotor and brake, as well as packaging the electronics, was also influenced by the high acceleration hardness requirements.

*Martin Marietta Aerospace, Orlando, Florida

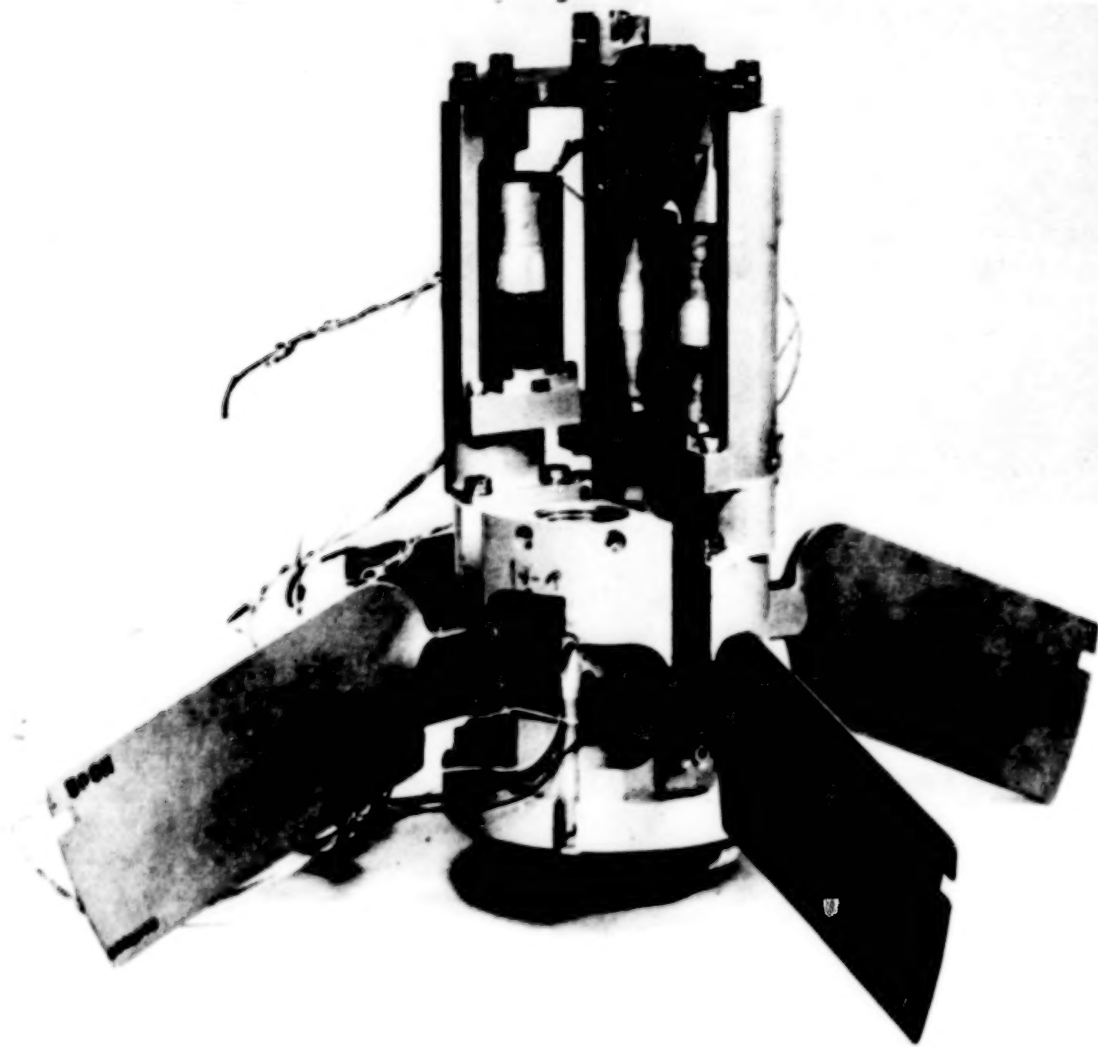


Figure 1. EM-CAS

The ability of an EM-CAS to meet the requirements of small guided projectiles has been demonstrated through detailed analysis, computer simulation, breadboard testing, and five prototype 10,000g canister launches. Breadboard testing using motors from 3 vendors demonstrated that the EM-CAS could meet bandwidth and slew rate requirements for a typical small missile (155 mm). Power analysis and bench tests demonstrated that power requirements are not prohibitive for a direct drive servomotor EM-CAS.

Overall, an EM-CAS using a samarium cobalt servomotor will compete favorably with pneumatic and hydraulic systems because of its inherent simplicity, reduced weight and envelope, and increased bandwidth (over pneumatic). Cost studies indicate that the EM-CAS will also be price competitive.

BREADBOARD DEVELOPMENT

The objectives of breadboard development were to establish EM-CAS technology and expand and verify the EM-CAS data base. To meet these objectives, the breadboard was designed with maximum flexibility for

accepting different motors and gear reducer configurations (spur gear, worm gears, ball screws, etc.) while incorporating tailored electronics.

The mechanical assembly shown in Figure 2 consists of existing projectile pitch shaft fin, bearing, and feedback potentiometer; as well as a tension spring loading fixture and adjustable mounting brackets which accept different motors and gear reducers.

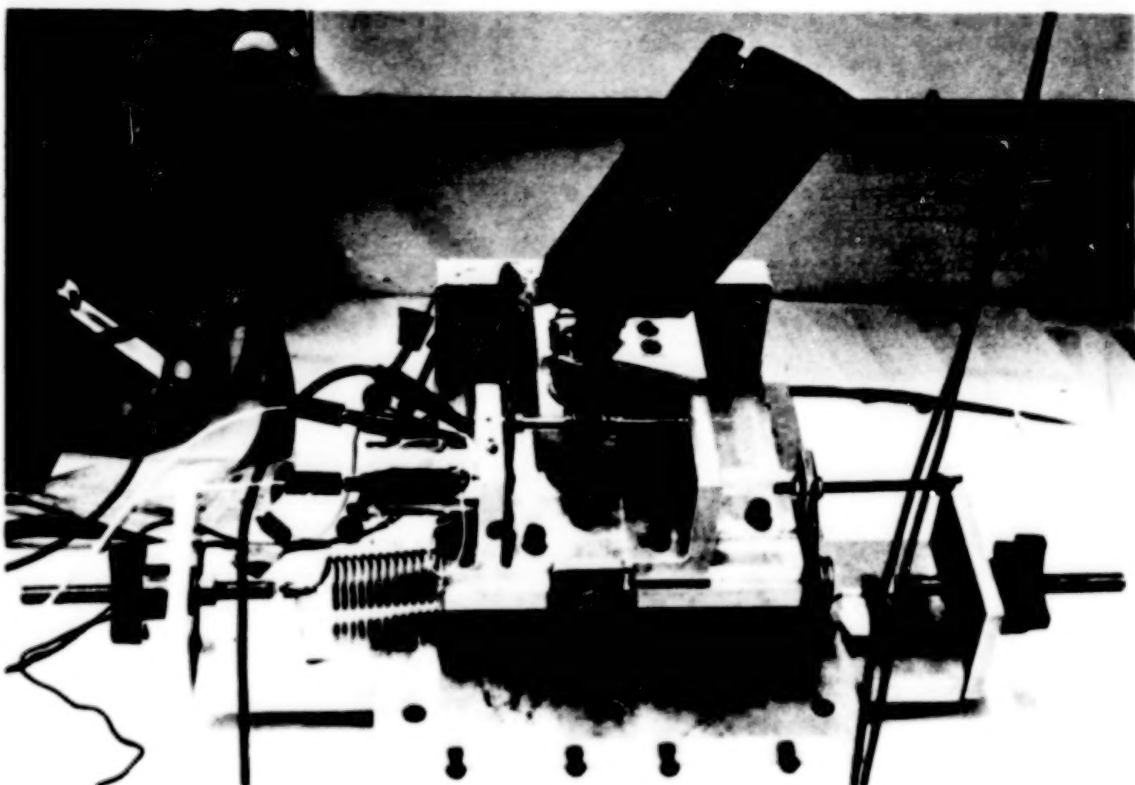


Figure 2. Mechanical Assembly

Tests were performed on two brush motors (Simmonds Precision and Inland Motors) and one brushless motor (MPC). Gear ratios were selected for each motor based on motor speed/torque capability and on a compromise between output load and frequency response. Tests were run for each motor to find frequency response, step response, and stall torque. Frequency response of 22 to 29 Hz, fin rates of 500 degrees per second, and stall torques up to 31.4 Nm (278 in lb) were demonstrated.

EM-CAS PROTOTYPE REQUIREMENTS

EM-CAS prototype requirements, primarily based on 155 mm projectile specifications, are summarized in Table I. Using these prototype requirements, dc motor/brake requirements were established (Table II).

EM-CAS SYSTEM DESCRIPTION

A photograph of the electromechanical actuator for a 155 mm cannon launched projectile is shown in Figure 1. Three independent axis of control (pitch, yaw plus roll, and yaw minus roll) requires three motor and gear train combinations. For expediency, simplicity, and lower cost, it was decided that all three motor and gear reducers are identical even

Table I. Prototype Requirements

Stall Torque (min per fin)	6.22 Nm (55 in lb)		
Loaded Rate (5.09 Nm per fin min)	120 deg/sec		
Shaft Deflection-Yaw/Roll Axes	± 22 deg		
Pitch Axis	± 17 deg		
Duty Cycle Duration(-25°F to +145°F) (all fins)			
Command	<u>Offset</u>	<u>Torque Rate/Fin</u>	<u>Duration</u>
$d_c = 3 \sin 20t$	2.33 deg	0.339 Nm/deg (3 in lb/deg)	50 sec
$d_c = 5 \sin 20t$	2.33 deg	0.339 Nm/deg (3 in lb/deg)	20 sec
			Total 70 sec
Frequency Response (+2.5 deg command)			
Axis	Offset	Torque Rate	Frequency Response
Pitch	10 deg	0.283 Nm/deg (2.5 in lb/deg)	12.1 Hz min at -80° lag
Yaw/Roll	15 deg	0.142 Nm/deg (1.25 in lb/deg)	14.32 Hz min at -75° lag
Environment			
Temperature (soak)	-25°F to +145°F		
Set Back	10,000g		
Set Forward	1,900g		
Lateral	750g		
Angular	75,000 rad/sec ²		
Radial	345g		
Electrical Power Requirements	Use Existing Battery (28600 Joules allowance)		

Table II. Torque Motor and Brake Performance Requirements

Parameter	Symbol	Unit
Torque (rated)*	T _r	0.106 Nm (15 in oz)
Current (armature rated)*	I _r	6.5A (6.5 amps)
Voltage (armature rated)	V _p	25V (25 volts)
Speed (rated)*	RPM	6000 min ⁻¹ (6000 rpm)
Maximum Applied		
Armature Voltage	V _{tm}	35V (35 volts)
Maximum Applied		
Armature Current	I _{tm}	16.7A (16.7 amps)
Torque constant*	K _{tm}	0.0162 N _p A/(2.3) in oz/amp
Rotor Inertia (max)	J _t ^m	21.2g cm ² (3x10 ⁻⁴ in oz-sec ²)
Armature Resistance at 25°C	R _A	2.1Ω (2.1 ohms)
Coulomb Friction (max)	T _c	0.00752 Nm (1.064 in oz)
Envelope (motor and brake)		3.175 cm Ø x 7.62 cm long (1.25 in Ø x 3 in long)
Brake Torque	T _b	0.071 Nm (10 in oz static dynamic)
Brake Voltage (dc)	V _b	30 ± 5V (30 ± 5 volts)
Brake Reaction Time (max)	t _b	0.010 sec (0.010 sec)
Brake Current (max) (25°C)	I _b	0.150A (0.150 amps)
Brake Inertia (max)	J _b	1.13g cm ² (0.16x10 ⁻⁴ in oz-sec ²)
Environment - As per Table I		

*Worst case tolerances and temperatures

though the pitch axis requirements were essentially twice the yaw/roll axis. The fins, fin shaft and bearing arrangements, feedback potentiometers, battery location, and all other useable parts that could be retained from a prior 155 mm missile system were used. The spur gear/worm gear combination was selected for the gear reducer because of breadboard demonstration, hardness, availability, low cost, and other lesser trade study criteria.

The electronics was packaged in the aft end of the control housing due to envelope and structural constraints and because a large inherent heat sink is available. Photographs of the major components and the complete assembly with fins folded are shown in Figures 3 and 4.

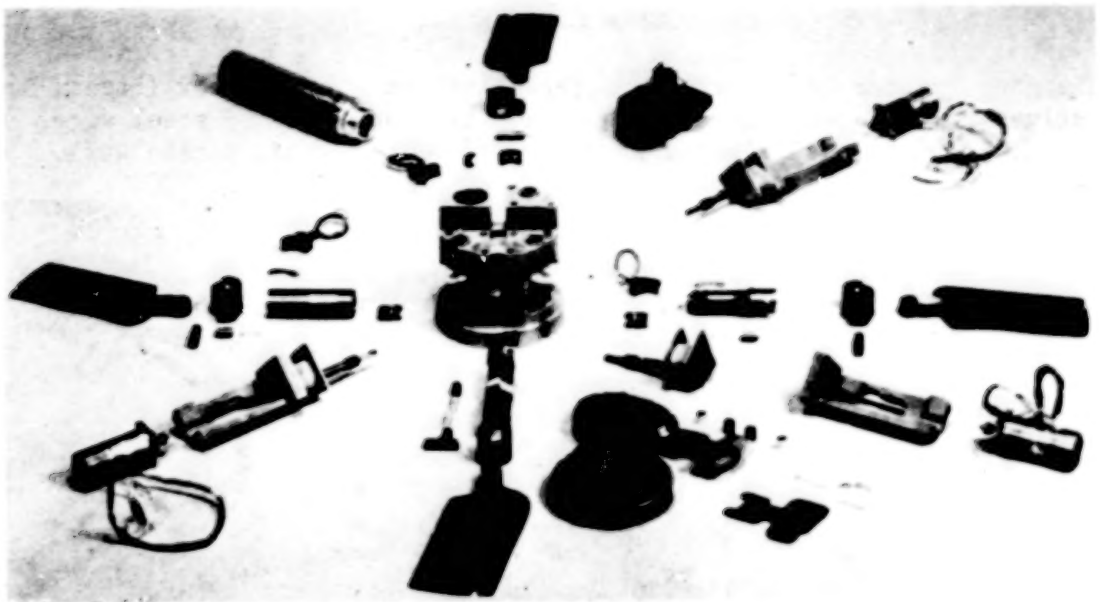


Figure 3. Major Components

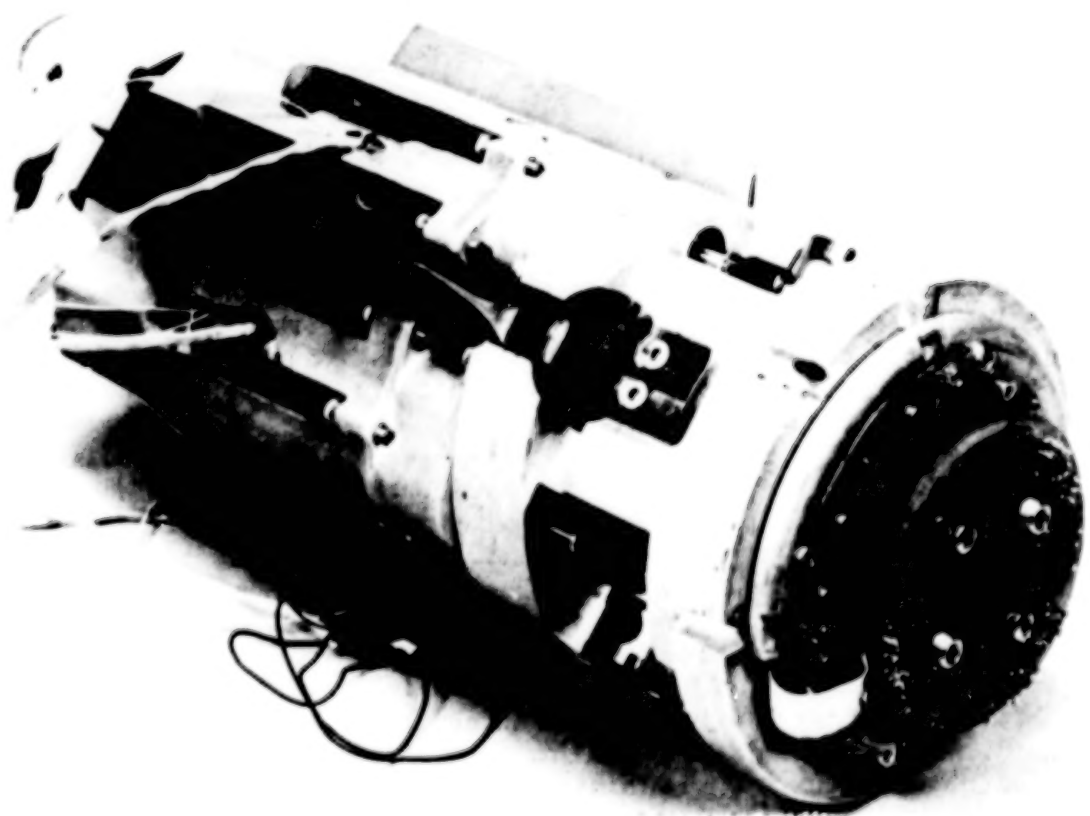


Figure 4. EM-CAS Electronics End with Fins Folded

GEAR REDUCER

The gear reducer consists of a 3.89/1 aluminum spur gearbox (Figure 5) which drives a worm gear segment with a two-threaded hardened steel worm. The overall gear ratio from motor shaft to fin output shaft is 194.44/1.

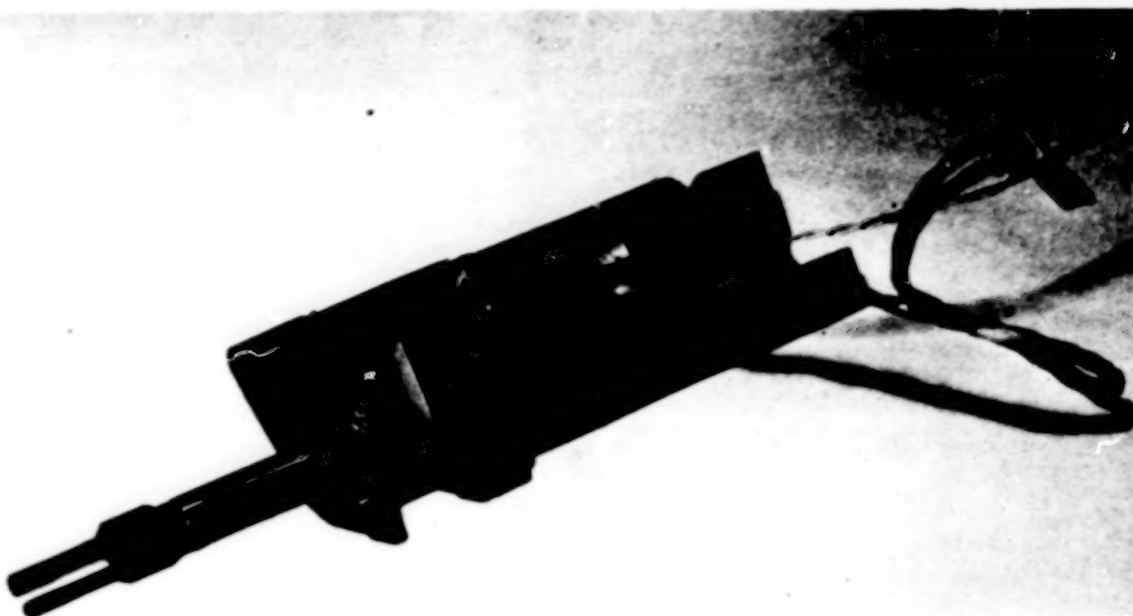


Figure 5. Gear Reducer

All spur gears are 2024-T4 aluminum, AGMA-12 precision from Pic Gear Corp. The worms and worm gears were purchased from Reliance Gear Co., Ltd. Worm gear material is QQ-S-763 class 10 steel (440B), and the worm is heat treated 1117 steel.

The gearbox was designed to provide flexibility in changing gear ratio and to minimize backlash on the output worm shaft. Gearbox ratios from 2/1 to 7/1 are feasible permitting selection of overall reducer ratios from 100/1 to 350/1. A gearbox ratio of 3.89/1 (194.44/1 overall) has proven optimum for the selected motor.

The bearings (KP3AL and KP3A) used in the gearbox were standard aircraft ball bearings supplied by TRW. The KP3A bearing was installed to carry the forward and aft thrust loads of the worm shaft in addition to radial loads. Any axial movement of the worm shaft translates directly into backlash on the output fin shaft. To minimize axial movement, the shaft was shimmed tightly on each side of the KP3A thrust bearing, and the bearing was installed with a 0.0178 mm (0.0007 in) mean tight fit in the aluminum housing and a 0.0076 mm (0.0003 in) mean tight fit on the steel shafts. This installation reduced internal bearing axial movement from 0.076 mm (0.003 in) to 0.013 mm (0.0005 in) as demonstrated by tests. Additional assurance of minimizing worm shaft axial movement was obtained by installing a disk spring beneath the KP3AL gearbox bearing and pre-loading the worm shaft to 68 Kg (150 lb) of thrust load.

Additional investigation to minimize backlash considered the required gear precision and centerline location tolerance. Results of this analysis are shown in Figure 6 where fin backlash is plotted against axis center tolerance for AGMA-10, AGMA-12, and AGMA-14 gears. Maximum backlash tolerated by the actuator fin shaft was established at 0.25 degree.

This analysis assumes no play in the gear shaft bearing. As a result of this analysis, AGMA-12 gears and 0.051 mm (0.002 in) axis center tolerance were selected.

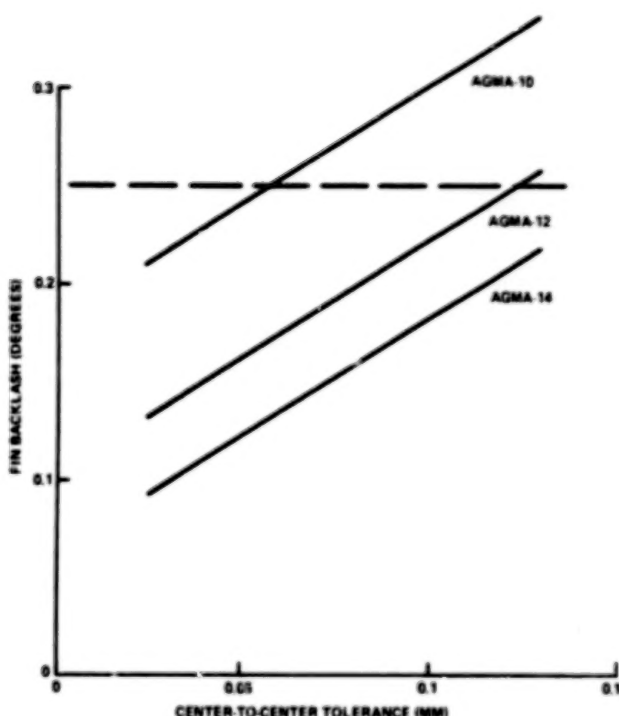


Figure 6. Centerline Tolerance Effects on Backlash

The spur gears and worm gear set are lubricated with FEL-PRO C100 grease which contains stabilized molybdenum disulfide and lead in an organic viscous carrier. The ball bearings were supplied presealed and prepackaged with lubricant conforming to MIL-G-23827.

Gear Reducer Trade

A trade study of various gear reducers was made for the purpose of designing the cheapest actuator which is capable of operating for a minimum of 70 seconds at the specified duty cycles and using an existing system battery. Results of this trade study are shown in Table III.

The single worm, the lowest cost and least efficient reducer, will only give 58 seconds of flight duration. The double-threaded worm will provide 70 to 82 seconds of flight duration and costs slightly more than the single worm. The four-threaded worm concepts offer little increased flight duration to justify the cost increase. The spiroid gear concept gives less duration for a higher price; however, it has the positive feature of almost zero backlash. The spur/bevel gear will achieve the same flight duration as the ball screw (max of 85 to 88 seconds) for a lower cost; however, it probably cannot be packaged in the available envelope. The ball screw is too expensive and will probably not withstand the 10,000g setback launch loads. Cost and high packaging risk eliminates the spur/bevel gear from further consideration. For these reasons, the double-threaded worm was selected for the EM-CAS prototype.

Table III. Reducer Trade

	SPUR/BEVEL	BALL SCREW	SINGLE WORM	2-WORM	4-WORM	SPIROID	4-WORM
DIA PITCH	0.52917M (48 dP)	— —	0.52917M (48 dP)	0.52917M (48 dP)	0.52917M (48 dP)	— (24 dP)	1.05833M (24 dP)
OTHER GEARS	0.26458M (96 dP)						
RATIO	NOMINAL 200/1	200/1	200/1	200/1	200/1	200/1	200/1
MAXIMUM OBTAINABLE	250/1	248/1	600/1	300/1	250/1	400/1	250/1
STAGES	4	2	2	2	3	2	3
WEIGHT (KG) (COMPONENTS ONLY) (LBS)	0.837 (1.845)	0.313 (0.69)	0.472 (1.04)	0.476 (1.05)	0.658 (1.45)	0.680 (1.50)	0.680 (1.50)
COST S/CAS (PARTS ONLY)	\$258	\$443	\$105	\$168	\$205	\$250	\$205
COST S/CAS	+153	+338	0	+63	+100	+145	+100
MAXIMUM MOTOR (INM) TORQUE (IN OZ)	0.088 (12.46)	0.0866 (12.26)	0.165 (23.32)	0.124 (17.54)	0.1074 (15.2)	0.2304 (32.6)	0.1023 (14.48)
MAXIMUM CURRENT LIMIT (AMPS)	5.24	5.16	9.81	7.38	6.39	13.71	6.09
BATTERY ENERGY (JOULES)	7071/ 6839	7038/ 6869	10.435/ 7916	8662/ 7324	7936/ 7100	10522/ 10383	7686/ 7068
DURATION-MIN (SEC) MAX (SEC)	85 88	85 88	58 76	70 82	76 85	57 58	78 85
BACKLASH - MAX (DEG)	0.05	0.20	0.20	0.26	0.3	0	0.3
10,000g SENSITIVE	LOW	VERY HIGH	LOW	LOW	LOW	LOW	LOW
PACKAGING RISK	HIGH	MED.	LOW	LOW	MED	HIGH	MED
SELECTION	2	6	3	1	4	7	5

Gear Reducer Efficiency Analysis

Gear efficiency prediction is inexact because surface finish, lubricant, temperature, rubbing speed, accuracy of teeth, and installation all influence gear effectiveness in transferring power from one gear to the other.

According to Mark's Engineering Handbook, the efficiency of worm gearing is approximately (dependent on thread angle (ψ) and coefficient of friction (f)) as follows:

$$\text{Efficiency, } E = \tan \psi \frac{(1 - f \tan \psi)}{\tan \psi + f} \quad \begin{aligned} \psi &= \text{Thread Helix Angle} \\ f &= \text{Coefficient of Friction} \end{aligned}$$

Friction data from several sources using different lubricants indicate that friction factors for hard steel rubbing on hard steel with pressures of 2.76×10^6 KPa (400 KSI) are 0.058 for graphite and 0.033 for molydisulfide. A grease consisting of molydisulfide and graphite was selected for this application.

For cylindrical worm gears (EM-CAS type) the variation of friction coefficient with rubbing speed for a carburized and ground steel worm and phosphor bronze gear was shown to vary from 0.08 to 0.03 for rubbing speeds from 12 to 254 cm/sec.

Using friction coefficient of 0.03 to 0.08 as boundaries, worm gear efficiency is plotted versus helix angle (ψ) in Figure 7. Breadboard test data for two different helix angles ($4^\circ 46'$ and $9^\circ 28'$) are also shown for comparison. Based on this data, EM-CAS worm gear efficiency of 60 percent to 80 percent is predicted.

Schematically, the gear train consists of four spur gears driving a worm gear set as shown in Figure 8. Assuming worm gear efficiencies predicted in Figure 7, overall gear reducer efficiency (from motor input to aerodynamic fin output) is predicted to vary with motor speed from 50 to 60 percent.

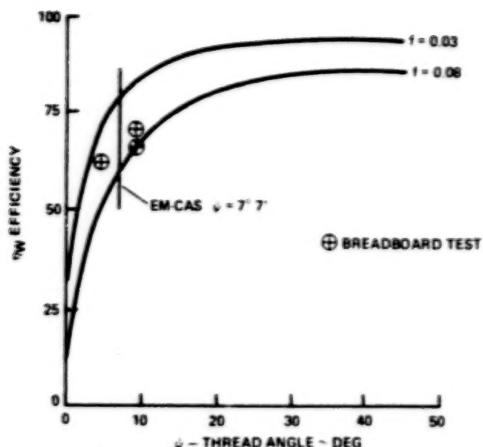
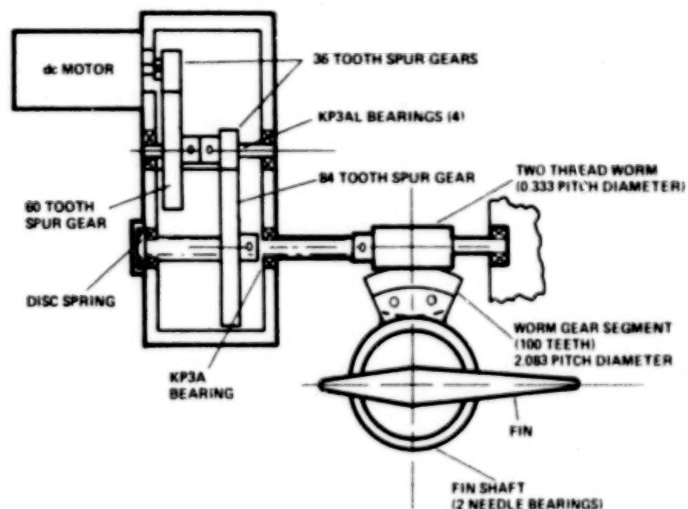


Figure 7. Worm Gear Efficiency

Figure 8. Gear Reducer Schematic



Gear Reducer Efficiency Test Results

Gear reducer efficiency tests were made to determine the effectiveness of the reducer in transmitting power to the aerodynamic fin. Separate tests had to be made on the dc motor, dc motor/gearbox, and EM-CAS to determine reducer losses and separate these losses into gearbox (spur gear) and worm gear components. These tests were made using the dynamometer test setup shown in Figure 9 and the EM-CAS test fixture.

Motor torque-speed performance with and without gearbox are compared in Figure 10. The gearbox efficiency curve, also shown, was derived from this test data and plotted against motor torque. Conclusions derived from this data indicates that at high torque (low motor speed), gearbox efficiency (N_{GB}) approaches 92 percent, as predicted, and reduces as torque decreases.

To estimate worm gear efficiency, it was necessary to operate the complete CAS under different load conditions and subtract the fin shaft bearings and gearbox losses. Results of these tests are plotted in Figure 11 showing that overall reducer efficiency is highly dependent on worm gear efficiency and that worm gear efficiency is 34 percent lower than predicted from analysis and breadboard test data. Detailed inspection of the worm and worm gear hardware revealed worm surface finish rougher than 20 microinch (RMS) and worm gear tooth surface finish rougher than 65 microinch

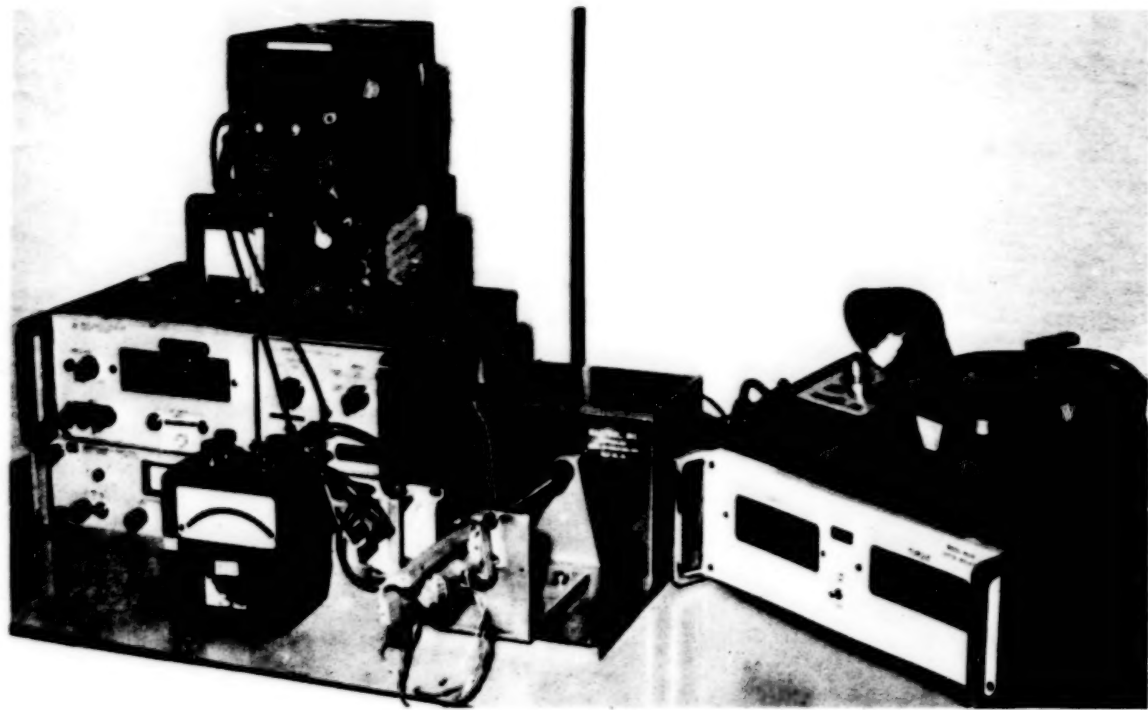


Figure 9. Dynamometer Test Set Up

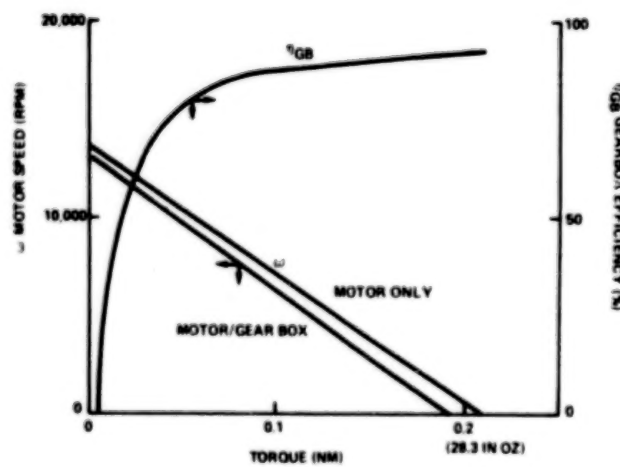
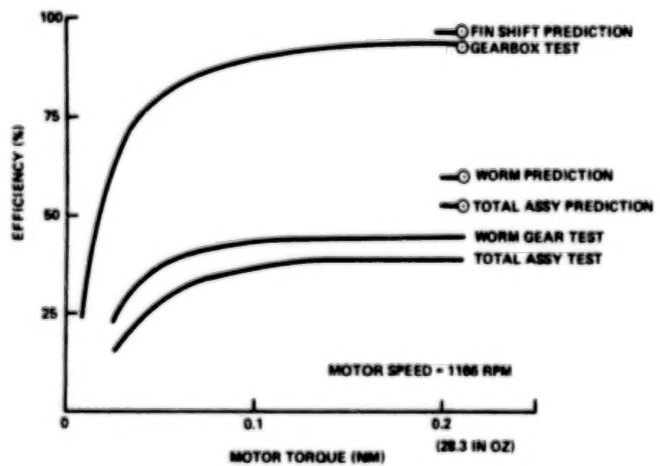


Figure 10. Gearbox Efficiency

Figure 11. Component Efficiency



(RMS). This compares with the breadboard worm and worm gear finishes which are smoother than 20 microinch (RMS). Test data found in literature indicates that the friction coefficient can increase from 80 percent to 300 percent as surface finish changes from 2 to 65 microinch (RMS). Therefore, rough surface finish is the most likely reason for the observed low efficiency of the worm gear.

DC MOTOR AND BREAK ASSEMBLY

The dc motor and brake assembly was designed, fabricated, tested and supplied by Inland Motors, Division of Kollmorgen Corp. A photograph of the disassembled unit is shown in Figure 12. The complete unit consists of a dc brush motor assembly and a brake assembly. The dc motor assembly consists of three main subassemblies: armature, field, and brush ring.

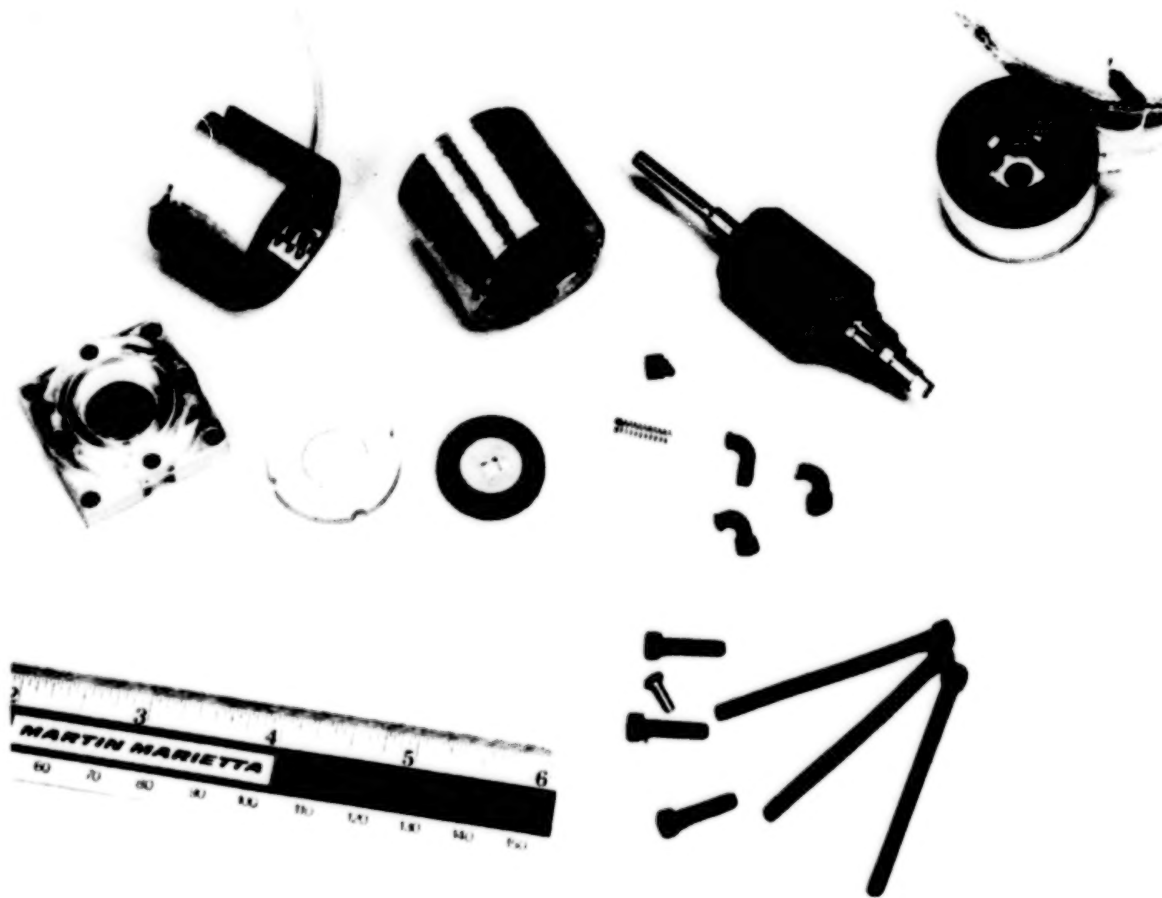


Figure 12. Disassembled Motor/Brake Assembly

The armature (rotor) assembly is made of thin laminations to reduce eddy current effects at high speeds and are bonded together to form the armature core which is insulated and wound with heavy insulation magnet wire.

The field assembly (stator) is the stationary outside case of the motor. Four radially oriented samarium cobalt magnets are bonded to a cold rolled steel yoke section and held physically in place on all four sides by shoulders.

A very small commutator diameter was chosen for this application to provide for better commutation at the higher operating speeds. In addition,

four cartridge brushes are used to provide better high speed commutation. The four brush housings, in addition to the two EMI capacitors, and wiring and shielding connections, are molded into a plastic housing which is sandwiched between the stator housing and spacer (aft bearing support). The rotor is mounted on two special load transfer bearings which limit ball load due to "set back" and "set forward" launch accelerations.

The brake consists of an armature, clapper, spring and housing assembly. The brake is failsafe which engages when power is off. The brake disengages the clapper from the armature when greater than 20 volts is applied to the brake coil. The brake will engage when this voltage reduces to approximately 5 volts.

The motor is designed to be pilot centered and flange mounted with four screws. Actual torque/speed test data on Inland Motor S/N 15 is plotted in Figure 13. For this motor, torque constant (K_T) measures 0.01674 Nm/amp (2.37 in oz/amp).

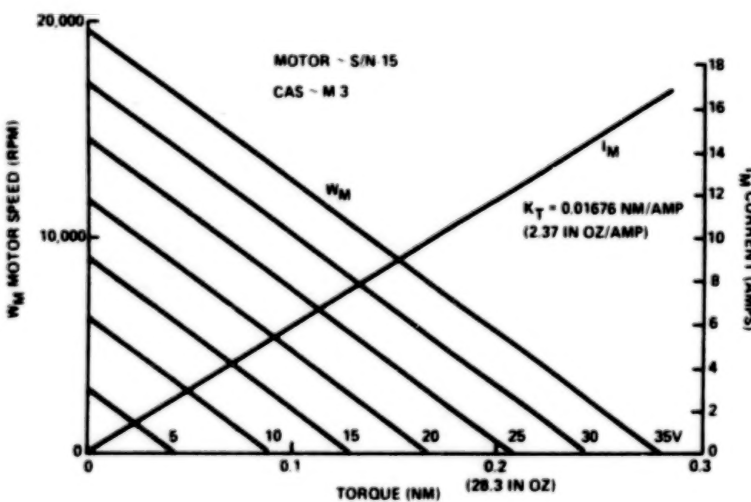


Figure 13. Motor Torque/Speed Characteristics

ELECTRONICS

The electronics package was designed, fabricated, assembled, and tested by Martin Marietta and consists of four shaped printed wiring fiberglass boards, an aluminum heat sink, and the required electronic components.

The first printed wiring board (PWB) is a two-layer board and carries the pitch, yaw plus roll (Y&R) and yaw minus roll (Y-R) command and feedback amplifiers. Error voltage is produced by summing the guidance commands with feedback position voltage.

The second PWB is a two-layer board and carries the dynamic lead/lag compensation amplifiers and the voltage limiting amplifiers.

PWB number 3 is a two-layer board and is attached to the aluminum heat sink which provides mounting for the four sets of complimentary pair of PNP and NPN Darlington power transistors. The board also provides capacitors to minimize crossover distortion and provides the circuitry to the power transistors.

The fourth PWB is a six-layer board and provides the amplifier for the summing junction currents proportional to commands and motor feedback currents proportional to motor speed. Phase lead compensation is provided for the phase lag due to the motor armature inductive lag.

CAS BENCH TESTS

Performance Tests

Performance tests were conducted to demonstrate compliance with the requirements. Low efficiency of the worm gear impacted the pitch axis in stall torque performance and the yaw/roll axes in frequency response performance. Both problems were solved by increasing electrical current limits in all three axes. A performance summary of the pitch and yaw/roll axis is listed in Table IV.

Table IV. Performance Summary

ITEM	REQUIREMENT	PITCH	EM-CAS AXIS		COMMENTS
			YAW+ROLL	YAW-ROLL	
STALL TORQUE (NM)	12.44	13.68			Pitch
(NM)	6.22		9.89	9.89	Yaw/Roll
LOADED RATE (DEG/SEC)	120	264	357	385	
FREQ. RESPONSE (HZ)					
AR = -3 dB	12.1 Hz	18 Hz	17.5 Hz	17.5 Hz	
ØLag = -75°	14.32Hz		18.0 Hz	18.0 Hz	
-80°	12.1 Hz	17.5Hz			

The required stall torque is 6.22 Nm/fin (55 in lb per fin) or 12.4 Nm pitch (110 in lb pitch). To eliminate the effects of inertia, stall torque was measured by imposing a slow triangle wave command into the EM-CAS electronics. For a pitch current limit increase of 50 percent, pitch axis stall torque increased 50 percent from 9.125 Nm (80.7 in lb) to 13.68 Nm (121 in lb).

Minimum loaded vane rate performance requirements are 120 deg/sec at 5.088 Nm/fin (45 in lb per fin)(10.18 Nm pitch/fin). The EM-CAS demonstrated 264 deg/sec in pitch and 357 deg/sec in the yaw/roll axes.

The ability of each actuator to follow triangle, square, and sine waves is evident in Figure 14. Very little backlash is displayed with the triangle and sine waves as the actuator crosses the zero axis. Note also that closed loop position error is very small. The zero overshoot shown in the square wave indicates damping close to critical which is also indicated in frequency response data.

Higher performance from the EM-CAS is possible by increasing current limits and gains; however, this increased performance requires additional battery power which reduces flight duration.

EM-CAS Battery Test

A series of tests on the EM-CAS were performed using energy supplied by a standard 1 7/8-inch diameter by 5 3/4-inch long thermal battery. Twelve tests were run: three ambient, five cold (-25°F), and four hot (+145°F). The purpose of these tests was to verify that the existing standard thermal battery could provide sufficient energy to operate the EM-CAS with simulated worst case flight duty cycles for a minimum of 70 seconds.

Other required loads were simulated with a 20 ohm resistor, and the three motor brakes released and held during tests using the B+ cell.

Eleven of these tests were performed with the initial electronic package which had the original current limits. One final battery test was conducted with the increased current limits required to meet stall torque and frequency response requirements.

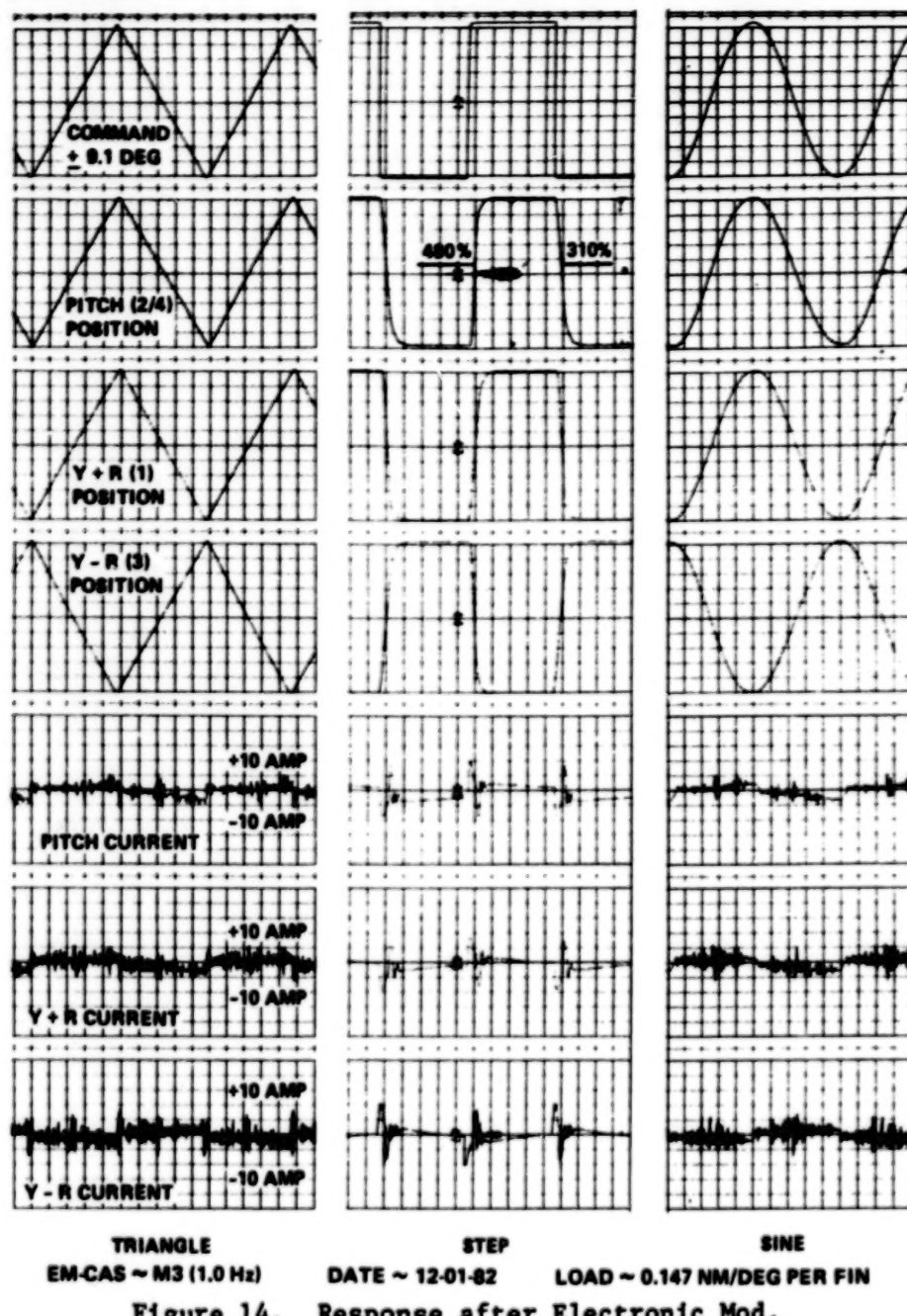


Figure 14. Response after Electronic Mod.

A comparison of average battery terminal voltage minimums for ambient, cold and hot soak conditions is shown in Table V. Battery terminal voltage minimums for the final battery test (high current limits) are shown in the last column of Table V.

Table V. Average Minimum Voltage/Time Conditions

TIME (SEC)	AMBIENT		COLD		HOT		FINAL TEST	
	+B	-B	+B	-B	+B	-B	+B	-B
3	34	32.5	33.5	33.2	33.5	31.5	36	35
50	32	29.0	31.2	32.7	32.2	30.2	35	32
70	29.5	28.5	26.2	30.4	29.7	27.7	34	30
100	29.5	21.0	21.7	25.2	29.2	23.8	34	26

*70 to 100 sec maximum current is supplied by the negative (-B) cell.

It is concluded from these series of tests that the existing thermal battery has sufficient capacity, even at high current limits, to operate the EM-CAS for the required flight duration.

MISCELLANEOUS TESTS

Miscellaneous tests during development to minimize failure risk included bearing thrust and "slop" investigations, and a hydrogen embrittlement study.

A thrust load test on the KP3A bearing selected to support the worm shaft was conducted to show bearing operability after a 50 percent thrust overload was imposed. As installed in the EM-CAS gearbox, the bearing showed acceptable operation after 1000 percent of recommended thrust load had been imposed, and the unsupported bearing withstood up to 400 percent of recommended thrust load before failure.

Hence, the selected KP3A bearing will safely carry the 1020 pound thrust load during launch without damage and will provide effective CAS operation afterwards.

Measurements were made on eight KP3A bearings to establish relative axial displacement between inner and outer bearing races for estimating bearing effects on backlash. Axial displacement on the free bearings varied from 0.051 to 0.102 mm (0.002 to 0.004 in). The bearings were then pressed into an aluminum housing and axial displacement was again measured. Results show that bearing axial displacement after pressing was less than 0.0127 mm (0.0005 in) in all measurements. These results showed that all bearings supporting the worm shaft must be pressed into their respective housings to minimize backlash.

Standard hydrogen embrittlement tests were performed on M4 and M6 metric screws which had been heat treated after plating.

CANNON LAUNCH TESTS

A total of five EM-CAS units were canistered and exposed to the gun launch environments as listed in Table VI. Three units (M1, M2 and M3) were assembled by Martin Marietta. Two assemblies (D1 and D2) were produced by Diehl GmbH & Co., West Germany. The pitch axis gearbox with a Lucas motor, assembled by Diehl, was present in the M1 unit. The Y+R and Y-R axes had Martin Marietta gearboxes and Inland motors.

Table VI. Canister Launch Test Summary

Unit	Date Launched	Unit Temp. °F	Setback g's	Acceleration	Post Launch Results
M1	7-16-82	Ambient	9,356		Circuit Card Spacers Failed
D1	8-18-82	-45°F	10,058		No Structural Anomalies
M2	8-18-82	-45°F	10,084		Circuit Card Screws Failed
D2	9-09-82	+145°F	9,960		No Structural Anomalies
M3	9-09-82	+145°F	9,900		No Structural Anomalies

All five 83.5 Kg (184 lb) projectiles were launched and parachutes recovered at the Redstone Arsenal in Huntsville, Alabama, using the 203 mm (8 in) cannon.

Hardware failures in the first and third tests were attributed to perimeter screws on the heat sink which were too long. The package was loose and free to move on the four perimeter screws during setback acceleration. The phenolic spacers in the first launch absorbed the setback

shock and failed. The substitution of aluminum spacers produced a more efficient joint which was capable of transmitting the circuit card inertia to the two M5 screwhead shoulders with subsequent tensile fracture. With the shorter length screws installed in the last tests, no further failure occurred.

PROBLEMS ENCOUNTERED AND SOLVED

Mechanical and electronic problems encountered and solved during development are summarized in Table VII. Excessive shaft axial clearance coupled with bearing clearances made the actuator pitch axis sensitive to limit cycle. This appeared as backlash to the actuator and when the shaft was properly shimmed, the problem disappeared.

Table VII. Problems Encountered and Solved

<u>Problem</u>	<u>Solution</u>
Excessive Shaft Axial Clearance	Redesigned Shaft Retainer to Accept Shims
Collar Flange Interference with Housing	Chamfered Housing
Rubbing Segment Gear Rollpin	Installed Shorter Pin Flush with Bottom
Motor Wiring/Cover Interference	Special Cutouts in Gearbox Covers
Phenolic Bushing Failure	Changed Material to Aluminum
Electronic Package Screw Failure	Reduced Perimeter Screw Lengths to Prevent Blind Hole Bottoming
Low Gear Reducer Efficiency	Increased Motor Current Limit
PWB Numbers 1 and 2 Cross Talk	Added Grounded Copper Shield to M1, Circuit Changes on M2 and up Eliminated Requirement
PWB Numbers 2, 3 and 4 Conductor Errors	Hard Wired Correctly and Epoxyed in Place
Heat Sink Grounding	Added Grounding Screw
Darlington Transistor Noise Sensitivity	Added Filter Capacitor and Epoxyed to PWB Number 3
Heat Sink Screw Head Position Inspection	Added Cutouts in Heat Sink
Low Bandwidth in Current Amplifier	Added R-C Integrator in Feedback Circuit (Epoxyed in Place)
Spacer Frame Component Interference	Spacer Frame Modification

The phenolic bushing failure on the first cannon launch was solved by using an aluminum material, and the screw failure on the third launch was solved by using shorter perimeter screws and confirming proper seating by visual inspection.

Cross talk between boards, conductor errors and grounding problems were finally solved by circuit changes and hardwiring. Conductor and component modifications were epoxied to the printed wiring board after checkout, and survived the cannon accelerations very well. Circuit changes had to be made to balance outputs and increase current limits for stall torque and bandwidth requirements.

CONCLUSIONS

Specific 1982 objectives were achieved as follows:

1. The assembly configuration and components of a prototype EM-CAS were established and optimized.
2. The performance capability of the prototype EM-CAS was demonstrated in laboratory tests.

3. The prototype EM-CAS for small missile high-g applications was demonstrated by exposure of 5 separate units to 10,000g launch environment using the 203 mm cannon at MICOM in Huntsville, Alabama.

In addition to specific objectives, the following was demonstrated:

1. 12 thermal battery tests, (4 hot, 5 cold and 3 ambient) operating the EM-CAS for greater than 83 seconds under worst-case duty cycle, were performed.
2. The EM-CAS is 14 percent lighter and 20 percent smaller than the present pneumatic CAS.
3. Cost studies show that the EM-CAS will be cost competitive with the pneumatic CAS.

Blank Page

TWO HUNDRED PASSAGE THREE-WAY VALVE - FRACTION COLLECTOR

Jay L. Keffer*

ABSTRACT

This paper describes the design and operation of a fraction collector used to direct flow of separated biological materials from 197 capillary tubes to either a collection tray or to a waste tank. This mechanism uses a 28-volt dc gear motor driving twin cams to force 197 needles through a self-sealing silicone rubber septum, where they inject the material in 197 separate pockets in a collection tray. The position of the collector tray is sensed by two optical limit switches. The time sequences are controlled automatically by an electronics control monitoring module.

INTRODUCTION

This fraction collector is part of a biological materials processing unit that by 1987 is scheduled to lead to commercial marketing of new medicines unobtainable without the benefit of zero-g. The processing unit is called the Continuous Flow Electrophoresis System (CFES) and is currently being operated in the middeck of the Space Shuttle (Figure 1). While not new, the electrophoresis process has been greatly improved by a continuous flow arrangement yielding higher purity and greater quantities of certain proteins by separating them from other biological materials. Although many of the proteins are obtainable on earth, the processes used are so limited by gravity that only research quantities are available. In space, however, away from the adverse effects of gravity, it may be possible to obtain these proteins in the quantities and purities needed to effectively treat diseases.

Electrophoresis processing involves the separation of biological materials from their surrounding medium by passing a fluid between walls across which an electrical potential has been established (Figure 2). Different cells take on different charges and move to different positions across the column as the medium is pumped upward. These cells will stabilize in specific streams, where they will be collected by 197 collection tubes, each leading to a needle mounted in the fraction collector.

The Shuttle middeck processing unit consists of three modules: the Fluids System Module (FSM), which is the largest of the three, the Electronics Control and Monitoring Module (ECMM), and the Sample Storage Module (SSM). The fraction collector is located at the top of the FSM.

REQUIREMENTS

The function of the fraction collector is to divert all flow through 197 tubes from the separation column to either a waste tank or to a collector. The total flow rate is less than 100 ml/min at a system pressure that is less than 70.3 gms/cm² (one psig). Fluid viscosities greater than water but less than glue is to be expected. Dead volumes are minimized to prevent areas where biological growth could occur. Finally it should be inert to the biological products to prevent contamination.

*McDonnell Douglas Astronautics Company, St. Louis, Missouri

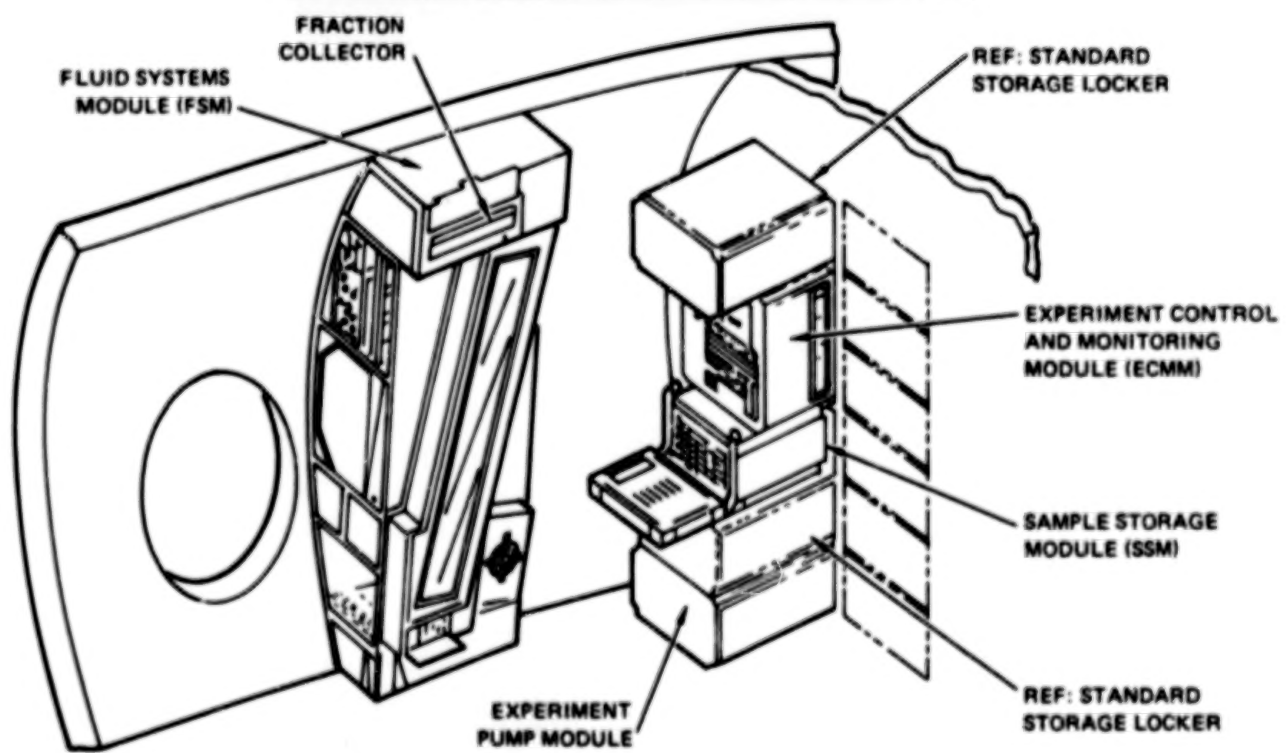
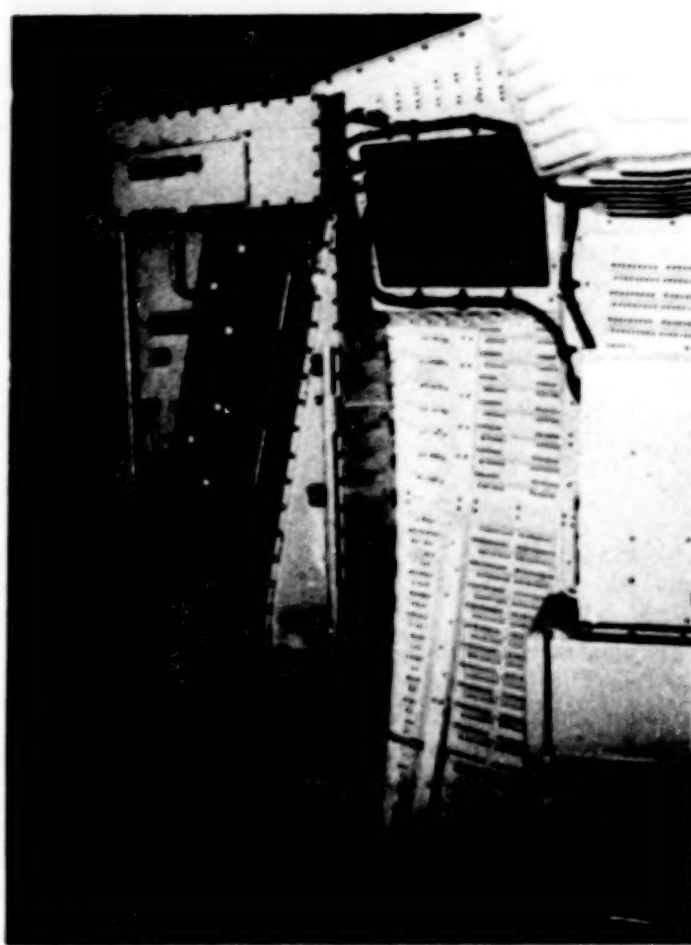
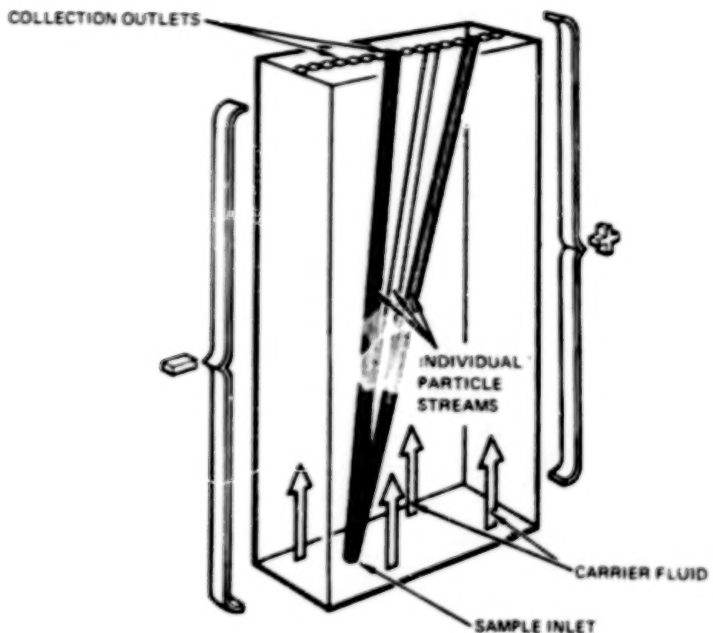


FIGURE 1 MIDDECK ELECTROPHORESIS SYSTEM



CONTINUOUS FLOW ELECTROPHORESIS SEPARATES THE SAMPLE INTO INDIVIDUAL PARTICLE STREAMS.

FIGURE 2 THE ELECTROPHORESIS SYSTEM

TRADE STUDIES

Each of the design concepts considered for the fraction collector involved the use of an array of 197 needles penetrating a self-sealing septum material. It is necessary for the septum material to reseal under system pressure after the needles are retracted. To verify this septum valving concept for use in the electrophoresis process middeck flight unit, development tests were performed to select the best needle configuration/septum material combination that requires the least penetration and retraction forces and has the best sealing qualities. In addition, a needle configuration that minimizes the possibility of septum coring was of primary importance to prevent septum leakage and to ensure all needles continue to flow even after septa penetration.

The selected needle configuration is a 20 gauge closed pencil point single side port arrangement (Figure 3). The side port is a slot that provides for a greater flow area than a round port without compromising the needle strength due to a reduced cross-section. The cone point aligns the forces through the needle centerline to ensure the needle will penetrate straight through the septa without straying. In addition, this side ported arrangement is self-cleaning with no dead volume.

The selected septum material is a 30 durometer medical grade silicone rubber. The maximum penetration force was measured at 771 grams (1.7 pounds) per needle on a single needle test at a rate of five cycles per minute. The retraction forces were not significantly different since most of the force is spent overcoming friction between the needle and the septa material.

It was discovered later in the development cycle that multiplying the penetration force from a single needle test times 197 needles is not a true representation of the total force required to penetrate the septum material with an array of 197 needles simultaneously. Instead, a factor of two should

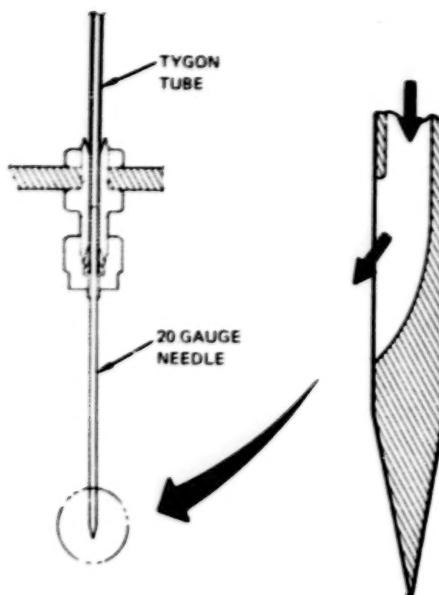


FIGURE 3 SELECTED NEEDLE CONFIGURATION

be applied to the calculated force using the method above. It is theorized that the additional force can be attributed mostly to the variations in needle straightness and needle parallelism causing interactive forces as they are forced through the septum material.

SYSTEM DESCRIPTION

Operation of the fraction collector (Figure 4) requires the astronaut to insert or remove collector cassettes. Other operations are handled automatically by the ECMM. The procedure is to open the access door to the collector area by turning two quarter turn latches, insert a cassette by engaging the two guide rails and pushing the cassette in until the ball plunger falls into place. A definite snapping action is felt at this point. The access door is then closed and latched. When the ECMM determines that collection is to take place the motor is energized forcing the septum material on top of the cassette against the septum material on the bottom of the waste manifold effecting a seal (Figure 5). Further upward travel forces the array of 197 needles through this stack of septum material into individual pockets in the cassette. When the mechanism reaches top dead center an optical limit switch is tripped to stop the motor. The mechanism will remain in this position for a predetermined amount of time, usually about 10-12 minutes as the cassette is being filled, then the motor is energized again forcing the waste manifold down causing the needles to withdraw from the cassette. The last part of the downward stroke is used to provide a gap between the cassette and the waste manifold to facilitate cassette removal and to seat the waste manifold against four stacks of four belleville washers. At bottom dead center another optical limit switch will stop the motor. At this time, the ECMM will prompt the astronaut to remove the cassette and place it back into the SSM.

The fraction collector consists of a welded aluminum structural frame supporting four guide shafts, the drive mechanism, the carriage assembly, a septum plug/spacer assembly, the waste manifold, the needle head, the 197 passage connect, two side latches, and finally a collector cassette that requires astronaut handling for insertion and removal.

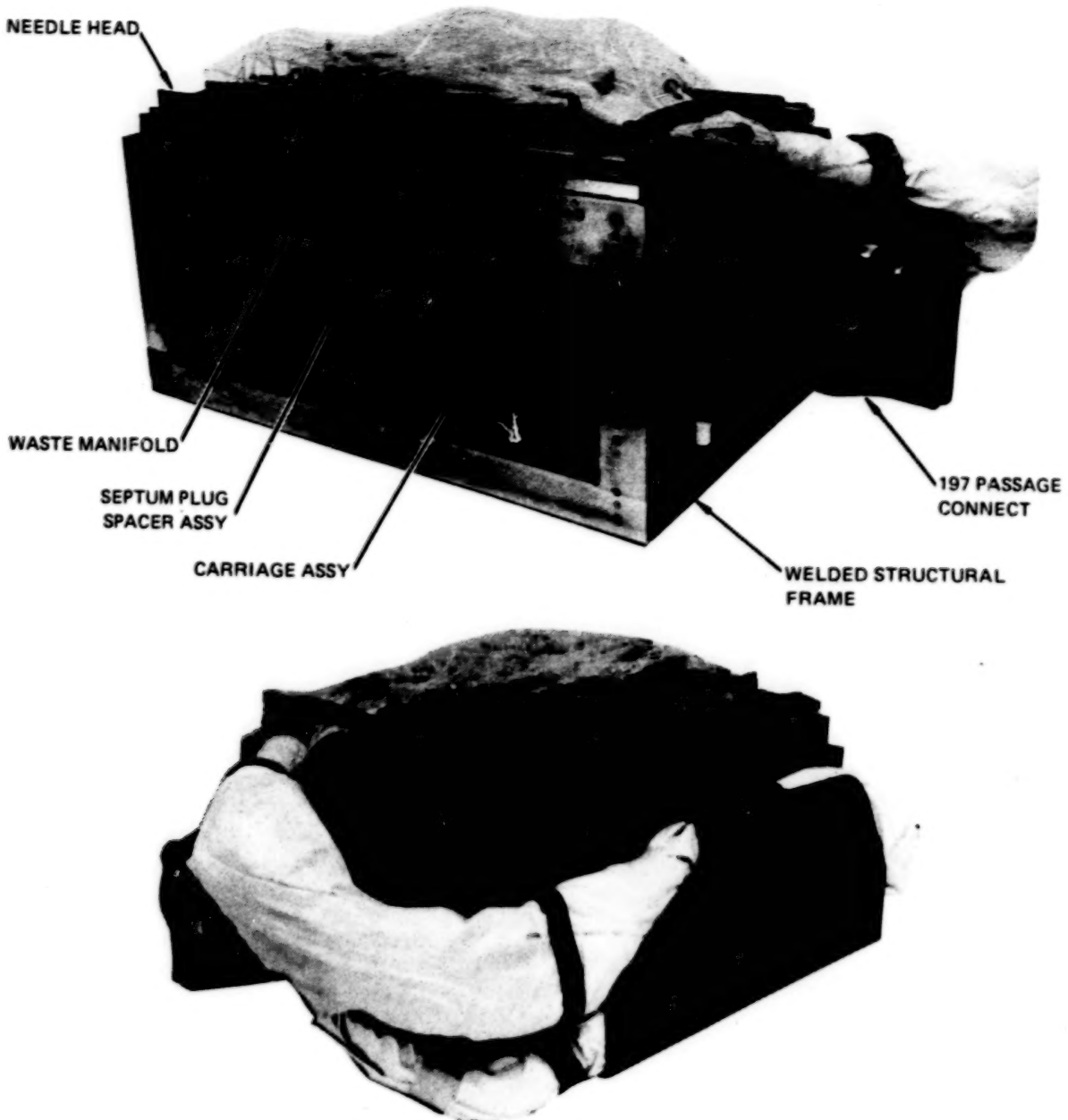


FIGURE 4 FRACTION COLLECTOR

The drive mechanism (Figure 6) includes a 28-volt dc gearmotor with a reduction ratio of 941/1. This motor is capable of delivering 2424 newtons (545 pounds) of vertical force at a rate of five cycles per minute at the maximum moment arm of one centimeter (.393 inch). At stall torque, 6494 newtons (1460 pounds) of vertical force is supplied by the motor at the maximum moment arm. The motor has a pinion gear mounted on the drive shaft that engages a line of three other pinions of equal diametric pitch to drive twin cams. With this gearing arrangement, the cams move in opposite rotational directions to keep the applied force symmetric about the four 1.27 centimeter (one half inch) diameter guide shafts. The cams are extra light duty aircraft bearings mounted off center to provide a total stroke of 1.99 centimeters (.785 inch).

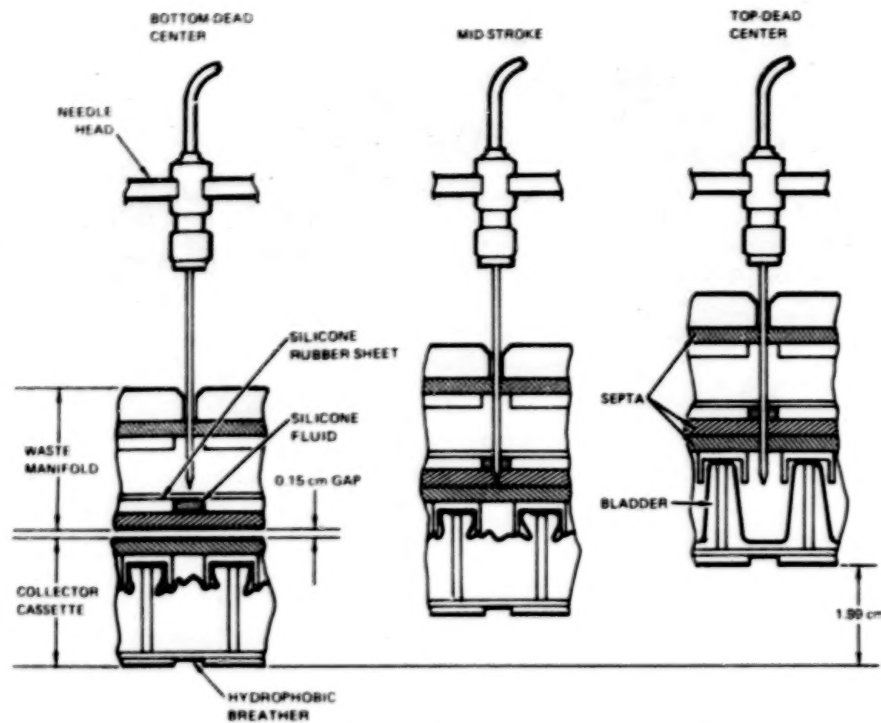


FIGURE 5 FRACTION COLLECTOR OPERATION

The vertical force is applied by the cams to the carriage assembly through two oblong shaped holes that allows the bearings to move freely from side-to-side as it rotates. This assembly provides a platform for insertion of collector cassettes up to 7.62 centimeters (three inches) in height. To date, only 2.54 centimeter (one inch) high cassettes have been used in flight; therefore, a spacer is required to make up the difference in height. Two bronze bearings are located on each of the four shafts and are spaced 6.10 centimeters (2.40 inches) apart to prevent binding. These bronze bearings are porous and are saturated with 350 centistokes silicone fluid for lubrication.

The septum plug/spacer assembly serves two purposes. First, it occupies the space necessary so that a 2.54 centimeter (one inch) high cassette can be accommodated. Second, it contains a mechanism consisting of two scissor jacks that raises a flat platform with 200 .953 centimeter (3/8 inch) square silicone rubber closed cell sponge pads that engage the needle penetrations in the septum material located on the bottom of the waste manifold. This is done by manually rotating two knobs located on the front of the spacer assembly. This was necessary as an insurance policy to prevent water seepage during launch and reentry. It was expected that 773 gms/cm^2 (11 psi) would be experienced during launch due to the water head, the launch g's, and the random vibration environment in the Shuttle middeck. The spacer contains a ball plunger to give a positive indication that the collector cassette is in position and properly aligned beneath the array of 197 needles.

The waste manifold is a shallow rectangular shaped stainless steel pan with a bolted on lid that collects the flow from all 197 tubes and directs

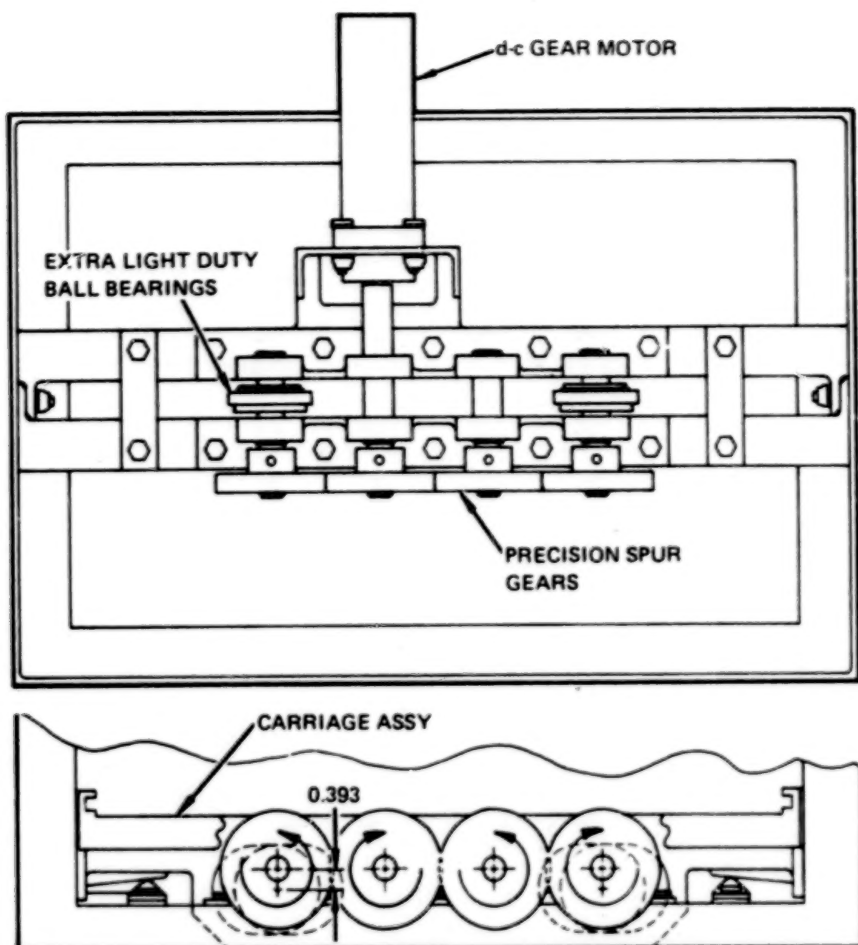


FIGURE 6 FRACTION COLLECTOR DRIVE MECHANISM

that flow to a waste tank when sample collections are not being made. Both the bottom and top of the waste manifold have an array of 200 .476 centimeters (3/16 inch) diameter holes covered over by a sheet of bonded on 30 durometer medical grade silicone rubber septum. One needle passes through the manifold in each of the 197 holes. Three holes are not used. The self sealing characteristics of the septum on the underside of the manifold was improved by injecting 1000 centistoke silicone fluid in the volume of each of the holes and capturing it with the septum on the underside and a .079 centimeter (1/32 inch) thick bonded on silicone rubber sheet on the inside. The top side septum which is sandwiched between two metal sheets provides a dynamic seal around each of the needles. The needles are never pulled out of this septum during operation. The top metal sheet provides a conical lead-in for each of the needles to facilitate needle installation.

The needles head (Figure 7) provides a mount for each needle assembly. An aligning tool was used when installing the needles into the needle head to ensure they were all parallel. The jam nuts were left loose enough to provide freedom of movement of the needle of about $\pm 10^\circ$ and then was locked in place with RTV 730 material. This was done to prevent any interaction between the needle due to nonparallelism or straightness variations that might cause a sideward force of the needle in the rubber resulting in leakage. This proved to be a necessary and a very important step in the assembly procedure.

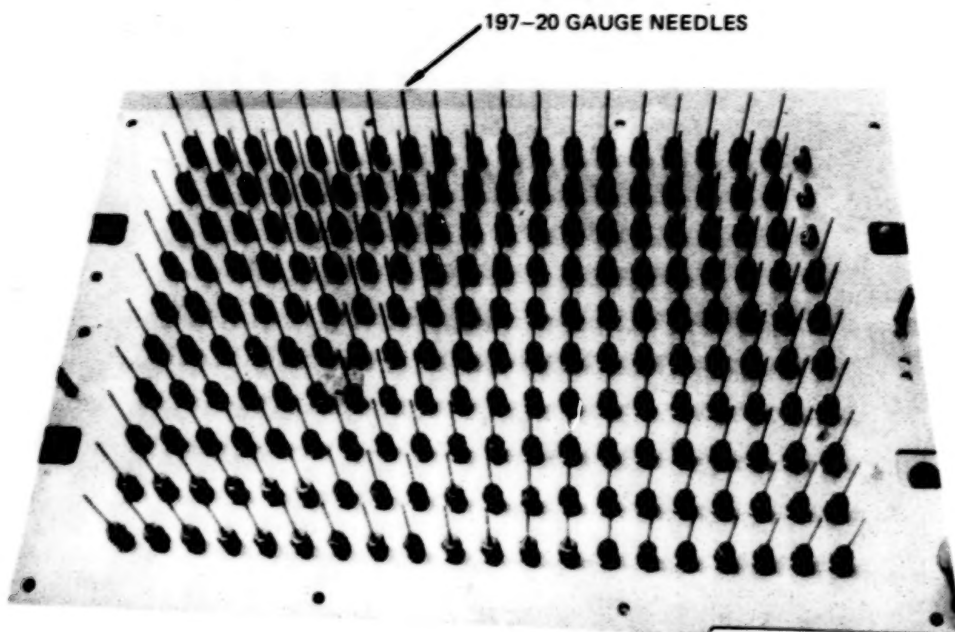


FIGURE 7 NEEDLE HEAD

A connect/disconnect is provided in the 197 tubes between the separation column and the fraction collector to facilitate removal/installation of either unit. The connect is 8.26 centimeters (3.25 inches) in diameter and consists of two mating stainless steel halves that are keyed together with dowel pins to ensure proper continuity of each tube. A thin .079 centimeter (1/32 inch) gasket is placed between the halves. The gasket seals both to the outside and around each of the 197 holes. This assembly is held together with a marman V-band clamp. Each tube was placed through the connect to the interface plane and then all were bonded in place with Hartel two part epoxy. This arrangement reduced the dead volume to near zero and also minimized metal contact with the buffer solution.

The two side latches (Figure 8) provide two functions. First, they pull the waste manifold off of the needles on the down-stroke. Second, they lock the manifold down when the cams reach bottom dead center. This prevents the manifold from getting excited during the vibration environment of launch and reentry.

Each latch consists of a ratchet, which is bolted to the waste manifold, a pawl, that is free to rotate about a clamp-up bushing on the carriage assembly and a fulcrum, that forces the pawl to rotate on the down-stroke.

The ratchet has two surfaces. On the up-stroke the pawl elevates and rotates up to the top surface of the ratchet. On the down-stroke the pawl pulls against the ratchet forcing the waste manifold off of the needles. During the last part of the downward motion the pawl is forced to rotate off of the top surface of the ratchet to the bottom surface, by the fulcrum, providing a gap between the waste manifold and the collector cassette facilitating removal and insertion of the cassette. The cams continue to rotate until bottom dead center is reached at which time the pawls pull the waste manifold against four stacks of four belleville washers. This provides the clamp-up force required to hold the waste manifold during launch and reentry dynamic environments.

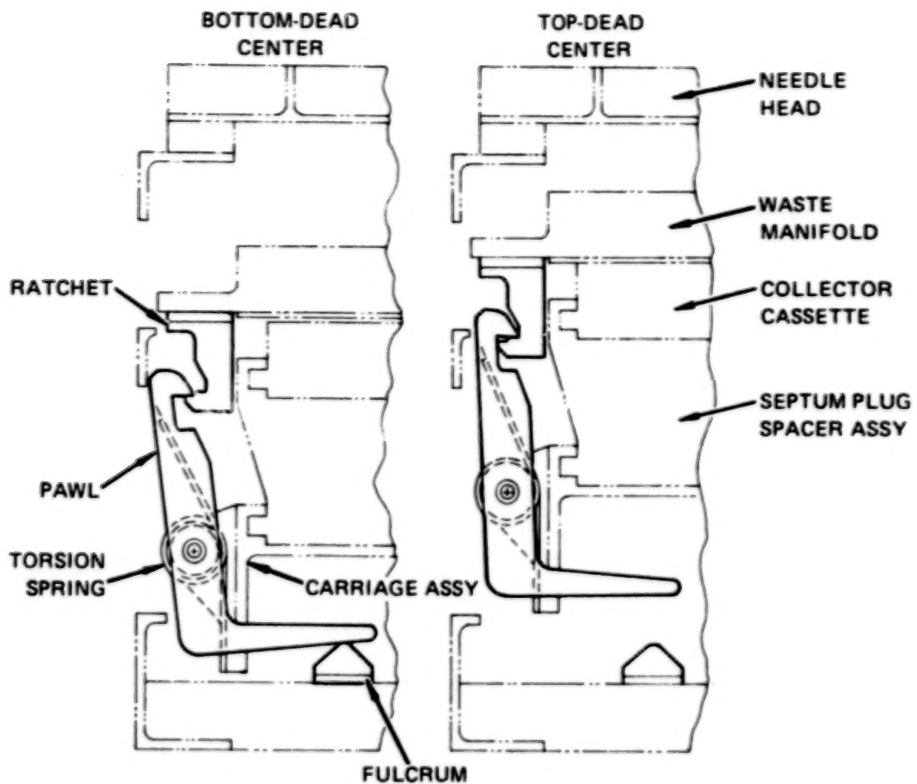


FIGURE 8 SIDE LATCH ARRANGEMENT

The collector cassette (Figure 9) resembles an egg carton consisting of a molded medical grade polyvinyl chloride bladder with 200 individual pockets in a 10 by 20 array covered with a polycarbonate sheet that is bonded to the ridges around the opening of each of the pockets. The assembly is then covered with a sheet of septum material that is bonded in place sealing around each pocket. These pockets are evacuated prior to use. Each pocket holds about 2.5ml of fluid. A machined aluminum frame provides the grid work for each of the pockets. The frame also has rails on all four sides that either engage the carriage assembly or the SSM where the cassettes are stored when not in use. The bottom of the cassette frame is covered by a sheet of hydrophobic material which is held in place by a bolted on aluminum sheet with 200 holes. As the pockets are being filled this hydrophobic material will vent the displaced air but prevent any water from passing through.

SAFETY ASPECTS

Several steps were taken to ensure the safety of the astronaut while interfacing with the collector. The fraction collector is rendered inoperable when either the access door is opened or when there is no cassette in place. This is accomplished by a plunger switch sensing the door position and a micro-switch with a roller leaf that engages a cammed surface on the cassette guide rail. In addition, the needle points are not exposed to the astronaut when he is inserting or removing a cassette, but are inside the waste manifold during this operation.

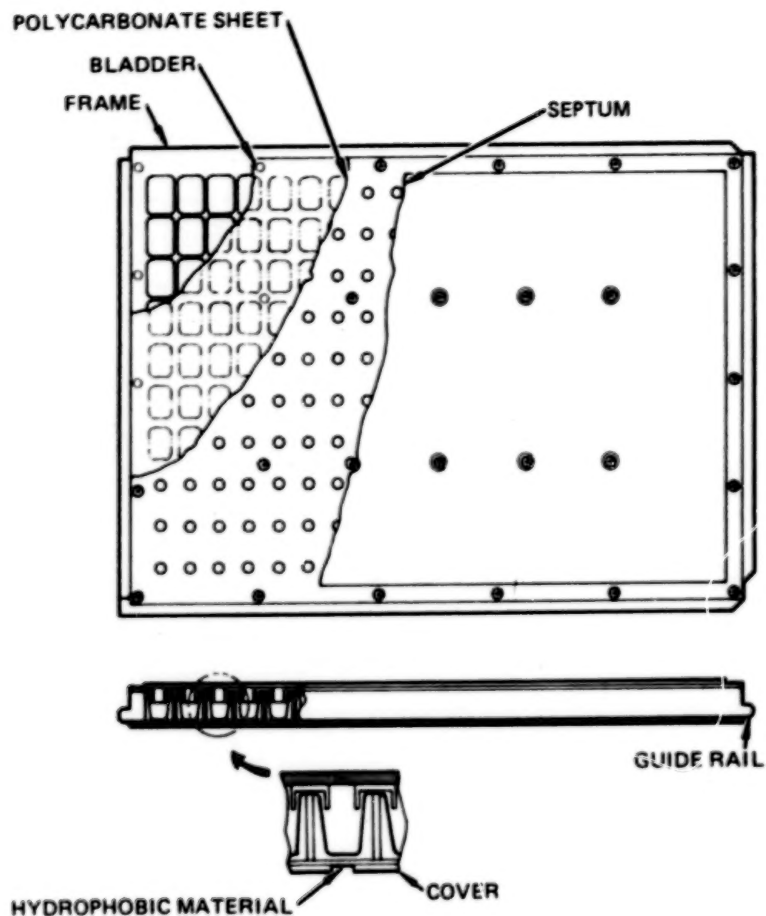


FIGURE 9 COLLECTOR CASSETTE

CONCLUSIONS

A two hundred passage three-way valve has been developed that collects the biological fractions from the continuous flow electrophoresis system. The forces required to drive an array of 197 20-gauge needles through a stack of septum material (.313 inch thick) is approximately two times the single needle force times 197.

NUTATION DAMPER SYSTEM

Donald R. Sevilla*
Jet Propulsion Laboratory
California Institute of Technology
Pasadena, CA

ABSTRACT

The Nutation Damper System is a three function mechanism designed for the Galileo Spacecraft, a spin stabilized deep-space probe to Jupiter. By damping the movement of a large deployable science boom acting as an outboard pendulum, the nutation damper rapidly stabilizes the spacecraft from dynamic irregularities.

The system includes the boom deployment device and the ultra-low friction boom hinge. This paper describes the mechanism, the degree to which friction, stiction and lost motion have been eliminated, and the unique test methods that allow its performance to be measured.

INTRODUCTION

The Galileo spacecraft is the first large, spin-stabilized space probe designed by Jet Propulsion Laboratory and is intended to be the most stable science platform ever sent into deep space. This stability is in part delivered by the active nutation damping of the craft by a large deployable science boom acting as an outboard pendulum. This pendulum action of the deployable science boom is provided by a specialized zero friction boom hinge, and the damping is produced by coupling the boom to the spacecraft bus with the Nutation Damper (essentially a flight-qualified fluid shock absorber). The damper, hinge and science boom deployment strut are the three elements that compose the Nutation Damper System.

Spacecraft Dynamics

Figures 1 and 2 help to illustrate the difference between spacecraft wobble and nutation. Wobble is due to the spacecraft being

*The research described in this paper was performed by the Jet Propulsion Laboratory, California Institute of Technology, under contract with the National Aeronautics and Space Administration.

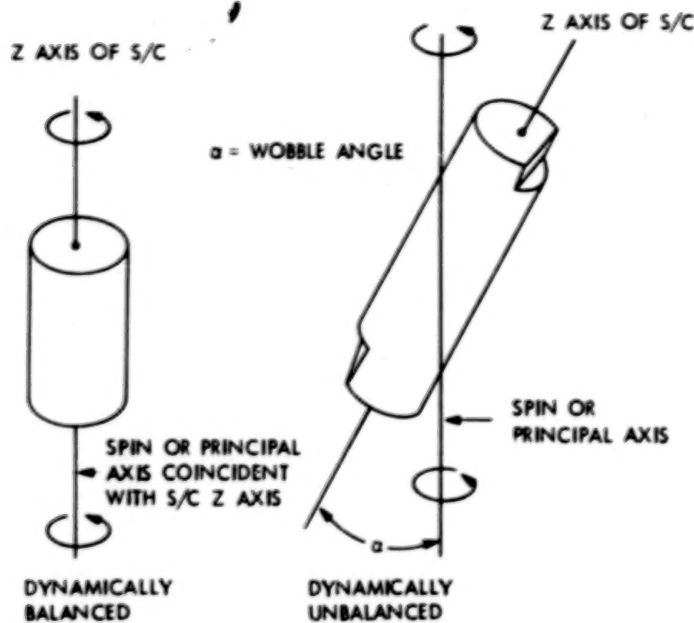


Figure 1. Spacecraft Wobble Only--Z Axis of Spacecraft Not Coincident With Principal Axis

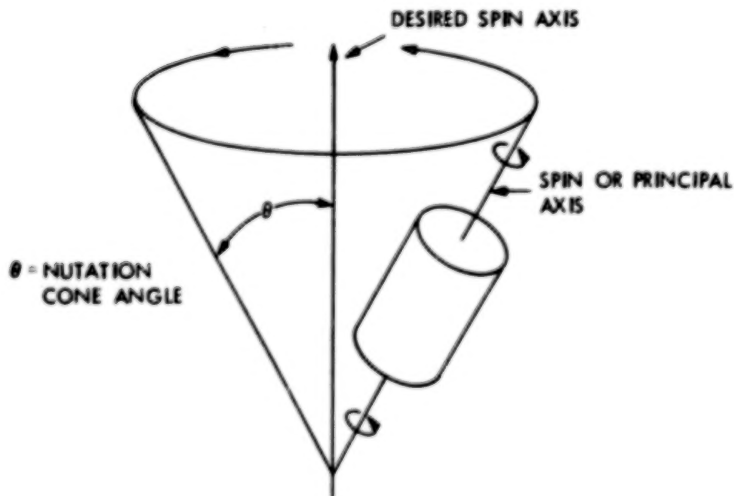


Figure 2. Spacecraft Nutation Only (No Wobble)

dynamically unbalanced, such that the spin (or principal axis) is not coincident with the Z axis of the spacecraft. On the other hand, nutation is the action of the spin axis of the spacecraft circulating in a "cone" about a desired spin axis. This action takes place when the spacecraft is disturbed by outside forces such as attitude correction maneuvers, fuel slosh, or if the main engine thrust vector does not pass directly along the principal axis. Figure 3 shows how the science boom will act as an outboard pendulum under the action of the nutating spacecraft if it is allowed to pivot at its base. By

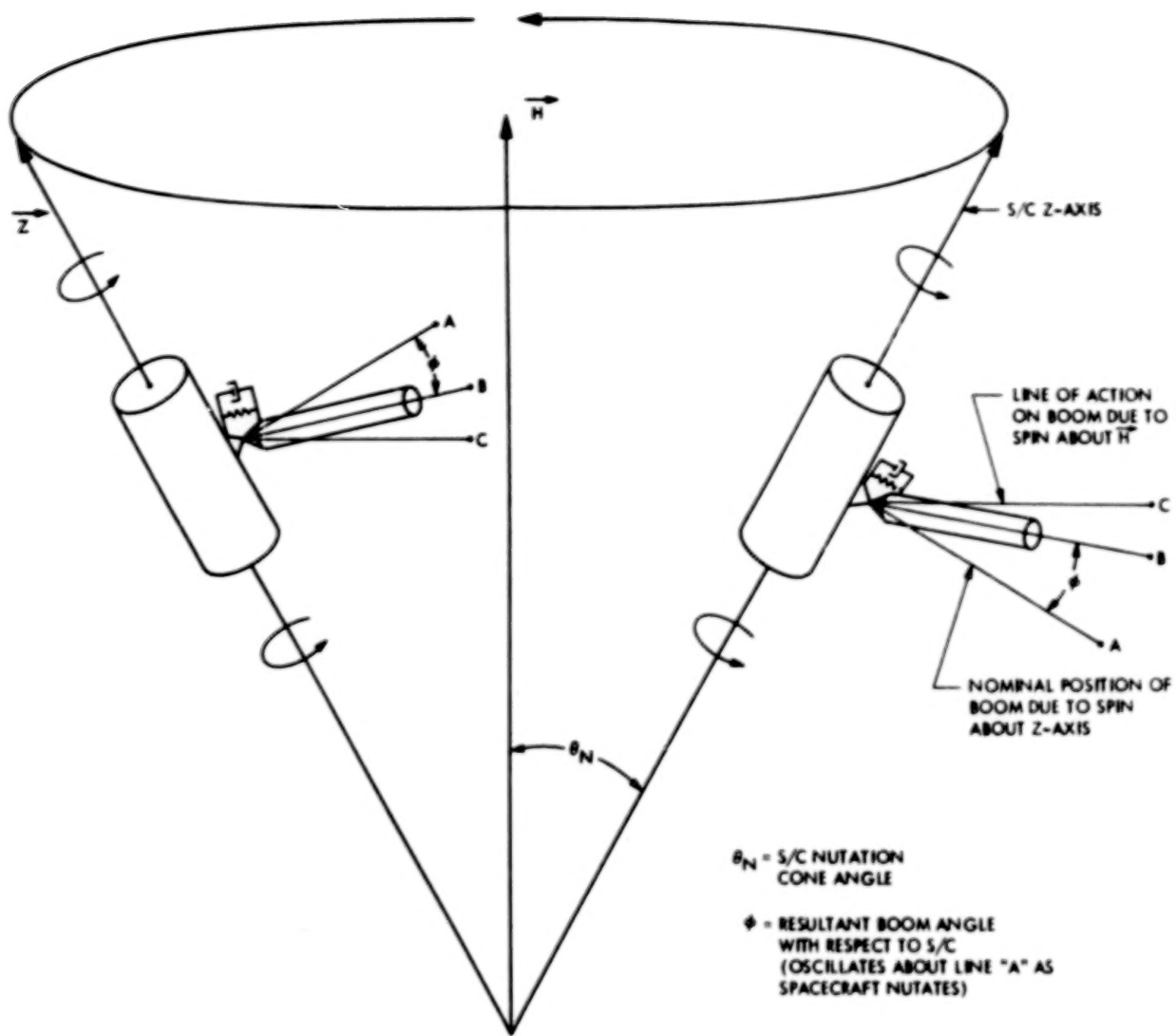


Figure 3. Boom Oscillation With Nutation

damping the motion of the boom, the time for the spacecraft to return to the desired spin axis is greatly reduced. This damping of spacecraft nutation provides an ultra-stable platform in inertial space for the science instruments, allowing science data to be gathered within minutes after spacecraft attitude changes.

What Was Required ?

The system engineers, when considering stability problems with the spacecraft, asked for a pendulum with 2 commandable hinge spring rates and excursions. Although a variety of spacecraft models were configured over the years, this pendulum (the science boom) eventually was required to have about its hinge a normal cruise spring rate of 335 N-m/rad (247 ft-lb/rad) with a maximum excursion of ± 6 degrees. A commandable stiffer spring rate of 2000 N-m/rad

(1475 ft-lb/rad) with a maximum excursion of \pm 2 degrees was to be used during orbital insertion engine burns. The stiffer spring rate would compensate for boom sag during thrust by limiting the movement at the base of the boom. Again after numerous configuration changes, the damping constant of the boom eventually converged to 2455 N-m-sec/rad (1800 ft-lb-sec/rad). Because the mechanism was to be a silicone fluid filled damper and the damping-constant was not an extremely critical value, a tolerance of +100% and -50% was selected. The +100% tolerance allowed room for within-specification damping function over an environmental temperature range, and would provide a larger damping-constant target during development. The -50% tolerance provided within-specification redundancy to the mechanism.

The movement of the boom was required to have absolutely zero backlash. The excursions of the boom during 98% of the life of the spacecraft will fall below 4.4 mrad (1/4 degree) and thus full damping is required in that travel. Also, to insure theoretical pendulum action of the boom in this travel range near zero stiction (break-out force) is a must, and thus ultra-low friction is a design driver. The spacecraft requirement was for stiction torque of the boom (the minimum torque for movement of the boom) to be less than .039 N-m (.35 in-lb) about the hinge. Therefore, the major design effort was toward this goal.

Description of the Mechanism

Figure 4 is a sectional view of the deployment strut component of the mechanism. The strut consists of a large compressed deployment spring to pull the science boom up into position. Due to its size, this spring was fabricated out of titanium wire to save weight. The outboard end of the strut has a Dow Corning 510 silicone fluid filled chamber, and a boss on the deploy rod inside this chamber acts as a fluid orifice to provide damped movement. This damper limits the speed of the boom while allowing a large deployment force margin (see Figure 5). The deployment rod is guided by moly-impregnated Vespel bushings and sealed by O-rings on each end of the fluid chamber. An inboard and outboard felt wiper excludes any possible dirt contamination to the O-rings. Boom deployment is halted smoothly by an Elgiloy rebound spring, thus limiting the deceleration forces. Vespel latch fingers at the outermost end of the rod prevent any bounce-off. With 18,000 centistoke fluid, the maximum pressure in the chamber during deployment is 3.4 MPa (480 psig).

The silicone fluid in the deploy damper is volume and temperature compensated from - 60° C to + 65° C by the addition of a series of evacuated nickel bellows inside the deploy rod. This chamber is O-ring sealed and connected to the damper chamber by an orifice through the wall of the rod. The bellows act as an accumulator by compressing or expanding as the fluid is heated or cooled. This is accomplished by filling the deploy damper in a vacuum chamber at the hot temperature. In addition, a strip heater and temperature

BLANK

PAGE

213

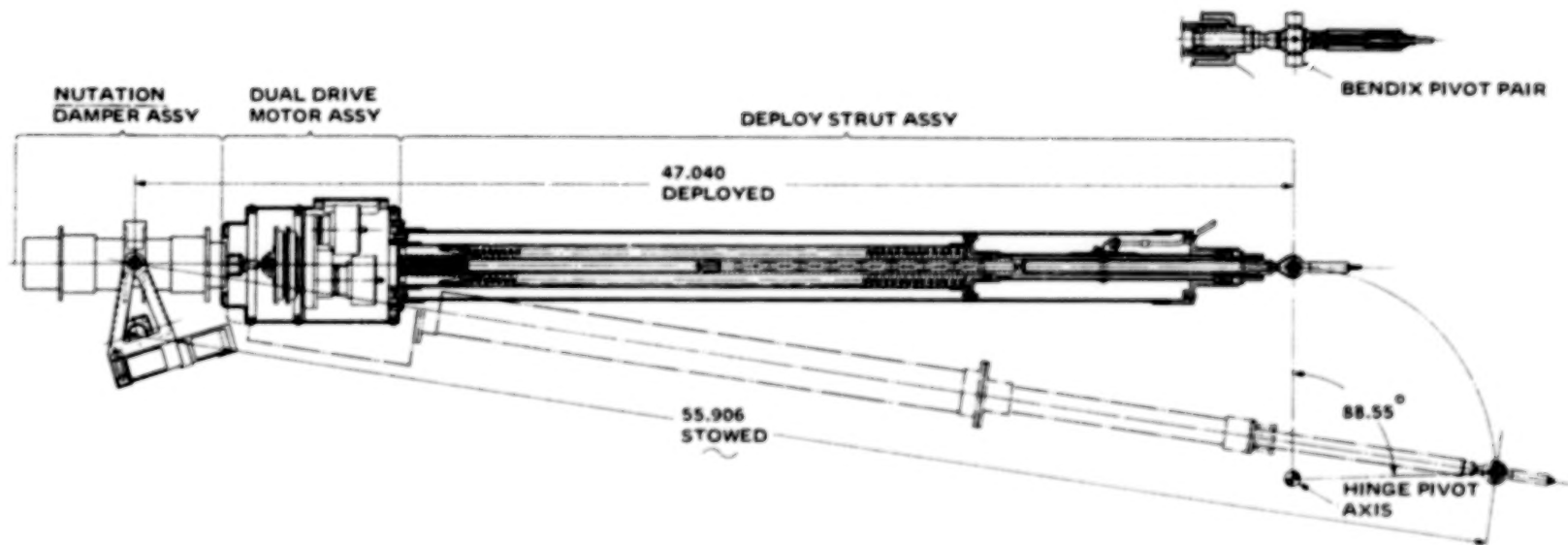


Figure 4. Section Drawing Deployment Strut

213

BEST AVAILABLE COPY

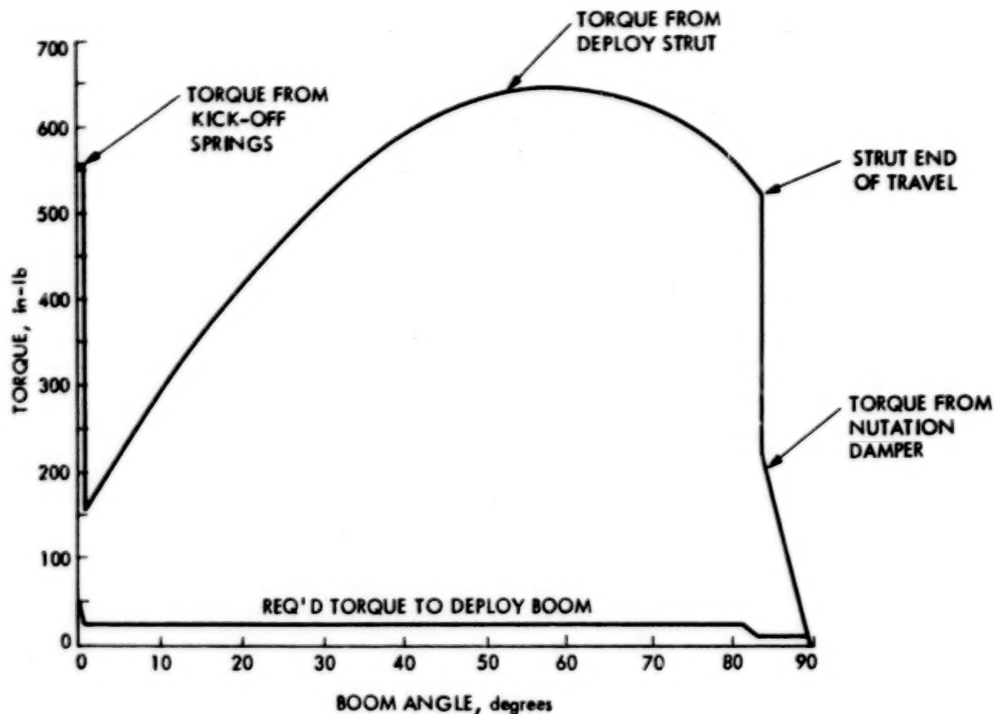


Figure 5. Deployment Torque vs. Boom Angle

transducers are attached to the outside of the damper tube to provide a controlled fluid temperature during deployment only.

Relatively late in the development of the mechanism, the launch loads analysis showed that the combination of the fiberglass spring tube and the titanium deploy damper and rod could deflect too much during launch. A boron-composite overtube was added that stiffens the entire strut. This overtube is allowed to slip fit on the outboard end to avoid any thermal expansion stresses.

Once the science boom has been deployed, the deploy strut acts only as a coupler from the nutation damper to the hinge. Figure 6 shows some prototype hardware on a spacecraft cable mock-up. The deploy strut (sans overtube) is seen between a large can containing a dual-drive motor assembly and the hinge. The nutation damper attaches the whole mechanism to the spacecraft bus. While the hinge pivots on spherical bearings to deploy the boom, it must allow oscillatory motion of ± 6 degrees with near zero friction, and absolutely no backlash. Any bearing here would have some unacceptable stiction torque. The solution was to attach the boom hinge to the spacecraft outrigger with Bendix flexural pivots, which would allow frictionless motion for the required amplitude.

Large 25 mm (one inch) diameter cantilever style pivots, custom fabricated by Bendix out of titanium, were structurally bonded into the bores of special spherical bearings. These bearings have a groove

BLANK

PAGE

215

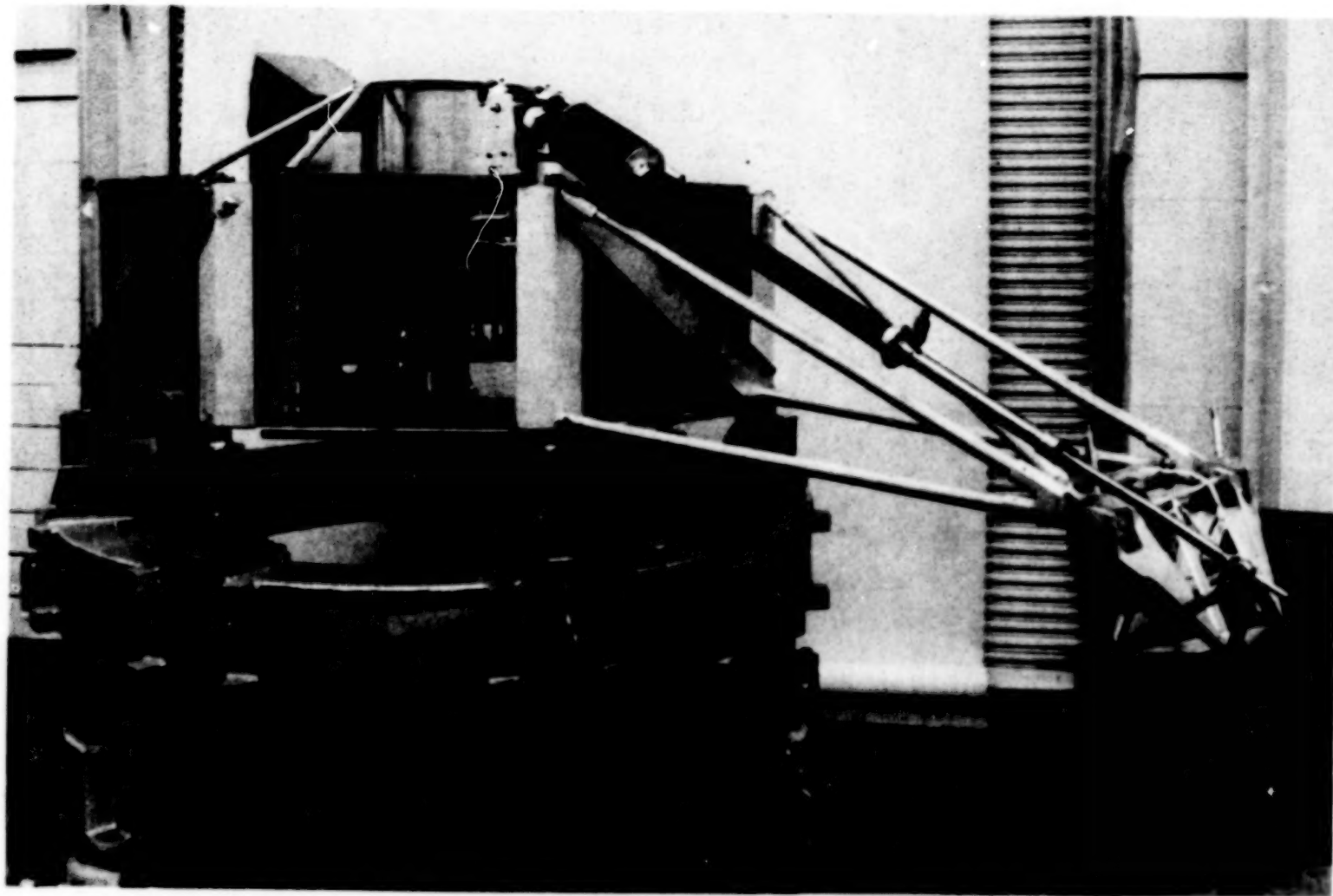


Figure 6. Nutation Damper System Prototype

215

BEST AVAILABLE COPY

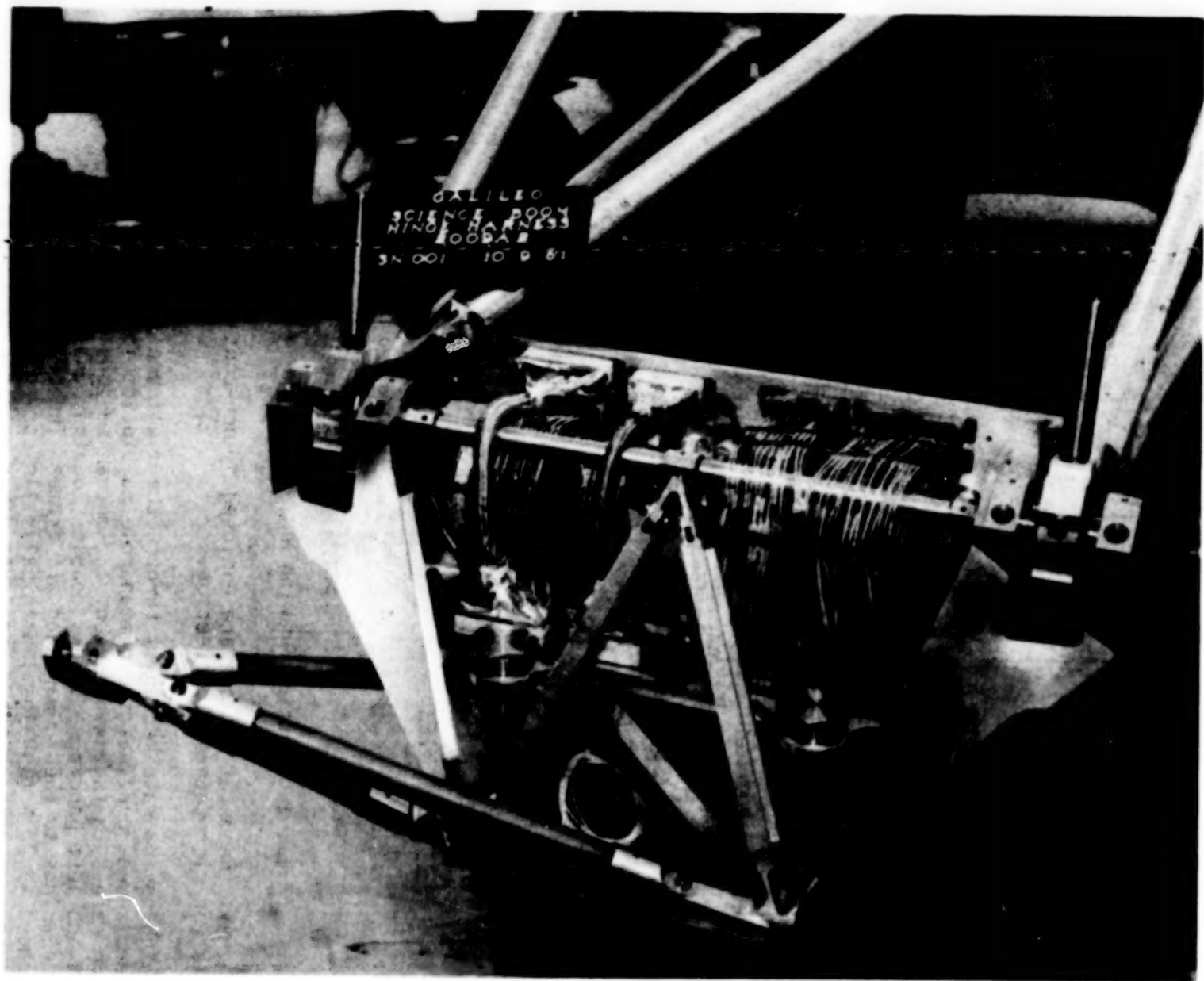
ground into the ball and an access hole through the outer race to allow the installation of a spring loaded ball detent mechanism. Thus the boom hinge is supported by the ends of the flexural pivots and the outrigger supports the outer race of the bearings (Figure 7). The boom rotates about the spherical bearings during deployment, and when the boom is in position, a ball is spring driven into the groove of each spherical bearing to lock it up. The boom then pivots only on the flexures. This identical technique is applied at the male rod-end on the end of the deploy rod (Figure 4) using 8 mm (5/16 inch) diameter flexures. Since this method of pivoting the boom is completely frictionless, the only contributors to a possible boom stiction would then be the 200 conductor hinge cable assembly or the nutation damper itself. Tests on the hinge and cable assembly (discussed later) at temperature showed the stiction due to the cable assembly to be less than .0003 N-m (.0027 in-lb).

The nutation damper assembly shown in Figures 8 and 9 is basically an ultra-low friction shock absorber. While the section drawing appears complex, in actuality the configuration is simple. The damper can be seen as three parts; the high spring rate mechanism through the midline of the device, and two redundant dampers. Each damper element is composed of a main frame (in the center) that slides by a pair of linear ball bushings on a guide shaft that is rigidly fastened to a forward and aft frame. The fluid chambers are created by attaching two welded metal bellows between the frames. Since the main frame is fixed to the spacecraft bus, and the forward/aft frame and guide shaft combination is connected to the science boom hinge by the deployment strut, it can be seen that as the boom oscillates up and down the fluid chambers will alternately be compressed or expanded. The boom displacement of $\pm 6^\circ$ equates to a nutation damper translation of $\pm 22\text{mm}$ (.85 inches.) The fluid orifice between the alternating high and low pressure chambers consists of an annular ring sandwiched between the duplexed linear ball bushings. Flats on the guide shaft provide a fluid passage to the orifice. This orifice and the viscosity of the fluid are what control the damping value of the mechanism. As configured with 50 centistoke silicone fluid, the maximum pressure in the bellows is less than 183 KPa (12 Psig).

The silicone fluid is volume and temperature compensated from - 60° C to + 65° C with the temperature compensation (T.C.) bellows fixed through the aft frame. This chamber is pressure regulated by a compression spring on the bellows guide rod inside the damper guide shaft. The fluid passage to the chamber is from the forward damper bellows through a hole into the fill plug cavity and through a .15 mm diameter (.006 inch) orifice into the guide shaft. This orifice is sized to prevent T.C. bellows pump-up from the oscillating pressure in the damper. In operation, the temperature of the silicone fluid is regulated from + 20 ° C to + 35° C with two redundant heater and temperature transducer assemblies, each containing four series/parallel resistive heaters and two temperature transducers. The damping-constant changes approximately 30% over this temperature

BLANK

PAGE



217

Figure 7. Science Boom Hinge

217

BEST AVAILABLE COPY

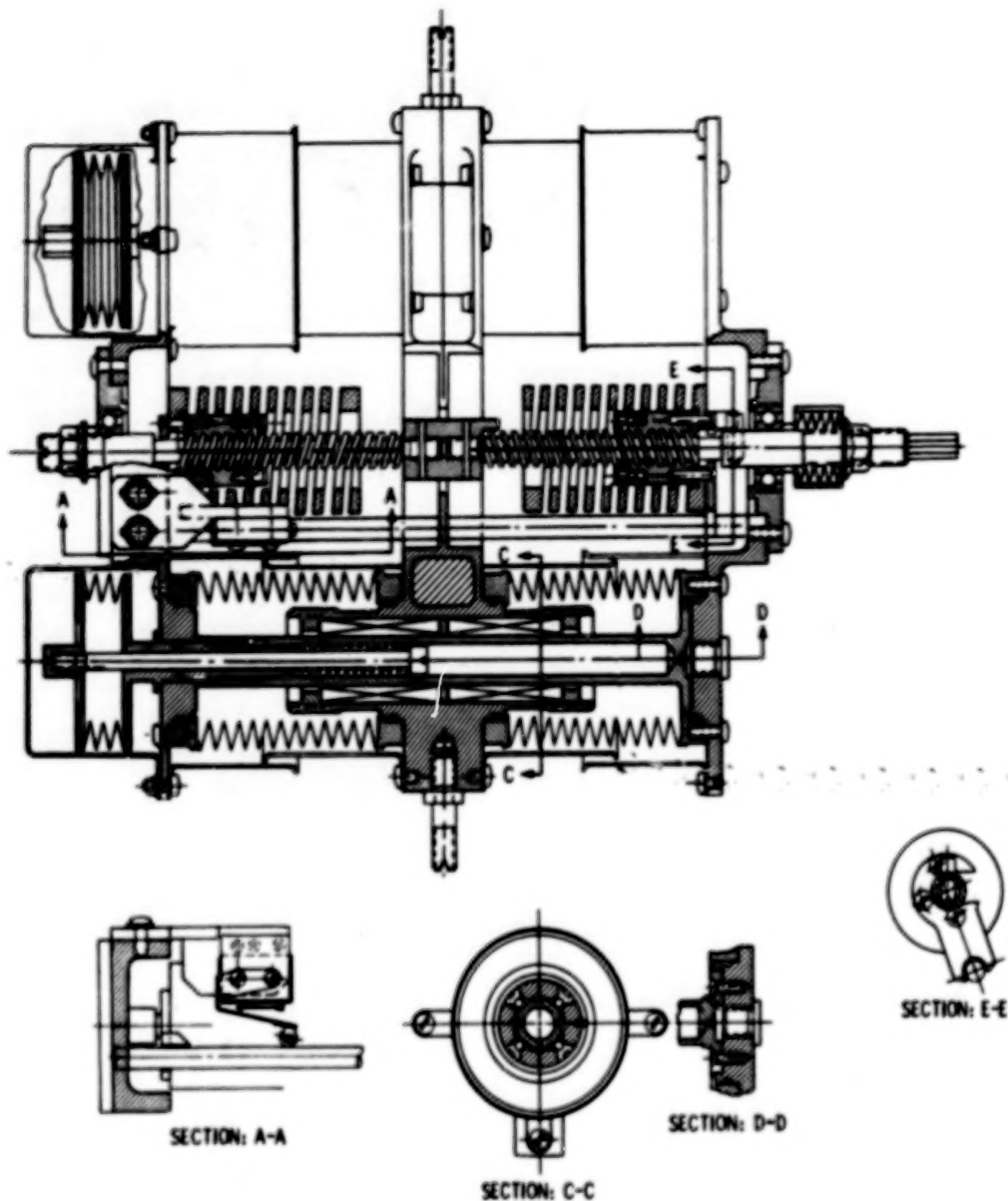


Figure 8. Section Drawing Nutation Damper Assembly

range. All the metal bellows are enclosed by non-contacting aluminum shells for micrometeroid protection.

The high spring rate mechanism through the midline of the nutation damper is what provides the commandable multiplication of the hinge spring rate by a factor of seven. The mechanism consists simply of right and left hand acme screws coupled together and fixed through ball bearings to the forward and aft frames. The bearings are preloaded to 22 N (100 lbs.) with bellville spring washers to insure that there is no backlash. Acme nuts carry machined helical titanium springs that are driven against the main frame. The stroke of the nuts are controlled by non-jamming stops, and the nuts are kept from

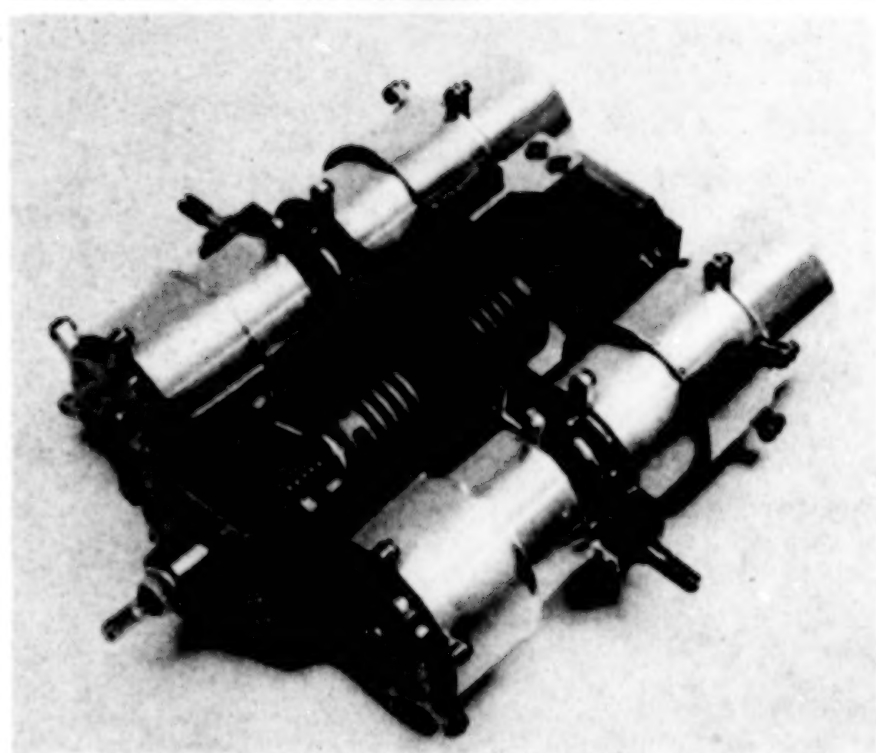
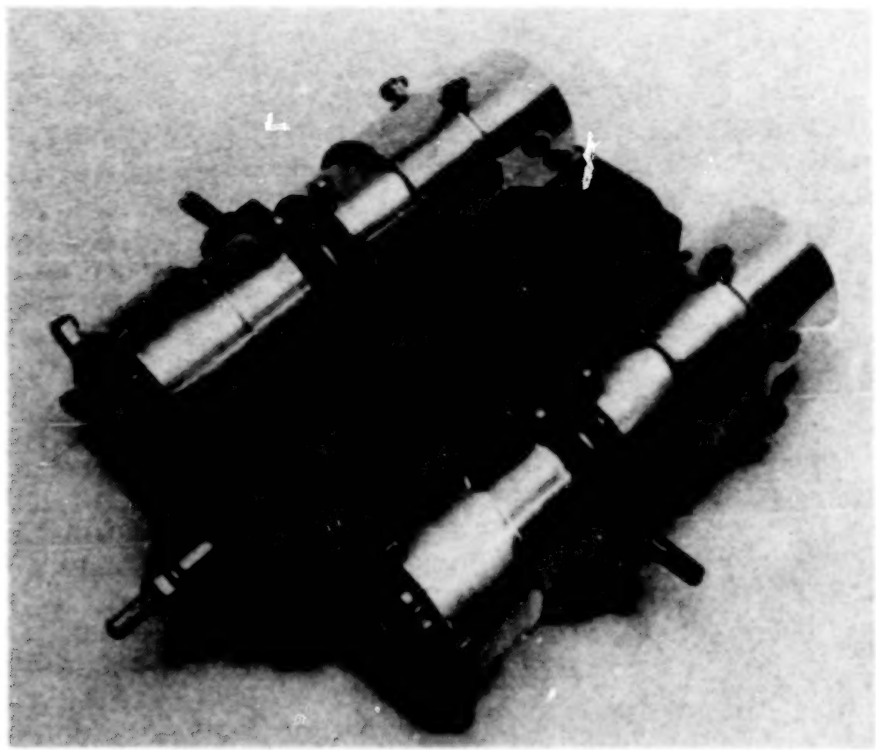


Figure 9. (a) Nutation Damper--Cruise Mode
(b) Nutation Damper--High Spring Rate
Mode Engaged

rotating by engagement to an antirotation rod. Both the acme screws and the antirotation rod pass through clearance holes in the main frame. Any contact would cause boom friction since the screws and rod are oscillating with the boom. The steel screw/brass nut combination is lubricated by silicone fluid-impregnated felt wipers on both sides of each nut.

The acme screws are driven by a dual-drive motor assembly (described in Packard, 1982) mounted in the can outboard of the nutation damper. Briefly, the dual-drive motor assembly is a two-motor completely redundant geared driver with no internal single point failures and is an extremely reliable method to actuate spacecraft mechanisms. By using a "sloppy hex" input on the forward acme screw, a flex coupling was deemed unnecessary. The total torque required to engage the high spring rate mode is .56 N-m (5 in-lb) and the total torque required to hold the springs engaged is a minimum of .19 N-m (1.72 in-lb). The dual-drive actuator provides a torque output of 5.7 N-m (50 in-lbs) and a restraining torque of 3.4 N-m (30 in-lb). The motor running time is not controlled by limit switches. Instead, the motor is run for a fixed length of time (110 seconds) to engage and disengage the mechanism. Since the mechanism is operated nominally in approximately 25 seconds, the motor assembly is stalled against the non-jamming stops for the additional time. A telemetry switch indicates high spring rate mode engaged.

Measurement of Performance

Characterising the performance of the devices presented here posed a particular problem. Over twenty various aspects of design and performance were qualified during development, with the majority of the tests listed below:

Helium Leak	T. C. Bellows Pumping
NDA Dynamic Stiction	ACME Screw Efficiency
Temp/Vol Compensation	Cable Wrap Dynamic Stiction
Dynamic Spring Rate	Running Friction (Deployment)
Life	O-Ring/Bearing Breakaway
Damping (Static)	Deployment Damping
High Temp No-Leak	Latch Breakaway
Deploy Time vs Temp	Detent Breakaway
Spring Tube Strength	Low Temp Vac No-Leak
Bonding Shear	Vibration (Sine and Random)

Most of these tests were fairly conventional methods of proof testing performance such as vertical hinge-line deployment tests or O-ring breakaway friction tests, and will not be covered in this paper. However, the ultra-precise demands of the system required the development of new test methods. Of particular interest is the dynamic testing of nutation damper and boom hinge stiction, dynamic spring rate versus static spring rate tests, and dynamic versus "static" damping tests.

Dynamic Stiction

The nutation damper had been optimized for the lowest friction possible by holding machining tolerances extremely tight and performing multiple stress-relieving of the titanium hardware during fabrication to control precise parallelism of the moving parts. Also, honing the main frame bores for the linear bearings to .01mm oversize was found to minimize the running friction while still supporting the guide shafts with minimum slop. The performance of the system had to be measured as it was going to be operated; that is, dynamically at very small deflections. Though breakaway friction was measured by adding or subtracting weight to the vertically mounted device until it moved, the very act of how the weight was added varied the results. The end result of the program was to develop a dynamic method that was repeatable. What was done was to drive the nutation damper with a calibrated torque motor of well defined current versus torque characteristics. By fabricating an electrical drive source that provided a sinusoidal decaying or ascending current input to the motor, and plotting that current trace side-by-side the sinusoidal damper displacement trace, the dynamic stiction level would be known when the displacement trace ceased to follow the current trace. In other words, that motor would be providing torque at a level lower than is required to move the device. This threshold would be the dynamic stiction level.

The test set-up consisted of an I-beam pendulum pivoted by a Bendix cantilever flexure and driven by an Aeroflex frictionless torque motor at the pivot point (Fig. 10.) This motor is a limited rotation bearingless assembly that normally is held in position (cantilevered) by the hardware it is assembled to. Unfortunately, alignment difficulties required the motor to be assembled into a housing to support the armature on miniature instrument bearings. Dynamic stiction tests on the complete test set-up without the nutation damper proved that the apparatus' stiction was immeasurable. The damper was fastened to the beam about 21cm from the pivot and a target for a non-contacting linear transducer was mounted at the end of the beam about 65cm from the pivot. By changes in an R-F field, the transducer measured the movement of the target to a resolution of .002mm (.0001 inch) and thus measured the damper oscillations to a resolution of .0007mm (.00003 inch.) As the chart recorder trace in Fig. 11 shows, the stiction threshold for the damper on the down sweep is fairly evident as .017 N-m (.15 in-lb.) Optimization of the mechanism is shown by the fact that the stiction level is nearly identical on the upsweep also.

When the same test method was used to measure the stiction level of the hinge cable wrap assembly at room and cold temperature (less than -100°C), unexpected problems were encountered. Normally, testing at this cold a temperature is performed in a vacuum chamber in an environmental lab. However, because the hinge and cable assembly had nearly zero internal damping of its own it was susceptible to

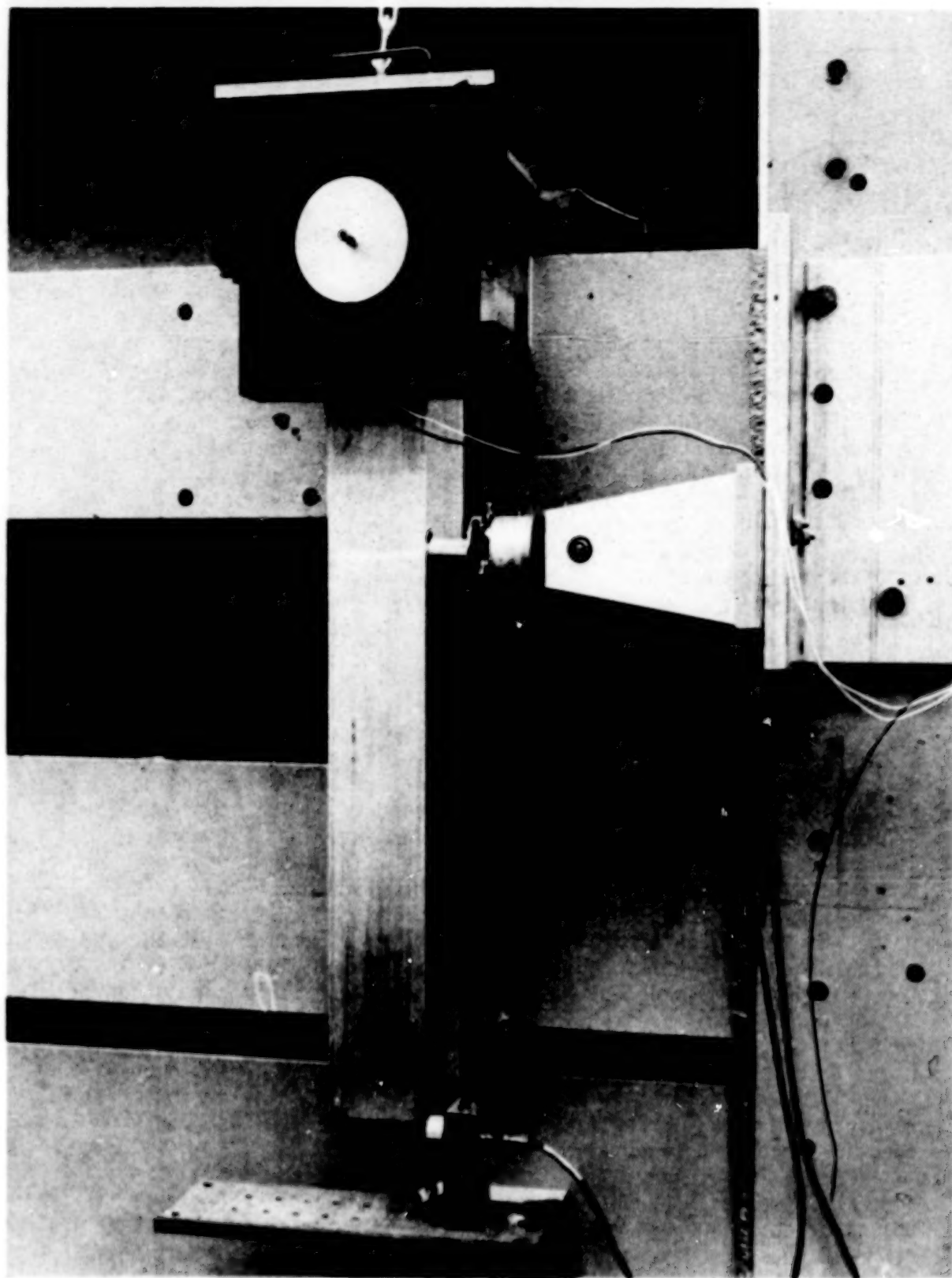


Figure 10. Stiction Torque Test Set-up--Nutation Damper

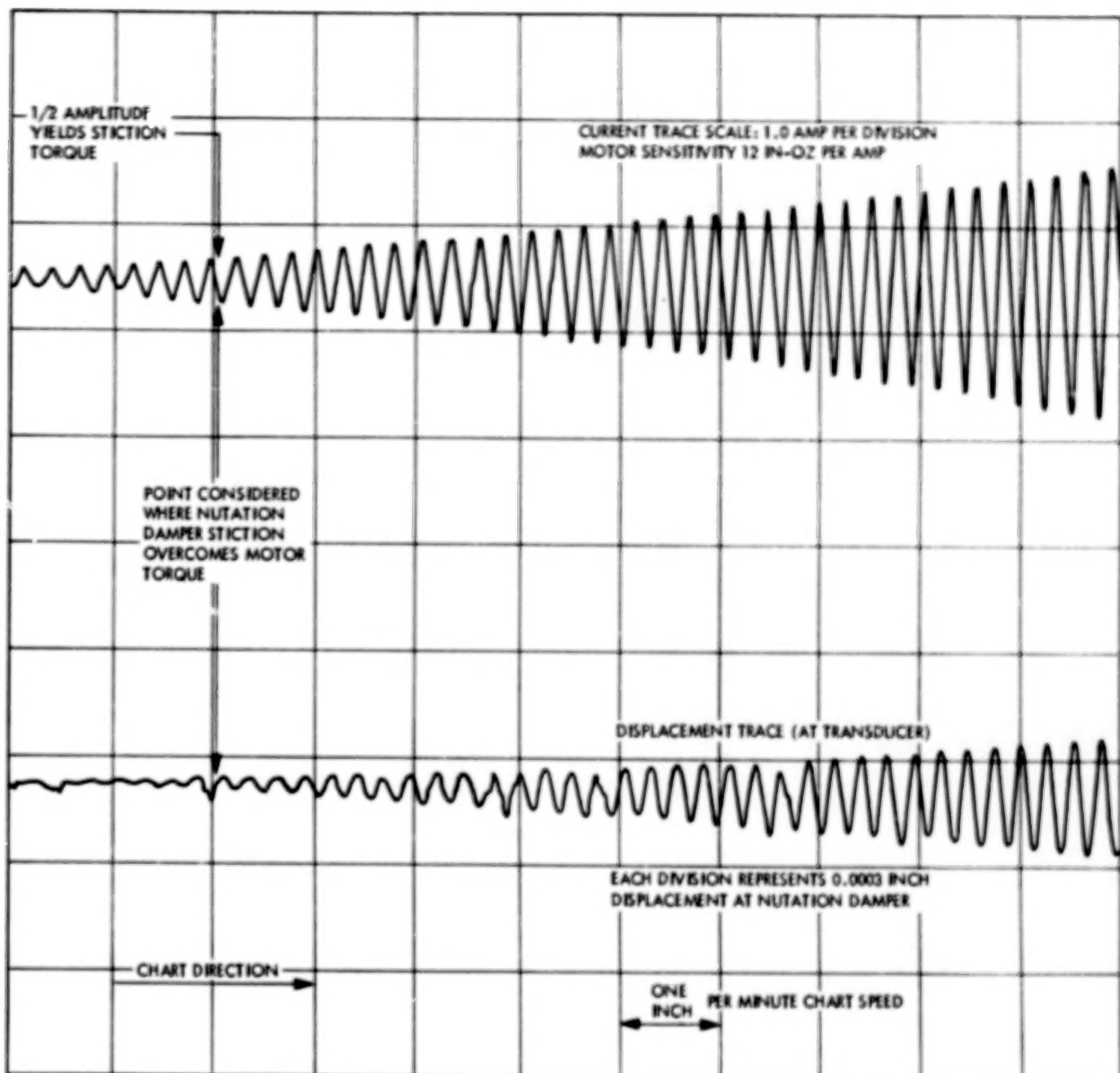


Figure 11. Sample Data--Dynamic Stiction Test

oscillations due to other sources. First it was seen that the vacuum and liquid nitrogen pumps attached to the chamber upset the test. When a run was performed with all pumps in the vicinity switched off, it was discovered that the entire building vibrated at a higher level than the torque that was being measured. By moving the testing back to the building where the nutation damper tests were performed, a sucessful test set-up was developed.

The hinge hardware was suspended by fiberglass thermal isolators in an insulated aluminum box that had clearance openings for the isolators, a fiberglass motor drive shaft, thermocouple wires and liquid and gaseous nitrogen lines (Fig. 12). A frame holding the

224

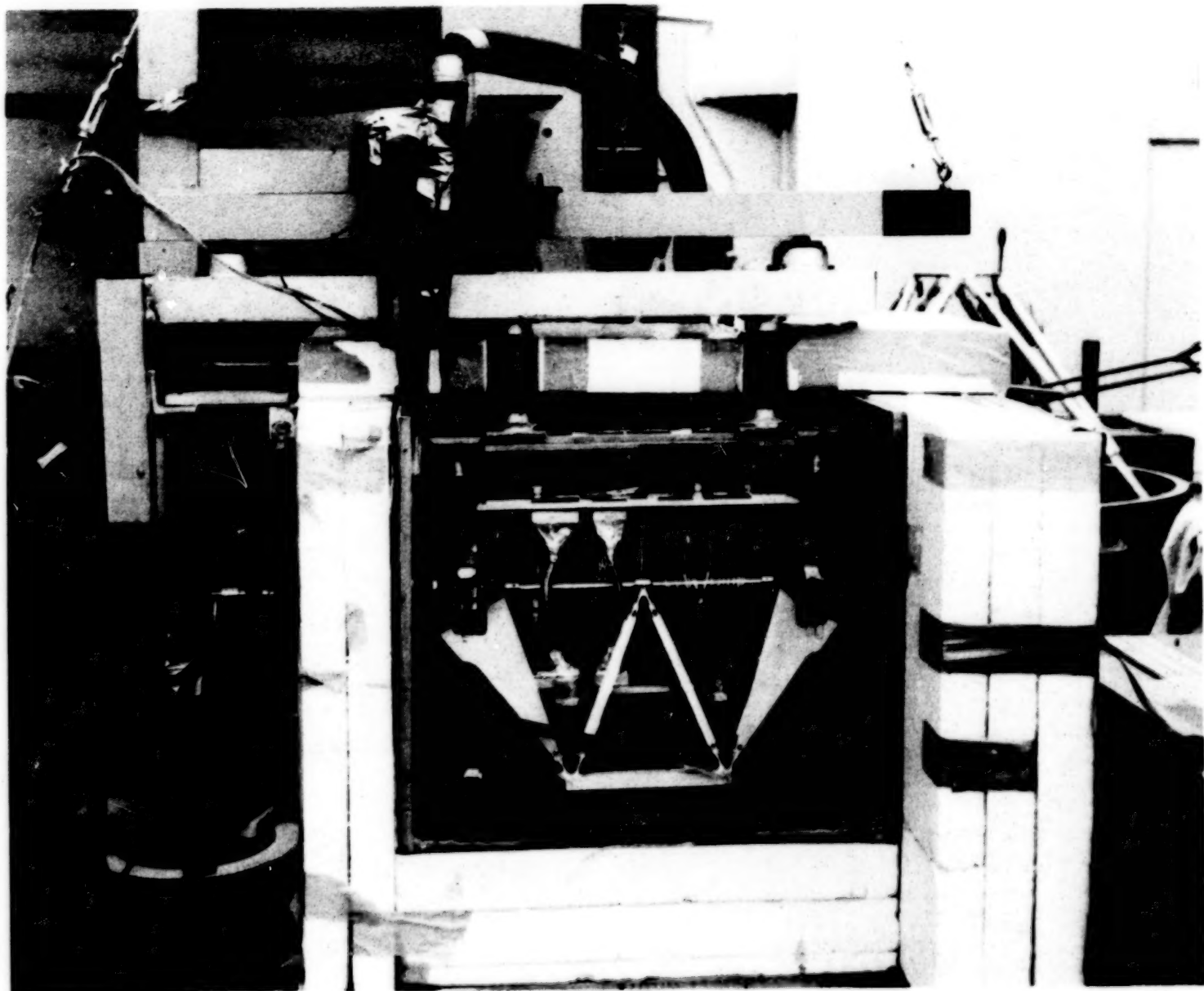


Figure 12. Stiction Torque Test Set-up--Science Boom Hinge

224

BEST AVAILABLE COPY

BLANK

PAGE

torque motor, linear transducer and the thermally isolated hinge assembly was mounted to the building superstructure through rubber vibration isolators. Two copper cold plates mounted on the inside walls of the box were liquid nitrogen fed in series, and the box was purged with cold gaseous nitrogen off the top of the LN₂ tank. After 10 hours of cooling, temperatures as low as -135°C were achieved in the structure with absolutely no icing problems. This was no easy feat, as previous to this set-up tests were rarely performed at less than -40°C in the atmosphere.

The test runs were performed after hours with all air conditioning equipment in the building shut down. The sensitivity of the test was such that it could be seen on the chart recorder when a truck drove by the building. Driving the hinge as a pendulum, the maximum resolution of the hinge oscillation was 2.7 arc seconds. The stiction of the hinge cable assembly was never actually measured. The displacement trace for the hinge would follow the motor current trace until both were lost in dither, the background noise or the limit of the mechanical and electrical set-up. Therefore, the stiction level had to be at most less than the dither level. This level was between .0007 N-m and .0002 N-m (.0062 and .0018 in-lbs.), depending on how much the chart recorder input was amplified.

Dynamic Spring Rate

Just as the dynamic stiction was measured on the nutation damper, the dynamic spring rate at small deflections could be measured also. By scaling the chart recorder to resolve the high current motor input at the start of the down sweep tests, the displacement versus force (calculated from motor torque input to the pendulum) of the damper/pendulum flexure combination would be shown. This would be an important piece of data as static spring rate testing is a rather inexact procedure when small deflections are used. By mounting the damper vertically and measuring the displacement of the frames as weight was added or subtracted, the spring rate was readily calculated. But as the magnitude of the weight was reduced for smaller and smaller deflections, the resulting displacement varied tremendously. Though in the 6mm to 25mm range the average spring rate of the damper was 2.8 N/cm (32 lbs/in), when deflections of less than .89mm (.035 inch) were used the calculated spring rate would vary from .18 N/cm to 6.73 N/cm (2 to 76 lb/in.) This was a haunting problem even when the weight used was liquid siphoned to a cup on the damper in as vibrationless a method as possible. By the dynamic method the spring rate of the damper is expected to be much more consistent. By measuring the dynamic spring rate of the pendulum and then the pendulum/nutation damper test set-up, the dynamic spring rate of the nutation damper will be resolved. As the damper has to be empty of silicone fluid for this test, it will be performed the next time the damper is disassembled.

Dynamic Damping Value

At the time of this writing, the dynamic damping test has not been performed. The damping value of the nutation damper was initially set by "static" damping tests; that is, displacing the center frame of the vertically held damper and recording the displacement versus time to return to the initial position. By mathematically curve-fitting the damping constant can be calculated. However, this method of measuring the damping value is in no way similar to the function of the device. It is possible that the actual dynamic damping characteristics would be different in the $\pm .89\text{mm}$ (.035 inch) oscillation at .01 hertz predicted service of the device. Therefore, tests are being prepared in which the damper will be driven by a motor at these values and the damping-constant will be calculated. By measuring the velocity of the damper in relation to the force input to the damper frame, the damping-constant is calculable. Since, by definition, damping is the force that is in-phase but opposite in direction to the velocity of the object, this data can be recorded concurrently on magnetic tape and manipulated by a computer to directly output the damping-constant.

Conclusions

Though the spacecraft requirements were severe in terms of the required precision of the Nutation Damper System, the design of the mechanism was initially promised as a "best effort." It was not known what performance level could be obtained. Some development was trial-and-error, but the design changed little throughout the program. The noteworthy achievement was being able to reliably gauge the performance of a mechanism by innovative test methods, allowing ultra-low friction levels to be resolved and separated from damping characteristics. These test methods showed that the Nutation Damper System will surpass the performance level required.

The device is currently scheduled to complete qualification level vibration and low temperature vacuum soak tests in early 1983 and will be delivered to perform in the spacecraft system testing in mid-1983. The Galileo spacecraft is scheduled to be launched to Jupiter in May 1986.

REFERENCE

1. Packard, Douglas T. Dual Drive Actuators. In Peter A. Minderman (chair), 16th Aerospace Mechanisms Symposium, presented at the John F. Kennedy Space Center, Kennedy Space Center, Florida, May 13-14, 1982. (NASA Conference Publication 2221)

PRACTICAL SMALL-SCALE EXPLOSIVE SEAM WELDING

Laurence J. Bement*

ABSTRACT

A small-scale explosive seam welding process has been developed that can significantly contribute to remote metal joining operations under hazardous or inaccessible conditions, such as nuclear reactor repair and assembly of structure in space. This paper describes this explosive seam welding process in terms of joining principles, variables, types of joints created, capabilities, and applications. Very small quantities of explosive in a ribbon configuration are used to create narrow (less than 0.5 inch), long-length, uniform, hermetically sealed joints that exhibit parent metal properties in a wide variety of metals, alloys, and combinations. The practicality of this process has been demonstrated by its current acceptance, as well as its capabilities that are superior in many applications to the universally accepted joining processes, such as mechanical fasteners, fusion and resistance welding, and adhesives.

INTRODUCTION

The demand is increasing for highly reliable, remote, metal joining processes for hazardous or inaccessible operations, such as nuclear reactor repairs or assembly of structure in Earth orbit or space. The NASA Langley Research Center-developed explosive seam welding process in creating narrow, long-length, uniform joints can contribute significantly to joining operations, due to many capabilities that exceed the universally accepted joining processes, such as mechanical fasteners, swaging, fusion welding, soldering, and adhesives. The purpose of this paper is to present this process in terms of the joining principles and variables, types of joints, capabilities, and current and potential applications.

EXPLOSIVE JOINING PRINCIPLES

Explosive welding produces metallurgical bonds that are impossible to achieve by any other joining process. The explosive welding process is accomplished by a high-velocity, angular collision of metal plates, which effaces the oxide films on both surfaces to allow interatomic (electron sharing) linkups through Van der Waal forces. (See References 1, 2, and 3.) The angular collision and parameters are shown in Figure 1. The several

*NASA Langley Research Center, Hampton, VA 23665.

million psi explosive pressure on top of the flyer plate produces velocities in the plate of several thousand feet per second. On impact, the kinetic energy is converted to skin-deep (less than 0.001 inch) melts, which are stripped from the surfaces and squeezed out by the closing angle. The closest analogous metallurgical bonding process is vacuum bonding in which surface oxides are mechanically removed under hard vacuum to allow interatomic linkups. Two explosive joining processes now exist, cladding and seam welding.

The explosive cladding process (Reference 1) utilizes bulk explosives, such as dynamite or nitroguanidine, to create an explosive pressure input that travels at a velocity of approximately 4000 to 10,000 ft/sec to create the angular collision. The loose-powder explosive is literally shoveled onto the flyer plate, which is spaced in parallel to the base plate. For example, in Reference 1, 175 pounds of dynamite was used in cladding a 0.125-inch thick, 4- by 8-foot lead sheet to a 0.25-inch thick steel plate. Explosive cladding is limited to approximately 10-foot lengths, due to the inability to maintain the collision parameters.

The explosive seam welding process (References 2 and 3) differs from cladding in the explosive used and the angular collision mechanisms. The explosive used is considerably more powerful, cyclotrimethylene-trinitramine (RDX), which is encased in a lead-sheathed "ribbon," as shown in Table I. The explosive load is measured in grains per foot (7000 grains per pound), and has a velocity of explosive propagation of 26,000 ft/sec. The plates are initially separated and the ribbon explosive is taped to the flyer plate. On initiation of the explosive, the center portion of the flyer plate is bent, as shown in Figure 2, to produce angular collisions on both sides. The resulting joint is highly uniform and less than 0.5 inch in width. As a comparison of efficiency, a 175-pound quantity of RDX could produce a continuous joint in 0.125-inch aluminum 49,000 feet long. With an approximate weld width of 0.25 inch, the total weld area would be over 1020 square feet, as compared to the 32 square feet in the cladding operation.

SEAM WELDING VARIABLES

The following explosive welding variables must be optimized for every joining configuration (References 2 and 3):

1. Plate materials
2. Plate thickness
3. Explosive quantity
4. Standoff (plate separation)
5. Surface finish and cleanliness
6. Mechanical shock

Metal alloys, conditions, and thickness present a wide range of density, mass, hardness, and malleability. These variables directly influence the quantity of explosive necessary to bend and accelerate the plates to achieve

explosive joining. As the above variables increase, more explosive is necessary.

A plate standoff or separation is required to achieve the high-velocity, angular collision. The amount of standoff can be as little as 0.010 inch, the maximum (to minimize material deformation and energy losses in bending) is 0.025 inch. This standoff can be achieved by shimming, fixturing, or machining. Any convenient shim may be used, including masking tape. A notch can be machined in the surface of either or both plates. The plates can be configured to present a parallel interface, or, to maximize efficiency, an angular interface (inverted "V") can be machined into one or both plates; that is, 5° angular faces, sloping from the center of the desired joining interface outward to a depth of 0.015 to 0.020 inch. An example of the latter approach follows in the applications section.

Surface cleanliness and smoothness must be carefully managed to achieve explosive joining success. The properties of substantial amounts of oxide films, such as rust or that on aluminum alloys, as well as water, grease, or oil, prevent the explosive joining process. Iron alloys must be polished and degreased to remove mill scale and corrosion-protective greases; 100 grit emory paper and an alcohol wipe, or other solvent that leaves no deposit on drying, is adequate. Stainless steel alloys need only degreasing. Pure aluminum has a minimal oxide film, requiring only degreasing. However, the aluminum alloys develop oxide films that prevent joining. These oxide films have considerably different properties than the parent metal. These oxide films are dependent on manufacturing processes and environmental exposure. Chemical etching to remove the oxide films allows reliable bonding under laboratory ambient over a several-week period. Since explosive joining is a "skin deep" process (0.001 inch penetration), surface scratches more than 0.003 inch deep prevent joining. A surface finish of 32 rms assures complete bonding. The surface finishes on virtually all sheet metal stock are smoother than 32 rms.

The mechanical shocks generated by the explosive pressure used to accelerate the plates and that generated on impact are the most damaging influence in the explosive joining process. The relative amplitude and influence is dependent on materials and structural configuration. These shock waves can not only damage sensitive structure in the area of the process, but can actually destroy a bonded joint immediately after its creation. Shock waves can be reduced by placing additional structure in the bond area. This additional structure can be a plate on the opposite side of a joining process (anvil), or clamping plate stock just outboard of the joining process. Once the joint has been made, the additional structure is removed. Adequate shock absorption can be achieved in the structure to be joined, particularly in thicker materials.

TYPES OF JOINTS

Four different types of lap joints and tube joining have been demonstrated, using explosive seam welding.

The four joint types are shown in Figure 3. The dissimilar-thickness joint was described earlier. The similar-thickness joint is created by placing explosive ribbons on both sides of the separated plates. The ribbons are simultaneously initiated by one blasting cap. The explosive pressures are exactly balanced. The sandwiched-butt joint combines the above two approaches to accomplish a butt joint. The scarf joint (Reference 4) is created by shifting the longitudinal axes of the explosive ribbon to create unbalanced forces. The plates are bent into axial alignment and joined in a single operation.

One setup for explosive seam welding to accomplish tube plugging is shown in Figure 4. Cylindrical plugs are machined to provide an "inverted V," angular interface, and are inserted into the tube. The explosive ribbon is wrapped around the outside circumference, opposite the inverted V, and initiated.

Tube joining is accomplished in the setup shown in Figure 5. Following tube insertion, the explosive is initiated by the blasting cap indicated. The inner tube is driven into the outer tube to accomplish the joining mechanism. The anvil ring prevents distortion of the female tube. Conversely, the outer tube (without the anvil ring) could be wrapped with explosive and driven into the male to accomplish the joining mechanism. The V-notch can be machined into either tube, or partially in both.

CAPABILITIES

The following is a general description of the capabilities of the explosive seam welding process.

1. Performs under hazardous conditions - This process can be used in hostile environments or conditions to reduce risks to personnel and facilities. The explosive materials (a number of different types are available with different characteristics) and joining process have a low sensitivity to environments, such as nuclear radiation, toxic atmospheres, inert gases, vacuum, hot (+450°F) and cold (-320°F) temperatures, and high-intensity light and sound. The recommended approach would be to install the explosive materials on the structure to be joined, prior to insertion into the hazardous environment or condition.

2. Remote - This process has the capability of hands-on operation to separation distances of miles. A totally confined explosive seam welding process has been developed, as shown in Figure 6 (Reference 5). The explosive ribbon is placed inside a flattened steel tube with closed end fittings, which accommodate the initiator and initiating method. On initiation, the explosive pressure is coupled through the tube wall to accomplish the welding mechanism, and the explosive products are contained within the tube. This method not only allows hands-on operation, but prevents the contamination of surrounding areas by the explosive products. Long-distance operation can be achieved by transmission of command signals to self-contained receiving units

which initiate the explosive mounted on the structure to be joined. This transmission approach is routinely applied to orbital and deep-space functions.

3. Simplicity - Once the explosive joining parameters have been established, the setup becomes purely mechanical. Minimal training is required, typically less than eight hours.

4. Material preparation - Machining, polishing, and/or chemical degreasing and cleaning are comparable to other joining processes. The explosive ribbon and blasting cap are simply taped or bonded to the materials to be joined.

5. High-strength, fatigue-resistant joints - This is a cold-working process which does not affect the parent metal properties. The area of the metallurgical bond can be created, through preselection of joining variables, to exceed the strength of the material thicknesses by a considerable margin. The resulting joints greatly exceed the fatigue strength (tension-tension and flexural) of fusion-welded joints (Reference 6).

6. Ability to join a wide variety of metals and alloys - Table II lists the metals and range of thicknesses in which 100% strength joints can be obtained (References 2 and 3). The plates to be joined were placed in parallel (except as noted), separated by 0.015 inch.

7. Ability to join metal combinations - This process can metallurgically join a wide variety of metal combinations, as well as different tempers and conditions. Table III provides a summary.

8. Ability to join very thin materials to very thick materials - The highest efficiencies in this process are achieved, using very thin flyer plates to thick base plates. Thin materials are most responsive to acceleration, as well as bending to achieve the necessary high-velocity angular collision. Furthermore, the thick base plates quickly dissipate deleterious shock waves. The thickness of the flyer plate is limited by its ability to resist being crushed and pinched off (0.001 inch in steel, 0.010 inch in aluminum). There is no upper limit on base plate thickness.

9. Ability to join a wide range of lengths and tube diameters - The minimum length that can be joined by this process is approximately 0.040 inch; there is no long-length limitation. The explosive ribbon is routinely manufactured in several hundred-foot lengths. The ribbon can be spliced with no loss in efficiency. The minimum tube diameter that can be joined by this process is approximately 0.040 inch with no upper diameter limit.

10. Ability to join complex shapes - This process can join a wide variety of shapes from flat stock to irregular shapes to tubes (cylindrical and non-cylindrical). The explosive ribbon is highly flexible and can be shaped to conform to a wide variety of contours. Shaping limits are: a bend radius of

0.063 inch on the ribbon's flat surface, and approximately a 1-inch radius to shape the ribbon on its edge, maintaining a single plane.

11. Joint uniformity and reliability - The joints created by this process exhibit a high degree of physical uniformity, in terms of the plate surfaces, areas, and thicknesses worked by the explosive pressure, bond areas, and joint strengths. The ribbon is manufactured to exacting aerospace standards; the explosive load in the ribbon varies less than 5% down the length. The plate surfaces are protected from lead embedment by masking or double-backed tape. The plate thicknesses of softer metals are reduced by approximately 0.005 inch by the explosive pressure. Once the joining variables are established, the resulting joint variations are caused by material preparation and machining and stock uniformity.

12. Inspectability - The joints can be evaluated nondestructively, using ultrasonic techniques, such as those described in Reference 7. Since the surfaces and thicknesses of the joints are highly uniform, the bond areas can be precisely located.

13. Hermetically sealed joints - The metallurgical bond created by this process has demonstrated absolute sealing ability. No leaks were detected (less than 1×10^{-9} cc/sec of helium at one atmosphere differential pressure, or the instrument's sensitivity limit) on a 12-inch diameter aluminum joint, before and after pressurization to 100 psi dry nitrogen. A surface finish of 32 rms is required.

14. Tooling - No tooling is required, provided the variables are controlled. However, the plates can be positioned by fixturing, or removable " anvils" can be used to maximize joining efficiency by reducing deformations and absorbing shock waves, as described in the explosive seam welding variables section.

15. Rapid operation - The explosive ribbon can be installed quickly; the installation can be mechanized and automated. On initiation of the explosive, the joining process proceeds at a velocity of 26,000 feet/second.

16. Low input-energy requirements - The explosive ribbon produces all the energy necessary to create a joint. Typical electric blasting caps, used to initiate the explosive, require approximately 0.1 joule (watt-sec). A number of other aerospace approaches for initiation can be used, such as mechanically actuated percussion primers (using human, hydraulic, pneumatic, or electrical energy sources), explosive transfer lines, or lasers. Each initiation method has its unique advantages and disadvantages in terms of cost, availability, safety, and system effects.

17. Balanced forces - The explosive joining setups can be configured to produce opposing explosive inputs to minimize or eliminate offsetting forces. For example, placing explosive ribbons on both sides of a structure (with simultaneous initiation), and cylindrical joints would generate symmetrically opposed forces.

18. Safety - The RDX explosive ribbon cannot be initiated by routine handling and cutting by personnel or electrical inputs (Reference 3). Other explosive materials, such as dipicramide, are available, that are insensitive to rifle fire and lightning. Dipicramide is stable to 450°F for 50 hours, and will burn with low energy output, but will not detonate. Simple procedures on controlling personnel accessibility, handling, and storage will preclude potential hazards. Electric blasting caps must use electrical shielding, grounding, and fail safe firing systems. The explosive products (lead fragments, pressure wave, and carbon-particle smoke) can be easily contained by several cubic-foot volume shielding. Since only small quantities of explosive are used, the explosive pressure attenuates to less than one psi within the first foot of distance from the source.

APPLICATIONS

Small-scale explosive seam welding has been accepted for one major application. Although joining problems are virtually unlimited, a number of other potential joining applications that take advantage of the unique capabilities of this process are presented here.

Present application - The first major application in which small-scale explosive seam welding will be used (scheduled for 1985) is in the repair of four nuclear reactors in Canada (Reference 7). A total of 390 fuel channels must be removed and replaced in each reactor. This process was developed and demonstrated in six months to make the final joint on the reactor face for each fuel channel. A 30 grains/foot ribbon will be double-backed tape to the internal circumference of the end fitting attachment ring (Figure 7) with the ribbon centered on the machined "V." An electrical blasting cap will then be installed on the butted interface of the ribbon. The fuel channel with attachment ring will then be inserted into the reactor, positioning the attachment ring opposite the bellows flange sleeve, as shown. The resulting joint has twice the bond area necessary to support the fail strength of the 0.030-inch wall thickness tube. This large bond area compensates for the known range of variables, such as surface finish and diametrical mismatches to 0.060 inch. One joint was subjected to 100 thermal cycles of 560°F to ambient with no loss in strength. The use of this process, instead of a robotic fusion welder, is anticipated to reduce personnel radiation exposure from 11.43 man-rems to 0.7 man-rem, and reduce reactor downtime from 78 hours to 1.6 hours.

Potential applications - Potential applications may include pipelines, sealing of vessels, and assembly of large space structures.

This process could be used in joining and sealing thin-walled tubing. For thick-walled tubing, the primary loads could be carried through bolted flanges, and the joint sealed with an explosively joined internal sleeve. Tubes could be plugged by using closed-end cylinders, joined to the internal diameter of the tube.

Vessels could be remotely capped and sealed, as shown in Figure 8, for disposal of hazardous wastes or to prevent contamination of materials. As an example of the latter, a sample from the surface of another planet could be returned to Earth. An attempt to bring a sealed sample from the moon failed on the Apollo program, using mechanical seals.

Remote assembly of large space structures could be accomplished, using the concept shown in Figure 9. The explosive ribbon would be installed inside the closed, conically domed cylinder. The cone would assist in guiding and inserting the mating cylinder, which is part of a second structure. The closed volume would fully contain the explosive products.

A second space application could be the erecting and rigidizing of erectable structures, as shown in Figure 10. A 13-column structure can be erected by shortening the length of the central telescoping tubes. When erected to the desired shape, the telescoping tubes would be joined. Again, the structure would contain the explosive products.

Space assembly of continuous large-area structures may be desirable. Figure 11 shows an 18-inch diameter cylindrical model in which all the 0.040-inch aluminum (bulkheads, neck, and outer cylinder) was explosively joined to substructure.

CONCLUDING REMARKS

The demand is increasing for highly reliable, remote metal joining processes for hazardous or inaccessible operations. This paper describes a small-scale explosive seam welding process in terms of joining principles, variables, types of joints created, capabilities, and applications.

Explosive welding requires a high-velocity angular collision of explosively driven plates to break up and efface the plates' oxide films to allow interatomic linkups. Explosive seam welding utilizes lead-sheathed, small-quantity, explosive ribbons that have been loaded with several different quantities of explosive to create narrow (less than 0.5 inch), long-length, uniform joints. Explosive quantity is tailored to the metal alloy's properties, as well as thickness. Other variables include plate separation methods, surface finish and cleanliness, and the mechanical shock created by the explosive pressure input and plate impact.

Four different types of lap joints and tube joining have been demonstrated. The capabilities of this process include: remote operation under hazardous conditions, 100% of parent metal properties, join a wide variety of metals, alloys, and combinations (including steel from 0.001 to 0.050 inch and aluminum from 0.010 to 0.187 inch), simple operations, uniform, inspectable, hermetically sealed joints and fast, safe operations.

The current application of this process is to make 390 steel tube joints in each of four active nuclear reactors. This process has the potential for

many hazardous and inaccessible operations, including assembly of structure in space.

The current development and acceptance of this small-scale explosive seam welding process has indicated that this process is indeed practical and has many capabilities that are superior in many applications to the universally accepted joining processes, such as mechanical fasteners, fusion and resistance welding, and adhesives.

REFERENCES

1. Otto, H. E.; and Carpenter, S. H.: Explosive Cladding of Large Steel Plates With Lead. Welding Journal, pp. 467-473, July 1972.
2. Bement, Laurence J.: Small-Scale Explosive Seam Welding. Presented at the Symposium on Welding, Bonding and Fastening, Williamsburg, VA, May 30 to June 1, 1972.
3. Bement, Laurence J.: Small-Scale Explosion Seam Welding. Welding Journal, pp. 147-154, March 1973.
4. Bement, Laurence J.: Explosively Welded Scarf Joint. Patent 3,842,485, November 22, 1974.
5. Bement, Laurence J.: Totally Confined Explosive Welding. Patent 3,797,098, March 19, 1974.
6. Otto, H. E.; and Wittman, R.: Evaluation of NASA-Langley Research Center Explosion Seam Welding. NASA CR-2874, August 1977.
7. Aikens, A. E.; and Bement, L. J.: Explosive Seam Welding Application to Reactor Repair. Presented at the 3rd Annual Conference of the Canadian Nuclear Society, Toronto, Canada, June 9, 1982.

TABLE 1

Cross-sectional Dimensions of Linear Ribbon RDX Explosive

Explosive Load, grains/foot	Thickness, inch	Width, inch
7	0.020	0.220
10	0.020	0.300
15	0.025	0.315
20	0.030	0.365
25	0.035	0.370
30	0.035	0.510

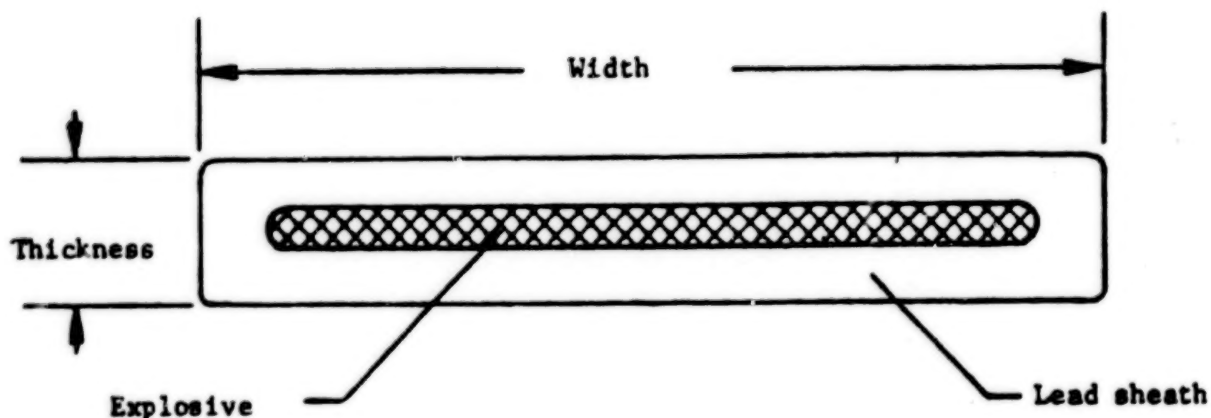


TABLE II

Like Metals Joinable by Explosive Seam Welding
(100% Strength Joints)

<u>Metal</u>	<u>Range of Thickness (inch)</u>
a. Iron/steel Low-carbon to 300 and 400 stainless	0.001 to 0.050
b. Aluminum - any fully annealed alloy and all age and work-hardened alloys except 2024 and 7075	0.010 to 0.188
c. Copper/brass	0.010 to 0.150
*d. Titanium (Ti-6Al-4Va)	0.005 to 0.050

*Each plate prebent 5° ——————

TABLE III

Metal Combinations Joinable by Explosive Seam Welding

- a. Low-carbon to series 300 and 400 stainless steel are joinable in any combination
- b. All aluminum alloys and conditions are joinable to any other alloy and condition, except a combination of 2024-T3, T4, etc. and 7075-T3, T6, etc.
- c. Any combination of copper, aluminum, and brass can be joined

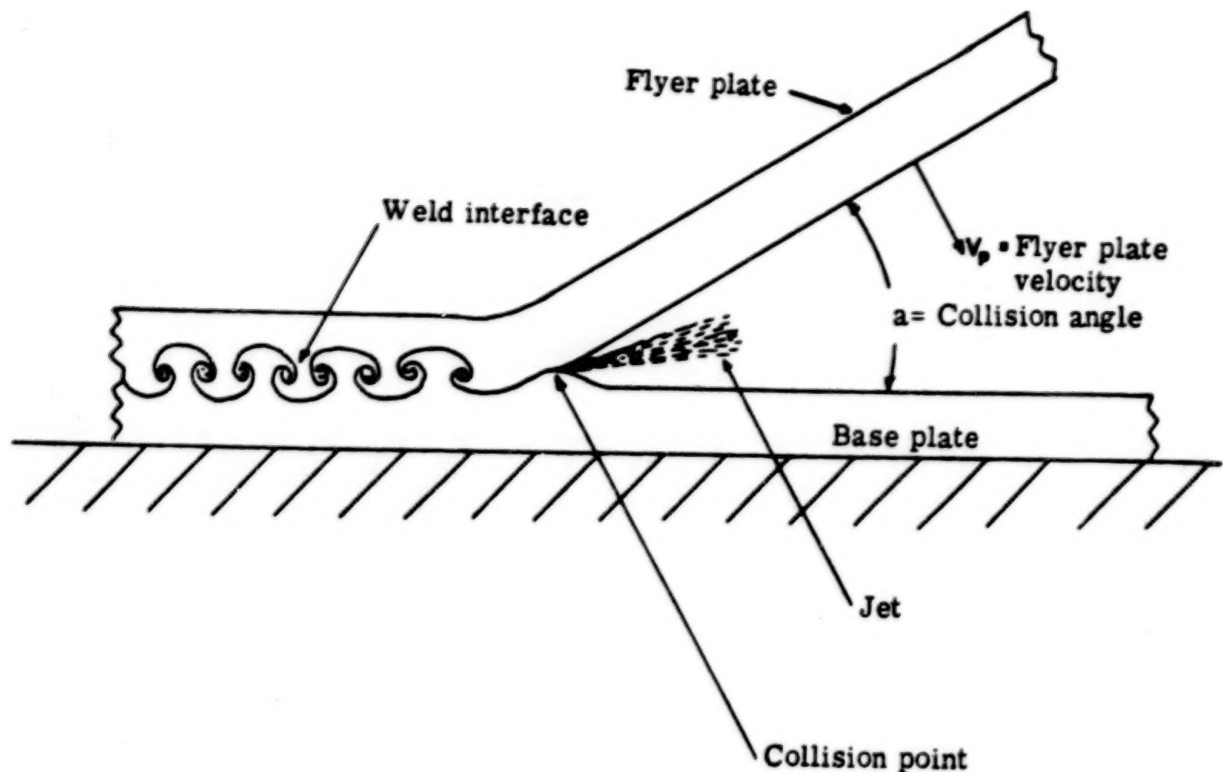


Figure 1.- High-velocity angular collision of metal plates in an explosive welding operation.

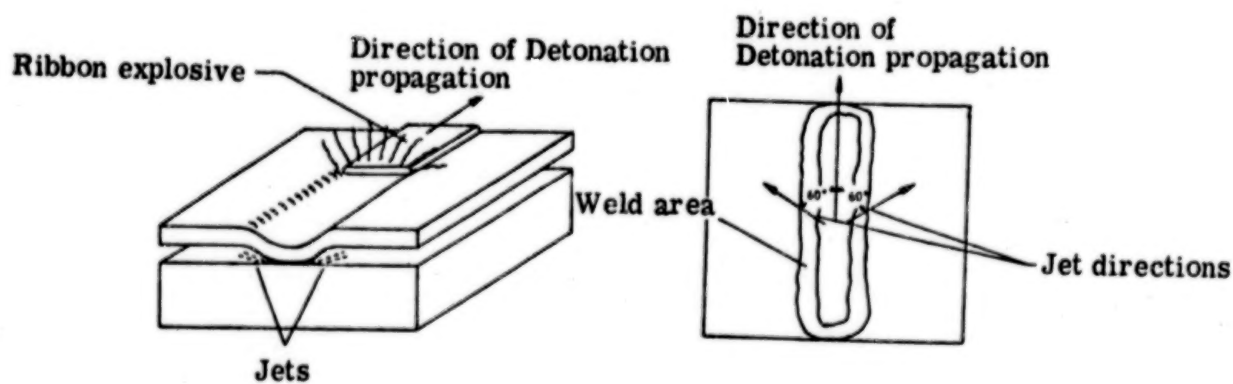


Figure 2.- Mechanisms involved in small-scale explosive seam welding process.

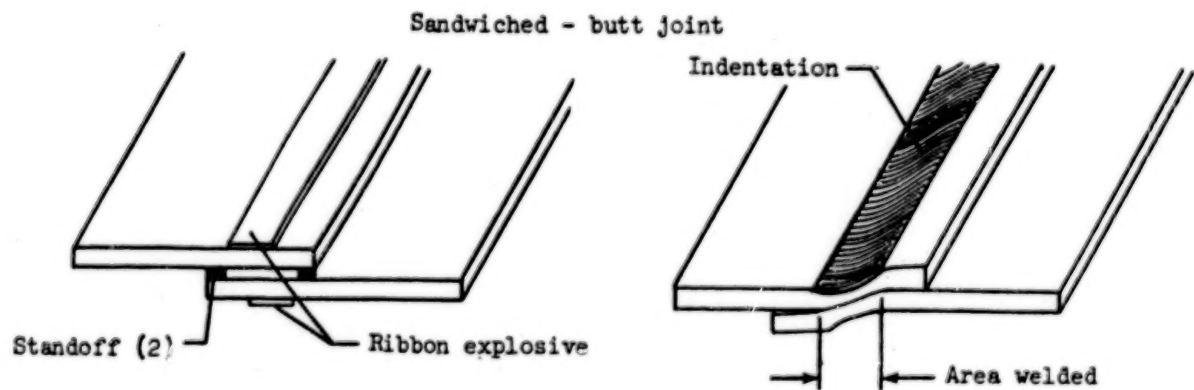
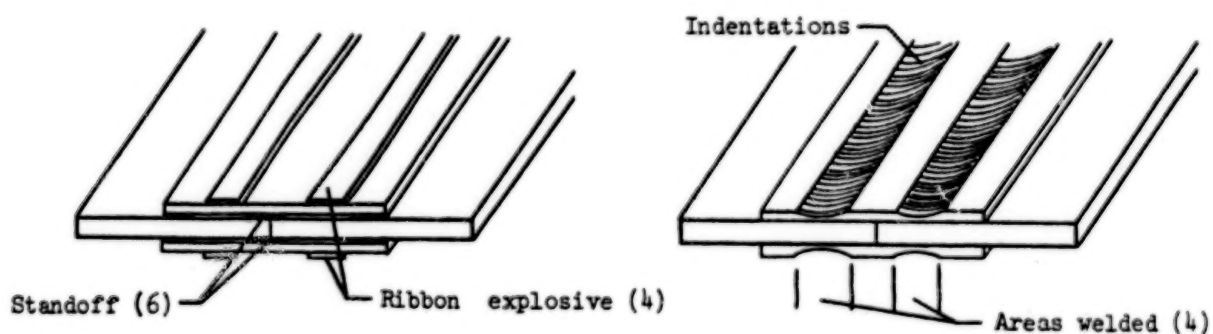
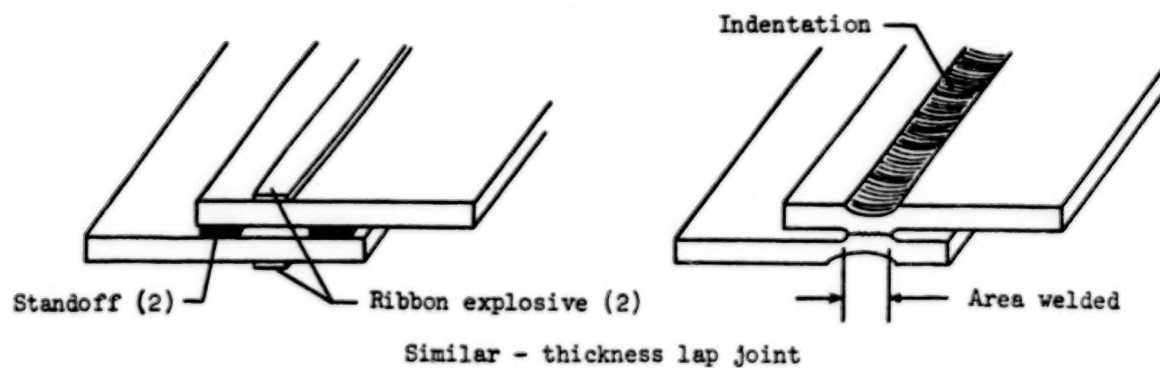
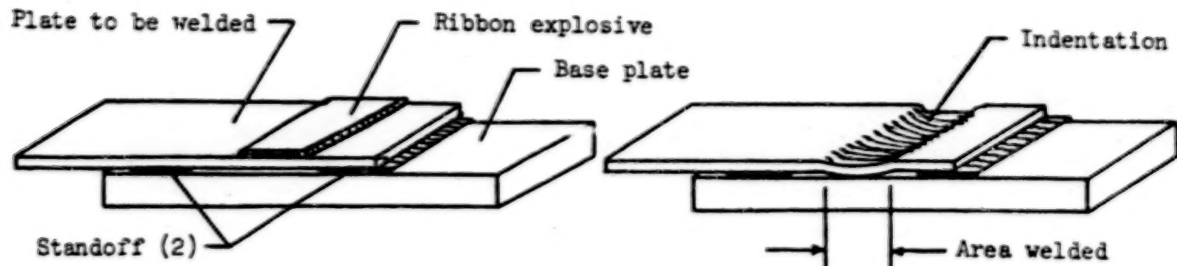


Figure 3.- Small-scale explosive seam welded joints.

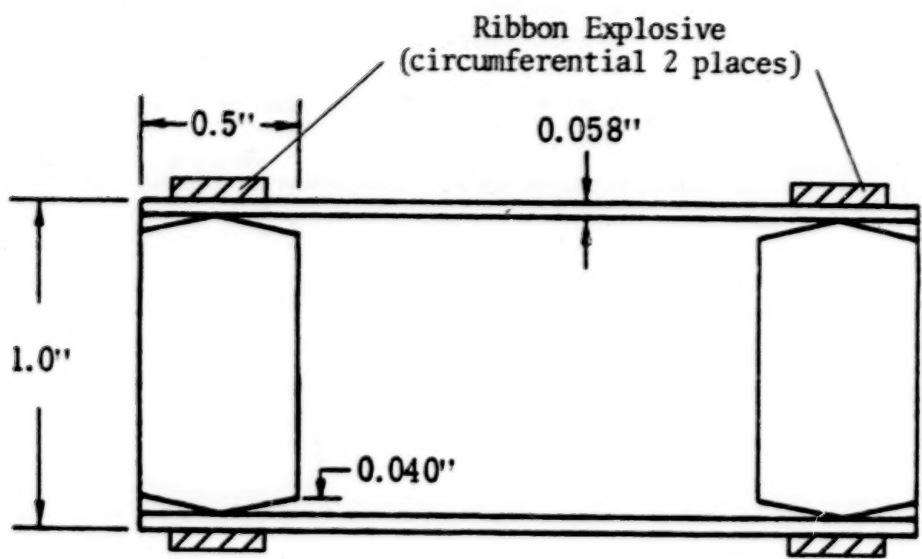


Figure 4.- Setup for explosive welding of 6061-T6 aluminum plug in 6061-T6 tube.

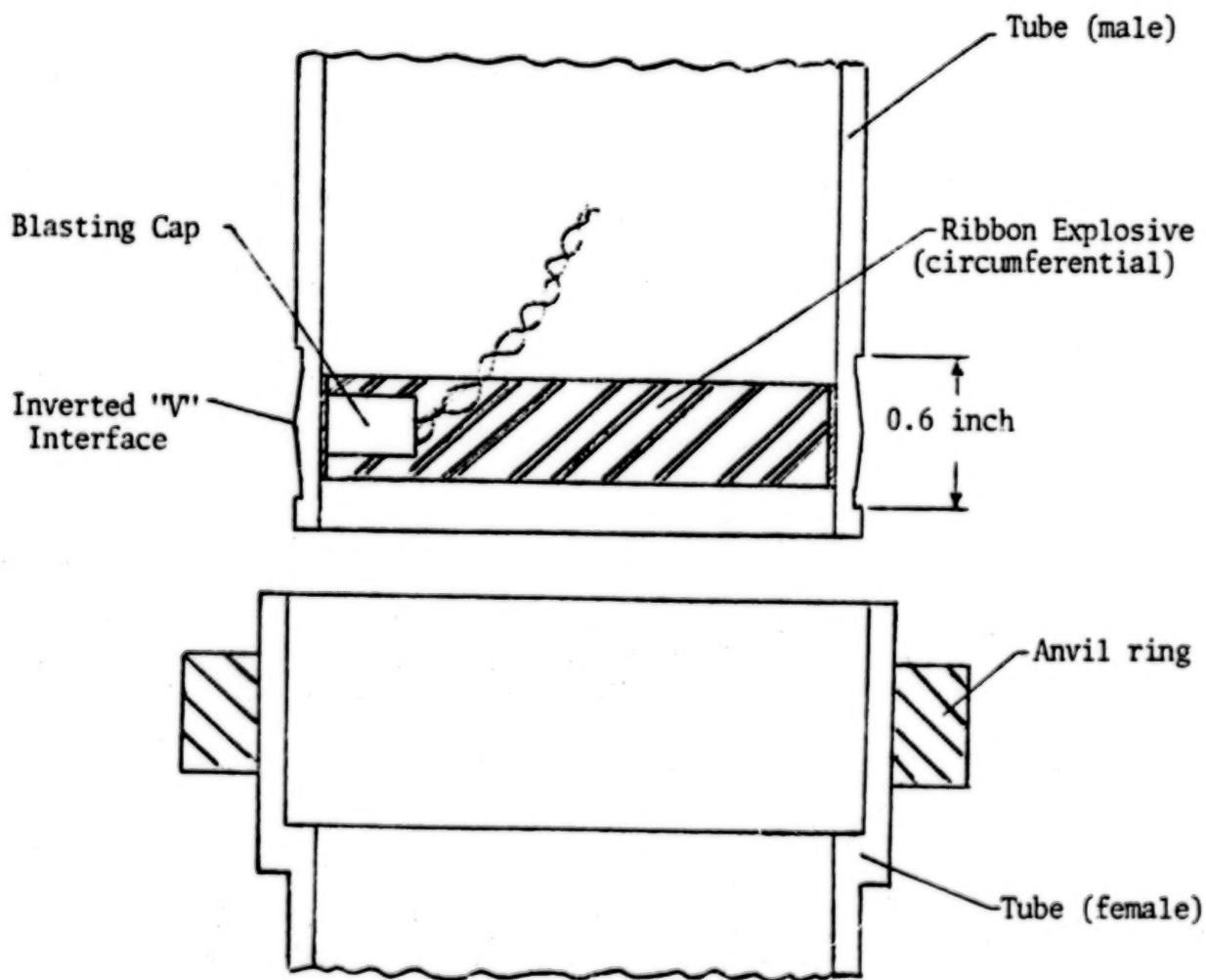


Figure 5.- Small-scale explosive seam welding setup for tubes.

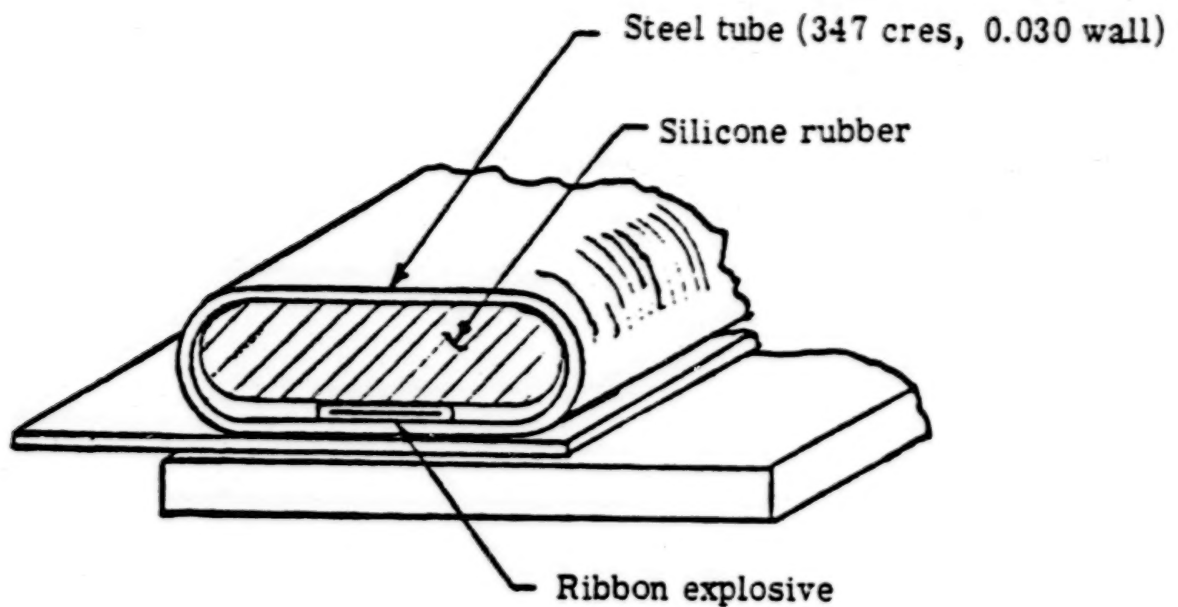


Figure 6.- Method for achieving a totally confined small-scale explosive seam weld.

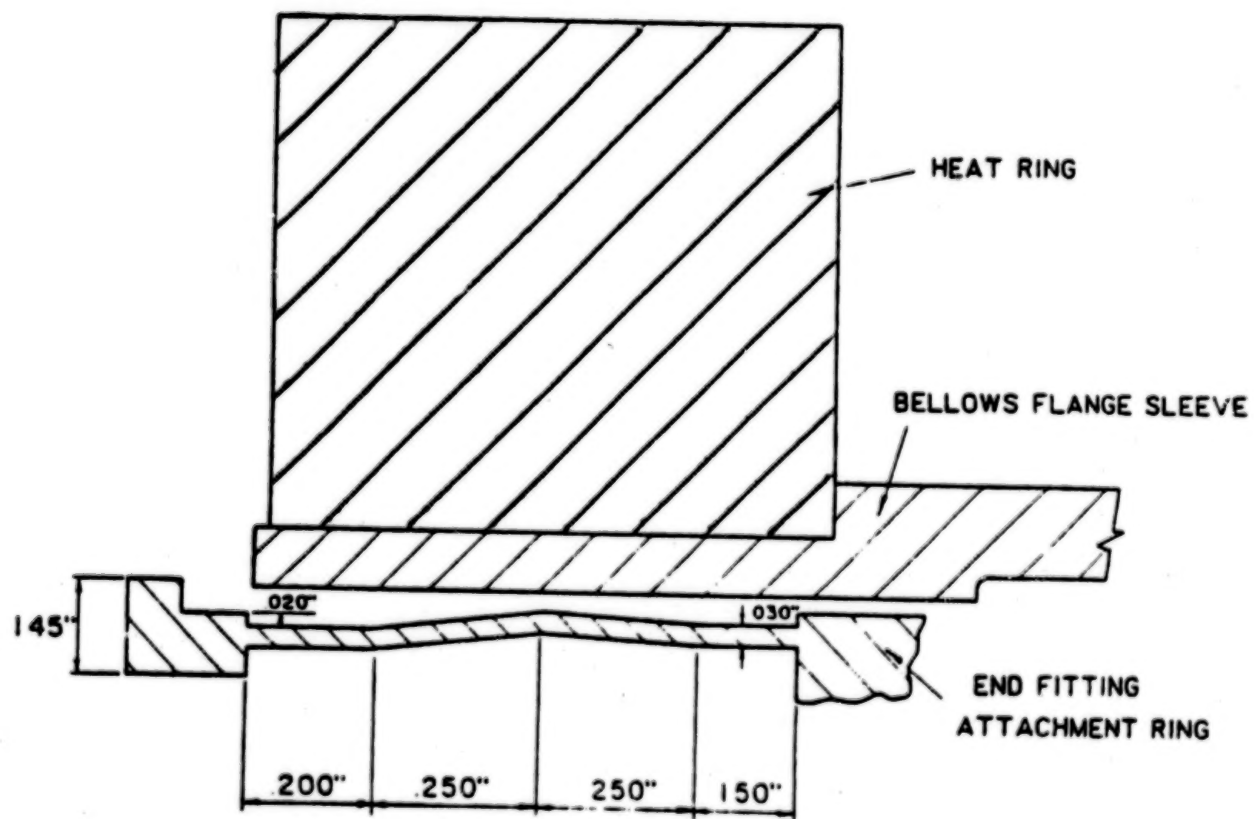


Figure 7.- Setup for explosive seam welding of nuclear reactor tubular joint.

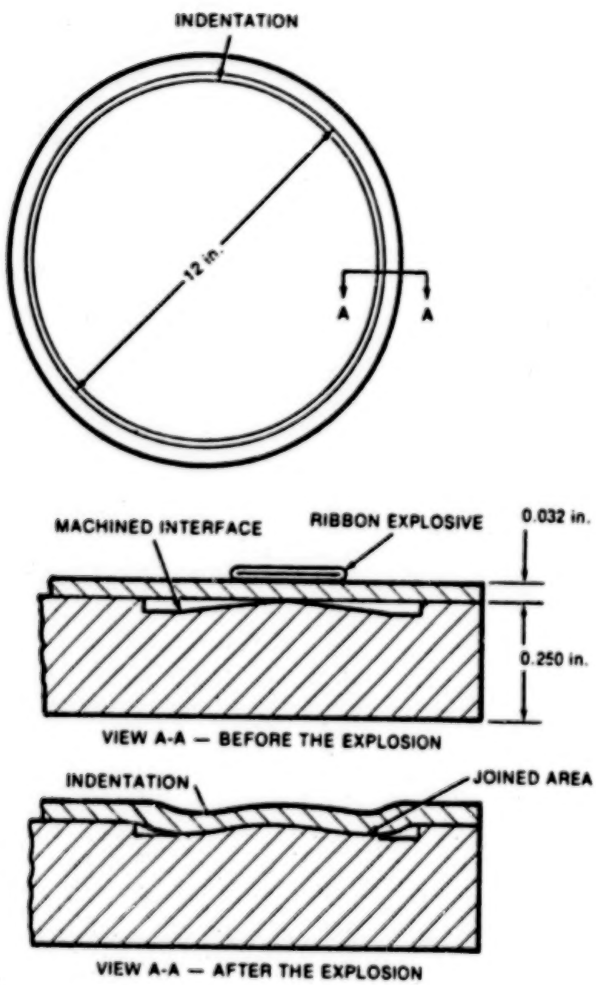


Figure 8.- Approach for closing and hermetically sealing a vessel.

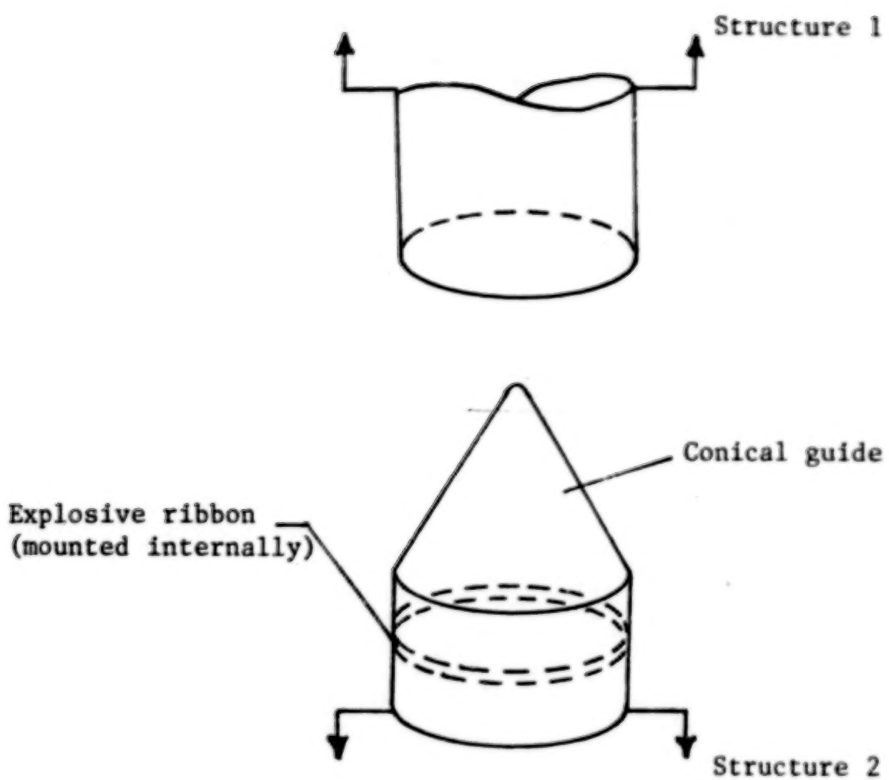


Figure 9.- Concept for totally confined, remote joining of structure in space.

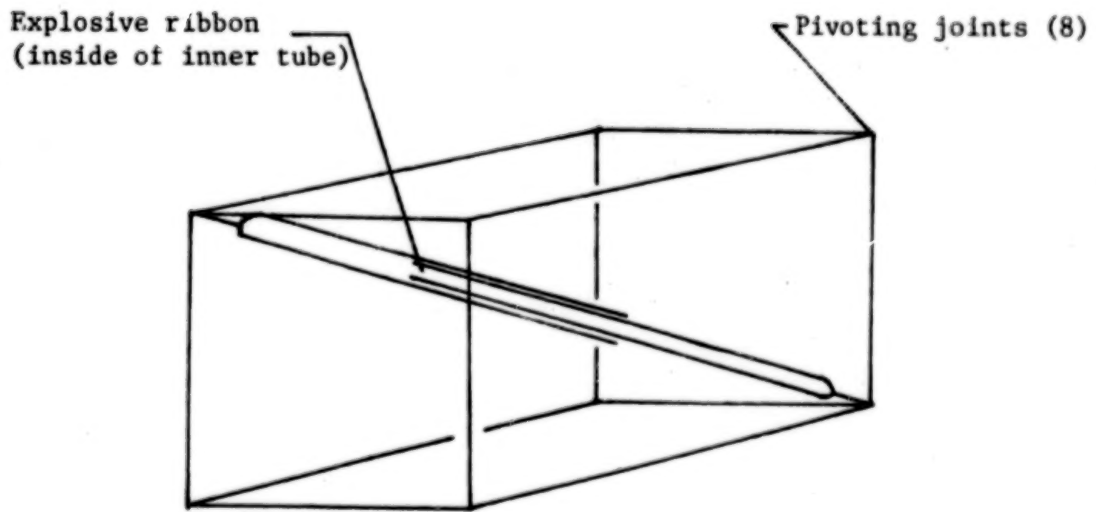


Figure 10.- Concept for totally confined, remote rigidizing of an erectable structure.

244

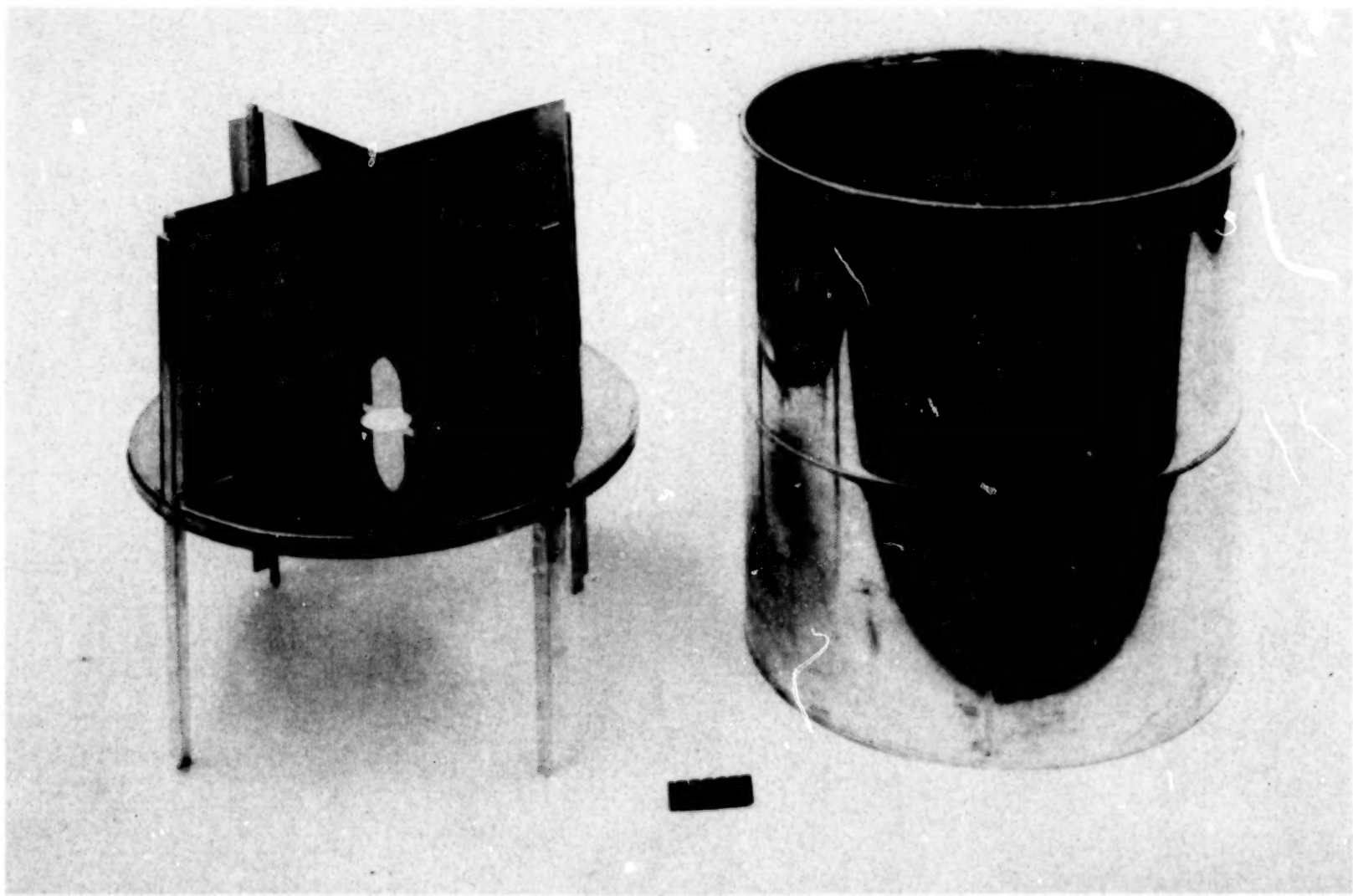


Figure 11.- Photograph of an 18-inch diameter model of a space station type structure fabricated by explosive seam welding; the internal structure of the model is shown on the left.

244

BEST AVAILABLE COPY

BLANK

PAGE

THE MANNED MANEUVERING UNIT
FLIGHT CONTROLLER ARM

Ken E. Falkner
Martin Marietta Denver Aerospace
Denver, Colorado

ABSTRACT

The Manned Maneuvering Unit (MMU) and its support equipment provide an extravehicular astronaut mobility, and the ability to work outside the confines of the Shuttle Orbiter payload bay. The MMU design requirements are based on the highly successful Skylab M-509 maneuvering unit. Design of the MMU was started as an R&D effort in April 1975 and Flight Hardware design was started in August 1979 to support a possible requirement for in-space inspection and repair of Orbiter thermal protection tiles. Subsequently, the qualification test and production activities were slowed, and the current projected earliest first flight is now STS-11 in January, 1984.

The MMU propulsion subsystem provides complete redundancy with two identical "systems". Each system contains a high pressure gaseous nitrogen tank, an isolation valve, a regulator, and twelve 1.7 lbf (7.5 N) thrusters. The thrusters are packaged to provide the crew member six-degree-of-freedom control in response to commands from translational and rotational hand controllers. The MMU control and electrical subsystems are also redundant and provide thruster logic, power conditioning and distribution, and heater power. An automatic rate stabilization mode is also available for the three rotational axes. As the original program schedule was short, extensive use of "off-the-shelf" components and proven assembly techniques were used. Included with the MMU is its airborne support equipment, the Flight Support Station (FSS), that provides for the propulsion subsystem recharge capability and activation of separation nuts using gas from the Orbiter GN₂ environmental control system. All mechanisms have been designed and tested to ensure proper operation within astronaut applied force capabilities during and after exposure to severe acoustic and thermal environments. The most complicated of these mechanisms is the flight controller arm.

This paper discusses the MMU control arm requirements, design, and developmental history.

INTRODUCTION

The MMU is based on the M-509 maneuvering unit, flown inside the Orbital Work Shop for 14 hours by five astronauts on the two Skylab missions. Subsequent to the Skylab program Martin Marietta received a contract from NASA-Johnson Space Center (JSC) in April 1975, to perform technology surveys, conceptual design, preliminary definition, and design of an MMU for the Space Shuttle Program. Also included was the design, fabrication of prototype hand controllers, and high fidelity mockups of the MMU and FSS. Amendments to the contract resulted in the development of the control laws; design and breadboarding of the control electronics; design, fabrication, and testing of propulsion components such as the three thruster module (TRIAD), regulator, and isolation valve; and establishment of the interfaces of the MMU and FSS with the astronaut, Extravehicular Mobility Unit (EMU), and Orbiter. The development effort provided the sound technical base for the design and development of the MMU and FSS for Shuttle use.

Full scale development of the MMU started in August 1979 to support a Space Shuttle thermal protection tile inspection and repair mission under contract to JSC. The MMU can also support Space Shuttle operations involving payload inspection, servicing, and repair; aid in large structure construction; and perform emergency rescue. The MMU is a self-contained system consisting of power, control, propulsion, structure and mechanisms, and thermal subsystems designed for Astronaut Extravehicular Activity (EVA). Key features are shown in Figure 1. Electrical power is provided by redundant silver-zinc batteries with a normal output of 750 Wh at 16.8 Vdc. The control subsystem contains three major elements, two hand controllers and a Control Electronics Assembly (CEA). They operate together providing signals to the propulsion subsystem allowing rotational and translational motion. The CEA contains gyros for automatic attitude hold and circuitry to convert hand controller deflections to thruster valve commands. The MMU structure is assembled using aluminum frames and skin. Mechanisms are provided for: three arm positions and arm length adjustment of five in. (127mm) total to accommodate different size astronauts from a five percentile female, to a 95 percentile male; and attachment to the EMU primary life support system (PLSS). Thermal control is provided using white paint on the outside and heaters on selected components. The CEA heat is rejected by radiation from MMU aft panels that are covered with silverized teflon.

The Flight Support Station (FSS), shown in Figure 2, is a piece of air-borne support equipment which will be structurally attached to fittings in the Orbiter payload bay (Fig. 3). It provides for storage of the MMU when not in use; allows the astronaut to don and doff the MMU using handrails and adjustable foot restraints; provides an interface for and control of the Orbiter's GN₂ environment control supply gas for recharging of the MMU; and interfaces with the Orbiter's power and instrumentation system while providing heater power for the MMU and FSS.

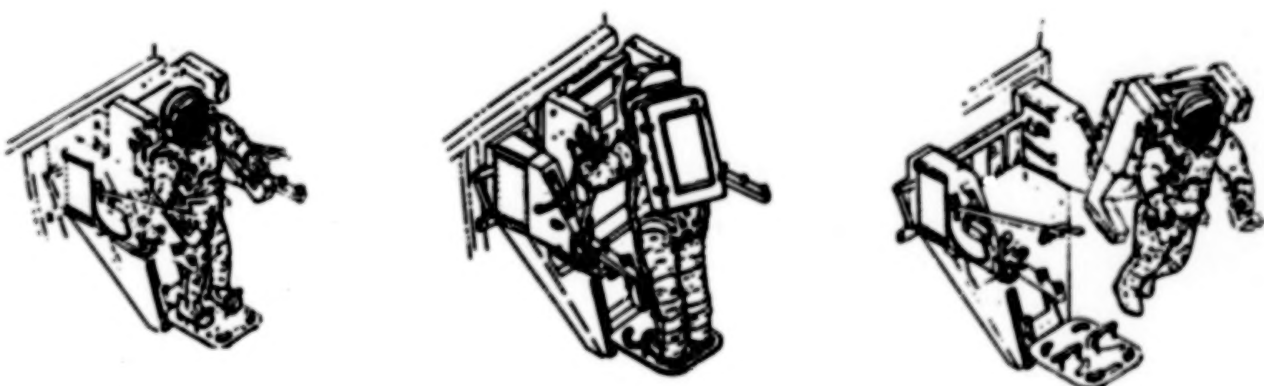
The function of the MMU arm is to situate the hand controllers in a position where their operation can be achieved without discomfort to the suited crewmember.



(a) Manned Manuevering Unit (b) EMU and PLSS

(c) MMU Latched to PLSS

Figure 1. Manned Manuevering Unit EVA System



Don/Doff Configuration

Servicing Configuration

Egress/Ingress

Figure 2. MMU Flight Support Station

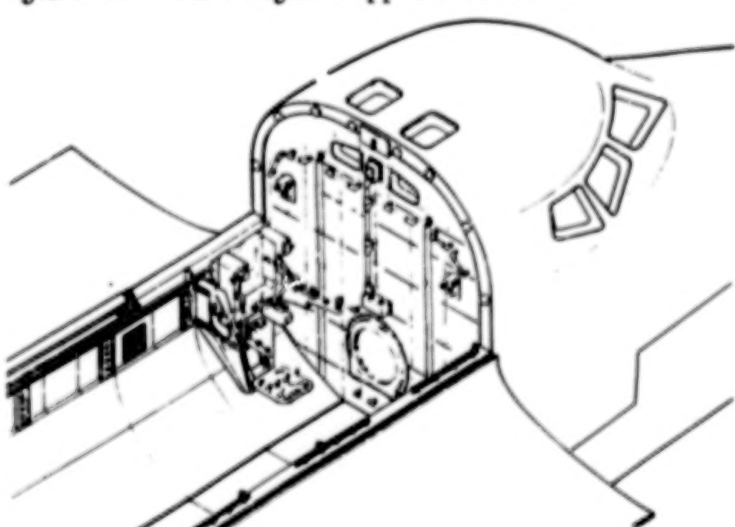


Figure 3. MMU Storage Location in Orbiter for Launch and Reentry

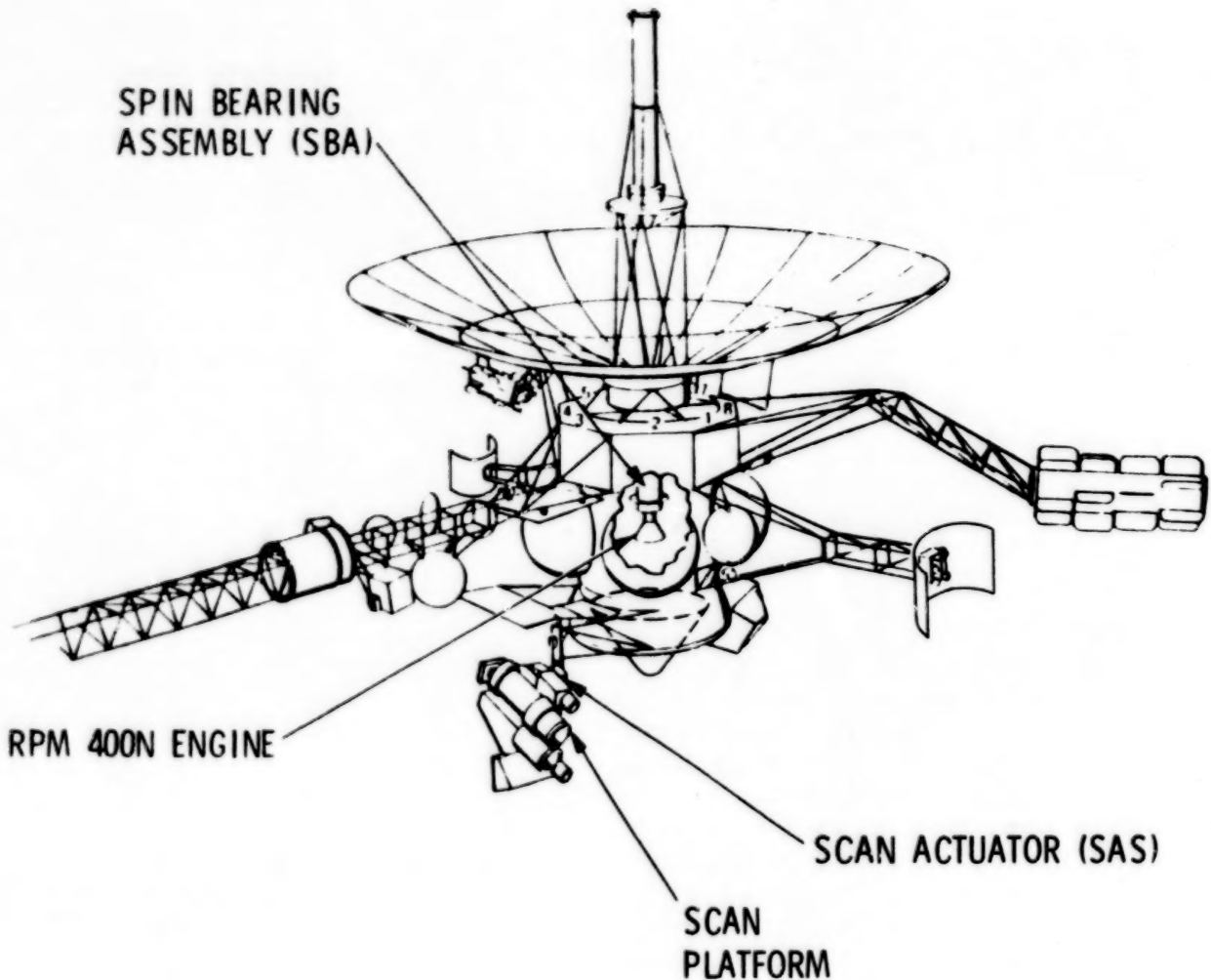


Figure 1. Galileo Spacecraft

SPIN BEARING ASSEMBLY CONFIGURATION

The SBA, Figure 2, has a fairly complex structure because it must provide a spun mounting for the 400 newton retropropulsion engine and a path for its fuel lines in addition to providing mechanical and electrical coupling between rotor and stator. This engine spins with the rotor so that any thrust vector misalignment will be averaged out during the long Jupiter orbit insertion burn. An engine support assembly is tied through the central engine support tube and a top cap to the SBA outer case. This case is mounted at the spacecraft rotor spin axis by struts which bolt to the central and lower case flanges.

Midway between the outer case and the central engine tube is a concentric despun tube whose end flange supports the spacecraft stator after flight deployment. A duplex bearing pair in the SBA

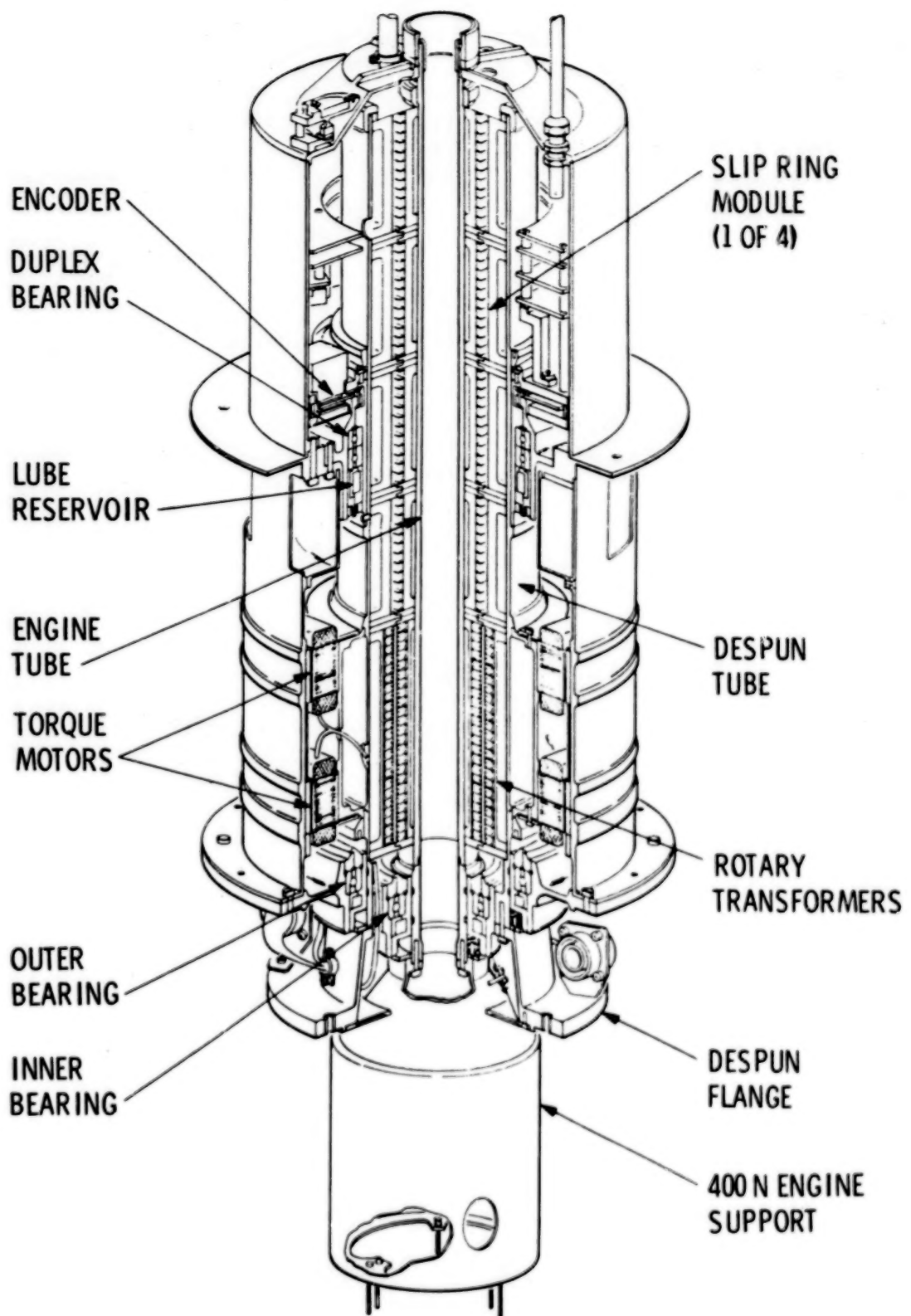


Figure 2. SBA Configuration

encoder is the primary rotating axial load transfer path between the spacecraft rotor and stator. Inner and outer bearings at the aft end of the SBA maintain the concentricity between the case, the despun tube, and the engine tube. These aft bearings are mounted in sliding sleeves so they cannot carry axial loads. They are preloaded by sets of coil springs which maintain a relatively constant preload in the presence of the radial thermal gradients which exist during portions of the mission. A more detailed description of the bearings and their lubrication system is provided below.

The annular volume between the despun tube and the engine tube contains a stack of 23 rotary transformers and 4 slip ring modules which, together with their associated wiring, provide electrical power and signal transfer between the spacecraft rotor and stator. In the annular space between the despun tube and the outer case are two redundant brushless DC torque motors and an optical encoder for rotor/stator relative position sensing.

Obviously, the complexity of the Spin Bearing Assembly created some difficult design and assembly challenges.

SPIN BEARING ASSEMBLY CHARACTERISTICS

The SBA is 0.75 m (29.5 in) long, the case diameter is 0.22m (8.6 in), and it weighs 31.2 kg (68.9 lb). All major structural elements are titanium. Each motor can provide a torque of 4.5 Nm. The drag torque is approximately 0.5 Nm (4.4 in-lb), primarily from the slip rings. Torque ripple must be less than 0.01 Nm except within discrete frequency bands where it is allowed to rise to 0.08 Nm. Ripple torque must be limited to minimize excitation of the spacecraft rotor flexible modes.

Rotary transformers allow 23 channels of digital data transfer at 800 kilobits/second and there are 48 slip rings for power and low frequency data transfer.

The 16-bit optical encoder provides a digital grey code output with a position resolution of 96 micro-radians (20 arc-seconds).

SCAN ACTUATOR SUBASSEMBLY CONFIGURATION

The SAS, Figure 3, is not as complex as the SBA. Its main housing mounts on the side of the spacecraft despun stator and contains the optical encoder position sensor. On a hollow shaft,

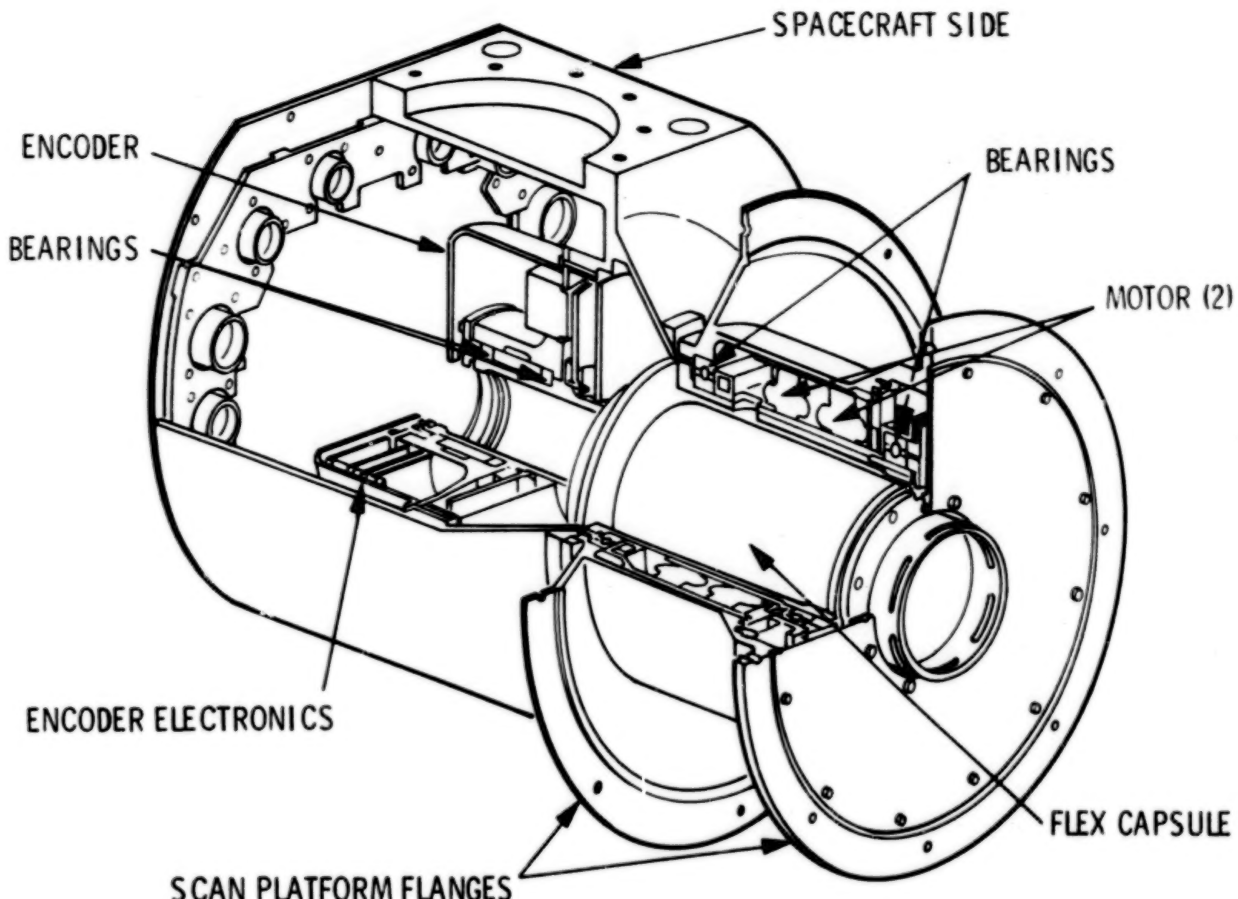


Figure 3. Scan Actuator Configuration

extending from the housing, are two bearings which support the SAS rotor. These bearings are spring loaded by a diaphragm within the rotor. The honeycomb scan platform, with its science instruments, is bolted to the rotor flanges. A 200-wire Flexible Circuit Assembly (FCA) is located within the hollow shaft to furnish electrical power and signal transfer between the stator and the scan platform. An FCA inner shaft drives the encoder rotor through a coupling diaphragm. This FCA shaft is supported at one end by the encoder bearings and at the other end by the SAS rotor end plate. Two redundant brushless DC torque motors drive the SAS rotor for scan platform pointing. Rotation is limited to 210° by stops on the case and the lower rotor flange.

SCAN ACTUATOR SUBASSEMBLY CHARACTERISTICS

The SAS is 0.35 m (13.8 in.) long, the lower rotor flange diameter is 0.26 m (10.3 in.), and it weighs 10.4 kg (22.9 lb.). All major structural elements are beryllium. Each of the redundant motors can provide a torque of 1.0 Nm. The average

drag torque is 0.04 Nm (5.7 oz-in.). Dahl parameters were established for system performance modeling at low tracking rates, and a maximum torque stiffness, σ , of 85 Nm/rad (12,000 oz-in./rad) was measured on the SAS engineering development unit.

As in the SBA, the 16 bit optical encoder provides a digital grey code output with a position resolution of 96 micro-radians (20 arc-seconds).

BEARING AND LUBRICATION SYSTEM

Certainly the key elements in the long term reliability of the actuators are the bearings and their lubrication. All bearings are ABEC Grade 7T with AFBMA Grade 5 balls. Rings are 52100 chrome alloy steel, balls are 440C stainless steel. The ball separators, chosen for a low and consistent drag torque, are TEFLON toroids. The large SBA bearings have a 11.43 cm (4.75 in.) bore, a 1.27 cm (0.5 in.) cross section, with 0.635 cm (0.25 in.) balls. All SBA bearings operate with a 22.7 kg (50 lb.) preload at a 20° contact angle for the encoder duplex pair and a 30° contact angle for the spring loaded aft bearings. The inner SBA bearing has a 5.08 cm (2.0 in.) bore and the same cross section and ball size as the larger bearings.

The SAS rotor bearings have a 10.16 cm (4.0 in.) bore, a 1.27 cm cross section, with 0.635 cm balls. They operate with a 18.1 kg (40 lb.) preload at a 30° contact angle. The SAS encoder separated duplex pair has a 5.08 cm (2.0 in.) bore, a 0.635 cm cross section, with 0.32 cm (0.25 in.) balls and they run with a 9 kg (20 lb.) preload at a 30° contact angle. All of the flight bearings were supplied by the Split Ball Bearing Division of MPB Corporation, Lebanon, New Hampshire.

All of the bearings receive a tricresyl phosphate pretreatment followed by lubrication with Kendal KG-80 oil. This lubricant was chosen for its radiation resistant qualities and its successful performance history in numerous similar applications. Each bearing cavity contains an acrylic copolymer (MICROWELL) lubricant reservoir which provides a sacrificial vapor supply to minimize the loss rate of the bearing oil through the 0.018 cm (0.007 in.) bearing cavity gaps. Sperry Flight Systems' lubrication loss analysis predicts, as the worst case, that at least 65% of the bearing lubricant will remain at the end of a seven-year mission.

A bearing design verification unit, using flight quality SBA parts, was built and subjected to flight unit vibration and thermal-vacuum test environments. It ran, in vacuum, at Sperry

for about one year prior to shipment to the Jet Propulsion Laboratory, where it continues to run. Bearing drag torque, about 0.06 Nm (8.0 oz-in), has been relatively stable, as have the bearing torque ripple characteristics. Since the SAS bearings and lubrication system are very similar to the SBA, the test is also furnishing confidence in the reliability of the SAS design.

Bearing system design required difficult tradeoffs between good bearing design practice, the "zero" torque desires of the pointing control system designers, and the stiffness requirements of the spacecraft structural analysis group. The bearings are very lightly loaded in space, yet they must carry significant loads during shuttle launch and environmental tests. The aft SBA bearings approach their stress limit during sine vibration tests at the "heart stopping" retropropulsion engine/engine tube cross axis resonance. Lead times for high quality bearings always present fabrication schedule problems. Some bearing deliveries were delayed by a chlorine corrosion problem which was traced to the trichloroethylene used to clean parts prior to the TCP treatment.

TORQUE MOTORS

Sperry Electro-Components of Durham, NC, supplied the two-phase, 24 pole, brushless DC torque motors for the SAS and the SBA. Torque constant for the SAS motors is 1.27 Nm/A (0.94 ft-lb/A) and for the larger, heavier SBA motors it is 5.29 Nm/A (3.9 ft-lb/A). Both utilize samarium cobalt magnets.

Individual motors in a pair are rotationally oriented to minimize the magnetic cogging torque and external magnetic field of the combination. Even with this cancellation, the external field of the SBA pair exceeded the 10 nano-tesla maximum allowable radial field at one meter, so the SBA will require external compensation. Spacecraft fields must be tightly controlled to preclude interference with the measurement of external fields by the Galileo magnetometer.

OPTICAL ENCODERS

Optical encoders are used in both actuators to supply position information to the system control computer and for torque motor commutation. These encoders were supplied by BEI Electronics, Inc. of Maumelle, AR. The SAS encoder, Figure 4, is a direct design derivative of the encoders used in the Shuttle Remote Manipulator System (Canadarm). Its big brother, the SBA encoder shown in Figure 5, has a larger center bore to fit over the SBA despun tube.

322

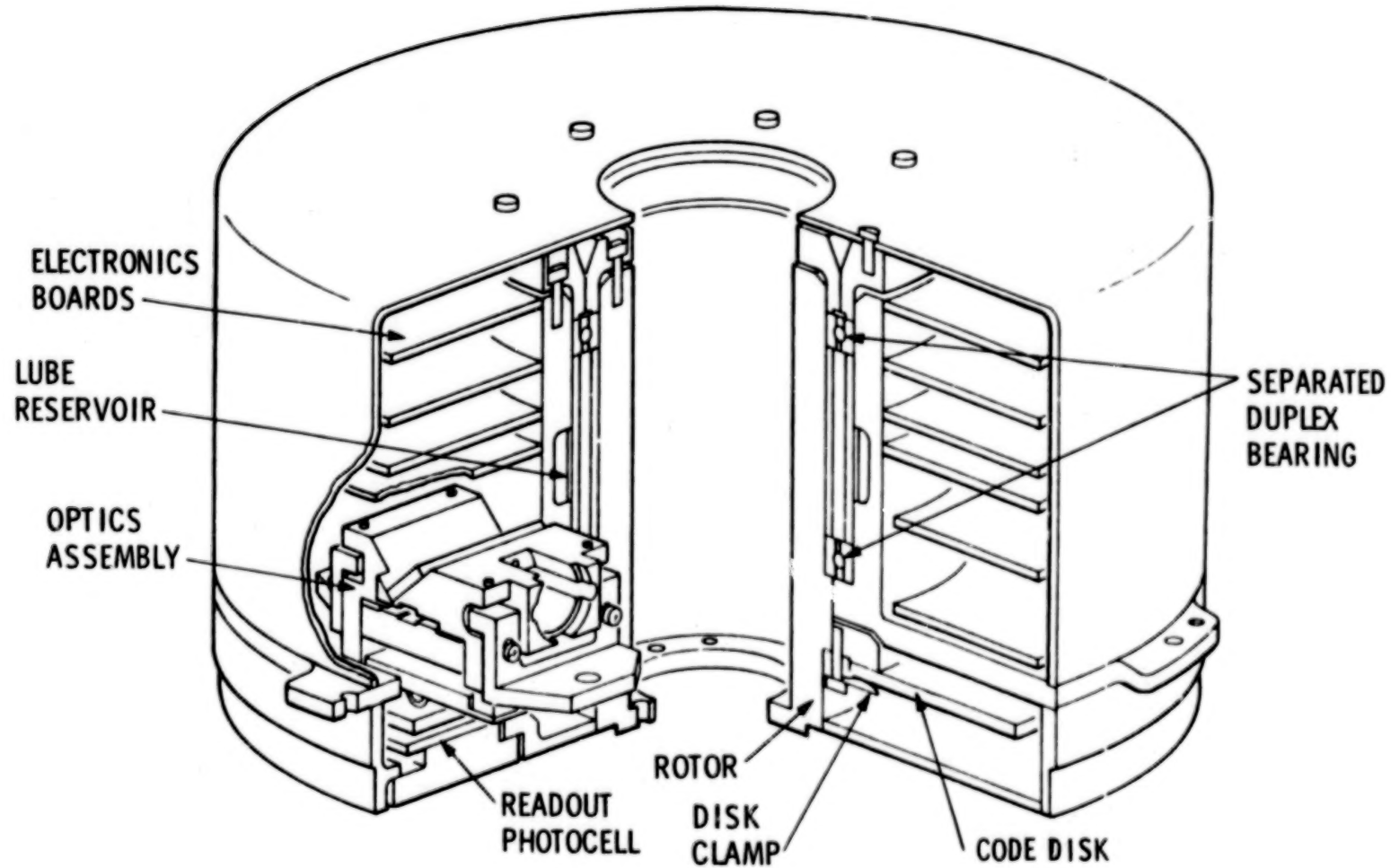


Figure 4. SAS Optical Encoder Cross Section

322

BEST AVAILABLE COPY

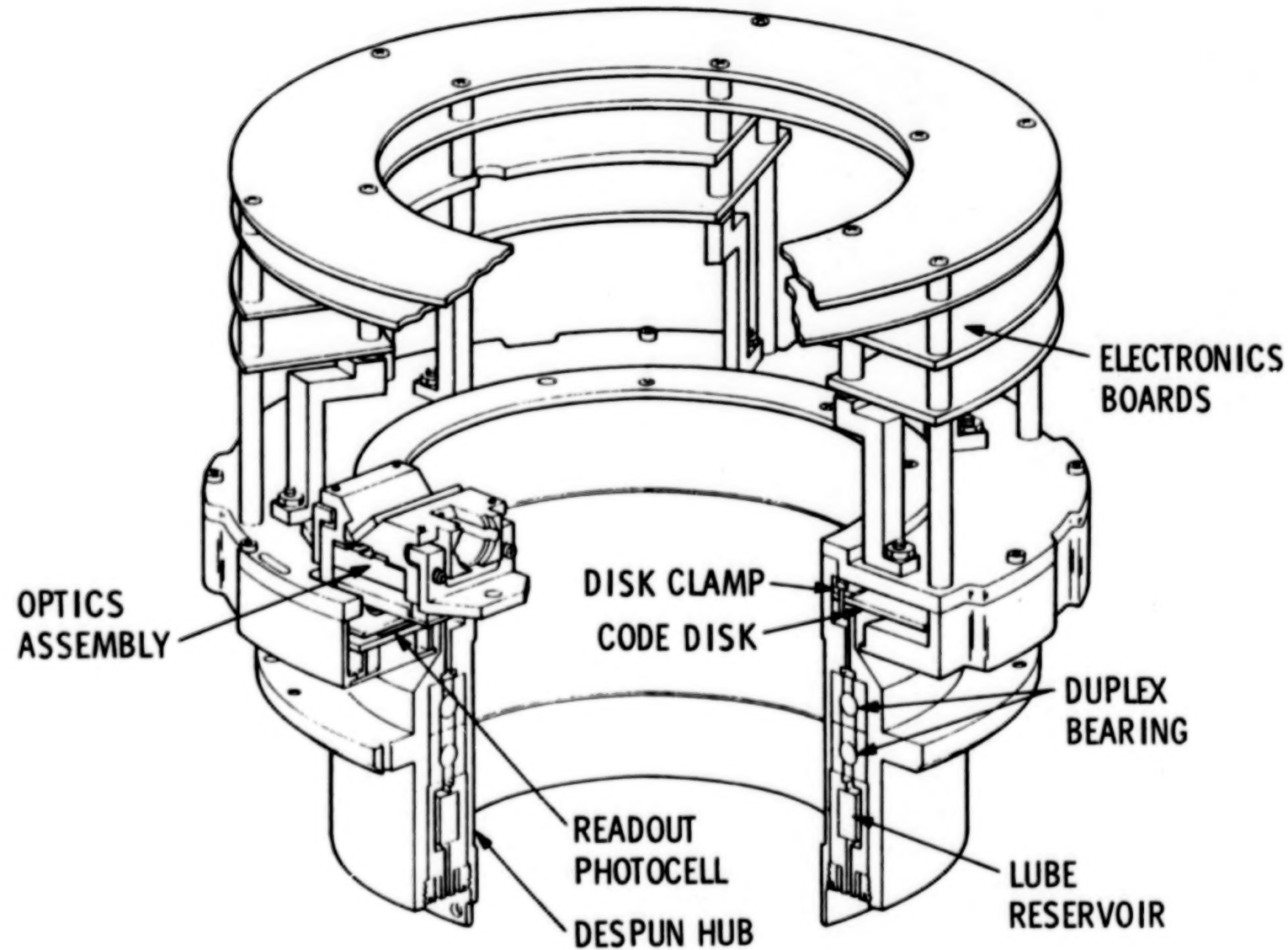


Figure 5. SBA Optical Encoder Cross Section

Redundant electro-optics assemblies, positioned 180° apart around the glass code disc, are used to read the 16-bit position information. Position resolution, as mentioned earlier, is 96 micro-radians (20 arc-seconds) and the allowable peak-to-peak error, at the code transitions, is 120 micro-radians (25 arc-seconds).

Achieving the code disc radial stability needed to meet this peak-to-peak error requirement proved to be difficult, time consuming, and, of course, expensive. Piece parts for the initial engineering development encoders were machined from 410 CRES to save schedule time. This material, the bearing material, and the glass used for the code disc have fairly closely matched coefficients of thermal expansion and the BEI procedure for mounting the glass disc on the rotor hub worked normally. Flight encoder piece parts were machined from titanium for the SBA and beryllium for the SAS. These changes were made to reduce weight and to match the other structural elements of the actuators. Stable code disc mounting for the titanium SBA encoders was fairly easy but getting a SAS code disc to remain stable throughout the thermal environment required many attempts, with attendant schedule slips. In retrospect, it probably would have been better to have changed the glass material to achieve a better thermal coefficient match.

SIGNAL AND POWER TRANSFER

The complex, and often conflicting, mechanical requirements imposed on the SAS and SBA are complicated by the added requirements imposed on them because they are also an integral part of the spacecraft electrical cabling system. As such, they must provide rotating electrical circuit paths for 28 VDC power; 2.4 kHz, 50 V, square wave power; low voltage digital logic power and signals; high frequency digital bus data; temperature transducer signals; gyro rebalance loop signals; and pyro firing circuits. Each of these circuit types comes with its own redundancy, shielding and isolation, and electrical parameter requirements. In total, the cabling system required 200 wires through the SAS and 96 through the SBA.

FLEXIBLE CIRCUIT ASSEMBLY

Because of its limited rotation, the SAS can use flexible circuit tapes to provide the required circuit paths. This Flexible Circuit Assembly (FCA), Figure 6, was supplied by the Electro-Tech Corporation of Blacksburg, VA. It contains four, 50 wire, etched copper circuit tapes manufactured from DuPont PYRALUX WA/K copper-clad laminate and cover sheet. The tapes are

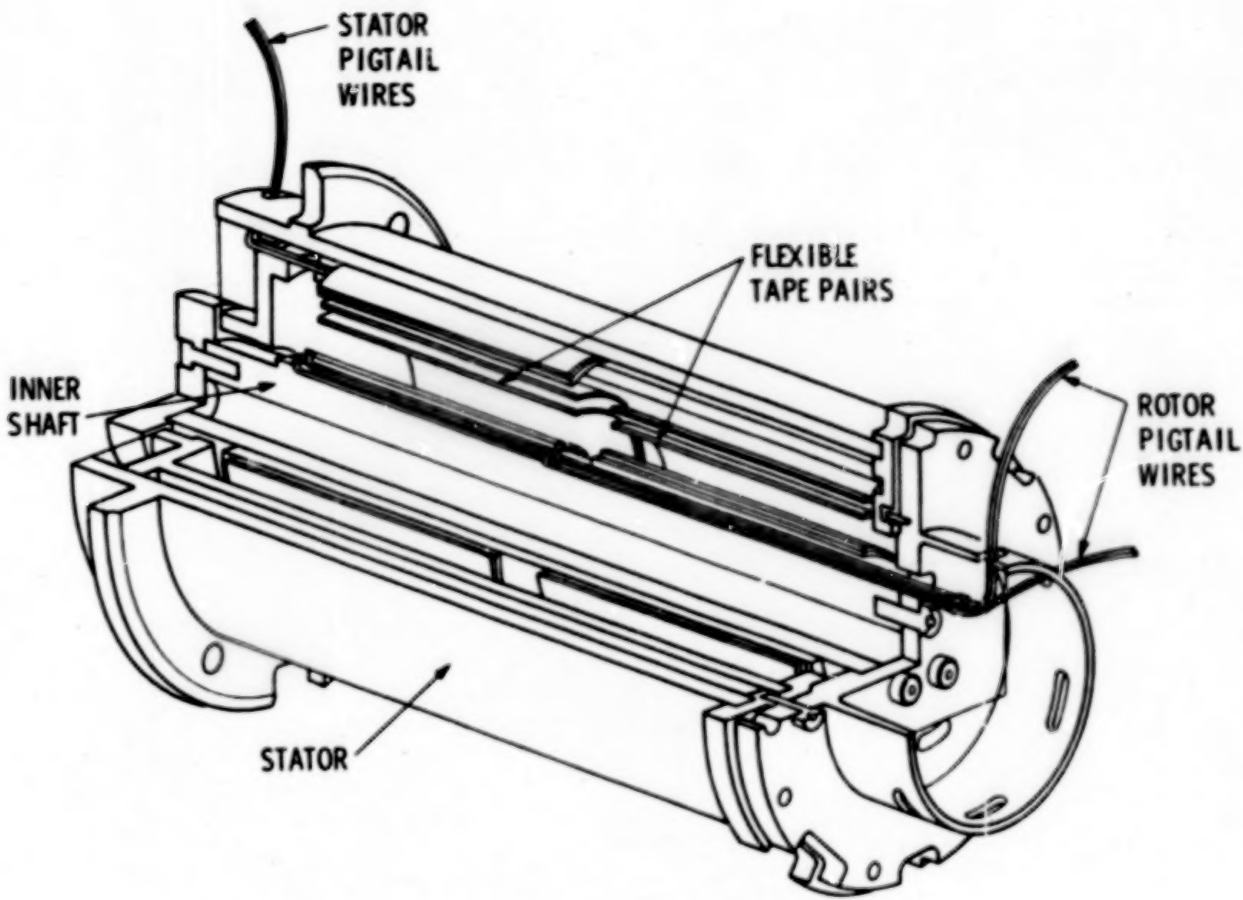


Figure 6. SAS Flexcapsule Cross Section

arranged in pairs with one pair wound clockwise and the other counterclockwise to minimize spring torque effects. Maximum allowable torque to rotate $\pm 105^\circ$ is 0.02 Nm (3.0 oz-in.).

Cross-coupling is minimized by the assignment of circuits within the tapes. A circuit "high" has its return path on the same trace in the adjacent tape layer and the highs and returns alternate across each tape. The maximum allowable capacitance of any trace to the FCA rotor and stator is 125 pico-farads. The maximum pickup allowed in a circuit pair is 250 millivolts when an adjacent pair is excited with a 100 volt peak-to-peak, 2.4 kHz, square wave with a 0.5 micro-second rise and fall time.

Two-foot wire pigtails extend from the FCA stator end for connection to the SAS back plate connectors during SAS assembly. Pigtails on the rotor end terminate at scan platform instrument connectors. These pigtails contain a variety of wire types and sizes including #24, #26, and #28 AWG in single wires, twisted pairs and triplets, shielded and unshielded, with two different insulation types. Keeping track of all these wires through the

assembly process and handling this multi-limbed device, without damaging wires, were major tasks.

ROLL RINGS

In its initial design stages, the SBA used the Sperry roll rings to accomplish power and signal transfer between the two sections of the spacecraft. These unique devices, illustrated in Figure 7, consist of inner and outer rings (which are much like bearing races) with a thin circular flexure rolling between them as they rotate. Flexure and ring cross-sectional curvatures are designed so that the flexure rolls on its outer edges provide redundant contact points and a small amount of wiping action to keep the surfaces clean. Predicted drag torque for a stack of 100 roll rings was 0.01 Nm, certainly a desirable attribute for a pointing actuator.

As the roll ring development and test progressed, a series of problems occurred. First, obtaining uniform platings on the rings and flexures with adequate adhesion was difficult. As these plating problems were resolved and as significant amounts

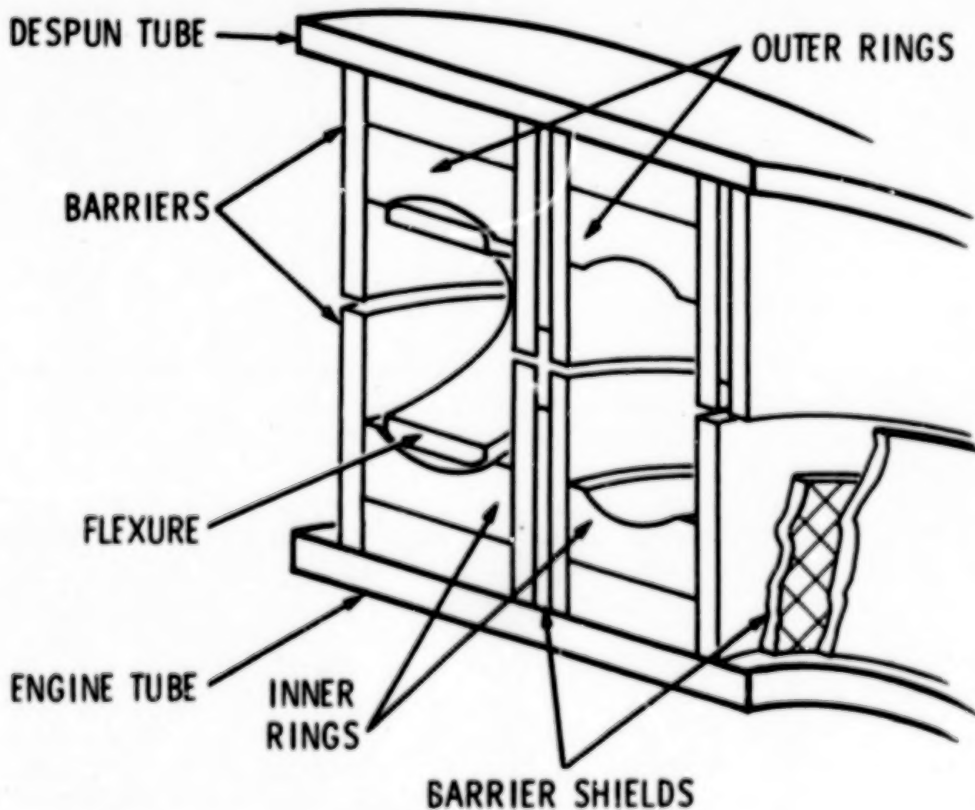


Figure 7. Cross Sectional View of Two Roll Ring Circuits

of rolling test time accumulated, flexure breakage began. Flexure stress is determined by a trade-off between desired flexibility, contact pressure, and fatigue life. Sperry had used published fatigue stress data which proved to be inadequate for the flexure configuration. They initiated a series of flexure fatigue tests which furnished the data necessary for a successful flexure design tradeoff.

Meanwhile, many of the units tested could not meet the electrical interruption requirements of the digital data transfer system. Devices which were electrically quiet while running in air became noisy after a period of operation in a vacuum. Information was obtained in a literature search which showed that the coefficient of friction between unlubricated gold surfaces increases dramatically in a vacuum. This led to an explanation for the random momentary interruptions. As the contact surfaces cleaned up during vacuum operation, the flexure could climb out of its normal track, thereby losing its redundant contact at one edge. This unstable condition would continue until the edge in contact encountered some surface anomaly, which would cause it to skid back into its normal track. During the skid, circuit interruptions could occur, particularly if the anomaly was some form of surface contamination.

The obvious answer was to lubricate the roll rings, following the practice in gold-on-gold slip ring technology. Lubrication was tried, successfully, but this led to a difficult situation. With the roll rings unlubricated, life tests could be accelerated. With lubrication, they could not, and it was not possible to adequately prove the reliability of a lubricated electrical contact in the time available.

Due to the recurring problems with the roll rings, a backup development effort had been initiated utilizing proven dry lube silver slip rings and rotary transformers and in December 1980 an SBA design change was directed.

Sperry has continued development of the roll rings with their own funds. The original lubricated devices are still running, with excellent electrical characteristics. Steady progress has been made in resolving the problems inherent in running roll rings unlubricated. In the author's opinion, these devices will eventually provide a significant improvement in rotating electrical joint technology.

SLIP RINGS

The SBA contains 4 slip ring and brush block assemblies with 12 equal width rings in each module. Two paralleled brushes ride

on each ring, about 180° apart, to provide contact redundancy. Two different size brush tips are used, one rated at 3 amperes per brush pair, the other at 0.4 amperes per pair. Each of the 4 brush block assemblies contains a different mix of high and low power brush pairs to give 31 high and 17 low power paths through the SBA.

The design uses dry lube silver-on-silver technology which has been proven in many space applications. Brush tips are molded from 85% silver, 12% molydisulphide, and 3% graphite. Rings are plated up, starting with copper, followed by fine silver, which is then covered with hard silver. Ring and brush block assemblies were supplied by the Electro-Tech Corporation of Blacksburg, VA.

There were two major concerns in the application of slip rings in the SBA. The first was the amount and the characteristics of the wear debris generated during the 11-million revolution, 7-year mission life. Excess debris, containing long silver slivers, could generate internal shorts or arcing which would cause spacecraft system failures. Several measures were taken to reduce this concern. First, all interior conductive surfaces were covered with insulating materials to block shorts to the spacecraft structure. Next, physical and electrical circuit isolation was provided which will allow continued operation of the spacecraft systems in the presence of ring to ring short circuits. Then, an accelerated life test was run to demonstrate that the hard silver ring surface did not tend to generate long slivers. After 13.5 million revolutions, the longest sliver found in the debris was 0.076 cm (0.03 in.) long. Total quantity of debris formed and brush tip wear rates closely matched the results reported from several other sources.

The second major concern was that the brush tips might lift under launch vibration, causing circuit interruptions and the potential for ring surface and brush tip damage. Brush pressures were set at the high end of industry standard practice and early module testing showed that the brushes would not lift.

When the engineering development SBA was tested, brush bounce did occur during both sine and random vibration inputs. Tests and analysis disclosed an unfortunate combination of resonances in the engine tube, the despun tube, and the brush leaf springs which could cause both of the redundant brushes to lift simultaneously. Extensive brush bounce tests were performed which demonstrated that the contact surfaces would not be damaged and the brush tips would not chip or fracture under sustained vibration. Spacecraft systems using the slip rings were reviewed and some changes were made to allow continued operation with momentary circuit interruptions. Shuttle launch vibration data

was analyzed and the random vibration test requirement in the range between 100 Hz to 1 kHz was reduced from $0.1 \text{ G}^2/\text{Hz}$ to $0.068\text{G}^2/\text{Hz}$. At this test level brush bounce did not occur.

ROTARY TRANSFORMERS

Rotary transformers are used for digital data transmission between the spun and despun sections of the spacecraft. Preliminary design of these devices was performed at the Jet Propulsion Laboratory with Sperry Flight Systems making the design refinements necessary for their application in the SBA.

Transformer construction is shown in Figure 8. Assembly of the inner and outer transformer sections is similar. Ten turn coils of #36 AWG wire are wound on ceramic bobbins. These bobbins are placed between two manganese-zinc ferrite half cores which are cemented into titanium core holders. Assembly tooling maintains concentricities while the cement joints are cured. In

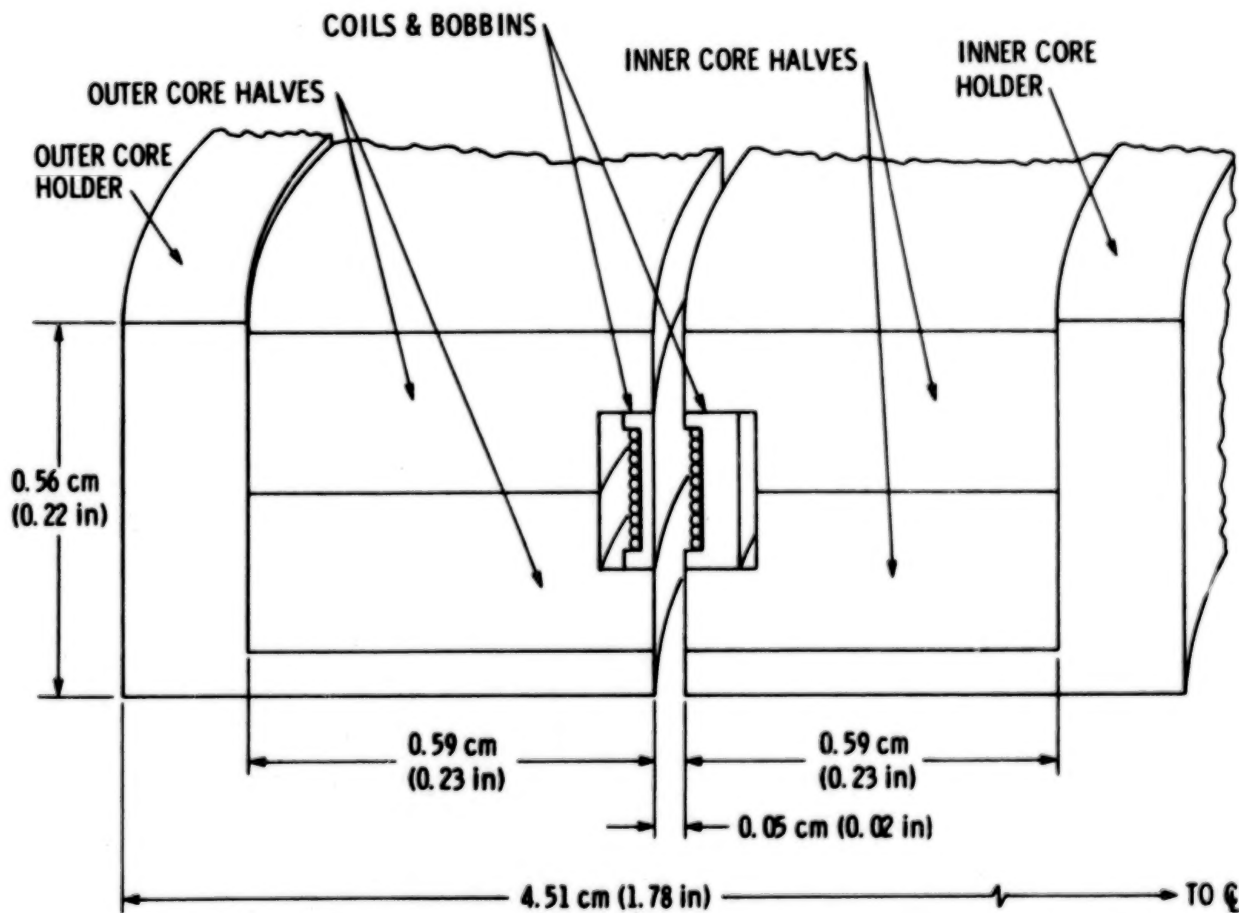


Figure 8. Rotary Transformer Cross Section

the unassembled condition the bobbins and cores are quite fragile, requiring careful packaging and handling, but once assembled, they are much less susceptible to damage. Transformer cores (MN-31) were supplied by Ceramic Magnetics of Fairfield, NJ, and the coil windings by Standard Industries of La Mirada, CA.

Rotary transformers have many characteristics which make them ideal digital signal transfer devices. There is no wear or torque drag, they are quite insensitive to axial or radial mis-alignments, and they are highly reliable. Their primary difficulty is associated with the design of the driver and receiver circuits required to couple data across the magnetic gap. Mechanism designers prefer a wide gap to minimize tolerance stackup problems, while circuit designers prefer a narrow gap to reduce leakage inductance. The Galileo rotary transformer radial gap is 0.05 cm (0.02 in.). The resulting nominal electrical parameters, including effects of the twisted shielded lead wire, is shown in Table 1.

TABLE 1. Rotary Transformer Electrical Parameters

TEST PARAMETER	WINDING		MEASUREMENT FREQUENCY
	INNER-SPUN	OUTER-SPUN	
Open Circuit Impedance Phase Angle	395 Ohms 84°	370 Ohms 85°	800 kHz
Open Circuit Impedance Phase Angle	33 Ohms 75°	34 Ohms 76°	80 kHz
Short Circuit Impedance Phase Angle	76 Ohms 83°	76 Ohms 83°	800 kHz
DC Resistance	3.52 Ohms	3.54 Ohms	N/A
Resonant Frequency	1.46 MHz	1.66 MHz	N/A

SUMMARY AND ACKNOWLEDGEMENT

These two actuators, and their component parts, presented a wide variety of technological challenges to everyone involved in their design, fabrication, and test. Engineering development units and flight versions have been built, successfully tested, and are well into integration with the Galileo spacecraft systems. The ultimate degree of success cannot be measured until mission completion, sometime in the 1990's, but the progress to date is certainly due to the professional competence and dedication of many individuals whose contributions are gratefully acknowledged.

The research described in this paper was carried out by the Jet Propulsion Laboratory, California Institute of Technology, under contract with the National Aeronautics and Space Administration.

Reference to any specific commercial product, process, or service by trade name or manufacturer does not necessarily constitute an endorsement by the United States Government or the Jet Propulsion Laboratory, California Institute of Technology.

Blank Page

A COMPACT MAGNETIC BEARING FOR GIMBALLED MOMENTUM WHEEL

K.Yabu-uchi, M.Inoue, S.Akishita, C.Murakami* and O.Okamoto*

Mitsubishi Electric Corporation, Amagasaki, JAPAN

*National Aerospace Laboratory, Tokyo, JAPAN

ABSTRACT

A three axis controlled magnetic bearing and its application to a momentum wheel are described. The four divided stators provide a momentum wheel with high reliability, low weight, large angular momentum storage capacity, and gimbal control. Those characteristics are desirable for spacecraft attitude control.

INTRODUCTION

Momentum wheels are widely employed for attitude control of satellites because the control system is simple and highly reliable. For example, according to the pitch attitude error sensed by certain attitude sensors, the wheel spin rate is changed so that the spacecraft may correct the attitude error around the pitch axis. At the same time, the large angular momentum stored in the wheel passively stabilizes the roll/yaw motions.

Although the system is simple and reliable, it does not meet the requirement of high roll attitude accuracy. For that purpose, precise active roll attitude control may be desired. The momentum wheel mounted on a gimbal mechanism might be one of the candidates (Ref.4). An example is seen in Fig.1 where the momentum wheel is supported by two pairs of bearings whose rotating axes are usually parallel with roll or yaw axis of the spacecraft. The two gimbal torquers provide the roll/yaw attitude control. However, the mechanically suspended gimballed momentum wheel has the disadvantages of its large size and mass, as well as of the disturbance torques at the gimbal bearings.

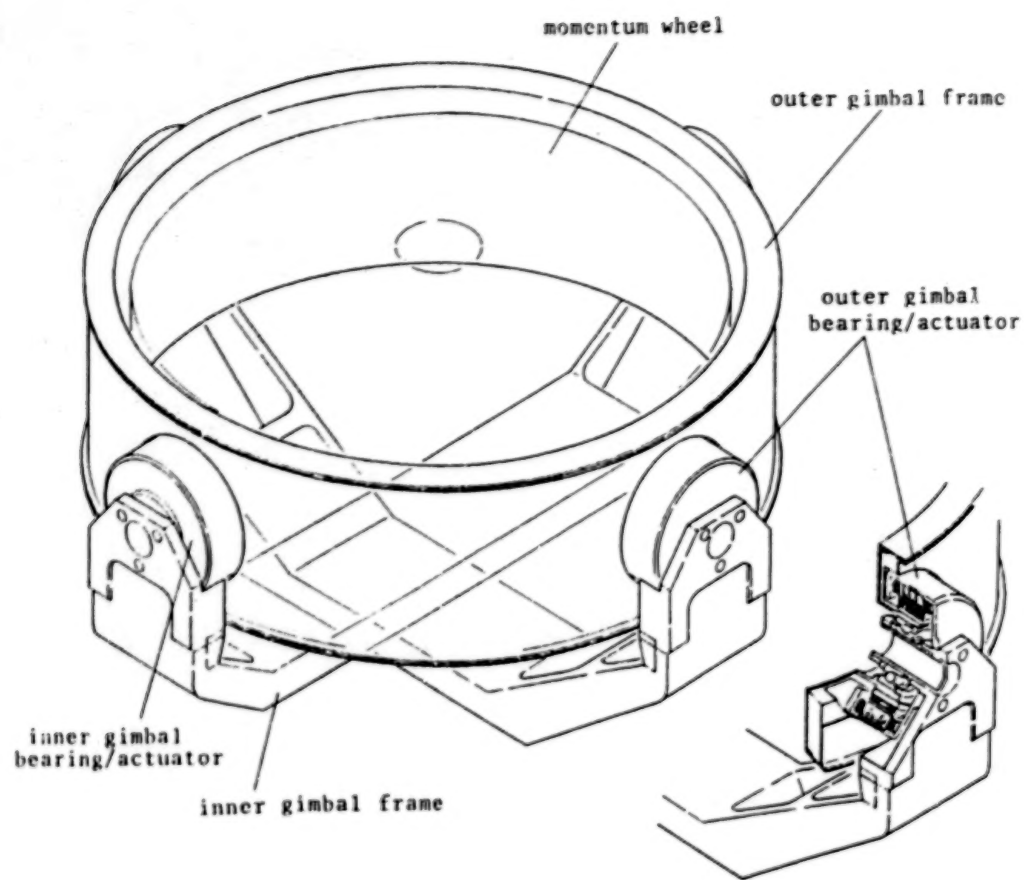


Fig. 1 Conventional gimballed momentum wheel

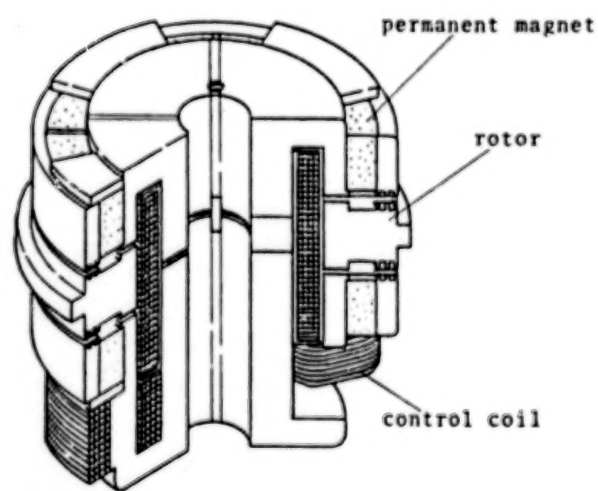


Fig. 2 Magnetic bearing with active axial/gimbal control

But the magnetically suspended momentum wheel is expected to be used as an attitude control device. As the magnetically suspended rotor has no contacts with stators, the difficult problems such as abrasion, frictional disturbances, lubrication in a vacuum environment, etc. have been eliminated, and long lifetime and high accuracy are achieved.

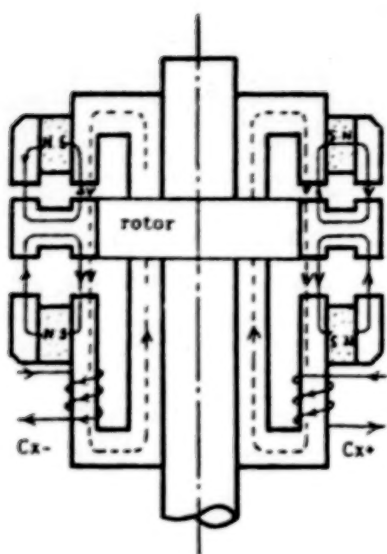
In addition, the rotor is able to tilt (gimballing) its spin axis within a clearance between the rotor and the stator. Though the gimbal angles might be rather small (1.0 degree at most), such vernier attitude error correction is sufficient if it is used with some other coarse attitude control devices such as thrusters or magnetic torquers (Ref. 1). Above all, the rotor gimballing without any contacts means that it does not require heavy mechanical gimbal frames seen in Fig. 1. and there are no frictional disturbances.

A magnetic bearing has to stabilize five degrees of freedom of the rotor: one axial, two gimbal and two radial motions. But the five active control mechanisms make the system complex and less reliable. The magnetic bearing to be described in detail has three active controllers, an axial and two gimbal ones. Two radial motions of the rotor are passively stabilized by the help of samarium cobalt permanent magnets (Ref. 1,2).

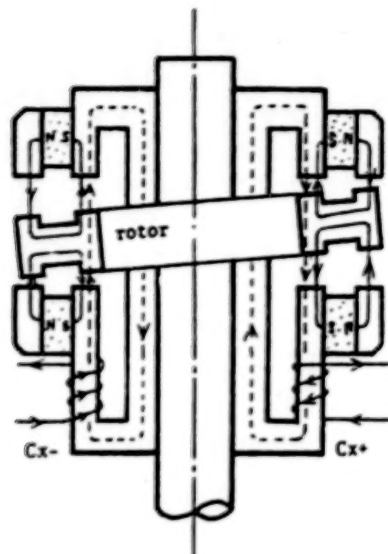
BEARING CONTROL MECHANISM

Figure 2 is a schematic illustration of the three axis controlled magnetic bearings. The stator is composed of four equivalent segments, each of which has the active axial position control and passive radial stability.

Figure 3 shows the magnetic flux flows in the bearing. In each segment, there are three flux loops: two of the permanent magnets and one of the control current. Consider the segment of right hand side of Fig. 3(a): The flux of the permanent magnets flows clockwise in the upper loop, while it flows counterclockwise in the lower loop. On the other hand, the flux of the control current may have alternating direction, so that the biased flux densities at the inner two gaps may be modulated by the control currents. When the control flux is counterclockwise, for example, the flux density in the upper inner gap become dense, while it becomes weaker in the lower inner gap, and vice versa. The unbalanced flux densities generate the control force to raise or lower the rotor.



(a) axial control mode



(b) gimbal control mode

Fig.3 BEARING CONTROL MECHANISM

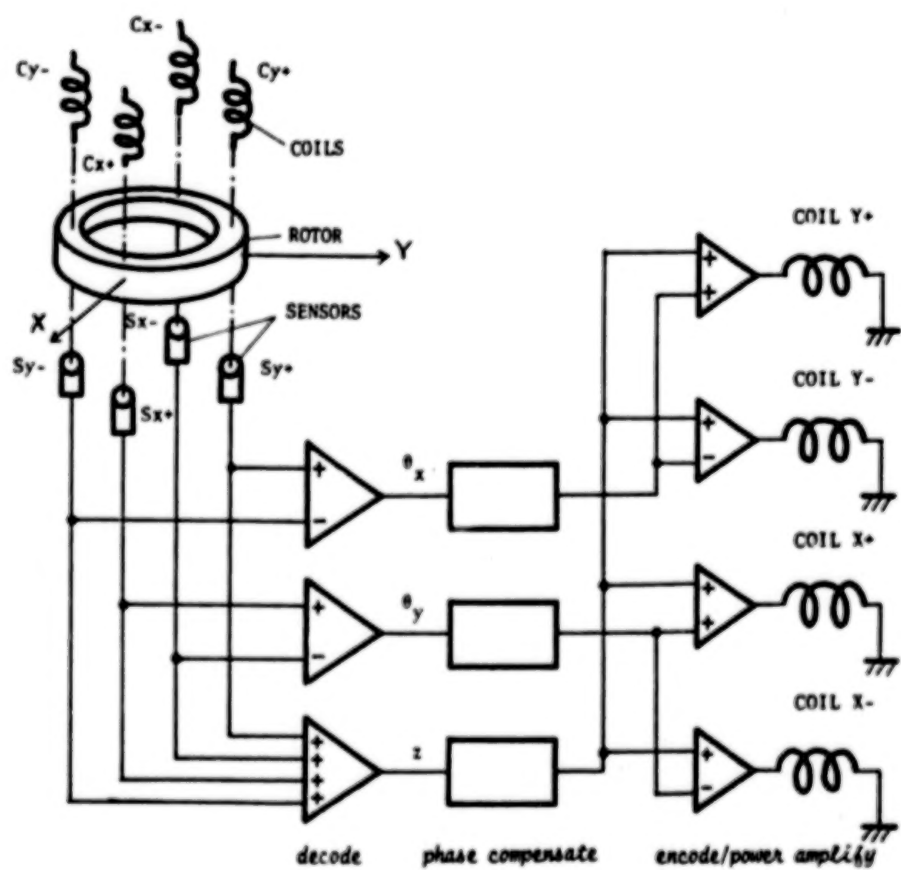


Fig.4 BEARING CONTROL ELECTRONICS

Figure 3(a) indicates the axial control mechanism of the magnetic bearing. The control currents in the control coils $Cx+$ and $Cx-$ yield the coaxial flux flows. The two unbalanced axial forces drive the rotor in an axial direction. In the Fig. 3(b), however, each control flux has an opposite direction at the inner gaps so that the two unbalanced axial force become a gimbal control torque.

The active axial and gimbal control electronics is seen in Fig. 4. Four axial position sensors are located beneath the rotor. Summing up the four sensor outputs yields an average axial displacement of the rotor (z), and subtraction of the outputs between the opposite sides yield two tilting (gimbal) angles θ_x and θ_y . These three signals θ_x , θ_y and z are phase compensated then distributed to the four control coils in order to correct the position errors of the rotor.

MECHANICAL DESIGN OF THE MAGNETIC MOMENTUM WHEEL

In order to stabilize the attitude of a biased momentum spacecraft, a large amount of angular momentum storage capacity with a light weight is required. This requirement is fulfilled by a high spin rate and a flywheel with a large inertia-mass ratio. In addition, the wheel must have sufficient stiffness to endure the heavy acceleration during launch.

In the case of a mechanically supported wheel, careful lubrication design and assembly must be done in order to meet the severe requirement of reliability. The magnetic suspension has removed the burden. But the design of this type of magnetic bearing was not so easy since the stator was divided into four segments each of which had a complex configuration with various materials: samarium cobalt, soft iron, stainless iron and damping copper. To ensure the accurate machining and assembling, many jigs were prepared.

A cross section, a photograph and an assembly drawing of the magnetic gimbaled momentum wheel are shown in Figs. 5 to 7. A spoked flywheel design provided a high inertia-mass ratio. Five pairs of spokes connected the wheel ring and the center hub. The wheel ring, the spokes and the center hub were machined out of one super duralumin block so that the number of wheel parts was decreased. That also made the wheel easy to assemble and highly reliable and reduced the weight. But the machining became more difficult and it took much more time.

Even as the centrifugal force became a hoop stress in the thick wheel ring, those thin spokes would well sustain the load at a high spin rate. In order to bear the large axial acceleration during launch and the gimbal reaction torques, the spokes had the form of thin blades and the two spokes are connected in the middle as was seen in the figures to increase the resonance frequency.

The baseplate is not only a mechanical interface between the wheel and the spacecraft but also a reference of the angular momentum vector since the four position sensors placed on the plate detects the tilting (gimbal) angles of the spin axis. As the base plate is fixed to the spacecraft directly, the alignment of the momentum vector is accurate.

A brushless DC motor whose stator coils were composed of thin copper films, insulated and formed by fiber reinforced plastics is seen in Fig. 7. Three coils were laminated around a cylinder for each three phases. The total nine coils had 1.8 mm in thickness. The thin stator coil and small permanent magnets, which yield sufficient magnetic field to generate drive torques, made the motor considerably compact. The motor phase angle was identified by the three commutation sensors, which also played a role of tachometer whose output was 24 pulses/rev.

The performances of the momentum wheel are as follows.

Maximum Angular Momentum	70 Nms
Maximum Speed	10,000 rpm
Maximum Gimbal Angle	0.5 deg.
Maximum Motor Drive Torque	0.02 Nm
Maximum Gimbal Reaction Torque	5.0 Nm
Weight (without electronics)	5.5 kg
Bearing Power consumption (zero gimbal position)	8 W
Motor Power consumption (maximum torque)	50 W
Supply Voltage	18 V, -18 V
Motor	15 V

BLANK

PAGE

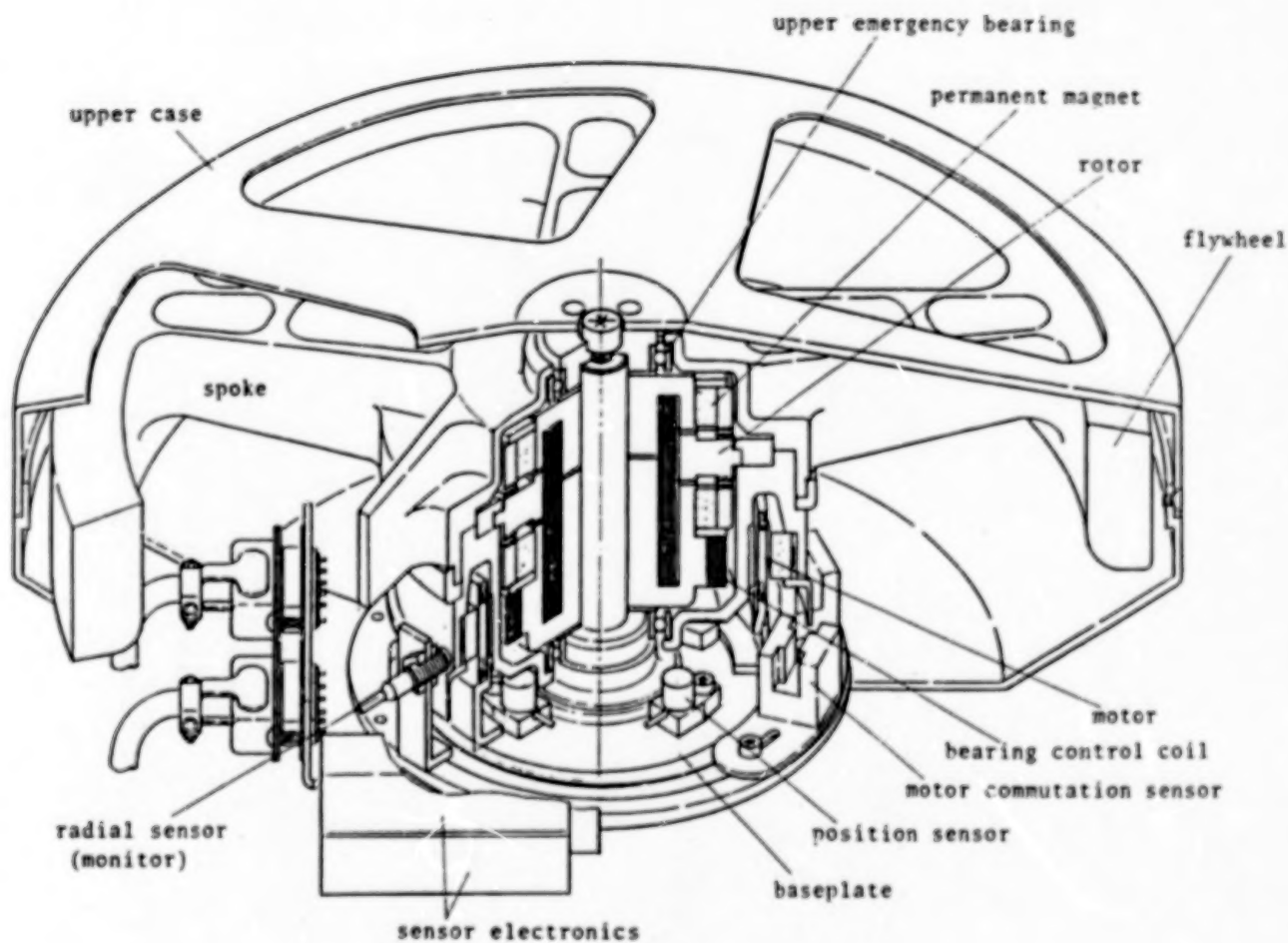


Fig. 5 Cross section of the magnetic wheel

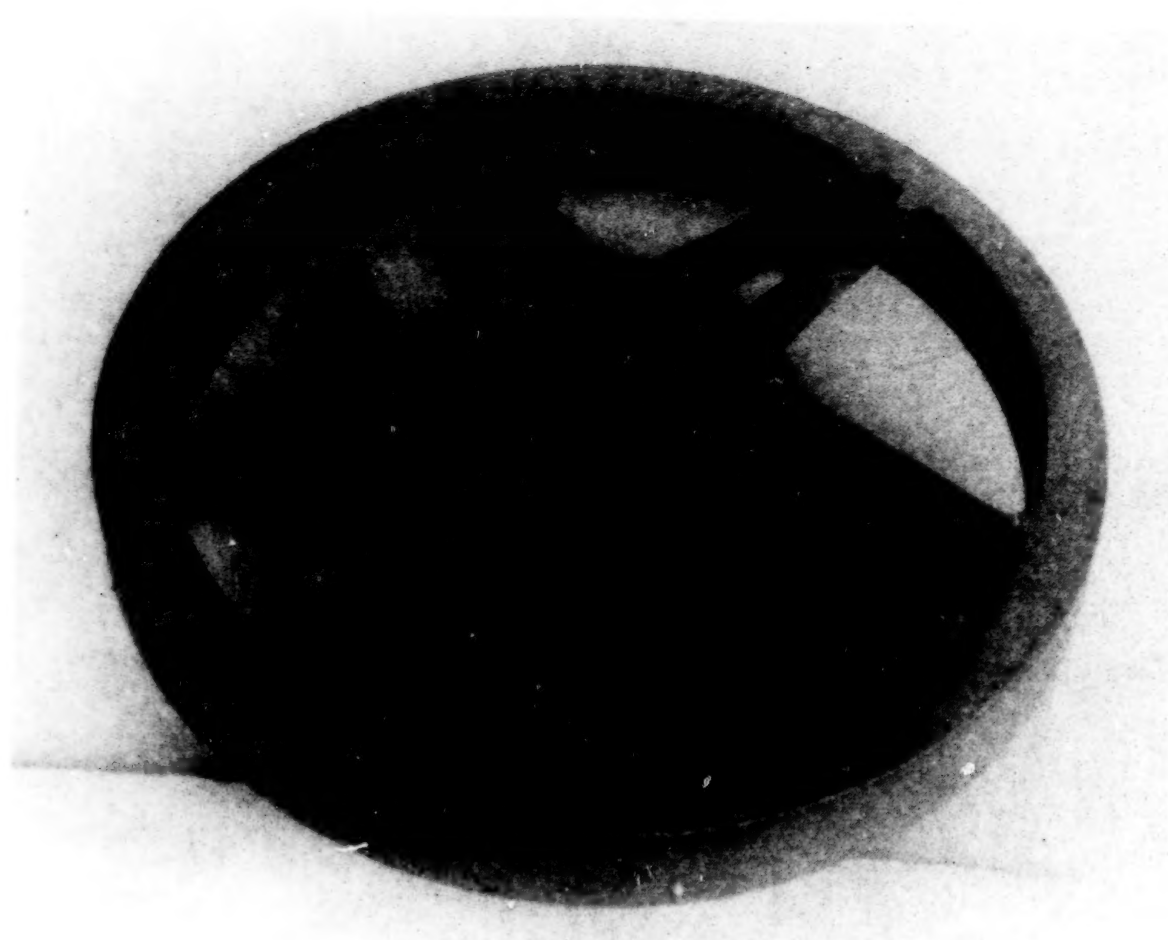


Fig. 6 Magnetically suspended gimballed momentum wheel

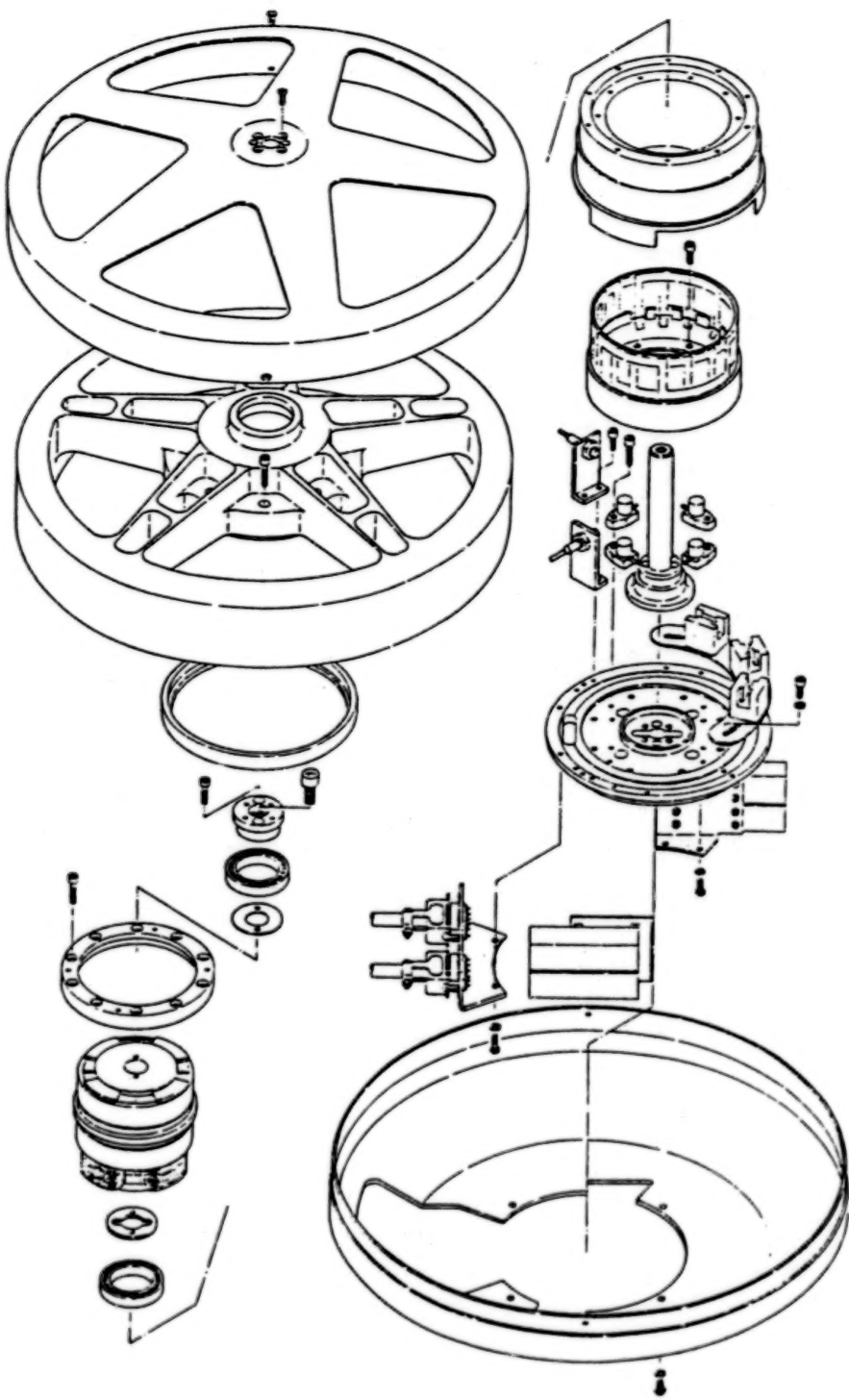


Fig. 7 Assembly drawing of the magnetic wheel

CONCLUSION

A magnetic bearing with a new mechanism, active axial/gimbal control and passive radial centering, was proposed. The magnetic bearing had suitable characteristics for attitude control of biased momentum spacecraft since it had light weight and gimbal control.

In applying the magnetic bearing to the momentum wheel, some philosophy about the mechanical design was described. The magnetically suspended gimballed momentum wheel displayed small size, large angular momentum storage capacity and high reliability.

REFERENCES

- 1) Murakami, C. et al. "A New Type of Magnetic Gimballed Momentum Wheel and Its Application to Attitude Control in Space", 33rd Congress of International Astronautical Federation, IAF 82-330, Paris, Oct. 1982.
- 2) Knoerrechen, H. and Lange, T., "Modular Design and Dynamic Tests on Active Bearing Momentum Wheel", IFAC-ESA Symposium on Automatic Control in Space, Noordwijkerhout, July, 1982.
- 3) Poubeau, P.C. "Satellite Flywheel with Magnetic Bearing and Passive Radial Centering", J. Spacecraft and Rockets, Vol. 17, No. 2, 1980.
- 4) Scott, E.D. and Rubbo, J.E., "Double Gimballed Reaction Wheel Maneuvering and Attitude control System", J. Spacecraft and Rockets, Vol.12, No.8, 1975.

HINGE LATCH MECHANISM

John C. Walker*

ABSTRACT

The device described in this paper is a modular hinge latch mechanism. It is used to latch and preload four motorized hinges after their deployment. The paper describes design requirements, hardware development and initial testing of this hinge latch module. A special effort has been made to cover the design philosophy incorporated into this hardware.

INTRODUCTION

This latch meets the hinge-lock requirements for a large space shuttle-flown satellite. The satellite has two solar panels and one antenna which are deployed after it disembarks from the shuttle. A schematic of the satellite's stowed and deployed configurations is shown in Figure 1.

Each of three types of hinges is equipped with a latch mechanism designed to reliably clamp the hinges shut under all combinations of dynamically induced loading. Upon command, the latch must also unclamp, allowing the antenna and solar panels to be restowed. The latch mechanism is modular and common to the three hinge types. Installation of the latch module in each hinge type is illustrated in Figure 2. An adjustment allows the preload to be customized for each hinge. Before being installed in flight hardware, each module is calibrated in a fixture such that the actual preload generated by the device is measured by a strain gauge.

The latch mechanism is a double over-center four-bar linkage. Preload is generated by driving the linkage into a latched position where a spring beam is deflected. The crank link is driven into adjustable eccentric stops by a reversible motor/gearbox. The adjustments allow control of a critical design parameter, over-center distance. While over center in the latched position, the preload generated at the latch tip keeps the linkage biased against its stop. While over center in the unlatched position, a compression spring-plunger assembly provides the bias force.

Latched and unlatched linkage positions are sensed by microswitches. The switch modules are adjusted relative to the eccentric stops to yield 2.54 mm (.100 in) trip arm motion.

*Ball Aerospace Systems Division, Boulder, Colorado

The latch mechanism is electronically and mechanically redundant - with the exception of the gearbox. Dry film lubrication is used on the linkage and gearbox, with Bray Oil Company 3L38RP grease used on the motor ball bearings. A lightweight, compact design was achieved through the use of 6Al-4V titanium and Carpenter Custom 455 stainless steel.

REQUIREMENTS

The general design requirements for this device consist of:

- Temperature: -54°C to +71°C (-65°F to +159.8°F)
- Humidity: 0-100% RH nonoperating mode for up to five days
0-55% RH during storage
- Electrical: 21-35 Vdc power for motors and switches
- Switches: Latched and unlatched position indicators
- Stress Factors of Safety: 1.5 on Ultimate Tensile Strength
1.2 on Yield Strength
- Fasteners: All fasteners employ means of positive locking
- Outgassing: Materials to meet requirements of NASA JSC SP-R-0022
- Redundancy: All electrical and mechanical devices shall be redundant, with the exception of the gearbox
- Drive Torque: Static drive torque under worst-case conditions shall be twice the maximum load
- Minimum Preload: Solar Array Hinge (SAH) 3343 N (752 lb)
Antenna Inboard Hinge (AIH) 1879 N (422 lb)
Antenna Outboard Hinge (AGH) 1467 N (330 lb)

LINKAGE - SPRING BEAM

The latch mechanism contains a double over-center four-bar linkage. Linkage hardware is illustrated in Figure 3. Preload is generated by driving the linkage into a position where a spring beam is deflected. Being biased over center while in the latched position allows preload to be maintained with the motor power off. The over-center action, while in the unlatched position, eliminates the need for a motor brake. The high mechanical advantage produced when the linkage goes over center minimizes the size of the motor/gearbox required to drive the mechanism.

Linkage design was optimized on a computer. Final linkage geometry maximizes mechanical advantage near the latched over-center position. Constraining the design was the requirement that the same latch module must fit into all three hinge types. A computer plot of mechanical advantage vs. crank angle is shown in Figure 4. Once the linkage is defined, the motor/gearbox torque requirement is a function of the latch beam spring rate and the preload requirement. The beam spring rate is found by setting a beam deflection which is "large" (10X) relative to thermal expansion effects. The worst-case thermal expansion change in latch-beam to latch-tip position is .05 mm (.002 in). Thus, the latch-beam deflection was set to .50 mm (.020 in). This sets a spring rate since the preload associated with this deflection is known for each hinge. Small beam deflections require lower drive torques since the preload is being generated in the high mechanical advantage section of the linkage action.

Beam deflection is set with an adjustable latch tip. The tip has a spherical radius such that it may accommodate ± 1 deg of misalignment. The maximum pull-in capability of the latch is 12.7 mm (.50 in).

The linkage uses redundant journal bearings throughout. The connecting link and lever link bearing pins are free to rotate in either of their bushings. The crankshaft is mounted in two pairs of concentric bushings.

MOTOR

The drive motor is a reversible dc torque motor with samarium cobalt magnets. The motor is sized to deliver a minimum of .325 N·m (2.90 in-lb), which is twice the maximum static load. The motor delivers this at minimum voltage (21V) and maximum temperature (+71°C). The motor was selected for its high motor constant (K_m). This means it is very efficient at turning electrical input power into mechanical output torque. The actuation time requirement dictated torque to be more important than power in this application. The samarium cobalt magnets contribute to the high motor constant and are insensitive to demagnetization during high current pulses. Motor redundancy is achieved by mounting two motors on one shaft. The primary operating mode uses one motor at a time. A summary of the motor's operating characteristics is given in Table 1.

GEARBOX

High motor torque allows the use of a single-stage gearbox. A single-stage gearbox is desireable because it minimizes size, weight and complexity. The motor pinion is cantilevered off the motor shaft while the output gear is cantilevered off the linkage crankshaft. The gearbox output gear is integral with the crankshaft. The crankshaft drives the crank link through an involute spline.

The gears were designed per AGMA standards. Spur gearing was chosen for high efficiency and jam-free operation. Gear mesh characteristics are listed in Table 2.

Peak loading on the drive train occurs when the motor drives the crank link into the unlatched eccentric stop. The effects of motor torque and inertial loading are combined in the dynamic simulation of Figure 5. This simulation assumes that the motor is running at maximum no-load speed when it impacts the stop. To keep drive train stresses at an acceptable level, the output gear has been designed to act as a torsion spring. The peak dynamic load was reduced from 75.7 N·m (670 in-lb) to 44.7 N·m (396 in-lb) through this cushioning effect.

The gear tooth stresses due to this load are:

Tooth Strength (Motor Pinion Bending Stresses)

- Actual 849 M·Pa (123,160 psi)
- Allowed 1379 M·Pa (200,000 psi) ($S_{ult} = 1.5$)
- Margin 0.08

Tooth Durability (Mesh Contact Stresses)

- Actual 2065 M·Pa (299,500 psi)
- Allowed 2637 M·Pa (382,500 psi) ($S_y = 1.2$)
- Margin 0.06

In order to endure high contact stress without pitting, the gears are being case-hardened to RC 60 minimum with the ionitride process. The case depth will be .08-.12 mm (.003-.005 in) to ensure subsurface shear stresses will not flake the case off.

SWITCH MODULE

Each latch mechanism contains two switch modules. One indicates when the linkage (crank link) is in the latched position while the other indicates the unlatched crank link position. Two microswitches are mounted in each switch module for redundancy. One trip arm actuates both microswitches when the crank link has depressed the contact button 2.54 mm (.100 in). The microswitch trip points are individually adjusted relative to the trip arm. Redundant compression springs bias the trip arm against an adjustable down stop. Figure 6 illustrates how these components are configured.

MATERIAL AND LUBRICANTS

The structural components used in the latch mechanism are made from 6Al-4V titanium. This alloy was chosen because of its corrosion resistance and strength-to-weight ratio. Titanium accounts for approximately 39% of total latch module weight. The more highly stressed components are made of passivated Carpenter Custom 455 corrosion-resistant steel. These components in-

clude the gears, links, stops and journal bearings. The steel is heat treated to tailor its strength vs. toughness properties for each application. Custom 455 accounts for approximately 25% of the total latch module weight. The close match (within 20%) in thermal expansion coefficients between these two materials keeps bearing clearances and gear-mesh backlash relatively constant. The bulk of the remaining module weight (31%) is made up of the various materials used in the drive motor. The total latch module weight is 62.3 N (14.0 lb).

Two basic lubricant types are used in the latch module. A dry, bonded lubricant is the preferred type for intermittently operated devices which must survive long nonoperating periods. This is because it has a low evaporation rate and no surface creep. For applications with low total travel and moderate contact stresses, Ball Aerospace Systems uses a bonded molybdenum disulphide-based dry lubricant. This lubricant has been used at all latch module moving interfaces except the motor ball bearings and brushes. The motor ball bearings use a molybdenum disulphide-based grease to endure the high contact stresses encountered here. The motor brushes are made of a silver/molybdenum disulphide material, Stackpole SM 476. This material has been tested to twice the required latch motor life and found to wear only .018 mm (.0007 in) at each brush block.

DEVELOPMENT PROBLEMS AND SOLUTIONS

Thermal Effects on Preload

Thermal effects strongly influence drive requirements and worst-case loading. Because of the over-center linkage's mechanical advantage characteristics, the drive torque requirement is minimized by decreasing the preload spring deflection. That deflection must not be made so small that thermal expansion/contraction causes large preload variations. Thermal expansion/contraction effects on preload must be accounted for in the nominal preload setting and in worst-case structural loading, as indicated in Table 3.

Peak Drive Train Loading

When the crank link is driven into the "hard" eccentric stops, loads occur which are much higher than the motor's stall torque. A single stage, low reduction gearbox increases this peak loading since gearbox stiffness is proportional to the inverse square of gear ratio. To lower stresses to an acceptable level (a 41% reduction) the output gear is designed to act as a cushion between the motor rotor inertia and the eccentric stops.

Preload Spring Selection

A significant weight reduction was brought about by using the mounting structure itself as the dominant spring. Preload is generated in this device through the deflection of a spring. Initially, the lever link was designed as

the dominant spring in this system. Choosing the lever link drove the spring rate requirements of the hinge-to-latch mounting structure up in order to achieve the desired deflection. This increased hinge weight.

CONCLUSIONS

This mechanism achieves all hinge latch design requirements with a compact modular unit. The hinge latch module has a calculated reliability of .9997 for its design life. Design philosophy stresses redundancy where redundancy does not overcomplicate the design or vastly increase the parts count. The use of easily accessible adjustments on critical performance parameters yields increased machinability and lower cost. Computer automation of the linkage analysis (which would have been done graphically) allowed Design Engineering the time to optimize latch performance. Design response to changes in hinge latch requirements is also greatly enhanced through this automation.

Development testing of the hinge latch module is under way. Initial testing has substantiated the computer predictions of preload generation and drive torque requirements associated with a given preload setting. The development test hinge latch module is shown in Figure 7.

ACKNOWLEDGEMENT

I would like to thank Hilary Lane and Gloria Bucco for their invaluable assistance in compiling and editing this paper. I also thank George Ahlborn for his work on the lubrication section and Lew Martin for his dynamic simulation of the latch impact.

REFERENCES

1. John C. Walker; SAAM Hinge Latch Mechanism; BASD TN82-20; 11 November 1982.
2. Dave Paule; Hinge Latch Loads; BASD SER B8650-81-041 27 July 1981.

Table 1
MOTOR OPERATING CHARACTERISTICS

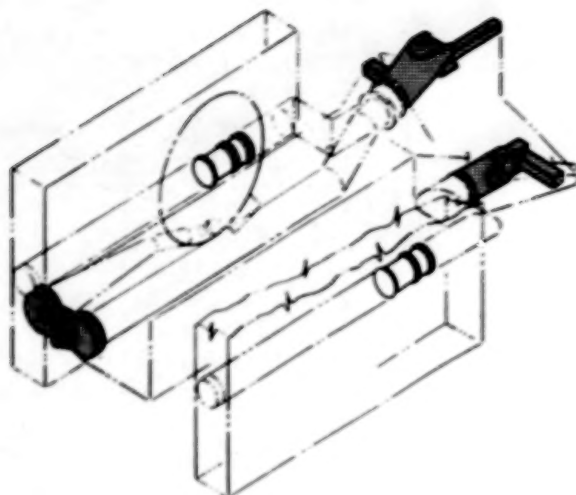
MOTOR TYPE	DC TORQUE WITH BRUSHES
MAGNETS	SAMARIUM COBALT
MOTOR CONSTANT	.209 N·m/ $\sqrt{\text{Watt}}$ (29.6 in-oz/ $\sqrt{\text{Watt}}$)
RESISTANCE	54Ω
MAXIMUM NO-LOAD SPEED	25.2 rad/s (241 rpm)
TORQUE CONSTANT	1.54 N·m/A (218 in-oz/A)
BACK EMF CONSTANT	1.54V/(rad/s)
ROTOR INERTIA	.125 mm·Kg·s ² (.173 in-oz-s ²)
WEIGHT	22N (5.0 lb)

Table 2
GEAR MESH CHARACTERISTICS

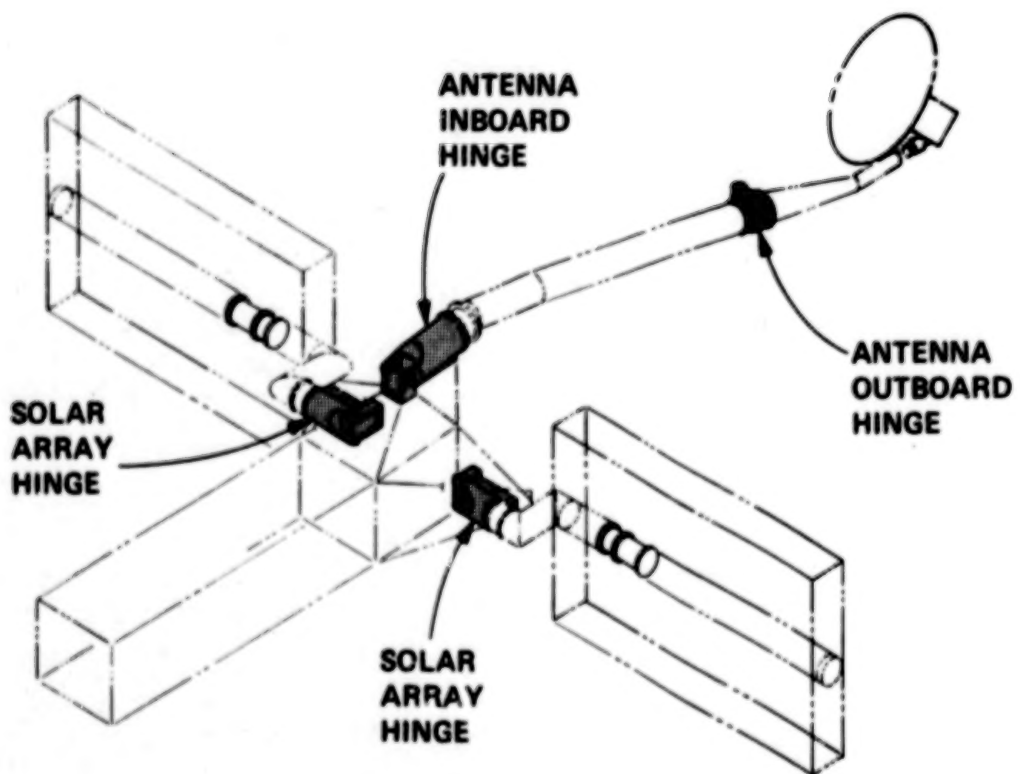
TOOTH TYPE	SPUR GEARS
TOOTH FORM	FULL DEPTH INVOLUTE
AGMA QUALITY NUMBER	Q7A
PRESSURE ANGLE	25 deg
DIAMETRAL PITCH	48
GEAR RATIO	17.833:1
CENTER DISTANCE	59.8 mm (2.354 in)
MINIMUM FACE WIDTH	7.04 mm (.277 in)

Table 3
PRELOAD VARIATION DUE TO THERMAL EXPANSION
AND INSTRUMENTATION UNCERTAINTIES

	Required Preload	Minimum Preload	Nominal Preload (22°C)	Maximum Preload
SAH	3340N (752 lb)	4010N (902 lb)	4420N (993 lb)	4990N (1120 lb)
AIH	1880N (422 lb)	2250N (507 lb)	2390 (537 lb)	2550N (574 lb)
AOH	1468N (330 lb)	1760N (396 lb)	1830N (412 lb)	1900N (428 lb)



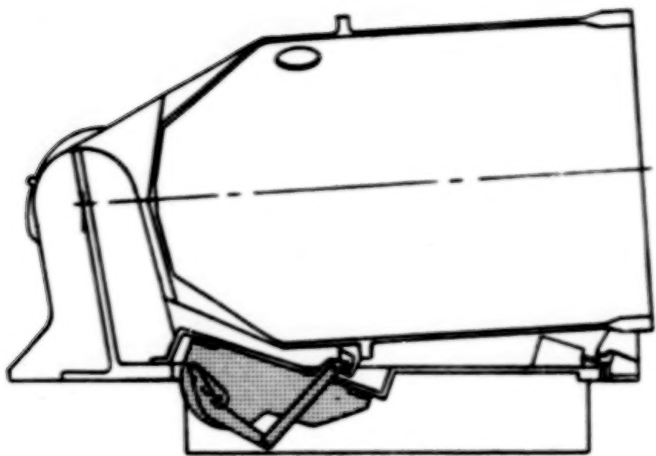
STOWED



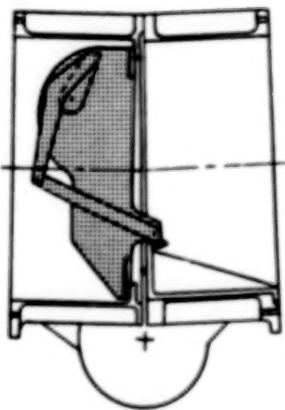
DEPLOYED

A/N 2972

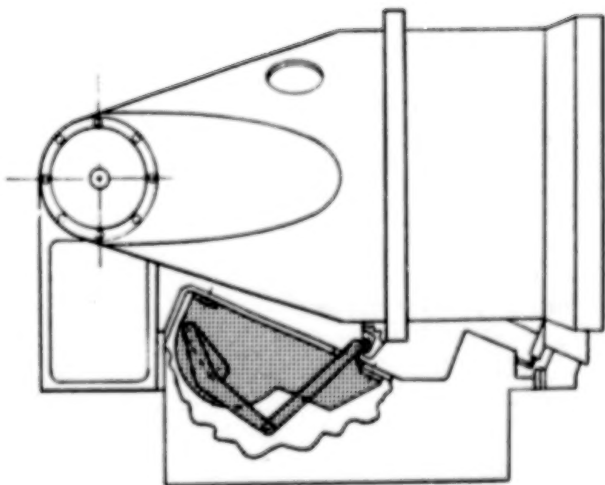
Figure 1 Stowed and Deployed Hinge Configurations



ANTENNA INBOARD HINGE



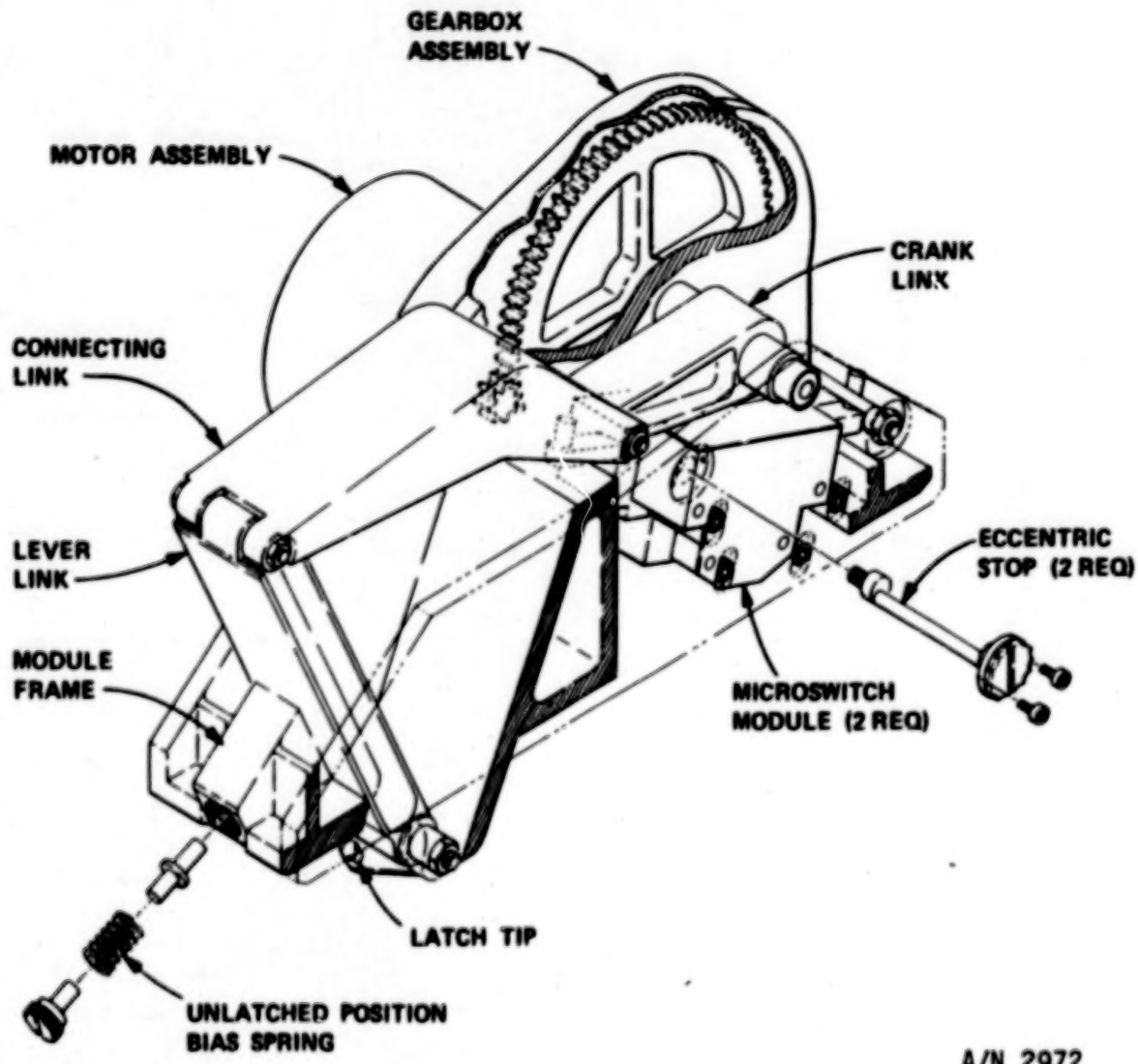
ANTENNA OUTBOARD HINGE



SOLAR ARRAY HINGE

A/N 2972

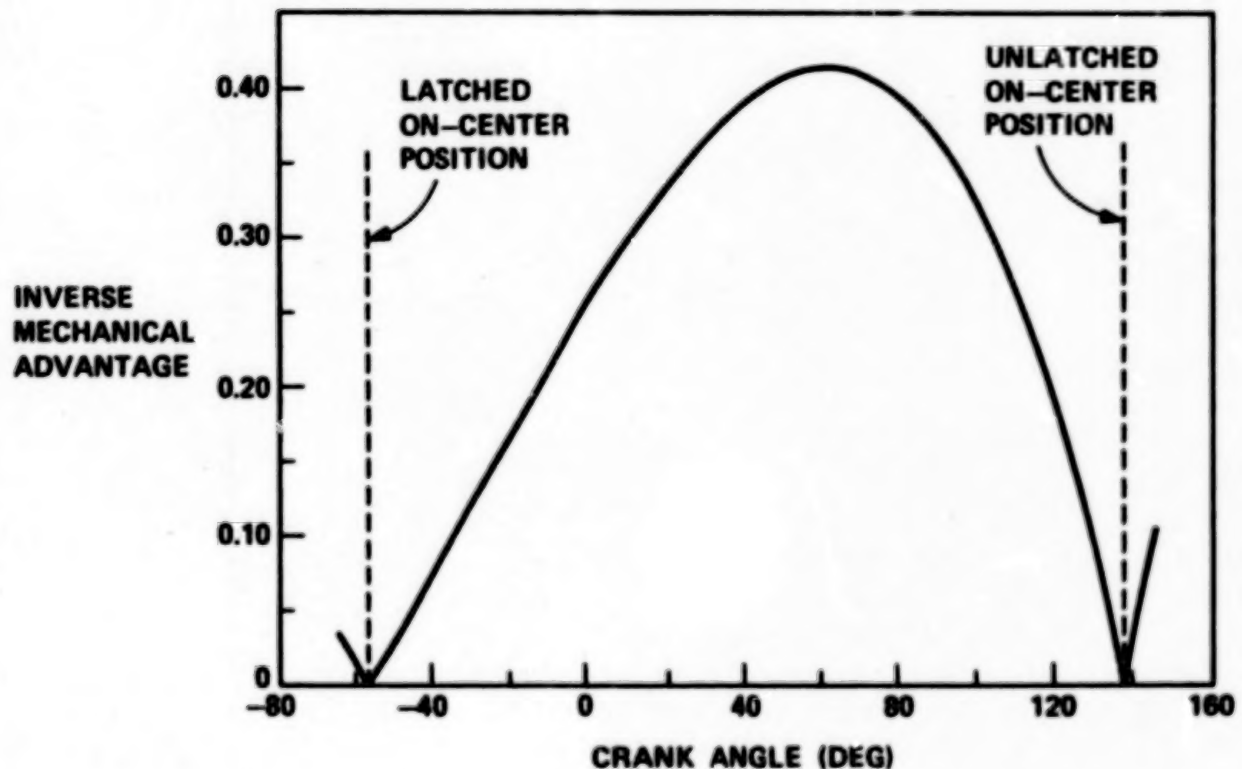
Figure 2 Latch Module Installations



A/N 2972

Figure 3 Hinge Latch Module

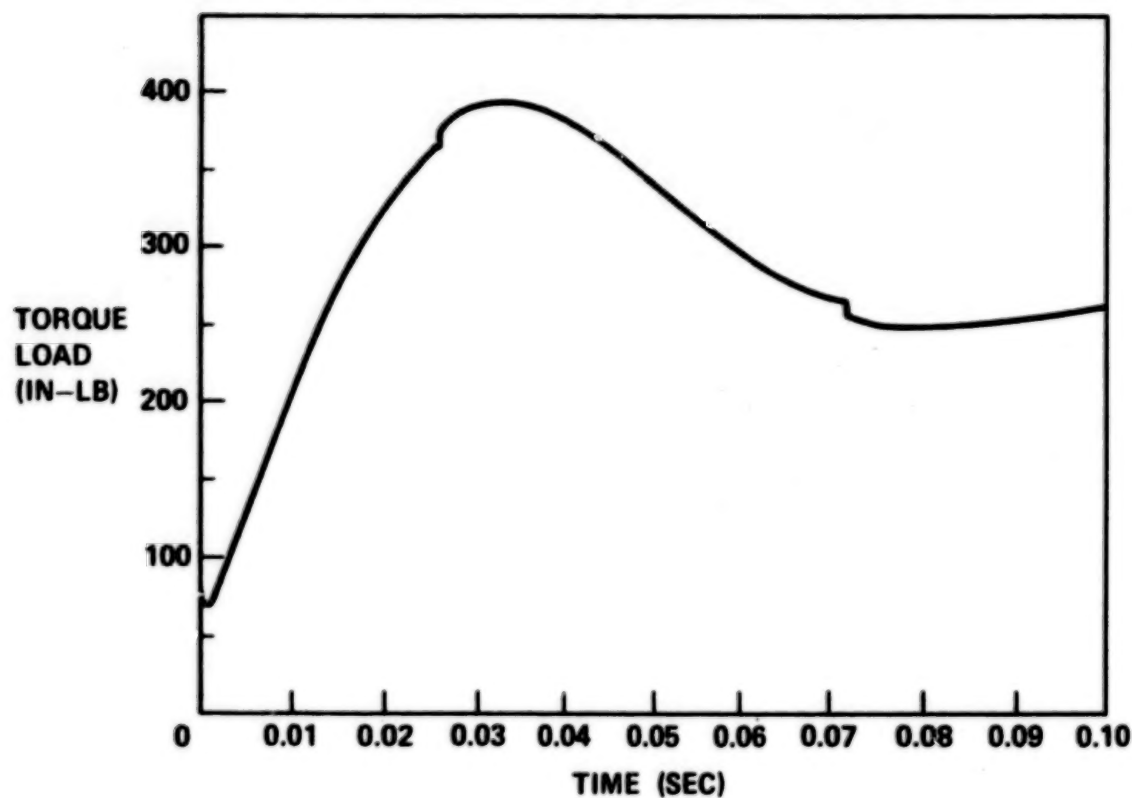
INVERSE MECHANICAL ADVANTAGE VS. CRANK ANGLE
FULL LINKAGE TRAVEL



A/N 2972

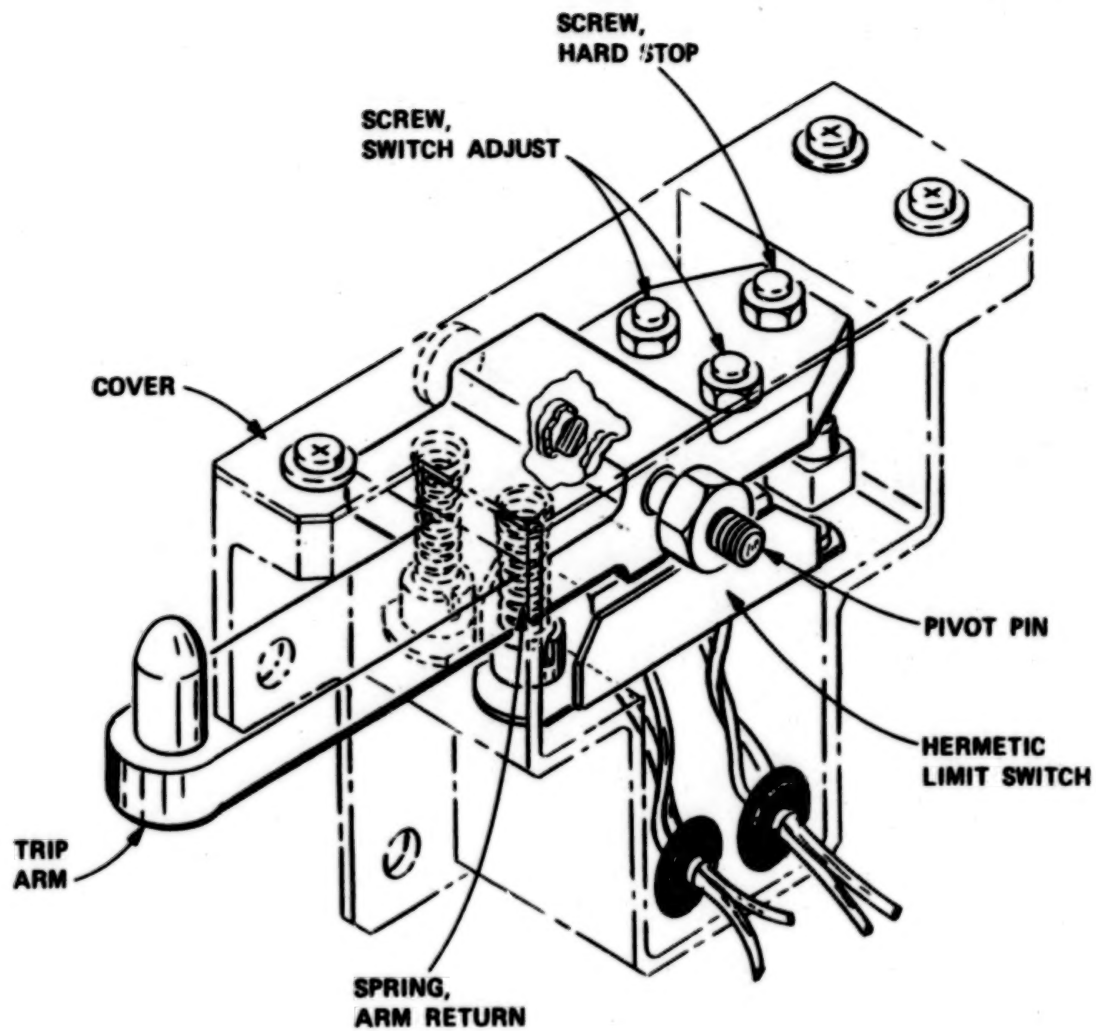
Figure 4 Linkage Mechanical Advantage

CRANKSHAFT TORQUE LOAD VS. TIME
LOADS INDUCED WHEN LINKAGE IS DRIVEN INTO STOP



A/N 2972

Figure 5 Dynamic Loading



A/N 2972

Figure 6 Switch Module

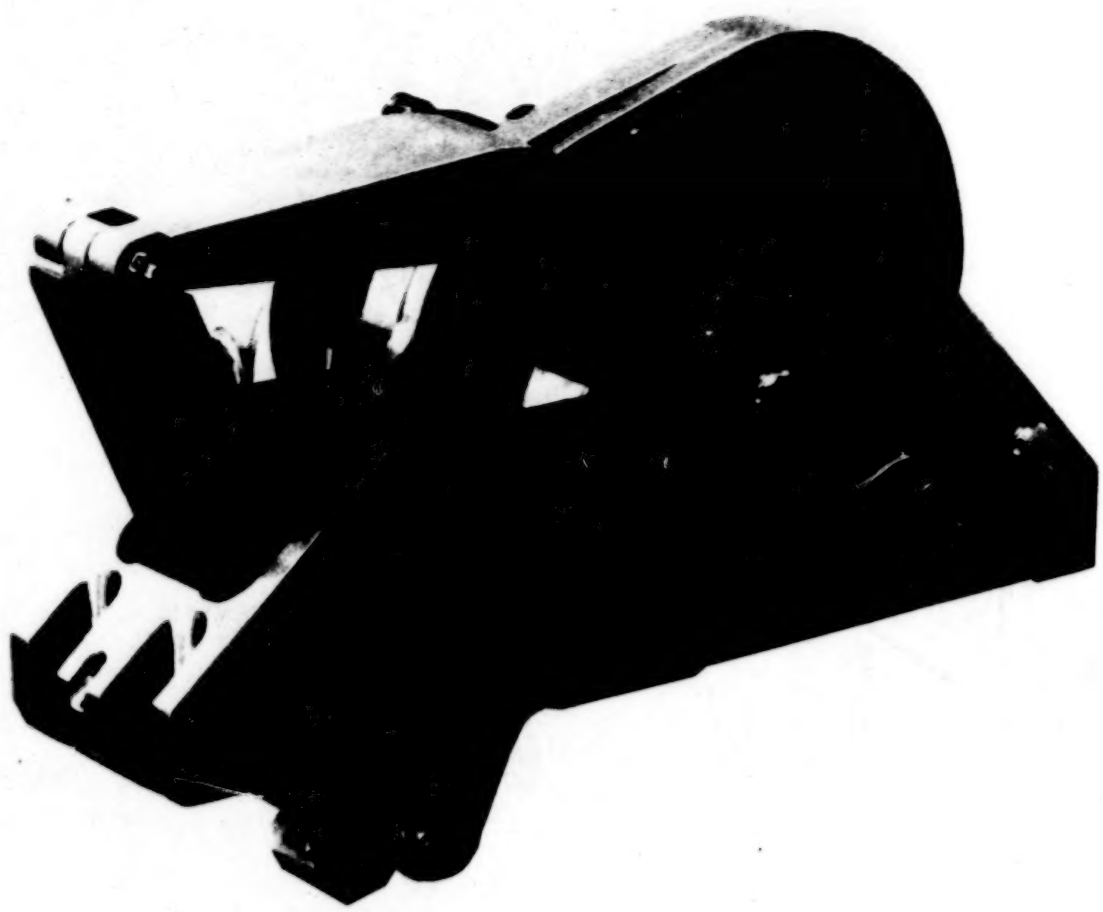


Figure 7 Development Test Latch Module

THE EVOLUTION OF A RELEASE-ENGAGE MECHANISM FOR USE ON THE ORBITER

John Calvert*

ABSTRACT

The Release-Engage Mechanism (REM) is designed to secure a deployable payload in the orbiter during launch and to enable the payload to be released, deployed, and reattached for re-entry.

This paper presents the following: (1) the initial design concepts of the Release-Engage Mechanism; (2) the problems encountered during assembly, (3) the abnormalities that occurred during vibration testing, (4) the incompatibility of the Remote Manipulator System and REM operation, and (5) the resulting modifications to the REM that assured its successful performance on two Shuttle flights.

INTRODUCTION

In the development of payloads for the Space Transportation System, it was found that a mechanism would be required that could secure a deployable payload in the orbiter during launch, release the payload upon reaching orbit to permit acquisition of scientific data, and re-secure the payload for re-entry.

The requirements for this mechanism provided many new and unique design problems, one of which was a connection that could safely secure a large payload during launch but could be easily separated upon reaching orbit. The basic concept selected was to insert and retract a pin from a matching hole in mating pieces. The hole was an integral part of a supporting structure. The pin was attached to the payload. The mechanical action of inserting and retracting the pin was accomplished by motors and driving linkages that were part of the supporting structure.

The mechanism also had to have an operational capability compatible with the Remote Manipulator System (RMS). The RMS was used to deploy, maneuver, and berth the payload. When the initial concepts for the REM were being conceived, RMS operational data was not available.

ORIGINAL REQUIREMENTS

The original requirement for the Release-Engage Mechanism (REM) was for it to be used with the Induced Environmental Contamination Monitor (IECM). The IECM is a deployable

*NASA George C. Marshall Space Flight Center, Alabama.

scientific package that will detect and map contaminants in and around the cargo bay of the orbiter. The IECM takes data while attached to the orbiter and while being maneuvered by the Remote Manipulator Arm. The IECM is rectangular, 1.23 meters (48.5 inches) long, 0.85 meters (33.5 inches) wide, by 0.77 meters (30.57 inches) high, and weighs 370 kilograms (816 pounds).

The REM has three interfaces: (1) structural interface with the IECM; (2) structural interface with the orbiter support structure, in this case the development flight instrumentation pallet; and (3) operational capability of the Remote Manipulator System (RMS). The positional accuracy of the RMS was ± 5 centimeters in any axis from a given point and one degree of rotation about any axis.

The IECM/REM Assembly was designed for the following load requirements:

IECM/REM LOAD FACTORS

x	+4.5	-0.4
y	+3.3	-3.3
z	+3.5	-3.1

ORIGINAL DESIGN CONCEPT

The design concept selected for development (figures 1a, 1b, and 2) had the following major design features: (1) two deployable rails, forward and aft, bolted to the payload (each rail had two structural pins, one round and one square); (2) motors, gear train and linkages which provided the latching and securing force for the payload; (3) an electrical feed-through system for the payload; and (4) the center frame or mounting structure. The center frame provided the four mating holes (nut plates) for the structural pins on the deployed rails. The center frame also provided a large flat surface area used in berthing the payload. Five position indicator switches were included as a design feature of the center frame. When actuated, these switches indicated that the payload was in a ready-to-be-latched position.

DESIGN CONSIDERATIONS

The structural pin-nut plate interface was of primary concern during the initial design effort. This interface provided the structural load path between the payload and Shuttle during launch and re-entry. It also had to be capable of separating and remating in orbit. Figure 3 shows the structural pins in the nut plates with the IECM installed.

Clearances between the pin and nut plate had to be kept small to minimize shock loads to the payload during vibration testing and launch and to provide a firm load path between the payload and orbiter.

It was realized that unnecessarily small clearances between the pin and nut plate would require the four pins to be manufactured, assembled, and maintained in near-perfect alignment so the pins could be mated with their respective nut plates. The alignment problem was complicated by the requirement that the payload and rails must be deployed in orbit, subjected to

a changing thermal environment and, therefore, configuration distortion outside the orbiter bay. The four pins had to remain in alignment so they could be re-inserted into their respective holes for re-entry. A clearance of 0.02 millimeter (0.0008 inch) was selected. The transfer of metal between the pin and nut plate during vibration was also of concern.

The material selected for the initial pin-nut plate design was chrome-plated, 4130 steel heat-treated to 160 ksi for the pin and 301 stainless steel for the nut plates. Two different shapes for the structural pins were selected, one cylindrical and one square. The cylindrical shape could transmit load in two directions. The square pin, when mated with a rectangular hole, would allow for uneven thermal expansion/contraction between the payload and REM center frame in a horizontal or x-axis direction. A 0.16 centimeter (0.06 inch) gap was allowed. The 0.02 millimeter (0.0008 inch) clearance was maintained in the vertical or z-axis direction. A 0.32 centimeter (0.125 inch) gap between the aft deployable rail and its mating nut plates was specified to allow for the payload contraction in the y-axis direction.

The mating or sliding surfaces of the pin and nut plate were highly polished to reduce friction forces and make the latch/unlatch smooth. No lubrication was used between the sliding surfaces of the structural pin and nut plate.

The berthing procedure for the deployed payload was for the RMS to place the sliding surfaces or three feet of the deployed rails on the designated areas of the center frame (figure 1) and slide the rails against the side fence and forward into a ready-to-latch position. At this time, the five ready-to-latch switches would give an indication that the payload was within 0.25 centimeter (0.1 inch) of the desired position. A latch command could then be given. The above procedure was required to allow the RMS to position the pins into the required alignment to enter the nut plates. The latching action, a forward movement of 3.5 centimeters, mated the pins into the nut plates and also made the electrical feed-through connection for the payload.

The gear train (figure 4) has redundant motors driving through a series of spur gears, a differential and worm/worm gear final drive. The gear train has a reduction of 2812 to 1. A motor torque of 2.4 kg-cm (34 in-oz) produces an output torque of 31.8 kg meters (230 ft lbs). The motors have an integral spring-loaded brake that prevents the latching system from being back-driven, although the final worm/worm gear absorbs much of the back-drive load. The gears are lubricated with Brayco grease 3L-38RP. The gear train is thermally isolated, and heaters are used to keep the grease from solidifying. The heaters assure that the gear train will operate at low temperatures. The gear train rotates a bell crank. This movement, transmitted through a solid adjustable link-and-latch link, pushed the pins on the forward rail into their mating holes. Figures 5a and 5b show the latching linkage in unlock and lock positions, respectively. The latch/unlatch indicator switches serve two purposes: (1) they indicate to the REM operator the status of the payload and (2) they automatically cut power to the gear train motor when the bell crank reaches the desired position. The adjustable link provides the means of equalizing the pre-load between the round and square pin.

During a study made of the locking linkage kinematics, it was noted that the two latch links rotated different amounts for the same bell crank rotation (figure 6a). A close examination revealed that one latch link traveled approximately 0.5 centimeter farther than the other during latch/unlatch operations. This uneven travel resulted in only one latch link being in contact

during latch/unlatch operations. An adjustment was available so that each latch link would apply equal force when the payload was in the latched position. Because of the spacing of the structural pins and aligning restraints provided by the center frame, this uneven movement was not a problem.

After assembly, the unit with the IECM installed was subjected to three axes of vibration testing. A latch/unlatch cycle was attempted between each axis of testing. The structural pins could not be retracted from their mating nut plates after each vibration test. A fine black powder was generated by the chrome-plated pins abrading the stainless steel nut plates. The powder generated was enough to close the 0.02 millimeter (0.0008 inch) gap between the pin and nut plate and cause binding. The problem was corrected by increasing the gap to 0.076 millimeter (0.003 inch) and by adding Brayco 3L-38RP grease to the interface. The vibration tests were then successfully completed.

During a thermal vacuum test to determine the REM lower operational temperature, it was found that, at temperatures below -125°F, the grease used on the structural pins solidified to such a degree that an unlatch/latch operation could not be performed. At the time the thermal vacuum test was performed, this operational temperature was acceptable.

To determine if the RMS could perform the berthing procedure for the payload described earlier and place the payload in the required ready-to-latch position, the REM was shipped to Johnson Space Center for testing in the Manipulator Development Facility (MDF). The berthing procedure required the RMS to place the payload and deployed rails on the surface of the REM, and while maintaining contact with the REM surface with the three berthing feet, move the payload 15.2 centimeters (6 inches) in the x-direction, and then, upon making contact with the side fence, move the payload 15.2 centimeters (6 inches) in the y-direction. The berthing procedure was performed by the RMS operator viewing the operation on two closed circuit television monitors.

Several problems were identified during these tests. It was found that, when the payload deployed by the RMS was constrained from movement in one direction, accurate control of the payload could not be maintained in the other direction. With the RMS arm in some positions, and the payload constrained in one direction, a command to move in one direction would result in payload movement in the opposite direction. As stated, the payload had to be moved 30.5 centimeters while maintaining contact with the three berthing feet on the center frame surface. This requirement for constrained movement and the friction force of the feet sliding on the center frame surface transmitted to the RMS made this procedure undesirable. Complicating the procedure further, the feet could not be seen by the television cameras with the payload installed. This made the movement of the payload into the required latching position difficult. The close positioning, 0.25 centimeter (0.1 inch) required to close the ready-to-latch switches was also very ~~difficult~~ and sometimes impossible to obtain.

Several times during berthing attempts, the payload rails would be placed into positions so that the rails would hang up and could not be freed by the RMS operator. This prevented the payload from either being locked up with the REM or from being moved away for another

berthing attempt. Successful berthing of the payload was sometimes achieved, but it was not a smooth nor consistent operation. When berthing and lock up could be achieved, the average time required was approximately 30 minutes.

As a result of these tests, it was decided changes must be made to the REM hardware which would (1) remove all possibility of payload hang up during the berthing process, (2) provide highly visible markings on the REM that could be used by the RMS operator for orientation of the payload, (3) increase the payload capture range of the REM, and (4) expedite the berthing process.

A new method of berthing was also required. Instead of having to move the payload along the surface of the REM, a straight down motion of the payload would be attempted. This motion was easier to accomplish with the RMS, and the hardware changes would enhance this method.

The unit was shipped back to MSFC where the following design changes were made to the REM: (1) four "Y" guides were mounted to the center frame; (2) guide rods were attached to the deployed rails; (3) ready-to-latch switches were included to give an indication that the payload was ready to be latched over a 0.6 centimeter range; and (4) pin and nut plate lead-in configurations were changed to increase the permissible misalignment for a successful latch-up. The original configuration of the REM is shown in figure 2. Figures 7a and 7b show the configuration after modification.

The four guide rods and "Y" guides were desired by the RMS operators for two reasons. The 10 centimeter opening at the top of the "Y" guides would provide a large target for the rods on the deployed rails when the RMS operator attempted to berth the payload. As the payload was moved close to the center frame, the physical restraint of the "Y" guide placed the payload in the desired position for latch-up. The second reason for the rod and "Y" guide was for visibility. Alternating light and dark horizontal stripes, equally spaced and at equal distances above the center frame surface, were painted on the "Y" guides. The outboard ends of the rods were also striped for better visibility. The height reference of the horizontal stripes was an important aid and improved the berthing procedure. The physical restraint of the "Y" guides was both an advantage and disadvantage. The advantage was that, with the rods in the confines of the "Y" guide while maintaining a plane parallel to the center frame, the payload would be placed in a position that successful latch-up would be achieved. The disadvantage was that the frictional force generated by contact of the rod on the surface of the "Y" guide had to be overcome by the RMS. This surface on the "Y" guide was coated with Emralon 334, a dry lubricant, to minimize the frictional force.

The original type of switch selected to give a ready-to-latch indication was also changed. The original switch would provide an indication only when the berthing feet were positioned to within 0.25 centimeter of the surface of the center frame. This was a very stringent requirement on the RMS operator. Also, the actuation arm of the switch was deformed during the Johnson Space Center testing. Therefore, a larger and stronger switch having a 0.6 centimeter indication capability was selected, and redundant switches were provided.

The original blunt nose design of the pin and nut plate is shown in figure 6b. The redesign of the pin and nut plate is shown in figures 6c, 8a, and 8b. This redesign in configuration allowed the pin to be out of alignment with the mating hole approximately 1 centimeter and still be guided into the hole by the latching motion.

Also shown on figure 8b is a new configuration for the latch link. Figures 5a and 5b show the original configuration. The monoballs that were originally the contact between latch link and deployable rails were also the primary area of hang-up for the deployable rails. A hook on the deployable rails had thin fingers that could become lodged between the separate monoballs and could not be removed by the RMS operator. This area was totally invisible to the RMS operator. The latch links were replaced by a solid latch line. In addition to removing the hang-up potential of the monoballs, a conical shape was specified on the top surface that would provide a guiding surface for the hook as it was brought down vertically into ready-to-latch position (figure 8b).

After the new configuration was vibration tested, the REM was shipped back to Johnson Space Center for further testing in the MDF. These tests indicated that the added aids and larger capture range of the REM made it compatible with RMS capability. In addition to the testing at JSC in the manipulator docking facility, berthing tests using a flight-type of arm were conducted at SPAR, the Canadian manufacturer of the RMS. This testing also indicated that the RMS and the REM were compatible for joint operations on a mission.

The last modification required on the IECM REM before flight was to allow operational capability down to -200°F. As stated earlier, the grease applied to the structural pins solidified at -125°F, making operation at lower temperatures impossible. Several dry lubricants were considered before NPI 425 was selected for testing. After the lubricant was applied, the pins were burnished to remove all excess. Vibration testing was again performed and the REM operated satisfactorily. The thermal vacuum test was successfully accomplished at a temperature of -210°F.

Three REMS have been built, the first for qualification testing. The second unit was flown with the IECM on STS3 and STS4. It was not operated on STS3 because of the failure of an aft bulkhead camera and the RMS elbow camera, which were needed to safely berth the IECM. However, the unit was satisfactorily operated on STS4.

The third unit was flown on STS3 with the Plasma Diagnostic Package, which was deployed and berthed three times on this flight. The PDP/REM is scheduled to be flown again aboard Spacelab 2.

The IECM/REM has been operated through two cycles in flight and the PDP unit through three cycles. The average time required to berth a payload has been approximately six minutes, with one berthing of the PDP being accomplished in four minutes.

A fourth REM is being designed for a GSFC payload, SPARTAN, a 1134 kg (2500 lb) payload to be launched in July 1984.

BLANK

PAGE

363

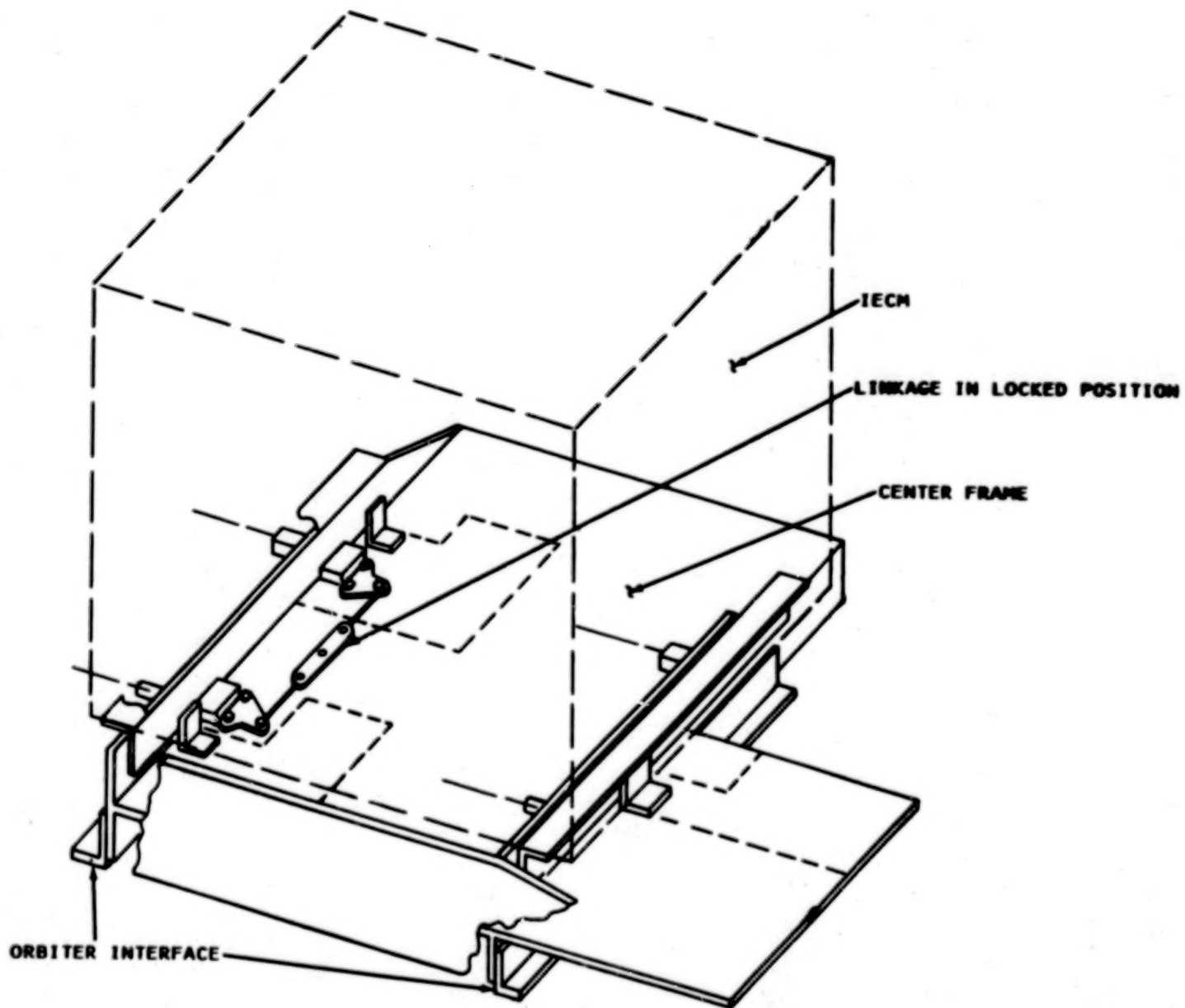


Figure 1a. Original Concept REM in Latched Position.

363

BEST AVAILABLE COPY

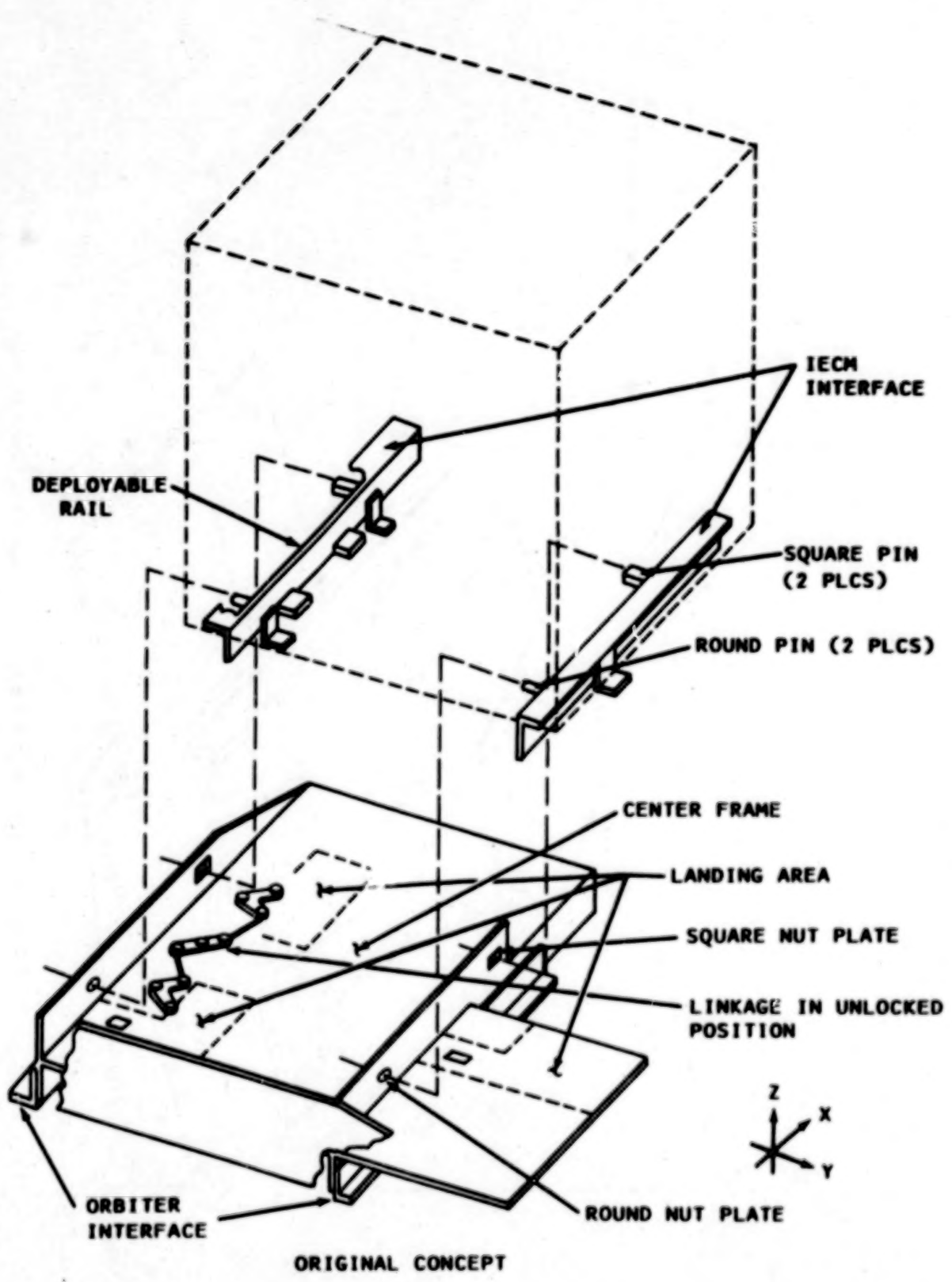


Figure 1b. REM with Payload Deployed.

BLANK

PAGE

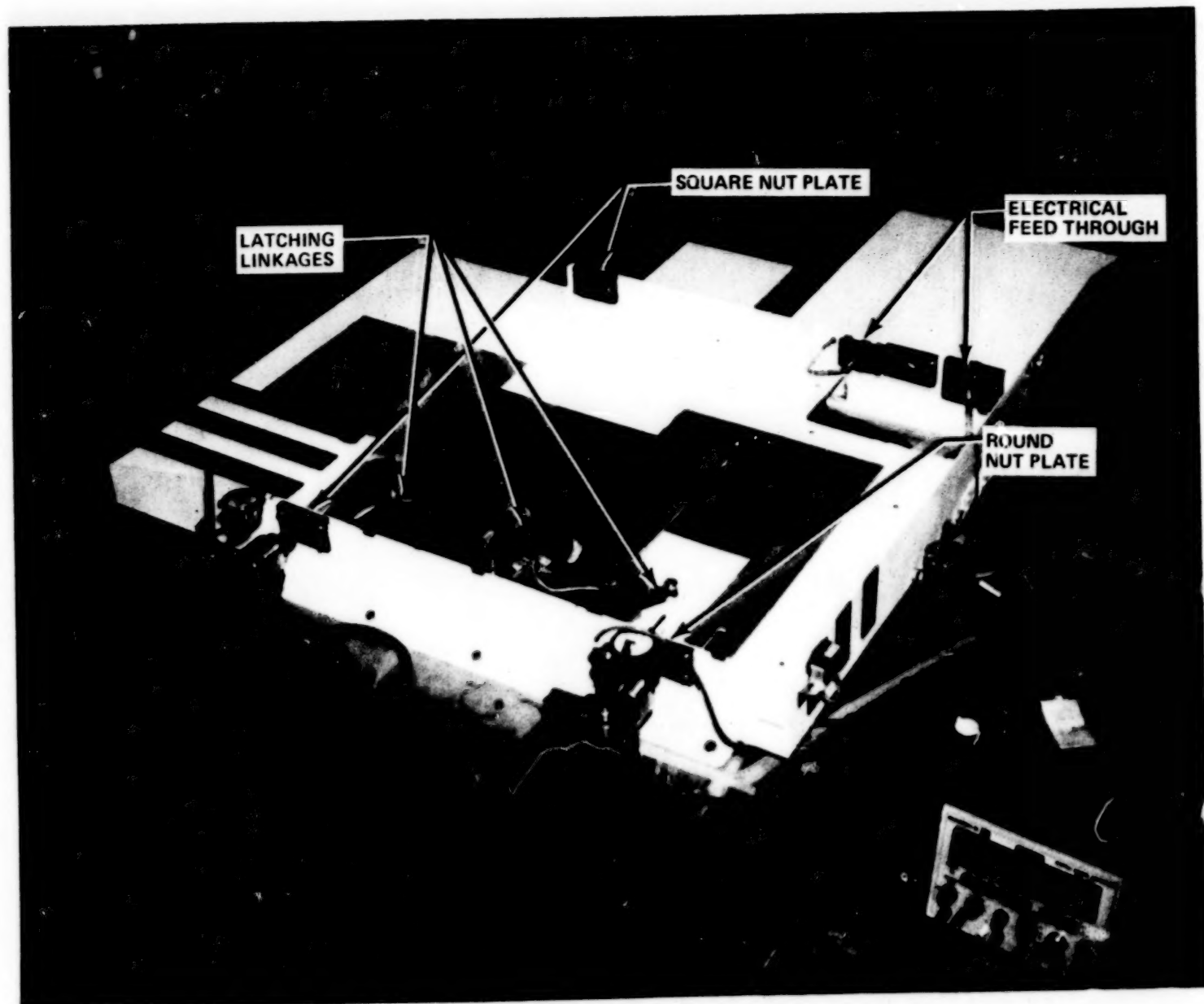


Figure 2. Center Frame Assembly and Calibration Equipment.

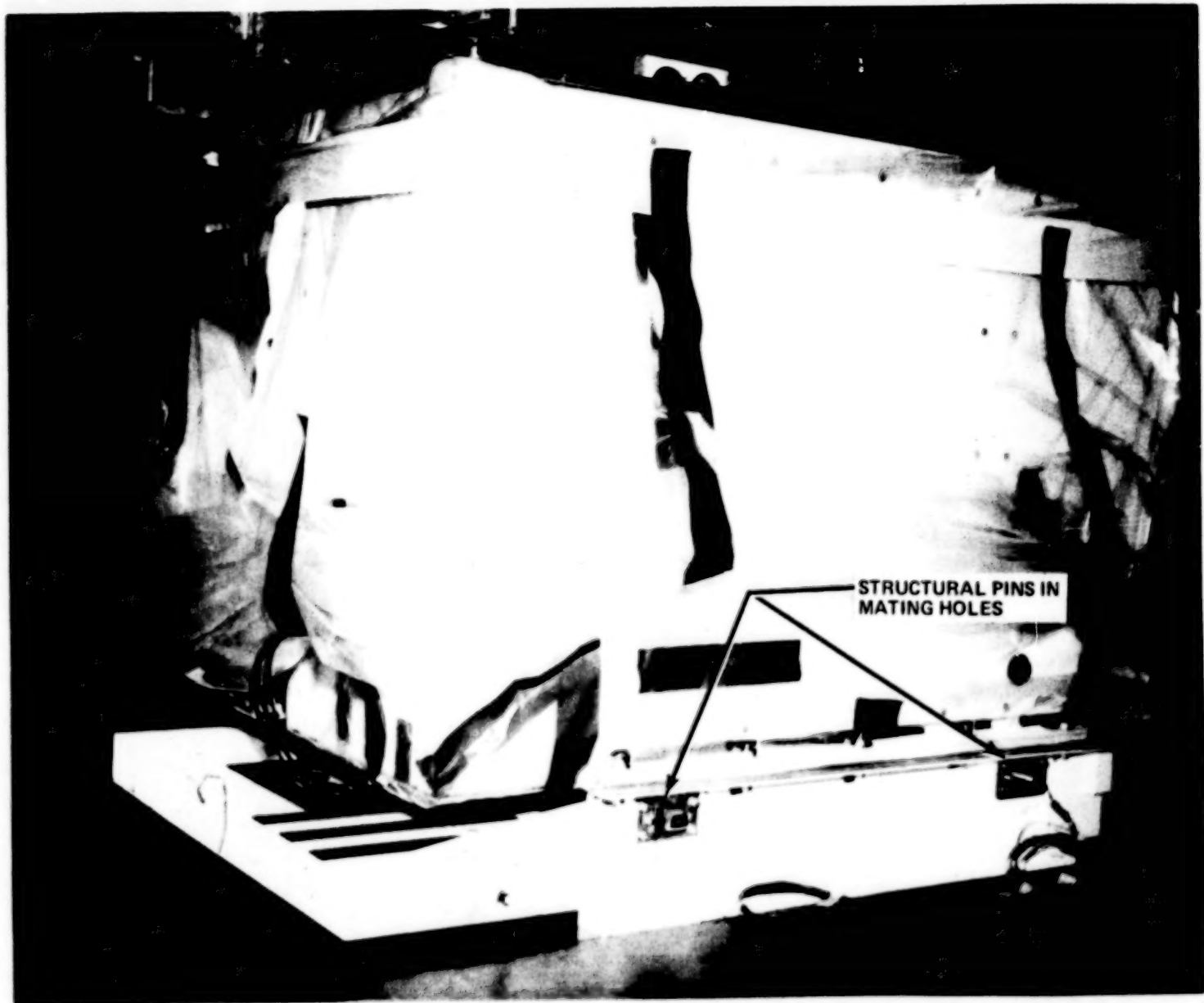


Figure 3. Release Engage Mechanism with Induced Environmental Contamination Monitor Installed.

366

BEST AVAILABLE COPY

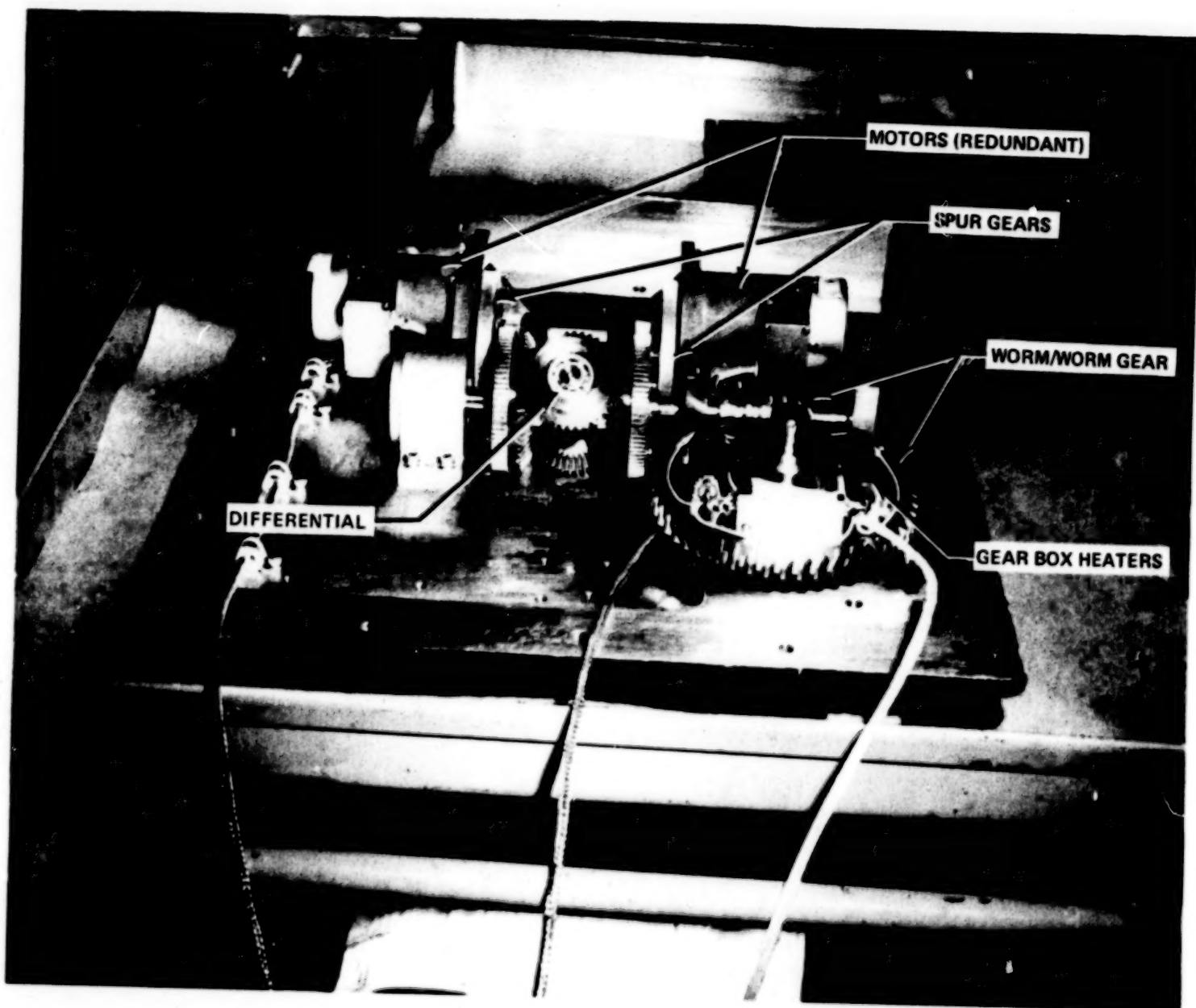


Figure 4. REM Gear Train.

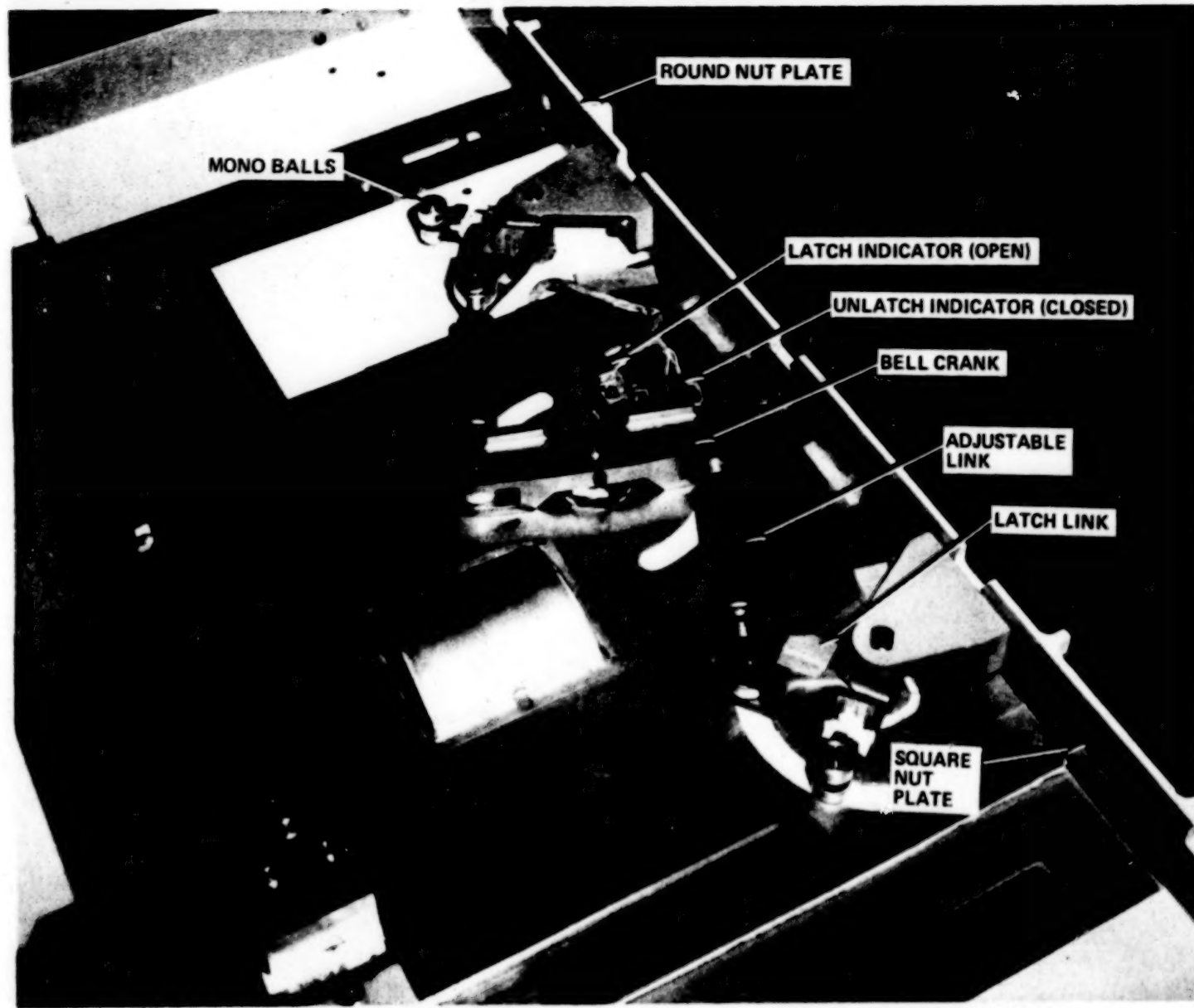


Figure 5a. Latch Linkage in Unlock Position.

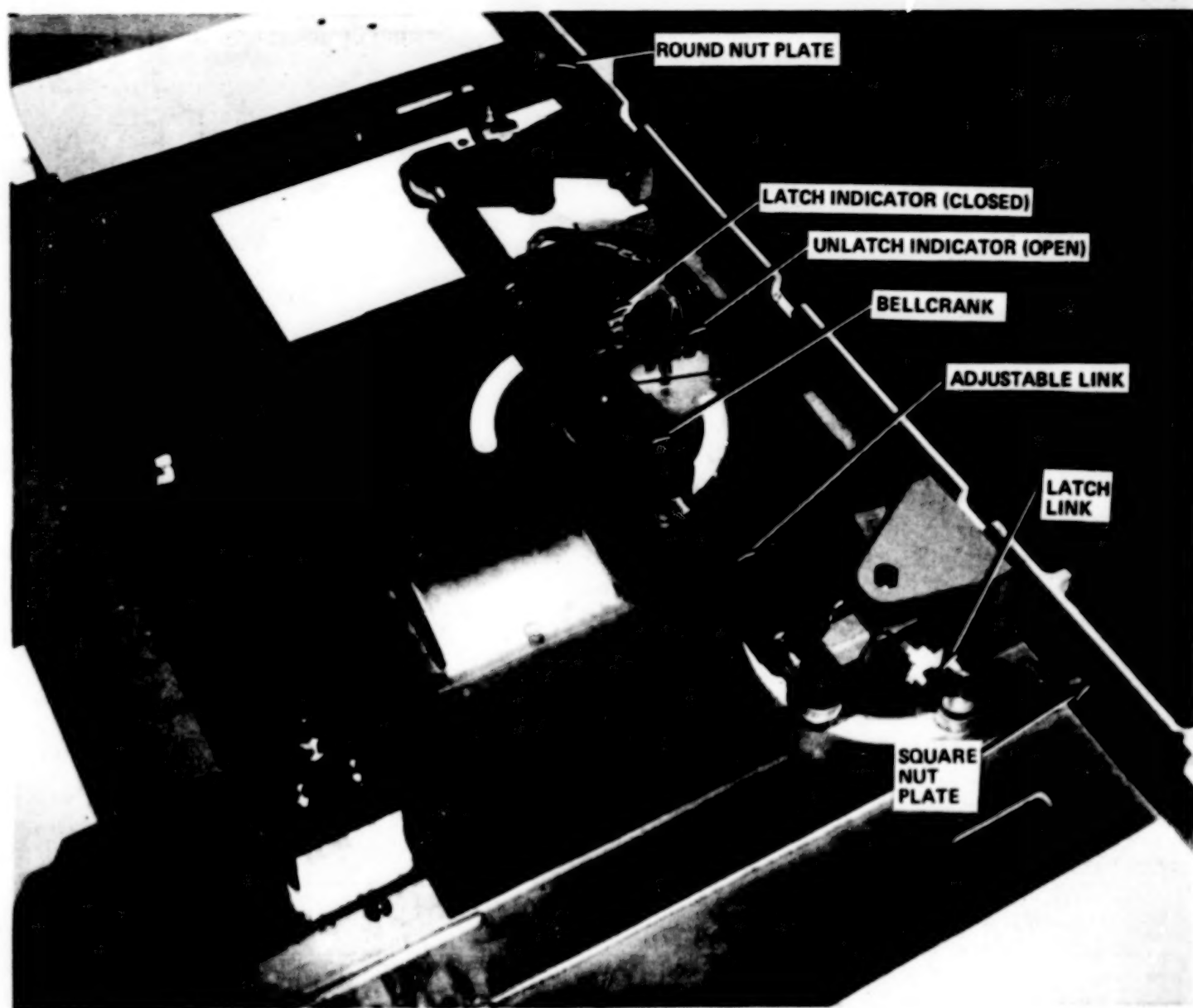


Figure 5b. Latch Linkage in Lock Position.

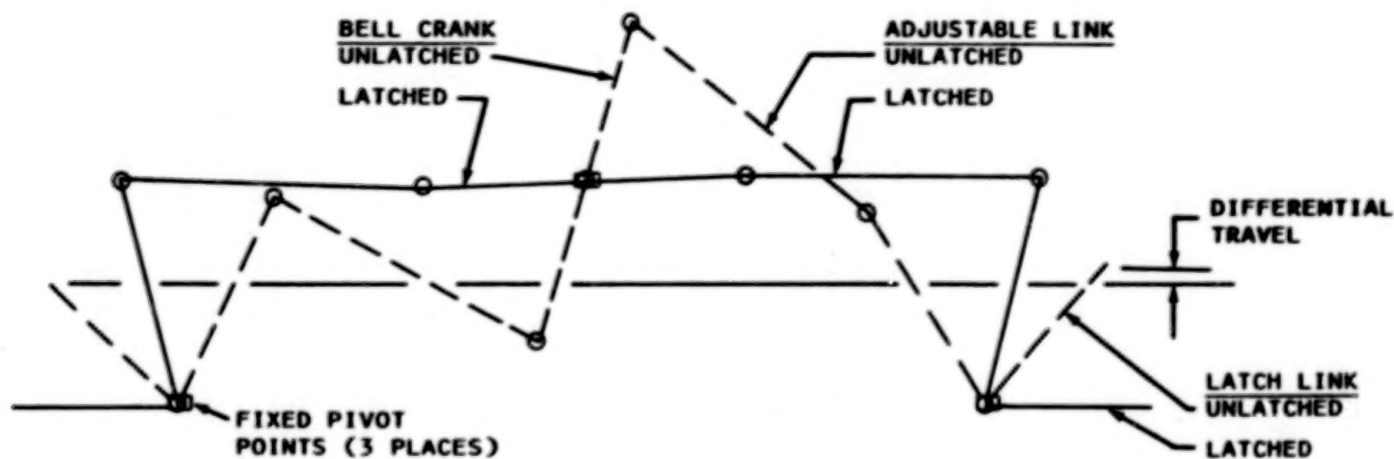


Figure 6a. Kinematics of Latching Linkage.

370

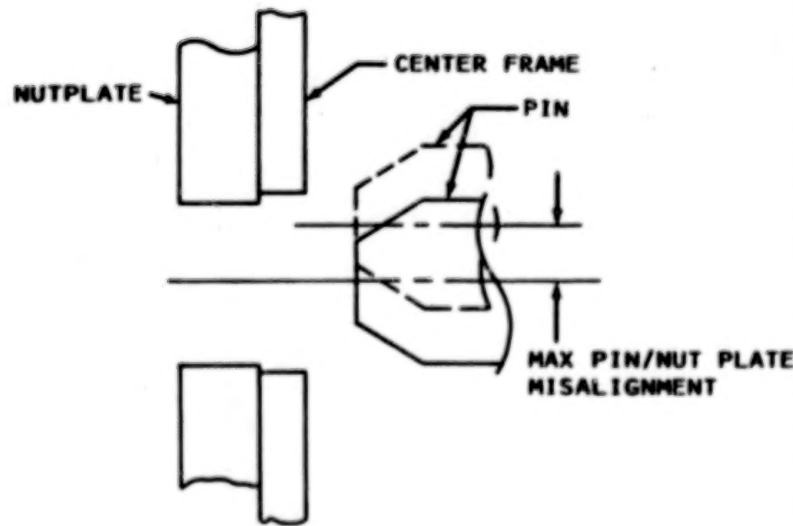


Figure 6b. Original Configuration.

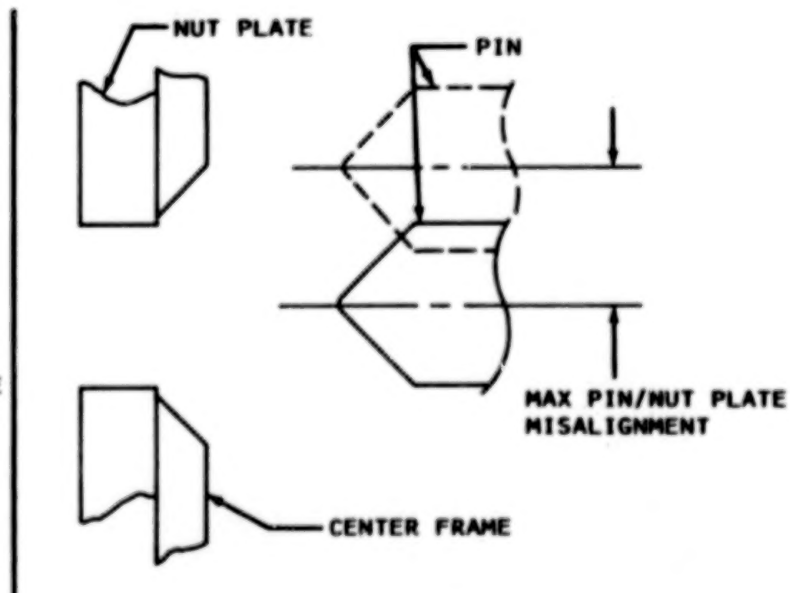


Figure 6c. Redesigned Configuration.

371

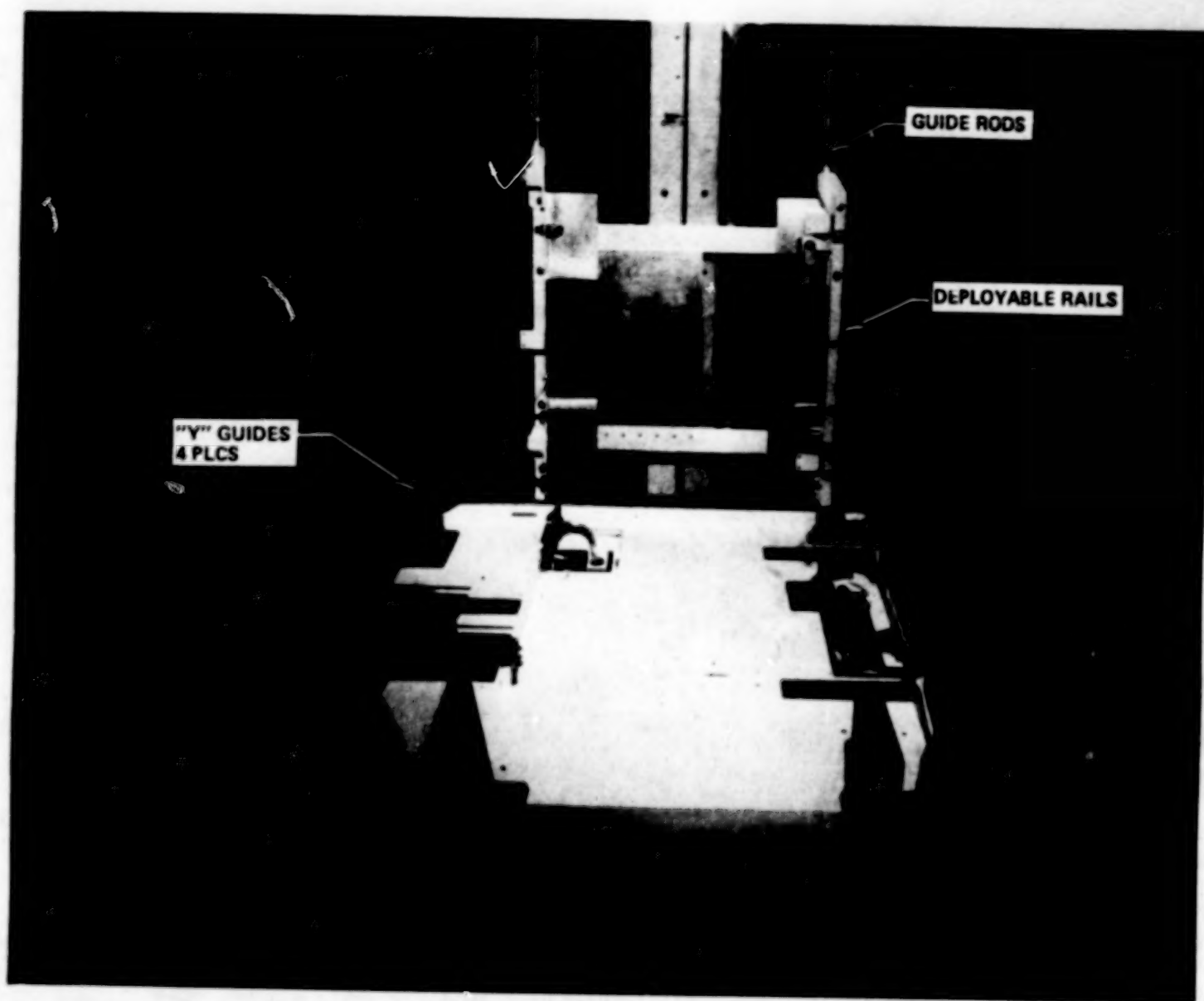


Figure 7. Reconfigured REM (Overall View).

371

BEST AVAILABLE COPY

372

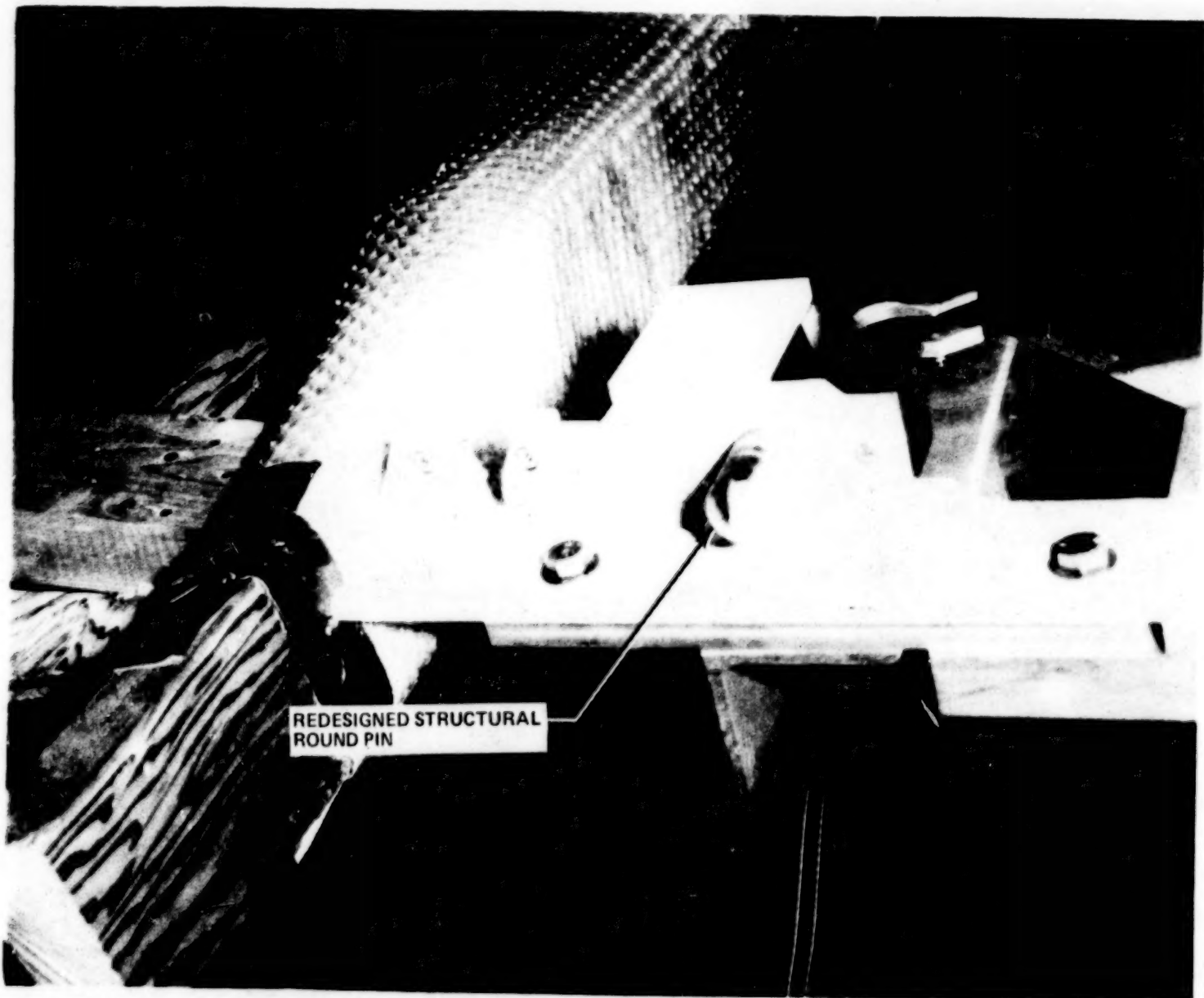
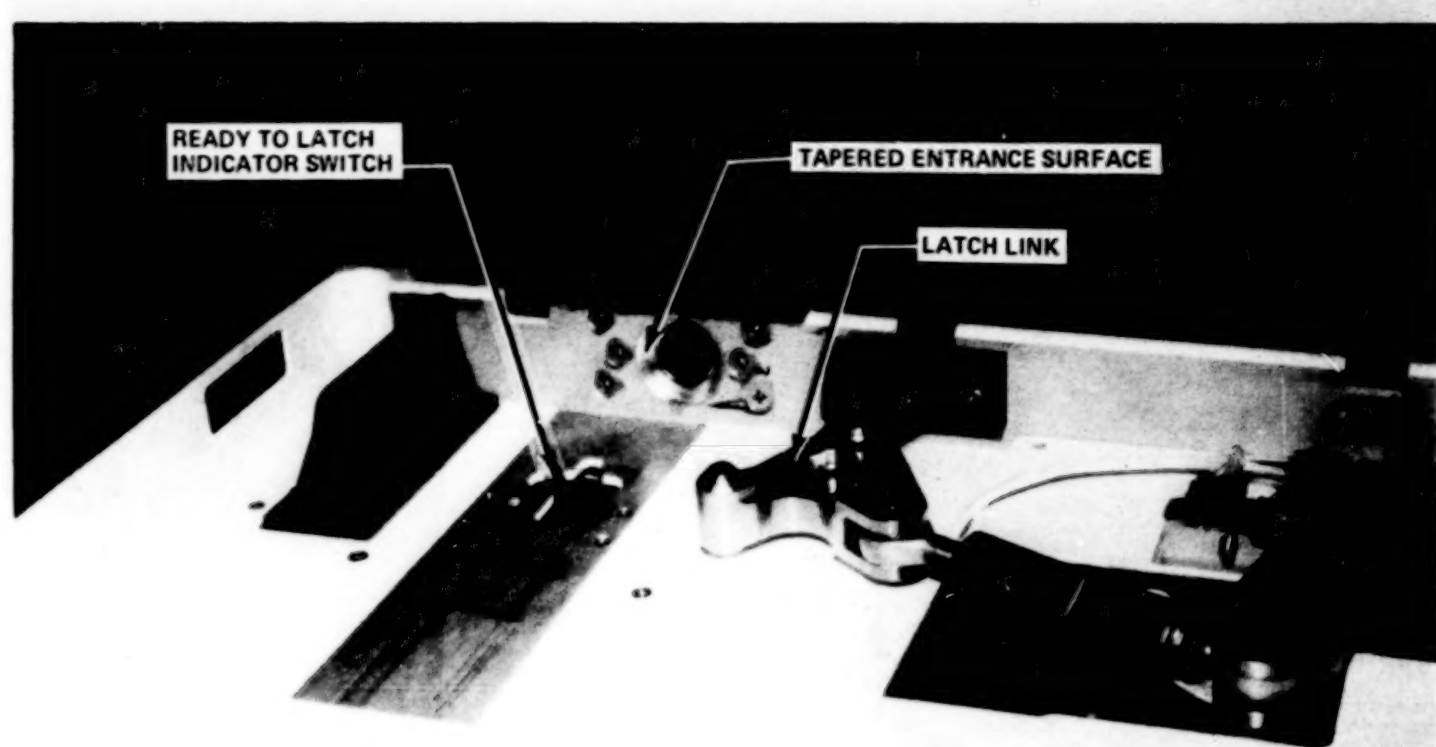


Figure 8a. Reconfigured REM (Round Pin).

372

BEST AVAILABLE COPY



373

Figure 8b. Reconfigured REM (Center Frame).

Blank Page

PAYLOAD RETENTION FITTINGS FOR SPACE SHUTTLE PAYLOAD GROUND HANDLING MECHANISM

By Vincent Cassisi*

ABSTRACT

New ground fittings for Space Shuttle payload handling were designed, built, and tested by Government and contractor personnel at the NASA John F. Kennedy Space Center (KSC), Florida, from May 1981 through November 1982. Design evolution of the Space Shuttle Orbiter payload retention fittings, which contained a load-sensitive split bushing in a pillow-block housing, created an incompatibility between the interfacing ground and airborne equipment. New fittings were designed and successfully used beginning with the fifth Space Shuttle flight, STS-5. An active hydraulic spring system containing a gas accumulator in the hydraulic system provided the load relief required to protect the Orbiter bushing from damage.

INTRODUCTION

The NASA KSC Design Engineering Directorate, in conjunction with the Planning Research Corporation, began design of new payload retention fittings in May 1981. Several other contractors and NASA Centers, including Rockwell International Corporation, The Aerospace Corporation, Martin Marietta Corporation, and Lyndon B. Johnson Space Center, also contributed through participation in design reviews. The new fittings were designed and tested, and production units were installed and successfully used for payload installation on STS-5 on November 11, 1982.

The Space Transportation System (figure 1) consists of two solid rocket boosters with an external fuel tank supported between them and an Orbiter cantilevered from the side of the external tank. Thus, the solid rockets support the entire Space Shuttle vehicle. At the launch pad, this entire assembly rests on the mobile launcher platform. The rotating service structure (RSS) can be moved so that the payload changeout room (PCR) encloses, but does not hold, the Orbiter to allow installation of payloads at the launch pad.

Payloads are held by the Orbiter at the longeron beam and keel points using standard payload trunnions. The longeron trunnions are 8.26 cm (3.25 in) in diameter and approximately 22.23 cm (8.75 in) long, and the keel trunnion is 7.62 cm (3 in) in diameter and approximately 29.21 cm (11.5 in) long. All have a chrome plating polished to 8 root-mean-square.

On the longeron beam of the Orbiter, there is a primary trunnion restraint that reacts the loads in the X and Z directions but allows movement in the Y direction. The longeron beam also has a secondary restraint that reacts the trunnion loads in the Z direction but allows free movement in the X and Y

*Vincent Cassisi, NASA KSC, Florida

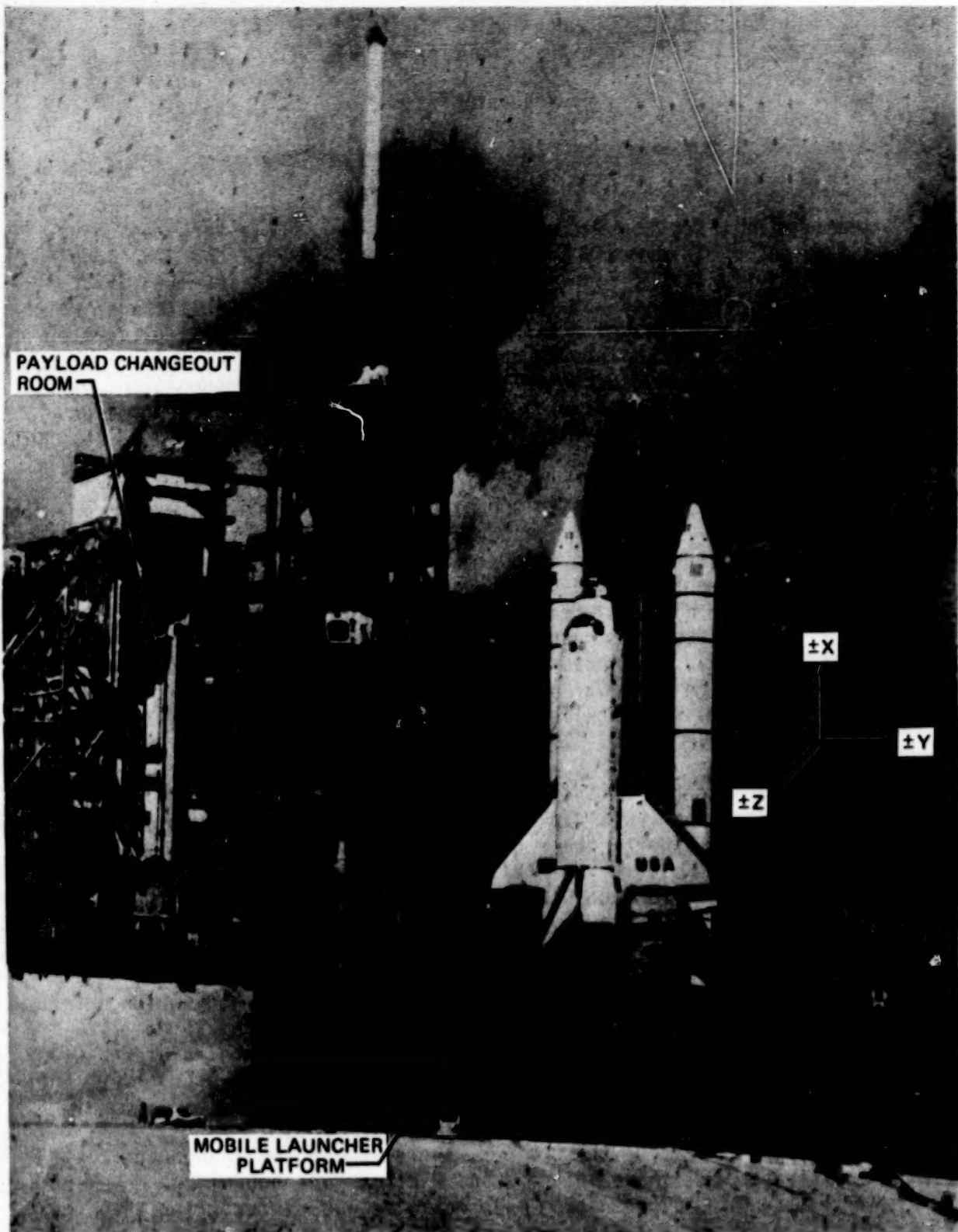


Figure 1. View of Launch Pad

directions. The keel restraint reacts trunnion loads in the Y direction but allows free movement in the X and Z directions.

The primary Orbiter fitting is firmly attached to the longeron beam, while the secondary fitting is allowed to slide in the X direction only. The trunnion interface with the Orbiter longeron fittings is a split spherical bearing to allow slight angular misalignment of the trunnion due to deflection, etc. This split bearing is prevented from rotating out of its housing by a small pin that will shear with a 13,344-N (3,000-lbf) load. The bore surface of the bearing has a Teflon coating to reduce friction from sliding motion and to protect the polished trunnion, which has a diametrical clearance of 0.003 to 0.010 cm (0.001 to 0.004 in).

The Orbiter keel fitting is attached to the bottom of the Orbiter payload bay. When open, it presents about a 22.86-cm (9-in) diameter hole. Closing draws two V-shaped halves together linearly in the X direction until at the closed position only a 7.62-cm (3-in) hole remains. The clearance is also 0.003 to 0.010 cm (0.001 to 0.004 in). A damage load limit is in effect to prevent Brinelling the trunnion and receptacle during centering. Finally, the payload keel has to be mated with the Orbiter fitting without the operator's being able to see either one, since there is no means of access or remote sensing.

Located in the PCR is the payload ground handling mechanism (PGHM) (figure 2), which is used to install and remove payloads from the Orbiter. It consists of a bridge, a vertical stem section hanging from the bridge, and adjustment devices attached to the front of the stem. Various mechanisms provide gross X and Z direction adjustments. Two payload fitting support beams on the front provide attach points for payload support fittings that are the support points for the payload trunnions before and during the transfer to the Orbiter fittings. The old fittings were rigid and not adjustable once the trunnions were placed on them.

The Space Shuttle vehicle is on the mobile launcher platform (an entirely separate structure from the RSS containing the PCR/PGHM with the payload) at the time of payload insertion or removal. With any winds, the two structures oscillate at different frequencies: the Orbiter at 0.56 Hz and the RSS at approximately 3 Hz. At the elevation of the payloads in the PCR, the relative motion at 180.04-m/s (35-kn) winds amounts to approximately ± 0.318 cm (± 0.125 in) in the X direction and 0.635 cm (0.250 in) in the Z direction. This motion far exceeds the 0.003- to 0.010-cm (0.001- to 0.004-in) clearances available. This clearly indicated the need for a completely different ground fitting.

DESIGN DETAILS

The decision to create a new generation of ground fittings to prevent damage to the Orbiter and trunnions carried an additional list of restraints and requirements that had to be met. The new fittings had to be capable of being attached as close as 70 cm (27.56 in) apart vertically anywhere along the 16.154-m (53-ft) long support beams in 10-cm (3.94-in) increments. The

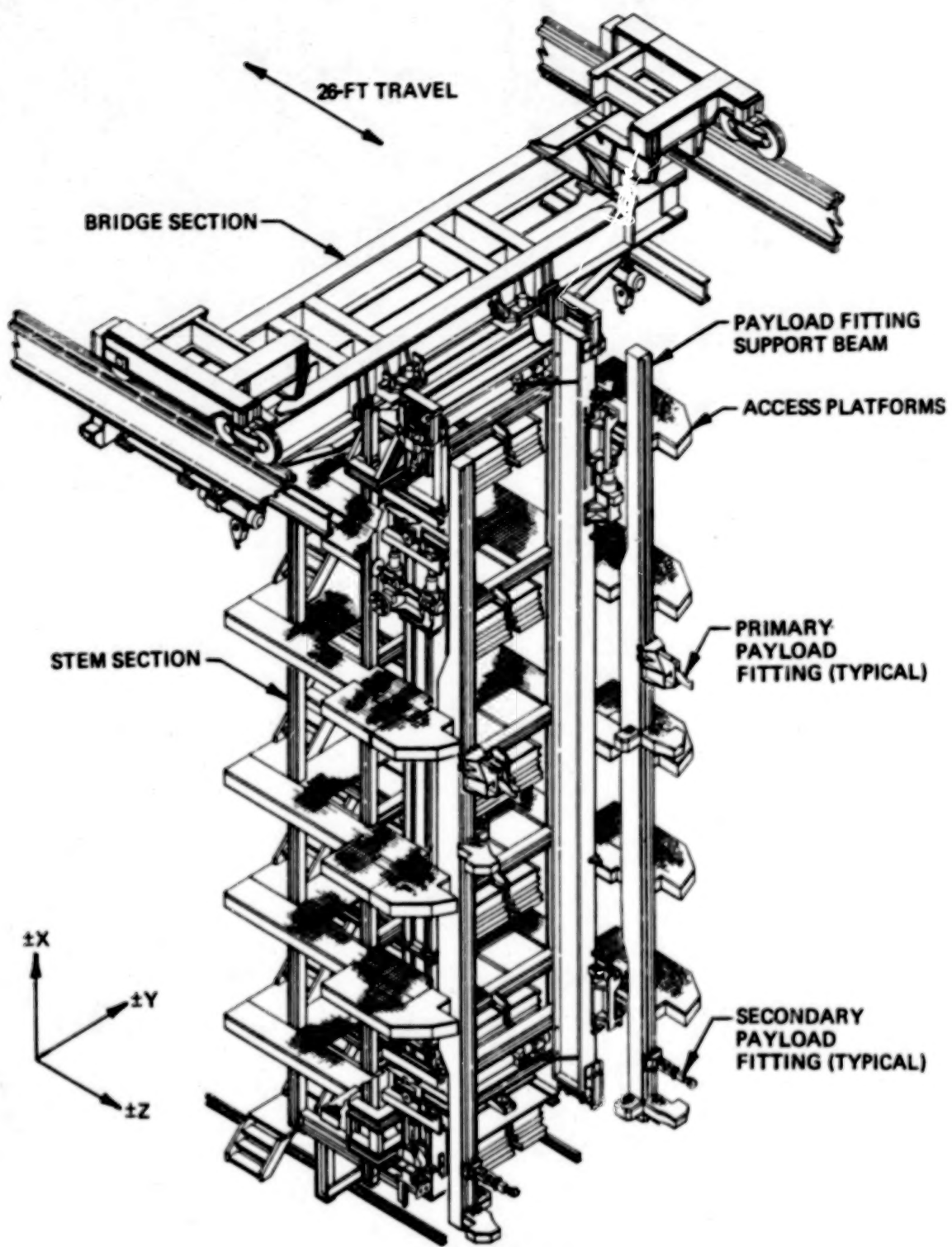


Figure 2. Payload Ground Handling Mechanism Assembled

maximum static load requirement per primary fitting was 173,472 N (39,000 lbf) in the X direction concurrent with $\pm 71,168$ N ($\pm 16,000$ lbf) in the Z direction. The secondary position only had the $\pm 71,168$ -N ($\pm 16,000$ -lbf) requirement in the Z direction.

The new fittings had to preclude damage to the polished finish of the trunnion. Such damage would change the coefficient of friction and cause higher Y-Y loads during flight.

Since we are dealing with class 100,000 clean rooms, the fittings could not cause contamination. Since some payloads also contained solid rocket propellant and liquid oxidizers, the fittings had to meet restrictive hazardous-area requirements.

Design safety margins for strength had to be 3 to 1 on yield. Further restrictions decreed no possible attachment to the Orbiter in any manner except the insertion of the trunnion. Clearances had to be maintained between the ground equipment and Orbiter equipment including the robot arm (remote manipulator system), hinges, cables, etc. on the Orbiter.

It was also desired to have the fittings designed for use on either side of the payload (not left or right hand only). The load exerted on the trunnion had to be known in addition to the trunnion position and amount of movement. Motion had to be linear, allowing fine adjustment in any direction without any unintentional movement in the other two axes. The new fittings were also required to be compatible with the remaining existing PGHM. The new 100.33-cm (39.5-in) cantilever from the face of the payload fitting support beam was greater than for the old fittings [was 45.72 cm (18 in)] but had to be kept reasonable to minimize the higher moments and the reinforcing required. Finally, the new design had to be completed; the prototype unit had to be built and tested; and the 20 production fittings had to be fabricated, tested, and delivered to meet the launch schedule while staying within the budget.

The ground fittings were separated into two designs according to function (figures 3 through 6): a primary fitting that had to support a 173,472-N (39,000-lbf) vertical load combined with a $\pm 71,168$ -N ($\pm 16,000$ -lbf) horizontal load, and a secondary fitting that had to support a $\pm 71,168$ -N ($\pm 16,000$ -lbf) horizontal load. The primary fitting required precisely controlled linear motion capability in all three perpendicular axes for alignment under load. A cantilevered horizontal trunnion support beam was supported on rollers and adjusted horizontally against the load with a double-acting hydraulic cylinder. This system was enclosed in a housing that was allowed to move only vertically by a second single-acting hydraulic cylinder. This housing was located within another structure that contained both the lateral movement mechanism and the means of attachment at various vertical locations as needed. The secondary fitting contained a horizontally positioned double-acting hydraulic cylinder that held and precisely moved the payload in the Z (in-out) direction but allowed free movement vertically and laterally through use of universal and wrist joints. Limiting loads to the sensitive Orbiter elements was achieved by use of a gas accumulator in the hydraulic system (figure 7).

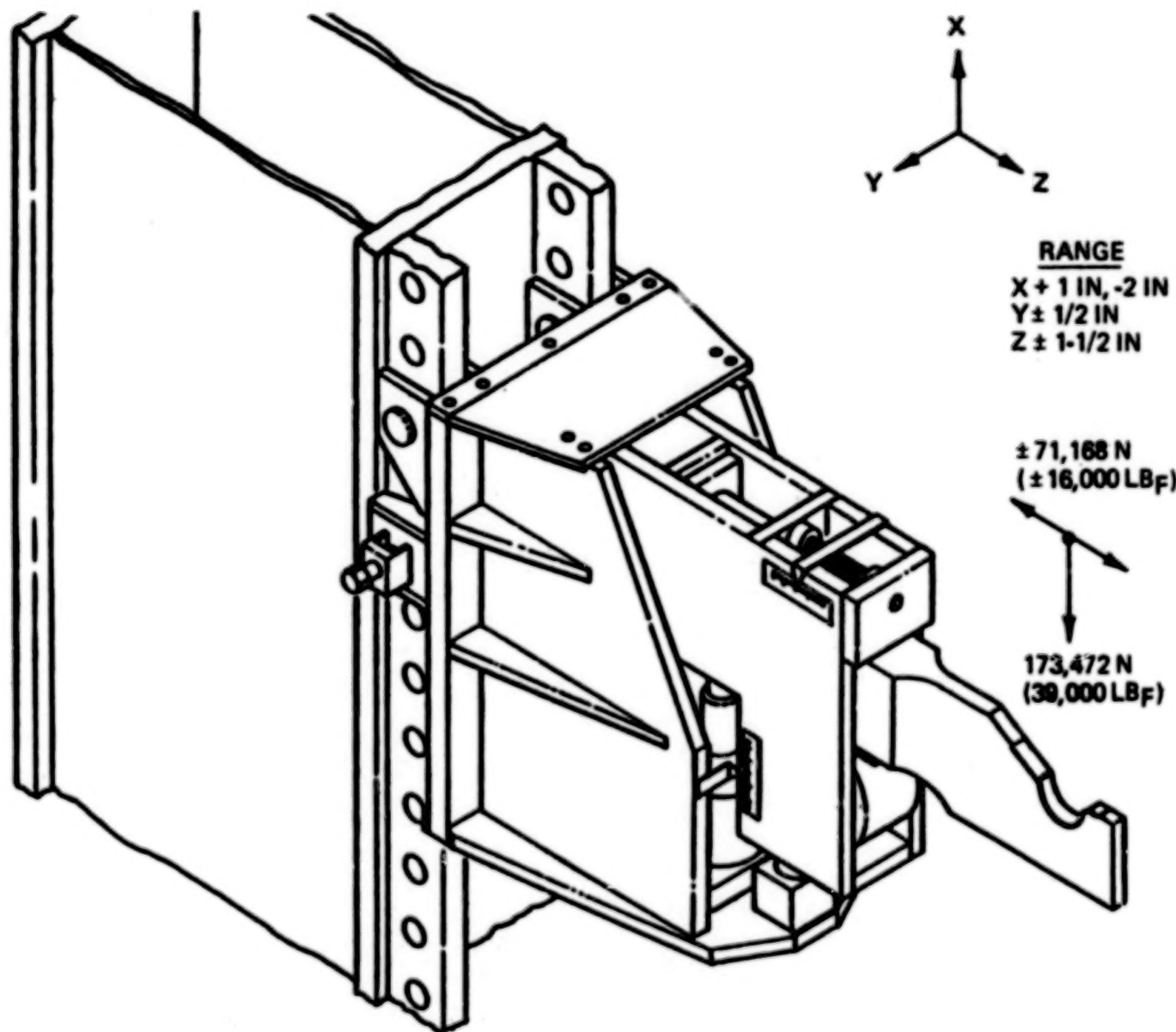


Figure 3. Primary Payload Support Fitting Mounted to Support Beam

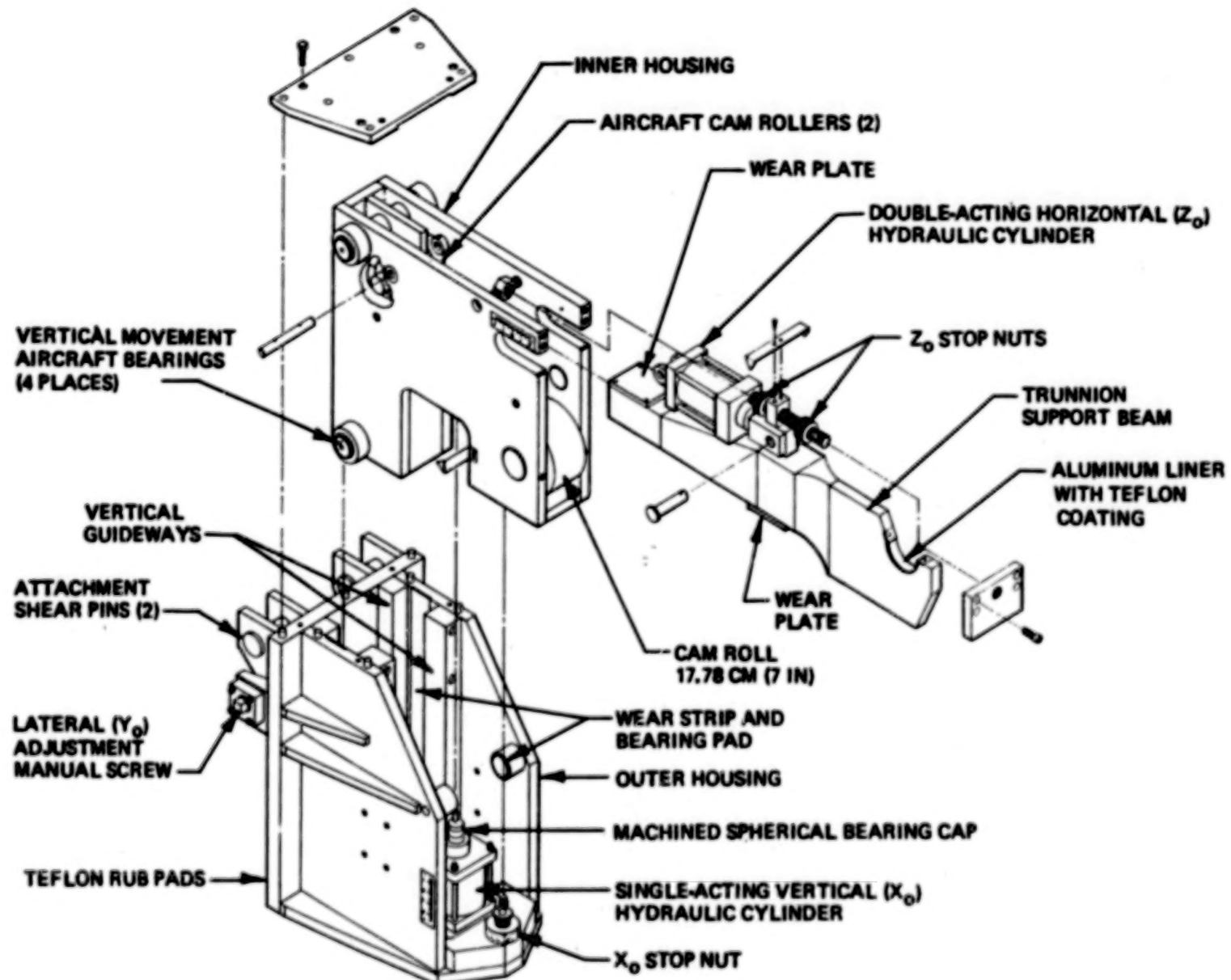


Figure 4. Primary Payload Support Fitting – Exploded View

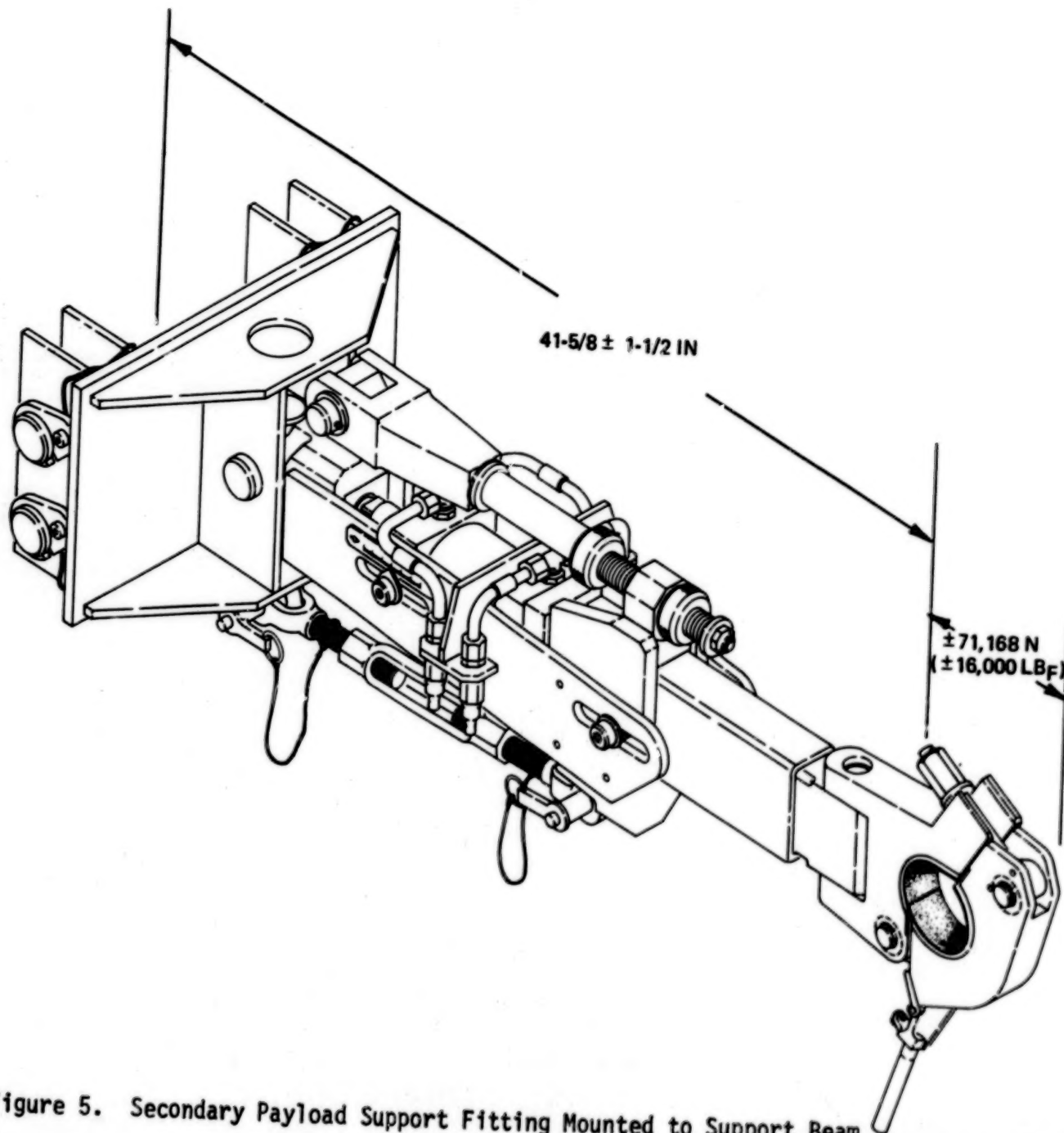


Figure 5. Secondary Payload Support Fitting Mounted to Support Beam

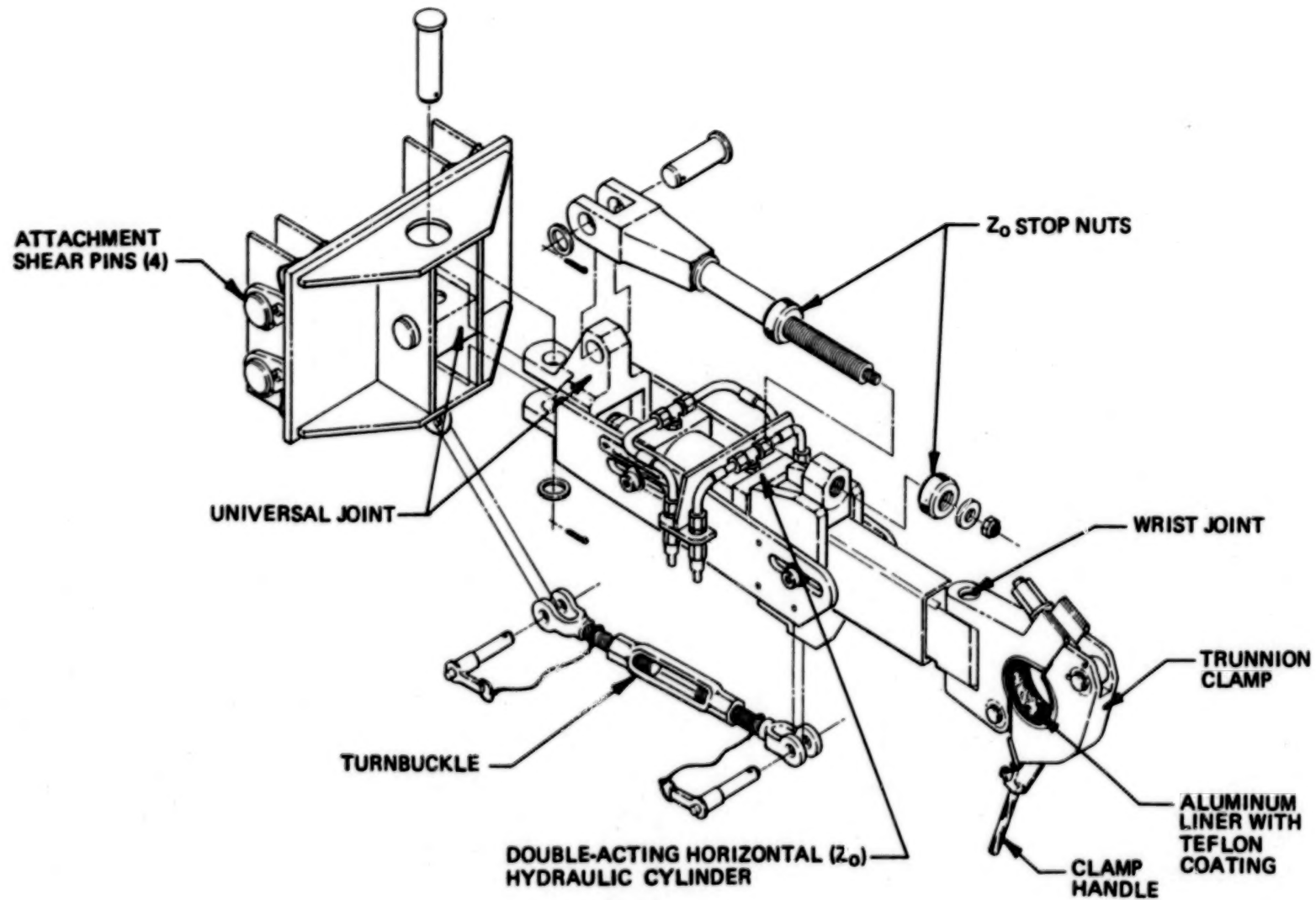


Figure 6. Secondary Payload Support Fitting Exploded View

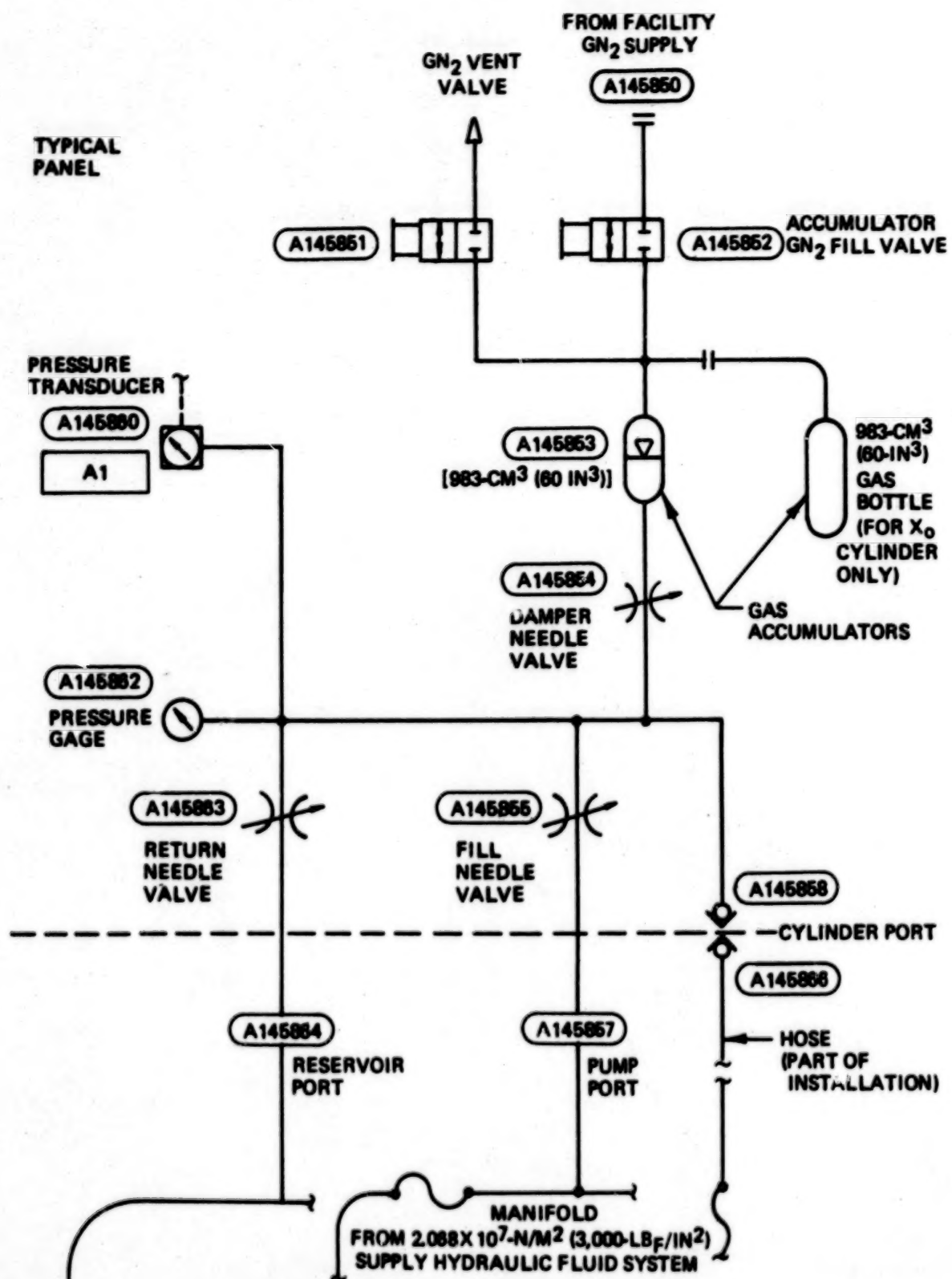


Figure 7. Typical Hydraulic Control Panel (Duplicated for Each Direction of Motion of Each Cylinder)

The cylinders could exert the required holding forces and needle valve positioning but still be soft and yielding to limit these loads during Orbiter motions and/or mismatch during installation.

The keel installation required a horizontal movement allowance combined with a load limitation. This was accomplished by allowing the closing lateral load on the payload keel (from the Orbiter keel fitting) to deflect the horizontal cylinders. Once the keel was locked, the payload was realigned laterally with the primary fitting lateral adjustment mechanism.

The primary requirements that guided the design were that the fitting be able to move linearly in the X, Y, and Z directions and that the load be transferred to the Orbiter without damaging the spherical bushing shear pins. A hydraulic system was designed that would not only provide the force to support and move the load but, by using a gas accumulator in the system, would also provide a load-relief spring to limit the interface loads and allow self-alignment during installation. This created a soft hydraulic system (rather than a hard, rigid system) that could limit the interface loads and move with the Orbiter motion. Figure 7 shows a schematic of the hydraulic system for moving one hydraulic cylinder in one direction. The accumulator gaseous nitrogen (GN_2) fill valve is used to precharge the gas accumulators to a value that depends on the spring constant required. To assume the load, the fill needle valve is opened, allowing liquid from the $2.068 \times 10^7 \text{-N/m}^2$ ($3,000\text{-lbf/in}^2$) supply system to enter both the accumulator and cylinder. The pressure increases, compressing the gas and building up force on the face of the cylinder piston until the pressure times the piston area is sufficient to raise the load. At this point, the pressure of the compressed gas is the same as the pressure on the face of the piston. Any additional liquid introduced into the system will only move the piston at constant pressure (theoretically). Any increase or decrease of load on the piston rod will unbalance the force across the piston face. As the piston moves to balance the force, it either compresses or expands the gas slightly until the new pressure times the piston area equals the new force. The change of force divided by the amount of movement it causes is the spring constant. High-point bleeds are used to bleed air out for good spring-rate calibration. Varying the damper needle valve will vary the dynamic response of the system by varying the flow rate between the accumulator and the cylinder. Opening the return needle valve will lower the load by allowing the pressurized liquid to escape to the central reservoir. A pressure gage reads out in lbf/in^2 gage, and the transducer feeds data to a digital readout that displays values in lbf . This system is repeated for each of the three powered directions on a primary fitting and each of the two powered directions on a secondary fitting. The central hydraulic system consists of redundant pumps, the central reservoir, and control panel. Haskell air-driven pumps were selected due to their successful industrial record of running on plain deionized water at high pressures. Here, they are used with 5% lubricant in the water and at lower pressure, which should yield high reliability. (Water is used because it is not likely to damage a payload if spilled.)

The primary fitting holds the polished payload primary trunnion on a liner made of 7076-T6 aluminum coated with Lear Siegler Fabroid G2 Teflon bearing material to protect the trunnion from damage by steel parts. The Teflon was added after tests showed galling of the aluminum and transfer of aluminum to the trunnion surface.

The trunnion support beam is 2.54 cm (1 in) wide to fit the area on the trunnion allocated to ground handling. Depth under the trunnion was minimized to avoid interference with Orbiter attachments 19.89 cm (7.83 in) below the trunnion, and this required heat treatment of AISI 4340 steel to meet the 3-to-1 margin on yield. The beam is cantilevered for clearance to the Orbiter fittings and is supported by a 17.78-cm (7-in) cam roll bearing below and two precision aircraft cam rollers at the top rear to support the X load. To meet the overall height limitation, the beam was tapered at the rear.

All rollers bear on wear plates that are shimmed to provide true linear Z motion. The Z load is taken by a double-acting hydraulic cylinder attached to the protrusion on the trunnion support beam over the 17.78-cm (7-in) roller. Pinned ends on the cylinder prevent moments on the cylinder rod that would side load the seals. The trunnion support beam, supporting rollers, and hydraulic cylinder are all structurally supported by the inner housing. This inner housing, which serves to provide the linear X direction motion, is supported on the single- (upward) acting hydraulic cylinder that has a machined spherical bearing cap on the rod end to reduce side loads on the seals. Four more aircraft bearings, two per side, are located to travel in the vertical guideways attached to an outer housing. The cylinder was located as close to the payload as possible in order to reduce the moment carried by the X rollers, which were spaced as far apart as possible to minimize their size and reduce overall height.

Lateral stability is provided by Teflon-coated wear strips and adjustable bearing pads that are located between the trunnion support beam and inner housing and between the inner and outer housings. The outer housing provides the overall enclosure and the means of attachment to the support beam at the desired location by using shear pins through both clevis ears and support beams on each side of the fitting. These pins, high strength for minimum size, are finished to 16 root-mean-square to provide a sliding surface with the Garlock DU Teflon-coated insert bearing sleeves that line the attachment holes on the fitting support beam.

The width between the clevis ears is 2.54 cm (1 in) wider than the lug on the beam, which allows the fitting to be moved in the lateral (Y-Y) direction ± 1.27 cm (± 0.5 in) by sliding the pin through the bearing sleeves. This is accomplished by using a coarse-thread manual screw that is located directly below the shear pins. This screw can be mounted on either side of the fitting, depending on accessibility, and will push or pull the fitting laterally on the sleeves. One screw is located on each primary trunnion fitting. Thus, to move a payload laterally, the screws to both fittings are operated simultaneously. A 0.64-cm (0.25-in) in-and-out free-sliding travel is designed into each screw. This prevents a screw on one side from binding up the screw on the other if they are erroneously turned at a different rate or in

different directions. The lower rear portion of the outer housing also has Teflon rub pads that bear against the front surface of the support beam lugs.

The X adjustment provides a range of movement of up 2.54 cm (1 in) and down 5.08 cm (2 in) from the null position. This allows the fitting to be lowered 5.08 cm (2 in) to clear the half diameter [4.13 cm (1.625 in)] of the trunnion for withdrawal.

In order to protect the payload and the Orbiter from colliding with each other in the event of a hydraulic failure, two mechanical stops were devised with manual follow nuts to minimize the free-fall distance. These nuts are positioned approximately 0.95 cm (0.375 in) from engaging to allow float with the Orbiter relative motion but to catch if failure occurs. They also are snugged up to support the loads whenever hydraulics are secured and pressure brought down during nonoperating periods.

Since the secondary fitting had to support $\pm 71,168$ N ($\pm 16,000$ lb_f) in the Z direction but offers no resistance in the X and Y directions, the design evolved into a stiff arm with a universal joint and a wrist. A clamp was devised that would firmly grab the trunnion and was lined with Teflon on aluminum for the same reason as was the primary fitting. A vertical-axis wrist was used to connect the clamp to the body of the fitting with a universal joint allowing unrestricted movement in the X and Y directions. The main body of the fitting consists of the double-acting hydraulic cylinders and the surrounding structure. The cylinder is mounted with the rod end toward the universal joint and the cylinder being pushed/pulled with respect to the rod. This surrounding structure is designed to eliminate bending due to frictional forces acting on the clamped trunnion as the trunnion moves vertically. (Bending the rod and cylinder would cause seal problems.) A turnbuckle supports the fitting prior to attachment to the payload. The secondary fitting also has the same gas accumulators for compliance to loads as does the primary fitting and has the mechanical stop screw with adjustable stop nuts.

CONCLUSION

A primary and a secondary fitting were built for test purposes and showed that the fittings were fully capable of preventing damage to the Orbiter and trunnion. Although early testing caused galling of the aluminum, the Teflon coating added later did provide full protection. The measured friction in the system from rollers, rub guides, seals in the hydraulic system, etc. proved to be somewhat greater than expected and varied with the magnitude of load. This extra damping allowed the full-open use of the damper needle valve. Physically, the fittings met all the size, cleanliness, compatibility, and strength requirements (figures 8 through 11). Ten primary and 10 secondary production fittings were fabricated, with 16 additional pairs destined for KSC Launch Complex 39 Pad B and Vandenberg Air Force Base, California.

STS-5 payloads were installed by the new fittings without problems. Final cost was within the original budget estimate.



Figure 8. Primary Fitting During Development Tests

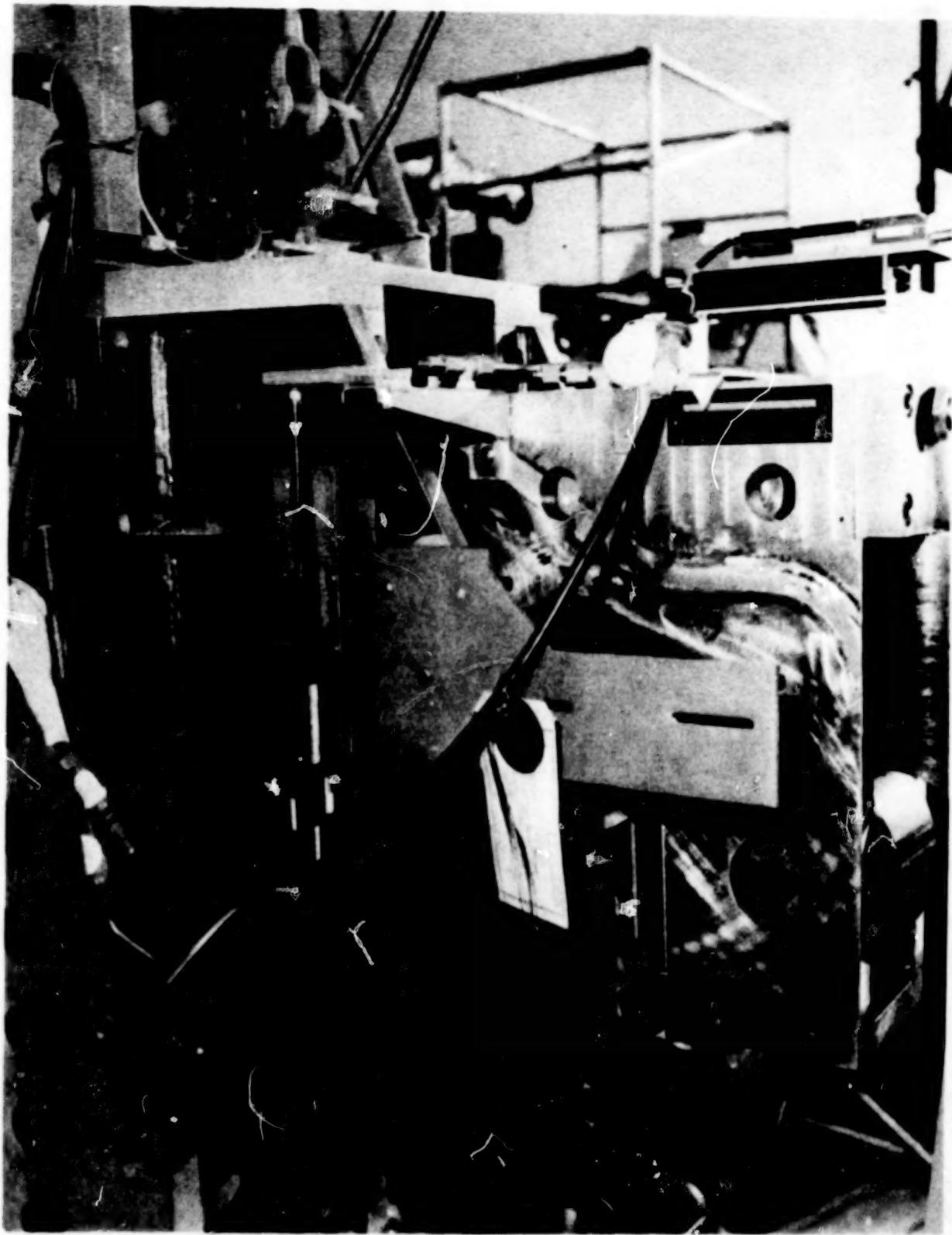


Figure 9. Primary Fitting

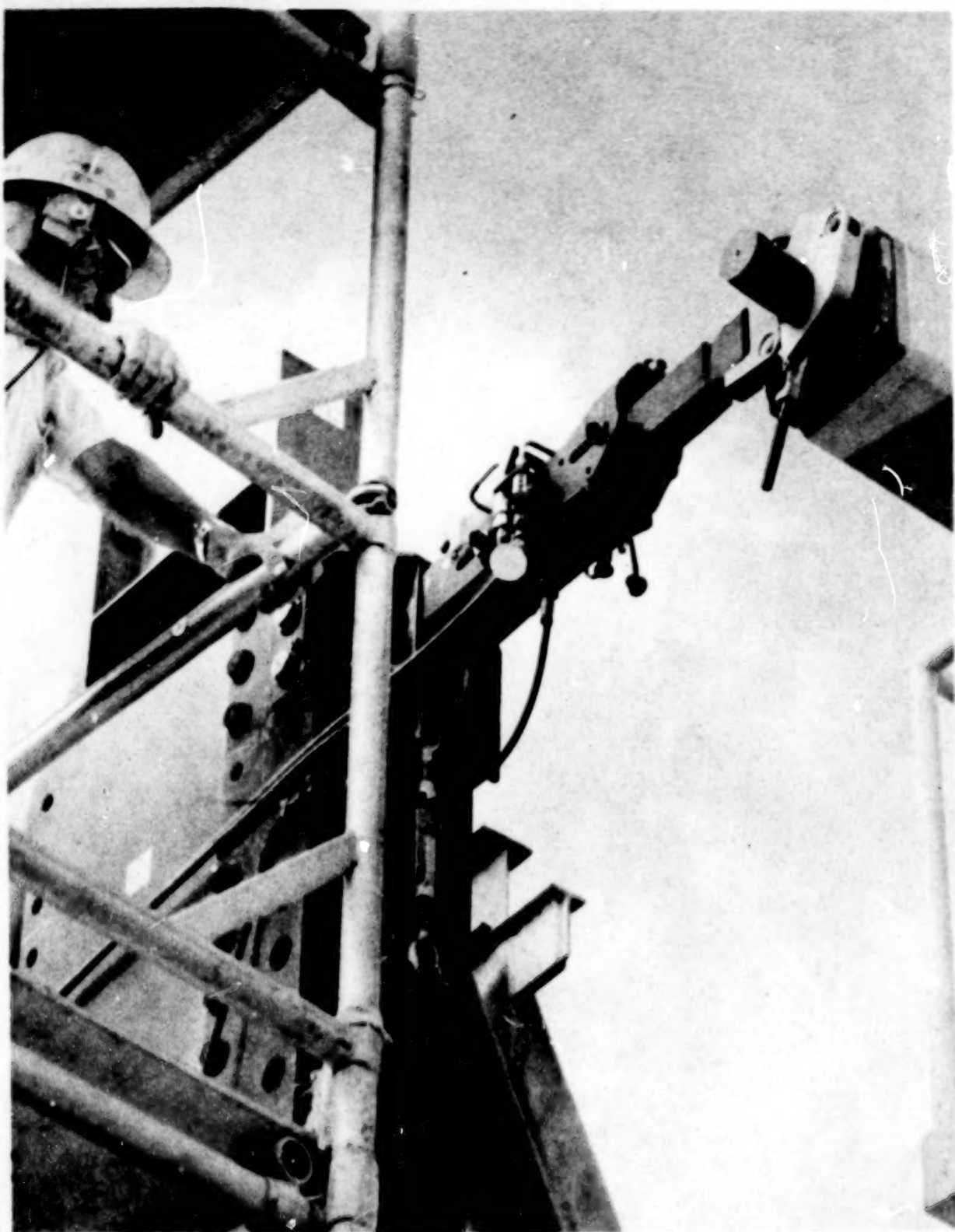


Figure 10. Secondary Fitting During Development Tests

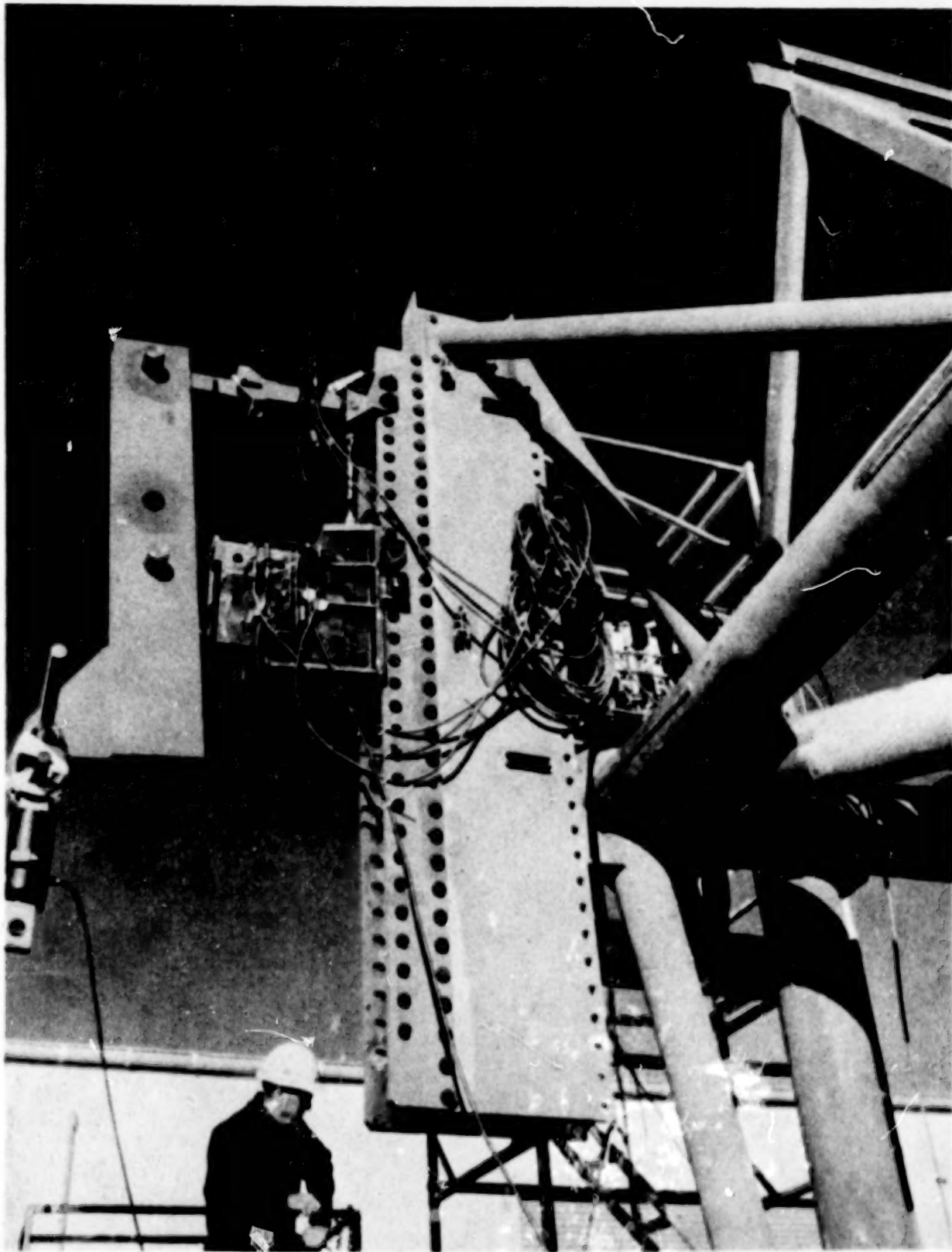


Figure 11. Secondary and Primary Fittings on Test Stand

1. Report No. NASA CP-2273	2. Government Accession No.	3. Recipient's Catalog No.	
4. Title and Subtitle 17th AEROSPACE MECHANISMS SYMPOSIUM		5. Report Date May 1983	
		6. Performing Organization Code	
7. Author(s)		8. Performing Organization Report No.	
9. Performing Organization Name and Address Jet Propulsion Laboratory Pasadena, CA 91109		10. Work Unit No.	
		11. Contract or Grant No.	
12. Sponsoring Agency Name and Address National Aeronautics and Space Administration Washington, DC 20546 and California Institute of Technology Pasadena, CA 91109 and Lockheed Missiles & Space Company, Inc. Sunnyvale, CA 94088		13. Type of Report and Period Covered Conference Publication	
		14. Sponsoring Agency Code	
15. Supplementary Notes			
16. Abstract The proceedings of the 17th Aerospace Mechanisms Symposium held at the Jet Propulsion Laboratory in Pasadena, California, on May 5-6, 1983, are reported in this NASA Conference Publication. Technological areas covered include space lubrication, aerodynamic devices, spacecraft/Shuttle latches, deployment, positioning, and pointing. Devices for spacecraft tether, magnetic bearing suspension, explosive welding, and a deployable/retractable mast are also described.			
17. Key Words (Suggested by Author(s)) Space lubrication Latch/relatch Tether satellite Magnetic bearings Deployment devices Electrodynamic control Actuators Umbilical system Nutation damper Thermal distortion Retractable mast Multipassage valve Explosive welding		18. Distribution Statement Unclassified - Unlimited Subject Category 39	
19. Security Classif. (of this report) Unclassified	20. Security Classif. (of this page) Unclassified	21. No. of Pages 404	22. Price A17

For sale by the National Technical Information Service, Springfield, Virginia 22161

NASA-Langley, 1983